Foam as a soil conditioner in tunnelling: physical and mechanical properties of conditioned sands

by
MIGUEL ÁNGEL PEÑA DUARTE

A thesis submitted for the degree of
Doctor of Philosophy at the University of Oxford

St. Catherine's College Trinity Term, 2007

Abstract

Foam as a soil conditioner in tunnelling: physical and mechanical properties of conditioned sands

A thesis submitted for the degree of Doctor of Philosophy at the University of Oxford

Miguel Ángel Peña Duarte

St. Catherine's College, Trinity Term 2007.

Earth pressure balance (EPB) tunnelling machines are commonly used for the construction of tunnels in soft soils. These machines use the excavated soil in a pressurised head chamber to apply a support pressure to the tunnel face during excavation. How well an unstable face is supported in an EPB machine depends on effectively transferring a constant pressure from the support medium to the surface of the face. If the support pressure is not constant, but instead changes, the varying pressure inevitably leads to collapse of the face or heave on the surface ground. A machine may be designed to work in "Ideal ground" conditions. However, natural soils rarely have these properties, and conditioning of the soil is usually necessary to change its properties to suit the machine. Effective soil conditioning significantly improves the machine performance and control of the soil flow through the screw conveyor. However, for soil conditioning as commonly used in practice, the effects of different conditioning treatments on soil properties and the machine performance are not clearly understood, and problems with EPB machine operations related to the soil properties are often encountered.

This thesis presents experimental investigations of direct shear box tests on conditioned sands, compressibility tests on conditioned sands and a model EPB screw conveyor operating with sandy soils. Index tests were performed to investigate effects of foam and polymer conditioning treatments on the plastic fluidity of different Leighton Buzzard (L.B.) sands and Thanet sand. The index tests allowed assessment of conditioning treatments for sandy soils, and optimum ranges of treatments for Leighton Buzzard sand and Thanet sand are suggested.

In the series of shear box tests, performed on conditioned Thanet sand and conditioned L.B. sands, one of the most important findings was that the pore water pressure controls the strength of the sand foam mixtures. An increase in foam injection ratio (FIR) might produce an increase of pore water pressure and a decrease of shear stress.

In the series of compressibility tests, performed on conditioned Thanet sand and conditioned L.B. fine sand, one of the most important findings was that increasing FIR does not increase maximum gas expelled. The FIR and the initial relative density of the specimen have to be related to the capability of the specimen to retain the gas and establish a coexistence between grains of soil, water and gas bubbles.

Finally, from the series of model (1:10 scale), screw conveyor tests, performed on conditioned Thanet sand, conditioned L.B. fine sand and conditioned Garside sand, it can be concluded that the Oxford screw conveyor model can be used as a trial machine to study the effects of different operating conditions on conditioned sand specimens similar to those used on site. This can allow choice of conditioning methods to improve the performance of an EPB machine at a given site.

Acknowledgments

No DPhil thesis is ever the product of one person's efforts, and certainly this one was no different. It would never have become reality without the help and suggestions of many supportive friends and colleagues.

My biggest thanks go to Professor Guy Houlsby who has been an extremely conscientious supervisor of my work. His guidance and thoughtful suggestions have been invaluable throughout the course of this study. His critical commentary on my work has played a major role in both the content and presentation of my discussion and arguments.

I am indebted to Mr. Robert Sawala for many helpful discussions on practical aspects of my research and for always trying to put into practice my ideas. I am also grateful to the Maintenance group of the Engineering Science Department who were always there to give me a hand with my research. I must thank the technicians of Store and Workshop of the Engineering Science Department.

I would also like to thank many people who encouraged and advised me throughout the course of this study, John Lyon, Arthur Moss, Dr. George Milligan, Andrew Merritt, Xavier Borghi, Rafaelle Vinai, Byron Byrne, Mahin Jung, aunty Moira, Tony Bernado, Maya´s mother, Maya, David Wahl, Maria Sanchez, Carolina Venegas, Carolina Jorquera and Daniela Peirano.

Thanks to Fernanda San Martin for the gift which made possible this final thesis and Luis Sebastian Caballero for all the administrative stuff that he did on my behalf.

I also extend my appreciation to the several sources which provided various kinds of financial support for me during my period reading for the degree of D.Phil.: EPSRC, the Pipe-Jacking Association, Craig from Mortons, the house of St. Gregory and St. Macrina and CORFO. I was able to write up the final draft of my thesis while worked for Elif Ibérica Environmental sl in Madrid as Technical Manager. I am obviously very much indebted to the Director of Elif Ibérica Environmental sl, Alex Blumenfeld, for his understanding and giving me time off work to complete my DPhil thesis.

I am grateful to the Chilean community in Oxford for the beautiful friendship and nice time we had together in Oxford. I am forever indebt to Ciara Rogerson, Victoria Brewer and Aisha Jung for the care with which they reviewed the original manuscript; and for conversations that clarified my thinking on this and other matters.

Fernanda, thank you very much indeed for being there and here during this part of my life.

Last, but not least, I thank my family: my parents, María del Pilar Duarte Salvo, and Cesar Hernan Peña Ramirez, for giving me life in the first place, for educating me, for unconditional support and encouragement to pursue my interests, even when the interests went beyond boundaries of language, field and geography. My sister, Yessie Peña, for listening to my complaints and frustrations, and for believing in me. My brother Rafael Peña and Ana María Peña, for being there.

My apologies if I have inadvertently omitted anyone to whom acknowledgement is due.

I hope this end result does not let down most of you family and friends who have supported me all along, as well as you interested readers who are patient enough to explore the workings of my occasionally contentious mind.

Contents

Chapter 1. Introduction

1.1. Mechanized tunnelling: earth pressure balance machines

The mechanized tunnelling industry has developed very rapidly in the last 20 years, leading to research on various parts of its process: machine type (Banbendererde,1991), face stability (Anagnostou and Kovári, 1996), tunnelling induced settlement (Marshall, 1998; Burd et al, 2000), concrete jacking pipes (Ripley, 1989, Norris, 1992; Augarde and Burd, 2001).

One area of research is the study of the mechanical properties of excavated soil mixed with conditioners during the tunnelling process.

Mechanized tunnelling processes, in unstable ground, usually offer a support behind the tunnel face to prevent the ground collapsing. In this process the use of earth pressure balance (EPB) machines is particularly important. EPB machines (see Figure 1.1), where the excavated soil is used as the support medium for face, have been in operation for the last two decades starting in Japan in the early eighties (Japan, 2006). A good understanding of the mechanical properties of soil, mixed with conditioners, leads to better control of the tunnelling operation using EPB machines. The most common conditioners used in the tunnelling process are foams, polymers and clays.

In EPB machines, the soil is removed from the head chamber by means of a screw conveyor that dissipates the pressure difference between the chamber and the tunnel. Figure 1.2 shows the main components of an EPB machine.

In order to achieve optimum performance with EPB machines, the excavated soil must form a suitable plastic mass of soft consistency and low friction that can readily be extruded from the head chamber through the screw conveyor. Natural ground is not always suitable for EPB machine application, so modifications of its properties in the cutter head, head chamber or screw conveyor may be necessary. Vinai (2006) reports (see Figure 1.3), some grain size distributions for successful tunnel excavation with EPB shields. Soil conditioning with polymers and foams has become a popular practice in EPB tunnelling, specifically in the screw conveyor, to enhance the properties of the soil and suit them to the machine.

Tunnelling performance has been extensively improved by the combined use of EPB machine technologies and conditioning. There are still unexplained processes that require more understanding to allow an efficient application of soil conditioning. Above all, the mechanism

governing the extrusion process of the conditioned soil, and the interaction between soils and conditioned agents needs to be understood.

1.2. Soil conditioning in mechanized tunnelling: EPB machine

Soil conditioning agents are now widely used in the mechanized tunnelling industry to achieve optimum performance in different parts of the tunnelling process. Some of the characteristics that have made soil conditioning agents a key feature in the mechanized tunnelling industry include:

- Improvement of excavation rates, reduction of wear and reduction of power requirements at the cutter head;
- Improvement of the flow characteristics of the excavated soil;
- Better pressure control in the chamber and screw conveyor of an EPB machine; and
- Lubrication of the advancing tunnel shield or lubrication of pipes in pipejacking.

The mechanized tunnelling industry uses a variety of soil conditioning agents at different points in the process. The efficacy of different soil conditioning agents has been shown in particular applications, most of it being site and application specific. Houlsby and Psomas (2001) pointed out that the soil conditioning agents' efficiency can also be related to the specific proprietary brands of material, which may be held as confidential by commercial parties.

Because the support medium on EPB machines is the excavated material itself, the use of soil conditioning to achieve an "ideal ground" condition has special relevance. "Ideal ground" conditions consist of soils with a relatively high content of fines, with a consistency to form a low permeability, soft plastic paste when excavated.

How well an unstable face is supported in an EPB machine depends on effectively transferring a constant pressure from the support medium to the surface of the face. If the support pressure is not constant, but instead oscillates, the varying pressure inevitably leads to collapse of the face or heave on the surface ground. For the EPB machine, the support pressure in the working chamber is generated by thrusting the tunnelling machine against the face with the shield jacks. The rotating cutting wheel scrapes off the ground that is pressed into the working chamber. At the same time, the equivalent amount of spoil is removed from the working chamber by the screw conveyor. The rotation speed of the screw conveyor regulates the volume extracted and thus the support pressure in the working chamber. For instance, when the rapid dissipation of pressure from the EPB chamber is needed, it is vital that the soil volume is rapidly extracted and if the natural ground does not have a soft plastic paste consistency, the control of the pressure dissipation, from the EPB chamber, would not be possible. This might stop the excavation work

and produce delays in the project, which will reflect in the contractor's cost of the tunnelling operation. This clearly demonstrates that "ideal ground" conditions directly affect the performance of EPB machines. However, natural soils rarely have "ideal" properties, and conditioning of the soil is usually necessary to change their properties to suit the machine.

There is no single treatment to successfully condition different types of soil. Furthermore, many factors influence the specification and performance of soil conditioning treatments. For instance, within the geotechnical factors that influence the treatments required for effective conditioning of the soil are the size particle distribution, strength, permeability and water content.

Materials such as water, foams, polymers and bentonite slurries are used as conditioning agents. Each agent has different properties producing varying effects on the properties of the different soils. Their effect on different soils depends on whether they are used separately or in combination, their concentration, their injection ratio and, in the case of foam, its expansion ratio value. As mentioned earlier, commercial products are available as soil conditioning agents, with different types of foams, polymers and bentonite, for use in different ground conditions.

To date, research into soil conditioning in tunnelling has not established a realistic correlation between the amount of conditioners, such as foams and polymers, and their performance with soils. Most studies have present general guidelines on conditioning treatments for different soils and the importance of adding certain types of polymers and foams to obtain more suitable properties. For instance, Merrit (2004) studied polymer and foam properties, carried out consolidation tests with conditioned clay, fall cone tests on conditioned soil and carried out screw conveyor tests with conditioning clay soils; Bezuijen and Schaminee (2000) modelled the drilling with and EPB shield using foam; Bezuijen et al (1999) tested additives for earth pressure balance shields; and Quebaud (1998) studied the conditioning properties of foam in two types of sand. Unfortunately, the findings from these studies are not always applied. This has resulted in practical tunnelling applications being based largely on trial and error.

The effect of conditioning treatment on the properties of different soils and EPB machine operations is only understood to a limited extent. In order to improve the fundamental understanding of soil conditioning further research is needed. This will improve its use, thus reducing the related problems encountered in mechanized tunnelling projects.

1.3. Scope and aims of the research

Although some research has been carried out in investigating the properties of sands conditioned with foam and the operation of an EPB screw conveyor with this material, the practical use of soil conditioner in tunnelling applications is still based largely on trial and error.

This research has been sponsored by EPSRC and the Pipe Jacking Association (PJA). It was performed as part of a project in collaboration with the University of Cambridge, investigating soil conditioning agents in pipe jacking and mechanized tunnelling. The scope of the project includes laboratory investigation of soil conditioning for sands and clays, studies of model EPB screw conveyors operating with sand and clays, and field monitoring of EPB machines operating in a range of soils to investigate the effects of soil conditioning on the machine performance. Observation of the performance of EPB machines operating on the Channel Tunnel Rail Link (CTRL) project in London was carried out for the field monitoring phase of the research.

This thesis presents laboratory investigation of soil conditioning for sands, and of a model EPB machine screw conveyor operating with sandy soils. The effect of soil conditioning agents on the properties of sandy soils and the behaviour of conditioned sands, with different granulometry, under shear and compression is not well understood. Equally, the effect of varying operating conditions and soil properties on an EPB screw conveyor's performance is not completely understood. The research presented in this thesis was carried out to investigate these topics in the laboratory, in order to advance the fundamental understanding and practical application of soil conditioning for mechanized tunnelling machines.

The specific aims of this research presented in this thesis are summarized as follows:

- To develop of simple test methods suitable for assessing conditioning treatments for sands;
- To investigate properties of soil conditioning foams;
- To investigate the effects of foam and polymer conditioning treatments on sands;
- To identify an optimum conditioning treatment for sands with different granulometry;
- To study the behaviour of conditioned sands with foam and polymer in shear box tests, and conditioned sands with foam in consolidation and permeability tests;
- To study the influence of parameters, such as: foam expansion ratio, foam injection ratio, polymer injection ratio and diameter of soil particles in the results from shear box, consolidation and permeability tests; and
- To investigate the operation of the model screw conveyor operating with sandy soils.

1.4. Thesis outline

Chapter 1 introduces mechanized tunnelling and the role of soil conditioning in its operation. The scope and aims of the research presented in this thesis are summarised.

Chapter 2 is a review of the literature relevant to this research. The review covers soil conditioning agents, their effect on soil properties and EPB tunnelling operations, laboratory testing of conditioned soils and some case studies of soil conditioning in practice.

Chapter 3 reports testing performed to investigate properties of foams and conditioned sand. The observed effects of various foam and polymer conditioning treatments on the plastic fluidity of different Leighton Buzzard (L.B.) sands and Thanet sand are discussed, and optimum conditioning treatments for these soils are suggested.

Chapter 4 describes the modified shear box apparatus commissioned for this research. Design details of the apparatus components and instrumentation are given. This Chapter also presents the operation and shear box test procedures. A series of shear box tests, performed on conditioned Thanet sand and conditioned L.B. sands, are discussed.

Chapter 5 describes the compressibility apparatus commissioned for this research. Design details of the apparatus components and instrumentation are given. This Chapter also presents the operation and compressibility test procedures. A series of compressibility tests, performed on conditioned Thanet sand and conditioned L.B. fine sand, are discussed.

Chapter 6 describes the instrumented model EPB screw conveyor system commissioned for this research. The system's components and instrumentation are described. The screw conveyor operation and test procedure are summarised. A series of model screw conveyor tests, performed on conditioned Thanet sand, conditioned L.B. fine sand and conditioned Garside sand, are discussed.

Chapter 7 summarises the conclusions of this research, investigating soil conditioning for sand and the operation of EPB screw conveyors with sands. Some suggestions for further research topics are given.

Chapter 2. Background

2.1. Introduction

This chapter summarises important concepts used during this research, standard soil mechanics tests related to this research, and describes properties of some conditioning agents. Applications of conditioning agents and their effects on soil properties are discussed.

The current practice of soil conditioning for EPB tunnelling is reviewed. Laboratory tests and research on conditioned soil are discussed and some case studies of applications of soil conditioning in practice are reviewed.

2.2. Important concepts

The following concepts are used in the next chapters, therefore, they need to be described or defined.

2.2.1. Bubble properties

A bubble is the structure that gives the characteristic appearance to foam. This research is interested in liquid-gas foams, for instance: detergent foam. Its form is categorized as cellular, which means that the bubble forms cells surrounded by liquid. Thus, the bubbles that form liquid-gas foams are a two-phase system in which gas cells are enclosed by liquid. These bubbles can contain more or less liquid, according to circumstances. A dry bubble has little liquid (thin films), which may often be idealised as a single surface. The bubble takes the form of a polyhedral cell. The films meet in lines (the edges of the polyhedra) and the lines meet at the vertices. In two dimensions, the dry bubble consists of a polygonal cell (Weaire, 1999). See Figure 2.1.

Most bubbles (foams) exist because they have surfactants as constituents. Surfactants are surface active; they reduce the surface energy or tension associated with surfaces, thus stabilising the film against rupture. Wet foams have a completely different form to dry foams.

Weaire (1999) asserted that bubbles are always in a meta-stable state (a typically slow coarsening process which implies true equilibrium), even if the bubbles do not coalesce. This state is determined by the particular history of the bubble, meaning that even if a shearing force is applied and then turned to zero, the bubble state does not return to the original state before shearing.

The property of a bubble involves, for instance, its behaviour as a solid under low applied stresses. This behaviour will depend of the bubble size and wetness. For a typical detergent bubble, its shear modulus will be of the order of 10 Pa, in comparison with the value $8x10^{10}$ Pa for steel. Moreover, the elastic modulus (strain) has not been explored very much but it is known that the gas within the bubble has an elastic modulus of 10^5 Pa. Obviously, after a certain yield stress, the bubbles separate (foam flows), as topological changes occur indefinitely (see Figure 2.2). Weaire (1999) has studied, in detail, the physics of bubbles (foams) but others have focused on the interaction of bubbles with different environments, for example, the velocity of a bubble in a liquid.

It is important to estimate the velocity of the bubbles in order to estimate the time interval that the bubbles take in leaving the MAPC. The velocity of bubbles has been studied by different researchers. In 1996, Sam et al. studied the axial velocity profiles of single bubbles in water/frother solutions, using a video camera to follow the bubbles. Single bubbles rose in a straight line (rectilinear) when the bubble was small (equivalent diameter smaller than 1.4 mm) and with increasing diameter the motion became oscillating (zigzag or spiral). Figure 2.3 shows the effect of bubble frequency on bubble velocity. A single bubble was defined as the first bubble in the chain of bubbles. Sam et al. (1996) used Tate's law to calculate the spherical bubble diameter. Tate's law is used under constant flow conditions by a balance of the upward force acting on the bubble (buoyancy force) and surface tension. From Tate's law, an expression for the diameter equivalent of the bubble can be obtained,

$$d_e = \left[\frac{6 * d_o * \gamma * \cos \chi}{\left(\rho_w - \rho_g\right) * g} \right]^{1/3} \qquad [2.1]$$

Where:

d_o= Orifice diameter from where the bubbles come in to solution;

Y= Water surface tension in contact with air (It was used Y= 72 dyne/cm);

χ= Angle of contact of the bubble;

ρ_g= Density of gas;

ρ_w= Density of liquid; and

g= Gravity acceleration.

In equation [2.1] it is important to define the angle of contact of the bubble. Figure 2.4 shows the angle of contact of the bubble and the difference between it and the angle between the interface and the horizontal, ϕ_o. When the orifice edge forms an ideal right angle only two relations are possible between χ and ϕ_o: either $\chi = \phi_o$ or $\chi = \phi_o + \pi/2$ (Marmur and Rubin,

1973). No further comment regarding this is made as it is beyond the research objectives of this study.

Table 2.1 is obtained from Sam et al. (1996). In this table, the results are related to bubble shape and bubble path in presence of water and frother in the system.

Sam et al. (1996) presents three general pattern profiles of bubble velocity: rapid increase to a maximum value, a decrease and, if there is sufficient time, a constant velocity stage.

Further research has been carried out on bubble velocity. Zhang et al. (2003) resumes the research about bubble velocity profiles in a graph shown in Figure 2.5. This confirms what Sam et al. concluded in 1996.

Clift et al. (1978) presents terminal velocity of air bubbles in water at 20° C. See Figure 2.6. They propose that for d_e > 1.3 mm, the terminal velocity for a pure system (upper most curve in Figure 2.6) could be approximated by

$$U_T = \left[\left(2.14 * \frac{\gamma}{\rho_w * d_e}\right) + 0.505 * g * d_e\right]^{\frac{1}{2}} \quad [2.2]$$

Where:

U_T= Terminal velocity of bubble in a pure water system.

Clift et al. (1978) also present a discussion about wall effects on the shape of bubbles. The diameter ratio is defined as,

$$\lambda = d_e / D \quad [2.3]$$

Where:

D= Diameter of cylindrical containing wall; and

λ= Diameter ratio.

Clift et al. (1978) established that bubbles with λ < 0.6 tended to be flattened in the vertical direction, while the containing walls tended to cause elongation. As a result, the resulting shape may not deviate greatly from a sphere. For wall effects to have negligible influence (less than about 2%) on terminal velocities the following conditions shall apply:

$$\mathrm{Re} \leq 0.1 \qquad \lambda \leq 0.06 \quad [2.4]$$

$$0.1 < \mathrm{Re} < 0.1 \qquad \lambda \leq 0.08 + 0.02 * \log \mathrm{Re} \quad [2.5]$$

$$\mathrm{Re} \geq 100 \qquad \lambda \leq 0.12 \quad [2.6]$$

Where:

Re= Reynolds number.

Figure 2.7 shows some bubble shapes at different λ values.

Clift et al. (1978) presented a series of correlations to achieve bubble terminal velocity which are valid when:

1. Some surface-active contamination is inevitable;
2. Wall effects are negligible;
3. M (Morton number) $<10^{-3}$;
4. E_o (Bond number) <40; and
5. Re>0.1

The correlations are:

$$J = 0.94 * \left(H^*\right)^{0.757} \qquad (2< H^* \leq 59.3) \qquad [2.7]$$

and

$$J = 3.42 * \left(H^*\right)^{0.441} \qquad (H^* > 59.3) \qquad [2.8]$$

Where,

$$E_o = g * \left(\rho - \rho_{gas}\right) \frac{d_e^{\,2}}{\gamma} \qquad [2.9]$$

$$M = g * \left(\mu\right)^4 * \frac{\left(\rho - \rho_{gas}\right)}{\rho^2 * \gamma^3} \qquad [2.10]$$

$$H^* = \frac{4}{3} * E_o * M^{-0.149} * \left(\frac{\mu}{\mu_w}\right)^{-0.14} \qquad [2.11]$$

$$J = Re * M^{0.149} + 0.857 \qquad [2.12]$$

$$U_{Tclift} = \frac{\mu}{\rho * d_e} * M^{-0.149} * \left(J - 0.857\right) \qquad [2.13]$$

Where:

μ: Dynamic viscosity of layer of liquid on surface of bubble;

μ_w: Dynamic viscosity of surrounded media;

ρ: Density of layer of liquid on surface of bubble;

ρ_{gas}: Density of gas inside of bubble;

E_0: Bond number;

M: Morton number;

H^*: Correlation for contaminated bubbles obtained by Clift et al. in 1978;

J: Correlation for contaminated bubbles obtained by Clift et al. in 1978; and

U_{Tclift}: Bubble terminal velocity in contaminated water.

Clift et al. (1978) found that using the previous equations, the r.m.s. deviation between measured and predicted terminal velocities was about 15% for 774 tests with H*≤59.3 and 11% for 709 tests with H*>59.3.

Finally, it should be noted that Clift et al. (1978) described the shape of a bubble when λ>0.6. Such bubbles were called slug flow bubbles shape. Figure 2.8 shows an example of these slug flow bubble shapes.

2.2.2. Surface tension

Surface tension is a property that allows the surface of a liquid to behave as a membrane. Figure 2.9 shows the molecular basis for surface tension by considering the attractive forces that molecules in a liquid exert on one another. Figure 2.9 (a) shows a molecule within the bulk liquid, so that it is surrounded on all sides by other molecules. The surrounding molecules attract the central molecule equally in all directions, leading to a zero net force. In contrast, Figure 2.9 (b) shows a molecule on the surface. Since there are no molecules of the liquid above the surface, this molecule experiences a net attractive force pointing toward the liquid interior. This net attractive force causes the liquid surface to contract toward the interior until repulsive collisional forces from the other molecules halt the contraction at the point when the surface area is a minimum (Wiley, 2004). If the liquid is not acted upon by external forces, a liquid sample forms a sphere, which has the minimum surface area for a given volume.

The surface tension Y is the magnitude F of the force exerted parallel to the surface of a liquid divided by the length L of the line over which the force acts. Figure 2.10 exemplifies equation [2.14].

$$Y = \frac{F}{L} \qquad [2.14]$$

Where:

F= Force parallel to the surface of a liquid, N; and

L= Length of the line over which the force acts, m.

2.2.2.1. Pressure inside a soap bubble and a liquid drop

A soap bubble (see Figure 2.11), has two spherical surfaces, inside and outside, with a thin layer of liquid in-between. The pressure inside a soap bubble is greater than that on the outside. This difference in pressure depends on the surface tension Y of the liquid and the radius R of the bubble.

For the sake of simplicity, Wiley (2004) assumes that there is no pressure on the outside of the bubble ($P_o = 0$). If the stationary soap bubble is cut into two halves and is at rest, each half has no acceleration and so is in equilibrium and the net force acting on each half must be zero ($\Sigma F = 0$).

Using equilibrium of the bubble for the forces due to the surface tension and air pressure, it is possible to write Newton's second law of motion as:

$$\sum F = 0 \qquad [2.15]$$

$$-2 * Y * (2 * \pi * R) + P_i * (\pi * R^2) = 0 \qquad [2.16]$$

Where:

F= Net force acting on soap bubble;

R= Diameter of soap bubble; and

P_i= Pressure inside of soap bubble.

Solving equation [2.16] for the pressure inside the bubble gives:

$$P_i = 4 * \frac{Y}{R} \qquad [2.17]$$

If the pressure P_o outside the bubble is not zero, this result still gives the difference between the inside and outside pressures,

$$P_i - P_o = 4 * \frac{Y}{R} \quad \text{(spherical soap bubble)} \qquad [2.18]$$

Thus the difference in pressure depends on the surface tension and the radius of the sphere. What is interesting is that a greater pressure exists inside a smaller soap bubble (smaller value of R) than inside a larger one.

A spherical drop of liquid, like a drop of water, has only one surface, rather than two surfaces, for there is no air within it. Thus, the force due to the surface tension is only one-half as large as that in a bubble. Consequently, the difference in pressure between the inside and outside of a liquid drop is one-half of that for a soap bubble:

$$P_i - P_o = 2 * \frac{Y}{R} \quad \text{(spherical liquid drop)} \qquad [2.18]$$

Equation 2.18 is known as Laplace's law for a spherical liquid drop. This result also holds for a spherical gas bubble in a liquid. However, the surface tension Y is that of the surrounding liquid in which the trapped bubble resides (Wiley, 2004).

2.2.3. Strength of soil

Usually the strength of the soil is defined using the Mohr-Coulomb failure law:

$$\tau_{ff} = c + \sigma_{ff} * \tan\phi \qquad [2.19]$$

Where:

c: Cohesion intercept;

ϕ: Friction angle;

σ_{ff}: Normal stress at failure; and

τ_{ff}: Shear stress at failure.

Equation [2.19] can be reduced to a simpler expression depending on the type of soil being studied.

2.2.3.1. Dry sand

In the case of dry sand, the equation [2.19] can be reduced to,

$$\tau_{ff} = \sigma_{ff} * \tan\phi \qquad [2.20]$$

Where the cohesion intercept becomes zero because sand is a cohensionless material. This assumption is valid for normal stress at failure lower than 500 kN.

It is important to bear in mind the different values of ϕ that can be used. Three different values of ϕ are important in engineering.

Particle –to- Particle friction angle

Particle-to-particle friction angle is one of the factors that contribute to the strength of a soil. It increases the rougher the surfaces of the particle are.

Friction angle at the ultimate condition

This is reached when the sand strains without further volume change and with constant deviator stress. This means that the deviator stress and the void ratio achieved values which are independent of the initial void ratio. Normally it is represented by ϕ_{cv}. It is considered a material property.

Peak friction angle

This is calculated from the stresses existing at the peak of the stress-strain curve. This is not a material property thus it depends on the void ratio that existed prior to the application of a deviator stress.

2.2.3.2. Saturated sand

The physical interaction of the water with the soil is studied here. The water present in a soil affects it in the magnitude of the forces transmitted through the mineral skeleton. The behaviour of the sand is exactly the same as in dry sand, but now the pore water pressure of the soil must be included in the analysis.

$$\sigma' = \sigma - u \qquad [2.21]$$

Where:

σ: Total stress;

u: Pore pressure; and

σ': Effective stress.

Much research has been done in the analysis of saturated soil behaviour. According to Terzaghi's principle of effective stress.

$$\tau_{ff}' = \sigma_{ff}' * \tan\phi' \qquad [2.22]$$

Where:

τ_{ff}: Effective shear stress;

σ'_{ff}: Effective normal stress; and

ϕ': Effective friction angle.

The analysis of this sample in this condition is very simple, but the analysis of samples where more than two phases are present (solid, air and water) is rather more complicated.

2.2.3.3. Partially saturated sand

The state of saturation can be classified into categories:

1. High degree of saturation, in which the water in the voids is continuous and air exists as isolated pockets or bubbles; and
2. Low degree of saturation, in which the air is continuous and water is present as thin layers around and between the solid particles.

In sands, the critical degree of saturation between these two conditions is generally about 20% (Head, 1986).

Normally, these types of soils are characterized for having four phases (Fredlund, 1979) liquid, gas, solids and contractile skin (or air water interface). The contractile skin qualifies as a phase since it has differing properties to that of the contiguous materials and definite bounding

surfaces (Fredlund, 1979). The influence of the contractile skin is important because it behaves as an elastic membrane under tension, interwoven throughout the soil structure.

Fredlund et al. in 1978 noted, "From a behavioural standpoint, an unsaturated soil can be visualized as a mixture with two phases that come to equilibrium under applied stress gradients (i.e. soil particle and contractile skin) and two phases that flow under applied stress gradients (i.e. air and water)".

Finally, from a volume-weight standpoint for an unsaturated soil, it is possible to consider the soil as a three-phase system since the volume of the contractile skin is small and its weight can be considered as part of the weight of water (Fredlund, 1979).

The presence of gas in the sample is also very important because gas is highly compressible and the pressure in the two fluids (gas and liquid) may not be equal.

The shear stress equation defined by Fredlund, et al. 1978 for an unsaturated soil is:

$$\tau_{ff} = c' + (\sigma_f - u_a)_f * \tan\phi' + (u_a - u_w)_f * \tan\phi^b \qquad [2.23]$$

Where:

c': Intercept of the extended Mohr coulomb failure envelope on the shear stress axis where the net normal stress and the matrix suction at failure are equal to zero; it is also referred to as "effective cohesion" and is normally zero for a sand;

$(\sigma_f - u_a)_f$: Net normal stress state on the failure plane at failure;

u_a: Pore air pressure on the failure plane at failure;

ϕ': Angle of internal friction associated with the net normal stress state variable, $(\sigma_f - u_a)_f$;

$(u_a - u_w)_f$: Matric suction on the failure plane at failure; and

ϕ^b: Angle indicating the rate of increase in shear strength relative to the matrix suction, $(u_a - u_w)_f$.

The equation [2.23] is an equation for soils and, therefore for sandy soils c'= 0.

The entire development of how the previous equation is obtained goes beyond the objectives of this research, and can be referred to in Fredlund (1979) and Fredlund and Rahardjo (1993).

2.2.3.4. Research assumption regarding shear stress

As implied above, unsaturated soils clearly present a more complicated situation than saturated soils. Therefore, as the soil sample mixed with foam is saturated in its initial condition, it is assumed that the air foam bubbles are not free to move in the soil.

Furthermore, the Mohr-Coulomb failure for saturated soil is used as a framework for interpretation. See equation [2.22].

2.3. Shear tests

2.3.1. Direct shear box

The shear box apparatus was developed originally for the determination of the angle of shear resistance of re-compacted sands (Head, 1994). It provides a convenient way to relate the angle of shear resistance with the voids ratio. This test is especially suitable for sand, due to its cohensionless characteristics.

The direct shear test is a displacement-controlled test: the rate at which the soil is strained is controlled. A specimen of soil is placed into a shear box, and consolidated under an applied normal load.

The shear box is made of two separate halves, an upper and a lower. After the application of the normal load, these two halves of the box can be moved relative to one another, shearing the soil specimen on the plane that is the separation of the two halves. The direct-shear test imposes stress conditions on the soil that force the failure plane to occur at a predetermined location (on the plane that separates the two halves of the box). On this plane there are two forces (or stresses) acting - a normal stress due to an applied vertical load and a shearing stress due to the applied horizontal load.

The shear box apparatus can be made in different sizes. Commercial shear boxes are usually 60 mm square and 20 or 25 mm high. The device used for this research was (internal dimensions) 254 mm long, 155 mm wide and 207 mm high.

The shear box apparatus is suitable for a particle size of up to 37.5 mm. Additionally, the shear box apparatus can be used to measure the resistance of other engineering materials for friction between soil and manufactured materials such as concrete, fabric matting, reinforced materials; friction between materials and components used in laboratory testing, for instance, latex rubber and silicone grease on stainless steel (Head, 1994).

The direct shear test (DST), was formerly quite popular, but with the development of the triaxial test, which is much more flexible, it has become less popular in recent years. The advantages of the DST are:

1. Cheap, fast and simple - especially for sands; and
2. Failure occurs along a single surface, which approximates observed slips or shear type failures in natural soils.

A list of limitations for DSTs include:

1. Some uncertainty in the interpretation of results from shear box tests for providing a failure criterion for the soil;
2. No control can be exercised over drainage, except by varying the rate of shear displacement (Head, 1994);
3. The maximum length of travel of the apparatus limits the deformation that can be applied to the soil (Head, 1994);
4. The area of contact between the soil in the two halves of the shear box decreases as the tests proceeds (Head, 1994);
5. Failure plane is forced. It may not be the weakest or most critical plane in the field;
6. Non-uniform stress conditions exist in the specimen;
7. The principal stresses rotate during shear, and the rotation cannot be controlled; and
8. Principal stresses are not directly measured.

However, a number of advantages can be noted:

1. The principle is easy to understand;
2. The preparation of the specimens is relatively easy; and
3. The tests can be extended to bigger soil particles so the friction between soils and many other engineering materials can be measured.

2.4. Compressibility tests

The two main processes that will be often mentioned in this research are: consolidation and compression. Consolidation is a time-dependent process of volume change in soils as water is squeezed from the pores (Atkinson and Bransby, 1978), while compression is the relationship between the volume of the soil and the effective stress, which is a relationship independent of time (Atkinson and Bransby, 1978).

In this section some of the apparatus used in compressibility tests are described. Finally, in the last part of this section a brief summary of the most important theories of consolidation is given.

2.4.1. Apparatus

2.4.1.1. Rowe cell

Professor P.W. Rowe developed this apparatus at Manchester University. The sample is loaded hydraulically by water pressure acting on a flexible diaphragm.

One of the greatest advantages of Rowe cells is the possibility to control drainage and to measure pore water pressure during the course of consolidation tests. Moreover, tests in large samples provide more reliable data for settlement analysis and large samples permit reliable measurements of permeability to be made under known stress conditions and taking into account the effect of soil fabric (Head, 1986). The Rowe cell can enable samples with diameters up to 254 mm to be tested. For a better understanding, see Figure 2.12.

2.4.1.2. Continuous tests

During the last 35 years, numerous workers have proposed several alternative methods in order to reduce the testing period to within a day or two, or even a few hours as opposed to the days that a consolidation test could take using a usual type of consolidation test, load applied incrementally, on clays. This section describes some of these continuous consolidation tests.

For all these tests the following terminology for the effective stress is applied,

$$p = \frac{P}{A} \qquad [2.25]$$

$$p_t = p + p_b \qquad [2.26]$$

Where:

P: Net applied axial load;

A: Cross sectional area of the sample under continuous test;

p_b: Back pressure;

p: Net applied axial stress on sample during test; and

p_t: Total vertical stress on sample.

The net applied axial load is the load required to cause axial deformation additional to that needed to balance the initial back pressure.

It is important to highlight that the pore water pressure at the drained face during testing is equal to the back pressure in these three types of tests. Thus, the excess pore water pressure can be written as

$$\Delta u = u_u - u_d = u_u + p_b \quad [2.27]$$

Where:

u_u: Pore water pressure at the undrained end of the sample;

u_d: Pore water pressure at the drained end of the sample; and

Δu: Excess pore water pressure at the base of the sample.

In these three type of tests the mean pore pressure in the sample is normally calculated assuming a parabolic distribution,

$$\bar{u} = \frac{1}{3} * (2 * u_u + u_d) = \frac{2}{3} * \Delta u + p_b \quad [2.28]$$

Where:

$\bar{u}$: Mean pore water pressure in the sample.

And the mean effective stress is,

$$p' = p_t - \bar{u} \quad [2.29]$$

Where:

p': Mean effective stress.

Constant rate of loading (CRL)

The applied stress is increased at a constant rate to reach the required maximum value in a period which may be from a few hours to three days.

The selection of the rate of loading should achieve a balance between two extreme conditions. A very high rate of loading induces a large pore pressure in the base of the sample, resulting in the effective stress not being uniform throughout its height. A slow rate can maintain uniformity but the ratio of pore pressure to applied stress is too small to give reasonable results.

Several types of apparatus and methods have been used to obtain a steadily increasing load at a constant rate. For instance, a oedometer cell has been used, loading it with moving weight driven along a lever-arm at a constant speed, hydraulic loading of a Rowe cell, and a pneumatic system with an air regulator driven by a computer controlled stepper motor, pressurising an air /water interchange connected to a Rowe cell (Head, 1986).

Constant pressure gradient (CG)

The difference in pore pressure between the upper and lower faces of the sample is kept constant if the base pore pressure does not change. The distribution of pore pressure across the

thickness of the sample is assumed to be parabolic. Oedometer cells and Rowe cells have been used to carry out this test (Sällfors, 1975).

Constant rate of strain (CRS)

In this test the vertical deformation of the sample is applied at a constant rate. Strictly speaking this shall be referred as a constant rate of displacement test, but this is the same as constant rate of strain, if strain is always defined in terms of the initial ample height (Head, 1986).

A standard procedure for this test is given in ASTM Designation D 4186-82. The load is gradually applied to the sample by increasing the axial displacement (vertical strain) at a constant rate. The resulting increase in vertical stress and pore water pressure at the base are monitored while drainage against a back pressure takes place from the top surface.

2.4.2. Consolidation

Terzaghi in 1944 described the theory of consolidation (one dimensional theory), which couples the theory, laboratory testing and data analysis of a consolidation test. The governing equation obtained by Terzaghi (1944) is:

$$\frac{\partial u}{\partial t} = \frac{\mathrm{k}}{\gamma_{\mathrm{w}} * m_v} * \frac{\partial^2 u}{\partial z^2} \qquad [2.30]$$

$$m_v = \frac{a_v}{1 + e_o} \qquad [2.31]$$

Where:

u: Excess pore water pressure;

z: Material coordinate system;

k: Coefficient of permeability;

m_v: Coefficient of volume change;

a_v: Coefficient of compressibility; and

e: Initial voids ratio.

A new test called constant rate of strain (CRS) began to be studied around 1964 by Crawford. He noted that laboratory consolidation rates are, frequently, several millions times larger than rates experienced in the field. Crawford's CRS test results seemed quite similar to those of standard tests conducted using different load durations. The maximum excess pore pressure (obtained at the base of the sample) in the CRS test was approximately five percent of the applied pressure. Crawford (1964) concluded that the results presented a substantial influence of the rate of testing on the confined compression characteristics of undisturbed clay.

In this part of the section it will be reviewed interpretation of CRS in detail as it is very relevant to this research.

Schmertmann (1965) in a discussion of Crawford's paper (1964) agreed that preconsolidation pressure and voids ratio-effective stress relationships could be accurately determined from the CRS test, but he noted that c_v (coefficient of consolidation), and k (permeability), could not be determined by this test. He also noted that the CRS testing method's greatest asset is the short time required to obtain desired information. In 1969, Smith and Wahls tried to resolve the differences posed by the previous two authors. Smith and Wahls (1969) proposed a theoretical CRS model which is intended to enable the determination of both rate and magnitude of consolidation in a much shorter period of time than has previously been required using conventional procedures. They used the CRS test to determine the appropriate rate of consolidation for the soil element under test. The assumptions used in this theory are:

1. The soil is both homogeneous and saturated;
2. Both water and soil are incompressible relative to the soil skeleton;
3. Darcy's law is valid for flow through the soil;
4. The soil is laterally confined and drainage occurs only in the vertical direction;
5. Both the total and the effective stresses are uniform along a horizontal plane, i.e., stress differentials occur only between different horizontal planes; and
6. The coefficient of permeability, k, is a function of the average voids ratio $\bar{e}$ of the sample.

Smith and Wahls (1969) based their last two assumptions on a case where a relatively thin sample and slow rates of deformation were used in the CRS test. Thus, the governing equation obtained, expressed in Eulerian coordinates is:

$$\frac{1}{(1+e)} * \frac{\partial e}{\partial t} = \frac{\mathrm{k}}{\gamma_{\mathrm{w}}} * \frac{\partial^2 u}{\partial z^2} \qquad [2.32]$$

To obtain a unique solution for equation [2.32], Smith and Wahls (1969) assumed that the voids ratio distribution is a linear function of time, depending on just the space variable z .

$$e = e_o - r * t * \left[1 - \frac{b}{r} * \left(\frac{z - 0.5 * H}{H}\right)\right] \qquad [2.33]$$

Where:

r: Rate of change of average voids ratio (1/time);

b: A constant, depending on the variation of the voids ratio with depth and time;

z: Space variable;

H: Maximum drainage distance for a soil layer; and

e_o: Initial voids ratio.

The governing equation was solved using equation [2.33] (considering that $\frac{b}{r}$ variation is between zero (voids ratio at the base remains constant) and two (voids ratio is uniform with length)) and the boundary conditions,

$$u(0,t) = 0 \qquad [2.34]$$

$$\frac{\partial u}{\partial z}(H,t) = 0 \qquad [2.35]$$

Thus the solution for the pore pressure is,

$$u = \frac{\gamma_w * r}{k} * \left\{ z * H * \left[\frac{1 + e_o - b * t}{r * t * (b * t)} \right] + \frac{z^2}{2 * r * t} - \left[\frac{H * (1 + e_o)}{r * t * (b * t)} \right] * \left[\frac{H * (1 + e)}{(b * t)} * \ln(1 + e) - z * \ln(1 + e_B) - \frac{H * (1 + e_T)}{(b * t)} * \ln(1 + e_T) \right] \right\} \qquad [2.36]$$

Where e_T and e_B are obtained from equation [2.33] by substituting z =0 and z =H respectively.

Smith and Wahls (1969) simplified equation [2.36] assuming $(1+e) = (1+\bar{e})$ where $\bar{e}$ is the average voids ratio (and not a function of z) of soil mass. Thus, the equation obtained is:

$$u = \frac{\gamma_w * r}{k * (1 + \bar{e})} * \left[z * H - \frac{z^2}{2} - \frac{b}{r} * \left(\frac{z^2}{4} - \frac{z^3}{6 * H} \right) \right] \qquad [2.37]$$

Znidarcic et al. (1984) mentioned that the consequences of the previous substitution on the material properties have not been evaluated. Smith and Wahls (1969) calculated the average effective stress and the average coefficient of permeability, replacing the value of the pore pressure at the base of the sample, (u_b = H), in equation [2.37]. In this way, the effective stress-voids ratio and the voids ratio-permeability relationships can be obtained (assigning these values to the average voids ratio).

Smith and Wahls (1969) concluded that "*the slower the rate of strain, the more accurately the standard test results could be determined by the CRS test. However, the rate of strain must be sufficiently fast to produce reliable, measurable pore pressure to calculate the coefficient of consolidation* (c_v)*"*. They also concluded that the CRS test, and the assumptions on which it is based, are valid for tests in which the pore pressure developed at the base does not exceed some fixed percent of the applied stress. For the soil in their study (undisturbed Massena clay, remolded kaolinite and remolded calcium montmorillonite), this upper limit of pore pressure was

approximately 50% of the applied stress. Znidarcic et al. (1984) noted that this analysis has two problems. Firstly, the degree of accuracy of the obtained material properties is unknown as a consequence of the voids ratio linearity respect of the time and secondly, a need of reference test results to ascertain which value of b is suitable to obtain appropriate material characteristics.

In 1971, Wissa et al. established a new analysis for the CRS consolidation test. This analysis included transient (initial), and steady state conditions. This *"analysis applies to any variation of permeability, k , and coefficient of volume compressibility, m_v , as long as incremental small strains exist and the coefficient of consolidation, c_v , is constant"* (Wissa et al., 1971). The transient condition develops in the soil immediately after the piston is set in motion, thus it must be dissipated before steady state conditions are established.

Wissa et al. (1971) started their analysis with the governing equation of consolidation written in terms of strain,

$$\frac{\partial \varepsilon}{\partial t} = c_v * \frac{\partial^2 \varepsilon}{\partial z^2} \qquad [2.38]$$

Equation [2.38] could be obtained from Gibson et al. (1967) for a monotonic consolidation by neglecting the self-weight of the material, assuming infinitesimal strains, setting the coefficient of consolidation,c_V, to be constant. The strain, ε, is defined as,

$$\varepsilon = \frac{\Delta e}{1 + e_o} \qquad [2.39]$$

It is important to highlight that equation [2.38] *"does not require the permeability or coefficient of volume compressibility to have any particular relation to stress and strain so long as their ratio is independent of position, z. Thus there is no restriction on the form of the compression curve, except that the solution will be valid for small strains only."* (Wissa et al., 1971).

Wissa et al. (1971) defined a dimensionless variable to solve equation [2.38],

$$\varepsilon = -\frac{\partial D}{\partial X} \qquad [2.40]$$

Where:

X: Dimensionless parameter $X = \frac{z}{H}$;

H: Sample height at time t;

D: Dimensionless displacement $D = \frac{\upsilon}{H}$; and

υ: Vertical displacement, considered positive downwards.

Thus, the governing equation in terms of the dimensionless displacement is,

$$\frac{\partial^3 D}{\partial X^3} = \frac{\partial^2 D}{\partial X * \partial T} \qquad [2.41]$$

Where:

T: Dimensionless parameter $T = \frac{c_v * t}{H^2}$.

The boundary and initial conditions for this case are,

$$D(1,T) = D(X,0) = \frac{\partial^2 D(1,T)}{\partial X^2} = 0 \qquad [2.42]$$

$$D(X = 0,T) = \frac{r * H^2}{c_v} * T \qquad [2.43]$$

Using the separation of variables, boundary and initial conditions, equation [2.41] can be solved. Wissa et al.'s (1971) final solution to the governing equation in terms of strain is,

$$\varepsilon(z,t) = r * t * \left\{1 + \frac{1}{6 * T} * \left[2 - \frac{6 * z}{H} + 3 * \frac{z^2}{H^2}\right] - \frac{2}{\pi^2 * T} * \sum_{n=1}^{\infty}\left(\frac{1}{n^2} * \cos\left(\frac{n * \pi * z}{H}\right) * \exp(-n^2 * \pi^2 * T)\right)\right\} \qquad [2.44]$$

The first term in the right hand side of equation [2.44] represents the case if the strains were the same everywhere in the sample. The second term represents the deviation from the average strain in the steady state case. Wissa et al. (1971) says that the deviation must exist to provide the gradient necessary for a constant flow of pore fluid. The last term is the transient part of the solution, and describes the decay of the initial discontinuities set up when the test is started. For small values of time, the sample is in a transient state and the term containing the exponential function cannot be neglected. It is important to highlight, that if the strain rate is too high, the steady state may never be reached. Additionally, in order to calculate the coefficient of consolidation, it is necessary to obtain the ratio of strains at the two ends of the sample. As the strains can not be measured within Wissa et al.'s (1971) test sample, an additional assumption is necessary in order to relate the strains to the stresses. The relationships will be calculated at first assuming the soil to be linear and secondly nonlinear. Assuming steady state conditions in the first case (linear material i.e. constant coefficient of volume compressibility, $m_v = \frac{\Delta\varepsilon}{\Delta\sigma'}$ where, $\Delta\sigma'$ is the difference in effective stress between the top and bottom of the test specimen), the coefficient of consolidation obtained is the same expression that Smith and Wahls (1969) used,

$$c_v = \frac{\Delta\sigma}{\Delta t} * \frac{H^2}{2 * \Delta u} \quad [2.45]$$

Where:

$\Delta\sigma$: Difference in total stress between top and bottom of the test specimen; and

Δu: Excess pore water pressure difference; In the case of Wissa et al. (1971) it was equal to the excess pore pressure at the bottom of the test specimen.

In the case of a nonlinear material, Wissa et al. (1971) used the following assumption,

$$c_c = -\frac{de}{d(\log \sigma')} \quad [2.46]$$

Where:

C_c: Compression index.

Wissa et al. (1971) define a second index called strain index, C_ε, that at small strains is related to the compression index as,

$$-\frac{d\varepsilon}{d(\log \sigma')} = c_\varepsilon = \frac{c_c}{1+e} \quad [2.47]$$

Using the previous equation, Wissa et al. (1971) obtained the coefficient of consolidation for a nonlinear material,

$$c_v = \frac{H^2}{2 * \Delta t} * \frac{\log\left(\frac{\sigma_2}{\sigma_1}\right)}{\log\left(1 - \frac{u}{\sigma}\right)} \quad [2.48]$$

Where:

σ_2: Total vertical stress at time t_2;

σ_1: Total vertical stress at time t_1; and

Δt: Difference between time t_2 and t_1.

In the case of transient conditions, Wissa et al. (1971) use the last two terms in equation [2.44] to interpret the transient strain condition. Once those values are determined, Wissa et al. (1971) established a ratio between the strain on the top and bottom of the sample (in both, linear and nonlinear materials). This ratio depends only on T and, therefore, when this ratio is known, C_v or C_ε are known too.

Wissa et al. (1971) concluded that the CRS consolidation test is ideally suited for investigating the influence of secondary compression and reconsolidation on the compressibility behaviour of

soils. In Wissa et al. (1971) it is established that the numerical meaning of fast and slow rates of strain depends on the soil being tested; However, the conclusion that the optimum rate of strain to be used for a given soil is a trade-off between the speeds best suited for determining the e versus log σ_v curve and the best for obtaining values of c_v is valid no matter what soil is being tested.

Wissa et al. (1971) established that in practice, both can be accurately determined for Kaolinite by using rates of strain that result in $\frac{u}{\sigma}$ (excess pore pressure at the base) values of 2% to 5% (using these values the soil can be assumed to behave as a linear material having a constant, m_v, without introducing significant differences in the computed values of k and c_v.

Znidarcic et al. (1984) pointed out relevant arguments here. Firstly, Znidarcic et al. (1984) argued that even though Wissa et al.'s (1971)' analysis is theoretically consistent, the assumption that the coefficient of consolidation is constant throughout the test is rarely the case for soils. This would suggest that the results obtained by Wissa et al. (1971) are only approximated. Znidarcic et al. (1984) is categorical in pointing out that the linear model is never justified. Also, he mentions that the nonlinear model is not a good approximation to real soil behaviour, especially for soft, normally consolidated clays (because the compression index is not constant). These two assumptions lead to two distinct curves for the voids ratio-effective stress relationship in the transient state.

Znidarcic et al. (1984) established that in the case of a steady state, the assumption of a constant coefficient of consolidation is less restrictive. But, he noted that the steady state condition is a consequence of the assumption of a constant coefficient of consolidation and he is categorical again in stating that actually the steady state does not exist in the case of a real material.

Although Znidarcic et al. (1984) confronts the theory of Wissa et al. (1971), Wissa et al.'s (1971) theory has been used by many authors. For instance, in 1997, Sheahan and Watters carried out an experimental verification of the CRS consolidation theory. They carried out 9 CRS consolidation tests on resedimented Boston blue clay (BBC) using a specially instrumented, computer automated hydraulic consolidation device (see Figure 2.13). The specimen was loaded using one of three vertical strain rates (0.1, 1, and 3%/h), and pore pressures were measured at three points through the specimen height and at the base (see Figure 2.13). The CRS results were compared to the end of primary states in four incrementally loaded (IL) oedometer tests,

performed using standard procedures. At the two faster CRS rates, excess pore pressure (Δu) developed and two methods were used to compute vertical effective stress: the nonlinear CRS theory of Wissa et al. (1971), that depends in part on Δu measured only at the base; and the direct integration of measured Δu distribution through the specimen (isochrone distribution). The results show that at the two faster rates, the CRS tests based on the nonlinear CRS theory are consistent with those obtained using the isochrone method; results from the CRS tests at all three rates compare well with IL test results. The CRS behaviour of resedimented BBC is virtually independent of the strain rate across the range tested. At vertical effective stress levels at and above preconsolidation pressure, the CRS tests loaded at 1 and 3%/h yielded coefficients of consolidation and hydraulic conductivity values that agreed well with IL test values (see Figures 2.14 and 2.15). Sheahan and Watters (1997) support the validity of the nonlinear CRS theory and suggest that less structured clays, such as those tested by them, may have less rate dependence during consolidation than soils with strong interparticle bonding and structure.

2.5. Tunnelling background

The tunnelling industry has grown rapidly since the 1970s, having addressed several problems regarding the stability and security of the tunnels. This section gives a broad background of different tunnelling applications.

2.5.1. Pipe Jacking and microtunnelling

Trenchless technology has been the non-disruptive technique broadly used to install pipes in the ground. Two of the most well known methods in the field of trenchless technology are pipejacking and microtunnelling. For both processes, the principle is the same, and consists of using hydraulic rams to push up pipe sections to line the hole formed by a cutting head, or shield. Pipejacking and microtunnelling operations differ in the size of the internal diameter of the pipes used. Microtunnelling is used in pipes with a diameter of less than 900 mm and pipejacking is used in pipes with larger diameters.

A pipejacking or microtunnelling operation consists of four elements: face, line, jacking pit and top side surface (See Figure 2.16). The face is responsible for excavating and controlling the ground and loading the soil for conveyance (Thomson, 1993). The line transmits the jacking load without damage to the pipes. The different types of materials for pipes include concrete, clay, plastic, steel and ductile iron. The jacking pit and top side surface are not relevant in this study.

The main applications for pipejacking and microtunneling are line installations (sewers, house connections, pressure pipes), installation of ducts (non disruptive method), crossings and pipe replacement.

This section describes the two main techniques actually used to install pipes in the ground.

The following operational systems (how to dig the tunnels) can be applied to pipe jacking, taking into consideration the limitation that each operational system might have.

2.5.2. Tunnelling Systems

In general, all the following tunnelling operations have been called closed-face (mode) mechanical shield tunnelling (Naitoh, 1985), which uses, as a principal idea, a compressed chamber to stabilize the tunnel face (Muir Wood, 2000).

Some of the main problems that occurred in tunnelling operation systems at the beginning of the 1800s were solved by Pressurized Plenum Chamber Machines (Stack, 1982). This type of machine presented several problems such as: health problems for the crew, inability to hold the tunnel face and water contamination problems (e.g. by sulphuric acid) in sandy soils with concentration of lignite and pyrite (Stack, 1982).

The introduction of Slurry Machines solved the problem of the high ground water table, keeping the dewatering of the ground, with consequent ground subsidence, to a minimum. This new type of machine was called a Slurry Machine or Mud Circulation Machine.

In 1971, Barlett (Stack, 1982) made a prototype of a Bentonite Tunnelling Machine (see Figure 2.17). The advantage of using bentonite slurry is that it serves to support the face and acts as a vehicle for the removal of excavated soil.

Around the 1960's, the Japanese were looking for a method of tunnelling through soft ground and mining ground, below the water table, which would tunnel with high efficiency of excavation and reduction in the cost, and comply with the environmental regulations and laws on air and water pollution, industrial water and waste disposal, in force in main Japanese cities. To fulfil those requests they built the Earth Pressure Balance Machine (EPBM). They introduced two different types (EPBM and Water Pressure Machine), that work under the same design but for different ground conditions. Externally, the shields resemble the slurry unit, in that the cutter head consists of a rotating disc fitted with drag teeth. Slits on either side of each cutter arm allow the material excavated from the face to enter the cutter frame, and then a drum (like a

chamber behind the cutter head). In this drum chamber (excavation chamber), the material excavated from the face is collected and compressed. This material in turn forms a plug, which supports the face and prevents the ingress of ground water. By means of a screw conveyor, the material in the drum is then moved upwards. A constant pressure is maintained at the face keeping the rotating cutter frame (cutter wheel), and screw conveyor constantly filled with earth (Stack, 1982). See Figure 1.2 for shield machine earth pressure type and Figure 2.18 for shield machine water pressure type.

Further progress was made around the same time in 1973, when Mitsubishi built an Automatic Slurry Tunnelling Machine. This design, with an automatic control (Stack, 1982), resolved the problem when a "run" of ground occurred and more spoil was removed from the face than was warranted by the machine's rate of advance (producing subsidence).

Over the years, the various machines have progressed in different ways. For instance, in 1976, the company Daiho Construction Co. Ltd adapted a version of the EPBM, called Earth and Mud Pressure Balance Shields, to work without a full cutter head plate. The new cutter head consisted of 4 wings, which provide support. This unit is very effective in sandy or gravel soils devoid of natural mud and, thus, very permeable (Stack, 1982).

More recently, together with bentonite, other products such as foaming agents and polymers have been added to permit the pressure to be transmitted to the ground, rather than to the ground water (Muir Wood, 2000).

2.5.3. Earth Pressure Balance Machine (EPBM)

The research concentrates on soil conditioning and lubrication in the EPBM; therefore, a description of it will be made to clarify certain technical aspects.

The EPBM has been used since the 1960s, and have improved rapidly. The EPB shield presents advantages over the slurry and blind shields. For instance, it does not need a separation plant when it is working in grounds with a high percentage of silt/clay, mechanical excavation guarantees better performance, etc.

The EPBM works under a full-face mechanical excavation system. For every revolution of the tool carrier, the entire tunnel face is excavated.

Some of the advantages of the full-face mode are (Maidl et al., 1995),

1. The tunnel profile is cut very accurately without large "overbreak";

2. The contours of the tunnel face remain unchanged during tunnelling (except for depth of cut);
3. Relatively high advance rates can be achieved; and
4. In contrast to the open mode or partial open mode, the rate of progress in the full face mode is determined by the adaptation of the tools and excavation force of the ground, and not mainly by the machine driver.

The activities of the full-face mode include: the coupling of excavation (cutting tool performance), face support and removal of the excavation material (Maidl et al., 1995). The first point is not analysed here because it is not part of this research project. The second and the third points are discussed at a later stage.

2.5.3.1. Operational principle

The main idea is that the material excavated by the cutting wheel serves as a support medium.

The tools on the rotating cutter head excavate the ground. The ground does not fall into the excavation chamber, but is pressed through the openings of the cutting wheel, into the excavation chamber, where it is mixed with the plastic earth slurry. Through the pressure bulkhead, the thrust force is transferred onto the earth slurry. Thus, uncontrolled entering of the excavated ground into the excavation chamber can be avoided. Balance is reached when the earth and water pressure in place does not further compress the earth-slurry in the excavation chamber.

A screw conveyor removes the material from the excavation chamber. Moreover, the transport from the tunnel can be handled by belt conveyors, trucks, solid handling pumps, etc.

2.5.3.2. Ground conditioning

According to practical experience, the excavated material should have the following properties to serve as support medium:

1. Good plastic deformation;
2. Pulpy to soft consistency;
3. Low internal friction; and
4. Low permeability.

These properties ensure that the support pressure can be applied regularly onto the tunnel face and a regular flow of material to the screw conveyor can be guaranteed. Therefore, an economical selection of the drive torque of the cutting wheel and screw conveyor is possible.

Low permeability values permit the transfer of materials from the screw conveyor to the conveyor belt without the use of a lock at the end of the screw conveyor, so avoiding the undesirable flow of water out of the screw conveyor (decreasing pressure and making the flow of material difficult to control).

Due to the fact that the ground rarely has the above mentioned properties the ground has to be conditioned. The conditioning required depends on the ground type. This is defined according to grain size, water content (w), liquid limit (%), plasticity index (I_p) and consistency index (I_c, {liquid limit-w}/I_p). For instance, in the case of sandy soils, the important parameters are the first two of the list. For clays, the last four parameters are of more relevance to the behaviour of the soil.

The conditioning of the ground is carried out during the excavation at the tunnel face, in front of the cutting wheel, to avoid the clogging of the cutting wheel (cutting tools) with small openings, as well in the screw conveyor and excavation chamber.

In the case of sandy soils, high water permeability values have been reduced by the addition of bentonite materials, which reduce the missing percentage of fines, because the water in the pores is bound to the bentonite structure. Therefore, the material is changed into a plastic earth slurry with very good flow properties and a reduced permeability. Other additives, for example polymers with water absorption properties, can be injected.

As for every machine, the EPB has a range of applications. The Figure 2.19, taken from Maidl et al. (1995) shows three different curves. Curve (1), shows one of the best situations, where there is a minimum of 30% fine grains. This is a case where the soil might not need many additives, showing rather impermeable characteristics. Curve (2), presents much more permeable behaviour than curve (1). According to experience, the permeability coefficient of the soil should not exceed a value of 10^{-5} m/s at a maximum pressure of 2 bar (Maidl et al., 1995). Therefore, any soil between curves (2) and (3) might need additives to improve its flow properties and according to Maidl et al. (1995), the EPB shield must not be used under water pressure.

Taking into consideration what has been mentioned above and the practical cases, the use of conditioners enlarges the range of application of the EPB shield.

It is necessary to bear in mind, that with a high percentage of conditioning additives, the problem of separation (additives from the material), is transferred to the disposal site.

2.5.3.3. Controls

Normally, different parameters can be measured in the EPB shields, for instance speed of advance, torque, earth pressure, volume of excavation, flow of conditioner.

The earth pressure measurement values document the entire tunnel drive, making it possible to steer individual parameters via regulation circuits. The earth pressure is controlled through the regulation of the thrust speed of the push cylinders or the rotation speed of the screw conveyor. For instance, the earth pressure is increased by means of increasing the thrust speed of the push cylinders or by reducing the rotation speed of the screw conveyor, and it is reduced by reducing the thrust speed of the push cylinders or increasing the speed of the screw conveyor.

Maidl et al. (1995) describe a flow chart (regulation system), of an earth pressure balance shield. The flow chart describes a simple algorithm to control the earth pressure. It is vital to bear in mind that, through the regulation system, only the action of the shield operator during normal manoeuvres can be minimised, therefore continuous visual control of the most important measuring instruments is necessary.

2.5.3.4. Screw conveyor

Screw conveyors are a successful means to overcome the pressure difference between the tunnel face and the inside of the tunnel. Screw conveyor systems consist of a screw-type blade and a static screw casing, within which the screw-type blade rotates. The diameter of screw conveyors has increased to over 1200 mm with an increased transport capacity (Maidl et al., 1995).

The screw conveyor drive is adjustable, to facilitate control of the support pressure in the excavation chamber. With a high pressure difference, two screw conveyors with different speeds can be installed, one behind the other. A discharge gate and injection nozzles on the exit of the screw tube, for adding lubricants, are standard equipment (Maidl et al., 1995).

The flow of the excavated material in the screw conveyor varies according to the pressure differences, inclination and geometry of the screw conveyor, soil properties and lubrication. Different arrangements can be made to improve the extraction of material in the screw conveyor: For example if a bigger flow is needed, two screw conveyors in parallel can be installed rotating in opposite directions. Figure 2.20, shows a scheme of the flow of the ground through the screw conveyor. The scheme is based on a constant support pressure and does not consider the rotation of the earth slurry, the opening of the cutting wheel or the force of gravity.

For a central shaft screw conveyor, the biggest particle size amounts to 40% of the clear diameter (Maidl et al., 1995). Screw conveyors without shafts are able to transport bigger particle sizes than a screw conveyor with a central shaft.

The functions of the screw conveyor system are:

1. Removal of material from the pressurised excavation chamber into the tunnel (under atmospheric pressure);
2. Permeable ground sealing against pressurised water; and
3. Control of the support pressure in the excavation chamber through the controlled removal of material.

The way that screw conveyors resist the ground water pressure is through different closing or compaction systems. The creation of the sealing plug is facilitated by the injection of different additives into the screw conveyor, for instance bentonite, polymers. Moreover, this reduces the driving torque required.

2.5.3.5. Loads on an EPBM

It is helpful to introduce the origin of the relations that drive most of the analysis of ground loading and, therefore, tunnel loading, in cohensionless soils.

In 1944 Terzaghi developed an equation based on the arching theory and on the stress yielding analysis of a horizontal dry sand strip, to obtain the vertical pressure on the roof of a tunnel through sand.

This equation was obtained using the condition that the sum of the vertical components, which act on the slice, must be equal to zero (see Figure 2.21), obtaining a linear differential equation which once resolved gives,

$$\sigma_v = \frac{B*(\gamma - \frac{c}{B})}{K*\tan\phi} * (1 - e^{-K*\tan\phi*\frac{z}{B}}) + q * e^{-K*\tan\phi*\frac{z}{B}} \quad [2.49]$$

Where:

B: Half of slide width;

γ: Bulk unit weight of the soil;

c: Cohesion of the soil;

k: Lateral pressure coefficient;

ϕ: Friction angle of soil;

q: Surcharge;

z: Distance between the surcharge application line and roof of the tunnel; and

σ_v: Vertical pressure on the roof of the tunnel.

In the case of sand (cohesionless material), c=0.

Supporting of the face

Certain ground conditions and the presence of ground water may make face support necessary.

The optimum situation is when the tunnel face is stabilised, either by its inherent stability or by the slope of the soil in connection with special supports (Maidl et al., 1995). The methods of face support are generally only suited to counteract earth pressure, therefore the underground water conditions mechanical face support must be complemented by extra measures to prevent the ingress of water.

In EPBM, after the addition of conditioners (water, bentonite, foam etc.), the excavated material is transformed into "earth slurry" which stabilises the tunnel face.

Figure 2.22, shows a simplified description of the pressure distribution in the tunnel face. According to West (1986), the machine chamber is balanced, keeping the chamber pressure higher than the water pressure (C > A1 and D > B1), but somewhat lower than the sum of the water pressure and the earth pressure (C < A1+ A2 and D < B1 + B2). Intermediate values in the chamber pressure are chosen to avoid a blow to the surface (Monteith, 2002).

Comparing the practical issues with the theoretical analysis made by Terzaghi in 1944, regarding tunnels through sand, the pressure in the chamber pressure is the water pressure plus the height of "loose soil" (Terzaghi defined "loose soil" as the soil above the roof of the

tunnel, up to 2 or 3 times the diameter of the tunnel). Further details on the application of equation [2.49] are outside the objectives of this thesis.

Loads on the shield

The shield supports external and operational loads. External loads are due to earth, water and support pressure. Operational loads are all the loads arising inside the shield construction, due to machine technology and site operation (Maidl et al., 1995). Some of the operational loads are due to the push of cylinders, weight of the components.

It should be noted, that these design loads for the shield skin are purely theoretical. In reality, considerable variations arise due to the cover-cut (plastic ground or support fluid filling the gap between the surrounding ground and the shield skin), and to the asymmetrical position of the shield in the excavation profile. These variations are not included in this analysis, in order to simplify the analysis.

The effective vertical stress at the roof of the shield can be calculated using Terzaghi's equation (1944), where the surcharge, q, is the total pressure of the buildings and traffic above the shield, and the presence of ground water around the area. Using earth pressure analysis, and taking into account the water pressure (Terzaghi (1944) and PJA (1995)), the effective horizontal stress can be calculated and Coulomb's theory used to obtain the radial stress around the shield. Finally, integrating the radial stress through the perimeter of the shield, the radial force (per unit of length) on the shield is obtained,

$$F_r = \pi * D_e * \frac{(\sigma'_v + \sigma'_h)}{2} \qquad [2.50]$$

Where:

D_e: Diameter of the shield;

σ'_v: Effective vertical stress at the roof of the shield;

σ'_h: Effective horizontal stress; and

F_r: Radial force per unit of length on the shield.

Further details on the application of the equation [2.50], are outside the object of this thesis.

Push cylinders and frictional forces

Frictional forces and support pressure are the forces that the cylinders must overcome.

The radial loads create frictional forces around the shield skin, i.e.: horizontal and vertical loads, arising from cover, buildings and traffic on the surface, as well as the weight of the shield itself.

There are some ways by which the frictional forces can be reduced, for instance using a conical form of the shield, by over-cut, or by lubrication of the shield (e.g. bentonite, polymers and foams).

Values of the coefficient of friction, μ, are given by Maidl et al. (1995) for steel shield skin and different grounds. For instance, sand has a typical coefficient of friction of 0.45 and clay, a typical coefficient of friction of 0.2.

Using equation [2.50], and including the weight of the shield, the frictional force in the shield skin is:

$$F = \tan\delta * \left[F_r * l + F_{sh} \right] \qquad [2.51]$$

Where:

l: Length of the shield skin;

F_{sh}: Weight of the shield;

$\tan\delta$: Coefficient of friction as a function of the wall angle of friction δ between the shield and the soil; and

F: Frictional force on the shield skin.

For sand, the coefficient of friction can typically be reduced to half, by means of shield lubrication with bentonite, or other suspension materials (Maidl et al., 1995).

Thrust resistance from the face

Additionally, other resistance forces must be overtaken by the push cylinders to the resistance of the tunnel face (F_{supp}), for instance, the thrust resistance at the cutting edge, thrust resistance due to excavation tools (at the tunnel face) and steering shield resistance (mainly in curved areas). Therefore the thrust force of the push cylinders is,

$$F_{cyl} = F + F_{supp} + F_{cuttingedge} + F_{exc.tools} + F_{steering} \qquad [2.52]$$

It is important to clarify, that this value is not the final value to be used in practice. A factor of safety must be included, taking into account forces like increased cutting edge resistance when encountering obstacles (for instance, adhesion of soil on the cutting tools), increased shield skin friction forces and increased cutting edge resistance in injection areas, due to ground swelling pressure, which are difficult to calculate exactly.

Torque

The excavation tool wear is the variable that controls the operational speed of the cutting wheel, making it remain small. Normally, the rotational speed does not exceed 3 rpm.

Maidl et al. (1995) and Naitoh (1985) express the same empirical relation to determine the torque, where the torque is proportional to the third power of diameter of the shield. Both conclude that the constant of proportionality depends of the ground conditions expected. Thus, the use of additives decreases the torque required to excavate (see Figure 2.23).

2.6. Soil conditioning agents

As mentioned above, different products can be used as lubricants in pipejacking operations and as conditioning agents for EPB shield.

Three of the most used materials are as follows:

2.6.1. Bentonite slurries

Bentonite is a clay consisting essentially of smectite minerals, in particular montmorillonite, which is the most commonly used material. Therefore, bentonite slurries are montmorillonite clay minerals dispersed in water to create a fluid with density, viscosity, impermeable and thixotropic properties; depending on the quality and source of the bentonite, the chemistry of the water and the proportion of the slurry.

Only natural sodium montmorillonite, as well as certain sodium exchanged or calcium smectites, have the necessary properties for engineering use (ODOM, 1986).

Montmorillonite has a crystal structure with weak electrostatic bonds between layers. It is for this reason that interlayer cations (Na, Ca, Mg), are exchangeable and water can enter between the layers (ODOM, 1986). See Figure 2.24.

The exchangeable ions associated with smectite clays are easily and reversibly replaceable. Sodium is readily replaced by calcium and magnesium, so that smectite clays tend to be depleted in sodium when subjected to leaching conditions (ODOM, 1986). The exchangeable ions play a dominant role in the commercial use of montmorillonite. When sodium is the predominant natural exchangeable ion, the montmorillonite usually has a high swelling capacity. This will imply a high degree of dispersion and a high natural viscosity.

Sodium (Na)-montmorillonite's chemical and hydration properties, together with the electric potential of the particles and the size of its particles, make it suspendable (clay platelets or clay sheets), once added to water. Moreover, when it is added to water in larger concentrations (5% to 6%), it may cause higher resistance to shear. Additionally, when the shear stress on the

liquid is removed, the Na-montmorillonite particles attract each other to develop a rigid gel structure, which has thixotropic properties (ODOM, 1986). By contrast, Ca-Mg montmorillonite neither gives high viscosity values or displays thixotropic behaviour. Therefore, Ca and Mg montmorillonite are normally changed to Na form. This is made by an exchange process, mixing soda ash (sodium carbonate) with crude, moist clay.

Bentonite slurries for lubrication and soil conditioning are prepared by adding, typically, about 3% mass bentonite to water in a mixer to disperse the clay particles in the water and then leaving the slurry for a certain time to allow for sufficient hydration of the clay. When used as a lubricant for pipejacking or as a face support fluid for tunnelling, the dispersed platelets of a bentonite slurry form a thin filter cake on the surface of the excavated soil, which acts as a low permeability membrane and transmits the fluid pressure to effective stresses in the soil to stabilise the ground (Milligan, 2000).

According to Lyon (2001) the static part of the filter cake provides most of the lubrication and the dynamic part stabilises permeable ground to prevent collapse onto the pipes. Moreover, the permeability of the filter cake must be at least three times lower than that of the surrounding soil, to prevent excessive fluid loss into the ground.

All the bentonite slurry properties can be improved by mixing them with other conditioners to enhance their filter cake performance, either as a lubricant in pipe jacking (tunnelling), or as a conditioner agent in EPB machines.

2.6.2. Polymers

Polymers are any material whose molecular construction is a chain of some hundreds or thousands of repeating sub-units. These sub-units are referred to as monomers. If the chain is formed by more than one molecular species, it is called a copolymer. The length of the chains, the range of chain lengths occurring in a particular sample and the degree of branching, all have considerable effect upon the physical properties of the polymers.

In soil conditioning and lubrication processes, several polymers can be applied. For instance, natural polymers such as cellulose, semi-synthetic polymers such as carboxymethylcellulose (CMC), and polyanionic cellulose (PAC), and synthetic polymers such as polyacrylamides (PA) can be used (Milligan, 2000).

The most common polymers used in soil conditioning and lubrication are Polyacrylamide polymers. A wide range of polyacrylamides is possible, with molecular weights ranging from

several thousand to over 10 million and with an ionic character (monomers having positive or negative charges respectively) from 100% cationic to 100% anionic (Milligan, 2000)

2.6.3. Foams

In general, protein based and synthetic detergents are used as foaming agents. According to Milligan (2000) different foaming agents contain glycol-based boosters, fluorocarbons enhancers and soluble polymers, in different proportions, as well as various additives, such as inorganic salts, preservatives, solvents and stabilisers.

Different properties are obtained for foams regarding: the chemical composition of the foaming agents, its concentration and the expansion ratio (relation of the volume of foam by the volume of liquid in the foam).

The stability of the foams is of vital importance for tunnelling applications. For instance, highly stable foam can hold the face pressure and the earth pressure balance plug in the screw conveyor for an EPB machine, avoiding settlements or difficulties in the earth-slurry filter cake formation.

In practice, polymers are added to the foam to increase its stability, and stiffness and add lubrication to the foam properties.

2.7. Overview of previous work

This section mentions previous work, related directly or indirectly to this research.

2.7.1. Shear box

The shear box is used to measure the friction angle of different materials. The boundary conditions could vary regarding the type of shear box to be used.

The next section explains the various studies made, in order to analyze the results obtained by direct shear box tests and the effectiveness of the shear box as an apparatus to measure the interface friction angle between soil and any material.

2.7.1.1. Shear box apparatus

At this point it should be noted that the shear box apparatus was made according the improvements suggested by Jewell (1989), where the symmetric behaviour of the sample was achieved by fastening the top part of the shear box to the loading platen. Figure 2.25 (b) shows the arrangement used by Jewell (1989). Figure 2.26 shows the basic definition of direct shear tests.

The next analysis takes into account the configuration by a medium size direct shear test as it was assembled in the University of Oxford.

Boundary conditions (conventional tests)

The shear box is one of the most used laboratory tests to study soil behaviour under an applied load. Several studies have been carried out to ascertain the best way to analyse the results.

Taylor (1948) was one of the first to analyze the behaviour of cohesionless materials. He stated that the frictional resistance in sands is partly sliding friction and partly rolling friction. He added that the resistance to shear is also caused by a phenomenon called interlocking.

Taylor (1948) explains the factors contributing to shearing strength in sands. As previously mentioned, he demonstrated that shearing resistance in sand is formed of two parts. The first is the internal friction resistance between grains, which is a combination of rolling and sliding friction. The second is interlocking, which contributes to a large portion of the strength in dense sands. This phenomenon does not occur in very loose sands. Therefore, it can be deduced that the angle of internal friction does depend on the internal friction and the degree of interlocking. This led Taylor to suggest that a boundary energy correction should be applied to the maximum shear stress measured in constant (vertical stress) direct shear tests. The work developed by Taylor (1948) was corroborated by Wroth (1958) and Stroud (1971) when they showed that the tests could be correlated by the energy equation (flow rule),

$$\frac{\tau_{yx}}{\sigma_{yy}} - \frac{\dot{\varepsilon}_{yy}}{\dot{\gamma}_{yy}} = \left(\frac{\tau_{yx}}{\sigma_{yy}}\right)_{cv} \qquad [2.53]$$

Where:

τ_{yx} : Shear stress;

σ_{yy} : Vertical stress;

$\dot{\varepsilon}_{yy}$: Strain increment;

$\dot{\gamma}_{yx}$: Shear strain increment; and

$\left(\frac{\tau_{yx}}{\sigma_{yy}}\right)_{cv}$: Stress ratio at the critical state or $\tan^{-1}(\phi_{cv})$.

For further information see Cole (1967).

The horizontal plane is one of maximum stress obliquity

The assumption used in this research is that the horizontal plane is a direction of zero extension, and sand exhibits coaxility during plastic deformation.

This assumption has been used by Arthur, James and Roscoe (1964) for the earth-pressure test model and by Jewell (1980) applying it to the direct shear apparatus (DSA).

Therefore, taking into consideration that in a standard direct shear test only the boundary shear and vertical displacements are measured, and keeping in mind the fact that the horizontal direction is a direction of zero linear incremental strain (see Jewell (1980) and Jewell and Wroth (1987)),

$$\tan\phi_{ds} = \frac{\tau_{yx}}{\sigma_{yy}} \qquad [2.54]$$

$$\psi = \tan^{-1}\left(\frac{dy}{dx}\right) \qquad [2.55]$$

$$\sin\phi_{ps} = \frac{\tan\phi_{ds} * \frac{1}{\cos\psi}}{1 + \tan\phi_{ds} * \tan\psi} \qquad [2.56]$$

Where:

dy: Vertical displacement;

dx: Horizontal displacement;

τ_{yx}: Shear stress obtained from direct measurement in direct shear apparatus;

σ_{yy}: Vertical stress obtained from direct measurement in direct shear apparatus;

ϕ_{ds}: Direct shear angle of friction;

ϕ_{ps}: Maximum plane strain angle of friction; and

ψ: Angle of dilatancy.

Thus, the assumptions (Jewell and Wroth, 1987), made to analyze the results from a DSA are:

1. There is sufficient uniformity for the deforming sand to be described in terms of a single state of stress and incremental strain;
2. The orientation of the principal axes of stress and incremental strain coincide; and
3. The incremental strains at the peak stress ratio are plastic and there is zero linear incremental strain in the horizontal direction.

Bolton (1986) offered a mathematically simple flow rule (for plane strain), which defines the plane strain angle of friction in terms of relative density and mean stress level,

$$\phi_{ps} - \phi_{cv} = 0.8 * \psi_{\max} = 5 * I_R^{\circ} \quad [2.57]$$

$$I_R = I_D * (10 - \ln p') - 1 \quad [2.58]$$

Where:

ϕ_{cv}: Critical state angle of friction;

I_R: Relative dilatancy index ($0<I_R<4$);

I_D: Relative density; and

p': Mean effective stress at failure.

A clear correlation was obtained from Bolton (1986) between the dilatancy angle and the relative density for different types of sand. Bolton (1986) concluded that for the critical state angle of friction of 31º for Leighton Buzzard sand, the relative density is around 20%, and that the friction angle decreases with decreasing values of relative density. However, this reduction does not continue below 31º for Leighton Buzzard sand.

Finally, Jewell (1989) made a useful analysis of the different approaches to the DSA, showing that equation [2.57] will overestimate the plane strain angle of friction if the angle of dilation obtained by direct shear measurements is under estimated. Moreover, Jewell (1989) showed that the Bolton relationship would overestimate the plain strain angle of friction in highly dilatant soils (around +3°). Therefore, for highly dilatant material, Rowe's (1969) flow rule can be used to obtain a more precise plain strain angle of friction,

$$\frac{\tan \phi_{ds}}{\cos \phi_{cv}} = \tan \phi_{ps} \quad [2.59]$$

Where:

ϕ_{cv}: Critical state angle of friction;

ϕ_{ds}: Direct shear angle of friction; and

ϕ_{ps}: Maximum plane strain angle of friction.

As has been demonstrated, there are several ways to attain important values to analyze the information obtained from the shear box tests. In this case, taking the finding made by Jewell (1989) and explained by Pedley (1990), the best equation to use is the energy correction (flow rule) equation [2.53] obtained by Taylor (1948) and confirmed by Stroud (1971). This equation, together with equation [2.54] and equation [2.55], allow us to obtain the critical state angle of friction (ϕ_{cv}). This, together with the maximum angle of friction, are the design parameters to bear in mind.

2.7.1.2. Bolton's correlation

Houlsby and Psomas (2001) gave special attention to the Bolton (1986) correlation (equation [2.57]). They demonstrated that adding foam to sand allows one to extend Bolton's correlation to void ratios considerably higher than that at the loosest normal state of the sand. In their experiments, they found that foamed sands, at states much looser than the normal loosest state, exhibit angles of friction lower than ϕ_{cv}, which had perhaps been previously envisaged as a lower bound to the friction angle. Mobilized angles of friction, as low as 6º, were measured (Houlsby and Psomas, 2001). Figure 2.27 illustrates this.

2.7.1.3. Interface friction

The study of the interface friction is a multidisciplinary science that encompasses: friction, wear and lubrication. The study of these three factors is known as tribology, and has been defined as the science and technology of interacting surfaces in relative motion and of related subjects and practices (Dietz, 2000).

Different projects have been carried out either by tribology scientists or by soil mechanic engineers in order to understand better interface friction behaviour. Unfortunately, until very recently, soil mechanic literature (Uesugi and Kishida, 1986a) has included some findings by tribology scientists.

Dagnall (1980) classified the different irregularities found in the topography of a solid surface. These irregularities are: roughness, which is inherent in the production process or left by the actual machine agent, waviness, which is the component of topography on which roughness is superimposed (may result from machine or work piece deflection), and vibration or chatter, which is the general shape of the surface.

These previous concepts are of vital importance in the characterization of different surfaces, which can be obtained through the use of appropriate instruments, for example, contact stylus profilometry.

Moreover, attempts have been made to analyze concepts such as friction and wear since the 1950's. Archard (1953), for example, defined the wear equation as:

$$V = \frac{K * N * v_x}{H} \qquad [2.60]$$

Where:

V: Volume of worn material;

K: Coefficient of wear;

N: Normal Load;

ν_x: Sliding distance; and

H: Hardness of worn surface.

Various important issues arise in some of the concepts involved in the previous equations, regarding the analysis of interface friction for soil mechanics. For instance, the friction force is thought to be composed of two parts, adhesion and ploughing. The new concept here is ploughing, which has been found to occur when one of the surfaces is much harder than the other. No further comments will be made about these two concepts in this report. For further details see Dietz (2000).

Finally, it should be noted that the surface material's properties, such as hardness and texture, might change during the abrasive process, for instance, by abrasive particles (embedded within the surface material).

Maan and Broese Van Groenou (1977) measured the force required to plough the wear scars. They found that the asperity angle, surface hardness and normal load were found to be critical in friction and wear.

Regarding the movement of particles relative to surfaces, Fang et al. (1993) demonstrated that the movement of particles consist of rolling and sliding between two horizontal metal faces. Uesugi and Kishida (1986a) and Paikowsky et al. (1995), showed that large particles are more likely to slide on a given surface than smaller particles (which might explain why coarse sands have a higher stress ratio in direct shear interface tests than fine sands).

It is helpful to understand the influence of the roughness of the surface on the frictional coefficient. Therefore, Figure 2.28 shows the effects that steel roughness and sand type have on the frictional coefficients.

Uesugi and Kishida (1986a) postulated that long wavelength surface irregularities do not necessarily have a slope great enough to increase the coefficient of friction. The roughness' concept (R_{max}), used at that time, was the relative height between the highest peak and the lowest trough along a surface profile of 2.5 mm length. They proposed limiting the traverse length to D_{50} in order to measure the roughness of a surface. This also permits the correlation

of the surface roughness to the coefficient of interface friction. Before the change, it was not possible to make the correlation due to the missing particle variable in the evaluation of surface roughness. Also, a normalized roughness, R_n, was defined to correlate the coefficient of interface friction over a wide range of sand diameters (Kishida and Uesugi, 1987). Figure 2.29 shows the definition of R_{max} and R_n. Figures 2.30 and 2.31 show the coefficient of friction and surface roughness for a particle case, before and after the modifications, respectively.

Uesugi et al. (1989) found increases in cumulative interface displacement brought about by cyclic shear increased the interface friction coefficients in smooth surfaces. This was thought to be due to the generation of crushed particles debris, which encounter a given surface rougher than the original particles and, thus, mobilize a higher friction coefficient.

Dietz (2000) made interface tests using an adaptation of a standard direct shear box, known as winged direct shear apparatus (WDSA). Dietz proposed the roughness across the length as the best parameter to be correlated with the peak interface resistance because it is associated with a clear physical meaning (the scale above which the solid surface can be considered planar). Dietz concluded that the operational angle of interface friction represents a better estimation of the operative angle of interface friction occurring in the field. This is because sliding particles of relatively higher hardness than the surface increase the surface roughness in an anisotropic way, due to the ploughing of wear-scars. The rougher the surface, the more likely the particles are to roll and, thus, the dilatancy associated with each traverse increases with the traverse number. In addition, he stated that Jardine et al.'s (1993) conclusions about a constant resistance at large displacement was incorrect as a representative of a critical state because:

1. Interface resistance is not necessarily constant;
2. A constant volume condition is rarely achieved; and
3. The resistance is dependent on the relative roughness between the sand and the surface.

Dietz (2000) carried out different cyclic or reverse interface testing to validate his arguments. Despite the limited data, he observed that an increase in resistance coincides with traverses of the apparatus, which do not trigger dilatancy and are thus associated with particle sliding and consequential ploughing of the surface. Therefore, he proposed a similar correlation to that made by Bolton (1986), but now called a dilatant interface flow rule,

$$\delta_{peak} = \delta_r + 0.8 * \psi \qquad [2.61]$$

Where:

δ_{peak}: Interface angle of friction at peak;

δ_r: Operational angle of interface friction; and

ψ: Angle of dilation.

According to Dietz (2000), the previous relationship can be used to obtain δ_r, without the need of doing the reverse or cycling shear interface tests and obtaining reliable values of δ_{peak} from several tests.

2.7.2. Laboratory tests on conditioners and conditioned soils

Foam

As described in previous sections, foams consist of a particular material that has been used successfully in the tunnelling process.

The parameters that normally define the foam properties are the foam expansion ratio (FER), and the 25% drainage time. These two values are calculated using the Ministry of Defence standard 1995, where the FER is defined as the ratio between the volume of foam to the volume of liquid used to produce the foam and 25% drainage time as the time required for a sample of foam to lose 25% of its initial volume.

These two parameters, plus the foam injection ratio, defined as the ratio of volume of foam to the volume of excavated soil, govern the behaviour of the foam with the soil.

The foam is generated by a machine known as "foam generator", which can vary in size depending on the volume of foam required for the tunnel excavation. Compressed air is mixed with the foaming agent under pressure to produce stable air bubbles with an internal pressure greater than the atmospheric pressure dispersed throughout the liquid. According to Cash and Vine-Lott (1996), small uniformly sized air pores generally result in more stable foam, with the production of a microcellular foam with most pores less than 1 mm in diameter being desirable. Once the foam is added to the excavated ground it becomes part of the grain structure.

The air bubbles in the grain structure lower the density of the earth slurry and reduce the grain friction (Maidl et al., 1995). This allows for better control of the "earth slurry" pressure in the pressure chamber in an EPB machine because of the elastic properties of the "earth slurry" (air bubbles contract or expand according to an increase or decrease of pressure in the chamber).

Protein foams are more stable than synthetic foams as they have longer drainage times, being able to retain the liquid in the bubbles' walls for longer, to maintain strength. However, these are not used very frequently because they require a special handling due to their chemical composition, making them both difficult to work with on site (protein foams have a strong smell) and expensive. Synthetic foams tend to have lower stability due to their relatively rapid drainage time, but this can be increased by the addition of polymers.

Watertight properties in foam are achieved by the addition of polymers, creating a three-phase system (see section 2.6.2). Small amounts of polymers, for instance PHPA at concentrations ranging from 0.1-3% of the foam content, are recommended to increase stability, and stiffness and to add lubrication to the foam properties.

2.7.2.1. Tests conducted with foams

Chemical engineers have studied foam extensively. Some research has been carried out regarding foam solutions. Thomas et al. (1998) presented several methods that can be used to resolve the structure of liquid and solid foams by optical means only. One method is based on confocal imaging while a further two use variants of computerized axial tomography. Magrabi et al. (1999), characterized the bubble size distribution of aqueous foams, produced by a compressed air foam generator. Photographic methods were used to capture the evolution over time of bubble size profiles because such methods are non-intrusive and have the advantage of keeping the cell size distribution unchanged and eliminating any distortion caused by introduced probes. Foam was captured in a cubicle chamber and a CCD video camera, fitted with an objective lens, transferred the bubbles' images to a video recorder. Magrabi et al. (1999) also calculated the drainage time experimentally, using a sonic velocity method, placing two microphones and a speaker in to the foam sample. Moreover, Darton and Sun (1999) studied the effect of different surfactant on foam and froth properties.

Sand and foam

Civil engineers have long been committed to researching mixes of foam and sand, due to the influence of foam in the tunnelling process. Table 2.5 shows influence of foam on the working of an EPB shield.

Quebaud et al. (1998) made several tests to characterize foam (two types of foam and one type of polymer) and samples of foamed sand (two types of silicacous sand and one silicacous aggregate). They conducted tests in foamed sand to check their "plastic fluidity" for which they used the slump tests (assumed a slump value of 12 cm as optimal fluidity), adhesion tests, measuring the friction angle of the mixture on a sloped plate of stainless steel, permeability

tests, using a constant head permeameter (assuming critical values for permeability between 10^{-5} m/s and 10^{-6} m/s), and impregnation tests, using a confining cell to characterize the impregnation depth (simulating the injection process in the head front of a EPB shield). The tests carried out for foam solutions were consistency tests, half-life tests and compressibility tests.

The impregnation behaviour of foam in soils carried out by Quebaud et al. (1998) in a consolidation cell, is the first of such data regarding compressibility of foamed soils. Also tested was the compressibility behaviour of pure foam products, where the foam underwent different pressure changes between 0.1 to 0.4 MPa. Quebaud et al. (1998) concluded that after several compression/decompression cycles, the foam accelerates its drainage time, thus inducing a reduction in foam compressibility.

Quebaud et al. (1998) conducted several permeability tests but could not obtain satisfactory results when the soils were saturated. The fine siliceous sand, tested at different water contents, was not able to achieve permeability lower than 10^{-6} m/s. For the coarse sand, satisfactory permeability was reached when an equal injection ratio of foam, such as those used for optimal slump tests (12 cm optimal fluidity), where used. In addition, Quebaud et al. (1998) concluded that foam which has compound polymers as chains allowed the mixture to reach a permeability value lower than the recommended.

Quebaud's (1998) concluded that regarding the characterization of foam, the generation process is of great importance to the foam quality and that the use of polymers requires special attention (in the case of saturated and granular soils). Quebaud et al.'s (1998) conclusions regarding foamed soil tests are as follows:

1. Foam has a positive influence on the fluidification and lubrication of the mixtures;
2. Foam which does not have an important liquid phase is more appropriate (influence of air bubbles on soil lubrication);
3. Surfactant concentration is not vitally important, demonstrating that the sands react well with foam if the foam waterproofs the soil;
4. The foam was inefficient when the sand was saturated or when its fines content was low; and
5. The incorporation of a viscosifying agent (polymer) seems to help the foam to reach a satisfactory permeability.

Bezuijen and Schaminee (2000) reported on three model tests, in a situation comparable to the work scenario of an EPB shield. The results were compared with a conceptual model, based on results from existing literature, combined with results from earlier research which was carried out in the Netherlands. For the tests, sand-water-foam mixes were used, which were tested to obtain their permeability, compressibility and shear strength. The model was designed to simulate the drilling process of an EPB shield, as well as the removal of the sand-water-foam mixture from the mixing chamber, by means of a screw conveyor. One sand was tested with two different types of foams and another sand, with a different sized grains, was tested with one of the foams mentioned above. The conclusion achieved by Bezuijen and Schaminee (2000) was that changing the grain diameter of the sand seems to have a major influence on the results; The void ratio (therefore porosity as well), of the mix in the mixing chamber is critical for the amount of torque on the rotor; when the void ratio of the mix in the mixing chamber decreases to the maximum void ratio of the sand, the torque on the rotor increases dramatically.

Psomas (2001) evaluated the fundamental soil properties: compressibility, permeability and shear strength of foamed sand. In his research, he used two types of sand (fine and coarse), four types of foaming agents and a specific polymer mixture. He used a 60 mm direct shear box apparatus for the shear strength measurements, the 75 mm Rowe cell apparatus for compressibility and some permeability measurements. Psomas (2001) gives a more extended analysis of results for compression tests made in a 75 mm diameter Rowe cell. He carried out most of the tests in two stages: undrained and drained. The loading process was carried out during both stages, but the unloading process was always carried out in a drained stage. Psomas (2001) observed that foamed soils have significant compression at low vertical stresses (20-40kPa), occurring with the same intensity in undrained or drained conditions. By contrast, when the vertical stress is increased after 50 kPa, most of the compression happens at the drained stage. When mixes of bentonite-foam-polymers-sand were tested, the compression at low vertical stress was very small (smaller than 0.2 mm). In addition, when foam-polymer-sand was tested the compression appeared to occur in both stages, irrespective of the vertical stress. Psomas (2001) highlighted that bentonite/foam/sand mixes require a longer time to consolidate. Furthermore, he observed that foam remains in the soil even after 200 kPa of vertical stress. Psomas (2001) tried to get significant values of void ratio variation through a quality control process. Unfortunately, the comparisons of these values were not consistent. One of the main reasons for this, given by Psomas, was the lack of measurement of gas bubbles expelled with the drained water.

Psomas (2001), calculated the permeability in his experiments by two different methods. First, he obtained a permeability value from the indirect calculation of the results given by Rowe cell tests. Secondly, he used the constant head principle to measure a direct permeability. Unfortunately, the values obtained differ, but it should be highlighted that in the case of direct permeability measurements for foamed soil, values even smaller than 10^{-6} m/s were reached.

Psomas (2001), as Bezuijen and Schaminee (2000), found that for his compressibility tests, the foamed sand prepared with a high foam injection ratio (FIR), retained higher final void ratios than the dry sand (high vertical pressures of around 200kPa). This shows that the gas bubbles were very well integrated with the sand structure, even at high pressures, where the presence of foam bubbles was observed. Also, foamed sand at moderate and high FIR, when sheared, exhibited very low values of shear strength. Psomas (2001) concluded that permeability values of foamed sand mixtures showed a tenfold reduction compared to that of the saturated sand. Psomas (2001) observed that the particle size of the sand plays an important role regarding the fundamental properties of the foamed sand. The results did not appear to be dependent upon the type of foaming agent utilised (they affect just the drainage time). Instead, the FIR appeared to be more important. A mixture of polymer oil mixture was added to some of the foamed fine sand tests and all of the foamed coarse sand tests. The results from the shear box tests can be presented along with Bolton's correlation (1986) in the same graph; where foamed sand lies in a region below Bolton's range.

Kusakabe et al. (1999), Bezuijen et al. (1999) and Maidl (1995) proposed simple equations for foam injection ratio. Unfortunately, these equations take into account just the particle size distribution, without obtaining similar results for any given soil grading (Milligan, 2000).

Vinai (2006) designed and commissioned an EPB screw model, based partly on his experience using the device described later in this thesis, of 1500 mm screw conveyor, coupled to a tank, with an inclination of 30° on the horizontal. The inner diameter of the screw case is 162mm, the flights have a pitch of 100mm and the screw shaft has a 60mm diameter (see Figure 2.32). Although Vinai's screw conveyor is very well instrumented with a vertical displacement transducer, 2 earth pressure cells, 3 pressure cells along the screw and a torque meter, he does not measure the pore water pressure during his tests.

Comparing the results obtained between saturated and conditioned sand, Vinai (2006) discovered the following during his screw conveyor tests: the pressures measured on conditioned sand along the screw case are higher in comparison with the pressures recorded for

the saturated soil. He interpreted this to mean that the screw is properly filled with material and that the pressure in the tank acts along the screw as well; and finally that the conditioned material maintains its workability after the extraction. Vinai (2006) defined the parameter of workability for EPBMs as when the slump of the material is between 16 and 21 cm; the pressures in the tank, for saturated sand, are less homogeneous than on conditioned sand tests; the measured torque is higher with dryer conditioning parameter; the extraction ratio (i.e. the combined effect of plate lowering gradient and extracted weight gradient), is lower or uncontrollable on no conditioned sand; pressures along the screw case are lower and less smooth or higher on no conditioned sands; water content of the wet mix partially decreases during the test, since pressure removes water from the sand pores during the loading step.

Vinai (2006) also points out that the behaviour of cohesionless materials, during the extraction step with screw conveyor, does not fulfil EPB tunnelling requirements. This is because dry sand and dry gravel show higher torque recorded during the whole test (see Figure 2.33), and no conditioned materials show silo effects which would imply a consequent lighter pressure transmitted on the tank floor.

2.7.2.2. Bentonite Slurry

Milligan (2000) described bentonite slurries as lubricants.

Psomas (2001), used some mixes of bentonite-polymers–foam-sand for his research, where he concluded that the excess water in the mix breaks the foam structure and therefore, the real FIR is lower than the initial one prepared from the sand.

2.7.2.3. Polymers

Milligan (2000) mentions that polymers are often added to bentonite slurries used in pipejacking lubrication to enhance their properties. For instance, to reduce fluid loss and improve filter cake formation, small amounts of CMC and PAC polymers, typically less than 0.5%, are added to the slurry, the long chain molecules blocking soil pores to retain the bentonite particles in the filtercake. Merrit and Mair (2001) show the influence of different polymers in the swelling indices of different clays (See Figure 2.34). Quebaud et al. (1998) work with more viscous foams, which were based on surfactants and polymers. According to Quebaud et al. (1998) the more viscous foams did not have any effect on the consistency of the foams. He notes the difficulties of foam generation when polymers are added to the foam surfactant. Psomas (2001) also used some polymer additives in foamed sand mixtures but, unfortunately, the data is insufficient to be able to draw any conclusions.

2.7.3. Other studies on conditioned soils

2.7.3.1. Lubrication in the pipe jacking process

The same products used as soil conditioners in the tunnelling process (EPB shields), behave as a lubricant agent between the pipe and the ground in the pipejacking and microtunnelling process. The type of soil is the main factor in deciding the best lubricant to be used. In the case of unstable ground, saturated sands for instance, the lubricant must provide a support to the tunnel and, therefore, prevent its collapse. As a result, a lubricant that can form a filter cake around the pipe (soil interface), is suitable for this function.

The introduction of this lubricant in the soil interface decreases the operational cost of the projects, for instance, by decreasing the number of intermediate jacking stations and reducing the size of thrust system, due to the decrease in the jacking forces.

Milligan (2000) provides a summary of the various advantages of using lubrication in the pipejacking process. Milligan's recommendations, and the data presented before by Marshall (1998), represent most of the work already carried out regarding lubrication in the pipe jacking process.

The research carried out by Marshall in 1998, consisted of the collection of information on jacking loads and stresses at the pipe-soil interface. He investigated four different schemes in different ground conditions: London clay, dense fine sand below the water table, stiff glacial till and soft alluvial clay. Marshall (1998) distinguishes three different patterns of behaviour, illustrated in Figure 2.35. It is important to highlight that all the pipes used were concrete pipes, the lubricant agents were bentonite slurries, and that measure of consistency, quality and volume of the bentonite slurry were not taken in Marshall's research (Marshall, 1998).

The effectiveness of the bentonite slurry lubricant is shown in Table 2.2, for different soil types. Values of over 50% reductions in friction are observed for cohesionless soils.

Xavier Borghi and Robert Mair are carrying out a study of pipejacking forces in cohesive soils under lubricated conditions in the University of Cambridge. A load cell pressuremeter has been designed to be used in pipejacking lubrication tests (Borghi, 2002).

2.7.3.2. Clay and foam

Merritt (2004) presented an experimental investigation of soil conditioning for clays, and of the mechanics of a model EPB screw conveyor, operating with clay soils (see Figure 2.36). The dimensions of the screws used by Merritt (2004) are:

- Total screw length 1200 mm (both screws);
- Screw shaft diameter 43 mm (both screws);
- Screw flight diameter 102 mm (both screws);
- Radial flight-casing clearance 3 mm (both screws);
- Screw flight thickness 5 mm (both screws);
- Screw pitch average 80 (screw 1) and 133 (screw 2); and
- Flight helix angle 13.9° (screw 1) and 22.9° (screw 2).

Merritt (2004) also carried out many index tests, to investigate the effects of foam and polymer conditioning treatments on the undrained strength of London Clay samples. He suggested optimum ranges of treatments for London Clay. Merritt's EPB screw conveyor was a 1:10 scale model. He measured, with varying soil properties and conveyor operating conditions, the soil flow rates, the pressure gradients and casing shear stresses along the conveyor, and the screw torque during tests on consolidated kaolin and compacted conditioned natural clay soil.

Merritt (2004) found that the screw torque was constant, and the casing shear stress and total pressure gradient were constant along the conveyor, during a steady state conveyor operation with a constant soil flow rate. He also found, that the total pressure gradient is influenced by conveyor operating conditions, including the sample pressure, the discharge outlet restriction, the screw speed, and the screw pitch. He showed results where, depending on the operating conditions and the soil strength, the total pressure can increase or decrease along the conveyor. One of Merritt's findings was that the screw torque is proportional to the casing shear stress, however, he does not mention the direction of the casing shear stress. He also concluded that conditioning natural clay soils with polymers and foams, to form a soft plastic paste, allowed controlled operation of the screw conveyor, with uniform soil flow rates and pressure gradients. Finally, he presented a theoretical model which describes the screw conveyor operation. He found a close agreement between the predictions of the theoretical model and the measured pressure gradients and torques from the model screw conveyor tests.

Merritt (2004) carried out a thorough analysis of the geometry and the forces acting on the soil material in the screw. Merritt's theoretical model is developed for a single flighted screw of constant pitch and channel depth, assumed to fit closely inside the conveyor, so that the radial

clearance between the screw flight and the casing is neglected. The geometry of the screw conveyor, used by Merritt (2004) is defined in Figure 2.37. The axes systems used in the analysis are also defined in Figure 2.37. The (x, y) axes refers to the directions parallel and perpendicular to the screw axis. The (l, w) axes refers to the directions parallel and perpendicular to the screw flight. The dimensions shown in Figure 2.37, used by Merritt (2004), are:

- e, flight thickness;
- ϕ_f, flight helix angle;
- t, screw pitch;
- h, channel depth;
- D_s, shaft diameter; and
- D_f, flight diameter.

The helix angle of the screw represents the angle of the flight, with respect to the perpendicular of the screw axis, as shown in Figure 2.37. Merritt developed his theoretical model starting with considering the motion of an element of soil in the channel of the screw conveyor. He assumed that the screw channel is completely filled, with the soil in contact with the casing surface, the screw shaft and the two flight surfaces. The soil is assumed to flow along the screw channel like a plug. The direction of soil movement along the conveyor is variable, depending on the shear stresses acting on the soil plug and the conveyor operating conditions. As the screw rotates, the soil plug flows along the screw channel, moving relative to the casing and the screw. Figure 2.38, illustrates the motion of the screw and an element of the soil plug, viewed in plan at the top of the screw channel. As the screw rotates, point 'A' at the top of the flight moves tangentially, relative to the casing, in the direction perpendicular to the screw axis, represented by the velocity vector, V_{sy}. Point 'A' also moves relative to the soil plug in the direction parallel to the screw flight, represented by the vector V_{sl}. The soil plug moves relative to the casing at an angle, θ, to the direction of the tangential screw flight velocity, represented by the vector, V_{pc}. The soil also has a velocity component in the direction parallel to the screw axis, represented by the vector, V_{px}.

The angle, θ, represents the direction of soil flow relative to the tangential velocity of the screw flight at the casing surface. The angle of soil flow is variable, depending on the movement of the soil along the channel as the screw rotates, as determined by the shear stresses acting on the soil plug. The movement of soil in the axial direction is controlled by the angle, θ, determining the flow rate along the conveyor. Merritt (2004) establishes that:

- The minimum value of θ is zero, when the soil does not flow along the conveyor and is jammed in the screw channel;
- The maximum value of θ for controlled flow is $(90 - \phi_f)$, when the soil moves perpendicular to the screw flight; and
- Values of θ greater than $(90 - \phi_f)$ imply that the velocity of the soil along the screw channel, V_{sl}, is greater than the velocity of the screw relative to the casing, V_{sy}. In this case, the soil flows along the screw channel faster than the rotation of the screw.

From the velocity vector triangle shown in Figure 2.38, Merritt (2004) defines all the velocities. The magnitude of the vector, V_{sy}, at the top of the screw flight is known from the rotational speed of the screw, N, in rotations per second (i.e. rpm/60):

$$V_{sy} = \pi * D_f * N \quad [2.62]$$

$$V_{pc} = \frac{V_{sy} * \sin\phi_f}{\sin(\theta + \phi_f)} \quad [2.63]$$

$$V_{px} = V_{pc} * \sin\theta \quad [2.64]$$

Merritt (2004) pointed out that the angle, θ, defines the direction of the shear stress acting between the soil and the casing, which influences the pressure gradient along the conveyor and the torque to rotate the screw.

Merritt (2004) also analysed the forces acting on the soil. He neglected the weight of the soil in his analysis. He assumed that:

1. The shear stresses were uniformly distributed over shear surfaces formed at the interfaces of the soil and the screw channel surfaces;
2. The shear stresses were constant along the length of the conveyor casing;
3. Existed undrained shearing conditions; and
4. The soil volume remained constant in the conveyor (no drainage boundaries).

The forces taken into account in Merritt's analysis are shown by the free body diagram in Figure 2.39. A passive pressure is applied normal to the flight surface pushing on the soil, and the relative movement between the soil and the screw channel generates shear stresses acting on the surfaces of the soil plug. The shear stresses between the soil and the screw surfaces resist the movement along the screw channel. The shear stress between the soil and the casing surface provides a force component that causes the soil to flow along the screw channel, and generates a pressure gradient along the conveyor. As the screw rotates, the forces acting on the soil plug cause it to flow down the screw channel, and generate a pressure gradient along

the conveyor and a torque to rotate the screw. The definitions gave by Merritt (2004) about these forces are:

- F_{cs} is the force due to the shear stress on the casing, acting on the surface cdef;
- F_{cn} is the normal force acting on the surface cdef, due to the total pressure acting on the conveyor casing;
- F_{ss} is the force due to the shear stress on the screw shaft, acting on the surface abgh;
- F_{sn} is the normal force acting on the surface abgh, due to the total pressure acting on the screw shaft;
- F_{ps} is the force due to the shear stress on the screw flight pushing on the soil, acting on the surface abcd;
- F_{pn} is the force due to the passive pressure applied by the screw flight pushing on the soil. This force acts normal to the surface abcd in the direction of the w-axis;
- F_{ts} is the force due to the shear stress on the trailing screw flight, acting on the surface efgh;
- F_{tn} is the force, due to the active pressure, acting on the surface efgh in contact with the trailing screw flight. This force acts normal to the flight surface in the direction of the w-axis; and
- F_{pl} is the resultant of the forces Fp and Fp+dP acting normal to the surfaces adeh and bcfg, respectively. Fpl represents the force due to the change of total pressure over the length of the element, dL.

Merritt (2004) used the free body diagram (Figure 2.39) to develop his theoretical model.

2.7.4. Soil conditioning in EPB shields

In section 2.5.3 a practical analysis of the forces experienced by the EPB machines was described and the frictional forces to be overcome by the machine were shown. A qualitative analysis of the force needed to have a stable face was made in the same section. Further analysis of the forces acting in the EPB machines will not be done in this research. For a deeper analysis of the different models used, the literature of Jancsecz and Steiner (1994), and Anagnostou and Kovari (1996) might be of interest.

Taking into account the description of the forces made in previous sections, it is easy to get an idea of the benefit of using additives, either as conditioner or lubricant, in an EPB machine.

The EPB shield uses conditioners to extend its application to different types of ground and to generate the appropriate "earth slurry" to control the pressure on the excavation. The pressure

is controlled by the stabilization of the face, water tightness and pressure dissipation in the screw conveyor.

In general, the use of conditioners permits the adjustment of soil conditions to suit the machine, rather than adapting the machine to the ground conditions.

Thus, conditioners affect some soil properties in the head chamber of an EPB machine, which are of vital importance for the best operation of the EPB machine. Such properties are: permeability, which controls the pressure gradient between the face and the screw conveyor and the friction in the head chamber (decreasing torque (Maidl, 1995); compressibility, which allows for small differences between the excavated soil and discharged soil volume without resulting in great differences in pressure in the head chamber; rheological properties, which characterize the flow of material even when it is subjected to low shear stress (Milligan, 2000 and Maidl, 1995); and adhesion, which does not present a problem in cohesionless soils, but can be a problem in cohesive soils, increasing the wear of the cutting tools as well as increasing the torque needed for the excavation.

The aim, therefore, is to create a soft and compressible soil mass of low permeability with suitable flow properties and low shear strength.

Steiner (1996) and Janscecz (1997) realized that particle size distribution alone is not sufficient to determine the needs of soil conditioning of a fine-grained soil. A more effective approach requires looking at the type of soil, the plastic limits and the natural water content.

Milligan (2000) summarizes the different application of soil conditioning in tunnelling machines and the use of soil conditioning in EPB machines. See Tables 2.3 and 2.4, respectively.

The different conditioners have been described in previous sections. However, it is important to highlight that in practice, a shift from bentonite slurry to foam and polymer conditioners is occurring, avoiding expensive spoil handling (always bearing in mind the insitu properties of the soil).

Reports have been published on the use of soil conditioning in the EPB tunnelling process, for instance Peron and Marcheselli (1994), Williamson et al. (1999), Herrenknecht and Maidl (1995) and Webb and Breeds (1997). All these are based on practical cases where, so far, conditioning in the tunnelling process has succeeded.

2.8. Summary

This Chapter illustrated the principal areas related to tunnelling and soils, giving a broad idea of the technical background behind the research. The complexity of soil conditioning and lubrication in the tunnelling process were discussed.

The following topics were addressed:

1. Important concepts relating to the research were explained, such as bubble properties, surface tension and soil strength;
2. Shear tests, compressibility tests and their most common methods and apparatus were explained;
3. The evolution of tunnelling over the last few decades, together with the main features of EPBM, such as, its advantages, the operational principle, ground conditions, control of parameters and screw conveyor were explained;
4. A description of the main conditioners used in the tunnelling industry was given; and
5. An overview was offered of previous work carried out on conditioners and conditioned soils, highlighting the work developed by Quebaud et al. (1998) and Psomas (2001), as the pioneers working to identify the properties of foam-sand mixes according to standard methods.

Chapter 3. Sand and conditioner properties

3.1. Introduction

This Chapter describes the sands and sand conditioners used during this research. The Chapter presents the voids ratio and particle size distribution of Leighton Buzzard (L.B.) fine sand, L.B. graded sand, L.B. coarse sand, L.B. medium coarse sand, Thanet sand and Garside sand. The Chapter also reports the foam expansion ratio (FER) and drainage time properties of Versa foam, Foamex TR, Foamex EC, SLF20, CLB F4, T-7and Polyfoamer MCB foam conditioners. The properties of polymer conditioners such as Drillam MV, MEYCO® Fix SLF P1, MEYCO® Fix SLF P2 and TFA34 are also described.

Furthermore this Chapter presents the results of slump and flow cone index tests on conditioned sands. An attempt to study the drainage time of the foam conditioners mixed with sand is also reported in this Chapter. The results obtained are analyzed focusing on the FER and drainage time of the different foam conditioners and on the slump behaviour of the foam and polymer conditioners when mixed with sand. This analysis is used to draw some conclusions regarding the behaviour of the sand mixed with foam or polymer conditioners.

3.2. Sands tested

Six types of sand were used at different stages of this research. Slump and flow cone index tests described later in this chapter were carried out on conditioned L.B. fine sand, L.B. graded sand, L.B. coarse sand and Thanet sand. These sands were also used for shear box tests which are discussed in Chapter 4. The properties of L.B. medium coarse sand used to study the drainage time of foam conditioners when mixed with sand are also discussed. In compressibility tests (Chapter 5), L.B. fine sand and Thanet sand were used. Finally for the screw conveyor tests Thanet sand, L.B. fine sand and Garside sand were used.

The properties of the sands tested in this research are discussed below.

3.2.1. Leighton Buzzard sands

Leighton Buzzard sand has previously been used by Psomas (2001) in order to study the behaviour of sand conditioned with foam under shear and compression. In order to deepen the understanding of foam conditioner when mixed with sand, the same sand types used by Psomas (2001) were used in this research. However, to widen this understanding a new sand, L.B. graded sand, was also used.

The maximum (e_{max}) and minimum (e_{min}) voids ratios of L.B. fine sand and L.B. coarse sand are taken from Psomas (2001). The maximum and minimum density tests, described by Head (1992) and British standard BS1377 (BSI, 1975) were carried out for L.B. graded sand.

A fourth L.B. sand, L.B. medium coarse sand, was also used to study the stability of foam when mixed with sand. The maximum and minimum density tests were also carried out for this type of sand.

In general L.B. sands have silica content (SiO_3) higher than 91%. The L.B. sands were supplied by SIBELCO MINERALS AND CHEMICALS LTD (SIBELCO, 1999, 2001a, 2001b and 2001c). The product name for L.B. fine sand is L.B. DA 80F SAND, it has a light cream colour and a low sphericity/sub angular to sub rounded grain shape. The product name for L.B. coarse sand is L.B. DA 14/25. This has a brown colour and an angular grain shape. L.B. graded sand was created from a mix of three different L.B. sands. The sands used are L.B. fine sand, L.B. medium coarse sand and L.B. DA 8/16 sand. The product name for L.B. medium coarse sand is L.B. DA 1 COS SAND. It has a dark brown colour and a medium sphericity/sub rounded grain shape, while L.B. DA 8/16 sand has also a brown colour and a medium sphericity/sub rounded grain shape.

Figure 3.1 shows the grading curve of L.B. fine sand, L.B. coarse sand, L.B. graded sand and L.B. medium coarse sand. L.B. fine sand has grain sizes between 60 μm and 300 μm. L.B. graded sand has grain sizes between 60 μm and 2 mm. L.B. coarse sand has grain sizes between 60 μm and 1.2 mm. L.B. medium coarse has grain sizes between 200 μm and 1.2 mm. Table 3.1 shows the characteristic sizes of L.B. sands d_{10} (nominal effective size), d_{20}, d_{50} (modal size), d_{60} and U_c (uniformity coefficient = d_{60}/d_{10}). The voids ratio values used for L.B. fine sand, L.B. graded sand and L.B. coarse sand in this research are shown in Table 3.2 (ASTM D4254-00, Method C).

3.2.2. Thanet sand

The Thanet sand was donated by Nishimatsu- Cementation Skanska Joint Venture and came from the Channel Tunnel Rail-Link (CTRL) project. The behaviour of Thanet sand when mixed with five commercial foaming agents and four polymer agents was examined. The examination included mainly slump index test, shear and compressibility tests.

In general Thanet sand can be described as very dense, grey silty fine sand. The samples of Thanet sand were obtained from the Graham Road (GR) and Stratford Box (SB) shafts

excavated for the CTRL project. At these locations, the Thanet sand lies at depths of around 24.2 to 37.8 m. During the geotechnical investigation for the CTRL project boreholes were drilled at these sites and laboratory tests were carried out on Thanet sand. At different depths, together with the Thanet sand formation, irregular lenses of clay and gravel were found. Table 3.3 details the characteristic grain size and percentage of particle sizes at different depths for different boreholes. The first two characters in the sample column indicates Thanet sand, the second two characters are the acronyms for the shaft (where the sample was taken from), the characters before the "D" denotes the borehole number used to take the sample and the numbers after the "D" indicates the depth at which the sample of Thanet sand was taken from. Table 3.3 indicates that the Thanet sand used for this research consists essentially of fine sand particles. The fines content (silt and clay together) varied between 5% and 52%, showing a slight tendency to increase with depth. Four grading curves have been selected as representative of the different particle distributions found on site. Figure 3.2 shows these curves. Thanet sand has around 90% of Quartz and Feldspar content. The assessed values of permeability for Thanet sand are between 1 x 10^{-7} m/s to 5 x 10^{-5} m/s (CTRL, 1997).

The samples taken from the CTRL site were collected in plastic bags and sealed to retain the natural moisture content of the Thanet sand.

Once the Thanet sand arrived at Oxford University, samples were taken from different Thanet sand bags to determine its moisture content. The moisture content of the samples was around 11.85% with a standard deviation of 1.2. Moreover from the Thanet sand bags several samples were taken to estimate the percentage of particles of size smaller than 2 mm, between 2mm and 29 mm, and higher than 29 mm. It was estimated that there was a 10.4%, in weight, of particles between 2mm and 29 mm in dry Thanet sand.

3.2.3. Garside sand

Garside sand was selected in order to test the Oxford Screw Conveyor model with a coarser sand than Thanet and L.B. fine sands, but also to use MAPEI Polyfoamer MCB foaming agent with a sand of a similar characteristics to one to be used in a tunnelling project at Politecnico di Torino. The tests on this sand were carried out with assistance from Raffaele Vinai, a visiting student from the Politecnico di Torino.

Garside sand has a uniform gradation with a sub angular to rounded grain shape. Its composition is mainly Quartz (thus it is a silica sand). The brand name is GARSIDE 16/30 yellow. It was supplied by Garside Sands – Aggregate Industries. Figure 3.3 shows the grading

curve and Table 3.2 shows the maximum density, minimum density, minimum voids ratio and maximum voids ratio of Garside sand.

3.3. Conditioners

Eight foaming agents and four polymer agents were used in this research. All of them were used in conditioner index tests but only some were used for conditioned sand index tests, shear box tests on conditioned sand, compressibility tests on conditioned sand and screw conveyor tests on conditioned sand. Commercial conditioners were used, thus their chemical composition is not publicly available. The basic properties of conditioner agents used in this research stated by their suppliers are mentioned below.

3.3.1. Foaming agents

Eight foaming agents were used in the foam index tests. All were used in conditioned sand index tests and six in shear box tests. Just one of these foaming agents had been used for compressibility tests on conditioned sand. The screw conveyor tests were carried out on conditioned sands with two different foaming agents. Table 3.4 shows the properties of the foaming agents. All these foaming agents were liquid solutions based on anionic surfactants or glycol with some containing polymer additives. In general the chemical composition of foaming agents was tailored to achieve different properties for conditioning different types of soil.

Versa foam is recommended to be used for fresh or saltwater drilling, and is said to reduce water consumption with lubricating properties improving penetration rates (CETCO, 2002).

FOAMEX TR is recommended for use in all type of soils, even in very permeable soils. It is said to reduce the internal angle of friction of soil particles and also to minimize the interface friction between the metallic parts of the earth pressure balance shield and the soil particles (LAMBERTI, 2002). FOAMEX EC can also be applied to all type of soils and due to its natural polymer additive it is said to have a high mechanical resistance and excellent "lubricity power" (LAMBERTI, 2002). Although it is not clear precisely what is meant by that term, presumably it indicates that the conditioner would serve as a lubricant.

Polyfoamer MCB can be used with all type of soils to enhance the overall tunnelling performance, reducing the friction (between soil particles) and the interface friction (between soil particles and the metallic parts of the shield) during excavation (MAPEI, 2004). Foamer 300 can be applied in most soft ground conditions minimizing the friction of particles on the metallic part of the shield (MAPEI, 2004).

Unfortunately no information was available from KAO CORPORATION for T-7.

CLB F4 is said to be compatible with all kind of ground and ensures water-proofing, and particularly, preventing free water flow in the screw conveyor of an earth pressure balance machine (CONDAT, 1999).

MEYCO® Fix SLF 20 is said to be suitable for soft ground. It also lowers friction and abrasiveness at the cutter head through the screw conveyor and conveyor (MBT, 2004).

All these foaming agents are said to be environmentally friendly, containing no substance hazardous to the environment. Thus there is no restriction in their use for environmental reasons.

3.3.2. Polymer agents

Four polymer agents were used for conditioned sand index tests. Table 3.5 shows the properties of the polymer agents.

DRILLAM MV is a partially hydrolised poly-acrylamide (PHPA) synthetic polymer with excellent cuttings carrying capacity and inhibition of hydratable formations (water adsorption) (LAMBERTI, 2002).

TFA 34 it is also a PHPA polymer product, it is said to viscosify conditioned soils and reduce sticking of soils to steel surfaces.

MEYCO® Fix SLF P1 is a lubricating polymer generally used where the water content in the soil increases and foam alone is inadequate to modify the soil properties. It is said to be especially developed to bind water and fine particles, improving the cohesion of the soil (MBT, 2004).

MEYCO® Fix SLF P2 is a soil structuring polymer used in coarse sands. It is said to have good anti-segregation properties. It is recommended for soft ground tunnelling (MBT, 2004).

All these polymer agents are environmentally friendly and can be injected into excavated soils as water based solutions or as additives in foam solutions.

3.4. Index testing: apparatus, methods and results

The apparatus and methods used for index tests on foaming agents and conditioned sands are described in the next sections. The results obtained from these tests are also presented.

3.4.1. Foam generator

The foam generator built by Psomas (2001) was used during this research to produce foam for foam index tests, conditioned sand index tests and the conditioned sand used in the shear box, compressibility and screw conveyor tests.

The foaming agent was mixed with water in a bucket to achieve a total foam solution of around 7 litres (see Figure 3.4). Then the foam solution was poured inside the tank through the relief valve. Once the entire foam solution had been poured inside the tank the relief valve was closed and the tank pressurized. During this research the pressure in the tank was applied using a nitrogen (oxygen free) bottle. The tank was always pressurized to 800 kPa but the gas line pressure varies according to the type of experiments for which foam was needed. The gas line pressure was either 300 kPa or 350 kPa. The detail of the pressures used in the gas line is given in the following sections.

3.4.1.1. Bubble sizes

Different attempts were carried out to establish the size of the bubbles in the foam produced by the foam generator using Versa foam. The first two attempts were undertaken to test different arrangements looking at light disposition and foam containers.

The first of the attempts was made collecting foam in a plastic container and a picture was taken (birds eye view) with a Nikon D1X digital camera. The key factor here was that the foam was exposed to free air, which did not apply any external pressure to the foam surface. The second attempt was made using two platens of transparent acrylic separated by two spacers of 0.254 mm diameter and photographing with a SONY DKC-ID1 digital camera. During this attempt elastic bands were used around the acrylic platens to fix the position of the platen and also apply a constant pressure to the foam. The foam was placed between the acrylic platens and a picture was taken from above.

Finally some attempts were made to record the image of a mixture of L.B. fine sand and Versa foam. This was made using a commercial scanner. The sand was mixed by hand with Versa foam. The mixture was placed on the scanner screen so an image could be acquired.

A commentary on the images obtained from all these attempts is given in the following section.

Bubble images

The foam obtained using the set-up previously described looks like ordinary "shaving foam" (see Figure 3.5 (a)).

Two different attempts were made to test the different arrangements looking at light disposition and foam containers.

The best image was obtained when the foam was exposed to a free surface air (first attempt), which did not apply any pressure to the foam surface, is shown in Figure 3.5 (b). In the second attempt, using two acrylic plates and two spacers in order to create a constant gap between the plates, one the best images obtained is shown in Figure 3.5 (c).

In both attempts, it is possible to obtain the biggest bubble size by simple inspection. In the first attempt the biggest size was 0.5 mm and at the second attempt 1 mm. The second attempt gave a value double to that of the first, this was caused by the foam being forced between the two plates thus compressing the bubbles to half their free dimension (see Figure 3.5 (b)).

Finally Figure 3.5 (d) shows an image of L.B. fine sand and Versa foam acquired from the scanner. From the image the shape of grains and the plateau borders of structure of the foam can be identified. Unfortunately this image is not of a good enough quality to identify clearly the boundaries between the foam and the sand grains.

The size of the bubbles is extremely important, as the size of the bubbles may have a direct impact on the behaviour of the sand under shear stress. Therefore by measuring the size of the bubbles it may be possible to establish a correlation between them and the size of the sand grains, thus a good image of the size of the bubbles is vital. Unfortunately in order to achieve this, deeper work in this area needs to be carried out to establish a better arrangement which improves the image of the bubble size acquisition. Detailed research of the image analysis process and different techniques to improve the acquisition of foam and sand foam images are beyond the scope of this research, and the results shown here are just general guides for future research.

3.4.2. Foam index tests

The foaming agents were characterized by two index tests. The first test involved measuring the foam expansion ratio (FER), which is the ratio between the volumes of foam in a drainage pan

to the volume of foam solution. Say, for example, the weight of collected foam in a drainage pan of 1600 ml volume is 200 grams. Since 1 gram of foam solution is approximately 1 ml, the total foam solution contained in the foam sample is 200 ml. The FER is thus calculated as 1600 divided by 200 to give a result of 8. Figure 3.6 shows the brass drainage pan used for the FER tests. This pan fulfils the requirements of the Ministry of Defence Standard 42-40/Issue 1. It has a volume of 1600 ml and a glass valve with a bore, for drainage, of 1.6 mm diameter. The brass drainage pan has a total weight of approximately 2698 g. The second test is intended to give an index of the stability of the foam. This test is performed using the same brass drainage pan described previously. Dividing the weight of the foam sample by 4 gives the 25% volume, in ml, of solution contained in the foam. The time required in minutes for this volume of foam solution to drain from the aerated foam is referred to as the 25% drainage time. The 50% drainage time was also measured.

Most of the foaming agents tested in this research were of interest mainly because they were evaluated as possible conditioners for The Channel Tunnel Rail-Link (CTRL) project where Nishimatsu- Cementation Skanska Joint Venture was the contractors. The exceptions are Versa foam, Polyfoamer MCB and Foamer 300. Versa foam was selected as the original conditioner used for this research and Polyfoamer MCB and Foamer 300 are foaming agents used in a project carried out at Politecnico di Torino by Raffaele Vinai, who was a visiting student at Oxford during 2004.

The concentrations of the foaming agents were selected following the manufacturers recommendations for granular soils and the requirements set by Nishimatsu- Cementation Skanska Joint Venture.

3.4.2.1. Foam expansion ratio (FER)

The foam generator used to produce foam is described in section 3.4.1. Using Versa foam (2 % concentration), it was noted that the FER of any foam produced varied with the level of liquid within the tank. Figure 3.7 shows how the FER obtained for Versa foam, at different pressure settings in the foam generator (liquid and gas) increases as the level in the tank decreases. Observing these results it was decided to use foam produced between the 6.5 litre and 2.5 litre level in the foam generator tank. In this way, the use of foam that might be too dense (above 6.5 litre level, excess of liquid) or too weak (below 2.5 litre level, excess of gas) would be avoided. The best pressure setting for Versa foam, where foam with most stable FER was produced along the tank level, together with a FER production higher than 13 was produced, was proffered to be 8 bar liquid pressure and 3 bar gas pressure. Figure 3.8 shows 4 tests, with

average FER, between 6.5 litre and 2.5 litre tank level, of 15 ± 0.8. This set up, for Versa foam, was used in conditioned L.B. sand during shear box, compressibility tests and screw conveyor tests. This set up was not varied during these tests.

As was mentioned at the beginning of section 3.4.2, there was an interest to study the properties of certain foaming agents as conditioners for the CTRL project by Nishimatsu-Cementation Skanska Joint Venture. Bearing this in mind, the foam generator was set up for the best foam generation condition achieved when T7 was used. Using T7 at 1% concentration, the Oxford foam generator was set so that foam with an expansion ratio around 16.6 ± 1.1 was obtained. This was achieved with a pressure of 8 bar on the liquid side and 3.5 bar on the gas. The other foaming agents that appear in Table 3.6 (at different concentrations) were tested with the same pressures of 8 bar on the liquid side and 3.5 bar on the gas.

Figure 3.9 (a) shows the FER values for each foaming agent at different concentrations. The red lines on the middle of the bars are the standard deviation for the FERs calculated. All the foaming agents showed FER values higher than 10, except MEYCO® Fix SLF20 which could not produce foam due to the hardness of the water (concentration of calcium and magnesium ions; calcium carbonate concentration higher than 60 mg/l) in Oxford. Hard water makes the foaming agent's active components inactive. CLB F4 and T7 showed FERs higher than 15 for concentrations higher than 2%, and Foamex TR showed FER higher than 15 at concentration higher than 1%. The decrease in FER for T7 when the concentration increased from 1% to 1.5% was not normal. Rather, an increase in FER was expected. However, the FER difference at these two concentrations was no higher than 5 units in the worse case, thus the FER for T7 at a concentration between 1% and 1.5% could be assumed to be around 15.2. In general, with the exception of T7, all the foaming agents showed an increase of FER when the concentration increased (see Figure 3.9 (b)). It is interesting to observe that the increase in FER is not linear with the increase of concentration and also that the presence of polymer components in the foaming agents does not imply a higher FER than a foaming agent without polymer compounds (see Polyfoamer MCB and Foamer EC).

The foaming agents produced foams with different expansion ratios over different ranges of concentration. These measurements indicate that different foaming agents have varying behaviour in regard to the foam generation, with some foaming agents producing a high FER at low concentrations, and others producing a low FER at low concentrations. This is believed to result from the varying effects of the foaming agents on the surface tension of the solutions. The specific chemical compositions of the foaming agents, containing different surfactants at

varying concentrations as well as other additives, determines their influence on the surface tension of the solutions.

3.4.2.2. Drainage time

Figure 3.10 shows as an example, for T7 at 1% concentration, the type of results obtained for the variation of the percentage (in volume) of foam liquid in the brass pan at different FER during the drainage time test. In Figure 3.10 it can be observed that samples with high FER show a slightly higher percentage of volume retained inside the brass pan than samples with low FER at the beginning of the test. This difference decreases with time, achieving almost equal values at the end of the test, this is observed in all of the foaming agents. This behaviour was expected due to samples with low FER having a higher liquid content than samples with higher FER, thus the liquid runs faster out from the brass pan, but when almost all the liquid has been drained out just "dry foam" remains inside the brass pan, therefore the curves of foam liquid in the brass pan converge.

Table 3.6 shows the 25% drainage time (t_{25}) and the 50% drainage time (t_{50}) values measured for different foaming agents at different concentrations. Figure 3.11 shows the 25% drainage time, 50% drainage time and its standard variation for each foaming agent. It is clear that CLB F4 was by far the foaming agent with the longest drainage times. It had a 50% drainage time of at least four times the maximum 50% drainage time achieved with any other foaming agents tested (T7, Foamer 300, Polyfoamer MCB, Foamer TR, Foamer EC, Versa foam, MEYCO® Fix SLF20). All of which showed 50% drainage time less than 10 minutes. In general increasing the concentrations of the foaming agents increased the stability of the foam produced. Thus higher drainage times (25% and 50%) were obtained at a higher concentration for a specific foaming agent. Polyfoamer MCB and Foamer EC contain a polymer to improve stability but it did not show a higher drainage time than any other of foaming agents tested. In fact Polyfoamer MCB had a 50% drainage time at 1.5% concentration of 6 minutes, the lowest measured for all the foaming agents.

3.4.3. Conditioned sand index test

Prior to any test being carried out, it was necessary to produce the mixture of conditioned sand. The foam was mixed with sand in a Multi-flow mixer (see Figure 3.12) of 14 litres maximum capacity supplied by ELE International. The Multi-flow mixer has 4 blades. Two blades are fixed and the other two can rotate. One of the rotating blades is placed almost in the centre of the drum and has six vanes on its shaft; the other is a side scraper blade. All the blades together allow the materials (sand and conditioners) to be homogeneously mixed in about 1 minute. A known mass of sand was placed in the Multi-flow mixer. This was mixed with a known volume

of water. At this early stage the mixture sand-water was mixed by the Multi-flow mixer. When the sand was homogeneously mixed with water, the Multi-flow mixer was stopped and the mixture was pressed down in the drum of Multi-flow mixer in order to release any trapped air in the sand-water mix. Then, a known volume of foam or polymer was added to the volume of sand-water in the drum. The volume of foam added to the drum divided by the volume of soil (sand-water mixture) in the drum is called foam injection ratio (FIR) and the volume of polymer added to the drum divided the volume of soil (sand-water mixture) in the drum is called polymer injection ratio (PIR). The foam produced by the foam generator was collected by an acrylic plunger device. Two acrylic plungers were built of 1 and 0.4 litres each. Figure 3.13 shows the two plungers used during testing.

Conditioned sand was characterized mainly by two types of test, the slump and flow cone tests but also a special drainage time test was carried out on conditioned sand.

3.4.3.1. Slump test

Different sand-water-foam or sand-water-polymer mixtures were tested to study the influence of water content, FIR and PIR on the consistency of conditioned sand, and also their effect in the plastic fluidity of the conditioned sand. When the mixture of sand and conditioner was homogeneously mixed, the slump cone (British Standard 1881: Part 102 and ASTM C 143/C 143M) was filled up with the prepared mixture. The mixture of sand and conditioner was placed and compacted by rodding it into a mould shaped as the frustum of a cone (see Figure 3.14). The mould must be filled up in three layers, each one approximately one third the volume of the mould. Each layer must be rodded with approximately 25 strokes of the tamping rod, uniformly distributed over the cross section of the layer. After the three layers of conditioned sand have been placed and tamped inside the mould, it is raised and the mixture allowed to subside. The vertical distance between the original and the displaced position of the centre of the top surface of the mixture was measured and reported as the "slump" of the conditioned sand. A removable collar was added to the top part of the mould in order to avoid an excess of the mixture, at the end of the filling up process, falling on the table and disturbing the free movement when the mould was raised.

A standard terminology is used throughout this Chapter to identify the "plastic fluidity" of the conditioned sand according to the measurement of its slump. This terminology is given in Table 3.7 (Quebaud, 1996). Although no definition for the term "plastic fluidity" is given in the standards, it is defined for this research as the ease of flowing of a plastic fluid.

First of all, the slump results from the series of tests on Thanet sand conditioned with four different foaming agents at different concentrations and four different polymers also at different concentrations are shown. Finally, the results from a series of tests carried out on L.B. sands conditioned with Versa foam at 2% concentration are shown.

Thanet sand

Firstly, a series of seven mixing tests were made to evaluate the mixing behaviour of Thanet sand (at different initial water contents) with T7 foaming agent at 1.5% concentration (but with different foam injection ratios (FIR)). A water content of 22% (water content of Thanet sand before soil conditioner was applied, w_{sandw}) and FIR between 44.5 and 55.6 % produced a good quality of foam sand mixture. This was based on visual inspections for that particular foaming agent at that particular concentration. Mixtures using lower initial water content values together with lower FIR were very dry, and homogeneous mixtures between foam and sand could not be obtained. In these types of mixtures the foaming agent disappears into the sand structure. The values of w_{sandw}=22% and FIR between 44.5 and 55.6%, produced plastic mixtures that, under simple visual inspection, had a homogeneous composition, and a clear presence of foam in the sand structure.

Secondly, because the polymer injection ratio (PIR) required to obtain a suitable mixture with Thanet sand was unknown, it was necessary to perform three tests at three different PIR under the same concentration. These tests were carried out for MEYCO® Fix SLFP1 and MEYCO® Fix SLFP2. After this, a PIR of 17.2% was chosen as the maximum PIR to be tested with the other two polymers agents. The chemical composition of TFA34 and DRILLAM MV differed from SLFP1 and SLFP2, the first two being partially hydrolysed poly-acrylamide products (PHPA), increasing viscosity and reducing fluid loss, which worked better with sand when their concentration in water was near to 0.1%. Nevertheless, due to Nishimatsu- Cementation Skanska Joint Venture's own interest, higher concentrations were also tested.

Thirdly, water under an injection ratio of 17.2% was added to Thanet sand (the same volume as used for polymers) in order to observe the behaviour of Thanet sand conditioned just with water at the same ratio used for the polymer gents.

Finally, using the previous values four different foaming agents, four different polymer agents and water alone were tested. The results are shown in Table 3.8.

Table 3.8 shows the data for the mixtures used in the slump tests on conditioned Thanet sand. The natural water content (w_{thanet}) in the Thanet sand used during these tests was 10.35% or

13.14% depending of the batch of Thanet sand used. The total mass of Thanet sand and water in the mixing drum ($M_{totaldrum}$) was 12 kg and the water content of this mixture (w_{sandw}) was 22%. The last three columns in Table 3.8 report the volume of conditioner used (foam and polymer) in the mixture, the injection ratios of the conditioners used (FIR, PIR and water injection ratio) and the slump obtained in mm.

Most of the foamed Thanet sand tests showed a very plastic slump (between 100 and 150 mm), with Foamex TR and CLB F4 at 1.5% concentration and FIR 55.6% showed a fluid slump (over 160 mm); and CLB F4 at 1.5% concentration and FIR 36% showed a firm slump (below 50 mm) (see Figure 3.15 (a)). The plastic fluidity terminology according to slump range used in Table 3.7 has been shown in four zones in Figure 3.15 (a). The grey colour represents the firm slump zone, the green colour represents the plastic slump zone, the cyan colour represents the very plastic slump zone and the blue colour represents the fluid slump zone.

Polymers MEYCO® Fix SLF P1 and SLF P2, at PIR of 13.8% and 17.2% (for the given concentration) also showed very plastic slump behaviour. Increasing the PIR over 17.2% will imply fluid slump behaviour of the mixture (see Figure 3.15 (a)). DRILLAM MV can be applied at a concentration as low as 0.025% where its mixture with Thanet sand results in a very plastic slump (see Figure 3.15 (b)). Due to the similarity of the chemical composition between TFA34 and DRILLAM MV, it can be concluded that TFA34 might reach fluid slump if it is used at 0.025% concentration (see Figure 3.15 (b)).

Adding only water to Thanet sand generates a fluid slump (see Table 3.8), which is not optimum for operation in an earth pressure balance machine (EPBM). However, adding conditioners to Thanet sand an optimum mixture, in the plastic zone, for operation in an EPBM might be achieved

Leighton Buzzard sands

Following the experience from the slump tests on conditioned Thanet sand, it was decided to undertake further slump tests to determine the FIR, concentration of Versa foam and water content that produces mixtures suitable for EPBM operation (slump in the plastic zone). A total of 26 tests were carried out. Figure 3.16 shows six pictures of slump tests carried out on L.B. sands. The 26 slump test results are shown in Table 3.9. In this table, the relevant mixing values are also shown. W_{sandw} is the water content of the mixture L.B. sand and water before foam is added to the mix. W_{drum} is the water content of the foam water L.B. sand mixture after the foam has been added.

Figure 3.17 (a) shows how conditioned L.B. fine sand at water content of 26.7% (w_{sandw}), conditioned L.B. graded sand at water content of 15.8% (w_{sandw}) and conditioned L.B. coarse sand at water content of 6% (w_{sandw}) increased in slump when the FIR increased. However in Figure 3.17 (b) a point can be observed, for conditioned L.B. coarse sand, where high FIR together with high water content (w_{drum}) produced a very low slump value. This is due to drainage of foam from the mixture due to the high water content. Figure 3.17 (b) shows the values of the slump obtained during the tests next to the symbols in the graph. The size of the symbols varies according to the maximum measured slump value. The biggest symbol is for 240 mm of slump, obtained for conditioned L.B. coarse sand, and the size of symbol of the smallest slump, 25 mm for L.B. coarse sand, is scaled with respect to the highest slump measured (240 mm).

Although the drainage of foam due to high water content in the mixture was observed just in the case of tests carried out on L.B. coarse sand, it was expected that all types of sand would have a limiting water content, which when exceeded would cause the sand to behave in similar manner as conditioned L.B. coarse sand. This water content limit, at which the drainage of foam from the mixture starts increases in value as the content of fines in the sand increases. This behaviour has been quantitatively graphed and it is shown in Figure 3.18. The diagonal red line is the drainage limit line. Conditioned sand mixtures with a combination of values of water content and FIR that fall above this drainage limit line have a small slump due to the drainage of foam from the mixtures. Conditioned sand mixtures with a combination of values of water content and FIR that fall below this drainage limit line present decreasing slump values moving in diagonal lines to the left, going from a fluid slump zones (above 160 mm) to firm slump zones (lower than 50 mm). For sands with different contents of fines the drainage limit moves upwards when the content of fines increases. As can be seen from Figure 3.17, the values of slumps for the three different conditioned L.B. sands increase, from left to right, within the same type of sand. Thus it can be concluded that the attempt to establish a general behaviour of sands under slump tests, as the one shown in Figure 3.18, is unique for a specific type of sand with a specific granulometry.

3.4.3.2. Flow cone test

One minute before introducing the sand conditioned mixture inside the flow cone (see Figure 3.19), it was moistened by filling the cone with water. Before introducing the sand conditioned mixture, the water was allowed to drain from the cone. The discharge tube was plugged by a rubber stopper and the mixture of sand and conditioner was placed inside the cone (see the American Society for Testing and Materials Standard C 939). The cone was filled until the

conditioned sand mixture made contact with the level indicators. The times were recorded from the remove of the stopper till the first break in the continuous flow of conditioned sand mixture from the discharge tube. To evaluate if the flow cone test was applicable when measuring the efflux of sand conditioned mixture, the top of the cone was examined; if the sand conditioned mixture had passed sufficiently (i.e. light was visible through the discharge tube), the time indicated by the stop watch was noted as the time of efflux of the sand conditioned mixture. If this was not the case, the flow cone test was deemed not applicable for conditioned sand of this consistency.

The flow cone test was first calibrated with water. The cone was filled up with water and the time the water took to discharge from the cone was the time of efflux of water. This time must be 8 ± 0.2 seconds for 1725 ± 5 ml of volume of water inside the flow cone.

Flow cone tests were carried out on conditioned Thanet sand.

Thanet sand

None of the mixes on conditioned Thanet sand would flow through the flow cone apparatus, so that it was not possible to measure the time for flow. Thus the Flow cone test could not be used as an index test on conditioned Thanet sand.

3.4.3.3. Special drainage time test

In an attempt to study the influence of the sand in the stability of the foam, tests were carried out where sand and foaming agents were mixed and the drainage time required for a quarter and half of the volume of foam solution to drain from the aerated sand foam mixture was measured. This test was carried out with the sand foam mixture at atmospheric pressure and also under higher pressure than atmospheric. The devices used for both tests are shown in Figure 3.20 and Figure 3.21 respectively. The first device (Figure 3.20) consisted of a funnel, equipped with a plug and a tube of 6 mm internal diameter, 95 mm length and with 211 holes on its wall of 0.5 mm diameter. From these holes the liquid drained from the conditioned sand. The liquid drained out the funnel towards a stopcock at the bottom of the funnel. The stopcock (opening of 2 mm diameter) controlled the flow of the liquid towards a measuring cylinder. For the second device (see Figure 3.21), the smallest of the acrylic plungers was modified (see Figure 3.13). Its piston was turned around and a tube of 2.5 mm internal diameter, with holes bored through of half a millimetres, and length of 200 mm (inside the container) was placed inside of the acrylic container. The total number of holes for draining totalled 120. The tube was connected to an on-off valve with an opening 4 mm in diameter. On top of the piston, at the time of testing, a dead weight was placed (see Figure 3.21 (c)).

In both tests the mixing of sand and foaming agent was done by hand. The sand used for all these tests was L.B. medium coarse sand. In general a known volume of sand was poured into a graduated cylinder. It was weighted and after this the sand was poured into a bigger container where it was mixed with a known volume of foam. After this the mixture was placed either in the funnel device or in the acrylic container. For the first type of test, between 160 and 170 grams of sand was used. A very high foam injection ratio, between 400% and 600%, was used for the mixtures in order to have some drainage of liquid. In the second test, 2 kg and 4 kg of dead weights were used. Thus the pressures on the mixture were 12.6 kPa and 25.7 kPa respectively. In order to reduce the friction of the piston on the walls, both the container and the piston were greased. For each test a volume of 40 ml of sand was mixed with 200 ml of foam.

Conditioned sand at atmospheric pressure

Table 3.10 shows the results of the tests carried out using the funnel apparatus shown in Figure 3.20. Figure 3.22 shows drainage times (25% and 50%) of foam alone (Figure 3.22 (a)), conditioned L.B. medium coarse sand at 500% FIR (Figure 3.22 (b)) and conditioned L.B. medium coarse sand at 600% FIR (Figure 3.22 (c)). CLB F4 shows the highest drainage times (25% and 50%) in all the tests. When the FIR increases to 500%, CLB F4 increases its drainage time twofold, achieving a value of around 35 min. T7 and Versa foam show drainage time values lower than 10 minutes at FIR of 500% and 600%. These values are higher than the ones obtained when foam alone is tested. They showed an increase by a factor of about 1.5 of the value obtained on foam alone. The increase in concentration from 1.5% to 5% did not show a major increase in drainage time for Polyfoamer MCB, showing a 50% drainage time value around 10 minutes.

Figure 3.23 shows the drainage time variation for Versa foam, at 2% concentration, and T7, at 1.5% concentration, for different FIR. Null percentage of FIR is when the foam was tested in the apparatus without any sand. For both foaming agents (Figure 3.23 (a) and (b)) it can be observed that the drainage times (25% and 50%) decrease when the FIR increases from 400% to 500%. At 25% drainage time (t_{25}) a 12.5% maximum decrease was measured for Versa foam and 23.7% maximum decrease was measured for T7. For 50% drainage time the differences increases, measuring a 21.16% decrease for Versa foam and a 26.5% decrease for T7.

The previous phenomenon may be due to that at FIR of 400% the FER used for the foam was 11.5% higher than when the test was carried out at FIR of 500% for Versa foam, and the FER for T7 at FIR 400% was 16.4% higher that the FER for T7 at FIR 500% (see Table 3.10).

The fact that sand absorbed some of the foam liquid when it was mixed with foam (to wet the surface of its grains) has not been studied or taken into account in the drainage time measurements. This phenomenon will increase the drainage time, and needs to be further investigated.

Conditioned sand under pressure

Table 3.11 shows the results of the tests carried out using the device shown in Figure 3.21. A total of 14 tests where carried out, seven tests were carried out for Versa foam at 2% concentration and seven tests were carried out for CLB F4 at 1.5% concentration. The FIR was 500% for all the tests.

The aim of this test was to verify if the difference between CLB F4 and Versa foam would still remain under pressure, or if the behaviour of the foaming agents would change under pressure. Observing Figure 3.24 it is clear that the two pressures applied did not change the behaviour of the foams in the conditioned sand regarding the drainage time. CLB F4 showed higher drainage times (25% and 50%), although the FER for the tests carried out with this foaming agent were lower than for the tests carried out with Versa foam.

During testing, several difficulties were faced. First of all it was difficult to overcome the air gap between the mix and the piston. Secondly the friction between the piston and the pan walls is not constant, because during the tests some sand grains became stuck to the piston walls. Thus the pressure on the conditioned L.B. medium coarse sand was not constant. Finally, the fact that a small container was used, in order to apply a relatively small dead weight meant that a small amount of foam was also added to the sand, consequently little liquid was present in the conditioned sand. Thus a small variation of liquid flow could perturb the results.

It was observed during the tests that the pressure applied seemed to push out the foam from the pores of the sample. Therefore it was difficult to obtain a liquid drainage rather than a foam flow through the pipe. This migration of fluid through the soil voids was also recognized in field monitoring systems on construction sites, recording the increase of the pore pressure in front of the tunnelling machine when it is approaching.

3.5. Summary

This Chapter reported the sands and conditioners properties that were used during this research.

Section 3.2 described the different type of sands used in this research. The distribution of the size of grains, the maximum density and minimum density given for the L.B. fine sand, L.B. coarse sand, L.B. graded sand, L.B. medium coarse sand, Garside sand and Thanet sand

Section 3.3 describes the conditioners used in this research. Eight foaming agents were described here, Versa foam, Foamex TR, Foamex EC, Polyfoamer MCB, Foamer 300, T7, CLB F4 and MEYCO® Fix SLF 20. Four polymers were described, DRILLAM MV, TFA 34, MEYCO® Fix SLF P1 and MEYCO® Fix SLF P2.

Section 3.4 reported the apparatus, methods and results for index tests. First of all, a description of the foam generator used in this research together with a brief description of an acrylic plate arrangement used to estimate the size of the bubbles produced by the foam generator was given. The bubbles images obtained with the different arrangement described in sub section 3.4.1.1 were discussed. Bubbles of 0.5 mm in diameter maximum were observed.

Secondly, subsection 3.4.2 describes the devices used for the measurement of the foam expansion ratio and drainage time of foam. The FER and drainage time results obtained for the 7 foams mentioned previously were also presented in this subsection. A FER of around 15 ± 0.8 for Versa foam at 8 bar liquid pressure and 3 bar gas pressure in the foam generator was obtained. A series of tests carried out on all the foaming agents mentioned in section 3.3 gave measurements of FER between 12.5 and 19 at 8 bar liquid pressure and 3.5 bar gas pressure in the foam generator. In general it was also observed that FER increases when the foaming agent concentration is increased. The differences in FER values between the foaming agents, which were tested at different concentrations, were believed to result from the varying effects of the foaming agents on the surface tension of the solutions. The specific chemical compositions of the foaming agents, containing different surfactants at varying concentrations as well as other additives, determines their influence on the surface tension of the solutions.

Most of the foaming agents show 50% drainage time between 6 and 8 minutes, except for CLB F4 which shows 50% drainage time between 30 and 38 minutes at different concentrations. Foaming agents with a polymer as one of its compounds to improve its stability did not show a much higher drainage time than foaming agents which did not have a polymer compound.

Finally, in subsection 3.4.3 the testing equipment used for the index test on conditioned sand was described. The description of the devices used for the slump tests and flow cone tests was detailed. Furthermore, the procedure and apparatus used to measure the special drainage time

of foam on conditioned sand were described. In this subsection were also presented the results of the index tests for conditioned sands. Slump tests, drainage time tests and flow cone tests results were described. Slump tests on conditioned Thanet sand using different foams varied between 40 and 200 mm. Slump tests on conditioned Thanet sand using polymers varied between 40 and 215 mm. In general for T7 (1.5% concentration), CLB F4 (1.5% concentration), Foamex TR (1.5% concentration) and Foamex EC (2.5% concentration) using FIR of 45% and a sand water content of around 22% produced slumps in the very plastic zone which are suitable for EPBM operations. Slumps in the very plastic zone can also be obtained using MEYCO® Fix SFL P1 and P2 at concentrations between 0.5 and 1% with PIRs between 14 and 17%. For DRILLAM MV and TFA 34 with a PIR of 17.2% at concentrations between 0.025 and 0.05%, slumps in the very plastic zone can be obtained. For conditioned L.B sands the slump range, using Versa foam as a foam conditioner, varied between 0 to 240 mm at different FIRs.

Versa foam at 2% concentration at an average FER of around 13.5 was used for the slump tests on conditioned L.B. sands. Slumps in the very plastic zone for conditioned L.B. fine sand can be obtained at water content between 20 and 27% with a FIR between 20 and 22%. For conditioned L.B. coarse sand the very plastic zone can be achieved using sand with a water content around 6% and a FIR around 3%. In the case of conditioned L.B. graded sand a slump in the very plastic zone was achieved using at a water content of 15.8% and a FIR of 12%.

In general the slump increased with an increase in FIR and water content, reaching a limit, which is call the drainage limit, after which, due to the excessive water content in the conditioned sand, the foam is drained out of the mixture producing a very firm slump. All sands show the same behaviour, but with varying drainage limits according to their content of fines. A higher content of fines in the sand increases the drainage limit, thus also the water content at which this occurs.

The drainage time tests carried out on conditioned L.B. medium coarse sand, either at atmospheric pressure or under pressure show no change in the stability of the foam, CLB F4 being recording the longest drainage times.

In the end, with these tests, the study of the properties of the conditioners and sands used in this research was successfully completed. The results obtained here were used to select the conditioned sand mixtures for testing in the shear box apparatus, compressibility apparatus and Oxford screw conveyor apparatus.

Chapter 4. Shear box tests

4.1. Introduction

This Chapter describes the modifications made to a medium size shear box apparatus (MSSA) at Oxford University. The Chapter also discusses the shear box tests results on Leighton Buzzard (L.B.) fine sand, L.B. graded sand, L.B. coarse sand, and Thanet sand mixed with foam conditioners. The apparatus, instrumentation and methodology used during testing are discussed here.

In the last section of this Chapter an analysis of the results is carried out focusing on effective stress, shear stress, pore pressure and angle of friction. This analysis is used to draw some conclusions, regarding the behaviour of the sand mixed with foam conditioners and the effect of the foam conditioners on the angle of friction of the sand-water-foam mixtures.

4.2. Shear box apparatus

The MSSA has two halves (top half and bottom half) and a loading platen.

The bottom half is formed by two parts. A bottom part built of duralumin and acrylic, and a top part built of acrylic (Jewell, 1980). The bottom part has internal dimensions of 254 mm length, 155 mm width and 76 mm height. The bottom part has a layer of sand paper on its base to avoid the movement of particles of sand on it. The top part is a tank with internal dimensions of 380 mm length, 234 mm of width and 134 mm height. Figure 4.1 shows a schematic drawing of the shear box.

The top half is formed by an acrylic-duralumin body with two steel arms. Each arm is placed on one side of the top half. The internal dimensions of the acrylic-duralumin part are 254 mm length, 155 mm width and a maximum height of 131 mm (including a 10 mm gap for the strip of sponge placed between the two halves of the shear box. The strip of sponge is described in next sections). Thus the maximum initial size of a sample is 254mm length, 207 mm height and 155 mm width.

The loading platen is built of stainless steel and has a layer of sand paper on the surface that makes contact with the soil sample. The dimensions of the loading platen are 252 mm length, 154 mm width and 21 mm thickness.

As in most standard shear box apparatuses (Jewell, 1980), the vertical load during testing was originally applied by dead weights. Unfortunately, this system was not able to cope with the

large compression of the sample consisting of sand water foam mixtures. Furthermore, the interest in the study of the shear stress in the sand-water-foam mixtures made it necessary to avoid material escaping from the shear band of the shear box apparatus; which would occur in a normal shear box apparatus. Thus a series of modifications were carried out to allow the MSSA to cope with the large compression of a sand-water-foam mixture and assure that the sand-water-foam mixture did not drain from the shear band zone.

The most important modifications will be described in the next sections.

4.2.1. Shear box modifications

4.2.1.1. Loading platen

Originally (Jewell, 1980) the vertical load on the shear box was applied by dead weights. The original system does not work for samples that exhibit large compression behaviour. At large compressions the loading arm crashes with the shear box structure which makes impossible to complete the test. In this research the loading platen was modified in such a way that a constant vertical load could be applied to the samples that showed large compression behaviour.

Four steel rods were added to the top part of the platen. They slide on four clamps, which were used to fix the platen to the top half of the shear box apparatus even when large initial compression of the sand-water-foam mixture occurred. The rods were fixed to the top platen (see Figure 4.2). Each clamp has a hole in one side to allow for insertion of the rods, allowing the clamp to slide on the rod whilst fixing its position on the rod through the means of a locking system (see Figure 4.2 (a)). At the other side of the clamp two screws pass through, allowing the permanent fixing of the loading platen with the shear box top half. The top half of the shear box and the loading platen were clamped together when the constant vertical load had already been applied to the sample. At this point the four clamps were slid on the loading platen rods and the screws of the clamps were secured to the top half of the shear box. The locking system of the clamps was tightening so that the loading platen, clamps and top half of the shear box become one body (see Figure 4.3, where the top parts are clamped together during a test).

A linear slide way (see Figure 4.2 (b)) was also added on top of the loading plate to smooth the horizontal movement of the top part of the shear box during testing, while a vertical constant force was applied on top of the sample. Figure 4.4 shows the linear slide way, load cell and hydraulic ram. The linear slide way was fixed to the loading platen by two screws. Platen 2 was fixed on top of the linear slide way by four screws. Platen 2, the linear slide way and loading

platen were fixed together as a one body. Platen 1, screw 1 and the load cell were fixed to the ram. When the sample sand water foam mixture was placed inside of the shear box and the loading platen (with the linear side way and Platen 2) placed on top of the sample. The hydraulic ram shown in Figure 4.4 was lowered (together with Platen 1, screw 1 and load cell) till Platen 1 and Platen 2 made contact. When the platens made contact they were bolted together so that the loading platen, Platen 1, Platen 2, load cell and ram move together as one unit. This assures that the entire system can only assume one position under the ram, ensuring 100% repeatability.

The loading platen had also been adapted with an eight 5 mm diameter holes in order to allow liquids to drain during the testing. Furthermore, a wire mesh of 0.08 mm aperture was placed between the sand paper and the loading platen to avoid soil particles escaping from the apparatus. The sand paper was glued on top of the wire cloth layer. This drainage system is the only drain that the shear box apparatus has. It is assumed that the properties of the sand-water-foam mixture in the shear band zone are kept constant, although the drain holes are through the loading platen.

4.2.1.2. Hydraulic system

The force applied by the ram, is generated by a hydraulic system which is shown is Figure 4.5. The hydraulic circuit is shown in Figure 4.6. The accumulator (Bosch HY/AB 10/330 C5, 10 litre nominal volume and 330 bar maximum working pressure) is fed by the hydraulic pump (ENERPAC BPN 20000 series, 7.5 litre reservoir, 240 volt motor, Output volume 0.65 – 5.4 l/min, Oil pressure range 60-700 bar and manual valve operation). When enough oil is put in the accumulator the hydraulic pump is stopped and a Nitrogen bottle pressurises the accumulator to the desired pressure point, to achieve the vertical stress under which the shear box test will be carried out. The Nitrogen bottle, accumulator, in line pressure reducing valve and three port two way valve are connected to the ram during shear box testing (red line in Figure 4.6). When the shear box test has ended, the Nitrogen bottle and the accumulator are isolated from the system and the hydraulic pump together with ball valve 2 are connected to the system to retract the ram (blue line in Figure 4.6).

4.2.1.3. Strips of sponge and metal channels

Sponge

The strips of sponge are placed between the two halves of the shear box apparatus in order to contain the soil mixes inside the box and to allow vertical movement of the upper part of the

shear box during testing. Four sponge strips were added between the top half and bottom half of the shear box apparatus.

The sponge is commercially called "economy sponge" which was supplied by a company call PRIORY FOAM.

The sponge strips are named here by their length. This aids in the description of the strips of sponge used during the research.

The longest strips together with one of the shortest ones (see Figure 4.7 (a)) were placed in the bottom half of the shear box, and the second shortest strips were placed in the upper half of the shear box (see Figure 4.7 (b)). The sponges were glued using Araldite®, a commercial adhesive. The longest strips have a dimension of 308 mm length and 25 mm width, and the shortest strips have dimensions of 154 mm length and 25 mm width. Strips of sponge of 11.6 mm thickness were glued in the shear box apparatus, however, due to a chemical reaction between the adhesive and the sponge material, a final thickness of 10 mm was measured in the shear box apparatus.

Metal channels

Four steel stiff channels were placed over the sponges in order to protect them from wear and tear during testing. Furthermore they increase the strength of the sponge in the gap under high vertical stress avoiding bending of the strips and prevent the soil mix from escaping.

The dimensions of these stiff steel channels are shown in Figure 4.7 (c). The steel shims were bent at the broken lines, shown in Figure 4.7 (c), forming a right angle. Two longer channels were put together by gluing the shorter sides forming a channel with a "T" shape. The shorter channels that were used are shown in Figure 4.7 (c), which will be called "L" shape channels. Two "T" shape and two "L" shape channels are placed over the strip of the sponge in the shear box apparatus. The thickness of the metal shim was 0.1 mm.

4.2.1.4. Sealing system

Cling-film is used to seal the gap in the middle part of the shear box apparatus between the top and bottom half in order to assure that the sand-water-foam mixtures did not escape from the shear band of the shear box apparatus.

The cling film is placed inside the shear box apparatus as an impermeable layer covering the entire gap between the top half and bottom half of the shear box (see Figure 4.8). Cling-film is

also used on the top of the box to seal the space between the loading platen and the walls of the shear box apparatus.

A layer of grease (see Figure 4.8) was placed between both sides of the cling-film inside the shear box apparatus to decrease the friction of the soil mix with the walls of the shear box apparatus during testing.

4.2.1.5. Stopper system

The stopper system ensured that the samples were always vertically loaded at their centre, which coincides with the centre of gravity of the shear box apparatus.

The system consisted of two horizontal stoppers and a pin roll holder. The horizontal stoppers are used to keep the shear box in position before shear is induced. The holder kept the pin roll in position before the test started, the holder and stoppers are taken away just before the shear box test started. Figure 4.9 shows the stoppers and holder.

4.2.2. Shear box instrumentation

The shear box apparatus had been instrumented to monitor the vertical stress, shear stress, pore water pressure, vertical displacement and horizontal displacement during the experiments. The details and calibration of the various instruments and the data logging system are discussed in the following sections.

4.2.2.1. Vertical stress

The vertical stress was measured by a load cell placed between the ram and Platen 1 (see Figure 4.4). A 1000 kg force "z" shaped load cell was also used. The load cell was attached to the ram using a standard threaded bolt inserted into the load cell. The load cell was also attached to Platen 1 using a bolt which fitted a threaded hole at the bottom of the load cell.

The load cell (Maywood Instruments Limited U4000, range 1000 kgf and full scale output without amplification of 3.024mV/V) was calibrated using an Instron Machine. Its response was linear with a calibration factor of -0.6563 kN/V (output voltage from signal conditioner, see next sections).

Vertical force carried by sponge-metal channels system

A study of the compression behaviour of the sponge under loading was carried out in order to establish the vertical load carried by the sponge during a shear box test. The result of the study is shown in Figure 4.10 (a), which shows exponential compression behaviour of the sponge with

increasing loads. However, when the behaviour of the sponge between 0 kN and 0.1 kN is magnified, Figure 4.10 (b), an elastic behaviour is observed till approximately 0.5 mm of compression of the strip of sponge. In general a densification process of the sponge started around 7.24 mm of compression.

The previous results were related to the friction force produced during the shear box testing at a specific compression of the strip of sponge. Figure 4.11 shows the friction vertical load ratio for three different vertical loads. The friction is around 21.25% of the vertical load applied on the sponge and metal channels in MSSA. Thus knowing the compression of the strip of sponge, the vertical force carried by the sponge-metal channels system was determined (see Figure 4.10). With this load the friction value could be calculated, and the shear load measured during the shear box test could be corrected in order to obtain the real shear load needed to shear the sand-water-foam mixture during testing.

4.2.2.2. Pore pressure

One pore water pressure transducer was used in the shear box apparatus. The pore water pressure transducer is a Druck transducer PDCR 1810 with maximum pressure range of 0.35 bar gauge. The pore water pressure transducer was connected to the bottom half of the shear box apparatus. The calibration of the pore water pressure transducer was carried out in-situ. The shear box was filled with water at different levels while the readings from the pore water pressure transducer were recorded. The linear calibration factor of the pore water pressure transducer was of 24.422 kPa/V.

On the bottom of the shear box apparatus (and the top of the pore water pressure transducer) there was a recess where a Vyon ® filter was placed. This Vyon ® was previously saturated with de-aired water and installed flush with the shear box apparatus base bottom half so it did not disturb the sample when it was fixed into place. The Vyon ® allowed the water pressure to be measured at the bottom of the sample inside the shear box apparatus, avoiding the grains of soil touching the active face of the transducer.

4.2.2.3. Vertical displacement

The vertical displacement was measured by two RDP electronic LVDT D5/200 AG (with spring return armature and range ± 5 mm). The transducers were placed on top of the shear box top half. They were placed at opposite sides from the vertical axis of the shear box apparatus, in order to calculate an average value of the compression of the sample during testing. The left

vertical displacement transducer is shown in position in Figure 4.3. A calibration factor of 1.0033 mm/V was obtained for the left side transducer and 1.8042 mm/V for the right side transducer.

The vertical displacement transducers were attached to one of the two steel rods (see Figure 4.7) and were placed in front and behind of the shear box apparatus. As the top half of the shear box apparatus moved vertically it pushed the displacement transducer strokes reading the vertical displacement of the mixture in the shear box during testing.

4.2.2.4. Horizontal displacement

The horizontal displacement was measured by RDP electronic LVDT's ACT/2000 A (with spring return armature and range ± 50 mm). The transducer was clamped to the top part of the bench of the shear box apparatus (see Figure 4.5). The transducer follows the movement of the bottom half of the shear box apparatus which is pushed by a rod, activated by a drive unit (geared motor), at the left hand side of the shear box apparatus (see Figure 4.5). A calibration factor of -2.5595 mm/V was obtained. The horizontal displacement transducers can be seen in Figure 4.5.

The speed of shearing selected in the drive unit was 2 mm/min. This was the maximum speed that could be achieved by the drive unit arrangement.

4.2.2.5. Shear load

The shear stress was measured by a load cell placed at the right hand side of the MSSA (see Figure 4.5). A 10 kN force "z" shape load cell was used. The load cell was attached to a clamp fixed to the shear box bench. The load cell (Maywood Instruments Limited U4000, range 10 kN and full scale output without amplification 3 mV/V) was calibrated using an Instron Machine. Its response was linear with a calibration factor of -0.7065 kN/V.

4.2.2.6. Data-logging system

The data acquisition system is formed by System Windows 2000, Dell Pentium II (r) Processor. Additionally, a computer board PCI-DAS1200 (8 differential channels) with an analogue input section had been installed. The board had a resolution of 12bit, input of programmable ranges (±10V, ±5V, ±1.25, etc.) and a through out of 330 kHz (330000 samples per second).

In order to read the data from the computer board, it was necessary to install a signal conditioner. This transforms the signals from the instruments to signals of a magnitude readable

by the computer board. The system used was an RDP-electronics Module 600 housing with 3 DC, 2 AC panels (each panel with two channels) with one power supply.

4.3. Experimental results from shear box tests

A total of 38 tests were carried out using the MSSA described in the previous sections. Four types of sand were used in the MSSA. Ten tests using Thanet sand and foam, two tests on saturated Thanet sand, nine tests on L.B. fine sand and foam, eleven tests on L.B. coarse sand and foam and six tests on L.B. graded sand. The sands are described in Chapter 3. The foams used were CETCO Versa foam for L.B. sands and KAO T-7, CONDAT F4, FOAMEX TR and FOAMEX EC for Thanet sand. The foam properties and description are given in Chapter 3.

The selection of the foams for Thanet sand was made by Nishimatsu- Cementation Skanska Joint Venture. The Thanet sand was donated from one of its tunnelling site in the Channel Tunnel Rail-Link (CTRL) project. The concentrations of the foaming agents were selected following the fabricant's recommendations for granular soils and the requirements set by Nishimatsu- Cementation Skanska Joint Venture.

The selection of three types of L.B. sands for the shear box tests were made with the aim of to increase our understanding of the behaviour of foam conditioners with sand with different grain size distributions.

The materials (sand, water and foam) used for the tests were mixed in a small drum. The sand in its natural state was normally mixed with water and foam to produce enough mix to fill up the MSSA. The mixed materials were poured inside. The sealing system was around the two halves of the MSSA when the mixed material was poured inside the MSSA, in order that no liquid or foam could escape the MSSA. When the MSSA was filled up to the desired height the cling-film on the top half of the MSSA was folded on top of the sample, then the loading platen was put in position on top of the sample. A layer of grease was placed on the internal walls of the MSSA, before the mixed material was placed in it, to decrease the friction. With the mixed material inside the MSSA and the loading platen in position the lowering of the ram starts when Platen 1 and Platen 2 make contact. When this occurred both platens were bolted together and a constant pressure was applied on top of the sample. When the desired vertical load on top of the sample was achieved the loading platen was clamped to the top half of the MSSA. After this the lifting screws (Figure 4.9 shows the lifting screw at the right hand side of the MSSA, there is another lifting screw at the left hand side of the MSSA) were removed and an initial compression of the sample inside MSSA occurred. When the initial compression had achieved a stable value, the horizontal shear of the mixture started (at a rate of 2 mm/min).

4.3.1. Quality control process

A quality control process for the mixtures during all the stages of the mixture preparation and testing was carried out. Figure 4.12 shows a basic scheme, where the different measurements of the quality control process are pointed out. The figure also shows the different stages within the quality control process.

Figure 4.12 together with Tables 4.1, 4.2, 4.3 and 4.4 give the detailed information about the measurements carried out during the quality control process. In Figure 4.12 and in Tables 4.1, 4.2, 4.3 and 4.4 the light green, pink, light blue backgrounds identify the 3 main zones where the quality control process was carried out. The light green area is the zone before the drum where the water, foam and soil were individually measured in the laboratory. The pink area is the drum zone, where the water-foam- soil mixture was weighed and sampled. Finally the light blue zone is the shear box, were the mixtures were sampled at different stages and the water expelled from the test was measured.

The first measurements carried out were:

1. The FER (foam expansion ratio);
2. The mass of soil (dry), M_s;
3. The volume of water, V_w;
4. The volume of foam, V_f; and
5. The mass foam, M_f.

The first measurement made was of the water added to the sand in the drum. The mix was weighed after the water was added. Also the FER of the foam added to the sand was measured by weighing every batch of foam that was added to the mixture. The FER used to produce the mixtures that was to be tested in the MSSA was around 14 with a variation of ±6 between tests.

Once these measurements were carried out, the water, foam and soil were thoroughly mixed in the drum. For all tests, except the test carried out on Thanet sand, the samples (M_{sd}) were taken before the mixture in the drum were weighed (see Tables 4.1. to 4.4). From the mixture of water-foam-soil in the drum measurements were recorded following the parameters below:

1. The weighed mass of water-soil in drum, M_{ws};
2. The weighed mass water-foam-soil in drum, M_{fs};
3. The water content in drum, w_{drum};
4. The mass sample of mixture from drum, M_{msd}; and

5. The mass sample of dry soil from drum, M_{dsd}.

Furthermore the foamed sand remaining within the drum (which was not added to the MSSA), was weighed. The measurements carried out from foamed sand remaining in the drum were:

1. The mass of reminder mixture in drum, M_{fs_r}; and
2. The mass of mass of reminder dry soil in drum, M_{dsoil_r}.

A second sample was taken from the mix being placed in the MSSA. The following parameters were measured for this sample:

1. The water content of mixture before test in shear box, w_{bt};
2. The mass sample of mixture before test from shear box, $M_{ms\_sb\_bt}$; and
3. The mass sample of dry soil before test from shear box, $M_{ds\_sb\_bt}$.

When the mix was inside the shear box and the loading platen was placed into position (prior to the start of the test) the water expelled from the sample was measured. At this stage the following parameter was measured:

1. The volume of water expelled before test from shear box, V_{webt}.

When the test finished and with no further shear displacement, but with the shear box still loaded, a new measurement of the water expelled from the sample after testing was carried out. In this stage the following parameter was measured:

1. The volume of water expelled end of test from shear box, V_{weet}.

Finally, the last sample was taken from the middle of the MSSA (shear band) after the test finished (unloaded and loading platen removed). At this stage the following parameters were measured:

1. The water content of mixture after test in shear box, w_{at};
2. The mass sample of mixture after test from shear box, $M_{ms\_sb\_at}$; and
3. The mass sample of dry soil before test from shear box, $M_{ds\_sb\_at}$.

Tables 4.1, 4.2, 4.3 and 4.4, with the white background, show a series of calculated parameters obtained in the following form:

$$M_{ws\_drum} = M_s + M_w \quad [4.1]$$

Where:

M_{ws_drum}= Calculated mass of water-soil in the drum, kg.

The calculated mass of water-soil in the drum can be compared with M_{ws} calculating the error in the measurement:

$$\Delta M_{ws\_drum} = M_{ws} - M_{ws\_drum} \quad [4.2]$$

$$ERROR_{ws\_drum} = 100 * \frac{\Delta M_{ws\_drum}}{M_{ws}} \quad [4.3]$$

Where:

ΔM_{ws_drum}= Difference of weighed mass of water-soil in the drum and calculated water-soil in the drum, kg.

$ERROR_{ws\_drum}$= Error in measurement of water-soil mixture, %.

The $ERROR_{ws\_drum}$ was the first control to be carried out during the quality process. The second control occurred after the foam has been added to the water-soil mixture. The calculated mass of water-foam-soil in the drum can be compared with M_{fs} calculating the error in the measurement:

$$M_{ms\_drum} = M_s + M_w + M_f \quad [4.4]$$

$$\Delta M_{ms\_drum} = M_{fs} - M_{ms\_drum} \quad [4.5]$$

$$ERROR_{ms\_drum} = 100 * \frac{\Delta M_{ms\_drum}}{M_{fs}} \quad [4.6]$$

Where:

M_{ms_drum}= Calculated mass of water-foam-soil in the drum, kg.

ΔM_{ms_drum}= Difference of weighed mass of water-foam-soil in the drum and calculated water-foam-soil in the drum, kg.

$ERROR_{ms\_drum}$= Error in measurement of water-foam-soil mixture, %.

Equation [4.5] is valid for all tests, except those on Thanet sand. For the Thanet sand test the following equation has to be applied:

$$\Delta M_{ms\_drum} = (M_{fs} + M_{msd}) - M_{ms\_drum} \quad [4.7]$$

The $ERROR_{ms\_drum}$ is the same as pointed out in equation [4.6].

From the measurements taken in the quality control process two new water contents can be calculated using the V_{webt} and V_{weet}. This water contents are calculated using the following equations:

$$M_{mixsb\_bt} = M_{fs} - (M_{msd} + M_{fs\_r} + M_{ms\_sb\_bt}) \quad [4.8]$$

$$M_{ssb} = M_{s} - (M_{dsoil\_r} + M_{dsd} + M_{ds\_sb\_bt}) \quad [4.9]$$

$$w_{c\_bt} = w_{bt} - 100 * \frac{V_{webt}}{M_{ssb}} \quad [4.10]$$

$$w_{c\_at} = w_{bt} - 100 * \frac{V_{weet}}{M_{ssb}} \quad [4.11]$$

Where:

M_{mixsb_bt}= Calculated mass of mix in shear box, kg.

M_{ssb}= Calculated mass of soil in shear box, kg.

W_{c_bt}= Calculated water content of mixture before test in shear box, %.

W_{c_at}= Calculated water content of mixture after test in shear box, %.

This equation [4.9] is valid for all tests except those on Thanet sand. For the test on Thanet sand the following equations has to be applied:

$$M_{mixsb\_bt} = M_{fs} - (M_{fs\_r} + M_{ms\_sb\_bt}) \quad [4.12]$$

$$M_{ssb} = \frac{M_{mixsb\_bt}}{(1 + w_{bt} * 0.01)} - M_{peblessb} \quad [4.13]$$

Where:

$M_{pebblessb}$= Mass of pebbles for a mass of soil. Ratio of mass of pebbles to mass of soil with pebbles is equal to 0.104.

Equations [4.12] and [4.13] are needed because no M_{dsoil_r} was carried out during shear box tests on Thanet sand. It is also important to highlight that the ratio of mass of pebbles to mass of soil with pebbles was obtained after several tests in the laboratory. For M_{ssb} w_{bt} is used because it is the amount of water of the mixture in MSSA before the loading platen was placed on the MSSA.

In the case of the shear box tests on saturated Thanet sand the mass of M_{ssb} was obtained measuring the amount of soil that was placed inside the MSSA.

Finally a last error can be calculated between w_{at} and w_{c_at}. This error is pointed out in Tables 4.1, 4.2, 4.3 and 4.4. The following equations show how it is obtained:

$$\Delta w_{at} = w_{at} - w_{c\_at} \quad [4.14]$$

$$ERRORw_{\_at} = 100 * \frac{\Delta w_{at}}{w_{at}} \quad [4.15]$$

Where:

Δw_{at}= Difference of measured water content after test and calculated water content after test, %.

ERRORw$_{_at}$= Error in measurement of water content after test, %.

Figure 4.13 shows the variation of the water content measurements for all tests. One can observe that in 91% of the tests the w_{at} was the lowest water content measured. This could have been caused by the drainage of water out of the shear band zone when the material that is in upper part of the shear band zone was removed in order to take the sample. This could, assuming that w_{c_at} was correctly calculated, explain the big error value show by ERRORw_at unlike the other errors. It could also be that, assuming w_{at} is correct, V_{weet} does not represent the total shear band drained water, which might well result in a lower estimation of V_{weet}, thus over estimating w_{c_at} (See equation [4.11]). Improved methods in order to measure V_{weet} and w_{at} have to be implemented to minimize uncertainty in the water content values of the soil mixtures after the shear box test.

In 69% of the tests w_{c_bt} is lower than w_{bt}. The maximum difference between them is less than 4%. Looking at w_{drum} and w_{c_at} one can see in Figure 4.13 that the maximum difference was around 10%.

In Figure 4.14 M_{ws_drum}, M_{ms_drum} and w_{c_at} have been plotted with their error lines (same colours as the data line) in kilograms and in % respectively (see Tables 4.1 to 4.4). M_{ws_drum} shows a maximum error variation of around 0.1 kg while M_{ms_drum} shows a maximum error variation of 0.4 kg. The maximum error variation of w_{c_at} is approximately 6% respect of w_{at}.

The next sections presents the result obtained for the 38 shear box tests. First of all the typical results obtained for the shear box tests will be described using, as an example, one test, focusing in the sample vertical displacement, horizontal displacement, pore water pressure, normal and shear stresses measured. Later an interpretation of all the results will be carried out highlighting the shear stress, effective stress, angle of friction and pore water pressure.

4.3.2. Data presentation

The tests were performed at constant vertical pressures. The vertical pressure between the tests varied between 44 kPa and 58 kPa. The rate of shearing was 2 mm/min for all the tests. The shear box test was stopped when the mixtures inside the MSSA has reached around 7.2 mm of vertical compression or when the horizontal displacement of the mixture was between 18 mm and 22 mm.

General shear box test data is shown in Table 4.5. Most of the tests were carried out without problems but Th1, Th2 and Th3 experienced a problem in the sealing of the pore water pressure transducer. Although these tests are shown in the table they were omitted from the data analysed. This can be seen in Table 4.5, in the Condition column where are "no", showing that these tests were not satisfactory. Table 4.5 lists:

- The initial vertical compression (v_0), before the shearing of the mixture starts, and the maximum vertical compression (v_{max}) during the shear box test;
- The height of the mixture (H_0) after the initial vertical compression, and the minimum height of the mixture (H_{min}) at its maximum vertical compression;
- The maximum shear displacement (δ_{max}) reached at the end of the test;
- The dry density (ρ_{D0}) after the initial compression of the mixture in the MSSA, the dry density (ρ_{Dmax}) at maximum vertical compression of the mixture;
- The voids ratio just after the initial vertical compression, the minimum voids ratio (e_{sbmin}) reached at maximum vertical compression; and
- The average vertical stress ($\sigma_{average}$) during the entire shear box tests.

The type of data gathered during the shear box tests will be shown in the next sections.

4.3.2.1. Vertical stress, shear stress and pore pressure

The stress results obtained from the direct shear box tests are of the form shown by Figure 4.15 to 4.18, where the vertical stress, shear stress and pore pressure are shown for some typical test results of L.B. fine sand, L.B. coarse sand, L.B. graded sand and Thanet sand.

All four sands showed the following general behaviour respect the minimum and maximum value of pore water pressure achieved during the tests, varying just the reached values. The minimum pore water pressure value reached for L.B. fine sand, L.B. coarse sand, L.B. graded sand and Thanet sand were 2, 0.5, 0.9, and 7 kPa respectively. The maximum pore water pressure value achieved during the tests on L.B. fine sand, L.B. coarse sand, L.B. graded sand and Thanet sand were 6, 2.3, 7.4 and 33 kPa respectively.

Moreover, the value reached by the pore pressure, where each type of sand achieved a maximum pore pressure was of an order of 12% for L.B. fine sand, 4.6% for L.B. coarse sand, 15% for L.B. graded sand, and 70% for Thanet sand of the value of the average vertical stress. The previous behaviour in each type of sand was observed in all sands of similar type (See Figure 4.15 to 4.18)

L.B. fine sand

In general (see Figure 4.15) the average vertical stress on for L.B. fine sand tests was around 49 (kPa) which was steady after around 2 mm of shear displacement.

The shear stress increases at an approximately constant rate after 10 mm of shear displacement.

L.B. coarse sand

In general (see Figure 4.16) the average vertical stress on the L.B. coarse sand tests was around 49 (kPa) which was achieved after around 2 mm of shear displacement. During these tests the vertical stress tends to increase slightly as the shear displacement increased. This is a common phenomenon on L.B. coarse sand tested in MSSA. However, the variation of vertical stress is lower than 3.6 kPa which was less than 8% of the average vertical stress.

The shear stress increases at an approximately constant rate after 10 mm of shear displacement.

L.B. graded sand

In general (see Figure 4.17) the average vertical stress for the L.B. graded sand tests was around 50 (kPa) which was achieved around 1 mm of shear displacement for most of the L.B. graded sand tests but not for the G6 test. During this test the vertical stress tended to increase as the shear displacement increased. It was expected that L.B. graded sand tests would show a behaviour intermediate between L.B. fine sand and L.B. coarse sand. This is confirmed by looking at Figure 4.17.

The shear stress increased at constant rate after 9 mm of shear displacement.

Thanet sand

In this case, the vertical stress average value was around 46.5 (kPa) which was achieved after 1 mm of shear displacement.

The shear stress increased at a constant rate after around 12 mm of shear displacement.

4.3.2.2. Vertical displacement, Shear stress/vertical effective stress ratio and pore pressure/vertical stress ratio.

Figures 4.19 to 4.22 show some of the typical results of vertical displacement, shear stress/vertical effective stress ratio and pore pressure/vertical stress ratio values for L.B. fine sand, L.B. coarse, L.B. graded sand and Thanet sand respectively.

All four type of sand showed the following general behaviour:

1. No dilation through the shear box tests. In general the mixture of foam and sand did not dilate during shearing, on the contrary the mixture compressed.
2. The shear stress/vertical effective stress ratio increased at a constant rate after 10 mm of shear displacement.
3. A high compressibility was shown by the foam and sand mixtures observed.
4. The pore pressure/vertical stress ratio was nearly constant in each test. On L.B. fine sand tests it reached a minimum and maximum value of 0.045 and 0.13 respectively, on L.B. coarse sand tests it reached a value of around 0.01, on L.B. graded sand tests it reached a value of around 0.03 and on Thanet sand tests the value was between 0.2 and 0.7.

Differences in the behaviour of these sands were observed in:

1. L.B. graded sand G6 test show a small dilation (Figure 4.21), on the contrary all the other L.B. graded sand tests compress rather than dilate.
2. L.B. sands and Thanet sand, where L.B. sands conditioned with foam showed low pore pressure values, exhibiting a ratio pore pressure /vertical stress of 15%, 1.25% and 3.75% of the value of ratio shear stress/vertical effective stress for L.B. fine sand, L.B. coarse sand and L.B. graded sand respectively. While Thanet sand exhibited a ratio pore pressure/vertical stress of similar order of magnitude as the ratio shear stress/vertical effective stress.
3. The high pore pressure values were observed for he Thanet sand tests but not when the Leighton Buzzard sands were tested.
4. The ratio shear stress/vertical effective stress of L.B. fine sand, L.B. coarse sand, L.B. graded sand and Thanet sand did not level off at the end of the test. Exception to this behaviour was L.B. graded sand G6 test, which did level off.
5. The vertical displacement of L.B. fine sand and Thanet sand did not level off at the end of the test. L.B. graded sand G6 test did level off at the end of the test but for G1 and G4 the vertical displacement did not level off. G6 reached a final vertical displacement value of -0.34 mm. G1 and G4 tests reached a vertical displacement value between -4.4

and -5.1 mm. The vertical displacement for L.B. coarse sand did level off at the end of the test. Its final vertical displacement values were between 1.88 and -2.7 mm.

To carry out the data analysis it was choose a shear displacement value at which the energy dissipation or Taylor's energy correction $\tau/\sigma' + \Delta(\text{Vertical dispplacement})/\Delta(\delta)$ (Jewell, 1989) in the mixtures starts being almost constant. Figures 4.23 shows the energy dissipation for the typical results of L.B. fine sand, L.B. coarse sand, L.B. graded sand and Thanet sand. Figure 4.24 shows the punctual energy dissipation value at 12 mm and the average energy dissipation value from shear displacement above 10 mm for each typical test result. Figures 4.23 and 4.24 show how the punctual energy dissipation value at 12 mm is close to the average value of the energy dissipation above 10 mm of shear displacement on all the tests on L.B. sands. This difference (Table 4.6) between these too values is always lower than 0.019 (absolute terms). The only exception is shown by Thanet sands where the difference increases till 0.04 (absolute terms) in the case of Th8. Although the exception showed by Th8, it is decided that 12 mm shear displacement is representative enough of the results achieved during the tests at approximated constant energy dissipation value. Table 4.7 shows a general set of results for each of the shear box tests at 12 mm of shear displacement. These results are discussed in the next section.

4.3.3. Data analysis

In general it is interesting to observe the results of the shear box tests plotted with FIR.

Observing Figure 4.25, it is clear that when a mixture of sand, water and foam have FIR larger than 12 it might be possible to achieve a shear stress/vertical stress ratio lower than 0.6. This is consistent because low FIRs mean stiff mixtures, which offer higher resistance to shear than mixtures with high values of FIR. In the case of Thanet sand the shear stress can be reduced, by adding some foaming agent, to about 70% of the shear stress developed by the Thanet sand without conditioning. For L.B. fine sand a twofold increase of FIR can reduce its shear stress by 23%. A 20% increase in FIR for conditioned L.B. graded sand can produce a maximum reduction of 50% in its shear stress. Conditioned L.B. coarse sand shows no major reduction of its shear stress with increasing FIR, showing an average value of around 0.73 shear stress/vertical stress ratio. For L.B. coarse sand the use of FIR higher than 10 did not produce suitable mixes for tunnelling process (see Chapter 3, slump test section).

Figure 4.26 shows the values of coefficient of friction (shear stress/vertical effective stress ratio) for Versa foam and L.B. fine sand mixtures of around 0.61 (31.4º angle of friction in direct

shear). In the case of Versa foam and L.B. coarse sand mixtures the average coefficient friction in direct shear was around 0.73 (36º angle of friction in direct shear), which was 0.03 higher than expected (35º angle of friction, Bolton in 1986). The mixtures of Versa foam and L.B. graded sand showed an average coefficient of friction of 0.63 (angle of friction in direct shear around 32º). The two values of coefficient of friction shown for a pair of tests with equal FIR on conditioned L.B. graded sand is explained by the different water contents of the mixtures. In the tests with a coefficient of friction higher than 0.8 the water content measured is twice the water content measured for tests with coefficients of friction lower than 0.61. This means that an excess of water content (around 18%) suppresses the effect that foam can have in reducing the shear stress on conditioned L.B. graded sand. In this case a twofold increase in water content causes a maximum increase of 35% in the coefficient of friction. In general it is expected that when denser mixes of Versa foam and L.B. graded sand mixtures show an increase in the coefficient of friction in direct shear.

The results in Figure 4.26 seem to be placed inside a band. This band has been drawn between two dashed lines. The value that is placed below the lowest dashed band line belongs to G4. During the G4 tests it was observed that the shear pin was displaced from the centre of the load cell that reads the shear forces in the MSSA (see section 4.2.2.5). This could have cause a faulty reading of the shear load, recording lower values than the reality.

In general there is a slight decrease (0.2 for different sands) of the coefficient of friction when the FIR increases. This is quite different from Psomas (2001) results, where the decrease of the coefficient of friction was around 0.6. Psomas results are shown in Figure 4.27, but in terms of τ / σ (shear stress divided by total normal stress) not τ / σ' (shear stress divided by total effective normal stress), as Psomas did not measure pore pressure.

As can be seen in Table 4.5 and Table 4.7 the use of foam increased the voids ratio of the sand to values higher than those reached by sand alone (see Chapter 3, maximum and minimum voids ratio for sands). Thus, the next analysis of results was drawn bearing in mind the voids ratio values using the relative density definition by Bolton (1986). In Figure 4.28 and Figure 4.29 Bolton's correlation (Bolton, 1986 and 1987) is drawn assuming a critical angle of friction at constant volume of 35º (the critical angle of friction at constant volume for a L.B. coarse sand (Bolton, 1986)), and a critical angle of friction at constant volume of 31º (critical angle of friction at constant volume for a fine silica sand (Houlsby and Psomas, 2001)) respectively. This correlation is used because it addresses the influence of the voids ratio on the angle of friction. Nevertheless, Bolton only analysed conventional sand (Relative Density between 0 and 1)

which, as mentioned previously, cannot exist at the voids ratios encountered for the foam sand mixtures (Relative Density ≤ 0). Bolton's correlation assumes that the angle of friction falls with increasing voids ratios (decreasing Relative Density), but that reduction does not continue below the critical angle of friction (at Relative Density of 0.23). Figure 4.28 shows the shear box tests on sands with coarse content higher or equal to 50%. Conditioned coarse sand showed, as previously mentioned, no decrease in its angle of friction with respect to the angle of friction at a constant volume for L.B. coarse sand. The conditioned L.B. graded sand showed a minimum angle of friction of around 23.5º at a Relative Density of -1. This sand also showed typical behaviour near Bolton's correlation diagonal straight line, when positive Relative Densities (dense samples) are achieved for the mixtures. Figure 4.29 shows shear box tests on sands with fines content higher or equal to 50% and no coarse content. The results for conditioned L.B. fine sand showed no major reduction of its angle of friction with respect to the critical angle of friction at a constant value. A maximum reduction of 1° is achieved on conditioned L.B. fine sand tests. The results from the Thanet sand tests (Th11 and Th12 tests, Thanet sand without conditioning) agree with Bolton's correlation, plotted near the diagonal straight line.

Previous treatment of direct shear box test results (Psomas, 2001) with foamed soils did not consider the pore water pressure in the mixes during the tests. Thus, if we take into account the pore water pressure (and use effective stresses), it can be observed that the angle of friction for foamed sands, Figure 4.29, is not significantly lower than the critical angle of shearing resistance for fine silica sand. Even though in these tests the angle of friction is not significantly lower than the critical angle of friction at a constant volume (maximum difference achieved was 4.2°), the use of a much higher FIR may give a lower angle of friction further moving these values away from the critical angle of friction at a constant volume.

If the ratio of pore pressure/vertical stress ratio is plotted against FIR, Figure 4.30, this ratio does not show much difference between L.B. sand tests, on the contrary it will be interesting to analyse the differences between the conditioned Thanet sand mixtures and the conditioned L.B. sand mixtures. Plotting the same ratio against the Relative Density, Figure 4.31, it is possible to observe how in Thanet sand loose mixtures the pore pressure/vertical stress ratio increases. Implying that mixtures with higher ratios have lower shear strengths than mixtures at lower ratios (a black solid line is draw as the best fit straight line for the Thanet sand tests). However, the L.B. sand tests showed pore pressure/vertical stress ratios lower than 0.11 for all the tests. Therefore it seems that pore water pressure controls the strength of the foam sand mixtures, so an increase in FIR might produce an increase in pore water pressure and a decrease of shear stress; but different types of sand, with regard to fines content and water content, will have

different optimum set of parameters in order to decrease the shear stress, as is the case shown here between L.B. sands and Thanet sand (see sand properties in Chapter 3).

So, if the pore water pressure controls the strength of the sand foam mixtures it is very important to understand the flow of the liquid through the sand. An attempt was made to measure the drainage of liquid from the shear band in the shear box. It was observed that for different foaming agents the percentage of liquid drained from the shear band was different. This is illustrated in Figure 4.32 where, surprisingly, the highest percentage of liquid drained from the shear band was measured for CONDAT F4 and KAO T7. Looking at the stability test results in Chapter 3, CONDAT F4 was expected to have a more stable foam and remain longer with in the sand. This reveals that there are others parameters that need to be considered in the stability of the foam, for instance, the permeability of the soil. This is observed in the tests carried out with Versa foam from CETCO, where the coarser the sand the highest the liquid drained from the shear band. The equation used to calculate the % liquid drained from the shear band was:

$$\%\ \text{liquid drained from shear band} = 100 * \frac{W_{c\_bt} - W_{at}}{W_{c\_bt}} \qquad [4.16]$$

Figure 4.33 shows the % liquid drained from the shear band versus the FIR of the tests. A band of data is observed lying between the two black dashed lines. An attempt to relate the results to the w_{c_bt} (values that appear next to the data in Figure 4.33) showed that no clear relation can be observed. Although it is observed that coarser sands show higher percentage of liquid drained from the shear band at FIR lower than 12%, in the contrary finer sands show percentages of liquid drainage from the shear band closer to zero % at FIR above 35%.

4.4. Applicability of experimental results in EPBM tunnelling processes

The experimental results have shown that foams can be used to increase the voids ratio of the soil. At high voids ratios (high FIR) the angle of friction can be lower than at "conventional" voids ratios (FIR=0%), this is due to "replacement" of grains by bubbles in the structure. A lower angle of friction of the foam soil mixture is particularly significant for the EPBM tunnelling industry. A lower angle of friction has implications for reduced power consumption and reduced wear throughout the tunnelling process. Equally well, reduced resistance because of high pore water pressure could be useful.

In conditioned Thanet sand 70% of shear stress reduction can be achieved at FIR of 46%, w_{c_bt} around 21% and FER of 18 compared to the obtained no conditioned Thanet sand shear stress values. This would reduce in similar amount the torque achieved in an EPB machine. Thus its

power consumption when conditioned Thanet sand is handled may also be reduced around 70% from the power consumed when the same machine handles un conditioned Thanet sand. When in conditioned L.B. fine sand the FIR increases to 20%, it produces a reduction its shear stress by 23% at FER of 15 and w_{c_bt} of 27%. Thus the torque and power consumption in a EPBM handling L.B. fine sand may be reduced by 23% if just its FIR is increased to 20% (at FER of 15 and w_{c_bt} of 27%). When in conditioned L.B. graded sand the FIR is increased to 20% (from 12% to 16%) the shear stress is reduced by 50%, at FER between 13-14 and w_{c_bt} reduced from 18% to 8%. This will imply that the torque and power consumption of an EPBM when handling L.B. graded sand can be reduced by 50%. In the case of conditioned L.B. coarse sand it might no be possible to reduce torque and power consumption just using foam as a soil conditioning material. It might be necessary to use bentonite or another type of soil conditioning.

The wear on the screw conveyor of an EPBM can also be reduced applying foam as a soil conditioner. This is due to that coefficient of frictions measured in conditioned sands are lower than the one measured for unconditioned sands. Thus, as the coefficient of skin friction is proportional to the coefficient of friction, a wear reduction may occur on the screw conveyor of an EPBM handling conditioned sand rather than unconditioned sand. For instance conditioned L.B. fine sand coefficient of friction can be reduced 2% respect of the coefficient of friction measured for saturated L.B. fine sand. This implies that the coefficient of skin friction may be reduced 2% and thus the wear on the screw conveyor of an EPBM handling conditioned L.B. fine sand may be reduced 2%. In the case of conditioned L.B. coarse sand it is no possible to reduce the wear using only foam as a soil conditioner.

The operators of EPBM most no only follow the labelling of foam packaging to evaluate the stability of the foam, as it was shown at the end of section 4.3.3. They must also consider the permeability of the soil. This is the case for L.B. coarse sand.

4.5. Summary

This Chapter reported the equipment, procedure, results and analysis of 38 shear box tests on L.B. fine sand, L.B. graded sand, L.B. coarse sand and Thanet sand. The MSSA used to carry out these tests has been described.

Section 4.2 described the MSSA to carry out these tests. A detailed description of the hydraulic vertical loading system, sealing system and clamping system of the MSSA is given in this section.

Section 4.3 presents the experimental procedures and results of shear box tests. Section 4.3.1 shows the measured and calculated values during the quality control procedure. The quality control procedure is explained using Figure 4.12 and the results are shown in Tables 4.1 to 4.4, and Figures 4.13 and 4.14. Section 4.3.2 presents the main values that can be obtained from shear box tests, such as, shear stress, vertical stress, pore pressure, vertical displacement, shear stress/vertical effective stress ratio and pore pressure/vertical stress ratio using as an example F3, F4, F6, C3, C4, C11, G1, G4, G6, Th8, Th9, Th10. Section 4.3.3 analyses the results of all the shear box tests. The analysis is carried out at a shear displacement value where the energy dissipation has reached an approximated constant value during the test. The analysis is done focusing firstly on the values of shear stress/vertical stress ratio and shear stress/vertical effective stress ratio versus FIR for all the tests at 12 mm of shear displacement. Then the angle of friction for all the tests together with Bolton's correlation was plotted against the Relative Density of the mixture at 12 mm of shear displacement. Furthermore, the pore pressure/vertical stress ratio was plotted against FIR and Relative Density. Finally, results of measurement made of the drainage of liquid of some foam conditioner from the shear band of the MSSA during testing are analysed.

It is found that that foams can be used to increase voids ratio of the soil achieving a minimum value of Relative Density of -1 for some sands. The pore water pressure controls the strength of the sand foam mixtures. An increase in FIR might produce an increase of pore water pressure and a decrease of shear stress. However, different type of sands, in terms of its fine content and water content, will have different optimum combination set of parameters (reducing shear stress) in order to produce a mixture suitable for tunnelling processes, as is the case showed here between L.B. sands and Thanet sand. At low relative densities (high voids ratios, only sustainable through the addition of foam) sands might exhibit a low angle of friction if the combination of parameters such as FIR, percentage of fine content of the sand and water content is such that the addition of foam can reduce the angle of friction of the sand. This is evidenced by G4 and Th4 with an angle of friction measured in direct shear of 23.5° and 26.8° respectively. This also shows that the extension of Bolton's correlation (at a different slope) to negative Relative Density values (voids ratios considerable higher that at the loosest normal state) is possible.

In the experiments described here, foamed sands at states much looser than the normal loosest state were found to exhibit angles of friction lower than the angle of friction at constant volume. Angles of friction as low as 23.5° were measured.

From the attempt made to measure the drainage of liquid (important because it controls pore pressure) from the shear band in the shear box during testing, the more stable foam showed the highest percentage drainage from the shear band. It is possible to conclude that there are others parameters to be considered in the stability of the foam, for instance, the permeability of the soil.

Section 4.4 reported the applicability of the experimental results in EPBM tunnelling processes. The use of the MSSA as a tool to determine the behaviour of soil conditioned with foam under direct shear and how this conditioning lowers the angle of friction of the foam soil mixture. This is particularly significant for EPBM tunnelling industry; as such a reduction can reduce EPBM energy consumption and thus the costs in its operation.

Finally these tests demonstrated that the shear box tests can be used to study the behaviour of similar conditioned sand specimens used at a tunnelling site, under direct shear, where the effects of FIR on a particular type of sand are unknown. It also demonstrates that relevant information can be extracted from shear box tests whose outputs could deliver important changes in the tunnelling conditioning programme when EPB machines are used.

Chapter 5. Compressibility tests

5.1. Introduction

This chapter presents the design, of the apparatus, specifically made to separate the effects of water expulsion, gas expulsion and gas compression during consolidation and the principles that were used to achieve this.

This chapter also presents the results obtained when Leighton Buzzard fine sand and Thanet sand, mixed with Versa foam conditioner, are consolidated at a constant rate of vertical displacement. The instrumentation and methodology used during testing are also described here.

In the final section of this chapter a detailed analysis of the results is carried out, focusing on key soil parameters. This analysis is used to draw conclusions regarding the behaviour of the sand mixed with Versa foam, and the effectiveness of the Versa foam conditioner.

5.2. Compressibility apparatus

5.2.1. MAP consolidometer

The apparatus used in this project was a modification of the one developed by Prof. P. W. Rowe at Manchester University. A detailed description of the Rowe cell apparatus can be seen in Head (1986). Figure 5.1 shows the Rowe cell with its standard parts.

This new apparatus has been called the MAP consolidometer (MAPC). The design and construction of the MAPC were made to allow for the measurements of expelled gas, expelled water, pore pressures and vertical stress during the consolidation of the sample at a constant rate of vertical displacement. The vertical displacement of the MAPC was applied by an ELE Tritest 50 machine. A piping system connected to the MAPC permitted the measurement of the liquid expelled during consolidation. Figure 5.2 shows the piping system that was connected to the MAPC. The air/water interfaces, twin burettes and diversion valve are pointed out, the remaining parts of the system are explained in the next sections.

The MAPC was formed by the base of the Rowe cell apparatus and a new special design call MAPC top. The MAPC top included a glass capillary tube and an o-ring, placed on its top surface and on the MAPC top's bottom edge respectively. The MAPC top is attached to a perforated plate on which a filter mesh, with an aluminium ring used as support, has been placed. Figure 5.3 shows the different parts of MAPC.

The MAPC top part also included a load cell, a pressure transducer and a vertical displacement transducer. The load cell was placed between the upper plate of the MAPC top and the reaction bar of the ELE Tritest 50 machine. The pressure transducer was screwed into a connector placed on the wall of the conical part of the MAPC. The vertical displacement transducer was attached to one of the 4 stainless steel rods of the MAPC top. See Figure 5.4 and 5.5.
The base of the Rowe cell or the MAPC base included a pore pressure transducer and a positioning fixed shim. This pore pressure transducer was screwed into a connector placed on the bottom of the MAPC base. The position plate was used, together with the vertical displacement transducer, to measure the vertical displacement of the MAPC top part to the MAPC base.

The next two sections describe in more detail the perforated plate and filter mesh parts, and the MAP consolidometer top.

5.2.1.1. Perforated plate and filter mesh

A perforated plate was added to the bottom of the MAPC top part, in order to distribute the vertical stress applied uniformly over the sample and allow the liquid to flow through it.

A Grade 304 stainless steel woven wire mesh of 80 micron aperture and 50 micron wire was placed beneath the perforated plate. The mesh kept grains of sand away from the piping system. The permeability of the mesh was taken into account in the final permeability calculation of the sample. The mesh permeability was approximately 0.83×10^{-6} m/s (see permeability calculation in data presentation section 5.4.1).

5.2.1.2. MAPC top

The MAPC top part was designed to support a working vertical stresses of around 400 kPa. Four stainless steel rods together with a stainless steel upper plate (see Figure 5.3) were used to transmit the vertical stress during testing towards the reaction bar of the Tritest 50 machine.

The stainless steel conical part of the MAPC top part was designed to avoid bubbles released during consolidation becoming trapped on the interior surface. The conical wall had an angle of approximately 20º. In this way the released bubbles during consolidation of the sample will not be stuck inside of the conical part but will move towards the graduated capillary tube, where the volume of the gas expelled can be measured.

The upper plate had two perforations. The capillary tube passed through one of them and from the other one an arrangement was used to connect the vertical load cell with the upper plate. This arrangement kept the entire MAPC top part aligned with the MAPC base during testing. This arrangement can be seen in Figures 5.4, 5.5, 5.6 and 5.7.

The next two sections describe in greater detail the capillary glass tube, the o-ring and the grease arrangement.

Capillary glass tube

The capillary glass tube was needed to capture and quantify the gas released during consolidation of the sand foam mixtures. After some development the following arrangement was used. Two acrylic connectors together with two translucent solid silicone rubber stoppers (see Figures 5.7 and 5.8) were used to secure a tight seal at the top and bottom of the straight capillary tube (9 mm external diameter and 6 mm internal diameter). The bottom connector was fitted with a ¼ BSPT female thread (see Figure 5.9) in order to connect to a stainless steel tube, which connected the internal part of the conical wall with the straight capillary glass tube. This connector had a conical shaped cavity where a translucent solid silicone rubber was fitted and kept in place by an aluminium ring illustrated by Figure 5.9. The translucent silicone rubber was perforated in order to place the straight capillary tube inside. The top acrylic connector is shown in Figure 5.10. Its construction is similar to the bottom acrylic connector, but it included an extra cavity to place an acrylic handle which was used to release the internal pressure from the glass capillary tube. This connector also included a female thread on its side. This side connection was used together with the acrylic handle to release the pressure from the glass capillary tube.

The stainless steel tube, which connects the conical wall and the capillary glass tube, was fitted in place by standard stainless steel male connectors. The stainless steel tube (6 mm outside diameter) had a wall thickness of 0.3 mm which meant it was easy to bend, to achieve the right position in the capillary glass tube system. In order to assure complete sealing in the connection between the standard male connectors and the stainless steel tube, Loctite 542 thread sealant was used.

O-ring and grease

In order to seal the gap between the side wall of the MAPC top and the inside wall of the base of the Rowe cell (to avoid leaks from the foam sand sample) several arrangements using an o-ring system were tested.

After various tests the following arrangement was found to give a satisfactory seal and low friction. A circular cross section o-ring of 1.5 mm in diameter (see Figure 5.11). It proved to be successful sealing the MAPC up to internal pressures of 200 kPa, and generated low friction values (see section 5.3.2), allowing an unloading stage during the consolidation test.

A layer of grease was applied on the inside of MAPC base part. In this way the friction between the grains of sand and the base was kept at minimum. The grease also helped to decrease the friction between the MAPC top and MAPC base parts during testing.

Figure 5.12 and Figure 5.13 show the conical wall (with its o-ring), perforated plate and filter mesh.

5.2.2. MAP consolidometer instrumentation

The MAP consolidometer is instrumented with two pore water pressure transducers, a load cell and an LVDT transducer. Two cell volume change (CVC) devices were placed in the piping system connected to the MAPC after the diversion valve. The CVC devices were used to measure the volume of liquid expelled from the sample during consolidation.

The design and arrangement of the instrumentation are discussed in the following five sections.

5.2.2.1. Vertical stress

A 50 kN "z" shaped load cell was used. It was placed between the MAPC upper plate and the Tritest 50 reaction bar. The load cell was attached to the upper plate by bolts as explained previously; it was also attached to the reaction bar using the standard fitting on the Tritest 50. On the reaction bar of the Tritest 50 a special shackle (see Figure 5.5) was mounted to pull the entire MAPC top part upwards once the consolidation test was finished.

The load cell (Maywood Instruments Limited U4000 load cell, range 50 kN, full scale output without amplification 2.7mV/V, excitation voltage 10 V, non-linearity < ± 0.03 % full scale output) was calibrated using an Instron compression testing machine. Its response was linear with a calibration factor of -2.19 kN/V.

5.2.2.2. Pore pressure

Two pore water pressure transducers were used in the MAP consolidometer. Both are Druck transducers PDCR 4010 (pressure range 0-7 bar gauge, full scale output 98.64 mV/V for the pressure transducer placed on the MAPC top; full scale output 99.42 mV/V for the pressure

transducer placed on the MAPC base, excitation voltage 10 V, non-linearity < ± 0.08% full scale output).

One pore water pressure transducer was placed on top of the MAP consolidometer, and was connected through a brass junction to the internal part of the conical wall, see Figure 5.6. The calibration of this pressure transducer was carried out in-situ using a Digital Pressure Indicator 600 (DPI 600) (pressure connector 1/8 BSP or M8 male or female standard, pressure range maximum error of ± 0.1 % with ± 1 digits up to 35 bar; ± 0.2 % with ± 1 digits 35 to 70 bar, temperature effect ± 0.02 %/Cº, warm up time 10 min, resolution 0.005 %). The DPI 600 was connected to one of the air/water interfaces which itself was connected with a suitable set of tubes at a brass junction (see Figure 5.6). The brass junction's valves allowed the transducer to be isolated from the rest of the MAPC, leaving a straight connection passing by the air/water interface between the point of pressure application (air line) and the pore pressure transducer. The calibration factor of the top pore water pressure transducer is 29.11 kPa/V.

The second pressure transducer was placed at the bottom of the MAPC base. Its calibration was carried out using the DPI described above and connecting it in line, passing by an air/water interface, with the pore pressure transducer. The DPI was connected at the mid point between the air line and the air/water interface. The calibration factor of the bottom pore water pressure transducer was 25.775 kPa/V (see Figure 5.14). On the bottom of the MAPC base part there was a recess where a Vyon ® filter was placed. This Vyon ® was previously saturated with water and installed flush with the MAPC base bottom part so that it did not disturb the sample when it is in place. The Vyon ® allowed for the measurement of the pressure at the bottom of the sample inside the MAPC and retained the grains of soil in the MAPC, without contaminating the tube line of the bottom pore water pressure transducer.

5.2.2.3. Vertical displacement

The vertical displacement was measured by a LVDT RDP electronic transducer ACT 2000 A (type spring return armature, nominal stroke ± 50 mm, electrical output (not amplified) 1.6 V/V, input requirements 1 V to 7 V rms A.C. regulated at 5 kHz optimum, linearity < 0.5 % full stroke). The calibration factor of the LVDT electronic transducer was -3.997 mm/V.
The vertical displacement LVDT transducer was attached to one of the four steel rods of the MAP consolidometer. As the MAPC base part moved upwards it pushed the LVDT transducer armature which was fixed to the MAPC top part, which was static at the time of testing.

5.2.2.4. Cell Volume Change

The two CVC devices were placed in the consolidation test system in order to measure the volume of liquid expelled from the sample during consolidation. Each CVC device was equipped with a LVDT transducer. CVC 1 had a capacity of 100 cc and CVC 2 of 50 cc. The devices were calibrated using the twin burettes in Figure 5.2 and the LVDT transducers connected to them. CVC 1 had an LVDT transducer type RDP electronics ACT 500 C (type captive guided armature, nominal stroke ± 12.5 mm, electrical output (not amplified) 0.8 V/V, input requirements 1 V to 7 V rms A.C. regulated at 5 kHz optimum, linearity < 0.5 % full stroke). CVC 2 had a LVDT transducer type RDP electronics DCT 500 A (type spring return armature, nominal stroke ± 12.5 mm, electrical output (not amplified) ± 2 V d.c. nominal for working stroke, + 5 V d.c. ± 10 % regulated input, linearity < 0.5 % full stroke). The twin burettes were filled up with de-aired water and paraffin as described by Wykeham Farrance (1988). The paraffin was previously filtered to avoid any impurities entering into the twin burettes system, which could mislead the volume measurement. A dye known as Sudan powder was added to the paraffin to distinguish it from the de-aired water inside the burettes. By adjusting the valves beneath the twin burettes it was possible to raise the de-aired water in the left burette and at the same time, lower the de-aired water in the right burette (it was also possible to reverse the direction of the de-aired water by adjusting the valves in a different way). The output de-aired water from the twin burettes was sent to one of the CVC devices. In order to relate the change in volume of de-aired water to the displacement of the LVDT transducer connected on the CVC device, the graduation on the twin burettes was used. The calibration factors of CVCs 1 and 2 were -6.25 ml/V and -2.4 ml/V respectively.

5.2.2.5. Data-logging system

The data acquisition system based on a PC with a PCI-DAS1200 data acquisition card (8 differential channels) with an analogue input section was installed. The board had a resolution of 12bit, input of programmable ranges (±10V, ±5V, ±1.25, etc.) and a logging rate of 330 kHz (330000 samples per second).

In order to read the data from the computer board, it was necessary to install signal conditioners. These transformed the signals from the instruments into signals readable by the computer board. One of the systems used was an RDP-electronics Module 600 housing with 3 DC, 2 AC panels (each panel with two channels) and one power supply. The other two used were an RDP-electronics transducer indicator type E308 and type E309. The E308 provided signal conditioning for strain gauge type transducers and the E309 was designed for use with linear variable differential transformer (LVDT), half-bridge and similar A.C. transducers.

5.3. Compressibility tests experimental procedure

Nineteen tests are reported here. A group X of tests was carried out applying a continuous constant rate of vertical deformation during the undrained and drained stages. In the second group of tests, called Y, the continuous constant rate of vertical deformation was applied just under drained conditions (see Table 5.1). Any test referred to as "Finesand" was carried out on Leighton Buzzard fine sand and any test called "Thanet" was carried out on Thanet sand. Tests containing the word "foam" were those in which the sand under consolidation had foam as part of its components. If the letter "R" is included in a test name, that test included an unloading stage, which was carried out at the end of the consolidation test.

To explain how the MAPC was operated it is necessary to use an overview of the entire system in operation. Figure 5.15 and Figure 5.16 show the main parts of the MAPC system. Blue continuous lines were the piping lines used during testing. The red continuous lines are air lines. Blue dashed lines are not used during testing but are used during the calibration of the pore water pressure transducer, CVC calibration or other procedures other than consolidation of the sample. The blue dash-dotted lines are for optional use during consolidation. This means that the system can operate during consolidation using either CVC 1 or CVC 2. By closing and opening the relevant valves the CVCs could be added to or excluded from the consolidation system during testing. Once the CVC had been selected the diversion valve shown in Figure 5.15 rerouted the flow of liquid coming from the sample to either the top or bottom of the selected CVC.

Precise measurements of the heights in the system were made. Figure 5.17 shows the main heights considered during testing. This Figure does not show the parts of the system which were not used during consolidation. The right hand side air/water interface was added for completeness.

The Vyon® filter was placed at the bottom of the MAPC base before the sample was placed inside. The filter was saturated for 24 hours before testing. The line that connects the bottom of the sample and the bottom pore water pressure transducer was saturated (valves U5 and U8 opened, see Figure 5.14). As soon as de-aired water covered the top of the filter the injection of de-aired water was stopped. With the line saturated the sample was placed inside the MAP consolidometer base. After this, the top part of MAPC was placed on top of the sample using a crane system. The top part was locked into place using the locking system of the screwed rod of the Tritest 50 machine. Once the MAPC top part was in place, the MAPC internal conical wall was filled with de-aired water through valve U1 (see Figure 5.4), valve U3 and valve U9 (see

Figure 5.6). Once the de-aired water was expelled from the top part of the capillary tube, de-aired water was passed between valve U5 and U4 to achieve saturation between the pore water pressure transducers. The bleed valve was used to ensure saturation in this line (see Figure 5.7). Once this was completed the saturation process ended and all the valves were closed except for valve U5 (which connected the two pore water pressure transducers). The back pressure in the air/water interface was set up and valves U6, R1, R2, R4, R5, R6, R7, F, I, H and B were opened. Soon after this, the recording of data was initialized and 60 seconds later valve U5 was closed, valve U8 and valve U1 were opened. For the group X tests the vertical displacement (by raising of the Tritest 50 pedestal) was initiated immediately after valve U1 was opened. For the group Y tests the vertical displacement was initiated after opening valve U1 and the top and bottom pore water pressures had reached a stable value.

The consolidation tests were stopped when 20 mm of vertical displacement had occurred, or when 250 kPa vertical stress was achieved or when excessive amount of gas had been expelled, almost reaching the CVC. When any of these occurred, an unloading stage was initiated lasting for a few millimetres of vertical displacement (in the opposite direction but at the same speed). After this, the recording of data was stopped and the test ended.

The next three sections describe in more detail the important points of the MAPC test procedure.

5.3.1. Quality control

A rigorous quality control process during the preparation of the mixture of sand and foam for each specimen created was carried out. Measurements of weight, volume and water content were taken. The sand, water and foam, were weighed at various stages in the mixing process. The volume of water and foam were also measured. Finally three samples were used to measure the water content at three different stages of the mixing process. The first measurement was taken when the sand and water were mixed in the mixing drum. The second measurement was taken from the mixture of sand, water and foam from the mixing drum. The final sample was taken from the mixture placed in the MAP consolidometer base.

The quality control scheme carried out during each compressibility test is given in Figure 5.18. The top right side of the scheme illustrates how the sand, water and foam used in the mixture of foamed soil were measured at the very beginning of the compressibility test. After these measurements were completed a further sample was taken from the drum where the foamed soil was mixed, Stage 1. After Stage 1 the foamed soil was placed inside the MAPC base. One sample was taken from the mixture placed inside the MAPC base (Stage 2 box in Figure 5.18)

and the mixture of foamed soil reminding in the drum (Mix reminder box in Figure 5.18). When the foamed soil was placed inside of the MAPC base, the MAPC top part was placed above the foamed soil following the filling of the MAPC top part with water. During the loading part of the compressibility test the volume of water expelled during the test was measured by one of the CVC devices, pointed out in the bottom right side of Figure 5.18.

5.3.2. Friction

Different o-ring arrangements were tested in order to achieve the best combination of sealing and low friction during the consolidation tests. The 1.5 mm diameter circular cross section o-ring was selected for the consolidation tests. It was selected because it offered less friction in the loading and unloading stages than any other arrangement of o-rings. Figures 5.19 and Figure 5.20 show the friction results of the MAPC at 5 mm/min in the loading and unloading stages respectively. Figures 21 and 22 show the friction results of the MAPC at 0.3 mm/min in the loading and unloading stages. The results are plotted against the position of the piston measured from the top of the MAPC base as % of insertion from the edge of the MAPC base (height of MAPC base 126 mm). Looking at Figures 5.19 to 5.22 it is clear that friction increases at a higher vertical displacement rates. A friction force of 0.2496 kN was estimated for the loading stages at 0.3 mm/min and of -0.1506 kN for the unloading at the same vertical displacement rate. In tests where a 5 mm/min vertical displacement rate was used, a friction force of 0.4039 kN was estimated through the loading stage and -0.2241 kN for the unloading phase. These values are used to calculate the real vertical stresses obtained from the sample under consolidation.

5.3.3. Compression speed

The compression speed was selected considering values given in the literature for consolidation at constant rate of strain (CRS) and the peculiarities of working with mixtures of sand, water and foam. Finesand10 and Finesand26FoamR tests were carried out at 0.15 mm/min and 5 mm/min of vertical displacement respectively. All the other tests were carried out at 0.3 mm/min of vertical displacement.

5.4. Experimental results

Some typical results obtained from the consolidation tests using MAP consolidometer at CRS are shown in this section. The results are described using a specific test as an example.

5.4.1. Data presentation

The first group of results presented in this section are the specimen height and vertical strain rate from the time that the recording of data started. Figure 5.23 shows the typical results using Finesand13foamR as an example. The left hand axis shows the specimen height (pink solid line)

in meters and the right hand axis shows the vertical strain rate (dark blue solid line) in mm per min. The light blue dash single dotted line, dotted line and dash double dotted line show the start of undrained-loading, drained-loading and unloading respectively of the consolidation test. These results were obtained from the readings of vertical displacement transducer. These results are important to confirm that the tests were carried out under a constant rate of strain and also to know the variation in height of the sample at any time. At the beginning of the test during undrained-loading there was a time of approximately 90 seconds to achieve the constant vertical strain rate. This was due to the time needed by the Tritest 50 machine moving parts to achieve the vertical strain rate set point. The undrained loading was carried out until the pore water pressure achieved an approximately constant value. During drained loading the specimen showed a linear decrease in height at a constant vertical strain rate of 0.3 mm/min in this case. The drained loading was carried out until the specimen height had changed by approximately 20 mm or when 250 kPa vertical stress was achieved or when excessive amount of gas had been expelled. At the end of the drained loading stage the Tritest 50 machine was stopped for approximately 25 seconds or until a decrease in the vertical load was observed. After this the unloading stage was carried out. The beginning of the unloading showed similar behaviour to the beginning of the undrained loading till the vertical strain rate set point had been achieved. The unloading stage was carried out for a few millimetres of vertical displacement.

Using Finesand25foamR as an example, the second group of results presented in this section are shown in Figure 5.24. The vertical and effective vertical stresses are shown on the left hand axis and at the right hand side, pore water pressure at top of the sample, pore water pressure at the base (bottom) of the sample, excess pore water pressure and average pore water pressure in the sample from the time that the recording of data starts. These results are important for monitoring the effect of the foam conditioning on excess pore water pressure and effective stress during the consolidation tests under constant rate of strain. The vertical and effective vertical stresses are represented by black and red solid lines respectively. The pore water pressure at the top of the sample, pore water pressure at the base (bottom) of the sample, excess pore water pressure and average pore water pressure in the sample are indicated by grey, brown, green and pink solid lines respectively. The light blue dotted line and dash double dotted line show the start of the drained-loading zone and unloading zone respectively (this test did not have an undrained-loading zone thus the dash single dotted line is not indicated in Figure 5.24).

The basic equation to calculate the vertical stress is:

$$\sigma = \sigma_{lc} + \left[\frac{1}{2} * \rho_{bulk} * g * H\right] \quad [5.1]$$

The second term on the right hand side in equation [5.1] takes into account the average weight of the soil per unit area. A linear distribution of the weight of the soil is assumed. Where:

ρ_{bulk}: bulk density of soil, kg/m^3;

g: acceleration of gravity, 9.81 m/s^2;

H: height of specimen, mm;

σ_{lc}: vertical stress calculated from the load cell placed on top of the system (see Section 5.2.2.1), kPa, corrected by the friction force; and

σ: vertical stress, kPa.

The basic equations to calculate excess pore water pressure and average pore water pressure are:

$$u'_b = \left[\left(u_{bottom} - u_{top}\right) - \left(u_{bottom} - u_{top}\right)_0\right] + \frac{\rho_{water} * g}{1000} * \left(\frac{LVDT}{1000}\right) \quad [5.2]$$

$$u_w = u_{top} + \left[\frac{1}{2} * \rho_{water} * g * H\right] + \frac{2}{3} * u'_b \quad [5.3]$$

Where:

ρ_{water}: water density, 1000 kg/m^3;

u_{top}: pore water pressure at the top of specimen, kPa. This was calculated using the pore water pressure transducer placed at the top of the MAPC (see Section 5.2.2.2) and corrected by the vertical distance between the pore water pressure transducer and the top of the specimen;

u_{bottom}: pore water pressure at the bottom of the specimen, kPa. This was calculated using the pore water pressure transducer placed at the bottom of the MAPC (see Section 5.2.2.2) and corrected by the vertical distance between the pore water pressure transducer and the bottom of the specimen;

$(u_{top} - u_{bottom})_0$: pressure difference when the two pore water pressure transducers are connected directly together (see Section 5.3) at the beginning of the consolidation tests, kPa;

$(u_{top} - u_{bottom})_t$: pressure difference when the two pore water pressure transducer are not connected directly together but through the specimen at time t during consolidation, kPa;

LVDT: vertical displacement measured by the LVDT transducer placed on the MAP consolidometer top part (see Section 5.2.2.3), mm;

u'_b: excess pore water pressure at the base of MAPC, kPa; and

u_w: average pore water pressure in the specimen, kPa.

It is important to highlight that many times during consolidation tests a pore water pressure called the back pressure is used. In this research the "back pressure" was exactly the same as

u_{top}. The concept of excess pore pressure in equation [5.2] has already been explained in Chapter 2 (see also Gibson et al. 1989). In this research it is assumed that the process is quasi-stationary. This assumption is because the test was carried out at very slow rate of strain so it can be assumed that the pore water pressure did have enough time to dissipate. In equation [5.3] the second term on the right hand side represents one part of the hydrostatic pressure in the sample.

The basic equation to calculate the effective vertical stress is:

$$\sigma' = \sigma_{lc} - u_{top} + \left[\frac{1}{2} * (\rho_{bulk} - \rho_{water}) * g * H\right] - \frac{2}{3} * u'_b \qquad [5.4]$$

Where:

σ': effective vertical stress, kPa.

Taking into account equations [5.1, [5.2] and [5.3] the vertical effective stress was obtained, subtracting the average pore water pressure from the vertical stress.

Figure 5.24 shows a non linear increase of the vertical stress through the loading stage of MAPC test. Although just one test is represented by this figure, the non linear increase was observed in all tests. For tests that no have foam as part of the mixture, the rate of increase of total vertical stress was higher than those that have foam as part of their mixture. This was expected as specimens that have foam as part of the mixture are less rigid than just saturated sands at the same voids ratio.

As can be expected, both pore water pressures, top and bottom, show similar trends through the test. In general the pore water pressure results showed small peaks during the drained loading zone. These peaks were present in all of the tests and were induced when the diversion valve acted. The disturbance shown, at round 2750 seconds, in the pore water pressure readings during the unloading zone occurs when the valves that connect the sample inside the MAPC to the piping system are being closed. In general the excess pore water pressure was very low for all the L.B. fine sand tests but not for the Thanet tests. This is discussed in the next sections.

The third group of results (see Figure 5.25) are the volume of water in/out of the sample, volume of gas expelled from the sample and volume of the sample in the MAPC from the time that the recording of the data started. These results are important to see the effect of foam conditioning on the volume of water expelled from of the sample and the volume of gas

expelled from the sample during the test under constant rate of strain. The volume of water in/out of the sample and the volume of gas expelled from the sample are indicated by a blue solid line and red dots respectively. The volume of the sample in the MAPC is indicated by a pink solid line. The light blue dash single dotted line, dotted line and dash double dotted line show the start of undrained loading, drained loading and unloading of the consolidation test respectively. The volume of the sample is easily calculated from the readings of the vertical displacement transducer and the constant area of the MAPC base. The volume of water in/out of the sample is measured by the CVC devices. The volume of gas expelled from the sample was calculated from data observed during the test.

During the recording of liquid expelled from the specimen by the CVC small discontinuities of the slope can be observed in Figure 5.25. This occurred when the direction of filling of the CVC was changed from top to bottom or bottom to top. This can also be clearly observed in the pore water pressure measurements in Figure 5.24. These variations were not relevant for the analysis of the tests and were due to the use of the diversion valve (see Figure 5.15) where the manual operation means that the two separate pressure lines (one connected to the specimen in the MAPC and the other connected to the air/water interface) interact for a fraction of a second decreasing the pressure in the MAPC specimen.

Regarding the gas expelled, it is important to explain that the word "slug" is used to highlight the shape of the bubbles expelled from the specimen during the consolidation test. The body of these bubbles is elongated like a bullet. Equation [5.5] and [5.6] show how the pressure inside the bubbles was calculated using the water surface tension and the radius of curvature observed. In these equations the calculations were made at the time that the bubble were observed coming out of the MAPC.

The first basic equations to calculate the volume of gas expelled (accumulated) are:

$$P_{gtube[i]} = \frac{2 * \gamma}{r_{tube}} + u_{top[i]} \qquad [5.5]$$

$$P_{gcapillary[i]} = \frac{2 * \gamma}{r_{bubblecapillary}} + u_{top[i]} \qquad [5.6]$$

Where:

Y: water surface tension at 21.5 degrees Celsius, 0.07234 N m^{-1} (see Chapter 2);

r_{tube}: radius of curvature of "slug" gas bubble in plastic tube of MAPC system,1 mm;

$P_{gtube[i]}$: pressure of "slug" gas bubble in the plastic tube of MAPC system at time *i*, kPa;

$r_{bubblecapillary}$: radius of curvature of bubble trapped in capillary glass reduction, mm; and

$P_{gcapillary[i]}$: pressure of gas inside of bubble trapped in the capillary glass reduction at time *i*, kPa.

The volume of the gas expelled, at the time that the bubble was observed coming out of the MAPC, is calculated from the next two equations:

$$V_{gtube[i]} = N_{slug} * \frac{L_{slug}}{1000} * \frac{\left(\frac{\phi_{tube}}{1000}\right)^2}{4} * \pi \quad [5.7]$$

$$V_{gcapillary[i]} = \frac{4}{3} * \pi * \left(\phi_{bubble}\right)^3 \quad [5.8]$$

Where:

N_{slug}: number of "slug" gas bubbles seen in tube of MAPC system;

L_{slug}: length of "slug" gas bubble seen in the tube of MAPC system, mm;

ϕ_{tube}: internal diameter of tube, 2 mm;

$V_{gtube[i]}$: volume of gas in tube at time *i*, m^3;

ϕ_{bubble}: diameter of bubble trapped in the capillary glass reduction, m; and

$V_{gcapillary[i]}$: volume of gas trapped in the capillary glass reduction at time *i*, m^3.

Secondly it was important to estimate the bubble terminal velocity in order to calculate the time that the bubbles could take to reach the outside of the MAPC so a more precise estimate of the pressure of the gas inside of the bubble could be carried out.

As it has been reported by Sam et al (1996) and Zhang et al (2003) the maximum velocity of a bubble is achieved within the first seconds and decreases with time. In our case in order to simplify the calculation it was assumed that the velocity of the bubble with time followed the profile illustrated by Figure 5.26.

Using Tates' law (at the equilibrium stage), constant flow condition, the approximation made by Clift et al (1978) respect bubble velocity in contaminated water systems for spherical equivalent diameter bigger than 1.3 mm (replacing in equation [2.1] Chapter 2, d_0= 80x10^{-6} m, ρ_w= 1000 kg m^{-3}, ρ_g= 1.2 kg m^{-3}, g=9.81 m/s^2, χ=0 º, Y= 72 dyne/cm, d_e gets the value of 1.528 mm), and using Reynolds (Re= 520.3, with μ_w=9.7209x10^{-4} kg m^{-1} s^{-1} and U_T= 0.331 m s^{-1}), Bond (E_0= 0.314, equation [2.9] in Chapter 2) and Morton (M= 2.264x10^{-11}, equation [2.10] in Chapter 2) numbers the bubble terminal velocity in contaminated water (U_{Tclift}) is around 168.4 mm s^{-1} (see also equations [2.11] and [2.7] in Chapter 2, H*= 16.143 and J= 7.72).

An average distance was calculated as the average distance between imaginary straight lines drawn from the 5 mm holes on the perforated plate, and the water output point in the MAPC cone. The average distance that a bubble travelled in order to leave the MAPC was 104 mm. With the distance and bubble terminal velocity it was possible to calculate the estimated time that the bubbles took to leave the MAPC. This estimated time was 0.617 seconds.

Although the bubbles expelled from the specimen had a slug shape, these were assumed to be cylindrical (occupying the full cross section of the diameter) in order to simplify the calculations of the radii of curvature when the bubbles were in the plastic tube of the piping system. When a bubble was trapped in the capillary glass reduction its shape was very close to spherical.
Finally the equation to calculate the volume of gas expelled, at time that the bubbles was estimated to leave the specimen, was:

$$t_{specimen} = t_{recorded} - \frac{\mathrm{d}_{\mathrm{distance}}}{U_{bubble}} \quad [5.9]$$

$$P_{gasspecimen[i]} = \frac{2 * \gamma}{r_{tube} \text{ or } r_{bubblecapillary}} + u_{top[i]} \quad [5.10]$$

$$V_{gasspecimen[i]} = \frac{V_{gtube[i]} * \left(P_{gtube[i]} + 100\right)}{\left(P_{gasspecimen[i]} + 100\right)} \quad [5.11]$$

$$Vol_{gasspecimen[i]} = V_{gasspecimen[i]} + V_{gasspecimen[i-1]} * \frac{\left(P_{gasspecimen[i-1]} + 100\right)}{\left(P_{gasspecimen[i]} + 100\right)} \quad [5.12]$$

Where:

$\mathrm{d}_{\mathrm{distance}}$: average distance between the specimen and valve U1 or average distance between the specimen and glass reduction (see Figure 5.17), 182.5 mm and 104 mm respectively;

U_{bubble}: bubble terminal velocity in contaminated water, 168.4 mm s^{-1};

$t_{recorded}$: time at which bubbles are seen to go out of MPAC conical part, s;

$t_{specimen}$: time at which bubbles are estimated to leave the specimen, s;

$P_{gasspecimen[i]}$: pressure of gas in the specimen at time i $t_{specimen}$. It is calculated with u_{top} at i $t_{specimen}$, kPa;

$P_{gasspecimen[i-1]}$: pressure of gas in the specimen which preceded $P_{gasspecimen[i]}$, kPa;

$V_{gasspecimen[i]}$: volume of gas in the specimen at time i $t_{specimen}$, m^3;

$V_{gasspecimen[i-1]}$: volume of gas in the specimen which preceded $V_{gasspecimen[i]}$, m^3; and

$Vol_{gasspecimen[i]}$: accumulated gas volume expelled from the specimen at time i $t_{specimen}$, m^3.

Equations [5.9], [5.10], [5.11] and [5.12] show the final calculation used to obtain the accumulated gas volume expelled from the specimen at time $t_{specimen}$. Knowing the distance to

U1 and the glass capillary reduction zone it was possible to estimate the time of travelling from the surface of the specimen. With this value, and assuming a constant radius of curvature, the pressure of the gas inside of the bubble was estimated at a specific time inside the specimen. Furthermore, assuming that Boyle's law is applicable we can calculate the volume of gas expelled from the specimen at time $t_{specimen}$. The final accumulated volume was calculated from equation [5.12] applying Boyle's law.

Finally it is important to mention the assumptions used in this section part:

i. The radius of curvature of the "slug" gas bubbles in the plastic tube in MAPC piping system is constant and equal to 1 mm;
ii. The bubbles trapped in the glass capillary reduction (see Figure 5.9 in bottom acrylic connector) have a spherical shape;
iii. Temperature through the MAPC test is constant;
iv. Each single bubble keeps constant its radius of curvature (the bubbles do not break) between its departure time from the specimen until it is observed outside the MAPC conical part;
v. From the previous two points Boyle's law is applicable;
vi. Atmospheric pressure is equal to 100 kilopascals; and
vii. The velocity of the bubble rises very quickly in the first tenth of a second to reach a terminal velocity value that in this project has been called U_{bubble}.

The fourth group of results presented in this section are the vertical strain, expulsion & compression of gas and compression of gas of the sample in the MAPC versus the effective vertical stress from the time that the recording of drained loading starts. These results are important in estimating the amount of the total compression of the specimen during the MAPC test is represented by the compression of gas. These results are indicated in Figure 5.27 using as example Finesand13foamR. The vertical strain in the drained loading zone is indicated by a black solid line in Figure 5.27. The volume of expulsion & compression of gas are represented by the pink solid line in Figure 5.27. Finally the compression of gas of the sample in the MAPC is represented by the red dots in Figure 5.27. The dotted line shows the start of drained loading of the consolidation test. The vertical strain from the time that the drained loading starts was easily calculated from the readings of the vertical displacement transducer. The strain due to the expulsion/compression of gas is obtained subtracting from the vertical strain rate the difference between the changes of volume of water, which is divided per the volume of the specimen at the start of the drained loading. The strain of the specimen due to the compression of gas expelled from the sample was calculated subtracting from the strain of the specimen due

to compression/expulsion of gas the volume of gas expelled measured from the sample divided by the volume of the specimen at time t = 0. The following three equations show how to obtain these values:

$$\varepsilon' = \frac{H'_0 - H}{H_0} \quad [5.13]$$

$$\varepsilon'_{\exp-wg} = \varepsilon' - \frac{\left(\Delta V - \Delta V'_0\right)}{A * H_0} \quad [5.14]$$

$$\varepsilon'_{\exp-g} = \varepsilon'_{\exp-wg} - \frac{Vol_{gasspecimen[i]}}{A * H_0} \quad [5.15]$$

Where:

H_0: height of specimen at time t=0, m;

H'_0: height of specimen at t = start drained loading, m;

ε': strain of specimen in the drained loading zone;

ΔV: change of volume of water in/out sample, m^3;

ΔV_0: change of volume of water in/out sample at time t = start drained loading, m^3;

A: area of specimen in MAPC, m^2;

$\varepsilon'_{exp\text{-}wg}$: strain of specimen due to expulsion/compression of gas in the drained loading zone; and

$\varepsilon'_{exp\text{-}g}$: strain of specimen due to compression of gas in the drained loading zone.

In Figure 5.27 it is observed that the strain due to compression of the gas is almost identical to the strain due to the expulsion/compression of the gas during the drained loading test. This fact is observed in the majority of the tests, carried out in the MAPC. This will be further analysed in the following sections.

The fifth group of results presented in this section are the voids ratios of the sample in the MAPC versus the effective vertical stress recorded for the undrained loading starts. These results are important in order to compare the properties of the foamed soil tested in the MAPC with similar sand without foam. The total voids ratio was calculated from the measurement of the vertical displacement measured by the LVDT and the record of the total amount of soil mixture. The liquid voids ratio was obtained using the readings of the CVC device together with the quality control data at the start of the test. Finally to obtain the gas voids ratio, the liquid voids ratio was subtracted from the total voids ratio. These results are indicated in Figure 5.28 using as example Finesand25foamR. The specimen total voids ratio, gas voids ratio and liquid voids ratio are indicated by a red solid line, green solid line and a blue solid line respectively. The light blue dash single dotted line, dotted line and dash double dotted line show the start of undrained loading, drained loading and unloading respectively of the consolidation test.

The sixth group of results are the coefficient of permeability of the sample in the MAPC versus the effective vertical stress from the time that the recording of drained loading last. These results are important in order to evaluate the effect of foam conditioning in the permeability of Leighton Buzzard fine sand and Thanet sand. The typical results are indicated in Figure 5.29 using as an example Finesand25foamR. The coefficient of permeability was calculated using two approaches: parabolic distribution (Bolton, 1991) and constant rate of strain nonlinear theory (Wissa et al, 1971). Figure 5.29 illustrates the final coefficients of permeability for both approaches, $k_{intsoil}$ (first approach) and $k_{sh\text{-}soil}$ (second approach), after the mesh and perforated plate corrections. In this figure the solid green line represents the coefficient of permeability corrected for the mesh and for the perforated plate using the hydraulic gradient approach. The solid black line indicates the coefficient of permeability with the same corrections but using the constant rate of strain nonlinear theory (Wissa et al, 1971).

In the first approach the hydraulic gradient was calculated assuming (Bolton, 1991) that the excess pore water pressure in the specimen follows a parabolic distribution. Thus the hydraulic gradient is based on the parabolic isochrones maximum gradient at the output of the system (see Chapter 2 for theoretical background). Equation [5.19] gives the value of the coefficient of permeability after it has been corrected by the presence of the mesh on top of the specimen. During the calculation of permeability a second correction of the original value (see equation [5.20]) was carried out to count for the homogenization of the streamlines (see APPENDIX A) on the back of the perforated plate (Defrêche et al. 2002).

The value used for the coefficient of permeability of the mesh is as used by Psomas (2001). The permeability correction factor, R_k, is approximately 0.98. Details of the values used for its calculation can be found in APPENDIX A. The following equations were used to calculate the coefficient of permeability using the parabolic distribution approach:

$$\upsilon = \frac{q}{\mathrm{A}} \qquad [5.16]$$

$$i = 2 * \frac{\left(1000 * u'_{b2-1}\right)}{H_{2-1} * \rho_{water} * \mathrm{g}} \qquad [5.17]$$

$$k_{system} = \frac{\upsilon}{i} \qquad [5.18]$$

$$\frac{L_{specimen}}{k_{apsoil}} = \left(\frac{H_i}{K_{system}} - \frac{\mathrm{L}_{mesh}}{\mathrm{k}_{mesh}} \right) \qquad [5.19]$$

$$k_{\text{int}\,soil} = \frac{k_{apsoil}}{R_k} \quad [5.20]$$

Where:

q: flow rate, m^3/s;

A: cross section area of specimen, 0.0506 m^2;

v: Darcy velocity, m/s;

$u'_{b2\text{-}1}$: average excess pore water pressure between a suitable interval of time during the consolidation test, kPa;

$H_{2\text{-}1}$: average height of specimen between a suitable interval of time during the consolidation test, m;

ρ_{water}: water density, 1000 kg/m^3;

g: acceleration of gravity, 9.81 m/s^2;

i: hydraulic gradient, dimensionless;

K_{system}: coefficient of permeability of system without mesh correction, m/s;

R_k: permeability correction factor taken into account the perforated plate, dimensionless;

K_{apsoil}: coefficient of permeability of system corrected by effect of mesh, m/s;

$L_{specimen}$: thickness of specimen at any time in consolidation test, mm;

H_i: thickness of mesh plus height of specimen, mm;

L_{mesh}: thickness of mesh, 0.3 mm;

K_{mesh}: mesh coefficient of permeability, $8.3\ 10^{-7}$ m/s; and

$K_{intsoil}$: coefficient of permeability of specimen at any time in consolidation test corrected for effect of perforated plate, m/s.

In the second approach the coefficient of permeability was calculated using the CRS (constant rate of strain) nonlinear theory developed by Wissa et al. in 1971 (see Chapter 2). Equation [5.21] gives the displacement rate over time, which was used in equation [5.22], together with average height of the specimen in order to obtain the strain rate over time. Equation [5.23] defines the average vertical effective stress over time defined by Sheahan and Watters (1997). Finally using equation [5.24] the coefficient of permeability (without correction for the mesh or the perforated plate) was calculated.

$$d_{rate} = \frac{H_{2-1}}{t_{2-1}} \quad [5.21]$$

$$s_{rate} = \frac{d_{rate}}{1000 * H_{2-1}} \quad [5.22]$$

$$\sigma'_{sh} = \left(\left(\sigma_{lc} - u_{top} \right)^3 - 2 * \left(\sigma_{lc} - u_{top} \right)^2 * u'_b + \left(\sigma_{lc} - u_{top} \right) * \left(u'_b \right)^2 \right)^{\frac{1}{3}} \quad [5.23]$$

$$k_{sheahan} = \frac{-0.434 * s_{rate} * H^2_{2-1} * \rho_{water} * g}{2 * \sigma'_{sh} * \log\left(1 - \left(\frac{u'_b}{\sigma - u_{top}}\right)_{2-1}\right)} * 10^{-9} \quad [5.24]$$

Where:

t_{2-1}: suitable interval of time during the test, s;

d_{rate}: displacement rate over time, mm s^{-1};

S_{rate}: strain rate ratio, s^{-1}.

σ'_{sh}: average vertical effective stress of the specimen over Δt (time difference) in MAPC defined by Sheahan and Watters (1997), kPa; and

$k_{sheahan}$: average coefficient of permeability of the specimen over Δt (time difference), m s^{-1}.

The final value of the coefficient of permeability was obtained after $k_{sheahan}$ was corrected for the presence of the mesh and the perforated plate on top of the specimen. The procedure used in the correction was the same as that carried out on the first approach. Equation [5.25] shows the coefficient of permeability after mesh correction ($k_{sh-mesh}$) and equation [5.26] shows the coefficient of permeability after the perforated plate correction ($k_{sh-soil}$) was carried out.

$$\frac{L_{specimen}}{k_{sh-mesh}} = \left(\frac{H_i}{K_{sheahan}} - \frac{L_{mesh}}{k_{mesh}}\right) \quad [5.25]$$

$$k_{sh-soil} = \frac{k_{sh-mesh}}{R_k} \quad [5.26]$$

Where:

$K_{sh-mesh}$: Sheahan coefficient of permeability of the system corrected by effect of mesh, m/s; and

$K_{sh-soil}$: Sheahan coefficient of permeability of the specimen at anytime of consolidation test corrected by effect of perforated plate, m/s.

The theory behind the equations [5.23] and [5.24] has been described in Chapter 2. It is important to highlight that these equations are applied assuming that conditions during the test (see Chapter 2) are not transient. For transient conditions during the test, the Sheahan and Watters (1997) approach results in the parabolic distribution, thus the coefficient of permeability is calculated using equation [5.18].

Finally before starting to interpret and analyse the results it is interesting to look at Table 5.2, which shows a summary of some values obtained by the MAPC on Leighton Buzzard-water-Versa foam mixtures and Thanet sand-water-Versa foam mixtures. The values that appear in the table from left to right are: Foam injection ratio (FIR), voids ratio just before the consolidation test starts (e_0), relative density just before consolidation test starts (Dr_0), liquid

void ratio just before consolidation test starts (e_{w0}), gas void ratio just before consolidation test starts (e_{g0}), saturation degree just before consolidation test starts (S_{r0}), initial liquid content just before consolidation test starts (w_0), maximum effective vertical stress during the consolidation test (σ'_{max}), initial height of the specimen in millimetre just before consolidation test starts (H_0), maximum excess pore water pressure per effective vertical stress (u'_b/σ'), vertical strain rate (s_r), and vertical displacement rate during drained loading.

5.5. Interpretation of results

In this section the most relevant results are interpreted and analysed. The next subsections present and interpret the displacement rate, voids ratios, pore water pressures, coefficient of permeability, gas expelled and Boyle's law results obtained.

5.5.1. Displacement rate

Following the recorded data in the different tests it is important to highlight that a rate of deformation of around 0.3 mm min^{-1} is easy to maintain with the Tritest 50 machine and also gives enough time to achieve stable conditions during the tests. The 0.15 mm min^{-1} or the 5 mm min^{-1} produces unstable values through the MAPC test. These stabilities and instabilities can be observed in the tests that were carried out at these vertical displacement rates, Finesand10 and Finesand26foamR. Figure 5.30 shows the vertical displacement rate of Finesand10 and Finesand26foamR. In the case of Finesand10 many peaks can be seen in the rate of deformation line, deviation of even 0.15 mm min^{-1} shows that there is a minor problem in the gear system of the Tritest 50 at vertical displacement rate around 0.15 mm min^{-1}. Although on average a 0.11 mm min^{-1} rate can be achieved there may be a need for further consideration in case a different type of soil needs to be tested and a lower rate of deformation is needed. In the case of Finesand26foamR stable conditions were not achieved during the test. This seems to be due to the excessively fast rate which does not allow enough time to achieve a stable condition during testing, where quasi-stationary conditions occurred. This is discussed in the excess pore water pressure subsection.

In 89% of the tests a vertical displacement rate of around 0.3 mm min^{-1} was used. This gave stable consolidation rates and also enough time to achieve quasi-stationary conditions. As it can be seen in Table 5.2 the exact value of 0.3 mm min^{-1} is a reference value (speed value written on the Tritest 50) and in reality the vertical displacement values were around that. The difference between the real values and the desired reference value is due to the manner in which the vertical displacement rate is selected in the Tritest 50. In this research this deviation from the desired reference value is considered acceptable with no major influence on the results.

5.5.2. Voids ratio (strain)

Figures 5.31, 5.32, 5.33 and 5.34 show the voids ratio results for all the nineteen tests carried out with the MAP consolidometer at CRS. The voids ratio (e), liquid void ratio (e_w) and gas void ratio (e_g) are evaluated at the left hand axis.

Looking at Figures 5.31, 5.32, 5.33 and 5.34 it is possible to observe four groups (see Table 5.3):

1. 150 kPa $<\Delta\sigma'_{drainedloadig}$ <217 kPa and $e_{drainedloading}$ <1.05
2. 185 kPa $<\Delta\sigma'_{drainedloadig}$ <229 kPa and 1.05 < $e_{drainedloading}$ <1.28
3. 24.7 kPa = $\Delta\sigma'_{drainedloadig}$ and $e_{drainedloading}$ =2.29
4. 59 kPa $<\Delta\sigma'_{drainedloadig}$ <195 kPa and 1.38< $e_{drainedloading}$ <2.63

The first group is formed by Finesand10, Finesand14foamR, Finesand15foamR, Finesand18foamR, Finesand21foamR and Finesand22R. They also present percentage of voids ratio variation that occurred in the drained zone between 3.23% and 7.64% of the voids ratio just before the consolidation test starts (e_0)

The second group is formed by Finesand12foamR, Finesand17foamR, Finesand19foamR, Finesand20foamR, Finesand23foamR, Finesand24foamR, Finesand25foamR and Finesand26foamR. They also present percentage of voids ratio variation that occurred in the drained zone between 12.89% and 20.52% of the voids ratio just before the consolidation test starts (e_0).

The third group is formed by Thanetsand1foamR. Although this shows similar percentage of voids ratio variation of the voids ratio just before the consolidation test starts (e_0) than the second group, its $e_{drainedloading}$ exceeded the second group ranges. This can be explained by the fact that $\sigma'_{enddranedloading}$ did not exceed 25 kPa.

The fourth group is formed by Finesand11foamR, Finesand13foamR, Finesand16foamR and Thanetsand2foamR. They also present percentage of voids ratio variation that occurred in the drained zone between 22.21% and 36.85% of the voids ratio just before the consolidation test starts (e_0).

In some tests a constant voids ratio could be observed right at the beginning of loading, either under a drained or undrained loading stage. This may due to some delay in achieving the vertical displacement rate set at a constant value before the test starts in the Tritest 50

machine. These delays were no longer than 60 seconds and did not have major effects on the general behaviour of the specimen in the MAPC tests.

All the tests showed a voids ratio value at the end of the loading stage higher by at least 5.69% than the maximum voids ratio for that type of sand (see Table 5.3) with exception of Finesand10, Finesand14foamR, Finesand15foamR and Finesand22R. It is clear looking at Table 5.2 that for tests Finesand14foamR and Finesand15foamR the previous results, i.e. voids ratio at the end of the loading stage lower than maximum voids ratio for that type of sand, have a strict relation to their low gas void ratio content at the beginning of the loading stage. In the case of the saturated sands, the results (Figures 5.31 and Figure 5.33) were as expected, i.e. voids ratio at the end of the loading stage lower than maximum voids ratio for a saturated fine sand. The higher difference between the voids ratio value at the end of the loading stage and the maximum voids ratio for that type of sand was achieved in test Finesand16foamR where the voids ratio at the end of the loading stage was 22.52% higher than the maximum voids ratio for Leighton Buzzard fine sand. This difference was achieved at effective stresses around 60 kPa; although higher effective stresses were applied on other Leighton Buzzard sand tests such as Finesand25foamR where the voids ratio at the end of the loading stage was 7.97% higher than the maximum voids ratio for Leighton Buzzard fine sand at effective stresses around 230 kPa. In the case of Thanet sand, it was observed that the voids ratio value of Thanet sand water foam mixtures at the end of the loading stage were at least 52% higher than the maximum voids ratio for Thanet sand. In this case effective stresses no higher than 75 kPa were applied.

These results reveal that gas bubbles can exist in specimens of sand and water at vertical effective stresses as high as 230 kPa (see Table 5.2 and Table 5.3).

5.5.3. Pore water pressures and excess pore water pressure

Figures 5.35, 5.36, 5.37 and 5.38 show the pore water pressure results for all the nineteen tests in the MAP consolidometer. Pore water pressure at top of the sample (u_{top}), pore water pressure at base of the sample (u_{base}) and average pore water pressure (u_w) are evaluated in kilopascal at the right hand axis. The excess pore water pressure (u'_b) is evaluated at the left hand side axis. A light blue dashed vertical line is used to mark the start of the drainage of liquid from the sample and a light blue dash double dotted line shows the start of the unloading zone.

Figures 5.35, 5.36, 5.37 and 5.38 show that the excess pore water pressures obtained from L.B. sand water foam mixtures are lower than 0.73 kPa, during the drained loading zone, even reaching negative values at some points during the MAPC tests. Pore pressure values lower than 0.73 kPa are beyond the good accuracy resolution of the instrumentation, thus the negative

values measured sometimes during testing are due to limitations of the pore pressure instruments.

In an attempt to increase the excess pore water pressure, a higher rate of vertical deformation was used. Finesand26foamR shows how this attempt was unsuccessful. Although higher pore water pressures (almost two fold) in the specimen were achieved, the excess pore water pressure follows exactly the same pattern than the other L.B. fine sand water foam mixtures. Nevertheless, the behaviour of Thanet sand water foam mixtures was significantly different. These tests showed a minimum excess pore water pressure value of 10.65 kPa and a maximum value of around 13.61 kPa at the end of loading stage (see Table 5.4).

Table 5.4 shows the maximum ratio, in percentage, of excess pore water pressure per effective stress, u'_b/σ' during drained loading. The maximum ratio excess pore water pressure per effective stress is over 100% for tests on Thanet sand water foam mixtures. These are higher than the values obtained on L.B. fine sand water foam mixtures (lower than 19%).

5.5.4. Coefficient of permeability

Figure 5.39 and Figure 5.40 show the coefficient of permeability results obtained from Finesand22, Finesand13foamR, Finesand14foamR, Finesand23foamR, Finesand24foamR, Finesand25foamR, Thanetsand1foamR and Thanetsand2foamR. They have been plotted on a logarithmic scale. These figures show the permeability results calculated using the parabolic isochrones maximum gradient at the output of the system ($k_{intsoil}$) and the CRS (constant rate of strain) nonlinear theory developed by Wissa et al. in 1971 ($k_{sh\text{-}soil}$).

Figure 5.39 and Figure 5.40 show the coefficient of permeability calculated using equation [5.20]. The tests plotted on these figures are just an example of the results obtained from all the tests carried out. The average coefficient of permeability calculated from the Finesand22 test (2.25×10^{-3} m s^{-1}) is higher than the expected values. These results are two orders of magnitude higher than values obtained from the Kozeny-Carman equation (Head, 1994), 1.35×10^{-5} m s^{-1}, which is the permeability for the same type of sand at its maximum voids ratio. However, the values obtained for Finesand10, are one order of magnitude lower than values obtained from the Kozeny-Carman equation. It is not clear why Finesand10 shows this behaviour. In this research the permeability values obtained for Finesand22 are thought to be correct because they are closer to the theoretical values found in literature for similar types of sand.

The values of the L.B. fine sand water foam mixtures show a maximum reduction in the permeability (permeability value 2.39×10^{-4} m/s) of one order of magnitude at vertical effective stress of 78 kPa. These results are not continuous due to the low values of the excess pore water pressure. It is clear observing the Thanet sand water foam mixtures tests that when high excess pore water pressures are achieved in the specimens during the MAPC test, more stable and continuous values of coefficient of permeability can be calculated. The maximum u'_b values achieved during the Thanetsand1foamR and Thanetsand2foamR MAPC tests, after the loading stage, are around 13.6 kPa which is a eighteen times the maximum u'_b recorded on L.B. sand water foam mixture tests.

Figure 5.39 and Figure 5.40 also show the coefficient of permeability using the CRS nonlinear theory equation [5.26]. More precise coefficients of permeability can be obtained using this equation. The coefficient of permeability obtained for Finesand22 is also two orders of magnitude lower than the Kozeny-Carman value of 1.35×10^{-5} m s^{-1}. Within the L.B. sand water foam mixtures tested, Finesand24foamR shows a very stable coefficient of permeability throughout its loading stage. The coefficient is of one order of magnitude lower than Finesand22 (1.06×10^{-4} m/s). The Thanet sand water foam mixtures show a very stable coefficient of permeability and also lower values compared with L.B. sand water foam mixtures. Thanetsand1foamR shows a minimum coefficient of permeability (using Wissa theory 4.55×10^{-8} m/s and using isochrones curve theory 5.40×10^{-8} m/s) of at least two orders of magnitude lower than L.B. sand water foam mixtures. All these results exhibit a similar shape to the coefficient of permeability curves obtained by Sheahan and Watters in 1997 (see Chapter 2).

Table 5.4 shows a summary of relevant values related to the coefficient of permeability. From left to right this table shows: maximum excess pore pressure (u'_b), maximum ratio excess pore water pressure per effective stress (u'_b/σ'), minimum coefficient of permeability of the specimen using CRS theory ($K_{sheahan}$), minimum coefficient of permeability of the system using CRS theory corrected by effect of mesh ($k_{sh\text{-}mesh}$), minimum coefficient of permeability of the system using CRS theory corrected by effect of perforated plate ($k_{sh\text{-}soil}$), minimum coefficient of permeability of the system using the parabolic isochrones maximum gradient (k_{system}), minimum coefficient of permeability of the system using the parabolic isochrones maximum gradient corrected by effect of mesh ($k_{ap\text{-}soil}$), minimum coefficient of permeability of the system using the parabolic isochrones maximum gradient corrected by effect of perforated plate ($k_{int\text{-}soil}$), average coefficient of permeability of the system using CRS theory corrected by effect of perforated plate (over the drained loading stage) and coefficient of permeability of the system using the

parabolic isochrones maximum gradient corrected by effect of perforated plate (over the loading stage).

From Table 5.4 it can be observed that when the maximum excess pore water pressure gets small the permeability values tend to increase, making the specimen more permeable.

It has to be said that due to instrumentation limitations, as low as the excess pore water pressure value got more unreliable was the calculated permeability value.

For group 1 in section 5.5.2 the maximum u'_b/σ' recorded was 0.02% except from Finesand10 and Finesand22R (1% <maximum u'_b/σ'< 8%), which are saturated sands and have no foam. Group 2 in section 5.5.2 shows a maximum u'_b/σ' value of 3046% in Finesand17foamR but it did not show reliable calculated permeability values. This implies that the maximum u'_b/σ' happened at the beginning of the drained loading where σ' was very small. The next less high maximum u'_b/σ' value, where permeability was calculated, is 8.88% for test Finesand5foamR, with average $K_{sh\text{-}soil}$ of $4.62x10^{-4}$. The highest maximum u'_b/σ' values in group 3 and group 4 were 11536% and 53204% respectively. These values were obtained in the Thanet sand tests. The L.B. fine sand tests in group 3 and group 4 showed at least 10 times smaller maximum u'_b/σ' values than the values showed on Thanet sand tests.

It is possible to say that in tests on L.B. fine sand with foam was necessary to measure maximum u'_b/σ' of around 9% in order to produce measurable permeability values. Tests on Thanet sands with foam with maximum u'_b/σ' values recorded are higher than 11000% have produced measurable permeability values. Following this, it can be conjectured that the drainage conditions is very important because it controls ratio u'_b/σ' and permeability.

The mesh and perforated plate corrections had less than one order of magnitude of influence in the calculation of the permeability values as it can be seen in Table 5.4 in columns fourth, fifth and sixth for Sheahan method, and columns eight and ninth and tenth for the parabolic distribution approach.

For tests on L.B. fine sand with foam the permeability calculated with the Sheahan method showed the same order of magnitude value than the permeability calculated with the parabolic distribution approach. In the contrary tests on Thanet sand foam showed one order of magnitude of difference between both approaches. This implies that most of the drained loading

occurred under no transient conditions for tests on Thanet sand with foam and transient conditions for tests on L.B. fine sand with foam.

In general with increasing σ' the sand specimens with foam tends to become stiffer as it can be seen in Figure 5.39 and Figure 5.40, independently of the method used to calculate the permeability values.

5.5.5. Gas expelled

Visual inspections of the gas expelled during the MAPC tests were carried out. Using these visual measurements, the strain of specimen due to expulsion/compression of gas in the drained loading phase ($\varepsilon'_{exp\text{-}wg}$) and the strain of the specimen due to compression of gas in the drained loading phase ($\varepsilon'_{exp\text{-}g}$) were calculated. Figure 5.41, Figure 5.42 and Figure 5.43 show the ratio of compression due to accumulated gas expelled at different vertical strains for each test. Figure 5.41, Figure 5.42 and Figure 5.43 show also the total compression strain of the specimen (ε'), the compression strain due to expulsion/compression of gas in the drained loading phase ($\varepsilon'_{exp\text{-}wg}$) and the strain due to compression of gas in the drained loading phase ($\varepsilon'_{exp\text{-}g}$).

The strain due to the expulsion of water is the area between the vertical strain in drained compression line (black line) and the expulsion/compression of gas line (pink line). The strain due to the expulsion of gas is the area between the expulsion/compression line (pink line) and the compression of gas dots (red dots). The strain due to the compression of gas is the area between the compression of gas dots (red dots) and the x axis. The tests that are not shown had no expulsion of gas during the loading stage of MAPC test.

The maximum strain due to the expulsion of gas is lower than 4% of the total strain in 74% of the tests although gas was expelled even at high vertical effective stresses of around 300 kPa on L.B. foamed fine sand and at vertical effective stresses of around 60 kPa on Thanet foamed sand (see Table 5.5). 26% of the tests had a maximum strain due to the expulsion of gas higher than 10% of the total strain ratio. Finesand15foamR shows a maximum strain due to the expulsion of gas of around 30% of the total strain which is the maximum recorded of all tests. Within the foamed sand tests, Finesand12foamR and Finesand26foamR show the lowest maximum ratio of compression due to the expulsion of gas values. Both have a zero strain due to the expulsion of gas.

Table 5.5 also displays the maximum strain during the drained loading phase, the maximum strain due to expulsion/compression of gas in the drained loading phase ($\varepsilon'_{exp\text{-}wg}$), the maximum strain due to compression of gas in the drained loading phase ($\varepsilon'_{exp\text{-}g}$), maximum compression of

gas as a percentage of the specimen strain, maximum gas expelled as a percentage of the specimen strain and maximum water expelled as a percentage of the strain.

Figure 5.44 (d) shows how increasing the FIR does not necessarily increase the Maximum gas expelled. This makes sense if FIR results are complemented by Figure 5.44 (b) or Figure 5.45 (a) where initial relative density of the specimen has to be related to the capability of the specimen to retain the gas and establish a coexistent between grain of soil, water and gas bubbles.

Looking at Figure 5.45 (c) and using the results in Table 5.5 regarding to the lowest maximum ratio of compression due to the expulsion of gas values obtained for tests Finesand12foamR and Finesand26foamR, where they have zero gas expelled at opposite values of maximum water expelled and maximum compression of gas, it is possible to estimate a polynomial distribution of the maximum water expelled versus relative density and FIR. In Figure 5.45 (a) and Figure 5.45 (c) two polynomial curves have been drawn. These curves show the limits of a band where the values move. The change of concavity in these polynomial curves represents the change in quality of coexistent between grains of soil, water and gas bubbles to achieve a mixture suitable for tunnelling with an EPBM.

It can be said that one wants minimal expulsion of water and gas, so that in fact "good" mixes would be those in which most compression is due to gas compression rather than water expulsion. Thus in this series of tests there are 3 best mixes, which are Finesand14foamR, Finesand18foamR and Finesand26foamR. These showed less than 50% maximum water expelled but also the compression of the gas was higher than the gas expelled. Although Finesand15foamR showed maximum water expelled lower than 50% the maximum gas expelled was higher than the maximum compression of gas (see Table 5.5 and Figure 5.45).

5.5.6. Boyle's law

In many engineering applications the law of ideal gases can be applied until pressures between 690 and 1379 kPa, if the absolute temperatures are at least twice the critical temperatures (Marks, 1997). Therefore it is interesting to plot Boyle's Law for all the foamed sand tests. Figures 5.46, 5.47 and 5.48 show Boyle's Law defined as the product of the average pore water pressure in absolute terms (u_w+100) and the gas voids ratio (e_g). In this definition it is assumed that the pressure of the gas inside of the MAP consolidometer is equal to the average pore water pressure.

In Figures 5.46, 5.47 and 5.48 the phase of drained loading of each test is clearly marked. This phase is placed after the blue dash dotted line. In this phase (between blue dash line and double dotted dash line) most of the tests show a relatively constant relationship according to Boyle's Law.

Table 5.6 shows the detailed values of the parameter used in the calculation of Boyle's law. In the last column of Table 5.6 it can be observed that 94% of the tests, where Boyle's law theory can be applied, show a standard deviation lower than 5%. The only test that shows a standard deviation higher than 5% is Finesand14foamR, with a standard deviation value of 14.6% of its average Boyle's law value.

5.6. Applicability of experimental results in EPBM tunnelling process

MAP consolidometer tests can be used to determine how stable sand water foam specimens are at high effective vertical stresses. This is very important in tunnelling projects when faced any an unknown pressure for earth pressure balance and a foaming agent that could produce foam has the ability to coexist with in-situ soils at high effective stress is required (see Figures 5.31, 5.32, 5.33 and 5.34). This could reduce the cost of tunnelling projects avoiding unnecessary investment in no adequate soil conditioners for that specific excavated soil.

Soils with reduced permeability are often required in EPB machines. This normally occurs when cohesionless soils are excavated. In this case to have a way to measure the permeability of the in-situ soil when it has been altered by adding soil conditioners is crucial. Using the MAP consolidometer test we can qualitatively evaluate if foam conditioners have any permeability effect on the in-situ soil under study (see Figures 5.39 and 5.40). In the case of L.B. fine sand conditioned with foam it was possible to reduce the permeability in one order of magnitude regarding saturated L.B. fine sand. Nevertheless, the previous result depends of the maximum value achieved by the ratio u'_b/σ', which in case of L.B. fine sand conditioned with foam has to be higher than 9% in order to achieve reliable permeability values. In the case of Thanet sand conditioned with foam it is possible to have reliable permeability values at ratios of u'_b/σ' around 11000%. The tunnellers could set up any type of apparatus on site in order to measure the permeability of an excavated conditioned soil mixture. During this on site test they have to put attention to: FIR used, excavated soil mixture loading pressure and rate of water volume expelled from the excavated soil mixture. Having the previous parameters on mind a comparative evaluation of the permeability of the excavated conditioned soil mixture can be established for different conditioners regarding the excavated natural soil. This might reduce the

cost of excavation, avoiding unnecessary runs out of material during tunnelling causing unforeseen damage and accidents on site.

"Ideal" soil water foam mixtures are preferred by tunnellers who use EPB machines. Ideal mixtures that can be extracted easily from the screw conveyor and avoid uncontrolled flow of water out the screw. Unfortunately the "ideal" mixture needs to be changed throughout the excavation process as the soil type, water table and building area changes. Thus a history of the soil water foam mixture behaviour at different effective stresses is very useful to determine properties of the specimen at a specific effective stress levels which could be used to back calculate main mixture parameter, used on site by tunnellers, as FIR for instance.

Nowadays one of the main problems for the tunnellers is the disposal of the excavated soil. Here it has been demonstrated that the existence of bubbles in a soil water mixture produces, when the soil mixture is consolidated, a high volume of water out of the mixture (Figure 5.44 and Table 5.5) and a negligible volume of gas. Thus this idea can be used as a way to extract the water of excavated soils before disposal in order to decrease the use of the available land in landfill.

5.7. Summary

This Chapter reported the equipment, procedure, results and analysis of nineteen compressibility tests on L.B. fine sand water foam mixtures and Thanet sand water foam mixtures. The MAP consolidometer apparatus used to carry out these tests has been described.

Section 5.2 described the MAP consolidometer apparatus used to carry out the tests. The MAP consolidometer (MAPC) consists of a base of a standard 254 mm diameter Rowe cell apparatus and a conical top part designed to capture gas bubbles during consolidation. A 1.5 mm circular cross section o-ring was used to provide sealing between the MAPC base and top parts. The MAPC was instrumented to measure pore pressures, vertical stress, vertical displacement during consolidation and the water expelled during the drained stage of the consolidation test.

Section 5.3 presented the experimental procedure of MAPC tests. Nineteen tests were reported. Group X tests were carried out applying a continuous constant rate of vertical deformation during the undrained and drained stages. In the second group of tests, called Y, the continuous constant rate of vertical deformation was applied under drained conditions (see Table 5.1). A detailed explanation of the operation of the MAPC was given using Figures 5.15, 5.16 and 5.17. The consolidation tests were stopped when 20 mm of vertical displacement has occurred, or when 250 kPa vertical stress is achieved or when excessive amount of gas has been expelled,

almost reaching the CVC. When any of these happened, an unloading stage was initiated lasting for a few millimetres of the vertical displacement (in the opposite direction but at the same speed). After this, the recording of data was stopped and the test ended. This section also explained in detail other important points of the MAPC test procedure such as: quality control, friction and compression speed.

In section 5.4 the typical results of MAPC tests were presented together with the equation related to each parameter. Six groups of results were presented and explained. The first group of results were for the specimen height and vertical strain rate from the time that the recording of data started (see Figure 5.23). The second group of results were the vertical and effective vertical stresses, pore water pressure at top of the sample, pore water pressure at the base (bottom) of the sample, excess pore water pressure and average pore water pressure in the sample from the time that the recording of data started (see Figure 5.24). The third group of results (see Figure 5.25) were the volume of water in/out of the sample, volume of gas expelled from the sample and volume of the sample in the MAPC from the time that the recording of data started. The fourth group of results presented in this section were the vertical strain, expulsion & compression of gas and compression of gas of the sample in the MAPC versus the effective vertical stress from the time that the recording of drained loading started (see Figure 5.27). The fifth group of results were the voids ratios of the sample during in the MAPC versus the effective vertical stress from the time that the recording of undrained loading started (see Figure 5.28). The sixth group of results were the coefficient of permeability of the sample in the MAPC versus the effective vertical stress from the time that the recording of drained loading lasted (see Figure 5.29).

In section 5.5 the most relevant results were interpreted and analysed. The displacement rate, voids ratios, pore water pressures, coefficient of permeability, gas expelled and control of Boyle's Law results were obtained. Voids ratios higher than the maximum voids ratio of L.B fine sand and Thanet sand were recorded on L.B. fine sand water foam and Thanet sand water foam compressibility tests respectively at effective vertical stresses of around 200 kPa. Thanet sand water foam mixtures show ten fold higher values of excess pore water pressures (10 kPa) than L.B. water foam mixtures.

Permeability values, calculated by the isochrones curves theory, of the L.B. fine sand water foam mixtures show a maximum reduction of one order of magnitude (2.39×10^{-4} m/s), with respect to the saturated fine sand test (2.25×10^{-3} m/s), at vertical effective stress of 78 kPa. The permeability values calculated using Wissa theory show permeability of one order of

magnitude lower than Finesand22 ($2.48x10^{-3}$ m/s) in the case of Finesand24foamR ($1.06x10^{-4}$ m/s) for the L.B. sand water foam mixtures tested. The Thanet sand water foam mixtures show a very stable coefficient of permeability and also lower values (using Wissa theory $4.55x10^{-8}$ m/s and using isochrones curve theory $5.40x10^{-8}$ m/s) compared with L.B. sand water foam mixtures. Thanetsand1foamR show a minimum coefficient of permeability of at least two orders of magnitude lower than L.B. sand water foam mixtures (see Table 5.4). Nevertheless, the previous results depend of the maximum value achieved by the ratio u'_b/σ', which in case of L.B. fine sand conditioned with foam has to be higher than 9% in order to achieve reliable permeability values. In the case of Thanet sand conditioned with foam it is possible to have reliable permeability values at ratios of u'_b/σ' around 11000%. Following this, it can be conjectured that the drainage conditions is very important because it controls ratio u'_b/σ' and permeability.

The maximum ratio of compression due to the expulsion of gas was lower than 4% of the total strain ratio in 74% of the tests although gas was expelled even at high vertical effective stresses of around 300 kPa on L.B. foamed fine sand and at vertical effective stresses of around 60 kPa on Thanet foamed sand (see Table 5.5). 26% of the tests had a maximum ratio of compression due to the expulsion of gas higher than 10% of the total strain ratio. In this subsection it is clear that increasing the FIR does not necessarily increase the maximum gas expelled (see Figure 5.44 (d), Figure 5.44 (b) and Figure 5.45 (a)). The FIR and the initial relative density of the specimen have to be related to the capability of the specimen to retain the gas and establish a coexistent between grain of soil, water and gas bubbles. Furthermore a polynomial distribution of the Maximum water expelled versus relative density and FIR was estimated (see Figure 5.45 (a) and Figure 5.45 (c)). These curves show the limits of a band where the values move. The change of concavity in these polynomial curves represents the change in quality of coexistent between grain of soil, water and gas bubbles to achieve a desire mixture suitable for tunnelling with an EPBM. It is concluded that "good" mixes would be those in which most compression is due to gas compression rather than water expulsion. Thus in this series of tests there are 3 best mixes, which are Finesand14foamR, Finesand18foamR and Finesand26foamR. These showed less than 50% maximum water expelled but also the compression of the gas was higher than the gas expelled (see Table 5.5 and Figure 5.45).

Boyle's law theory is fulfilled in most of the MAPC tests in the drained loading zone. It can be observed that 94% of the tests where Boyle's law theory can be applied show a standard deviation, of the average value of the product of the average pore water pressure and the gas void ratio, lower than 5%.

Section 5.6 reported the applicability of the experimental results in EPBM tunnelling processes. High voids ratio values at high effective vertical stresses, permeability measurements, study of specimen behaviour at different effective vertical stresses and drying of soils are the outputs that this experimental research recommends tunnellers on EPBM applications to use.

Finally these tests demonstrated that the conditioning of L.B. fine sand and Thanet sand with foam to form materials suitable for controlled EPB machine operations can be successfully studied. It also demonstrated that relevant information can be extracted from MAPC tests whose outputs could deliver enormous changes in the tunnel operational costs avoiding: unnecessary runs out of material during tunnelling causing unforeseen damage and accidents on site, and unnecessary investment in no adequate soil conditioners for that specific excavated soil, when EPB machines are used.

Chapter 6. Screw conveyor tests

6.1. Introduction

This Chapter describes the main parts of the model earth pressure balance (EPB) screw conveyor commissioned at Oxford University. The apparatus, instrumentation and methodology using during testing are also described. Some screw conveyor test results, on Leighton Buzzard fine sand and Thanet sand mixed with Versa foam, and Garside sand mixed with Poly-foamer MCB conditioners are described here.

In the last section of this chapter an analysis of the results is carried out, focussing on the effect of the Oxford screw conveyor (OSC) model operating conditions on angle of friction on the conveyor casing, torque, casing shear stress and discharge efficiency. This analysis is used to draw some preliminary conclusions regarding the behaviour of sand mixed with foam conditioners, and the effect of the conditioners in screw conveyors.

6.2. Oxford model EPB screw conveyor

The screw conveyor apparatus used in this project is a modification of the one developed by Merritt at Cambridge University (Merritt, 2004). The screw conveyor commissioned for this research represents an approximately 1:11 scale model of a full scale EPB machine screw conveyor. The system has been equipped with instrumentation including Cambridge type load cells and pore pressure transducers, which are placed in the screw conveyor casing. A draw wire transducer is placed on top of the screw conveyor system tanks to measure the vertical displacement of the consolidation ram. The screw is rotated by an electrical motor which is controlled by a 650V (trade name) drive unit which has an option to measure the torque in the system.

The model screw conveyor can be operated with variable screw speeds, variable pressure on the sample and different sizes of discharge gates. Screws of different geometry can also be installed. The Oxford model EPB screw conveyor casing can be rotated by 45 degrees about the screw axis in order to study variations in Cambridge type load cell and pore pressure transducers measurements, for the same operational and sample conditions.

The next sections will describe the main parts of the Oxford model screw conveyor together with a more detailed description of its instrumentation.

6.2.1. General arrangement

An overview of the Oxford screw conveyor (OSC) is shown in Figure 6.1 and Figure 6.2. In Figure 6.1 the 650V drive, two jacking swivel wheels and AC induction motor are highlighted. The swivel wheels (three in total) are used to give a free horizontal movement to the OSC frame when the OSC casing is not bolted to the tanks. The swivel jacking wheels have a locking mechanism that fixes their vertical and horizontal position when it is needed. Using their swivel mechanism they can give precise vertical alignment of the OSC casing with the bottom flange of the tanks. The AC electric motor rotates the screw (inside the OSC casing), which could be operated at different speeds via the 650V drive. The 650V drive is also used to measure the torque applied by motor during testing.

In Figure 6.2 the reaction frame, tanks, conveyor casing, Rotex® coupling and motor gearbox are highlighted. The motor gearbox reduces the speed and increases the maximum torque of the motor by a factor of 61.7. The speed range obtained after the gear box for the OSC model, 4.6-23 rpm, is the same as the operational range used in screws by contractors on tunnelling sites. The rotational movement from the motor gearbox axis shaft is transmitted by a Rotex® coupling to a drive shaft which connects to the screw. The rotating screw extracts the sample placed inside the tanks. At the same time a vertical stress is applied on top of the sample by a piston which is held by the reaction frame. The sample therefore moves through the casing. The casing has in its wall Cambridge type load cells and pore pressure transducers.

The general arrangement of the system is shown in Figure 6.3 and Figure 6.4. The model screw conveyor was designed to represent an approximately 1:11 scale of a typical EPB machine screw conveyor. Medium to large diameter EPB machines typically have screw conveyor with a length in the range about 8 m to 12 m, and a diameter of about 0.8 m to 1.2 m. Based on these typical full scale dimensions, the model screw conveyor was designed with an internal diameter of 108 mm and a length of 1099 mm when connected to the flange of the tank.

The screw conveyor was instrumented at four sections along the length. Two Cambridge type load cells and one pressure transducer could be mounted in the casing at each section (see Cut c-d in Figure 6.5). The Cambridge type load cells measure the total normal and shear stress acting on the internal surface of the casing. The pressure applied on the sample in the tanks is measured by a gauge in a hydraulic system. The hydraulic system was designed by Gue (1984) to consolidate clay samples. The hydraulic system is not described here but details can be found in Gue (1984). The sample volume change is measured through the displacement of the piston, which descends into the container as the soil is extracted by the screw. The motor 650V drive

was configured to measure the torque provided by the motor to rotate the screw. The instrumentation set up can provide measurements of the screw conveyor operation through the total pressures and pore water pressures acting on the casing, the casing shear stresses, the effective stresses, the screw torque and the soil flow rate through the conveyor. These measurements could provide data for the investigation of the screw conveyor mechanics with different soil samples and conveyor operating conditions.

6.2.2. Tank

The tank models the pressure chamber of an EPB machine. The sample tank consists of two cylindrical duralumin (H15-TB) tubs, which are bolted together by flanges as shown in Figure 6.3. The assembled tubs are bolted to a duralumin base plate and placed in a load frame. The lower cylindrical aluminium tub has a hole in the wall with a flange for connection of the screw conveyor. When the conveyor is connected to the sample tank, the screw enters the tanks through this connection flange. A rubber o-ring seals the flange tank connection with the conveyor. The flange tank connection has been machined from duralumin. However, a stainless steel insert was placed on its internal wall in order to avoid excessive wearing of the aluminium by the soil grains. The total length of the flange tank connection was chosen to produce the same ratio of length of insertion of the screw into the tank to height of the sample tank as for the Cambridge screw conveyor apparatus (Merritt, 2004), in order to have similar basic dimensions for future comparative research. The vertical position of the flange was chosen following the same principle.

The sample in the tank is pressurised through a piston with a vertical load applied by a jack mounted in the loading frame. The dimensions of the tank, piston and jack are shown in Table 6.1. The piston wall has an o-ring (flexible rubber hose) to seal the gap between the piston and the tank (between 1.5 mm to 3 mm). To minimize the friction between the internal wall of the tank and the o-ring of the piston, a layer of grease was applied in the tank internal wall. The jack used to load the piston and pressurise the sample was connected to a nitrogen gas bottle at the end of the hydraulic system (see Gue, 1984). Gue (1984) use the hydraulic system at a maximum pressure of 11.8 MPa. Gue also calibrated the hydraulic rams using a proving ring to determine the losses due to friction: 4.25 % friction losses were found. Assuming a maximum working pressure of 11.8 MPa for the hydraulic system, the maximum pressure that could be applied to the sample is 577 kPa, including the 0.69 kPa from the mass of the piston and a 4.25 % loss due to friction. The pressure supplied to the jack was controlled with a regulator in the gas line and monitored with a dial gauge accurate to 50 kPa.

6.2.3. Conveyor casing

The conveyor casing models the inclined screw conveyor casing of an EPB machine. The conveyor casing was machined from a steel tube. A discharge outlet can be found at one side of the conveyor casing. This discharge outlet has a 3" pipe thread with a internal diameter of 85.5 mm that can be used with any commercial fitting in order to change the discharge outlet conditions. A drawing of the conveyor casing is shown in Figure 6.6. Table 6.2 shows also the main dimensions of the conveyor casing components.

In Figure 6.6 four instrumented sections can be observed. In each section two Cambridge type load cells and one pore water pressure transducer can be connected. The instrumented sections have 225 mm between them, with the first instrumented section 344.6 mm from the beginning of the screw and the last section 164.4 mm from the centre of the discharge point. The two ports for mounting the load cells are placed in the lower half of the casing with centres at 45° to the vertical axis and 90° between them (see Figure 6.5). When the load cells are mounted on the ports the active face of the load cell coincides with the internal face of the conveyor casing. The load cell ports have tapped holes to connect the load cell housing to the conveyor casing and an o-ring groove to seal this connection. The pore water pressure transducers were mounted through a tapped hole placed on the centre line of the conveyor casing between the Cambridge type load cells as shown in Figure 6.6. The pore water pressure connectors are shown in Figure 6.7. This connector makes the mounting process of the pore pressure transducers easier for each test, assuring complete sealing of the connection and also a flush end between the internal face of the conveyor casing and the Vyon® used on the top of pore pressure connector. The connector will be explained in a later section.

6.2.4. Screw drive shaft

The screw drive shaft was designed by Merritt (2004) to make the mechanical connection to transfer the torque driving the screw. The final assembly of the drive shaft consists of two steel plates bolted to the end of the flange of the conveyor casing, which house the shaft seals and bearings, the shaft adaptor piece and the drive shaft piece. Details of the two steel plates system (sealing and bearings) can be found in Merritt (2004) and no further details are given here. The connection between the assembled drive shaft and the screw shaft inside the conveyor is made through a shaft adaptor piece. A layout of Merritt's design is shown in Figure 6.8. Although the final design at Oxford is different from Merritt's design, the drive shaft design is exactly the same.

The connection between the assembled drive shaft and the screw shaft inside the conveyor is made from hexagonal bore steel tubes and the drive shaft tube has a circular cross section. The

shaft adaptor part was machined with a hexagonal section at one end to fit the screw shaft and a circular section at the other end to fit into the drive shaft tube. The adaptor part was fixed into the screw shaft by a 6 mm diameter silver steel shear pin which has a quoted ultimate shear strength between 365 MPa and 547 MPa (expected to fail at a torque between 253 Nm and 379 Nm), and a circular section of the piece passed through the hole in the conveyor end plate and into the drive shaft tube. The connection between the drive shaft and the shaft adaptor part was made with a transverse shear pin through the two pieces. This is a hardened steel dowel pin supplied by Ondrives Ltd. UK. This pin has a shear strength of 56 kN and it was expected to fail at a torque of around 1400 Nm.

The screw drive shaft is connected to the output of the gearbox through a flexible coupling (type Rotex® supplied by Ondrives Ltd. UK) rated for a maximum torque of 625 Nm. The coupling comprises two cast iron hubs connected with a flexible polyurethane part which compensate for small axial, radial and angular misalignments in the drive shaft. Figure 6.9, Figure 6.10 and Figure 6.11 show a detailed drawing of the torque coupling. The torque coupling hubs were provided with two bores to match a 16 mm key way. One hub of the coupling was fitted with a bush (see Figure 6.10) in order to fit the hexagonal end of the drive shaft and the other hub was used as provided by Ondrives Ltd. UK to fit the shaft of the gearbox.

The drive shaft provides the mechanical connection between the screw shaft and the gearbox. The torque is transferred from the gearbox through the flexible coupling to the drive shaft, which rotates in the shaft bearings. The transversal shear pin connector between the drive shaft and the shaft adaptor part transfers the torque to the screw shaft via the silver steel shear pin to drive the screw inside the conveyor casing.

6.2.5. Model screws

Two screws were designed and manufactured for the model conveyor. The two screws have exactly the same dimensions, with the only difference being that one has a tube of 43 mm outside diameter with a 1 1/8" hexagonal bore in its length as central shaft and the other screw does not have a central shaft. The screw with central shaft and the screw without central shaft are shown in Figure 6.12.

The screws were manufactured by Universal Augers Ltd. UK. The central shaft of the screws has been machined from mild steel and its screw flights have been welded to the shaft. The screw flight surfaces have been hard faced to reduce wear of the screws during testing. The screw geometries are shown in Figure 6.13, Figure 6.14, Figure 6.15 and Table 6.3.

The outer diameter of the screw flights was designed to provide a 3 mm clearance between the flights and the conveyor casing so the screw will fit inside the casing allowing for tolerance in its dimensions. The screw with central shaft (SCS) and the screw without central shaft (SWCS) have approximately 12.5 flights over the length.

The geometry of screw conveyors used in EPB tunnelling machine have helix angles between 15 to 25 degrees. The screws for the model conveyor were designed with geometries based on this typical range. The specific dimensions were chosen to suit length and diameter of the model conveyor and to give a significant difference in its central shaft in order to measure the effects on the conveyor operation.

6.2.6. Screw motor

The model screw conveyor is driven by a variable speed electric motor and a gear box mounted on the conveyor frame as shown in Figure 6.2. The gearbox shaft connects to the screw drive shaft through the flexible coupling as described in the previous sections. The motor and gear box were selected based on the requirement of a maximum torque of about 800 Nm with a speed range between 5 to 30 rpm. The gearbox and the electric motor used were supplied by Pujol Transmissions Ltd. The electric motor is an induction squirrel cage motor with an in line gearbox. The motor shaft fits directly into the hollow gearbox input shaft and requires no special oil seals on the motor. The motor and gearbox technical data are shown in Table 6.4. The motor has a power of 2.2 kW and a rated output torque of 14.79 Nm. With the reduction gearbox ratio of 61.7 the motor can provide an output torque of 848.9 Nm, for a gearbox efficiency of 93% (Pujol, 2005).

The speed of the motor is controlled by 650V AC drive unit. This unit will allow local or remote control operation of the motor and also record the torque applied by the motor during the screw conveyor operation. The next section will describe the 650V drive main features used during this research.

6.2.6.1. 650V drive

The 650V inverter has been designed to provide simple speed control for standard AC induction motors. In this research the 650V was programmed for a preset speed. Table 6.5 shows the technical data for the 650V drive unit. The drive unit was supplied by Eurotherm Drives. An RFI filter was included in the inverter unit to reduce the interference with the screw conveyor instruments, generated by the inverter controlling the frequency of the power supply to control the motor speed.

The ConfigEd Lite (CE Lite) software was used to configure the 650V Eurotherm Drives (Eurotherm Drives Limited (a) and (b), 2002). This software employs a graphical user interface and a drawing tool that allow a diagram to be drawn of the configuration for the 650V drive with specific functionalities. In general CE Lite can create configurations for the 650V drive, install configurations into the 650V drive, modify and retrieve configurations. The parameters in the configuration of the 650V drive are selected for an application of basic speed control with a drive set up in a Sensorless Vector Mode. This set up is recommended by the manufacturer for maximum torque control at low speeds.

In order to operate the drive in Sensor Less Vector Mode the drive needs to have detailed information about the motor. An Autotune was carried out in order to feed the driver with the maximum amount of information about the motor and automatically load them into the drive. In order to start the Autotune some values need to be entered. Table 6.6 show the initial parameter values for starting the Autotune.

Once the Autotune was completed the 650V drive was tuning to drive the screw conveyor. In order to do this CE Lite configuration software together with a control box were used.

A control box is used to change the operational speeds of the screw conveyor. This together with the CE Lite permits to run the motor at five different speeds and to measure the torque.

Figure 6.16 shows the internal circuit control box and the internal panel 650V driver. The serial connector which connects the terminals in the 650V with the switches in the control box is shown on the right hand side of the control box. The two connections that transmit the output voltage generated (torque measurement) by the operation of the motor via the drive are shown by the dashed line (terminal 5 and terminal 1 in the 650V drive front panel). This signal goes to the data acquisition system.

6.2.7. Screw conveyor instrumentation

The model screw conveyor is extensively instrumented to monitor the operation during experiments. The general arrangement of the instrumentation was described earlier and details and calibration of the various instruments and data logging system are discussed in the following sections.

6.2.7.1. Cambridge type load cells

Design of load cells

The Cambridge type load cells used in the model screw conveyor at Oxford University were designed by Merritt (2004). The design and other types of application for this type of load cell are described by Bransby (1973) and Martin (1994). In the OSC model four load cells were used to measure the total normal stress and shear stress acting at a point on the conveyor casing. The load cells were manufactured by Cambridge Insitu Ltd, UK.

Figure 6.17 shows an exploded view of the four main components of the Cambridge type load cell. The platen acts as the active face of the load cell. A hot-bonded rubber seal, placed around the edges, fixes the platen to the housing frame. The top of the load cell fits inside the housing frame and its top part is fixed to the platen with screws. The cover plate is placed and fixed over the base of the housing frame and the base of the load cell with screws (Merritt, 2004). The cover plate also has a central hole through which the load cell cable passes.

The Cambridge type load cells are fixed in the ports on the conveyor housing with screws. The load cell load platen coincides with the internal surface of the conveyor, so the normal and shear stresses acting on the conveyor are applied to the platen and transferred to the load cell (Merritt, 2004).

A pair of vertical webs at each end of the load cell measure the normal stress, and four horizontal webs measure the shear stress in the direction parallel to these webs. Figure 6.18 shows a drawing of the load cell dimensions and indicates the normal and shear web position.

Table 6.7 shows the general load cell specifications. Bransby (1973) describes the design of the normal and shear web sizes in order to prevent failure in compression or by buckling under the design loads. The design load capacities were based on the maximum stresses expected during the screw conveyor tests, increased by a factor of about 3.5 to prevent damaging the instruments and assuming a maximum allowable stress of 147 MPa for the webs. The load cells have a maximum load capacity of 1681 kPa normal stress applied in combination with the maximum shear stress of 586 kPa.

The total normal force acting on the platen is measured as the sum of the forces in the normal stress webs. The moment applied to the load cell from an eccentric normal force is measured through the difference in the forces carried by the two pairs of vertical webs. The output from the strain gauges on the shear webs is proportional to the shear force acting on the platen in

the direction parallel to the shear webs. The three strain gauges (normal, eccentric and vertical signals) circuits are wired to a nine core cable carrying the common power supply and the output for each circuit to the data logging system.

Figure 6.19 and Figure 6.20 show the layout of the Cambridge type load cell on the conveyor casing. Most of the tests were carried out using the load cell configuration shown in Figure 6.20 except for SCOD1 test which was the first trial test carried out. For tests SCOD2 to SCOD16, one load cell was placed at each section (see dashed line rectangular box with the number of the section at the left hand side) oriented as is shown in Figure 6.20.

The load cell housing is sealed to prevent entrance of water by the hot-bonded rubber between the platen and the frame, and Plastic Padding a sealer manufactured by Henkel Loctite Adhesives Ltd was used to seal the screws connecting the load cell to the platen. Figure 6.21 shows a photograph of one of the Cambridge type load cells used in this research.

Calibration of load cells

Each circuit for the strain gauges on the load cells is sensitive to loads applied in the direction of the web orientations. Each circuit also has a cross-sensitivity to loads applied in the other directions. The outputs of the three circuits are proportional to the normal load, shear load and moment applied to the platen. This results in a matrix of nine calibration coefficients relating the applied loads to the change in the circuit outputs.

$$\begin{bmatrix} V_A - V_{A0} \\ V_B - V_{B0} \\ V_C - V_{C0} \end{bmatrix} = \begin{bmatrix} a_{11} & a_{12} & a_{13} \\ a_{21} & a_{22} & a_{23} \\ a_{31} & a_{32} & a_{33} \end{bmatrix} \begin{bmatrix} N \\ S \\ M \end{bmatrix} \quad [6.1]$$

Where:

V_A, V_B: The outputs from the normal force circuits;

V_C: The output from the shear force circuit;

V_{A0}, V_{B0}, V_{C0}: Zero offsets of the circuits;

a_{11}, a_{12}, a_{13}, a_{21},..., a_{33}: Calibration coefficients; and

N, S, M: Normal load, shear load and moment applied to the platen.

With the calibration coefficients calculated, the matrix is inverted to calculate the applied load from the measured circuit outputs.

Coefficients a_{11} and a_{21} represent the direct sensitivity of the vertical webs to normal load. The coefficient a_{32} represents the direct sensitivity of the shear webs to the applied shear load. The coefficients a_{13}, a_{23}, a_{33} represent the sensitivity of the normal and shear webs to the moment

applied by an eccentric normal load. The coefficients a_{12}, a_{22} and a_{31} represent the cross sensitivities of the circuits to loads applied in the direction opposite to the orientation of the webs.

The load cells were calibrated following the calibration programme shown by Table 6.8. In this table the values between brackets are values used for some load cells where, for practical reasons, longer arm moments than 10 mm could be used.

In order to calibrate the load cells a loading system and a loading rig were used. Figures 6.22, Figure 6.23 and Figure 6.24 show the loading system and different views of the loading rig and loading system assembled together.

During calibration the output from each circuit was recorded for each load increment and the calibration coefficients determined from the slopes of regression lines fitted to plots of the input voltage against the applied loads. Figure 6.25 shows an example set of calibration results for a Cambridge type load cell. Table 6.9 shows the calibration coefficient value for a Cambridge type load cells.

6.2.7.2. Pore pressure

Pressure transducers were installed at sections 1, 2 and 3 in the ports indicated in Figure 6.6 in order to measure the pore water pressure between the soil and the interface with the casing. Three 7 bar range type PDCR 4010 pressure transducers manufactured by Druck Limited were used during the OSC tests.

A special connector was designed to make the connection of the pore pressure transducer in the casing easier. The schematic drawing of the connector has already been shown in section 6.2.3. Figure 6.26 shows an overview of the connector already assembled and a view of the connector together with a pore pressure transducer mounted in the OSC casing. A Vyon® disc is pushed into the top cavity of the connector which has been filled up previously with glycerine. The Vyon® disc was previously saturated with de-aired water in order to eliminate any trapped air in its pores. The Vyon® and the glycerine were put in the connector once the connector had been assembled to the pore pressure transducer. For each test a new de-aired water saturated Vyon® disc was used.

The transducers were calibrated under air pressure using the Digital Pressure Indicator 600 manufactured by Druck Limited. The transducers have a linear response over a full pressure

range. The calibration factor of the pore water pressure transducers in section 1, section 2 and section 3 were 7109.27 kPa/V, 7122.25 kPa/V and 7097.62 kPa/V respectively.

6.2.7.3. Piston vertical displacement

The piston vertical displacement was measured by a draw wire transducer. The transducer has a range of 1000 mm and its output voltage is linearly proportional to the extension of its cable. The draw wire transducer was mounted on the reaction frame above the tank sample as it is shown in Figure 6.3 and Figure 6.4. The cable of the draw wire transducer was connected to the top part of the piston and fixed in that position during the OSC tests. The cable was extended during the lowering of the piston into the tank during the conveyor operation. The transducer output indicates the sample height and was used to calculate the volumetric sample flow rate through the screw conveyor during the OSC tests.

This calibration curve was obtained fixing the draw wire transducer on a bench and recording the output voltage of the draw wire transducer at different extensions of its cable. The linear calibration factor of the draw wire transducer was -112.3 mm/V.

6.2.7.4. Torque

The voltage output signal (see section 6.2.6.1 and terminal 5 in Figure 6.16), from the 650V drive unit is proportional to the current drawn by the motor during its operation. The maximum current drawn by the motor is proportional to the maximum torque supplied by it. Using this property a calibration curve was obtained for the torque supplied by the electric motor to rotate the screw versus the voltage output signal obtained from the 650V drive unit. The calibration was carried out using the system shown in Figure 6.27.

Torque calibration system

The torque calibration system is formed by a flywheel, Guta Percha belt, "z" type load cell, calibration frame and shackles. The flywheel has a diameter of 305 mm and it is screwed on a boss which slides in the shaft of the gearbox. The "z" type load cell is screwed to the reaction bar placed on one side of the calibration frame and attached through a shackle to the Guta Percha belt. The belt is made of a special tree resin whose frictional property and load resistance were suitable for the motor torque calibration. The calibration system was designed to generate enough friction between the flywheel and the Guta Percha belt to achieve a maximum torque of around 300 Nm.

A series of tests at two different velocities, 5 rpm and 7 rpm, was carried out to calibrate the torque supplied by the electric motor. Figure 6.28 shows an example of a series carried out at 7

rpm with a dead weight applied of 54.21 N. The series has four steps. In step one the dead weight was placed in the system and then the motor was energized at 0 rpm. Then the motor was run at 7 rpm using the control box. After this the motor was driven to 0 rpm and finally it was switched off. The voltage output signal from the 650V drive unit and load in the "z" type load cell were recorded by a data acquisition system. This series was repeated for the following dead loads: 0 N, 8.8 N, 107.9 N, 168.3 N, 206.1 N, 217.5 N, 338 N, 387.2 N and 436.1 N.

The calculated torque (using the known dead weight and the "z" type load cell recorded load) was plotted against the difference in output voltage signal from the 650V drive unit between any time and the voltage produced at the beginning of the step 1 when the motor is not energized. The torque calibration curve obtained for the series of tests is shown in Figure 6.29. The curve that best fits the series of points is a polynomial of second order. Although this curve may underestimate torque between 100 Nm and 170 Nm, this approximation is thought to be enough for this application. The coefficient of determination, R, is around 0.99 which is valid to values of torques near 350 Nm which exceed the maximum torque design value of 300 Nm. The coefficients of the terms of the second order polynomial (to the power greater than zero) will be used to calculate the torque supplied by the motor to rotate the screw.

Once these coefficients were obtained the gearbox motor system was connected to the screw conveyor. As is shown in Figure 6.30 the OSC model was run several times at different speeds without soil material inside. This was done to establish the torque that the motor needs to supply to rotate the screw conveyor without any material in the casing. It was found that the torque needed for a range of speeds between 5 and 11 rpm is the same, 16 Nm, while when the speed is increased to 15 rpm a greater torque is needed, 28 Nm, to rotate the screw conveyor. These values were subtracted from the torque measurements obtained from running the OSC at a specific motor speed during the experiments. There are two spikes around 110 Nm that can be observed at 5 rpm. There is no clear explanation of why they have occurred, however the torque (16 Nm and 28 Nm) used for the range of speeds is no influenced by these spikes.

6.2.7.5. Data-logging system

The instruments installed on the OSC model were connected to a data logging system to record the measurements during the experiments. The instruments were plugged into channels in a junction box (see Figure 6.1 and Figure 6.2), which connects into a Mowlem Microsystem Autonomous Datalogging Unit (ADU). The analogue input module of the ADU accepts up to eight DC channels and also provides precision dc transducer supply of 10 V. Analogue to digital

conversion is performed to 12 bit accuracy (1 in 4096), with a full scale input range of ±10 V. The analogue to digital converter module also contains a pre-amplifier with eleven software selectable gain ranges (x1,x2,….,x1024), allowing even a ± 10 mV signal to be fed directly to the ADU. Once digitised, channel readings may (if desired) be stored in the ADU's battery backed internal memory (256 kByte). A built in microcomputer supervises all the aspects of the operation of the ADU and handles RS232 communications with the host PC. During the screw conveyor test the host computer executes a program called ControlPanel written in Microsoft Visual Basic 6.0 ®. This programme oversees the running of a test and handles all communication over the RS232 serial interface (running at 9600 baud). The data logging system was configured to read all eight Cambridge type load cells. However, during the tests carried out in this research just four Cambridge type load cells were used for testing. This means that a total of 12 strain gauges signals from the Cambridge type load cells were recorded by the ADU. Taking into account the signals from the pore water pressure transducers, the draw wire transducer and the voltage signal from the 650V drive, a total of 16 channels were recorded at one time of a maximum of 29 channels configured to be recorded. The miniature of the screen interface in Figure 6.31 shows 29 channels displayed every two seconds on the screen for any test. The Control Panel programme consists of five main parts. The first part is the initial zero reading of the channels recorded. The flow diagram in Figure 6.31 shows how, as soon as Control Panel is loaded, the com port is opened and the gain, offset and calibration coefficient of the channels are set. The maximum number of readings for a test of approximately sixty minutes at a logging rate of 0.9 seconds per reading line is also defined.

When the Zero Read button is clicked (see Figure 6.31) a routine, which is described at the right hand side in Figure 6.31, starts making absolute measurements on the specified channels using a filter of 50 Hz. Once the zero reading has been gathered by the ADU the channels are initialized again (SETZ command), which will read the data from the channels without the 50 Hz filter. It is not possible to use this filter for the reading of the channels during testing because it takes too long for the twenty nine channels to be read. After the channels have been initialized the memory used by the test in the ADU and the SCAN RATE of the test are set. Pressing the START button initiates the reading of the twenty nine channels each 0.9 seconds during the entire time the test last. The ADU checks the STATUS of the programme after each reading of the twenty nine channels. If the STOP button is clicked a FINISH instruction is send to the ADU which will end the test. If STATUS does not detect FINISH a new reading will take place. When the TEST TERMINATED state is reached the DATA RETRIEVAL starts recalling all the data from the memory of the ADU. The data will be written in a file, together with all the zero readings and calibration factors read at the beginning of the test.

6.3. OSC experimental results

A total of sixteen tests were carried out using the screw conveyor model system described in the previous sections. Three types of sand were used in the OSC tests. One test using Thanet sand and foam, five tests on L.B. fine sand and foam, one test on saturated L.B. fine sand, seven tests on Garside sand and foam and two tests on saturated Garside sand. Thanet sand and L.B. fine sand are much finer sands than Garside sand, which is a coarse sub angular to rounded quartz type of sand. The foams used were CETCO Versa foam, for Thanet sand and L.B. fine sand, and MAPEI Polyfoamer MCB for Garside sand.

The tests were carried out with assistance from Raffaele Vinai, a visiting student from the Politecnico di Torino. The selection of Garside sand was made to test the OSC model with a coarser sand type than Thanet and L.B fine sands, but also to use MAPEI Polyfoamer foaming agent with sand of a similar type to one to be used in a tunnelling project at Politecnico di Torino.

The materials (sand, water and foam) used for the tests were mixed in a wheel barrel. Three or four batches of dry sand were normally mixed to produce enough mix to fill the tank of the OSC model. The mixed materials were poured inside the tank. The casing discharge gate was closed when the mixed material was poured inside the tank, so no water escaped outside the OSC model. When the tank was filled up to the desired height the piston was put in position by sliding it inside the tank. A layer of grease was placed on the internal walls of the tank, before the mixed material was placed, to decrease the friction. With the mixed material inside the tank and the piston in position the rotation of the screw was started together with movement of the piston in the tank, applying a constant pressure on top of the mixed material which was extracted by the screw. The plug in the gate was taken off just before the rotation of the screw started.

Table 6.10 shows the initial amount of sand, water and foam used in each test to produce the mixture placed inside the OSC tank.

Tests were performed with varying pressure applied to the sample, with varying screw speeds and with different discharge conditions. The speed of the screw was varied with the speed toggles of the control box. The conveyor discharge conditions (gate diameter) were varied by connecting or removing a series of commercial adaptors shown in Figure 6.32, with diameters of discharge varying from 45 mm to 71.5 mm. Each test was stopped when the ram of the piston reached its maximum stroke or when the maximum testing, of about 1 hour, was achieved.

The next sections present the results obtained from the sixteen OSC tests. First of all the typical results obtained for the OSC tests will be described. One test is used as an example, focussing on sample height variation, normal and shear casing stresses measured, torque and flow rate variation. Later an interpretation of the results, during steady state conditions, will be carried out highlighting the effect of the different operation parameters on the casing shear stress, friction angle, torque and discharge efficiency.

6.3.1. Data presentation

The initial test parameters before the OSC tests started are shown in Table 6.11. The data gathered during the OSC tests is shown in the next sections. The values plotted in the following sections are the five point rolling average of the raw data of any parameter recorded from the tests. This was done to simplify the presentation of the data by smoothing the results.

6.3.1.1. Sample height, Piston displacement

The piston displacement was recorded at all times during the OSC tests using the draw wire transducer cable attached to it. With this value and knowing the initial height of the specimen (H_0, see Table 6.11) before the test started, the height of the specimen can be calculated at any time. Figure 6.33 shows an example for SCOD9 test, showing the piston displacement recorded and the sample height calculated (left hand side axis).

It can be seen in Figure 6.33 that the sample height variation decreases faster when the speed of the motor is increased and vice versa. This result is observed in all the tests. The sample height is important to calculate the volume of material extracted by the screw from the tank. This value will be used to evaluate the discharge efficiency, which is discussed in a later section.

6.3.1.2. Pressure on specimen

The pressure in the jack was measured by a gauge installed in the hydraulic system as described in section 6.2.2. This value is given in Table 6.11 as σ'_{piston} for all the OSC tests. Using the geometry of the jack and piston, and also considering the friction values estimated by Gue (1984), the pressure at the top of the specimen during the tests was calculated. The ratio of jack bore diameter to piston diameter was around 0.051. The friction losses estimated by Gue (1984) are of the order of 4.25% of the pressure in the jack. Thus the pressure at the top of the specimen is about 4.9% of σ'_{piston}. The pressure at the top of the specimen for each test is shown in Table 6.11 ($\sigma'_{topspecimen}$). The pressure at the top of the specimen was constant during the extraction of material from the tank last.

Figure 6.33 shows the pressure at the top of the specimen, $\sigma'_{topspecimen}$, at the right hand side axis for SCOD9 test. Visual inspection of the gauge in the hydraulic system was made at intervals during the test. No important variations were detected during the tests once the desired jack pressure was set.

The pressure at the top of the specimen models the pressure in the chamber of an EPB machine, which has to be regulated according the pressure exerted by the ground above the tunnelling machine. The maximum pressure applied during tests was about 152 kPa ($\sigma'_{topspecimen}$). The total stress at the line of the conveyor ($\sigma_{0lineconveyor}$) was also calculated. This takes into account the initial mass of the specimen inside of the tanks. Table 6.11 shows these values before and after the piston is placed on top of the specimen. The maximum $\sigma_{0lineconveyor}$ obtained was about 16.8 kPa before the piston was placed on top of the specimen and 168.8 kPa afterwards. Just the initial $\sigma_{0lineconveyor}$ is given because no accurate record of the mixture leaving the tanks was carried out. In general different pressures (see Table 6.11) were applied to the top of the specimen to see its effect in the OSC operation.

6.3.1.3. Speed

Different speeds of the motor were used during the series of tests to see its effect in OSC operation. 5, 7, 11 and 15 rpm were used at different stages during the tests (see Table 6.11). The speed was controlled by the control box described in section 6.2.6.1. The speeds correspond to values used on site for screw speeds of EPB machines. It has been found by experience that the speed of the screw affects the operation of the EPB machine, accelerating the internal pressure dissipation along the screw conveyor. Thus varying this speed in the OSC model would help a better understanding of its influence in the operation of screw in EPBM.

Figure 6.33 shows an example of speed variation for SCOD 9 test. Three motor speeds were tried during this test. The peak speed observed at the very beginning of the test was a free rotation of the screw in order to measure the torque of the motor before the material was placed inside. The screw was run for approximately two revolutions at 5 rpm.

6.3.1.4. Normal stress

The normal stress measured by the Cambridge type load cells was recorded during the OSC tests. The configuration of the Cambridge type load cells in the casing has been described in section 6.2.7.1.

The normal stress affects the coefficient of friction. An increase in the normal stress may produce a small decrease of the coefficient of friction. It is also known that less friction will decrease the torque required to extract material from the pressure chamber along the screw conveyor in an EPB machine. Thus the study of the normal stress variation at different operating conditions of the OSC model would help to increase the understanding of the effect of the use of foam during the extraction of sand.

The normal stress measured in each section in the OSC model was assumed to be the total normal stress in that section regardless of its orientation (with shear measurement perpendicular or parallel to screw axis, see Figure 6.20).

Figure 6.34 shows the normal stresses recorded at four sections along the conveyor casing during SCOD9 test. In the legend shown at the bottom right hand side of Figure 6.34, the first character "A" indicates the measurement of normal load and the number describes the load cell used for the measurement. The character "S" and number following it describes the section where it is placed in the casing.

The normal stress values shown in Figure 6.34 have similar order of magnitude, which is the common case for all the tests carried out on the OSC model.

During the filling of the tank (before plug off dashed dot line) a small increase of the normal stress is observed for all the load cells. Soon after the plug was taken off from the discharge gate (discharge diameter of 85.5 mm) the screw started to extract material from the tank. During 5 rpm speed of the motor the normal stress amplitude became bigger, which decreased when the speed motor was higher than or equal to 11 rpm.

A diagram of the OSC model is shown in Figure 6.34. In this diagram each section has been assigned a colour and a character. For instance section 1 is "S1" in a red colour. The normal stress lines also have the corresponding section colour to make its identification with the sections easier.

6.3.1.5. Shear stress

The shear stress measured by the Cambridge type load cells was recorded during the OSC tests. The configuration of the Cambridge type load cells in the casing has been described in section 6.2.7.1.

The shear stress measured in each section in the OSC model is part of the total shear stress in that section. In the following sections the total shear stress is calculated, taking into account the orientation of the shear stress (in shear perpendicular or parallel to screw axis, see Figure 6.20).

Figure 6.35 shows the shear stresses recorded at four sections along the conveyor casing during SCOD9 test. In the legend shown at the top left hand side of Figure 6.35, the first character "S" indicates the measurement of shear and the number describes the load cell used for the measurement. The second character "S" and number following it describes the section where it was placed in the casing.

The shear stress values shown in Figure 6.35 have similar order of magnitude, which is the common case for all the tests carried out on the OSC model. In absolute terms the value of shear stresses varies depending of the test carried out, but its order of magnitude is always similar.

During the filling of the tank (before the plug was removed) there was no increase of the shear stress for all the load cells. Soon after the plug was taken off from the discharge gate (discharge diameter of 85.5 mm) the screw started to extract material from the tank. During 5 rpm speed of the motor the shear stress amplitude became bigger, and decreased when the speed motor is higher than or equal to 11 rpm.

6.3.1.6. Pore pressure

The pore water pressures from three pore water pressure transducers in the screw conveyor casing were recorded during each test. The configuration of the pore water pressure transducers has been described in section 6.2.7.2.

Figure 6.36 shows the pore water pressure recorded at three sections along the conveyor casing during SCOD9 test. In the legend showed at the top right hand side of Figure 6.36, the first character "PT" indicates the measurement of pore water pressure and the number describes the pressure transducer used for the measurement. The second character "S" and number following it describes the section where it was placed in the casing.

During the filling of the tank (before the plug is removed) there was an increase in the pore water pressure for all the pressure transducers. The measurement of pore water pressures were not affected by the rotational movement of the screw as can be seen in Figure 6.36, but there was a gradual decrease in pressure along the conveyor casing, where the pressure transducer

placed closest to the tank shows higher pressure than the transducer in section 3. The pore water pressures also decreased with time as the test reached its end. The last two phenomena were observed in all the tests carried out on the OSC model.

6.3.1.7. Torque

The torque was calculated for all tests using the calibration curve obtained in section 6.2.7.4. The torque produced by the motor to rotate the screw is important in EPB machine operations because it has direct relation with the energy consumed during tunnelling operations. Higher torque will mean more current drawn by the motor and thus higher energy consumption. Therefore the study of torque variation at different operating conditions of the OSC model will help to increase the understanding of the effect of the use of foam on the torque needed during the extraction of sand in the screw conveyor of EPB machines.

Figure 6.37 shows the torque calculated from the measurement of current drawn by the motor during SCOD9 test. The black line is the total torque calculated without applying any filter, so this torque is called raw torque. The red line is the torque calculated applying a 5 point moving average to the raw torque. This will be called average torque. These two values are shown because although the average torque is a good way to eliminate the scatter from raw torque, there are some peaks in raw torque which are not in the same order of magnitude as the value obtained from average torque (the peaks in Figure 6.37 show a difference between its raw value and average value of around 90 Nm). It is important to highlight that these peaks can be produced by punctual extra power needed by the electrical motor to extract the soil material or by some residual electrical current induced in the motor cage. To find out the real cause of these peaks is beyond the remit of this chapter, however in order to minimize the peaks influence in further analysis only the average torque and the maximum average torque are taken into account.

When the motor was rotated without soil in the casing at the beginning of SCOD9 test (see Figure 6.37), although no material was inside the casing, a small torque of 10 Nm was calculated from the calibration curve. This occurred in all tests. This was due to the method used to calculate the torque, which relies on average values of varying electrical parameters. These parameters are influenced by temperature and other factors of the motor. The order of magnitude of this peak at the beginning of OSC tests was so small that it was not deemed important in the task of comparing the variation of torque under different operating conditions of the OSC model.

6.3.1.8. Flow rate

The flow rate was obtained using the geometry of the tank and calculating the variation of the height of the specimen over time in the tank during the OSC tests.

The flow rate is important because it can be used to evaluate the efficiency of extraction of material, by comparison with the maximum volumetric flow that can be extracted taking into account the geometry of the screw and the speed of the motor. In this way it can be determined if the material is been moved by the screw or whether the material in the casing is just rotating without moving along the screw. The latter will mean, for instance, that a smaller screw pitch is needed to move the material forward. The maximum volumetric flow will be described in the next section.

Figure 6.38 shows the volumetric flow rate of saturated Garside sand for SCOD9 test. The flow rate increases when the speed of the motor increases and the flow rate decrease when the speed of the motor decreases.

6.3.1.9. Efficiency

The efficiency is calculated as the ratio of the flow rate data described in the previous section and the maximum volumetric flow value shown in Table 6.12. The values in this table were obtained using the following equation:

$$Q_{\max} = \frac{\pi}{4} * \left(D_c^{\,2} - D_s^{\,2}\right) * \left(t - e\right) * \left(\frac{60 * N}{0.001}\right) \qquad [6.2]$$

Where:

D_c: Internal diameter of conveyor casing, m;

D_s: Screw shaft diameter, m;

t: Screw pitch, m;

e: Screw flight thickness, m;

N: Rotational speed of the screw, rpm; and

Q_{max}: Maximum volumetric flow at specific speed, l/hr.

The previous equation assumes that the conveyor casing is completely full of material and that the soil advances along the screw axis by a length equal to the screw pitch with each rotation. Thus the equation of efficiency is:

$$Q = -\Delta H * 0.001 * \frac{D^2_{\,T}}{4} * \pi * 1 * 10^{-6} * \frac{(36 * 10^5)}{\Delta t} \qquad [6.3]$$

$$\eta = 100 * \frac{Q}{Q_{max}} \quad [6.4]$$

Where:

ΔH: Displacement change of piston in the interval of time Δt, mm;

D_T: Internal diameter of tank, mm;

Δt: Interval of time of displacement change, seconds;

Q: Flow rate of steady state event, l/hr; and

η: Flow efficiency of steady state event, %.

The efficiency for SCOD9 test is shown in Figure 6.39. The overall trend of the discharge efficiency during this test was to decrease over time, achieving an approximately constant efficiency value of about 45% at the end of the test.

It is worth highlighting that from looking at Figure 6.39, one can say that the efficiency does appear to be related to the rotation rate. The efficiency tends to decrease when the speed increases and the efficiency tends to increase when the motor speed decreases. This will be discussed in following sections.

6.3.1.10. Steady state conditions

During the OSC tests different stages were observed after the plug was taken off (see red dashed dot line in Figure 6.33). Stages were decided by the speed of the motor and by the pressure applied on top of the specimen. For instance in test SCOD9, eight stages can be identified. Stage 1 occurs at $\sigma'_{topspecimen}$=0 and 5 rpm, stage 2 at 147 kPa and 5 rpm, stage 3 at 147 kPa and 11 rpm, stage 4 at 147 kPa and 15 rpm, stage 5 at 147 kPa and 5 rpm, stage 6 at 147 kPa and 11 rpm, stage 7 at 0 kPa and 11 rpm, and stage 8 at 0 kPa and 0 rpm. Table 6.13, Table 6.14 and Table 6.15 show all the stages for each test carried out on the OSC model.

The steady state events are named first using the test name, for instance SCOD9. Then after the hyphen the speed of the motor and after that in which stage the event has occurred. When a forward slash symbol is used it means that during the same stage a second steady state event occurred.

To analyse the data it was necessary to identify within the stages when volumetric flow was approximately constant so steady state conditions were achieved. For instance, normal stress, shear stress and pore water pressures were shown in steady state volumetric flow conditions (using the piston displacement and the speed of the motor) within stage 2 and stage 4 for

SCOD9 test in Figure 6.40 and Figure 6.41 respectively. In Figure 6.40 normal stress, shear stress and pore water pressure show approximately stable values over the time period. The normal stress and shear stress curve have a sinusoidal shape which is due to the effect of the screw flights passing by the Cambridge load cells during the steady state condition. The pore water pressure shows a much flatter response which was almost constant through the steady state condition. The normal and shear stress in Figure 6.41 show much flatter response than normal and shear stress in Figure 6.40. In Figure 6.41 normal and shear stress show almost constant values in some sections for specific periods of time. For instance in Figure 6.41 (a) the normal stress between 2408.2 seconds and 2414.2 seconds was constant around 3.2 kPa in section 4 (pink line).

What is observed in Figure 6.40 and Figure 6.41 was observed in general in all tests over the steady state volumetric flow conditions events for all the OSC tests. However, the more usual was Figure 6.41. This is discussed in the following sections.

Figure 6.42 shows the torque values under steady state volumetric flow conditions in stage 2 (SCOD9-5.2), stage 3 (SCOD9-11.3)and stage 4 (SCOD9-15.4). In this Figure the volts measured by the 650V drive unit are also plotted. V_0 is the average volt measured when the motor rotates the screw without any material inside. Due to the current fluctuations drawn by the motor the values of voltage (which is proportional to the current drawn by the motor) sometimes took values lower than V_0 during the test. This was not thought as a problem because this situation was expected as the V_0 value is based on a average calculation obtained from running the motor at 5 rpm, 11 rpm and 15 rpm (see Section 6.2.7.4). This condition means that small negative values of raw torque are calculated. It is for this reason that the average torque is used as a better approximation of the torque trend. However, the average torque does not seem to estimate the raw torque when peaks such as the one show in stage 4 occur. This situation is observed, with major or minor differences, in all the OSC tests. Bearing this in mind the values used for the analysis of the torque behaviour are: the maximum raw torque, the maximum average torque and the average torque over the steady state event.

Pressure gradients

Having identified the steady state events for each stage, an average value could be obtained for the normal stress, shear stress and pore water pressure analysed over that section during the steady state event. This was done for all the OSC tests. Figure 6.43 shows the values of normal stress, shear stress and pore water pressure variation along the length of the screw for SCOD 9 steady state events.

The normal stress showed an overall increase along the screw length, between sections S1 and S2, for all the steady state events. The earlier steady state events, SCOD9-5.2 and SCOD9-11.3, showed higher values than the later events (SCOD9-15.4, SCOD9-5.5 and SCOD9-11.6). The range of values for the normal stress measured varied between 2.5 kPa and 7.5kPa.

The shear stress shows similar behaviour along the screw length to the normal stress. An average value for all the steady state events of approximately 1.23 kPa can be estimated.

The pore water pressure values in all the stages were lower than 2 kPa. The pore water pressure showed a decrease (on average 0.8 kPa reduction) over the screw length in the earlier events (SCOD9-5.2 and SCOD9-11.3). The other steady state events showed very small pore water pressures (around 0 kPa). The pore water pressure at section 4 was inferred from regression lines fitted to the total pressure gradients extrapolated to a point of 1019.6 mm of the length of the screw.

The effective stress values vary between 2.4 kPa and 6.4 kPa. In all stages the effective stress tended to increase from section 1 to section 2. Between section 2 and section 4 the effective stress decreased to approximately 3 kPa on average.

Following the previous description, an average value can be calculated for the normal stress and pore water pressure over the length of the screw. The effective stress, for the interface between the material and the conveyor casing, could be calculated using the average values of normal stress and pore water pressure over the length of the screw. So the total pore water pressure change in Table 6.16 was calculated from the difference between the pressure at the discharge point and the measured pressure in section 1. The pressure at the discharge point was inferred from regression lines fitted to the total pressure gradients and extrapolated to a position of 1184 mm from the beginning of the screw (the mid point of the outlet). The total pressure gradient is the total pressure change divided by the difference in length between the pressure at the discharge point and the length of the pore water pressure at section one, which is 839.4 mm.

Table 6.16 shows all the steady state volumetric flow events that occurred within the stages of the OSC tests. The table shows:

1. The name of the test;
2. The initial relative density (D_{r0}) of that test;
3. The ratio of the final height and initial height of the specimen (H_f/H_0) in that test;

4. The maximum raw torque calculated in the entire test (T_{max});
5. The steady state events for the OSC tests;
6. The elapsed time during the steady state event (Δt);
7. The speed of the motor (N) during the steady state event;
8. The average pore water pressure ($u_{average}$) of the values measured by the pore pressure transducers during the steady state event;
9. The average normal stress ($\sigma_{average}$) of the values measured by the Cambridge load cells during the steady state event;
10. The average effective stress ($\sigma'_{average}$) using the average pore water pressure and the average normal stress during the steady state event;
11. The total pore water pressure change (Δu) during the steady state event;
12. The total pore water pressure gradient ($\Delta u/L$) during the steady state event;
13. The maximum raw torque (T_{rmax}) over the steady state event;
14. The maximum average torque (T_{avmax}) over the steady state event;
15. The average torque (T_{av}) over the steady state event;
16. The soil flow rate (Q) at the steady state event; and
17. The efficiency (η) over the steady state event.

To take into account the shear stress direction (parallel or perpendicular to the screw axis) in the steady state events for each stage, an average value can be obtained between section S.1 and S.2, S.2 and S.3, and S.3 and S.4. The following equation shows the general average casing shear stress calculated,

$$\tau_c = \sqrt{(\tau_{Sx-1})^2 + (\tau_{Sx+1})^2} \qquad [6.5]$$

Where:

τ_{Sx-1}= Average casing shear stress calculated in section X-1 during a steady state event, kPa;

τ_{Sx+1}= Average casing shear stress calculated in section X+1 during a steady state event, kPa; and

τ_c= Casing shear stress calculated in the centre of sections X-1 and X+1 during a steady state event, kPa.

It is important to highlight that due to the arrangement of the Cambridge load cells during the SCOD tests the previous equation was applied to all tests except SCOD1.

Thus the angle of friction was calculated using the following equation,

$$\delta = arc\tan\left[\frac{\tau_{caverage}}{\sigma'_{s(x-1,x+1)}}\right] \quad [6.6]$$

Where:

$\sigma'_{S(x-1,x+1)}$= Average effective stress calculated in the centre of sections X-1 and X+1 during a steady state event, kPa; and

δ= Angle of friction calculated in the centre of sections X-1 and X+1 during a steady state event, degrees.

The direction of friction is defined as.

$$\varepsilon = arc\tan\left[\frac{\left(\frac{\tau_{sx-1}}{\sigma'_{sx-1}}\right)}{\left(\frac{\tau_{sx+1}}{\sigma'_{sx+1}}\right)}\right] \quad [6.7]$$

Where:

σ'_{Sx-1}= Average effective stress calculated in section X-1 during a steady state event, kPa;

σ'_{Sx+1}= Average effective stress calculated in section X+1 during a steady state event, kPa; and

ε= Angle of direction of friction calculated in the centre of sections X-1 and X+1 during a steady state event, degrees.

The ε value achieves its maximum value when η is equal to 100% and the shear stress in parallel direction to the screw axis achieves its maximum value and the shear stress in perpendicular direction is equal to 0. When the shear stress in the perpendicular direction achieves its maximum value and the shear stress in parallel direction achieves its minimum value equal to 0 the efficiency is 0 and ε achieves its minimum value. It is important to emphasize that τ_{Sx-1} must always be the shear stress measured in parallel direction and τ_{Sx+1} must always be the shear stress measured in perpendicular direction to the screw axis

Finally, the direction of soil movement was calculated using the following equation,

$$\theta_c = \arctan\left[\frac{0.01 * \eta * \tan\phi_f}{(1 - 0.01 * \eta)}\right] \quad [6.8]$$

Where:

ϕ_f: Flight helix angle, degrees; and

θ_c: Calculated direction of soil movement, degrees.

As mentioned in Chapter 2 section 2.7.3, the calculated direction of soil movement and direction of friction must be equal, $\theta_c=\varepsilon$, assuming that the conveyor casing is completely full of material. This will be discussed in following sections.

The casing shear stress, angle of friction, angle of direction of friction and the calculated direction of soil movement were analysed during the steady state event over sections S1.2, S2.3 and S3.4, the mid points of sections S.1, S.2 and S.3 respectively. This was done for all the OSC tests. Figure 6.44 shows the values of casing shear stress, angle of friction and angle of direction of friction along the length of the screw for SCOD 9 steady state events in sections S1.2, S2.3 and S3.4.

In Figure 6.44 the casing shear stress shows an overall decrease along the screw length (towards the exit) for all the steady state events. The earlier steady state events, SCOD9-5.2 and SCOD9-11.3, show higher initial values (S1.2 and S2.3) than the later events (SCOD9-15.4, SCOD9-5.5 and SCOD9-11.6). The range of values for the casing shear stress calculated varies between 1.5 kPa and 2.5 kPa.

In Figure 6.44 the angle of friction shows an approximately constant value (24.5 degrees) between section S1.2 and section S3.4. This is discussed in the following sections.

In Figure 6.44 the angle of direction of friction increases over the length of the screw (towards the exit). The angle of direction of friction is between 30 and 50 degrees. When it is plotted versus the calculated direction of soil movement S1.2 shows the lowest values (see Figure 6.44 (d) red line around S1.2 label) while S3.4 shows the highest values (see Figure 6.44 (d) red line around S3.4 label). The angle of direction of friction does not show any trend when it is plotted versus the calculated direction of soil movement. This is discussed in the following sections for all the OSC tests.

Table 6.17 shows all the calculated data for OSC tests. In the table are shown the name of the test, the tangent value of the flight helix angle (ϕ_f), the steady state events during the test, the efficiency (η) over the steady state event, direction of soil movement (θ_c), average casing shear stress in the direction parallel to the screw axis ($\tau_{averagepar}$), average casing shear stress in the direction perpendicular to the screw axis ($\tau_{averageper}$), average casing shear stress ($\tau_{caverage}$), maximum casing shear stress (τ_{cmax}), average angle of direction of friction ($\varepsilon_{average}$), maximum angle of direction of friction (ε_{max}) and the average angle of friction ($\delta_{average}$). The following equations describe the parameters shown in Table 6.17:

$$\tau_{averagepar} = \frac{\tau_{S1} + \tau_{S3}}{2} \quad [6.9]$$

$$\tau_{averageper} = \frac{\tau_{S2} + \tau_{S4}}{2} \quad [6.10]$$

$$\tau_{c\,average} = \frac{\tau_{c(S1.2)} + \tau_{c(S2.3)} + \tau_{c(S3.4)}}{3} \quad [6.11]$$

$$\tau_{c\,\max} = Max(\tau_{c(S1.2)} + \tau_{c(S2.3)} + \tau_{c(S3.4)}) \quad [6.12]$$

$$\varepsilon_{average} = \frac{\varepsilon_{(S1.2)} + \varepsilon_{(S2.3)} + \varepsilon_{(S3.4)}}{3} \quad [6.13]$$

$$\varepsilon_{\max} = Max(\varepsilon_{(S1.2)} + \varepsilon_{(S2.3)} + \varepsilon_{(S3.4)}) \quad [6.14]$$

$$\delta_{average} = \frac{\delta_{(S1.2)} + \delta_{(S2.3)} + \delta_{(S3.4)}}{3} \quad [6.15]$$

Where:

τ_{S1}, τ_{S3}= Average casing shear stress calculated in section 1 (S1) and section 3 (S3) in parallel direction to the screw axis during a steady state event, kPa;

$\tau_{averagepar}$= Average casing shear stress in parallel direction to the screw axis over the steady state event, kPa;

τ_{S2}, τ_{S4}= Average casing shear stress calculated in section 2 (S2) and section 4 (S4) in perpendicular direction to the screw axis during a steady state event, kPa;

$\tau_{averageper}$= Average casing shear stress in perpendicular direction to the screw axis over the steady state event, kPa;

$\tau_{c(S1.2)}$, $\tau_{c(S2.3)}$, $\tau_{c(S3.4)}$= Casing shear stress calculated in the centre of sections S1 and S2, S2 and S3, and S3 and S4 respectively during a steady state event, kPa;

$\tau_{caverage}$= Average casing shear stress over the steady state event, kPa;

τ_{cmax}= Maximum casing shear stress over the steady state event, kPa;

$\varepsilon_{(S1.2)}$, $\varepsilon_{(S2.3)}$, $\varepsilon_{(S3.4)}$= Angle of direction of friction calculated in the centre of sections S1 and S2, S2 and S3, and S3 and S4 respectively during a steady state event, degrees;

ε_{max}= Maximum angle of direction of friction over the steady state event, degrees;

$\delta_{(S1.2)}$, $\delta_{(S2.3)}$, $\delta_{(S3.4)}$= Angle of friction calculated in the centre of sections S1 and S2, S2 and S3, and S3 and S4 respectively during a steady state event, degrees; and

$\delta_{average}$= Average angle of friction over the steady state event, degrees.

All these values are discussed and analysed in the next sections.

6.3.2. OSC interpretation of results

The first section discusses the different operating conditions under which OSC tests were carried out and the later sections discuss torque and efficiency.

6.3.2.1. Operating conditions

Discharge gate

In Figure 6.45 (a) both events, SCOD5-5.1 and SCOD3-5.4, are on conditioned L.B. fine sand (w_0 = 26.9%, $FIR_{theoric}$ = 20.6%) of equal $\sigma'_{topspecimen}$ (73.9 kPa), motor speed (5 rpm) and screw type (central shaft). Thus the only difference is the discharge gate type. SCOD5-5.1 has an A type gate discharge and SCOD3-5.4 has a B gate type. This implied a reduction of the gate of 16.3% (from 85.5mm to 71.5 mm in diameter). This reduction produced an increase in friction angle of approximately 88%.

These angles of friction show that the measurements made during these events was of the skin friction angle between the soil and the stainless steel material of the casing and not the internal angle of friction of the conditioned L.B. fine sand. Friction tests carried out by Potyondy (1961) between dry sand and saturated sand against smooth and rough steel show that the skin friction angle value is between 0.54 and 0.85 of the internal angle of friction of sands. Assuming that the L.B. fine sand has a ϕ_{cv} of around 31°, its skin friction angle on steel might be between 15° and 23.8°. When a discharge gate B type is connected an average angle friction of 22° is obtained. This falls inside the normal range of skin friction coefficients measured between sand and steel. However, the mixture going through the conveyor casing during SCOD5-5.1 event showed lower skin friction (see Figure 6.45 (c)) with steel than the values calculated by Potyondy (1961). The low value could either have been caused by some lubricating components going through the conveyor with the mixture during SCOD5-5.1, or by the presence of a more fluid mixture going through the conveyor. The latter seems to be the more obvious reason, if one observes the efficiency value for SCOD5-5.1 (see Table 6.17). SCOD5-5.1 achieved an efficiency value of 129.9%. In this case the material is extruded from the tank side to the motor side faster than it is removed by the flights. The opening A also produces very low effective stresses and casing shear stresses, where values lower than 5 kPa were recorded.

It seems that when the opening A (85.5 mm) was used the flow of material through the screw conveyor was easier, even achieving values of efficiency higher than 100%.

Screw type

In Figure 6.46 both events, SCOD5-5.1 and SCOD7-5.5, were on conditioned L.B. fine sand (w_0 = 27.1%, FIR = 20.75%) of equal $\sigma'_{topspecimen}$ (73.9 kPa), motor speed (5 rpm) and discharge

gate type (A). The only difference is the screw type. SCOD5-5.1 has a screw with a central shaft (CS) and SCOD7-5.5 has a screw without central shaft (WCS).

The events started with a difference in angle of friction of 6.9°, and over the length of the screw the friction angle increased faster for SCOD7-5.5 than for SCOD5-5.1. One of the reasons that might explain this is observed in Figure 6.46 (b). The effective stress through the conveyor, during SCOD7-5.5-WCS, reduces faster causing an increase in the angle of interface friction. It is interesting to observe that the average casing shear stress measured in both tests is similar, around 0.7 kPa for SCOD5-5.1-CS and 0.98 kPa for SCOD7-5.5-WCS. Although the amount of conditioned L.B. fine sand coming out of the system was not measured, the geometry of the screw type without central shaft indicates that when it is used there would be more volume to be filled inside the conveyor casing by the conditioned L.B. fine sand extracted from the tank. Thus a higher efficiency than SCOD5-5.1-CS would be expected. However the opposite was observed, leading to the conclusion that the mixture passed through the screw conveyor during these steady state events was heterogeneous, having a more homogenous fluid mixture during SCOD5-5.1-CS. This can be observed in Figure 6.47: at the time that the SCOD7-5.5 event started more conditioned L.B. fine sand had been taken out than when the SCOD5-5.1 event started. Figure 6.47 shows the volume of conditioned L.B. fine sand out of the tank for each event starting time. The thin dashed line marks the starting time of the SCOD5-5.1 event and the thick dashed line marks the starting time for SCOD7-5.5 event. At the starting times, 0.054 m^3 of conditioned L.B. fine sand had been taken out for SCOD7-5.5 event compared with 0.024 m^3 of conditioned L.B. fine sand for SCOD5-5.1. A more detailed series of tests must be carried out if further conclusions want to be made.

The average angle of friction for SCOD7-5.5 was 21.61°, which falls within the range given by Potyondy (1961). Thus during this event the conditioned L.B. fine sand was in contact with the steel casing during its three sections (S1.2, S2.3 and S3.4).

Pressure on the top of the specimen

Comparing two tests in Figure 6.48, of equal initial mixture conditions, saturated Garside sand (w_0 = 19.2%, FIR = 0%), and equal screw type (central shaft) but with different $\sigma'_{topspecimen}$, 98.3 kPa (SCOD8) and 147.1 kPa (SCOD9), it is clear that higher pressure produce a more homogenous distribution of the friction over the length of the screw. In the case of SCOD9 the increase of angle friction to values of around 25° along the screw length, 1.2° higher than Potyondy's values (1961), could mean that material tends to stick to the casing walls producing sand-sand friction contact rather than sand-steel contact. Although the internal angle of friction of coarse sands is around 35°, there is a clear constant trend along the screw, of SCOD9, which

might be use to validate this idea. The increasing angle of friction during SCOD8 may have been caused by the decreasing effective stress, between 6.7 to 3.1 kPa, on this test. This may mean that it is possible to increase the angle of friction during a test by increasing the specimen top pressure, going from soil-steel contact to soil-soil contact.

The casing shear stress values (see Figure 6.48 (c)) do not seem to be affected by the specimen top pressure. It is around 1.5 kPa for both tests.

For the case of conditioned soils it is not possible to make a totally valid comparison because conditioned tests of equal initial mixing conditions were not produced at two different pressures.

Motor speed

Steady state events in four different tests were analysed. In each test the specimen top pressure ($\sigma'_{topspecimen}$), its mixing properties (w_o%, FIR%), the discharge gate (A) and sand type (L.B. fine sand or Garside sand) were equal. Therefore the only difference within the tests was the motor speed.

In Figure 6.49 three events are analysed for SCOD6. SCOD6-5.1, SCOD6-5.3 and SCOD6-11.4. The friction angles show similar behaviour along the screw length. It is clear that the change of speed from 5 to 11 rpm in the different steady state events had little effect on the friction angle of saturated L.B. fine sand. The friction angle showed approximately the same tendency in each event. A slight decrease in friction angle between section S1.2 and section S3.4 could be observed. A value average of 7° friction angle lower in section S3.4 than in section S1.2 could be estimated. However, in general no clear influence of the motor speed on the angle of friction for L.B. fine sand in the conveyor casing of OSC model was observed. The effective stress value and the casing shear stress for SCOD6-11.4 were lower than the effective stress and casing shear stress recorded for the events SCOD6-5.3 and SCOD6-5.1. However, 1 kPa of difference is not really sufficient to draw any conclusion.

In Figure 6.50 three steady state events were analysed for SCOD8 at speeds of 5 rpm, 7 rpm and 15 rpm. This was a saturated Garside sand test where events at 98.3 kPa $\sigma'_{topspecimen}$ were analyzed. The motor speed shows no influence in saturated Garside sand because the angle of friction values for the different events show exactly the same tendency and roughly the same value. Over the length of the screw an increasing angle friction was observed. This must be a result of the reduced amount of liquid in the section closest to the discharge gate, making the extracted material drier than in section one, hence its extraction is more difficult.

In Figure 6.51 four steady state events were analysed for SCOD9 at speeds of 5 rpm, 11 rpm and 15 rpm. This is a saturated Garside sand test where events at 147.1 kPa $\sigma'_{topspecimen}$ were analyzed. The motor speed showed no influence in saturated Garside sand because the angle of friction values for the different events show exactly the same tendency and roughly the same value for all of them, approximately 24.5° over the length of the screw. The change of speed has no influence neither in the effective stress nor in the casing shear stress. These values show exactly the same tendency in all four tests. Values of effective stress between 3.2 and 4.8 kPa and values of casing shear stress between 1.6 and 2.4 kPa were observed.

In Figure 6.52 four steady state events were analysed for SCOD10 at speeds of 5 rpm, 11 rpm and 15 rpm. This is a conditioned Garside sand test where events at 73.9 kPa $\sigma'_{topspecimen}$ were analyzed. The tendency for all the events was the same for different motor speeds. Overall there was a decrease of friction over the length of the screw (towards the exit). This value can be estimated as 20.3° angle of friction between section S1.2 and S3.4. It is interesting to point out that Figure 6.52 (b) shows maximum differences in effective stress values between SCOD10-15.3 and SCOD10-5.1 of around 3 kPa. These differences were lower in casing shear stress values, Figure 6.52 (c), achieving values of around 1 kPa. The maximum effective stress value recorded was 7.88 kPa for SCOD10-5.1, in section S2.3. The maximum casing shear stress value is 2.97 kPa for SCOD10-5.1, in section S2.3. It is important to highlight that these maximum values have been recorded at a physical point where suppose to be less influence of the inlet to the conveyor from the tank and from the exit of the conveyor to outside, to the readings.

In general for the Garside sand, the use of conditioning tends to lower the angle of friction and also make it constant. Increasing the pressure top specimen, $\sigma'_{topspecimen}$, tends to steady the angle of friction curve along the screw length. A high $\sigma'_{topspecimen}$ together with an un-conditioned soil is more likely to produce soil-soil contact in the conveyor casing than soil-steel contact. This produces angle friction of around 26° (maximum value recorded for SCOD9-15.4) in the screw, which increments the energy demanded by the screw to extract the sand.

FIR

Steady state events in seven different tests were analysed. In each analysis the specimen top pressure ($\sigma'_{topspecimen}$), the motor speed, the discharge gate (A) and sand type (L.B. fine sand or Garside sand) were equal. Therefore the only difference were the mixing properties (w_o%, FIR%) at which the event occurred.

In Figure 6.53 the friction angle calculated for SCOD 6 (saturated L.B. fine sand) events shows similar behaviour over the length of the screw. Event SCOD6-5.1 occurred after 6 revolutions of the screw and SCOD6-5.3 started at around the 33rd revolution of the screw. This shows the consistency of the OSC model to measure friction angles of saturated L.B. fine sand. Although there was a slight tendency of the angle of friction to decrease over the length of the screw (towards the exit), an average value of 22.8° can be assumed for this test. SCOD5-5.1 showed an angle of friction visibly lower than the SCOD 6 events. The average angle of friction for SCOD5-5.1 can be estimated around 11.2°. This value is 49% of the angle of friction obtained for SCOD6 events. Thus a decrease of 51% in the angle of friction was produced due to conditioning L.B. fine sand with CETCO Versa foam. In event SCOD5-5.1 there was just one point, section S3.4, which showed a similar angle of friction to SCOD6 events. This could be due to conditioned L.B. fine sand getting drier through the length of the screw, increasing the porosity of the material which decreases the effective stress and thus increases its angle of friction. It is also interesting to highlight the liquid content (w_0%) of the events. For both tests it is almost the same; however, the amount of foam used is rather different. SCOD5-5.1 was produced from 29.8 litre of foam rather than the 0 litre of foam used to produce SCOD6 mixture. The casing shear stress was lower than 1.5 kPa in all tests, but the casing shear stress for conditioned test SCOD5-5.1 tends slightly to increase along the screw conveyor (towards the exit) while SCOD 6 tests tend decrease along the screw conveyor (towards the exit). Although these increases and decreases of casing shear stress in the tests were no of a big magnitude they helped to approximate the values of angle of friction at section S3.4.

Figure 6.54 shows that MAPEI Polyfoamer MCB had little effect in Garside sand at a FIR of 18.7% and w_0 of 20.2%. The conditioned Garside sand angle of friction has a constant value over the length of the screw while saturated Garside sand shows a slightly decreased angle of friction. The average angle of friction over the length of the screw, for conditioned Garside sand was around 20.5° and for saturated Garside sand was of 18.3°. These results could have been affected by the time when the steady state events were achieved in SCOD10. SCOD10-5.1 was achieved after 14 revolutions of the screw conveyor. It may be possible that by achieving steady state events earlier, after 3 or 4 revolutions of the screw, the MAPEI Polyfoamer MCB foam could show more influence on the angle of friction. However, it is clear that this conditioning effect reduces very soon after a steady state event has started. The recorded value of effective stress and casing shear stress for conditioned Garside sand have to be affected by the time at which the steady state events occurred. It was expected to see lower values of effective stress and casing shear stress for conditioned Garside sand than for saturated Garside sand. However,

the effective stress values for saturated Garside sand were placed between the two conditioned Garside sand events.

In Figure 6.55 the effect of foam conditioning at w_0 between 1.9% and 5.8%, and FIR between 37.4% and 18.7% was to stabilize the friction over the length of the screw. SCOD14-5.2 and SCOD12-5.2 steady state events show how FIR between 18% and 37% could do this. It is important to highlight that FIR was calculated assuming that the dry sand was in its loosest state when the mixture was prepared in the drum. The friction angle in these events went from 17.8° to an average value of 22.5°. Although SCOD15-5.5 was a conditioned event (FIR 57.5% and w_0 3%), its conditioning parameters had no effect on the angle of friction over the length of the screw, showing a constant rate of increase along the screw (towards the side of the motor). This could be due to the washing of the conditioner by the water through the conveyor, thus showing similar slope to an unconditioned event as is the case of the angle of friction of SCOD8-5.6 along the screw. The slope of the angle of friction curve over the length of the screw of SCOD14-5.2 and SCOD12-5.2 (together) is smaller than the slope of the angle of friction curve over the length of the screw of SCOD15-5.5 and SCOD8-5.6 (together). This reduction in the slope of its angle of friction curve was of 55%. It is interesting to observe that the effective stress for all the events was constant around 4.95 kPa except for SCOD15-5.5 which showed much higher values of effective stress. SCOD15-5.5 effective stress values decreased from 27.2 kPa in section S1.2 to 8.8 kPa in section S3.4. The tendency of the behaviour of casing shear stress was similar to the effective stress but the values are different. The casing shear stress was approximately 1.7 kPa for all the events except for SCOD15-5.5 for which the average value was approximately 7 kPa. It is not clear why this event shows such behaviour.

Figure 6.56 shows three steady state events for two conditioned tests. The difference in the tests lies in the amount of water used to produce the specimen. In SCOD12 no water was used and in SCOD14, 33% less water in volume than the volume of foam was used. Thus there was a liquid content of 5.8% for SCOD14 compared with 1.9% liquid content for SCOD12 (FIR of 37.4%). However, the absence of water had no effect on the angle of friction. The angle of friction, in the steady state events, was similar over the length of the screw, showing angles of friction values of SCOD14-11.3 in the middle of the angle of friction values of SCOD12 events. The total average across all steady state events was approximately 17.6°. The different behaviour of SCOD12-11.3/3, compared to SCOD12-11.3, may have been due to the drying of the mixture. This would make the specimen less homogeneously mixed, leaving part of the Garside sand with conditioned properties and another without conditioned properties or perhaps simply with no material passing continuously along the screw, and thus distribute the effective

stress and casing shear stress less homogeneously inside the conveyor casing during the same test. This could be the reason for the lower effective stress (around 1.5 kPa) and casing shear stress (around 0.46 kPa) values compared to events SCOD12-11.3 and SCOD14-11.3.

Figure 6.57 compares one non conditioned steady state event with two conditioned steady state events. It is not completely clear why at section S1.2 the friction is smaller for saturated Garside sand than for conditioned Garside sands. The only obvious reason is shown in Figure 6.57 (b) where the effective stress for the saturated Garside sand in S1.2 is around 6.7 kPa (four times the effective stress calculated for conditioned Garside sand). This can be attributed to an appropriate amount of water at the start of the event in that specific section (later in the sections the water is less), which produces an adequate lubrication thus increasing the effective stress due to the high normal stress and the low pore water pressure recorded (see Table 6.16). In general the effect of conditioning had no effect over the length of the screw. In some sections the angle of friction for SCOD8-15.5 was higher and in others lower than the conditioned Garside sands. Thus the conditioning was not very useful at this motor speed and specimen top pressure.

In general, Garside sand, at a FIR between 18% and 37%, and w_0 lower than 5.8%, produced an angle of friction lower than 24° over the length of the screw at an $\sigma'_{topspecimen}$ of at least 98.3 kPa. L.B. fine sand, at a FIR over 20%, and w_0 around 20%, produced an angle of friction lower than 25° over the length of the screw.

6.3.2.2. Average torque and average casing shear stress.

Figure 6.58 shows a graph of the average torque, T_{av}, of Table 6.16 against the average casing shear stress perpendicular direction of Table 6.17, $\tau_{averageper}$. Figure 6.58 also plots the theoretical average torque calculated by the following equation,

$$TheoreticalT_{av} = \tau_{averageper} * \pi * \frac{D_c}{2} * D_c * L * 1000 \qquad [6.16]$$

Where:

$\tau_{averageper}$= Average casing shear stress in perpendicular direction to screw axis, kPa;

D_c= Internal diameter of casing, 0.108 m;

L= Length of the screw, 1.25 m; and

Theoretical T_{av}= Theoretical torque, Nm.

Figure 6.58 (a) shows a good agreement between the calculated values and the theoretical torque value, although there are four points that fall far from the theoretical line. These points

are SCOD4-5.3, SCOD2-5.1/1, SCOD2-5.1 and SCOD3-5.4. For the case of SCOD4-5.3 where high torque and very low $\tau_{averageper}$ were calculated, the only explanation is that the soil mixture was jammed in a zone where no Cambridge load cells were placed. This would have generated the high torque recorded and a higher $\tau_{averageper}$, displacing the SCOD4-5.3 towards the theoretical line of torque (to the right of Figure 6.58 (a)). In the case of the other events, SCOD2-5.1/1, SCOD2-5.1 and SCOD3-5.4, the only conclusion that seems reasonable is that the average torque was not a valid representation for these events. Figure 6.58 (b) shows that when maximum average torque (see Table 6.16), T_{avmax}, is plotted, all the events tend towards the theoretical line of the torque and SCOD2-5.1/1, SCOD2-5.1 and SCOD3-5.4 approach the theoretical torque value line. One explanation for the differences between the torque values in SCOD2-5.1/1, SCOD2-5.1 and SCOD3-5.4 and the theoretical line of torque could be the stick of soil mixture material in the place where the load cells were placed, producing higher measurements of shear stress than was actually been experienced by the whole screw conveyor casing. This difference in shear stresses on the screw conveyor might produces the torque differences between the theoretical line of torque and the real torque experienced during the events.

In general 90% of the torque values recorded can be well estimated using together the T_{av} and T_{avmax} for all the OSC tests.

6.3.2.3. Average discharge efficiency and motor speed

Figure 6.59 shows the discharge efficiency vs motor speed for L.B. fine sand tests on the OSC model. In Figure 6.59 (a) there are two points that show discharge efficiency higher than 100%. This means that the conditioned L.B. fine sand during these steady state events was advancing along the screw axis by a length greater than the screw pitch (100 mm) for each screw rotation. Physically, it means that the soil mixtures during these events were very liquid, producing very low casing shear stress. Among these events is SCOD5-5.1 which also showed low angle of friction (see section 6.3.2.1) compared with saturated L.B. fine sand tests when they were tested on the OSC model. For all the other conditioned L.B. fine sand steady state events an average discharge efficiency of about 55% was calculated. In Figure 6.59 (b) all the saturated L.B. fine sand steady state events show discharge efficiency lower than 40% at 5 rpm and 11 rpm.

Figure 6.60 shows the discharge efficiency vs motor speed for Garside sand tests on the OSC model. Figure 6.60 (a) shows a wide range of values between 5.6% and 78%. The events which show values of discharge efficiency lower than 10% belong to tests SCOD12 and

SCOD14. The events in SCOD12 with discharge efficiency lower than 10% were events that belong to a test which started with a FIR of 37.4%, and a liquid content of 1.9%. It is important to highlight that these events occurred almost at the end of SCOD12 test. The event in SCOD14 with discharge efficiency lower than 10% is an event that belongs to a test which started with a FIR of 18.7%, and a liquid content of 5.8%. It is important to highlight that this event also occurred almost at the end of SCOD14 test. In general a decreasing trend of efficiency with increasing speed was observed. Figure 6.60 (b) shows values of discharge efficiency between 40% and 60% at any motor speed. The saturated Garside sand also showed a decreasing trend of efficiency with increasing speed of the motor.

Figure 6.61 shows the average direction of friction values, $\varepsilon_{average}$, vs calculated angle of soil movement for L.B. fine sand tests and Garside sand tests on the OSC model. As was mentioned in Chapter 2 section 2.7.3, it was expected that $\varepsilon_{average}=\theta_c$. This means that the values for average direction of friction should lie on the black line of Figure 6.61 labelled η_s=100%. Clearly, this was not the case. Thus, one may conclude that the assumption that the conveyor casing was completely full of material, as made in section 6.3.1.9, was incorrect.

Figure 6.62 shows the vector of velocities and the direction of movement of a soil element regarding the flight ad casing.

A relation between the calculated direction of soil movement and direction of friction that takes into account the voids in the casing during the test is shown in the following equation,

$$\tan\theta = \frac{\eta}{\eta_s - \eta} * \tan\phi_f = \tan\varepsilon_{average} \qquad [6.17]$$

Where:

η_s= Efficiency of solids, percentage of length solids over the total length available, %;

$\varepsilon_{average}$= Direction of friction, degrees; and

θ= Direction of soil movement deduced, taking into account the voids during extraction of material, degrees.

Equation [6.17] takes into account the voids of material during the SCOD tests and presents the expected relation between direction of friction and direction of soil movement. If equation [6.17] and equation [6.8] are re-arranged,

$$0.01 * \eta_s * \tan\varepsilon_{average} = 0.01 * \eta * (\tan\phi_f + \tan\varepsilon_{average}) \qquad [6.18]$$

$$\tan\theta_c = 0.01 * \eta * (\tan\phi_f + \tan\theta_c) \qquad [6.19]$$

If equation [6.18] is divided by [6.19] the resulting ratio is,

$$0.01 * \eta_s * \frac{\tan \varepsilon_{average}}{\tan \theta_c} = \frac{(\tan \phi_f + \tan \varepsilon_{average})}{(\tan \phi_f + \tan \theta_c)} \quad [6.20]$$

Re-arranging equation [6.20] one can get,

$$\varepsilon_{average} = \arctan\left[\frac{(\tan \theta_c * \tan \phi_f)}{(0.01 * \eta_s * \tan \phi_f + (0.01 * \eta_s - 1) * \tan \theta_c)}\right] \quad [6.21]$$

Equation [6.21] shows the direction of friction angle taking into account the voids of material during extraction in OSC tests. If the direction of friction is plotted using equation [6.21] for different values of efficiency of solids and different values of calculated soil movement, the black lines in Figure 6.61 are obtained. Most of the tests (88%) are placed between η_s=25% and η_s=100%. Although 61% of the tests are between η_s=50% and η_s=80%. The cases where η_s is higher than 100% mean that, with each rotation of the screw, solids were advancing along the axis by more than the screw pitch.

6.4. Applicability of experimental results in EPBM tunnelling process

Carrying out OSC tests can help to evaluate the efficiency of the use of foam as a conditioner for sand when it is used in an EPB machine. For instance, during this research it was seen that MAPEI Polyfoamer MCB has little effect in Garside sand when it is used at FIR values lower than 37%.

Carrying out OSC tests can help to ascertain if the foam conditioning used in sand during EPB tunnelling operations would have any lubricating effect. The angle of skin friction calculated during most of the tests using CETCO and MAPEI foam conditioners produced a skin friction angle typical for friction contact between sand and steel, between 15° and 23.8°. Although, sometimes lower values than 15° and higher values than 23.8° were achieved at specific operating conditions of the OSC model. These values were measured in some events during tests: SCOD2, SCOD5, SCOD9 and SCOD16. Events SCOD2-5.1/1, SCOD5-5.1, SCOD16-5.1/1 and SCOD16-11.2 had average angle of friction values lower than 15°. Events SCOD9-5.2, SCOD9-11.3, SCOD9-15.4, and SCOD9-5.5 has average angle of friction values higher than 23.8°. The events with a mixture L.B. fine sand and foam that showed angle of friction values lower than 15° started at w_0 around 27%, D_{r0} between -0.7 and -1, and FIR around 21%. They measured indifferently at 5 or 11 rpm, but both of them were carried out with a central shaft screw type and a gate diameter of 85.5 mm. The event with a mixture Garside sand and foam that showed an angle of friction value lower than 15° started at w_0 around 3.1%, D_{r0} around -0.008, and FIR around 60%. This was carried out with a central shaft screw and a gate diameter of 85.5 mm. SCOD9, which had events with average angle of friction higher than

23.8° started at w_0 around 19.22%, D_{r0} around 0.214, and FIR of 0%. This was carried out with a central shaft screw and a gate diameter of 85.5 mm.

From the previous events (average angle of friction<15° and average angle of friction>23.8°) the only events where the soil mixture advanced approximately along the axis by an amount similar to the screw pitch wit each rotation of the screw (90%<η_s<100%) were events SCOD2-5.1/1 and SCOD5-5.1, as it is shown in Figure 6.61. Thus it is recommended that when excavation through L.B. fine sand an addition of foam conditioner with similar properties to CETCO Versa foam are recommended to be used. Specifically FIR around 21%, w_0 around 27% in order to get D_{r0} between -0.7 and -1, in order to get low angles friction and thus low torque and power consumption while the soil is been excavated. This will also produce easy handling of this excavated material in the screw conveyor.

6.5. Summary

This Chapter reported the equipment, procedure, results and analysis of sixteen Oxford screw conveyor (OSC) tests mainly on L.B. fine sand water foam mixtures and Garside sand water foam mixtures. The OSC model used to carry out these tests was described.

Section 6.2 described the OSC model used to carry out the tests. The OSC model consisted of a tank and a horizontal instrumented screw conveyor casing. The tank modelled the pressure chamber of an EPB machine when a loading piston was pushed inside it in order to apply a constant vertical stress to the sand-water-foam mixture inside the tank. The conveyor casing modelled the inclined screw conveyor part of an EPB machine.

Section 6.3 presented the experimental procedures and results of OSC tests. Section 6.3.1 showed the main values that can be obtained from OSC tests, using as an example SCOD9 test. At the end of this section the steady state flow conditions were established as the common parameter to be used for further analysis in all the OSC tests. Section 6.3.2 analysed the results of all the OSC tests. The analysis was done focusing firstly on the different operating conditions under which the OSC tests were carried out. It seemed that when the opening A (85.5 mm) is used, the flow of material through the screw conveyor was easier, even achieving values of efficiency higher than 100%. The average angle of friction for tests carried out with a screw without central shaft can be around 21.61° assuring that for conditioned L.B. fine sand the extracted material was in contact with the steel casing during along the screw axis. The higher pressure on the top of the specimen produced a more homogenous distribution of angle of the friction over the length of the screw. It is clear that the change of speed from 5 to 15 rpm in the different steady state events had no major effect on the friction angle of sands. In general

for Garside sand, FIR between 18% and 37%, and w_0 lower than 5.8% produced angles of friction lower than 24° over the length of the screw at an adequate $\sigma'_{topspecimen}$. For L.B. fine sand, FIR over 20% and w_0 around 20% produced an angle of friction lower than 25° over the length of the screw. 90% of the torque values recorded could be adequately estimated by T_{av} and T_{avmax} for all the OSC tests. The assumption that the conveyor casing was completely full of material and that the soil advances along the screw axis by a length equal to the screw pitch with each rotation (in order to calculate the efficiency) seemed to be incorrect, this followed the results of average direction of friction and calculated direction of soil movement. During extraction of material the conveyor had voids of no material. When they are taken into account the efficiency of soil (η_s), for 61% of the steady state events, is between η_s=50% and η_s=80%, far from the original assumption of efficiency. There also were cases where solids were advancing along the screw axis by a length longer than the screw pitch with each rotation (η_s >100%).

Finally it is recommended a percentage of FIR (21%) and w_0 (27%) to be achieved in mixtures of soil and foam conditioner when tunnellers are being excavated though L.B. fine sand in order to produce easy handling of material along the screw conveyor, low torque and power consumption. This demonstrates that the OSC model can be used as a trial machine to study the effect of different operating conditions on similar conditioned sand specimens than a tunnelling site. This becomes even more relevant when controlled EPB machine operations need to be carried out but not enough information about the behaviour of the sand (present on site) mixed with foam conditioners is known by the contractors. This also demonstrated that relevant information can be extracted from OSC tests. Outputs from these tests could deliver enormous changes in the tunnel operational costs when EPB machines are used.

Chapter 7. Conclusions and future research

7.1. Introduction

This research has presented experimental investigations into soil conditioning for sands, shear box tests on foam conditioned sand, compressibility tests on foam conditioned sand and into the operation of a model EPB screw conveyor with sandy soils. Conclusions from the research are given in the summary at the end of each chapter. This chapter summarises the key conclusions drawn from the research and some suggestions for further research are also given.

7.2. Sand and conditioner properties

From the different index tests carried out in this research it can be concluded that:

1. Foam expansion ratio (FER), increases when the foaming agent concentration is increased. The differences in FER values between the foaming agents, which were tested at different concentrations, are believed to result from the varying effects of the foaming agents on the surface tension of the solutions. The specific chemical compositions of the foaming agents, containing different surfactants at varying concentrations as well as other additives, determine their influence on the surface tension of the solutions (see section 3.4.2.1);
2. The specific chemical composition of the foaming agents also affects the drainage time of the foaming agents. Most of the foaming agents tested in this research show 50% drainage time between 6 and 8 minutes, except for CLB F4, which shows 50% drainage time between 30 and 38 minutes, at different concentrations. Foaming agents, with a polymer compound to improve stability, do not show much higher drainage time than foaming agents which do not have a polymer compound (see section 3.4.2.2);
3. In general, for T7, CLB F4 and Foamex TR at 1.5% concentration, and Foamex EC at 2.5% concentration, using an FIR of 45% and a sand water content of around 22%, produce slumps in the very plastic zone, which may be suitable for EPBM operations. Slumps in the very plastic zone can also be obtained using MEYCO® Fix SFL P1 and P2, at concentrations between 0.5 and 1%, with PIRs between 14% and 17%. For DRILLAM MV and TFA 34, with a PIR of 17.2%, at concentrations between 0.025 and 0.05%, slumps in the very plastic zone can be obtained (see section 3.4.3);
4. Using Versa foam at 2% concentration (FER of around 13.5) slumps in the very plastic zone can be obtained for: conditioned L.B. fine sand (water content between 20% and 27% and FIR between 20 and 22%), conditioned L.B. coarse sand (water content of around 6% and a FIR around 3%) and conditioned L.B. graded sand (water content of 15.8% and a FIR of 12%) (see section 3.4.3.1);

5. In general, the slump increases with an increase in FIR and water content, reaching a limit, which is called the drainage limit, after which, due to the excessive water content in the conditioned sand, the foam is drained out of the mixture, producing a very firm slump. All sands would show the same behaviour, but with varying drainage limit, according to the content of fines. A higher content of fines in the sand increases the drainage limit, thus also the water content at which this occurs;
6. None of the mixes on conditioned Thanet sand would flow through the flow cone apparatus, so that it was not possible to measure the time for flow. Thus the Flow cone test could not be used as an index test on conditioned Thanet sand (see section 3.4.3.2);
7. The drainage time tests carried out on conditioned L.B. medium coarse sand, either at atmospheric pressure or under pressure show no change in the stability of the foam, CLB F4 being recording the longest drainage times (see section 3.4.3.3); and
8. The index tests (slump test and drainage time), are a very useful tool to study the properties of the conditioners and sands used in this research. This has been successfully completed. These results were successfully used to select the conditioned sand mixtures which were tested in the shear box apparatus, compressibility apparatus and Oxford screw conveyor apparatus.

7.3. Shear box tests

From the MSSA tests carried out in this research it is important to highlight that:

1. Foams can be used to increase voids ratio of the soil, achieving a minimum value of Relative Density of -1 for some sands;
2. The pore water pressure controls the strength of the sand foam mixtures. An increase in FIR might produce and increase of pore water pressure and a decrease of shear stress. At high voids ratios (high FIR) the angle of friction can be lower than at "conventional" voids ratios (FIR=0%), this is due to "replacement" of grains by bubbles in the structure;
3. Different type of sands, regarding their fines content and water content, have different optimum combination sets of parameters (reducing shear stress), in order to produce a mixture suitable for tunnelling processes. This is the case showed here between L.B. sands and Thanet sand. At low relative densities (high voids ratios, only sustainable through the addition of foam), sands might exhibit a low angle of friction if the combination of parameters such as FIR, percentage of fines content of the sand and water content is such that the addition of foam can reduce the angle of friction of the sand. This is evidenced by tests G4 and Th4 with angle of friction measured in direct shear of 23.5° and 26.8° respectively;

4. Bolton's correlation can be extended (at a different slope), to negative Relative Density values (voids ratios considerably higher than at the loosest normal state);
5. Foamed sands at states much looser than the normal loosest state were found to exhibit angles of friction lower than the angle of friction at constant volume. Angles of friction as low as 23.5° were measured;
6. From the attempt to measure the drainage of liquid (important because it controls pore pressure) from the shear band in the shear box during testing, where the more stable foam shows the highest percentage drainage from the shear band, it is possible to conclude that there are other parameters to be considered in the stability of the foam, for instance, the permeability of the soil;
7. The MSSA can be used as a tool to determine the behaviour of soil conditioned with foam under direct shear, defining how this conditioning lowers the angle of friction of the foam soil mixture. This is particularly significant for the EPBM tunnelling industry as such a reduction may reduce EPBM energy consumption and, thus, the costs of its operation; and
8. The shear box tests can be used to study the behaviour of similar conditioned sand specimens to a tunnelling site, under direct shear, where the effects of FIR on a particular type of sand are unknown. This will uncover relevant information which could deliver important changes in the tunnelling conditioning programme, where EPB machines are used. For instance conditioned L.B. fine sand coefficient of friction can be reduced 2% respect of the coefficient of friction measured for saturated L.B. fine sand. This implies that the coefficient of skin friction may be reduced 2% and thus the wear on the screw conveyor of an EPBM handling conditioned L.B. fine sand may be reduced 2%. In the case of conditioned L.B. coarse sand it is no possible to reduce the wear using only Versa foam as a soil conditioner.

7.4. Compressibility tests

From the MAPC tests carried out during this research, it can be concluded that:

1. Using foam as a soil conditioner in compressibility tests on sands, can produce voids ratios higher than the maximum voids ratio of sand without foam conditioning at effective vertical stresses of around 200 kPa;
2. Thanet sand/water/foam mixtures show ten fold higher values of excess pore water pressures (10 kPa) than L.B./water/foam mixtures;
3. The permeability of saturated L.B. fine sand (2.48×10^{-3} m/s), can be reduced by an order of magnitude when this is conditioned with foam (1.06×10^{-4} m/s);
4. The Thanet sand water foam mixtures show lower values of coefficient of permeability (4.55×10^{-8} m/s) than L.B. sand water foam mixtures (1.06×10^{-4} m/s). The Thanet sand

water foam mixtures show a minimum coefficient of permeability of at least two orders of magnitude lower than L.B. sand water foam mixtures;

5. The permeability results depend of the maximum value achieved by the ratio u'_b/σ', which in case of L.B. fine sand conditioned with foam has to be higher than 9% in order to achieve reliable permeability values. In the case of Thanet sand conditioned with foam it is possible to have reliable permeability values at ratios of u'_b/σ' around 11000%. Following this, it can be conjectured that the drainage conditions is very important because it controls ratio u'_b/σ' and permeability;
6. Even at high vertical effective stresses (around 300 kPa on L.B. foamed fine sand and at around 60 kPa on Thanet foamed sand), the maximum ratio of compression, due to the expulsion of gas, is lower than 4% of the total strain ratio in 74% of the tests;
7. Increasing FIR does not mean increasing the maximum gas expelled. The FIR and the initial relative density of the specimen have to be related to the capability of the specimen to retain the gas and establish a coexistence between grain of soil, water and gas bubbles. It is concluded that "good" mixes would be those in which most compression is due to gas compression rather than water expulsion. Thus in this series of tests there are 3 best mixes, which are Finesand14foamR, Finesand18foamR and Finesand26foamR. These showed less than 50% maximum water expelled but also the compression of the gas was higher than the gas expelled (see Table 5.5 and Figure 5.45);
8. Boyle's law theory is fulfilled in most of the MAPC tests in the drained loading zone;
9. The outputs that have to be used by tunnellers on EPBM applications from this experimental research are high voids ratio values at high effective vertical stresses, permeability coefficient measurement, study of specimen behaviour at different effective vertical stresses and drying of soils. The tunnellers could set up any type of apparatus on site in order to measure the permeability of an excavated conditioned soil mixture. During this on site test they have to put attention to: FIR used, excavated soil mixture loading pressure and rate of water volume expelled from the excavated soil mixture. Having the previous parameters on mind a comparative evaluation of the permeability of the excavated conditioned soil mixture can be established for different conditioners regarding the excavated natural soil. This might reduce the cost of excavation, avoiding unnecessary runs out of material during tunnelling causing unforeseen damage and accidents on site; and
10. "Ideal" soil water foam mixtures are preferred by tunnellers who use EPB machines. Ideal mixtures that can be extracted easily from the screw conveyor and avoid uncontrolled flow of water out the screw. Unfortunately the "ideal" mixture needs to be

changed throughout the excavation process as the soil type, water table and building area changes. Thus a history of the soil water foam mixture behaviour at different effective stresses using the MAPC is very useful to determine properties of the specimen at a specific effective stress levels which could be used to back calculate main mixture parameter, used on site by tunnellers, as FIR for instance; and

11. Nowadays one of the main problems for the tunnellers is the disposal of the excavated soil. Here it has been demonstrated that the existence of bubbles in a soil water mixture produces, when the soil mixture is consolidated, a high volume of water out of the mixture (Figure 5.44 and Table 5.5) and a negligible volume of gas. Thus this idea can be used as a way to extract the water of excavated soils before disposal in order to decrease the use of the available land in landfill.
12. Finally these tests demonstrated that the conditioning of L.B. fine sand and Thanet sand with foam to form materials suitable for controlled EPB machine operations can be successfully studied. It also demonstrated that relevant information can be extracted from MAPC tests whose outputs could deliver enormous changes in the tunnel operational costs avoiding: unnecessary runs out of material during tunnelling causing unforeseen damage and accidents on site, and unnecessary investment in no adequate soil conditioners for that specific excavated soil, when EPB machines are used.

7.5. Screw conveyor tests

From the screw conveyor tests carried out during this research, it can be concluded that:

1. The analysis of the tests showed that: when the opening A (85.5 mm) is used, the flow of material through the screw conveyor was easier, even achieving values of efficiency higher than 100%, the average angle of friction for tests carried out with a screw without central shaft can be around 21.61° assuring that for conditioned L.B. fine sand the extracted material was in contact with the steel casing during along the screw axis, the higher pressure on the top of the specimen produced a more homogenous distribution of angle of the friction over the length of the screw, the change of speed from 5 to 15 rpm in the different steady state events had no major effect on the friction angle of sands, Garside sand (FIR between 18% and 37%) at w_0 lower than 5.8% produced angles of friction lower than 24° over the length of the screw at an adequate $\sigma'_{topspecimen}$, L.B. fine sand (FIR over 20%) at w_0 around 20% produced an angle of friction lower than 25° over the length of the screw, 90% of the torque values recorded could be adequately estimated by T_{av} and T_{avmax} for all the OSC tests;
2. The assumption that the conveyor casing is completely full of material and that the soil advances along the screw axis, by a length equal to the screw pitch with each rotation in order to calculate the efficiency, appears to be incorrect following the results of the

average direction of friction and calculated direction of soil movement. During the extraction of material the conveyor has voids of no material. When they are taken into account, using the efficiency of soil, η_s, shows that 61% of the steady state events are between η_s=50% and η_s=80% which is far from the original assumption of perfect efficiency. There were also cases where solids advanced along the screw axis by a length longer than the screw pitch with each rotation (η_s >100%); and

3. It is recommended a percentage of FIR (21%) and w_0 (27%) to be achieved in mixtures of soil and foam conditioner when tunnellers are being excavated though L.B. fine sand in order to produce easy handling of material along the screw conveyor, low torque and power consumption. This demonstrates that the OSC model can be used as a trial machine to study the effect of different operating conditions on similar conditioned sand specimens than a tunnelling site. This becomes even more relevant when controlled EPB machine operations need to be carried out but not enough information about the behaviour of the sand (present on site) mixed with foam conditioners is known by the contractors. This also demonstrated that relevant information can be extracted from OSC tests. Outputs from these tests could deliver enormous changes in the tunnel operational costs when EPB machines are used.

7.6. Future research

Considerable scope remains for further research into soil conditioning for EPB machines and screw conveyor operations. Some suggestions to extend the research presented in this thesis are given below.

The index tests used here were useful for identifying effective conditioning treatments for the soils tested in this research. Similar tests could be performed with other sandy soils, either in the laboratory or on site, for specific tunnelling projects, to build up a database of optimum conditioning treatments for different soils. The effects of parameters such as different surfactant properties, conditioning agent concentrations, and combinations of different agents on the properties of conditioned sands could also be investigated further. A database and improved knowledge of effective conditioning treatments for different soils based on standard index tests would be of use for tunnelling practice. The size of the foam bubble, produced by the foam generators, and also the variation of the size of the foam bubbles, when they contribute to the soil structure, have not been clearly defined in this research. Some tests for measuring the foam bubble size were described in Chapter 3, but these have not been further investigated. Some research and development of test methods to investigate foam bubble size variation, and its effect in foam soil conditioning treatments, may help improve EPB machine operations.

Some results from the model screw conveyor tests indicated that foam conditioning treatments provided lubrication to reduce soil-steel interface shear stresses. Sand-steel interface shear tests could be performed in the MSSA with conditioned sand soils, or with conditioning agents introduced to the interface. Such tests would allow direct measurements of the effects of different conditioning treatments on soil-steel interface shearing behaviour.

Further research is possible with the MSSA on conditioned soils for e.g. test on different sands to observe the effect of foam in its internal angle of friction. This will complement the results obtained in this research. Modifications to the current MSSA, in order to improve the measurement of the drained liquid during shearing, are advised. With these modifications a more precise control of the drainage of liquid could be carried out, and these results could be compared with the stability property of the foam itself, in order to establish a relationship between foam properties and foam-soil interaction under specific loads. In this way, more reliable data could be obtained regarding the real stability of foam when it is mixed with sand in an EPBM.

The gas measurement system used in the compressibility test may be improved. During the current research, when an excess of bubbles were expelled, the test was stopped to avoid the bubbles reaching the CVC. The design of a new system, where the bubbles expelled by the sample during compression can be trapped, will minimize the danger of bubble contamination in the CVC and extend the range of vertical compression of the samples. In this way, the presence of foam bubbles in the conditioned soil sample at higher effective stresses than 200 kPa could be studied. It will also be interesting to modify the current MAPC in order to observe the state of the conditioned soil sample after the compression test (Thomas, 1987). If this was carried out, the final voids ratio of the conditioned soil could be obtained from an insitu measurement and compared with the indirect measurements of volume change. This would help to corroborate the results presented in this research regarding the percentage of compression of the gas in the conditioned soil.

Further research is possible with the Oxford screw conveyor. Tests using higher sample pressures would be interesting in order to identify the maximum pressure that can be controlled by the screw conveyor. Conditioning agents are normally injected into the screw conveyor on EPB machines. Tests could be performed to investigate the effects of injecting conditioning agents into the conveyor at different points. This application of soil conditioning provides a lubricating layer around the casing surface, which can reduce the screw torque and also influence the pressure gradient. Tests could be performed to further investigate the effects of

varying screw geometries. Different screw pitches could be used to compare with the results already obtained. Modifying the OSC, in order to automatically control the opening gate, would increase the operation range option of the OSC making it more similar to the EPB machine's control system.

7.7. Final remarks

Due to the need of further research in the practical use of soil conditioner in tunnelling, which is still based on trial and error, this experimental investigation has provided to develop a simple test methods for assessing conditioning treatment for sands; investigate properties of commercial soil conditioning foams; investigate the effects of foam and polymer conditioning treatments on sands; identify an optimum conditioning treatment for sands with different granulometry; study the behaviour of conditioned sands with foam and polymer in shear box test, conditioned sand with foam in consolidation and permeability tests; study the influence of parameters such as: FER, FIR, PIR and diameter of soil particles in the results from shear box, consolidation and permeability tests; investigate the operation of the Oxford model screw conveyor operating with sandy soils; and demonstrated consistency between findings of recommended conditioned sand mixtures for EPBM by slump tests (Chapter 2) and minimal angle of friction of shear box/screw conveyor tests (Chapter 3 and Chapter 6) measured on conditioned sand mixtures. In this way this research aids to advance the fundamental understanding and practical application of soil conditioning for mechanized tunnelling machines.

References

Anagnostou, G. and Kovari, K. 1996. Face stability conditions with earth-pressure-balanced shields. Tunnelling and underground space technology, Volume 11, Issue 2, pg.165-174.

Archard, J.F., 1953. Contact and rubbing of flat surfaces. Journal of Applied Physics, Volume 24, Issue 8, pg. 981-988.

Arthur, J.R.F., James, R.G., Roscoe, K.H, 1964. The determination of stress fields during plane strain of a sand mass. Geotechnique, 14, Number 4, 283-306.

ASTM C 143/C 143 M. Standard test method for slump of hydraulic-cement concrete.

ASTM C939-97. Standard test method for Flow of Grout for pre-placed-aggregate concrete (Flow Cone Method).

ASTM D4186-82 (CRS). ASTM standard: standard test method for one-dimensional consolidation properties of saturated cohesive soils using controlled-strain loading.

ASTM D4254-00 Method C. ASTM standard: standard test methods for minimum index density and unit weight of soils and calculation of relative density.

Atkinson, J.H. and Bransby, P.L., 1978. The mechanics of soils. An introduction to the critical state soil mechanics, McGraw Hill, London.

Augarde, C.E. and Burd, H.J., 2001. Three-dimensional finite element analysis of lined tunnels. Int. J. Num. Analyt. Meth. Geomechanics, 25,243-262.

Banbendererde, S., 1991. Tunnelling machines in soft ground: a comparison of slurry and EPB shield systems. Tunnelling and underground space technology, Volume 6, Issue 2 , 1991, Pages 169-174.

Bezuijen, A. and Schaminee, P.E.L., 2000. Model experiments using foam simulating the drilling with and EPB shield. Internal report, Geodelft. Delft, Netherlands.

Bezuijen, A., Schamine, P.E.L. and Kleijan, J.A., 1999. Additive testing for earth pressure balance shields. 12th Europe Conf. on soil mechanics and Geotech. Engng., Amsterdam, June.

Bolton, M.D., 1986. The strength and dilatancy of sands. Geotechnique 36, No1, 65-78.

Bolton, M.D., 1987. The strength and dilatancy of sands. Geotechnique 37, No2, 219-226.

Bolton, M. D., 1991. A guide to soil mechanics. Chung Hwa Book Company (Hong Kong) Ltd.

Borghi, F. X., 2002. Lubrication in pipe jacking and soil conditioning for EPB-shield tunnelling. First year report submitted in February 2002. University of Cambridge.

Bransby, P.L., 1973. Cambridge contact stress transducers. Cambridge University Engineering Department Report CUED/C-SOILS/LN-2.

BS 1377-4:1990. British standard: Methods of test for soils for civil engineering purposes. Compaction-related tests.

BS 1881:Part 102:1983. British standard. Testing Concrete. Part 102. Method for determination of slump.

BSI, 1975. Methods of test for soils for civil engineering purposes. Gr10 British standards Institution. BS 1377:1975.

Burd, H.J., Houlsby, G.T, Augarde, C.E, and Liu, G, 2000. Modelling Tunnelling-Induced Settlement of Masonry Buildings. Proc. ICE, Geotechnical Engineering, 143, 17-29 ISSN 1353 2618.

Cash, T. and Vine-Lott, K.M., 1996. Foam as a tunnelling aid: its production and use. Tunnels and tunnelling, Vol. 28, No 4, 22-23.

CETCO EUROPE Ltd.,2002. Drilling Products DPPA 100, Colloid Environmental Technology Company, Polymer and Additive product Line.

Clift, R., Grace, J.R., Weber, M.E., 1978. Bubbles, drops and particles. Academic Press.

Cole, E.R.L., 1967. The behaviour of soils in the simple shear apparatus. PhD Thesis, Cambridge University.

CONDAT, 1999. EARTH PRESSURE BALANCE T.B.M., CONDAT Specific Products.

Crawford, C.B., 1964. Interpretation of the consolidation test. Journal of the soil mechanics and foundations division. Proceedings of the American society of civil engineers. ASCE Vol. 9o, No SM5, September, pp 87-102.

CTRL, 1997. London Tunnels West Geotechnical Design Basis Report. Channel Tunnel Rail Link Technical Report No. 220-RUP-LCEEH-00025-AA, February 1997.

Dagnall, H., 1980. Exploring surface texture. Rank Taylor Hobson (January 1980).

Darton, R.C., Sun, K.H., 1999. The effect of surfactant on foam and froth properties. Institution of chemical engineers. Trans. IChemE., Vol 77, Part A, September.

Dietz, M.S., 2000. Developing an holistic understanding of interface friction using sand within the direct shear apparatus. PhD thesis, University of Bristol.

Dufrêche, J., Prat, M., Schmitz, P., Sherwood, J.D., 2002. On the apparent permeability of a porous layer backed by a perforated plate. Chemical Engineering Science 57, 2933-2944.

Eurotherm Drives Limited (a), 2002. 650 AC Drive, Frames 1, 2, 3. Software Product Manual, HA467872U001 Issue 2. Compatible with Version 4.xSoftware.

Eurotherm Drives Limited (b), 2002. 650V, 650 Series, Frames 1, 2, 3. Software Product Manual, HA467649U002 Issue 2. Compatible with Version 4.xSoftware.

Fang, L., Kong, X.L., Su, Y.J., and Zhou, Q.D., 1993. Movement patterns of abrasive particles in three-body abrasion. Wear, Volumes 162-164, Part 2, pages 782-789.

Fredlund, D.G. and Rahardjo, H., 1993. Soil Mechanics for Unsaturated Soils, John Wiley & Sons, New York, pp.517. June.

Fredlund, D.G., 1979. Appropriate concepts and technology for unsaturated soils. Canadian geotechnical journal, Vol. 16, pp. 121-139.

Fredlund, D.G., Morgenstern, N.R. and Widger, R.A., 1978. The shear strength of unsaturated soils. Canadian geotechnical journal, Vol. 15, No.3, pp. 313-321.August.

Gibson, R.E., England, G.L. and Hussey, M.J.L., 1967. The theory of one-dimensional consolidation of saturated clays, I- Finite Non-linear consolidation of thin homogeneous layers. Géotechnique 17:261-273.

Gibson, R.E., Schiffman, R.L., Whitman, R.V., 1989. Geotechnique, Vol. 39, No1, pp.169-171.

Gue, S. S., 1984. Ground heave around driven piles in clay. DPhil thesis, University of Oxford.

Head, K.H., 1986. Manual of soil laboratory Testing. Vol. 3: Soil testing laboratory manuals.

Head, K.H., 1992. Manual of soil laboratory Testing. Vol. 1: Soil classification and compaction tests. –2nd ed.

Head, K.H., 1994. Manual of soil laboratory Testing. Vol. 2: Permeability, shear strength and compressibility tests. –2nd ed.

Herrenknecht, M. and Maidl, B., 1995. Applying foam for an EPB shield drive in Valencia (translated from German). Tunnel 5/95, 10-19.

Herrenknecht, 2006. Web page source www.herrenknecht.com. August 2006.

Houlsby, G., Psomas, S., 2001. Soil conditioning for pipejacking and tunnelling: properties of sand/foam mixtures. Proc. Underground construction 2001. International exhibition & symposium. London Docklands, UK, pp. 128-138.

Jancsecz, S and Steiner, W (1994). Face support for a large mix-shield in heterogeneous ground conditions. Proc. Tunnelling 94, IMM, London, UK.

Janscecz, S., 1997. Modern shield tunnelling in the view of geotechnical engineering: A reappraisal of experiences. Proc. 14th Int. Conf. On soil mechanics and foundation engineering, Hamburg, 1415-1420.

Japan, 2006. Shield Tunneling Association of Japan. Web page source: http://www.shield-method.gr.jp/english. August 2006.

Jardine, R.J., Lehane, B.M., and Everton S.J., 1993. Friction coefficients for piles in sands and silts. Soc. Underwater Tech. 28: Offshore site investigation and foundation behaviour, pp 661-677.

Jewell, R. A, Wroth, C.P., 1987. Direct shear tests on reinforced sand. Geotechnique 37, No. 1, 53-68.

Jewell, R. A., 1980. Some effects of reinforcement on the mechanical behaviour of soils. PhD Thesis, Cambridge university.

Jewell, R. A., 1989. Direct shear test on sand. Geotechnique 39, No 2, 309-322.

Kishida, H and Uesugi, M., 1987. Tests of interface between sand and steel in the simple shear apparatus. Géotechnique, 37, No 1, 45-52.

Kusakabe, O., Nomoto, T., and Imamura, S., 1999. "Geotechnical criteria for selecting mechanized tunnel system and DMM for tunnelling". Panel discussion, Proceedings of 14th Int. Conf. on Soil Mech. and Found. Engng.. (Hamburg, 1997). Vol. 4, pp. 2243-2440, Balkerma, Rotterdam.

LAMBERTI, 2002. Earth Pressure Balance Shield, conditioning agents. http://www.lamberti.com/products/Products_List.pdf

Lyon, J., 2001. Personal conversation. CETCO Europe representative.

Magrabi, S.A., Dlugogorski, B.Z., Jameson, G.J., 1999. Bubble size distribution and coarsening of aqueous foams. Chemical engineering science, 54, 4007-4022. Available on internet from Elsevier Science ltd.

Maidl, B., 1995. Erweiterung der einsatzbereiche der erddruckschilde durch bodenkonditionierung mit schaum. PhD thesis Ruhr Universität Bochum, Germany. In German.

Maidl, B., Herrenknecht, M., Anheuser, L., 1995. Mechanised shield tunnelling. John Wiley & Sons.

Mann, N., and Broese Van Groenou, A., 1977. Low speeds scratch experiments on steels. Wear, Vol. 42, Issue 2, pages 365-390.

MAPEI, 2004. Machine Tunnelling Application, MAPEI UTT PRODUCT DATA SHEET.

Marks, 1997. Manual del Ingeniero Mecánico, 9a Edición, Tomo 1. McGraw-Hill. ISBN:970-10-0662-3

Marmur, A., Rubin, E., 1973. Equilibrium shapes and quasi-static formation of bubbles at submerged orifice. Chemical Engineering Science, Vol. 28, pp. 1455-1464.

Marshall, M., 1998. Pipe jacked tunnelling: jacking loads and ground movements. DPhil Thesis, University of Oxford.

Martin, C.M., 1994. Physical and numerical modelling of offshore foundations under combined loads. DPhil thesis. University of Oxford.

MBT, 2004. Products, UGC International.http://www.degussa-ugc.com/MBTUGC/Home/default.htm

Merritt, A.S. and Mair, R.J., 2001. Investigation of lubrication and soil conditioning for tunnelling and pipe jacking in clay soils. Proc. Modern Tunnelling Science and Technology, Kyoto, Japan.

Merritt, A.S, 2004. Conditioning for clay soils for tunnelling machine screw conveyors, PhD thesis, University of Cambridge.

Milligan, G., 2000. Lubrication and soil conditioning in tunnelling, pipejacking and microtunneling. A state of the art review, geotechnical-consulting group.

Ministry of Defence, 1995. Foam liquids, fire extinguishing (Concentrates, foam, fire extinguishing). Defence Standard 42-40/Issue 1, Annex B.

Monteith, G., 2002. Personal communication. Mechanised Tunnelling Manager. Barhale Construction plc.

Muir Wood, A., 2000. Tunnelling: Management for design. Taylor & Francis Books Ltd Spon Press.

Naitoh, K., 1985. The development of earth pressure balanced shields in Japan. Tunnels & Tunnelling: the international journal of underground works, Vol. 17, No. 5.

Norris, P., 1992. The behaviour of jacked concrete pipes during site installation. D.Phil. Thesis, University of Oxford.

Odom, I.E., 1986. Na/Ca montmorillonite: properties and uses. American colloid company manuscript.

Paikowsky, S.G., Player, C.M., and Connors, P.J., 1995. A dual interface apparatus for testing unrestricted friction of soil along solid surfaces. Geotechnical Testing Journal, No 2, 18, 168-193.

Pedley, M. J., 1990. The Performance of soil reinforcement in bending and shear. DPhil Thesis, University of Oxford.

Peron, J.Y. and Marcheselli, P., 1994. Construction of the passante ferroviario link in Milan, Italy, lots 3P, 5P, and 6P, excavation by large earth pressure balanced shield with chemical foam injection. Tunnelling 94, Institution of mining and metallurgy and British tunnelling society, Chapman and Hall, London, UK, 679-707.

P.J.A., 1995. Pipe Jacking Association: Guide to best practice for installation of pipe jacks and micro-tunnels.

Potyondy, J.G., 1961. Skin friction between various soils and construction materials. Geotechnique 11:339-355.

Psomas, S., 2001. Properties of foam/sand mixtures for tunnelling applications. MSc. Thesis, University of Oxford.

Pujol, 2005. Personal communication with Pujol Transmissions Ltd.

Quebaud, S., 1996. Contribution à l'étude du percement de galleries par boucliers à pression de terre: amelioration du creusement par l'utilisation des produits moussants. PhD Thesis, University of Lille, France.

Quebaud, S., Sibaï, M. and Henry, J.P., 1998. Use of chemical foam for improvements in drilling by earth-pressure balanced shields in granular soils. Tunnelling and Underground Space technology, Vol. 13, No 2, pp. 173-180.

Ripley, K.J., 1989. The performance of jacked pipes. D.Phil Thesis, University of Oxford.

Rowe, P.W., 1969. The relation between the shear strength of sands in triaxial compression, plane strain and direct shear. Geotechnique 19, No1, 75-86.

Sam, A., Gomez, C.O., Finch, J.A.,1996. Axial velocity profiles of single bubbles in water/frother solutions. International Journal of Mineral Processing, 47, 177-196.

Schmertmann, J.H., 1965. Discussion of "Interpretation of the consolidation test". Journal of the soil mechanics and foundations division. Proceedings of the American Society of Civil Engineers. ASCE Vol. 91, No SM2, March, pp 131-135.

Sheahan, T., Watters, P., 1997. Experimental verification of CRS consolidation theory. Journal of Geotechnical and Geoenvironmental Engineering. Vol. 123, No 5, May 1997.

SIBELCO, 1999. Civil engineering department fax contact with Hepworth Minerals and Chemicals Ltd.

SIBELCO, 2001a. Telephone and fax contact with David Marsden (Technical Sales Engineer)

SIBELCO, 2001b. Email contact with Mr. James Wylie (Sales Admin Manager).

SIBELCO, 2001c. Email contact with Mr. James Wylie (Sales Admin Manager).

Smith, R.E. and Wahls, H.E., 1969. Consolidation under constant rate of strain. J. Soil Mechanics and Foundation, Div. ASCE. Ann Arbor, Micigan, pp. 519-539.

Stack, B., 1982. Handbook of mining and tunnelling machinery. John Wiley & Sons.

Steiner, W., 1996. Criteria for selecting mechanised tunnelling systems in soft grounds. North American tunnelling' 96, Ozdemir (ed.), Balkema, Rotterdam, 483-491.

Stroud, M.A., 1971. The behaviour of sand at low stress levels in the simple shear apparatus. PhD thesis, University of Cambridge.

Sällfors, G., 1975. Preconsolidation pressure of soft, high-plastic clays. PhD thesis, Chalmers University of Technology, Göteborg, Sweden.

Taylor, D.W., 1948. Fundamentals of soil mechanics. New York:John Wiley & Sons. Eleventh Printing March, 1960.

Terzaghi, K., 1944. Theoretical soil mechanics. Second edition London: Chapman and Hall, Ltd.. John Wiley and Sons, Inc. New York.

Thomas, P.D., Darton, R.C., Whalley, P.B., 1998. Resolving the structure of cellular foams by the use of optical tomography. Ind. Eng. Chem. Res., 37, 710-717.

Thomas, S.D., 1987. The consolidation behaviour of gassy soil. DPhil Thesis, University of Oxford.

Thomson, J.C., 1993. Pipejacking and microtunneling. Blackie Academic & Profesional.

Uesugi, M., Kishida, H, and Tsubakihara, Y., 1989. Friction between sand and steel under repeated loading. Soils and Foundations, Vol. 29, No 3, pp. 127-137.

Uesugi, M., Kishida, H., 1986a. Influential factors of friction between steel and dry sands. Soils Fdns. 26, No 2, 29-42.

Vinai, R., 2006. A contribution to the study of soil conditioning techniques for EPB TBM applications in cohesionless soils. Dottorato di Ricerca in Geoingegneria Ambientale, XVIII Ciclo. Politecnico di Torino.

Weaire, D., Hutzler, S., 1999. The physics of foams. Clarendon Press, Oxford.

Webb, R. and Breeds, C.D., 1997. Soft ground EPBM tunnelling- west Seattle, Alki tunnel. Tunnelling 97.The Institution of Mining and Metallurgy, 501-504.

West, G., 1986. Innovation and the rise of the tunnelling industry. Cambridge University Press.

Wiley, 2004. Information obtained from Wiley's web page: http://he-cda.wiley.com/WileyCDA/. October 2004.

Williamson, G.E., Traylor, M. T., Mikiya, H., 1999. Soil conditioning for EPB shield tunnelling on the south bay ocean outfall. Part of RETC paper proceedings. Document provided by George E. Williamson, Vice-president of underground Division in Traylor Bros., Inc.

Wissa, A.E., Christian, J.T., Davis, E.H., Heiberg, S., 1971. Consolidation at constant rate of strain. Journal of the soil mechanics and foundations division, Proceedings of the American Society of Civil Engineers, ASCE 97, No SM 10, paper 8447, pp. 1393-1413.

Wroth, C.P., 1958. The behaviour of soils and other granular media when subjected to shear. PhD thesis, Cambridge University.

Wykeham Farrance, 1988. Twin burette and single burette volume change apparatus WF/12510 /12520 /12550. Technical literature.

Zhang, Y., Sam, A., Finch, J.A., 2003. Temperature effect on single bubble velocity profile in water and surfactant solution. Colloids and Surfaces A: Physiochem. Eng. Aspects, 223, 45-54.

Znidarcic, D., Croce, P., Pane, V., Ko, H., Olsen, H., Schiffman, R., 1984. The theory of one dimensional consolidation of saturated clays. III Existing testing procedures and analysis. Geotechnical Testing Journal, 7 No 3, 123-133.

Tables

d_e (mm)	Bubble shape		Bubble path	
	water only	30 ppm frother	water only	30 ppm frother
0.9	sph/obl	sph	rec	rec
1.5	obl	sph/obl	osc	rec
2.2	obl/pro	obl	osc	slightly osc
2.7	pro	obl/pro	osc	slightly osc

sph = spherical, obl = oblate ellipsoidal, pro = prolate ellipsoidal, rec = rectilinear, osc = oscillatory.

Table 2.1. Bubble shape and path in the presence and absence of frother (Dowfroth 250) about 20 cm above the orifice (Sam et al, 1996)

Scheme No.	Pipe ID (mm)	Soil type	Cover (m)	Mean frictional resistance (kN/m)		Reduction in friction (%)
				Unlubricated	Lubricated	
4	1200	Dense silty sand	7-10	23	9	59
5	1200	Sand and gravel	4-7	100	10	90
6	1500	London clay	6-8	-	13	
7	1000	Dense silty sand	5-8	- - -	9 42 (break) 3	 79(increase) 93
8	1800	Stiff glacial clay	6	48	15	69
9	1500	Very soft clay	5.5-6	25	14	44

Table 2.2. Reduction in fricitional resistance for stages 2 and 3 schemes (Marshall, 1998).

Location	Open or closed face TBM[1]	Slurry shield/mix shield machines	EPBM[2]
Tunnel face	Lubricate cutters and spoil; reduce wear and power requirements	Improve slurry properties to provide optimum filter cake in soil; reduce wear and power requirements	Lubricate cutters and spoil; reduce wear and power requirements; permeate soil face and reduce water inflows; start process of modifying excavated material
Machine head	Improve muck flow through head; reduce friction and wear	Prevent clogging with plastic clays; reduce wear with abrasive soils	Help soil to obtain a plastic state of suitable consistency; prevent re-compaction of plastic clays; prevent clogging; reduce friction and wear; provide compressible material to reduce pressure fluctuations
Spoil handling system	Reduce water content to improve handling	Improve dispersion of excavated soil in slurry; reduce wear with abrasive soils; improve performance of separation plant	Produce suitable plastic state in spoil for controlled flow through screw conveyor; reduce permeability of spoil to prevent excessive water flow through screw conveyor; reduce friction, wear and power requirements for screw conveyor; reduce water content of muck for easy handling
Spoil tip	Improved spoil quality for easier disposal or re-use for construction purposes	Improved spoil quality for easier disposal or re-use for construction purposes	Improved spoil quality for easier disposal or re-use for construction purposes
Tunnel bore	Use in slurry to support tunnel bore and provide lubrication of pipes in pipe jack construction	Use in slurry to support tunnel bore and provide lubrication of pipes in pipe jack construction	Use in slurry to support tunnel bore and provide lubrication of pipes in pipe jack construction

1. TBM = tunnel boring machine 2. EPBM = earth pressure balance machine

Table 2.3. Possible applications of soil conditioning in tunnelling machines (Milligan, 2000).

Soil type	Mining characteristics	Treatment	
Plastic clays	Tend to reconstitute with little loss of strength in machine chamber.	High dosage of foam at head to keep excavated material as separate pieces.	
Laminated, silty or sandy clays	Break up better, but still tend to re-constitute, slightly abrasive, form plug.	Possibly none other than water to reduce shear strength to acceptable value; in stiffer clays, medium dosage of foam at head. Possibly add lubricant to foam to reduce abrasion.	
Clayey sands and gravels.	Flow easily, may form plug if fines content in excess of 10%; highly abrasive.	Add lubricant polymer at head to reduce wear; add water-absorbing polymer at screw if required to form plug and control water inflow.	
Silty fine sands	Do not flow, do not form plug, allow ground water inflow, highly abrasive; problems increase with larger particle sizes.	Foam with polymer additive to stiffen foam and provide lubrication; approximate dosage rates for polymer:-	0.1%
Sand/gravel			0.25%
Gravel and cobbles			1 - 3%
Cobbles and boulders	Tend to congregate in clumps in head and/or jam screw.	Large dosages of additive to keep cobbles separate in head and provide water control and lubrication.	

Table 2.4 Summary of use of soil conditioning in EPB machines (Milligan, 2000).

Parameter	Foam influence
soil consistency	• To give to the soil a pseudo-hydraulic state, that is to say able to transmit pressures • To give to the soil a pseudo-plastic state, able to create a pressure gradient along the extraction screw
ground permeability	• To make the excavated soil almost impermeable
homogeneity	• To make the mixing between soil and foam easier, in order to obtain a paste with the required qualities
sticking compaction (fine soils)	• To avoid the colmation of muck due to the sticking of the clay • To avoid an overcon-solidation of the fine elements under the mechanical action of the cutting head and the screw
friction	• To help the muck circulation from its excavation to its storage • To reduce the abrasive behaviour of some soils
confining regulation	• To fill the empty spaces of the expanded soil in order to reduce the pressure variations
impregnation (granular soils)	• To give an apparent cohesion to the soil at the head front through its impregnation in a limited depth

Table 2.5 Foam influence on the working of an EPB shield (Quebaud et al, 1998).

Sand	d_{10}	d_{20}	d_{50}	d_{60}	U_c
	μm	μm	μm	μm	
L.B. fine sand	90	127	160	175	1.94
L.B. graded sand	134	171	460	610	4.55
L.B. coarse sand	655	810	930	980	1.50
L.B. medium coarse sand	295	407	510	540	1.83
L.B. DA 8/16 sand	1110	1210	1440	1526	1.37
Garside sand	625	675	830	890	1.42

Table 3.1. Sand characteristic sizes.

Sand	ρ_{dmin}	ρ_{dmax}	e_{max}	e_{min}	Particle density
	kg/m^3	kg/m^3			Mg/m^3
L.B. fine sand$^+$	1387.4	1646.0	0.910	0.610	2.65
L.B. graded sand*	1694.9	1895.7	0.564	0.398	
L.B. coarse sand$^+$	1480.4	1778.5	0.790	0.490	
Thanet sand*	1204.8	1518.0	1.200	0.746	
Garside sand*	1483.0	1669.0	0.787	0.588	

+ value obtained from Psomas, 2001.

* value measured in this research

Table 3.2. Maximum density, minimum density, minimum voids ratio and maximum voids ratio of L.B. fine sand, L.B. graded sand, L.B. coarse sand, Thanet sand and Garside sand.

Sample	Test	Location	Depth	Percentage of particle sizes				D_{10}	D_{20}	D_{50}	D_{60}	Uc
			m	Clay	Silt	Sand	Gravel	μm	μm	μm	μm	
TSGR1109D26.43-26.8	1	Graham Road	26.43-26.8	7	12	81	0	7	66	129	150	21.4
TSGR1109D28.95-29.45	2	Graham Road	28.95-29.45	<=8		92	0	65	78	118	131	2.0
TSGR1109D29.75-30.25	3	Graham Road	29.75-30.25	3	8	89	0	54	155	179	187	3.5
TSGR1109D31.28-31.75	4	Graham Road	31.28-31.75	8	13	79	0	7	60	97	108	15.4
TSGR1109D32.5-33	5	Graham Road	32.5-33	4	11	85	0	28	69	93	104	3.7
TSGR1109D34.75-35.3	6	Graham Road	34.75-35.3	10	12	78	0	3	50	88	100	38.7
TSGR1109D35.45-35.95	7	Graham Road	35.45-35.95	9	17	74	0	3	30	84	95	31.7
TSGR1109D37.25-37.75	8	Graham Road	37.25-37.75	13	25	62	0	-	8	74	85	-
TSGR1109D38.5-39	9	Graham Road	38.5-39	18	34	48	0	-	3	55	74	-
TSGRSR7422D27.2-27.6	10	Graham Road	27.2-27.6	<=14		85	1	-	70	128	146	-
TSGRSR7422D27.6-28.1	11	Graham Road	27.6-28.1	<=14		85	1	-	66	113	127	-
TSGRSR7422D28.1-28.55	12	Graham Road	28.1-28.55	7	11	82	0	3	64	100	121	40.5
TSGRSR7422D28.6-29.1	13	Graham Road	28.6-29.1	<=10		90	0	63	71	113	126	2.0
TSGRSR7422D29.1-29.6	14	Graham Road	29.1-29.6	<=7		93	0	78	138	173	181	2.3
TSGRSR7422D29.6-30.08	15	Graham Road	29.6-30.08	<=7		93	0	66	77	108	119	1.8
TSGRSR7422D30.1-30.6	16	Graham Road	30.1-30.6	<=5		95	0	69	75	113	125	1.8
TSGRSR7422D30.6-31.1	17	Graham Road	30.6-31.1	<=12		88	0	-	68	95	116	-
TSGRSR7422D31.1-31.52	18	Graham Road	31.1-31.52	2	15	83	0	50	62	87	100	2.0
TSGRSR7422D31.6-32.1	19	Graham Road	31.6-32.1	0	20	80	0	35	60	88	110	3.1
TSGRSR7422D32.1-32.6	20	Graham Road	32.1-32.6	<=5		95	0	68	75	100	118	1.7
TSGRSR7422D33.1-33.6	21	Graham Road	33.1-33.6	3	25	72	0	4	30	83	97	22.6
TSGRSR7422D33.6-34.1	22	Graham Road	33.6-34.1	<=8		92	0	65	70	96	116	1.8
TSGRSR7422D34.1-34.6	23	Graham Road	34.1-34.6	3	29	68	0	8	20	80	90	12.0
TSGRSR7422D34.6-35.1	24	Graham Road	34.6-35.1	1	21	78	0	13	57	84	94	7.2
TSGRSR7422D35.1-35.6	25	Graham Road	35.1-35.6	<=12		88	0	-	70	94	116	-
TSGRSR7422D35.6-36.1	26	Graham Road	35.6-36.1	<=13		87	0	-	66	91	101	-
TSGRSR7422D36.1-36.6	27	Graham Road	36.1-36.6	9	34	57	0	2	6	67	83	36.1
TSGRSR7422D37.1-37.6	28	Graham Road	37.1-37.6	7	13	80	0	4	60	86	95	25.7
TSSB1138D24.2-24.7	29	Stratford box	24.2-24.7	<=7		93	0	66	76	100	117	1.8
TSSB1138D26.17-26.67	30	Stratford box	26.17-26.67	3	9	88	0	40	68	93	101	2.5
TSSB1138D28.1-28.6	31	Stratford box	28.1-28.6	5	7	88	0	40	68	93	110	2.8
TSSB1138D30.11-30.56	32	Stratford box	30.11-30.56	8	11	81	0	6	63	90	100	16.7
TSSB1138D32.64-33.10	33	Stratford box	32.64-33.10	8	11	81	0	6	63	89	100	16.7
TSSBSR2120D30-30.6	34	Stratford box	30-30.6	6	6	59	19	30	70	115	129	4.3
TSSBSR2120D36.35-36.8	35	Stratford box	36.35-36.8	10	13	77	0	2	50	84	95	47.5

Table 3.3. Thanet sand characteristics at Graham Road and Stratford box shafts from the CTRL project.

Supplier	Foaming agent	Chemical nature	Density kg/m^3	pH	Recommended concentration (%)	Recommended FER range
CETCO Europe, U.K.	Versa foam	Biodegradable synthetic polymeric foaming agent (solution of the sodium salt of an alcohol ether sulphate)	1020	7.5	1-2	No available
LAMBERTI s.p.a., Italy	Foamex TR	Liquid foaming agent based on anioninc surfactants (30-50% Alkylethoxysulphate sodium salt)	1050-1060	6-8 (at 1% concentration)	0.5-1.5	5-20
	Foamex EC	Liquid foaming agent based on biodegradable anioninc surfactants (sulphoric ester) in association with natural polymer	1040	6-8 (at 1% concentration)	2-4	5-20
MAPEI, UTT Italy	Polyfoamer MCB	Liquid foaming agent based on biodegradable anioninc surfactants (sulphoric ester) in association with synthetic polymer	1000-1100	6-8 (at 1% concentration)	1.5-5	No available
	Foamer 300	Liquid foaming agent based on biodegradable anioninc surfactants (30-50% Alkylethoxysulphate sodium salt)	1050-1060	6-8 (at 1% concentration)	0.5-2 (Normal); 1-2.5 (high water pressure)	No available
KAO CORPORATION, Japan	T-7	Liquid solution of poly(oxy-ethylene), sulfo(alkyl) sodium salt	No available	8	0.5-2	12-20
CONDAT Lubrifiants, France	CLB F4	Liquid based on alkylether sodium sulphate (anionic surfactant)	1090 (at 20°C)	7.1 (at 5% concentration)	2-8	6-32
MBT Europe, Switzerland	MEYCO® Fix SLF20	Liquid solution of polyoxyethylene alkyl ether surfactant	1005-1015 (at 20°C)	6.5-8	2-6	7-12

Table 3.4. Properties of foaming agents used in this research: suppliers foaming agent information.

Supplier	Polymer agent	Chemical nature	Density kg/m^3	pH	Recommended dosages
LAMBERTI s.p.a., Italy	DRILLAM MV	Anionic polyacrylamide in liquid emulsion	1050	6-8 (at 0.5% concentration)	0.2-0.4% (concentration in water or foam solution)
CONDAT Lubrifiants, France	TFA 34	Anioninc polyacrylamide in liquid emulsion	1150	7.5 (at 1% concentration)	0.1-1% (concentration in water)
MBT Europe, Switzerland	MEYCO® Fix SLF P1	Water soluble liquid poly(alkylene oxide)	1035-1045	6.5-7.5	0.3-3% (concentration in foam solution); 0.2 - 2 kg/m^3 (volume of soil excavated)
	MEYCO® Fix SLF P2	Liquid solution derivated from vegetable oils	900-950	8.5-10.5	0.3-1.5% (concentration in foam solution); 0.1 - 0.9 kg/m3 (volume of soil excavated)

Table 3.5. Properties of polymer agents used in this research: suppliers polymer agent information.

Foaming agent	Concentration	Number of tests		FER	t_{25}	t_{50}	Stand. Deviation		
	%	FER	Drainage time		min	min	FER	t_{25}	t_{50}
Versa Foam	2	5	5	14.5	4.48	6.65	1.8	0.45	0.54
Foamex TR	1.5	13	5	16.8	5.46	7.78	0.8	0.44	0.65
	1	13	4	16.4	5.44	7.81	1.2	0.64	0.84
Foamex EC	4	21	4	14.1	5.55	8.01	1.0	0.65	0.85
	2.5	27	4	13.8	5.37	7.89	1.4	0.51	0.74
Polyfoamer MCB	5	6	6	12.7	4.25	6.53	1.0	0.28	0.21
	1.5	6	6	12.7	3.84	6.06	1.3	0.28	0.26
Foamer 300	2.5	6	6	12.9	4.07	6.30	1.2	0.37	0.51
	0.5	6	6	12.5	4.18	6.45	1.4	0.27	0.35
T-7	2	15	5	18.9	4.98	6.92	0.8	0.57	0.74
	1.5	8	6	14.1	4.54	6.80	1.4	0.38	0.49
	1	30	7	16.6	4.86	6.97	1.1	0.40	0.74
CLB F4	5	13	2(1)	17.8	19.97	37.48	0.8	1.60	3.51
	2.5	26	4	17.0	16.60	31.31	0.8	2.85	5.44
	1.5	7	5	13.9	15.30	30.80	1.8	0.74	1.25
MEYCO® Fix SLF20	2,5	0	0	-	-	-	-	-	-
	5	0	0	-	-	-	-	-	-

( ) = Number of test for t_{50}

Table 3.6. FER, 25% and 50% drainage times of foaming agents (Foam generator at 8 bar liquid pressure and 3.5 bar gas pressure)

Plastic fluidity	Slump range mm
Firm	10 to 40
Plastic	50 to 90
Very plastic	100 to 150
Fluid	>= 160

Table 3.7. Plastic fluidity terminology according to Slump range.

.

Type of conditioner	Name of conditioner	Concentration	Type of sand	M_{thanet}	w_{thanet}	$M_{wateradded}$	$M_{totaldrum}$	w_{sandw}	$V_{totaldrum}$	V_{foam} or $V_{polymer}$	FIR or PIR or Water injection ratio	Slump
		%		kg	%	kg	kg	%	litre	litre	%	mm
Foam	T7	1.5	Thanet	10.85	10.35	1.15	12	22	8.19	2.95	36.0	135
				10.85	10.35	1.15	12	22	8.19	3.77	46.0	145
				11.13	13.14	0.87	12	22	8.99	4.00	44.5	125
				11.13	13.14	0.87	12	22	8.99	5.00	55.6	155
	CLB F4	1.5		10.85	10.35	1.15	12	22	8.19	2.95	36.0	40
				10.85	10.35	1.15	12	22	8.19	3.77	46.0	120
				11.13	13.14	0.87	12	22	8.99	4.00	44.5	140
				11.13	13.14	0.87	12	22	8.99	5.00	55.6	165
	Foamex TR	1.5		11.13	13.14	0.87	12	22	8.99	4.00	44.5	125
				11.13	13.14	0.87	12	22	8.99	5.00	55.6	202
	Foamex EC	2.5		11.13	13.14	0.87	12	22	8.99	4.00	44.5	100
				11.13	13.14	0.87	12	22	8.99	5.00	55.6	165
Polymer	MEYCO® Fix SLF P1	1		11.13	13.14	0.87	12	22	8.99	1.24	13.8	104
				11.13	13.14	0.87	12	22	8.99	1.55	17.2	175
				11.13	13.14	0.87	12	22	8.99	1.86	20.6	215
	MEYCO® Fix SLF P2	0.5		11.13	13.14	0.87	12	22	8.99	1.24	13.8	95
				11.13	13.14	0.87	12	22	8.99	1.55	17.2	148
				11.13	13.14	0.87	12	22	8.99	1.86	20.6	210
	TFA 34	0.05		11.13	13.14	0.87	12	22	8.99	1.55	17.2	112
		0.1		11.13	13.14	0.87	12	22	8.99	1.55	17.2	77
		0.3		11.13	13.14	0.87	12	22	8.99	1.55	17.2	40
		0.6		11.13	13.14	0.87	12	22	8.99	1.55	17.2	8
	DRILLAM MV	0.025		11.13	13.14	0.87	12	22	8.99	1.55	17.2	154
		0.05		11.13	13.14	0.87	12	22	8.99	1.55	17.2	117
		0.2		11.13	13.14	0.87	12	22	8.99	1.55	17.2	60
Water	water	100		11.13	13.14	0.87	12	22	8.99	-	17.2	240

Table 3.8. Slump test results on conditioned Thanet sand (Foam generator at 8 bar liquid pressure and 3.5 bar gas pressure)

Type of conditioner	Name of conditioner	Concentration	Type of sand	M_{sand}	$M_{wateradded}$	$M_{totaldrum}$	w_{sandw}	$V_{totaldrum}$	V_{foam}	FER	w_{drum}	FIR	Slump
		%		kg	kg	kg	%	litre	litre		%	%	mm
Foam	Versa foam	2	L.B. fine	12	4.12	16.12	34.3	8.3	0.0	-	34.3	0.0	0
				12	3.5	15.5	29.2	8.4	0.0	-	29.2	0.0	0
				12	3.5	15.5	29.2	8.2	2.3	13.9	30.5	28.0	no measured*
				12	3.2	15.2	26.7	9.4	2.6	14.8	28.1	28.0	200
				12	3.2	15.2	26.7	8.7	1.3	14.4	27.4	15.0	95
				12	3.2	15.2	26.7	8.8	2.2	13.9	28.0	25.0	190
				12	3.2	15.2	26.7	8.7	1.9	14.4	27.8	22.0	135
				12	2.3	14.3	19.6	9.8	2.0	13.9	20.7	20.0	110
			L.B. coarse	12	2.7	14.7	22.5	8.3	0.0	-	22.5	0.0	no measured**
				12	2.7	14.7	22.5	8.3	0.0	-	22.5	0.0	no measured**
				12	1.8	13.8	15.0	8.6	0.0	-	15.0	0.0	no measured**
				12	3.58	15.6	29.8	13.5	0.0	-	29.8	0.0	no measured**
				12	2.7	14.7	22.5	8.1	2.2	13.5	23.9	27.3	0
				12	1.8	13.8	15.0	8.2	2.2	13.1	16.4	26.9	25
				12	0.7	12.7	6.0	8.5	2.4	15.8	7.3	28.4	240
				12	0.7	12.7	6.0	8.5	1.3	15.0	6.7	15.4	185
				12	0.7	12.7	6.0	8.5	0.7	15.1	6.4	8.3	175
				12	0.7	12.7	6.0	8.5	0.3	15.9	6.2	3.6	158
				12	0.7	12.7	6.0	8.5	0.2	13.3	6.1	2.0	130
				12	0.6	12.6	5.0	8.5	0.3	13.5	5.2	3.6	150
				12	1.8	13.8	15.0	8.5	2.3	11.4	16.6	26.6	25
				12	1.2	13.2	10.0	8.5	1.2	13.9	10.7	14.2	>200
			L.B. graded	12	2.6	14.6	21.3	7.0	0.0	-	21.3	0.0	0
				12	1.9	16.6	15.8	7.0	1.1	12.6	16.6	15.7	155
				12	1.9	13.9	15.8	7.0	0.8	13.4	16.4	12.0	130
				12	1.9	13.9	15.8	7.0	0.8	14.3	16.3	12.0	130

* stiff mix but slump broke in the middle after cone was taken off

** slump segragates no keeping standard shape when cone was taken off

Table 3.9. Slump test results on conditioned L.B. sands (Foam generator at 8 bar liquid pressure and 3 bar gas pressure)

Foaming agent	Concentration	Foam								Sand conditioned								
		Number of tests		FER	t_{25}	t_{50}	Stand. Deviation			Number of tests		FIR	FER	t_{25}	t_{50}	Stand. Deviation		
	%	FER	Drainage time		min	min	FER	t_{25}	t_{50}	FER	Drainage time	%		min	min	FER	t_{25}	t_{50}
Versafoam	2	4	4	13.6	3.25	5.18	1.8	0.23	0.26	1	1	400	15.6	4.79	11.01	0.0	0.00	0.00
										2	2	500	13.8	4.19	8.68	1.7	0.04	0.30
										2	2	600	14.2	4.16	7.84	0.3	0.10	0.17
CLB F4	1.5	3	3	14.7	8.82	18.81	1.7	0.42	1.37	2	2	500	13.4	14.13	35.43	1.2	0.99	1.98
										2	2	600	14.3	13.68	32.74	1.7	0.96	0.35
T 7	1.5	6	6	14.0	2.98	4.75	1.6	0.58	0.72	1	1	400	18.3	4.39	10.97	0.0	0.00	0.00
										2	2	500	15.3	3.35	8.06	0.8	0.00	1.17
										4	4	600	14.9	3.60	7.19	1.3	0.19	0.52
Polyfoamer	1.5	0	0	-	-	-	-	-	-	5	5	500	10.5	3.80	8.33	2.1	0.23	0.49
MCB	5	0	0	-	-	-	-	-	-	4	4	500	13.0	4.69	10.01	1.4	0.60	0.86
Foamer 300	0.5	0	0	-	-	-	-	-	-	4	4	500	13.6	4.82	11.41	2.3	1.06	4.04

Table 3.10. FER, 25% and 50% drainage times of foaming agents using funnel device for conditioned L.B. medium coarse sand stability test (Foam generator at 8 bar liquid pressure and 3.5 bar gas pressure)

Foaming agent	Concentration	FIR	Sand conditioned																	
			Pressure kPa																	
			12.6									25.7								
			FER	t_{25}	t_{50}	Average			Stand. deviation			FER	t_{25}	t_{50}	Average			Stand. deviation		
	%	%		min	min	FER	t_{25}	t_{50}	FER	t_{25}	t_{50}		min	min	FER	t_{25}	t_{50}	FER	t_{25}	t_{50}
Versafoam	2	500	10.7	1.92	3.4	12.8	2.2	4.4	1.4	0.4	0.7	12.0	1.9	3.6	13.7	2.8	6.1	1.5	0.8	2.3
			14.1	2.40	4.75							14.8	3.47	6.44						
			12.2	1.65	4.33							14.4	2.92	8.10						
			13.1	2.61	4.21															
			14.1	2.28	5.25															
CLB F4	1.5		8.1	8.4	22.5	10.1	10.1	24.2	2.0	2.2	2.8	10.4	5.6	17.8	11.5	9.6	21.2	1.1	3.2	12.6
			10.2	12.6	27.4							12.8	8.6	-						
			12.0	9.4	22.6							12.0	12.5	-						
												10.9	11.8	24.6						

Table 3.11. FER, 25% and 50% drainage times of foaming agents for conditioned L.B. medium coarse sand under pressure.

M_{ssb}	kg	9.2	8.1	8.0	8.8	8.2	8.8	8.5	8.0	8.9
$M_{pebblessb}$	kg	0	0	0	0	0	0	0	0	0
M_{mixsb_bt}	kg	11.8	10.2	9.1	11.2	9.2	11.1	9.5	9.6	11.2
ERRORw_at	%	-32.7	-13.7	-58.5	-20.0	-14.6	-27.9	-39.7	-19.9	-27.4
Δw_{at}	%	-5.0	-2.9	-3.1	-4.0	-1.1	-5.5	-3.1	-2.3	-5.4
w_{c_at}	%	20.3	24.0	8.5	24.3	8.5	25.2	10.8	14.1	25.0
w_{c_bt}	%	27.3	26.7	9.6	26.6	10.2	27.1	13.3	16.2	26.7
$ERROR_{ms\_drum}$	%	-0.81	-0.82	-0.51	-0.66	-0.51	-0.74	-0.51	-0.15	-0.38
ΔM_{ms_drum}	kg	-0.123	-0.125	-0.069	-0.101	-0.070	-0.112	-0.069	-0.022	-0.058
M_{ms_drum}	kg	15.3	15.3	13.7	15.3	13.7	15.3	13.7	14.5	15.3
$ERROR_{ws\_drum}$	%	-0.52	-0.57	-0.27	-0.46	-0.29	-0.53	-0.34	-0.10	-0.25
ΔM_{ws_drum}	kg	-0.078	-0.086	-0.037	-0.070	-0.039	-0.080	-0.046	-0.015	-0.038
M_{ws_drum}	kg	15.2	15.2	13.6	15.2	13.6	15.2	13.6	14.4	15.2
$M_{ds\_sb\_at}$	kg	0.099	0.082	0.105	0.073	0.069	0.094	0.080	0.080	0.107
$M_{ms\_sb\_at}$	kg	0.114	0.099	0.110	0.088	0.074	0.113	0.087	0.090	0.128
w_{at}	%	15.3	21.1	5.4	20.2	7.4	19.7	7.7	11.7	19.6
V_{sweet}	litre	0.641	0.531	0.355	0.541	0.301	0.351	0.212	0.505	0.336
V_{webt}	litre	0.000	0.310	0.265	0.339	0.158	0.182	0.000	0.337	0.186
$M_{ds\_sb\_bt}$	kg	0.096	0.060	0.087	0.069	0.067	0.103	0.077	0.072	0.109
$M_{ms\_sb\_bt}$	kg	0.122	0.078	0.099	0.090	0.075	0.133	0.087	0.086	0.140
w_{bt}	%	27.3	30.5	12.9	30.4	12.2	29.2	13.3	20.4	28.8
M_{dsoil_r}	kg	2.6	3.7	3.8	3.0	3.7	3.0	3.3	3.9	2.9
M_{fs_r}	kg	3.1	4.8	4.4	3.8	4.3	3.8	3.8	4.7	3.7
M_{dsd}	kg	0.099	0.089	0.090	0.086	0.064	0.098	0.097	0.076	0.102
M_{msd}	kg	0.128	0.114	0.100	0.113	0.072	0.126	0.108	0.090	0.133
w_{drum}	%	30.0	28.3	11.1	31.4	11.3	28.9	11.8	17.9	30.4
M_{fs}	kg	15.2	15.2	13.6	15.2	13.6	15.2	13.6	14.5	15.2
M_{ws}	kg	15.1	15.1	13.6	15.1	13.6	15.1	13.6	14.4	15.2
FER	kg	13.7	16.4	15.8	15.4	15.6	12.8	14.6	14.6	12.8
FIR	%	22	20	20	15	15	10	10	20	10
Foaming agent		Versa foam, Cetco, 2%								
M_f	kg	0.139	0.104	0.114	0.085	0.084	0.071	0.062	0.134	0.070
V_f	litre	1.9	1.7	1.8	1.3	1.3	0.9	0.9	2.0	0.9
V_w	litre	3.2	3.2	1.6	3.2	1.6	3.2	1.6	2.4	3.2
M_s	kg	12	12	12	12	12	12	12	12	12
Test		F1	F2	F3	F4	F5	F6	F7	F8	F9
Sand type		L.B. Fine sand								

Table 4.1. Initial mixed material data for shear box tests on L.B. fine sand.

M_{ssb}	kg	10.2	10.1	9.6	9.6	9.7	9.5	10.2	9.4	9.5	9.2	9.3
$M_{pebblessb}$	kg	0	0	0	0	0	0	0	0	0	0	0
M_{mixsb_bt}	kg	10.8	11.5	10.2	10.3	11.1	10.2	11.6	10.1	10.2	9.7	9.8
ERRORw_at	%	24.9	-7.2	-85.0	-116.3	-46.5	-65.8	17.5	10.3	-105.7	9.8	-28.4
Δw_{at}	%	1.6	-1.0	-3.3	-4.4	-5.8	-1.4	2.3	0.7	-4.1	0.6	-1.7
w_{c_at}	%	4.9	14.2	7.2	8.1	18.1	3.6	10.7	6.2	8.0	5.1	7.5
w_{c_bt}	%	4.9	16.3	7.4	8.4	19.2	5.1	12.5	6.2	8.2	5.1	7.5
$ERROR_{ms\_drum}$	%	-0.21	-0.30	-0.12	-0.05	-0.19	-0.08	-0.21	-0.10	-0.09	-0.01	0.02
ΔM_{ms_drum}	kg	-0.026	-0.042	-0.016	-0.007	-0.026	-0.010	-0.029	-0.013	-0.011	-0.001	0.002
M_{ms_drum}	kg	12.7	13.9	12.9	13.0	13.9	12.9	13.8	12.9	12.9	12.7	12.8
$ERROR_{ws\_drum}$	%	-0.17	-0.25	-0.06	0.02	-0.12	-0.02	-0.16	-0.05	-0.04	0.06	0.06
ΔM_{ws_drum}	kg	-0.021	-0.034	-0.008	0.002	-0.016	-0.002	-0.022	-0.007	-0.005	0.008	0.007
M_{ws_drum}	kg	12.7	13.8	12.9	12.9	13.8	12.9	13.8	12.9	12.9	12.7	12.7
$M_{ds\_sb\_at}$	kg	0.113	0.114	0.082	0.109	0.084	0.105	0.086	0.122	0.092	0.126	0.093
$M_{ms\_sb\_at}$	kg	0.121	0.129	0.086	0.113	0.094	0.107	0.097	0.130	0.096	0.133	0.098
w_{at}	%	6.5	13.3	3.9	3.8	12.4	2.2	13.0	6.9	3.9	5.6	5.8
V_{weet}	litre	0.000	0.411	0.030	0.109	0.103	0.282	0.285	0.000	0.025	0.000	0.000
V_{webt}	litre	0.000	0.206	0.010	0.087	0.000	0.141	0.103	0.000	0.012	0.000	0.000
$M_{ds\_sb\_bt}$	kg	0.110	0.117	0.083	0.121	0.073	0.115	0.089	0.134	0.092	0.120	0.088
$M_{ms\_sb\_bt}$	kg	0.115	0.139	0.089	0.132	0.087	0.122	0.101	0.142	0.099	0.126	0.095
w_{bt}	%	4.9	18.3	7.5	9.3	19.2	6.6	13.6	6.2	8.3	5.1	7.5
M_{dsoil_r}	kg	1.6	1.7	2.2	2.2	2.1	2.3	1.7	2.3	2.3	2.6	2.5
M_{fs_r}	kg	1.7	2.0	2.5	2.4	2.6	2.6	2.0	2.5	2.6	2.8	2.7
M_{dsd}	kg	0.111	0.121	0.107	0.114	0.111	0.105	0.090	0.121	0.115	0.134	0.112
M_{msd}	kg	0.114	0.141	0.112	0.121	0.125	0.111	0.103	0.127	0.120	0.139	0.117
w_{drum}	%	3.5	16.3	5.4	5.7	12.6	5.7	14.1	4.7	5.0	3.4	4.2
M_{fs}	kg	12.7	13.8	12.9	13.0	13.8	12.9	13.8	12.9	12.9	12.7	12.8
M_{ws}	kg	12.7	13.8	12.9	12.9	13.8	12.9	13.8	12.9	12.9	12.7	12.7
FER		14.9	13.7	14.4	13.2	12.2	14.2	12.5	12.0	13.8	9.0	12.7
FIR	%	2	10	5	10	7.5	7.5	5	5	7.5	3	5
Foaming agent		Versa foam, Cetco, 2%										
M_f	kg	0.011	0.063	0.031	0.068	0.052	0.045	0.034	0.037	0.046	0.029	0.035
V_f	litre	0.2	0.9	0.4	0.9	0.6	0.6	0.4	0.4	0.6	0.3	0.4
V_w	litre	0.7	1.8	0.9	0.9	1.8	0.9	1.8	0.9	0.9	0.7	0.7
M_s	kg	12	12	12	12	12	12	12	12	12	12	12
Test		C1	C2	C3	C4	C5	C6	C7	C8	C9	C10	C11
Sand type		L.B. Coarse sand										

Table 4.2. Initial mixed material data for shear box tests on L.B. coarse sand.

M_{ssb}	kg	10.1	10.1	10.1	9.4	11.6	11.7
$M_{pebblessb}$	kg	0	0	0	0	0	0
M_{mixsb_bt}	kg	10.9	11.2	11.2	10.4	13.9	14.0
ERRORw_at	%	-21.2	-55.9	-83.9	-86.4	-3.7	-3.1
Δw_{at}	%	-1.3	-2.9	-4.0	-3.1	-0.6	-0.5
w_{c_at}	%	7.4	8.1	8.8	6.6	17.3	17.9
w_{c_bt}	%	7.4	8.5	9.8	7.8	17.4	17.9
$ERROR_{ms\_drum}$	%	-0.05	-0.15	-0.18	-0.22	-0.31	-0.20
ΔM_{ms_drum}	kg	-0.006	-0.020	-0.024	-0.029	-0.045	-0.029
M_{ms_drum}	kg	13.0	13.3	13.3	13.4	14.5	14.6
$ERROR_{ws\_drum}$	%	-0.01	-0.08	-0.12	-0.13	-0.28	-0.16
ΔM_{ws_drum}	kg	-0.001	-0.011	-0.016	-0.017	-0.041	-0.023
M_{ws_drum}	kg	13.0	13.3	13.3	13.3	14.5	14.5
$M_{ds\_sb\_at}$	kg	0.123	0.119	0.104	0.124	0.105	0.107
$M_{ms\_sb\_at}$	kg	0.131	0.125	0.109	0.128	0.122	0.125
w_{at}	%	6.1	5.2	4.8	3.6	16.7	17.4
V_{weet}	litre	0.000	0.200	0.232	0.464	0.177	0.170
V_{webt}	litre	0.000	0.161	0.132	0.355	0.162	0.173
$M_{ds\_sb\_bt}$	kg	0.107	0.129	0.085	0.109	0.100	0.103
$M_{ms\_sb\_bt}$	kg	0.115	0.142	0.095	0.122	0.119	0.123
w_{bt}	%	7.4	10.1	11.2	11.6	18.8	19.4
M_{dsoil_r}	kg	1.7	1.6	1.8	2.4	0.1	0.1
M_{fs_r}	kg	1.9	1.8	1.9	2.7	0.3	0.3
M_{dsd}	kg	0.101	0.102	0.104	0.102	0.141	0.100
M_{msd}	kg	0.108	0.111	0.114	0.112	0.169	0.120
w_{drum}	%	6.6	8.9	8.7	10.0	19.6	20.1
M_{fs}	kg	13.0	13.3	13.3	13.3	14.5	14.5
M_{ws}	kg	13.0	13.2	13.2	13.2	14.5	14.5
FER		13.0	12.1	15.4	13.1	15.7	14.2
FIR	%	6	8	12	16	8	12
Foaming agent		Versa foam, Cetco, 2%					
M_f	kg	0.039	0.056	0.065	0.105	0.036	0.061
V_f	litre	0.5	0.7	1.0	1.4	0.6	0.9
V_w	litre	1.0	1.3	1.3	1.3	2.5	2.5
M_s	kg	12	12	12	12	12	12
Test		G1	G2	G3	G4	G5	G6
Sand type		L.B. Graded sand					

Table 4.3. Initial mixed material data for shear box tests on L.B. graded sand.

M_{ssb}	kg	7.9	6.4	6.3	6.3	6.6	6.8	6.9	6.8	7.3	7.2	8.4	8.2
$M_{pebblessb}$	kg	0.91	0.74	0.73	0.74	0.77	0.79	0.80	0.79	0.85	0.83	0.98	0.95
M_{mixsb_bt}	kg	10.6	8.7	8.7	8.6	9.1	9.3	9.4	9.4	9.9	9.7	-	-
ERRORw_at	%	-17.5	-7.9	1.8	-17.3	-12.4	-10.0	-9.1	-1.1	-14.6	-8.7	-	-
Δw_{at}	%	-3.1	-1.7	0.4	-3.2	-2.5	-2.0	-1.7	-0.2	-2.6	-1.6	-	-
w_{c_at}	%	20.7	22.6	23.9	21.8	22.6	21.8	21.0	20.8	20.6	19.9	-	-
w_{c_bt}	%	20.7	22.6	23.9	21.8	22.6	21.8	21.0	20.8	20.6	19.9	-	-
$ERROR_{ms\_drum}$	%	-2.34	-1.96	-1.62	-2.29	-2.60	-1.91	-1.71	-0.78	-1.22	-1.90	-	-
ΔM_{ms_drum}	kg	-0.32	-0.27	-0.23	-0.32	-0.36	-0.27	-0.24	-0.11	-0.17	-0.27	-	-
M_{ms_drum}	kg	14.19	14.19	14.27	14.25	14.24	14.28	14.25	14.27	14.21	14.29	15.01	15.00
$ERROR_{ws\_drum}$	%	-0.76	-0.45	-0.45	-0.63	-0.64	-0.57	-0.35	-0.42	-0.34	-0.56	-0.65	-0.40
ΔM_{ws_drum}	kg	-0.105	-0.063	-0.063	-0.088	-0.089	-0.079	-0.049	-0.059	-0.047	-0.078	-0.097	-0.060
M_{ws_drum}	kg	14.0	14.0	14.0	14.0	14.0	14.0	14.0	14.0	14.0	14.0	15.0	15.0
$M_{ds\_sb\_at}$	kg	0.061	0.065	0.075	0.077	0.086	0.062	0.060	0.072	0.074	0.074	-	-
$M_{ms\_sb\_at}$	kg	0.072	0.079	0.093	0.091	0.104	0.075	0.072	0.087	0.088	0.088	-	-
w_{at}	%	17.6	20.9	24.3	18.6	20.1	19.8	19.3	20.6	18.0	18.3	-	
V_{weet}	litre	0.000	0.000	0.000	0.000	0.035	0.123	0.105	0.141	0.000	0.070	0.000	0.000
V_{webt}	litre	0.000	0.000	0.000	0.000	0.035	0.123	0.105	0.141	0.000	0.070	0.000	0.000
$M_{ds\_sb\_bt}$	kg	0.056	0.063	0.070	0.075	0.078	0.055	0.048	0.074	0.064	0.060	-	-
$M_{ms\_sb\_bt}$	kg	0.068	0.077	0.086	0.091	0.096	0.068	0.059	0.091	0.078	0.072	-	-
w_{bt}	%	20.7	22.6	23.9	21.8	23.1	23.6	22.6	22.9	20.6	20.9	-	-
M_{dsoil_r}	kg	-	-	-	-	-	-	-	-	-	-	-	-
M_{fs_r}	kg	3.1	5.1	5.2	5.1	4.6	4.5	4.4	4.6	4.0	4.2	-	-
M_{dsd}	kg	0.058	0.081	0.059	0.079	0.072	0.076	0.051	0.066	0.086	0.054	-	-
M_{msd}	kg	0.1	0.1	0.1	0.1	0.1	0.1	0.1	0.1	0.1	0.1	-	-
w_{drum}	%	21.5	23.6	23.8	21.6	22.6	23.6	22.7	24.3	20.7	22.3	32.0	32.0
M_{fs}	kg	13.8	13.8	14.0	13.8	13.8	13.9	14.0	14.1	13.9	14.0	-	-
M_{ws}	kg	13.9	13.9	13.9	13.9	13.9	13.9	14.0	13.9	13.9	13.9	14.9	14.9
FER		15.2	18.3	17.6	19.9	15.9	17.9	15.0	18.6	18.7	18.7	0.0	0.0
FIR	%	26.6	34.8	46.3	46.5	36	46.5	36.0	46.5	36.2	47.6	0	0
Foaming agent		KAO T-7, 1.5%				CONDAT F-4, 1.5%		FOAMEX TR, 1.5%		FOAMEX EC, 2.5%		NOTHING	
M_f	kg	0.185	0.186	0.268	0.248	0.233	0.274	0.247	0.264	0.215	0.282	0.000	0.000
V_f	litre	2.8	3.4	4.7	4.9	3.7	4.9	3.7	4.9	4.0	5.2	0.0	0.0
V_w	litre	2.5	2.5	2.5	2.5	2.5	2.5	2.5	2.5	2.5	2.5	3.6	3.6
M_s	kg	11.5	11.5	11.5	11.5	11.5	11.5	11.5	11.5	11.5	11.5	11.4	11.4
Test		Th1	Th2	Th3	Th4	Th5	Th6	Th7	Th8	Th9	Th10	Th11	Th12
Sand type		Thanet sand											

Table 4.4. Initial mixed material data for shear box tests on Thanet sand.

Sand type	Test	Condition	Mssb	v_0	v_{max}	H_0	H_{min}	δ_{max}	ρ_{D0}	ρ_{Dmax}	e_0	e_{sbmin}	$\sigma_{average}$
			kg	mm	mm	mm	mm	mm	kg/m^3	kg/m^3			kPa
L.B. Fine sand	F1	ok	9.2	-0.002	-4.3	186.4	182.1	18.2	1253	1282	1.12	1.07	48.5
	F2	ok	8.1	-0.442	-5.3	168.5	163.2	19.0	1221	1261	1.17	1.10	51.0
	F3	ok	8.0	-1.192	-5.4	165.2	159.9	18.3	1237	1278	1.14	1.07	49.2
	F4	ok	8.8	-0.002	-3.7	178.9	175.2	19.0	1255	1282	1.11	1.07	49.6
	F5	ok	8.2	-0.736	-5.4	167.7	162.3	18.3	1237	1278	1.14	1.07	48.9
	F6	ok	8.8	-0.209	-2.9	176.2	173.3	18.2	1274	1296	1.08	1.05	47.7
	F7	ok	8.5	-0.339	-3.6	169.1	165.5	18.4	1281	1309	1.07	1.02	44.8
	F8	ok	8.0	-0.901	-5.3	164.5	159.2	18.1	1231	1271	1.15	1.08	46.1
	F9	ok	8.9	-0.173	-3.5	177.2	173.7	18.2	1270	1296	1.09	1.04	47.7
L.B. Coarse sand	C1	ok	10.2	-0.001	-0.6	178.9	178.3	18.2	1451	1456	0.83	0.82	57.9
	C2	ok	10.1	-0.079	-1.3	177.3	176.0	18.5	1444	1455	0.84	0.82	51.5
	C3	ok	9.6	-0.134	-1.9	172.5	170.5	18.3	1408	1424	0.88	0.86	49.5
	C4	ok	9.6	-0.180	-2.3	175.2	173.0	18.2	1390	1408	0.91	0.88	51.1
	C5	ok	9.7	-0.121	-1.0	170.3	169.3	18.3	1449	1457	0.83	0.82	54.9
	C6	ok	9.5	-0.118	-1.9	167.3	165.4	18.3	1439	1455	0.84	0.82	50.5
	C7	ok	10.2	-0.010	-0.6	178.4	177.8	18.3	1446	1451	0.83	0.83	55.5
	C8	ok	9.4	-0.077	-2.1	167.3	165.2	18.1	1430	1449	0.85	0.83	48.4
	C9	ok	9.5	-0.179	-2.5	173.2	170.7	18.1	1389	1409	0.91	0.88	47.7
	C10	ok	9.2	-0.285	-2.8	169.9	167.1	18.2	1370	1393	0.93	0.90	47.9
	C11	ok	9.3	-0.245	-2.7	171.7	168.9	18.2	1380	1403	0.92	0.89	47.6
L.B. Graded sand	G1	ok	10.1	-0.665	-4.4	167.7	163.3	18.2	1526	1567	0.74	0.69	52.4
	G2	ok	10.1	-0.598	-4.4	170.8	166.4	18.3	1506	1546	0.76	0.71	45.9
	G3	ok	10.1	-0.670	-4.5	168.7	164.3	18.3	1514	1555	0.75	0.70	45.7
	G4	ok	9.4	-1.870	-5.1	160.8	155.6	18.2	1487	1536	0.78	0.73	45.7
	G5	ok	11.6	-0.039	-0.5	172.4	171.9	18.3	1716	1721	0.54	0.54	50.9
	G6	ok	11.7	-0.038	-0.6	167.4	166.8	18.4	1773	1779	0.49	0.49	53.0
Thanet sand	Th1	no	7.9	-0.420	-4.6	186.0	181.3	22.1	1127	1157.7	1.35	1.29	46.1
	Th2	no	6.4	-0.476	-4.9	156.9	152.1	21.3	1078	1113.9	1.46	1.38	44.1
	Th3	no	6.3	-0.840	-5.4	166.6	161.1	20.0	996	1031.5	1.66	1.57	46.2
	Th4	ok	6.3	-0.650	-5.1	163.8	158.6	20.2	1028	1062.4	1.58	1.49	46.8
	Th5	ok	6.6	-0.310	-4.2	164.6	160.4	20.2	1068	1097.9	1.48	1.41	47.0
	Th6	ok	6.8	-0.450	-5.7	174.0	168.3	20.1	1034	1070.5	1.56	1.48	46.0
	Th7	ok	6.9	-0.250	-4.2	174.2	169.9	19.4	1054	1081.2	1.51	1.45	46.4
	Th8	ok	6.8	-0.360	-6.0	178.0	172.0	18.5	1019	1056.0	1.60	1.51	46.5
	Th9	ok	7.3	-0.360	-4.0	170.0	166.1	19.5	1151	1179.4	1.30	1.25	46.6
	Th10	ok	7.2	-0.480	-4.9	172.9	168.0	19.5	1106	1139.4	1.40	1.33	46.3
	Th11	ok	8.4	-0.300	-1.7	176.1	174.4	18.7	1282	1295.5	1.07	1.05	50.1
	Th12	ok	8.2	-2.100	-1.8	173.3	171.5	19.5	1272	1286.3	1.08	1.06	51.0

Table 4.5. General data on shear box tests

Test	Average energy dissipation between 10 mm shear displacement and the end of shear box test	Standard deviation of energy dissipation between 10 mm shear displacement and the end of shear box test	Energy dissipation value at 12 mm shear displacement	C-A
	A	B	C	D
F3	0.779	0.010	0.797	0.018
F4	0.813	0.017	0.810	-0.002
F6	0.741	0.012	0.735	-0.006
C3	0.749	0.013	0.730	-0.019
C4	0.775	0.011	0.772	-0.003
C11	0.773	0.017	0.762	-0.010
G1	0.702	0.011	0.691	-0.011
G4	0.611	0.010	0.608	-0.003
G6	0.814	0.007	0.806	-0.007
Th10	0.827	0.023	0.800	-0.027
Th9	0.784	0.015	0.770	-0.013
Th8	0.852	0.037	0.892	0.040

Table 4.6. Energy dissipation for average shear displacement above 10 mm and at 12 mm.

Sand type	Test	Condition	D_{r12}	e_{12}	σ_{12} kPa	$(\tau/\sigma')_{12}$	$(\tau/\sigma)_{12}$	$(u/\sigma)_{12}$	ϕ_{mob12} degrees
L.B. Fine sand	F1	ok	-0.55	1.08	49.6	0.56	0.5	0.06	29.1
	F2	ok	-0.68	1.12	51.0	0.59	0.6	0.04	30.7
	F3	ok	-0.58	1.09	49.1	0.59	0.5	0.10	30.3
	F4	ok	-0.56	1.08	49.8	0.67	0.6	0.08	33.8
	F5	ok	-0.58	1.09	48.8	0.58	0.5	0.11	30.2
	F6	ok	-0.47	1.05	48.0	0.64	0.6	0.04	32.8
	F7	ok	-0.40	1.03	45.1	0.65	0.6	0.06	32.9
	F8	ok	-0.62	1.10	45.9	0.59	0.5	0.07	30.5
	F9	ok	-0.47	1.05	48.1	0.66	0.6	0.04	33.3
L.B. Coarse sand	C1	ok	-0.10	0.82	60.5	0.75	0.75	0.00	37.0
	C2	ok	-0.11	0.82	52.6	0.72	0.70	0.02	35.7
	C3	ok	-0.24	0.86	49.8	0.72	0.71	0.02	35.6
	C4	ok	-0.31	0.88	51.3	0.74	0.72	0.03	36.5
	C5	ok	-0.10	0.82	57.9	0.78	0.77	0.02	38.1
	C6	ok	-0.10	0.82	51.0	0.75	0.74	0.02	37.0
	C7	ok	-0.12	0.83	58.0	0.75	0.74	0.01	36.9
	C8	ok	-0.13	0.83	48.4	0.72	0.71	0.02	35.7
	C9	ok	-0.31	0.88	47.9	0.72	0.70	0.03	35.9
	C10	ok	-0.38	0.90	47.9	0.69	0.69	0.01	34.6
	C11	ok	-0.34	0.89	47.8	0.71	0.70	0.01	35.3
L.B. Graded sand	G1	ok	-0.80	0.70	52.5	0.57	0.57	0.01	29.7
	G2	ok	-0.95	0.72	46.2	0.61	0.58	0.05	31.2
	G3	ok	-0.89	0.71	46.0	0.55	0.52	0.06	29.0
	G4	ok	-1.03	0.73	45.4	0.43	0.40	0.08	23.5
	G5	ok	0.14	0.54	53.1	0.81	0.78	0.04	39.1
	G6	ok	0.44	0.49	56.1	0.83	0.80	0.03	39.6
Thanet sand	Th1	no	-0.25	1.30	46.8	0.41	0.38	0.07	22.1
	Th2	no	-0.46	1.40	44.0	0.30	0.26	0.14	16.9
	Th3	no	-0.89	1.59	46.4	0.19	0.14	0.23	10.6
	Th4	ok	-0.72	1.51	46.7	0.50	0.21	0.59	26.8
	Th5	ok	-0.52	1.43	47.3	0.52	0.31	0.41	27.3
	Th6	ok	-0.68	1.49	46.1	0.51	0.22	0.57	26.9
	Th7	ok	-0.61	1.46	46.7	0.60	0.24	0.61	31.0
	Th8	ok	-0.75	1.53	46.7	0.63	0.18	0.71	32.2
	Th9	ok	-0.14	1.25	46.9	0.66	0.53	0.20	33.4
	Th10	ok	-0.33	1.34	46.5	0.66	0.30	0.54	33.4
	Th11	ok	0.32	1.05	50.4	0.71	0.64	0.10	35.5
	Th12	ok	0.29	1.06	50.8	0.69	0.59	0.14	34.4

Table 4.7. Shear box test data at 12 mm of shear displacement

Group type	
X	**Y**
Test	**Test**
Finesand10	Finesand24foamR
Finesand11foamR	Finesand25foamR
Finesand12foamR	Finesand26foamR
Finesand13foamR	Thanetsand1foamR
Finesand14foamR	Thanetsand2foamR
Finesand15foamR	
Finesand16foamR	
Finesand17foamR	
Finesand18foamR	
Finesand19foamR	
Finesand20foamR	
Finesand21foamR	
Finesand22R	
Finesand23foamR	

Table 5.1. Groups of consolidation tests carried out in the research.

Test name	FIR %	e_0	Relative Density, Dro	e_{w0}	e_{g0}	Saturation degree, Sr_0 %	Initial liquid content, w_0 %	σ'_{max} kPa	Initial height of specimen, H_0 mm	[a]Maximum u'_b/σ' %	[a]Vertical strain rate, s_r % s^{-1}	[a]Vertical displacement rate mm/min
Finesand10	0.0	0.75	0.55	0.75	0.00	99.97	28.12	242.84	89.20	6.21	0.0021	0.11
Finesand11foamR	43.8	1.65	-2.47	0.84	0.81	50.89	31.70	108.70	89.20	1.55	0.0070	0.33
Finesand12foamR	22.0	1.23	-1.08	0.80	0.43	65.18	30.33	231.06	89.20	1.73	0.0063	0.32
Finesand13foamR	43.7	1.44	-1.78	0.65	0.79	45.29	24.69	207.83	90.20	3.09	0.0062	0.31
Finesand14foamR	15.0	0.99	-0.28	0.86	0.13	87.04	32.61	353.26	92.20	1.33	0.0050	0.26
Finesand15foamR	10.0	0.98	-0.24	0.81	0.17	82.56	30.58	348.89	91.20	-7.72	0.0052	0.27
Finesand16foamR	43.8	1.73	-2.73	0.79	0.94	45.68	29.80	60.17	89.20	0.30	0.0070	0.32
Finesand17foamR	22.0	1.32	-1.36	0.82	0.50	62.12	30.89	217.51	89.20	-14.75	0.0063	0.31
Finesand18foamR	10.0	1.06	-0.51	0.80	0.26	75.52	30.31	218.99	89.20	-13.50	0.0055	0.28
Finesand19foamR	20.0	1.35	-1.48	0.59	0.76	43.86	22.39	216.36	89.20	-4.22	0.0064	0.31
Finesand20foamR	15.0	1.25	-1.12	0.42	0.82	33.88	15.94	216.39	89.20	-1.51	0.0066	0.32
Finesand21foamR	10.0	1.12	-0.70	0.41	0.71	36.88	15.61	216.48	89.20	-8.26	0.0050	0.25
Finesand22R	0.0	0.67	0.81	0.67	0.00	100.01	25.23	222.33	89.20	0.43	0.0050	0.26
Finesand23foamR	31.5	1.39	-1.59	0.38	1.01	27.14	14.19	215.19	89.20	18.63	0.0069	0.33
Finesand24foamR	15.0	1.18	-0.90	0.55	0.63	46.45	20.69	215.00	91.20	6.64	0.0061	0.32
Finesand25foamR	15.0	1.16	-0.85	0.40	0.76	34.59	15.19	230.37	93.20	7.34	0.0057	0.31
Finesand26foamR	15.0	1.28	-1.23	0.49	0.79	38.32	18.48	196.13	89.20	2.74	0.0927	4.66
Thanetsand1foamR	46	2.29	-2.41	0.82	1.47	35.82	30.99	24.75	89.70	348.91	0.0066	0.26
Thanetsand2foamR	36.0	2.63	-3.15	0.79	1.84	29.96	29.70	74.76	89.20	294.35	0.0070	0.34

[a] Values caculated during the drained loading of the specimen

Table 5.2. Summary of consolidation test results.

Tables

Test name	e_{max}	e_{min}	e_0	$e_{drainedloading}$	$e_{enddrainedloading}$	$\sigma'_{enddrainedloading}$ kPa	$\Delta\sigma'_{drainedloading}$ kPa	$100*(e_{drainedloading}-e_{enddrainedloading})/e_0$ %	$100*(e_{enddrainedloading}-e_{max})/e_{max}$ %
Finesand10			0.75	0.74	0.69	242.84	239.76	7.60	-24.55
Finesand11foamR			1.65	1.65	1.04	106.03	105.20	36.85	14.14
Finesand12foamR			1.23	1.23	1.01	228.58	229.36	17.93	11.22
Finesand13foamR			1.44	1.38	1.06	203.06	195.97	22.21	16.93
Finesand14foamR			0.99	0.91	0.87	341.24	164.70	3.48	-4.15
Finesand15foamR			0.98	0.90	0.87	343.55	180.72	3.23	-4.35
Finesand16foamR			1.73	1.61	1.11	60.17	60.47	28.58	22.52
Finesand17foamR			1.32	1.24	1.03	211.88	212.69	15.57	13.25
Finesand18foamR	0.91	0.61	1.06	1.00	0.96	216.96	155.63	3.73	5.82
Finesand19foamR			1.35	1.26	1.05	207.57	194.04	15.11	15.48
Finesand20foamR			1.25	1.15	0.99	213.70	196.22	12.89	8.31
Finesand21foamR			1.12	1.05	0.96	214.20	196.87	7.64	5.69
Finesand22R			0.67	0.66	0.63	218.60	216.82	5.49	-31.05
Finesand23foamR			1.39	1.26	0.98	212.02	200.91	20.52	7.69
Finesand24foamR			1.18	1.18	0.98	210.09	209.94	17.01	7.66
Finesand25foamR			1.16	1.16	0.98	230.37	228.74	15.57	7.97
Finesand26foamR			1.28	1.28	1.00	187.56	185.55	21.47	10.27
Thanetsand1foamR	1.200	0.746	2.29	2.29	1.83	24.74	24.74	20.22	52.49
Thanetsand2foamR			2.63	2.63	1.89	73.76	73.74	28.03	57.64

Table 5.3. Summary of voids ratio results at the end of drained loading.

Test name	[a]Maximum u'_b kPa	[a]Maximum u'_b/σ' %	[a]Minimum $k_{sheahan}$ m/s	[a]Minimum k_{shmesh} m/s	[a]Minimum $k_{sh\text{-}soil}$ m/s	[a]Minimum k_{system} m/s	[a]Minimum $k_{ap\text{-}soil}$ m/s	[a]Minimum $k_{int\text{-}soil}$ m/s	[a]Average $k_{sh\text{-}soil}$ m/s	[a]Average $k_{int\text{-}soil}$ m/s
Finesand10	0.81	7.82	5.20E-07	5.19E-07	5.29E-07	1.67E-08	1.66E-08	1.69E-08	6.95E-06	6.83E-06
Finesand11foamR	0.07	2.27	-	-	-	2.67E-06	2.69E-06	2.74E-06	-	2.07E-04
Finesand12foamR	0.10	3.07	-	-	-	1.69E-07	1.68E-07	1.72E-07	-	2.18E-04
Finesand13foamR	0.14	1.01	1.50E-05	1.59E-05	1.62E-05	1.71E-07	1.71E-07	1.74E-07	8.37E-05	9.02E-05
Finesand14foamR	0.07	0.02	8.18E-07	8.18E-07	8.34E-07	2.01E-06	2.02E-06	1.74E-07	6.66E-05	1.64E-05
Finesand15foamR	-0.32	-0.09	-	-	-	-	-	-	-	-
Finesand16foamR	0.02	3134	-	-	-	1.59E-06	1.60E-06	1.64E-06	-	1.59E-04
Finesand17foamR	-0.59	3046	-	-	-	-	-	-	-	-
Finesand18foamR	-0.58	-0.27	-	-	-	-	-	-	-	-
Finesand19foamR	-0.18	-0.10	-	-	-	-	-	-	-	-
Finesand20foamR	-0.04	-0.03	-	-	-	-	-	-	-	-
Finesand21foamR	-0.35	-0.32	-	-	-	-	-	-	-	-
Finesand22R	0.02	1.12	1.04E-04	1.81E-04	1.84E-04	1.06E-05	1.11E-05	1.13E-05	2.48E-03	2.25E-03
Finesand23foamR	0.73	0.83	3.34E-07	3.33E-07	3.41E-07	2.17E-07	2.16E-07	2.21E-07	1.58E-04	2.39E-04
Finesand24foamR	0.31	1.19	7.97E-06	8.21E-06	8.37E-06	1.47E-06	1.48E-06	1.51E-06	1.06E-04	3.55E-05
Finesand25foamR	0.34	8.88	6.94E-06	7.11E-06	7.24E-06	2.86E-08	1.20E-06	1.22E-06	4.62E-04	9.26E-05
Finesand26foamR	0.24	0.34	8.26E-05	1.32E-04	1.35E-04	5.65E-05	7.45E-05	7.59E-05	1.35E-04	4.32E-04
Thanetsand1foamR	13.61	11536	1.63E-07	1.62E-07	1.66E-07	8.14E-08	8.12E-08	8.29E-08	3.67E-06	9.52E-07
Thanetsand2foamR	10.65	53204	4.48E-08	4.46E-08	4.55E-08	5.30E-08	5.28E-08	5.40E-08	1.16E-06	9.99E-07

[a] Values caculated during the drained loading of the specimen
- Values lower than zero

Table 5.4. Summary of coefficient of permeability results using CRS theory and parabolic isochrones maximum gradient theory.

Test name	Maximum compression strain of specimen, [a]Maximum ε'	Maximum compression strain due to expulsion/compression of gas, [a]Maximum $\varepsilon'_{exp\text{-}wg}$	Maximum compression strain due to compression of gas, [a]Maximumrecordedvalue $\varepsilon'_{exp\text{-}g}$	Maximum gas expelled, (Maximum $\varepsilon'_{exp\text{-}wg}$-Maximum $\varepsilon'_{exp\text{-}g}$)	Maximum water expelled, (Maximum ε'-Maximum $\varepsilon'_{exp\text{-}wg}$)	Maximum compression of gas, 100*(Maximum $\varepsilon'_{exp\text{-}g}$/Maximum ε')	Maximum gas expelled, 100*(Maximum $\varepsilon'_{exp\text{-}wg}$-Maximum $\varepsilon'_{exp\text{-}g}$)/Maximum ε'	Maximum water expelled, 100*(Maximum ε'-Maximum $\varepsilon'_{exp\text{-}wg}$)/Maximum ε'
						%	%	%
Finesand10	0.0325	0.0000	0.0000	0.0000	0.032	0.0	0.0	100.0
Finesand11foamR	0.2295	0.0358	0.0274	0.0085	0.194	11.9	3.7	84.4
Finesand12foamR	0.0990	0.0195	0.0195	0.0000	0.079	19.7	0.0	80.3
Finesand13foamR	0.1313	0.0251	0.0223	0.0028	0.106	17.0	2.1	80.9
Finesand14foamR	0.0174	0.0087	0.0069	0.0018	0.009	39.6	10.7	49.7
Finesand15foamR	0.0160	0.0084	0.0036	0.0048	0.008	22.3	30.1	47.6
Finesand16foamR	0.1810	0.0614	0.0576	0.0037	0.120	31.8	2.1	66.1
Finesand17foamR	0.0885	0.0205	0.0175	0.0030	0.068	19.8	3.4	76.8
Finesand18foamR	0.0192	0.0113	0.0113	0.0000	0.008	58.8	0.0	41.2
Finesand19foamR	0.0869	0.0256	0.0029	0.0227	0.061	3.4	26.1	70.5
Finesand20foamR	0.0714	0.0279	0.0112	0.0167	0.044	15.6	23.4	61.0
Finesand21foamR	0.0404	0.0134	0.0126	0.0008	0.027	31.1	2.0	66.8
Finesand22R	0.0220	0.0000	0.0000	0.0000	0.022	0.0	0.0	100.0
Finesand23foamR	0.1192	0.0364	0.0357	0.0007	0.083	29.9	0.6	69.5
Finesand24foamR	0.0921	0.0311	0.0298	0.0013	0.061	32.3	1.5	66.2
Finesand25foamR	0.0837	0.0252	0.0167	0.0084	0.059	20.0	10.1	70.0
Finesand26foamR	0.1205	0.0966	0.0966	0.0000	0.024	80.1	0.0	19.8
Thanetsand1foamR	0.1363	0.0513	0.0506	0.0007	0.085	37.1	0.5	62.4
Thanetsand2foamR	0.1969	0.0526	0.0510	0.0015	0.144	25.9	0.8	73.3

[a] Values caculated during the drained loading of the specimen

Table 5.5. Summary of maximum compression of gas, maximum gas expelled and maximum water expelled during loading of specimen in MPAC.

Test name	Number of points	$^{*av}u_w$ (as absolut pressure) kPa	$^{av}e_g$	BOYLE'S LAW, $^{*av}u_w * {}^{av}e_g$=constant	BOYLE'S LAW, standard deviation
Finesand10	N.A.	N.A.	N.A.	N.A.	N.A.
Finesand11foamR	1678	135.1	0.74	100.3	1.5
Finesand12foamR	734	136.0	0.40	54.7	1.0
Finesand13foamR	956	135.4	0.57	77.1	1.1
Finesand14foamR	163	131.6	0.03	4.1	0.6
Finesand15foamR	143	131.9	0.08	10.7	0.5
Finesand16foamR	1327	130.6	0.72	93.3	2.0
Finesand17foamR	675	124.8	0.38	47.8	0.6
Finesand18foamR	164	122.3	0.19	22.6	0.5
Finesand19foamR	656	124.0	0.62	76.8	0.6
Finesand20foamR	528	123.6	0.68	84.3	0.7
Finesand21foamR	376	123.1	0.61	75.4	0.4
Finesand22R	N.A.	N.A.	N.A.	N.A.	N.A.
Finesand23foamR	871	124.7	0.83	103.7	1.0
Finesand24foamR	700	126.0	0.59	74.0	0.7
Finesand25foamR	668	107.7	0.72	78.0	0.5
Finesand26foamR	62	139.7	0.67	92.3	0.9
Thanetsand1foamR	959	129.6	1.37	177.3	0.6
Thanetsand2foamR	1394	128.9	1.72	222.0	1.0

N.A. No applicable Boyles's law

[*] Values caculated adding 100 kPa to the average pore water pressure

[v] Average values over the drained loading zone

[a] Values caculated during the drained loading of the specimen

Table 5.6. Summary of Boyle's law theory values during drained loading of specimen in MPAC.

Tank and Piston components	Dimension, mm
Tank diameter	450
Tank internal height	890
Jack bore diameter	101.6
Jack rod diameter	50.8
Jack stroke	450
Piston diameter	447
Piston thickness	22

Table 6.1. Tank and Piston dimensions.

Casing tube components	Dimension, mm
Conveyor casing length	1009.2
Assembled conveyor length	1099.2
Casing outer diameter	127
Casing internal diameter	108
Discharge outlet internal diameter	85.5
Discharge outlet length (from casing outside wall)	37.5

Table 6.2. Casing tube components.

Geometry parameters	Screw type	
	Central shaft	Without central shaft
Conveyor length, L (mm)	1250	
Casing diameter, D_c (mm)	108	
Flight diameter, D_f (mm)	102	
Shaft diameter, D_s (mm)	41.3	0
Channel depth, h (mm)	30.35	
Screw pitch, t (mm)	100	
Flight thickness, e (mm)	4.5	
Flight helix angle, ϕ_f (degrees)	17.3	
Shaft helix angle, ϕ_s *(degrees)	37.6	
Average helix angle, ϕ_a (degrees)	23.95	
D_f/L	0.082	
D_s/D_f	0.405	0
t/D_f	0.980	
e/D_f	0.044	

* Shaft helix angle for Screw type wihout central shaft is calculated using the diameter of the shaft generated by the flights over its length, which is 41.3 mm

Table 6.3. Screw dimensions.

Motor and gearbox supplier	Pujol transmissions Ltd.
Power supply	400 V at 50 Hz
Motor model	100Ls-4
Motor code	3604112020-41201005
Motor type	Induction squirrel cage motor
Motor phases	3
Motor number of poles	4
Rated motor power, kW	2.2
Rated motor speed, rpm	1420
Rated motor output torque, Nm	14.79
Motor flange diameter, mm	250
Motor shaft diameter, mm	28
Gearbox type	SPC 195/250/28
Gearbox code	3060223100
Gearbox lubricant	Shell Omala oil 320
Reduction gear box ratio	61.7
Output gearbox speed range, rpm	4.6 - 23
Gearbox efficiency, %	0.93
Rated gearbox output torque, Nm	848.9

Table 6.4. Motor and gearbox technical data

Inverter supplier	Eurotherm drives
Inverter type	650V
Frame	2
Power output, kW	2.2
Nominal input voltage, V	380 to 460 (±10%)
RFI filter	Yes
Keypad	Remote keypad fitted (RS232)
Eurotherm controllers	Software Config Ed Lite version 6.04
	Keypad
Driver 650V software	651 Firmware version 4.6

Table 6.5. 650V drive technical data.

MAX SPEED, Hz	47.4
MOTOR CURRENT, A	5.3
BASE FREQUENCY, Hz	50
NAMEPLATE RPM, rpm	1420
MOTOR POLES	4
MOTOR VOLTAGE, V	400

Table 6.6. Initial Autotune values.

.

Load cell dimensions	**w x l (t) x h**
	mm
External	30 x 30 x 24
Normal stress web	3 x 1 x 8
Shear stress web	2 x 0.55 x 6
Load platen plan	32 x 32
Load cell capacities	**kPa**
Maximum normal stress on platten (with zero shear stress)	1719
Maximum shear stress on platten	586
Maximum normal stress on platten (at maximum shear stress on platten)	1681
Load cell material properties (HE15N)	**MPa**
0.1% Proof stress, σ_p	220
Maximum working stress on the web (2/3 σ_p)	147
Young's modulus	70000

Table 6.7. Cambridge type load cell specifications.

Calibration programme							
Calibration type	Applied loads	Normal load	Normal stress	Shear load	Shear stress	Normal load eccentricity	Moment applied
		N	kPa	N	kPa	mm	Nm
Normal stress calibration	Normal load = at stages	0-1271.2	0-1241.4	0	0	0	0
	Eccentricity = 0						
	Shear load = 0						
Moment Calibration	Normal load = constant value	420.85	411	0	0	-10 (-15)	-4.2 (-6.1)
	Eccentricity = varies					to	to
	Shear load = 0					10 (15)	4.2 (6.1)
Shear stress calibration	Normal load = constant value	1271.2	1241.4	-148.1	-144.7	0	0
	Eccentricity = 0			to	to		
	Shear load = at stages both directions			148.1	144.7		

Table 6.8. Cambridge type load cells calibration programme.

Average coefficient	Value	Unit
a_{11}	0.0028	mV/V/N
a_{21}	0.0002	mV/V/N
a_{32}	0.002	mV/V/N
a_{13}	-0.1953	mV/V/Nm
a_{23}	0.0212	mV/V/Nm
a_{33}	0.2029	mV/V/Nm
a_{12}	-0.0014	mV/V/N
a_{22}	0.0126	mV/V/N
a_{31}	0.0028	mV/V/N

Table 6.9. Calibration coefficient value for Cambridge type load cells with parallel measurement of shear..

Test	Soil type	Foam conditioner	FER	Total water	Total foam	Total sand	Liquid content	FIR
				litre	litre	kg	%	%
SCOD1	Thanet sand	CETCO Versa foam, 2% concentration	14.89	71.8	52.1	138.3	54.4	45.6
SCOD2	L.B. fine sand			52.0	29.8	197.3	27.4	20.9
SCOD3	L.B. fine sand			52.0	29.8	200.2	27.0	20.6
SCOD4	L.B. fine sand			52.0	29.8	199.3	27.1	20.7
SCOD5	L.B. fine sand			52.0	29.8	200.8	26.9	20.6
SCOD6	L.B. fine sand			58.5	0.0	220.7	26.5	0.0
SCOD7	L.B. fine sand			52.0	29.8	197.9	27.3	20.9
SCOD8	Garside sand	MAPEI Polyfoamer MCB, 1.5% concentration	13.2	40.0	0	208.0	19.2	0.0
SCOD9	Garside sand			40.0	0	208.1	19.2	0.0
SCOD10	Garside sand			40.0	26.4	208.1	20.2	18.7
SCOD11	Garside sand			0.0	26.4	208.1	1.0	18.7
SCOD12	Garside sand			0.0	52.8	207.8	1.9	37.4
SCOD13	Garside sand			20.0	26.4	206.7	10.6	18.8
SCOD14	Garside sand			10.0	26.4	208.1	5.8	18.7
SCOD15	Garside sand			0.0	71.148	181.7	3.0	57.6
SCOD16	Garside sand			0.0	71.148	174.9	3.1	59.9

Table 6.10. Initial mixed material data.

Test	Soil type	Total dry sand tank	H_0	Dry density	e_0	Dr_0	w_0	σ'_{piston}	$\sigma'_{topspecimen}$	$\sigma_{0lineconveyor}$		Speed	Gate diameter	Screw type
										When just the material is inside	When piston is on top			
		kg	mm	kg/m^3			%	kPa	kPa	kPa	kPa	rpm	mm	
SCOD1	Thanet sand	123.9	890.0	910.0	1.91	-1.605	54.43	400	20.2	12.3	32.4	5	85.5; 45	Central shaft
								600	29.9		42.2	5; 7; 11		
SCOD2	L.B. fine sand	176.0	890.0	1243.2	1.13	-0.738	27.36	1050	51.9	13.8	65.7	5	85.5	Central shaft
SCOD3	L.B. fine sand	170.9	890.0	1207.6	1.19	-0.948	26.98	1050	51.9	13.4	65.3	5	71.5	Central shaft
								1500	73.9		87.3			
SCOD4	L.B. fine sand	170.8	890.0	1206.8	1.20	-0.953	27.09	1500	73.9	13.4	87.3	5	71.5	Central shaft
SCOD5	L.B. fine sand	170.8	890.0	1206.4	1.20	-0.955	26.89	1500	73.9	13.4	87.2	5; 11	85.5	Central shaft
SCOD6	L.B. fine sand	215.9	890.0	1525.1	0.74	0.575	26.51	1500	73.9	16.8	90.7	5; 11	85.5	Central shaft
								2500	122.7		139.5			
								3100	152.0		168.8	5; 15		
SCOD7	L.B. fine sand	177.5	890.0	1254.2	1.11	-0.676	27.29	1500	73.9	13.9	87.8	5; 11	85.5	Without central shaft
								2000	98.3		112.2	11; 15		
								2500	122.7		136.6	5; 11; 15		
								3000	147.1		161.0			
SCOD8	Garside sand	197.6	828	1500.9	0.77	0.156	19.23	1500	73.9	14.5	88.4	5	85.5	Central shaft
								2000	98.3		112.8	5; 7; 15		
SCOD9	Garside sand	194.3	808	1511.8	0.75	0.214	19.22	3000	147.1	14.3	161.4	5; 11; 15	85.5	Central shaft
SCOD10	Garside sand	206.2	835	1553.0	0.71	0.425	20.18	1500	73.9	15.3	89.2	5; 11; 15	85.5	Central shaft
SCOD11	Garside sand	198.0	835	1491.3	0.78	0.105	0.96	1500	59.1	12.3	71.4	5; 11; 15	85.5	Central shaft
								2500	122.7		135.0			
SCOD12	Garside sand	197.7	836	1487.2	0.78	0.083	1.92	2000	98.3	12.4	110.7	5; 11; 15	85.5	Central shaft
SCOD13	Garside sand	193.8	828	1471.9	0.80	-0.002	10.64	2000	98.3	13.2	111.5	5; 11; 15	85.5	Central shaft
SCOD14	Garside sand	192.8	824	1471.5	0.80	-0.004	5.77	2000	98.3	12.6	110.9	5; 11; 15	85.5	Central shaft
SCOD15	Garside sand	177.66	760	1469.8	0.80	-0.014	2.97	2000	98.3	11.3	109.6	5; 11	85.5	Central shaft
SCOD16	Garside sand	172.4	737	1470.8	0.80	-0.008	3.08	2000	98.3	11.0	109.2	5; 11	85.5	Central shaft

Table 6.11. Initial data for OSC tests..

Speed	Screw type	
	Central shaft	Without central shaft
	Qmax	Qmax
rpm	l/hr	l/hr
5	224.1	262.5
7	313.7	367.4
11	493.0	577.4
15	672.2	787.4

Table 6.12. Maximum volumetric flow.

Test		SCOD1										SCOD2	SCOD3					SCOD4			SCOD5						SCOD6										
Stage		1	2	3	4	5	6	7	8	9	10	1	1	2	3	4	5	1	2	3	1	2	3	4	5	6	1	2	3	4	5	6	7	8	9	10	11
Δt	seconds	1104	72	92	102	368	76	150	50	182	520	736	1123	156	28.1	327	250	13.5	23.4	401	453	94.5	104	73.8	33.3	50.4	165	104	284	158	174	320	17.1	137	36	289	155
Speed	rpm	5	5	0	0	7	0	11	0	5	5	5	5	5	5	5	5	5	5	5	5	11	5	11	5	5	5	11	5	11	5	0	0	5	11	15	5
σ'topspecimen	kPa	29.9	20.2	0	29.9	29.9	0	29.9	0	29.9	0	51.9	51.9	0	51.9	73.9	0	0	73.9	73.9	73.9	73.9	73.9	73.9	73.9	0	73.9	73.9	73.9	73.9	73.9	73.9	123	123	152	152	152
Gate	Type*	A	A	A	A	A	A	A	A	C	C	A	B	B	B	B	B	B	B	B	A	A	A	A	A	A	A	A	A	A	A	A	A	A	A	A
	ON-OFF**	OFF	OFF	OFF	OFF	OFF	OFF	OFF	OFF	OFF	OFF	OFF	OFF	OFF	OFF	OFF	OFF	OFF	OFF	ON	OFF	OFF	OFF	OFF	OFF	OFF	OFF	OFF	OFF	OFF	OFF	OFF	OFF	OFF	OFF	OFF

***Gate diameters: 85.5 mm = A; 71.5 mm = B; 45 mm = C
**** ON= closed; OFF=opened

Table 6.13. Stages in SCOD1 to SCOD6 tests.

Test		SCOD7																					SCOD8								SCOD9							
Stage		1	2	3	4	5	6	7	8	9	10	11	12	13	14	15	16	17	18	19	20	21	1	2	3	4	5	6	7	8	1	2	3	4	5	6	7	8
Δt	seconds	316	59.4	91.8	59.4	131	29.7	243	72	59.4	127	29.7	57.6	65.7	80.1	65.7	72.9	64.8	60.3	189	63	18.9	34.2	352	104	531	218	502	149	128	23.4	288	290	300	172	103	17.1	41.4
Speed	rpm	5	11	5	11	5	11	5	5	11	15	15	5	11	15	5	5	11	15	5	15	5	5	5	5	7	15	5	5	0	5	5	11	15	5	11	11	0
σ'topspecimen	kPa	73.9	73.9	73.9	73.9	73.9	73.9	73.9	98.3	98.3	98.3	123	123	123	123	123	147	147	147	147	147	147	0	73.9	98.3	98.3	98.3	98.3	0	0	0	147	147	147	147	147	0	0
Gate	Type*	A	A	A	A	A	A	A	A	A	A	A	A	A	A	A	A	A	A	A	A	A	A	A	A	A	A	A	A	A	A	A	A	A	A	A	A	A
	ON-OFF**	OFF	OFF	OFF	OFF	OFF	OFF	OFF	OFF	OFF	OFF	OFF	OFF	OFF	OFF	OFF	OFF	OFF	OFF	OFF	OFF	OFF	OFF	OFF	OFF	OFF	OFF	OFF	OFF	OFF	OFF	OFF	OFF	OFF	OFF	OFF	OFF	OFF

*Gate diameters: 85.5 mm = A; 71.5 mm = B; 45 mm = C

** ON= closed; OFF=opened

Table 6.14. Stages in SCOD7 to SCOD9 tests.

Test		SCOD10						SCOD11												SCOD12					SCOD13				SCOD14					SCOD15						SCOD16			
Stage		1	2	3	4	5	6	1	2	3	4	5	6	7	8	9	10	11	12	1	2	3	4	5	1	2	3	4	1	2	3	4	5	1	2	3	4	5	6	1	2	3	4
Δt	seconds	328	299	299	350	27.9	21.6	51.3	126	141	38.7	424	200	206	197	239	165	38.7	9	11.7	308	824	384	277	431	419	356	113	10.8	338	328	1235	109	28.8	564	230	92.7	217	79.2	585	267	8.1	328
Speed	rpm	5	11	15	5	5	0	5	5	11	15	15	5	11	15	5	11	15	0	5	5	11	15	5	5	11	15	15	5	5	11	15	5	5	5	11	0	5	5	5	11	5	5
σ'topspecimen	kPa	73.9	73.9	73.9	73.9	0	0	0	59.1	73.9	73.9	123	123	123	123	123	123	0	0	0	98.3	98.3	98.3	98.3	98.3	98.3	98.3	0	0	98.3	98.3	98.3	98.3	0	98.3	98.3	0	98.3	0	98.3	98.3	98.3	0
Gate	Type*	A	A	A	A	A	A	A	A	A	A	A	A	A	A	A	A	A	A	A	A	A	A	A	A	A	A	A	A	A	A	A	A	A	A	A	A	A	A	A	A	A	A
	ON-OFF**	OFF	OFF	OFF	OFF	OFF	OFF	OFF	OFF	OFF	OFF	OFF	OFF	OFF	OFF	OFF	OFF	OFF	OFF	OFF	OFF	OFF	OFF	OFF	OFF	OFF	OFF	OFF	OFF	OFF	OFF	OFF	OFF	OFF	OFF	OFF	OFF	OFF	OFF	OFF	OFF	OFF	OFF

*****Gate diameters: 85.5 mm = A; 71.5 mm = B; 45 mm = C
****** ON= closed; OFF=opened

Table 6.15. Stages in SCOD10 to SCOD16 tests.

TEST	D_o	H/H_o	Maximum torque, Tmax	Steady state event	Δt	Speed	Average pore water pressure, $u_{average}$	Average normal stress, $\sigma_{average}$	Average effective stress, $\sigma'_{average}$	Total pore water pressure change, Δu	Total pore water pressure gradient, $\Delta u/L$	Maximum raw torque, Trmax	Maximum average torque, Tavmax	Average torque, Tav	Soil flow rate, Q	η
			Nm		s	rpm	kPa	kPa	kPa	kPa	kPa/m	Nm	Nm	Nm	L/hr	%
SCOD1	-1.60	0.61	365.1	SCOD1-5.1/1	164	5	-0.57	-8.78	39.73	1.39	1.66	97.97	78.3	67.2	84.5	37.4
SCOD2	-0.74	0.64	138.5	SCOD2-5.1	170	5	8.44	23.68	15.24	-5.09	-6.06	59.8	15.2	3.2	281.1	125.3
				SCOD2-5.1/1	154	5	1.40	18.39	16.99	1.96	2.34	138.5	29.8	3.8	134.7	60.2
SCOD3	-0.95	0.47	119.6	SCOD3-5.4	195	5	0.19	29.50	29.30	2.77	3.30	37.9	13.3	4.7	115.4	51.4
SCOD4	-0.95	0.86	327.9	SCOD4-5.3	30	5	16.12	17.71	1.58	-24.8	-29.55	195.7	191.7	188.3	33.3	14.2
SCOD5	-0.96	0.47	95.5	SCOD5-5.1	144	5	15.73	19.27	3.54	-30.66	-36.53	2.0	2.0	0.4	290.7	129.9
SCOD6	0.57	0.83	180.9	SCOD6-5.1	61	5	0.60	3.45	2.85	-1.01	-1.20	7.4	1.8	0.6	25.3	11.4
				SCOD6-5.3	258	5	0.35	2.83	2.47	-0.28	-0.33	90.5	19.9	0.9	74.9	33.4
				SCOD6-11.4	37	11	-0.04	1.91	1.95	0.76	0.90	7.4	2.4	0.6	162.0	33.0
SCOD7	-0.68	0.51	179.5	SCOD7-5.5	90	5	1.11	3.96	2.85	3.74	4.46	13.1	7.4	3.2	140.2	53.5
SCOD8	0.16	0.50	119.0	SCOD8-5.2	229	5	1.77	6.27	4.50	-1.03	-1.22	110.2	25.0	2.7	113.1	50.8
				SCOD8-7.4	164	7	1.10	5.18	4.08	0.09	0.10	29.9	7.2	2.0	138.0	43.9
				SCOD8-15.5	121	15	0.54	5.92	5.38	0.037	0.04	119.0	38.8	16.2	268.5	40.0
				SCOD8-5.6	498	5	0.54	5.74	5.20	0.07	0.08	95.5	22.1	3.0	93.5	41.6
SCOD9	0.21	0.51	128.4	SCOD9-5.2	135	5	1.24	5.41	4.17	-1.26	-1.50	38.1	18.1	6.8	120.7	54.0
				SCOD9-11.3	104	11	1.00	5.19	4.19	-0.77	-0.92	49.0	38.7	29.3	246.5	49.9
				SCOD9-15.4	59	15	0.11	3.97	3.86	-0.089	-0.11	128.4	42.7	20.6	274.7	40.7
				SCOD9-5.5	78	5	0.03	4.02	3.99	-0.09	-0.11	27.1	10.8	4.6	90.4	40.2
				SCOD9-11.6	50	11	-0.10	4.03	4.12	0.03	0.03	40.9	34.8	22.4	208.1	42.2
SCOD10	0.43	0.49	136.0	SCOD10-5.1	123	5	1.58	7.32	5.74	-4.63	-5.51	38.1	29.2	6.9	109.1	48.8
				SCOD10-11.2	157	11	1.34	6.18	4.84	-3.50	-4.17	136.0	51.1	19.8	241.2	48.9
				SCOD10-15.3	72	15	0.79	4.66	3.87	-1.17	-1.39	26.2	19.5	12.5	304.5	45.3
				SCOD10-5.4	298	5	0.62	4.10	3.48	-0.71	-0.85	112.6	25.2	2.6	103.7	46.2
SCOD11	0.10	0.50	117.4	SCOD11-15.5	162	15	-0.51	2.20	2.70	-0.44	-0.52	104.5	24.1	9.5	229.4	34.1
				SCOD11-5.6	75	5	-0.62	2.07	2.70	-0.36	-0.43	15.9	5.0	2.0	93.7	41.4
				SCOD11-11.7	75	11	-0.72	2.07	2.80	-0.774	-0.92	117.4	24.4	4.7	171.1	34.4
				SCOD11-15.8	96	15	-0.81	2.25	3.06	-0.65	-0.78	31.7	18.9	8.5	250.2	37.1
				SCOD11-5.9	154	5	-0.74	2.59	3.34	-0.51	-0.60	102.9	21.8	2.1	92.2	41.5
				SCOD11-11.10	104	11	-0.96	2.62	3.58	-0.86	-1.03	35.4	15.1	3.2	209.8	42.3
SCOD12	0.08	0.57	189.7	SCOD12-5.2	108	5	0.05	5.64	5.58	-0.032	-0.04	147.3	56.7	29.2	122.7	55.0
				SCOD12-11.3	177	11	-0.49	4.44	4.93	-0.23	-0.28	64.9	54.3	43.0	253.4	51.4
				SCOD12-11.3/3	105	11	-0.59	0.85	1.44	0.12	0.14	35.4	28.2	19.4	36.4	7.5
				SCOD12-15.4	65	15	-0.55	0.87	1.42	-0.21	-0.25	50.8	30.3	17.8	66.7	10.0
SCOD13	-0.002	0.50	128.4	SCOD13-11.2	113	11	2.69	4.06	1.36	-1.742	-2.08	35.4	12.1	3.2	259.7	52.7
				SCOD13-15.3	184	15	0.29	2.28	1.99	0.51	0.60	121.3	35.7	7.6	182.4	27.1
SCOD14	-0.004	0.51	133.0	SCOD14-5.2	53	5	6.95	9.85	2.90	-10.04	-11.96	13.1	5.3	2.2	134.0	59.5
				SCOD14-11.3	118	11	0.14	5.12	4.99	-0.94	-1.12	40.9	32.6	23.2	255.3	51.8
				SCOD14-15.4	226	15	0.00	0.89	0.89	-0.01	-0.01	102.1	25.3	3.3	37.7	5.6
SCOD15	-0.01	0.54	195.7	SCOD15-5.2/2	142	5	6.99	7.98	0.99	-10.69	-12.74	112.6	8.2	2.7	164.8	73.4
				SCOD15-5.5	68	15	-0.16	17.87	18.03	-0.19	-0.23	95.5	88.5	79.0	139.6	62.2
SCOD16	-0.01	0.56	181.6	SCOD16-5.1/1	64	5	9.34	45.18	35.84	-13.93	-16.59	15.9	5.3	1.3	174.4	78.0
				SCOD16-11.2	21	11	0.58	58.47	57.89	-8.66	-10.32	131.4	122.5	115.3	311.1	62.2

Table 6.16. Measurements OSC tests.

TEST	Tan(ψ)	Steady state event	η	Direction of soil movement, θ_c	Average casing shear parallel orientation, $\tau_{averageparal}$	Average casing shear perpendicular orientation, $\tau_{averageperp}$	Average casing shear, $\tau_{caverage}$	Maximum casing shear, τ_{cmax}	Average direction of friction, $\varepsilon_{average}$	Maximum direction of friction, ε_{max}	Average angle of friction, $\delta_{average}$
			%	degrees	kPa	kPa	kPa	kPa	degrees	degrees	degrees
SCOD1	0.31	SCOD1-5.1/1	37.4	10.5	N.C.	N.C.	N.C.	N.C.	N.C.	N.C.	N.C.
SCOD2		SCOD2-5.1	125.3	57.1	1.35	5.24	5.80	6.2	26.03	31.4	19.44
		SCOD2-5.1/1	60.2	25.3	2.22	3.49	4.16	4.25	28.61	30.18	13.94
SCOD3		SCOD3-5.4	51.4	18.3	8.36	7.25	12.04	13.46	53.68	59.95	22.00
SCOD4		SCOD4-5.3	14.2	3.0	0.34	0.16	0.54	0.68	53.20	87.05	35.64
SCOD5		SCOD5-5.1	129.9	53.6	0.54	0.30	0.70	0.81	64.96	72.28	11.17
SCOD6		SCOD6-5.1	11.4	2.3	0.72	0.96	1.30	1.46	45.00	48.93	23.50
		SCOD6-5.3	33.4	8.9	0.51	0.84	1.02	1.16	42.46	45.85	22.04
		SCOD6-11.4	33.0	8.7	0.27	0.75	0.85	0.99	40.63	45.40	23.16
SCOD7		SCOD7-5.5	53.5	19.8	0.32	0.79	0.98	1.16	41.47	60.41	21.61
SCOD8		SCOD8-5.2	50.8	17.8	0.49	1.26	1.60	1.96	21.00	26.30	18.29
		SCOD8-7.4	43.9	13.7	0.33	1.09	1.20	1.29	14.47	20.80	16.76
		SCOD8-15.5	40.0	11.8	0.65	1.45	1.69	1.85	19.81	28.48	18.03
		SCOD8-5.6	41.6	12.5	0.52	1.43	1.58	1.67	15.06	24.73	18.02
SCOD9		SCOD9-5.2	54.0	20.2	1.02	1.41	2.07	2.49	38.81	45.89	24.23
		SCOD9-11.3	49.9	17.3	1.10	1.46	2.11	2.48	39.62	44.50	24.74
		SCOD9-15.4	40.7	12.1	1.09	1.34	1.87	2.11	42.67	47.88	25.03
		SCOD9-5.5	40.2	11.8	1.14	1.38	1.92	2.13	40.56	44.95	25.02
		SCOD9-11.6	42.2	12.8	1.01	1.38	1.82	2.00	37.99	40.91	23.29
SCOD10		SCOD10-5.1	48.8	16.6	1.02	1.75	2.44	2.98	39.57	45.66	20.80
		SCOD10-11.2	48.9	16.6	0.83	1.52	2.08	2.50	37.08	43.24	20.85
		SCOD10-15.3	45.3	14.5	0.52	1.23	1.50	1.74	28.58	31.67	19.32
		SCOD10-5.4	46.2	15.0	0.54	1.13	1.38	1.58	28.65	33.04	20.12
SCOD11		SCOD11-15.5	34.1	9.2	0.62	0.79	1.03	1.13	38.32	43.40	20.90
		SCOD11-5.6	41.4	12.4	0.54	0.73	0.94	1.07	36.58	43.27	19.15
		SCOD11-11.7	34.4	9.3	0.50	0.72	0.91	0.99	33.70	38.01	18.39
		SCOD11-15.8	37.1	10.4	0.50	0.80	0.97	1.08	29.87	33.30	17.58
		SCOD11-5.9	41.5	12.5	0.56	0.87	1.07	1.20	30.94	34.69	17.37
		SCOD11-11.10	42.3	12.9	0.57	0.93	1.13	1.27	28.11	31.24	17.52
SCOD12		SCOD12-5.2	55.0	20.9	1.08	1.63	2.18	2.49	32.46	37.26	19.82
		SCOD12-11.3	51.4	18.3	0.84	1.35	1.70	1.84	30.74	37.07	18.27
		SCOD12-11.3/3	7.5	1.5	-0.03	0.35	0.46	0.49	37.92	55.28	17.08
		SCOD12-15.4	10.0	2.0	0.01	0.39	0.53	0.56	40.79	48.36	19.78
SCOD13		SCOD13-11.2	52.7	19.2	0.36	0.49	0.58	0.90	56.24	88.14	20.37
		SCOD13-15.3	27.1	6.6	0.50	0.63	0.78	0.98	55.74	72.26	20.49
SCOD14		SCOD14-5.2	59.5	24.6	0.49	0.83	1.14	1.31	24.22	49.83	19.26
		SCOD14-11.3	51.8	18.5	0.73	1.26	1.62	1.82	34.79	44.61	17.37
		SCOD14-15.4	5.6	1.1	-0.13	0.18	0.29	0.46	60.62	86.43	18.59
SCOD15		SCOD15-5.2/2	73.4	40.7	0.46	0.41	0.59	0.93	30.66	59.76	29.95
		SCOD15-5.5	62.2	27.2	3.85	4.45	7.04	8.48	48.80	58.86	21.55
SCOD16		SCOD16-5.1/1	78.0	47.8	-2.06	0.66	3.39	4.68	14.78	34.21	7.26
		SCOD16-11.2	62.2	27.2	1.87	6.16	7.60	10.22	10.19	27.23	8.33

N.C. = data no calculated

Table 6.17. Calculated data OSC test

Figures

Figure 1.1. Herrenknecht S-300 Earth Pressure Balance Shield for Madrid. Maximum excavation diameter of 15.20 m and installed torque of 125268 kNm (Herrenknecht, 2006).

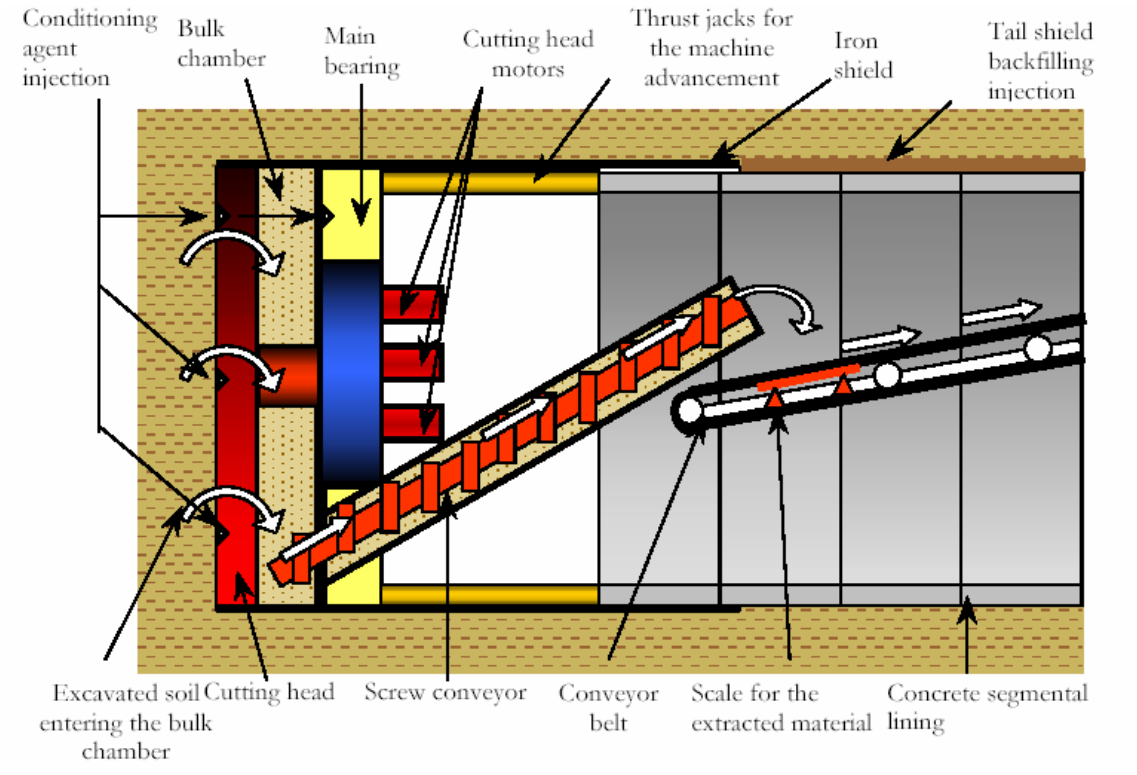

Figure 1.2. Main parts of an EPB machine (Vinai, 2006).

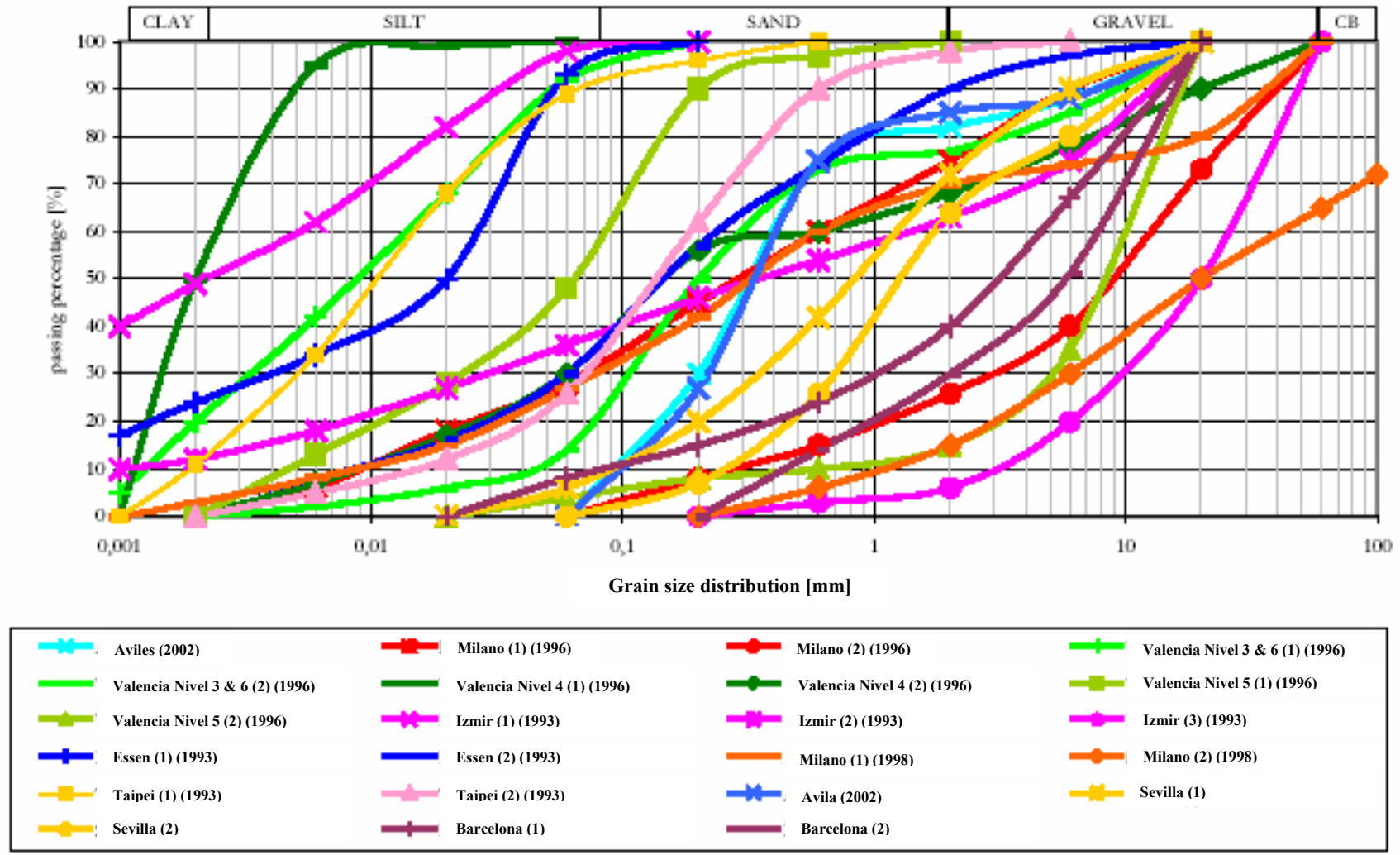

Figure 1.3. Grain size distribution for several EPB shields tunnel excavations (Vinai, 2006).

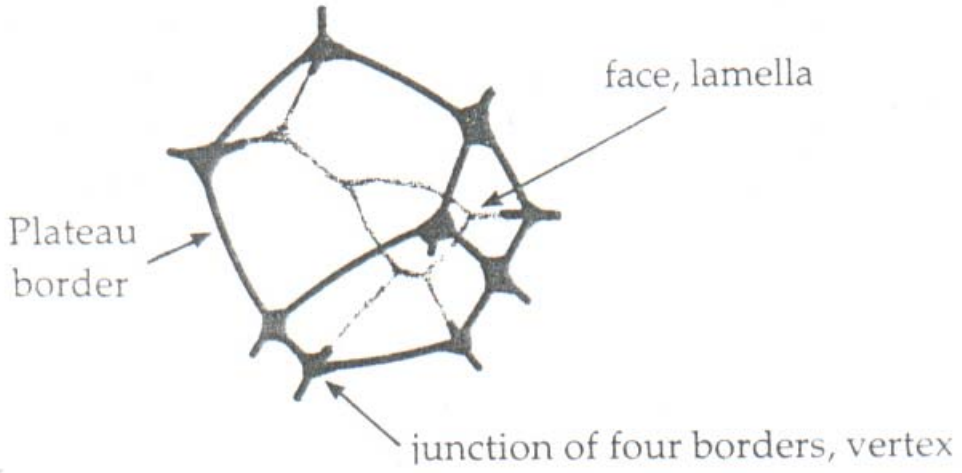

Figure 2.1. A three dimensional bubble cell whose faces are thin films, meeting in Plateau borders (Weaire, 1999).

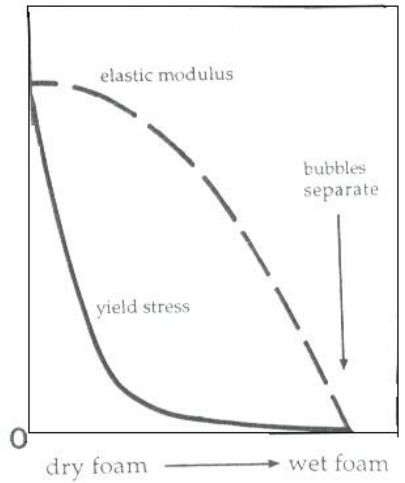

Figure 2.2. The shear modulus and yield stress depend strongly on the liquid fraction of the foam (Weaire, 1999).

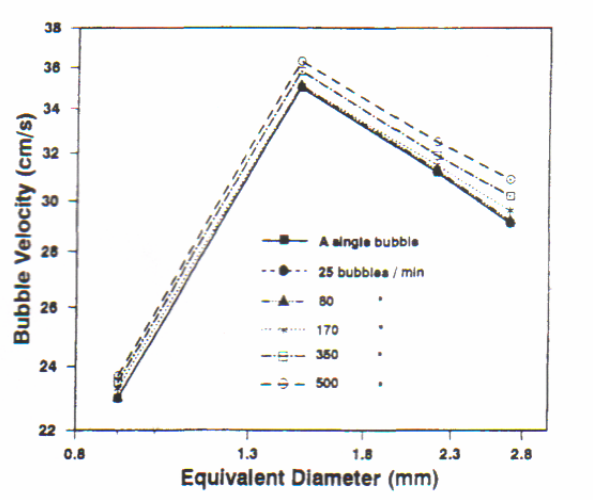

Figure 2.3. The effect of bubble generation frequency on velocity at a location ≈ 20 cm above the orifice in tap water (Sam et al, 1996).

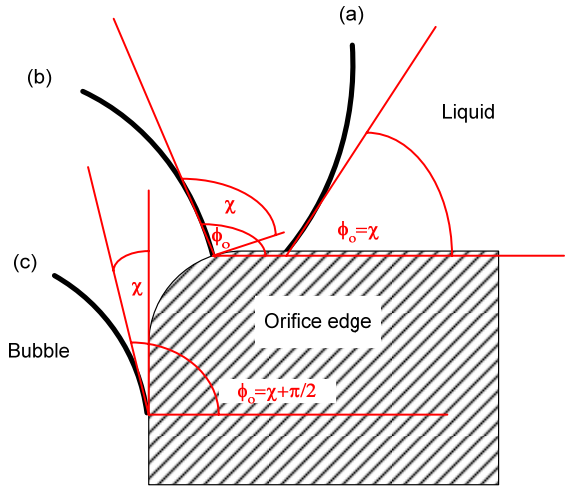

Figure 2.4. Angles on bubble formation (Marmur and Rubin, 1973).

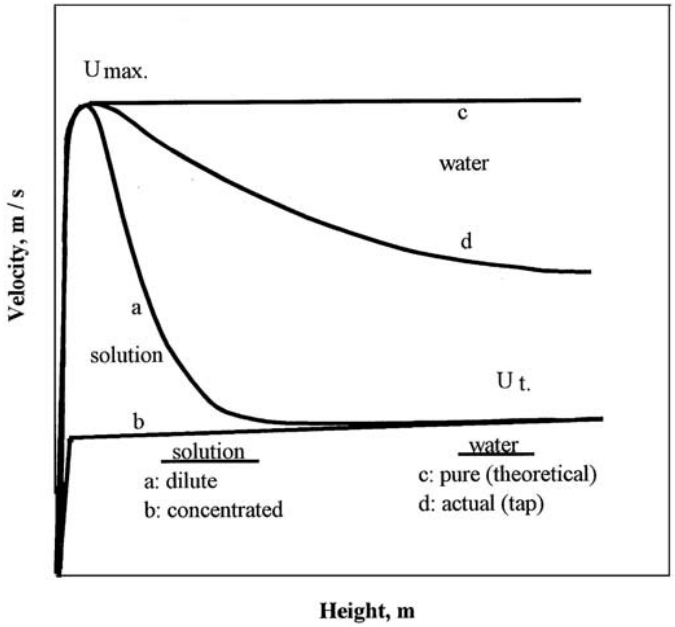

Figure 2.5. Typical bubble velocity profiles for a bubble rising in water and surfactant solution. Indicated are the maximum velocity (U_{max}) and terminal

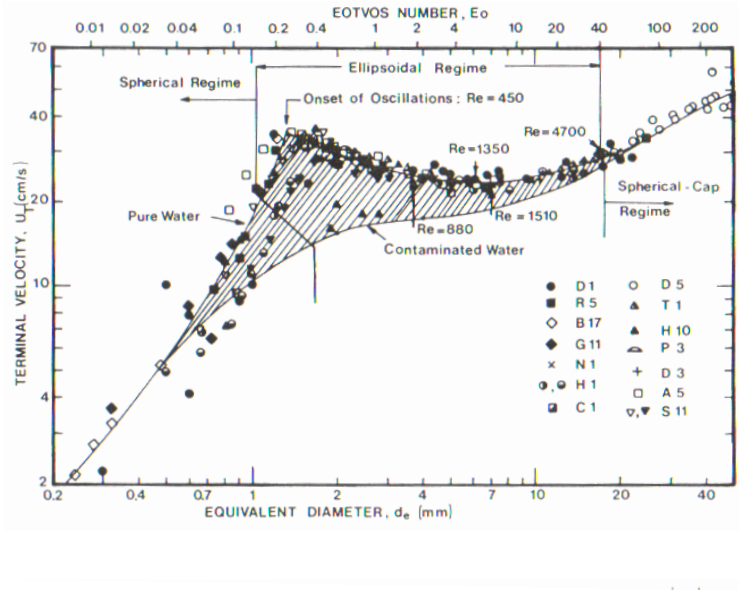

Figure 2.6. Terminal velocity of air bubbles in water at 20°C (Clift et al, 1978).

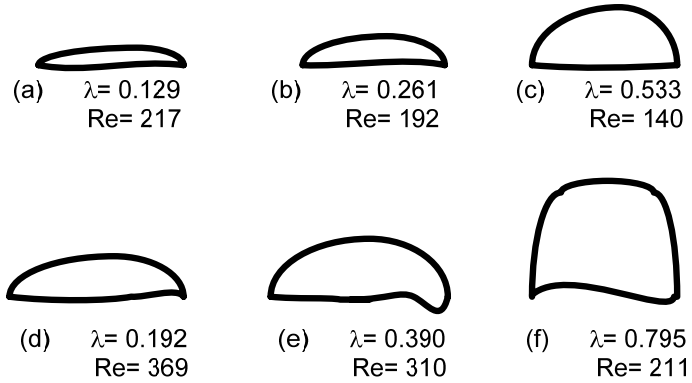

Figure 2.7. Bubble shapes traced from photographs showing the influence of λ on the shape of large bubbles (Clift et al, 1978).

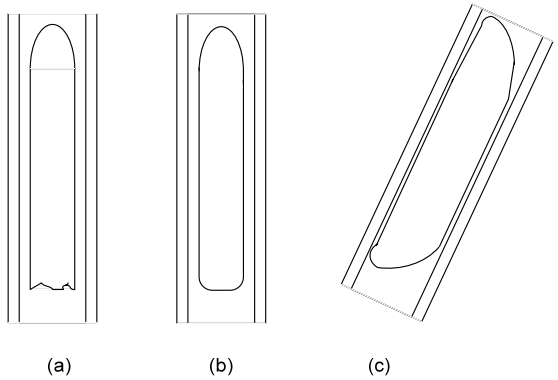

Figure 2.8. Slug flow bubble shapes: (a) $E_{oD} > 10^2$, $M<10^{-6}$ (low viscosity liquid), (b) viscous liquid, (c) inclined tube (Clift et al, 1978).

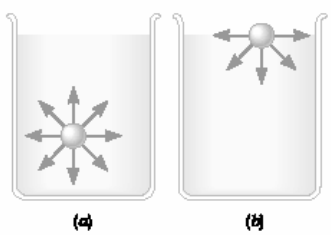

Figure 2.9. Molecule in a liquid: (a) a molecule within the bulk liquid and (b) a molecule in the surface (Wiley, 2004).

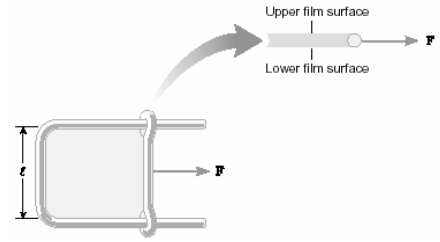

Figure 2.10. Surface tension definition (Wiley, 2004).

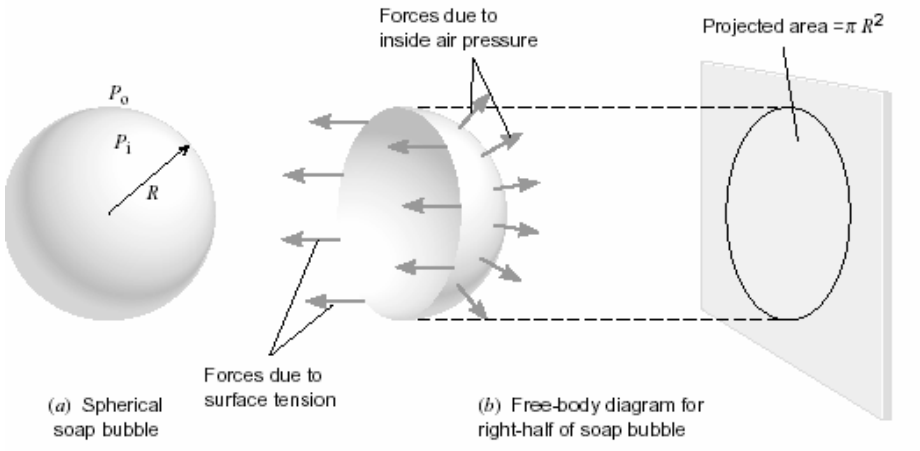

Figure 2.11. Surface tension: (a) spherical soap bubble and (b) free body diagram (Wiley, 2004).

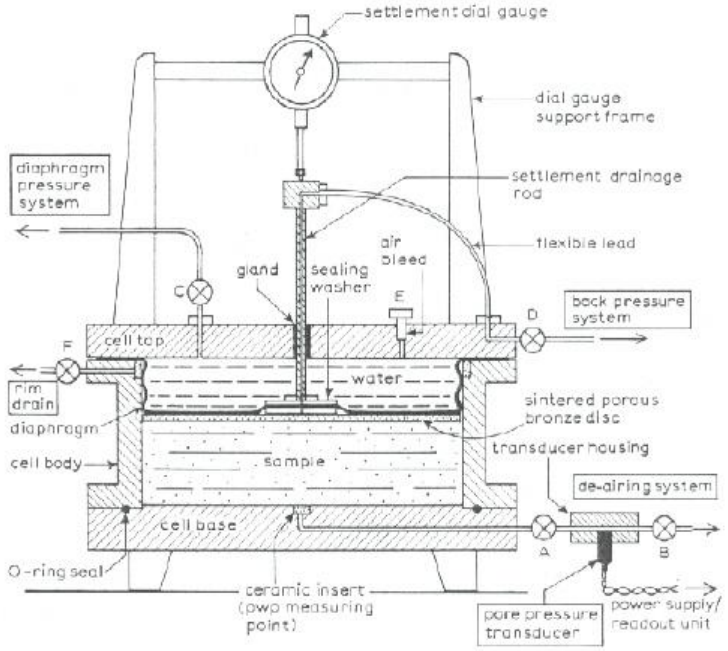

Figure 2.12. Main features of 250 mm diameter Rowe hydraulic consolidation cell (Head, 1986).

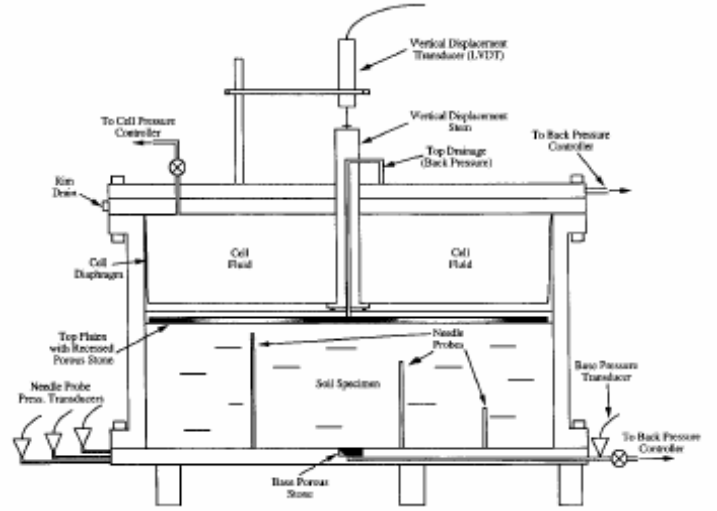

Figure 2.13. Cross section schematic of instrumented hydraulic consolidation (Rowe) cell (Sheahan and Watters, 1997).

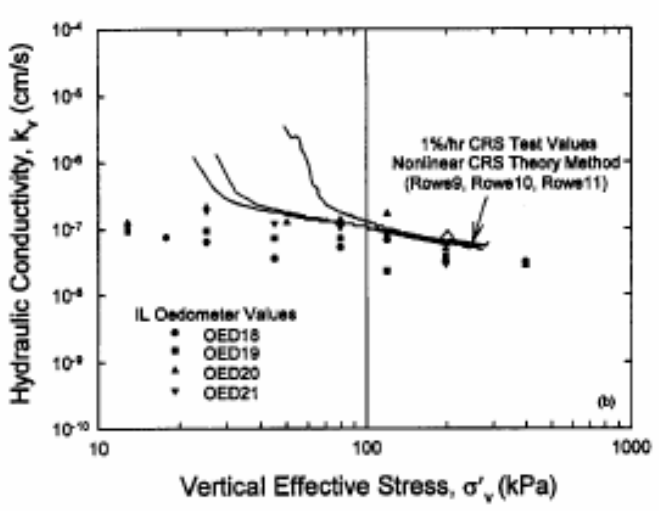

Figure 2.14. Consolidation parameter comparison, hydraulic conductivity versus stress level: 1%/h CRS tests versus IL Oedometer tests.

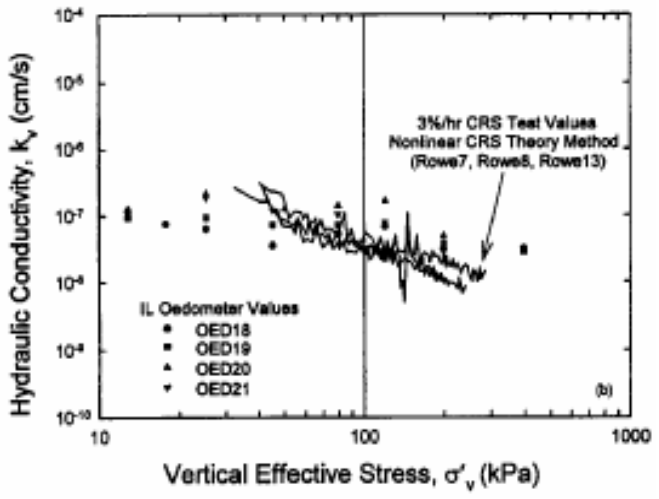

Figure 2.15. Consolidation parameter comparison, hydraulic conductivity versus stress level: 3%/h CRS tests versus IL Oedometer tests.

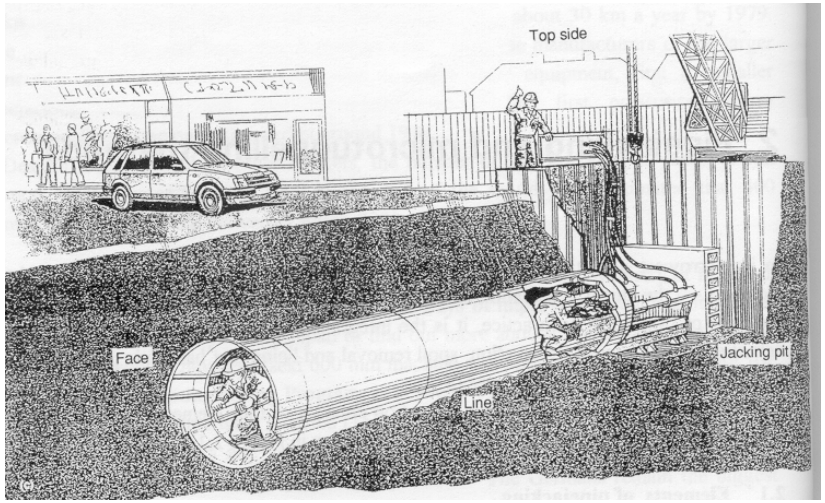

Figure 2.16. Elements of pipejacking (Thomson, 1993).

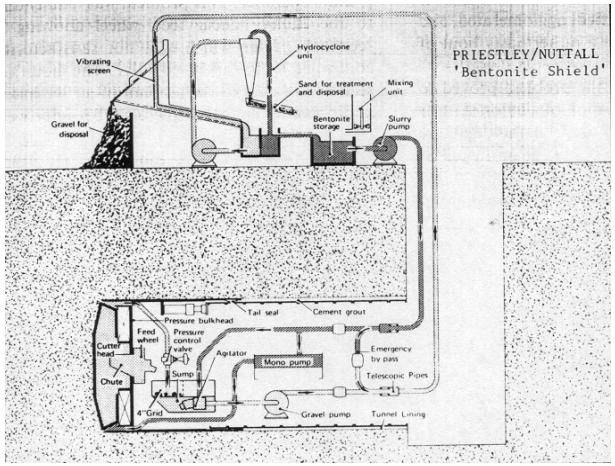

Figure 2.17. Barlett bentonite process (Stack, 1982).

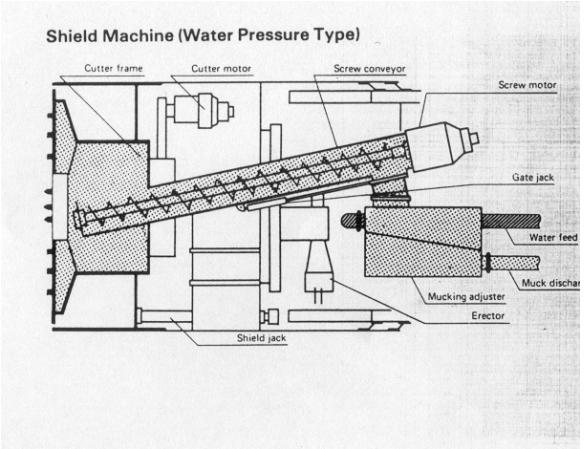

Figure 2.18. Shield machine: water pressure type (Stack, 1982).

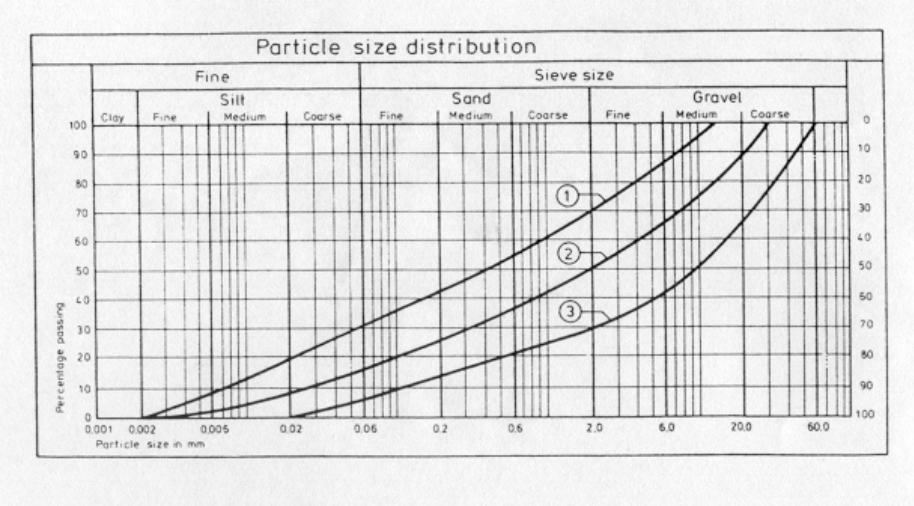

Figure 2.19. EPB shield range of application with regard to the particle size distribution of the ground (Maidl et al, 1995).

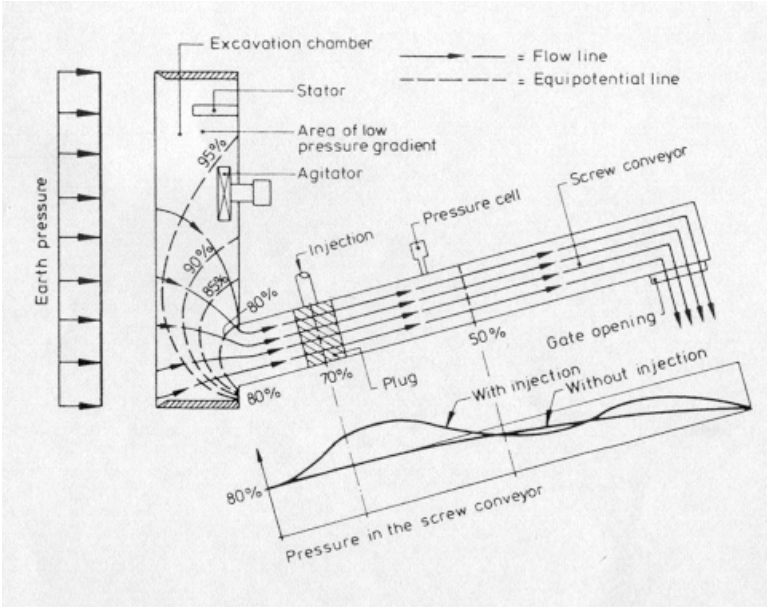

Figure 2.20. Flow configuration in the excavation chamber (Maidl et al, 1995).

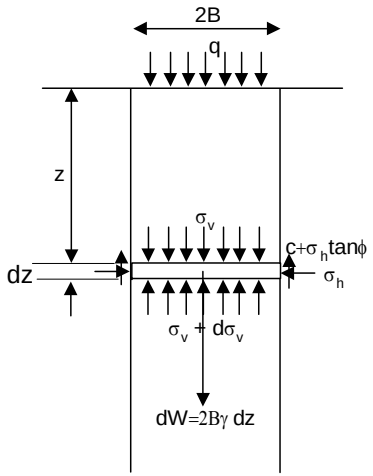

Figure 2.21. Diagram illustrating assumptions on which computation of pressure in sand between two vertical surfaces of sliding is based (Terzaghi, 1943).

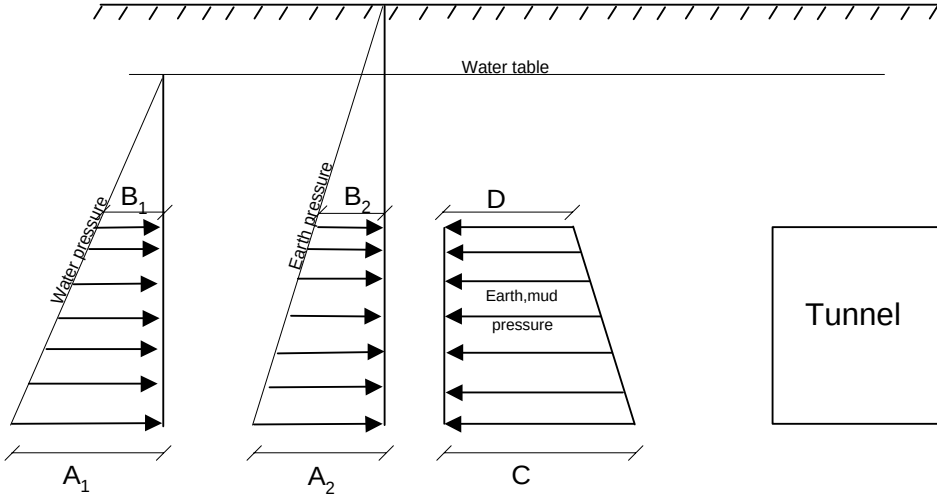

Figure 2.22. Earth pressure balance support (West, 1986).

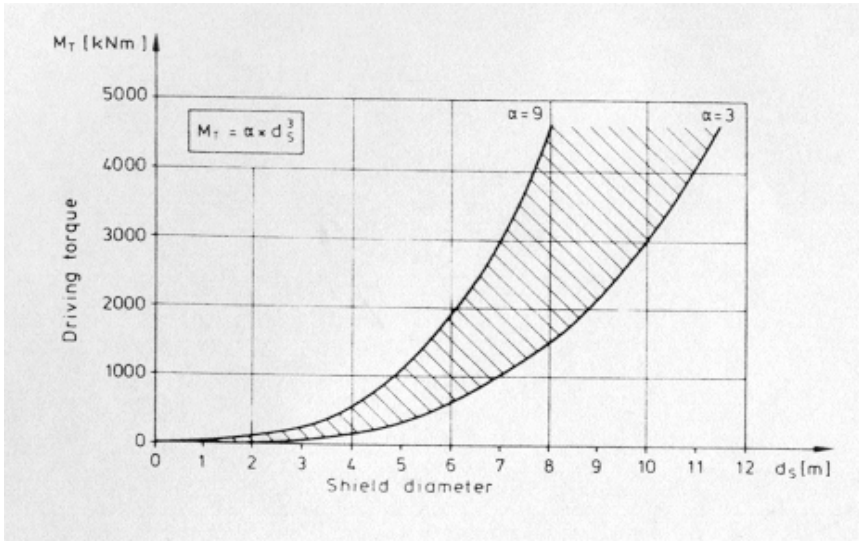

Figure 2.23. Relation between shield diameter and installed cutting wheel torque (Maidl et al, 1995).

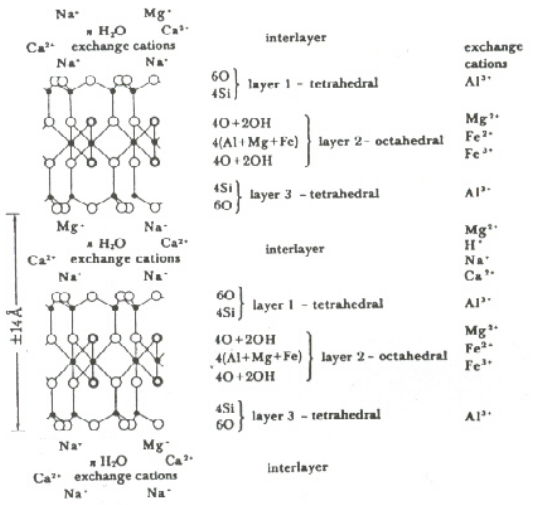

Figure 2.24. The structure of montmorillonite. The chemical composition shown is intended to illustrate the variations possible in the various sheets of the structure and in the interlayer space (Odom, 1986).

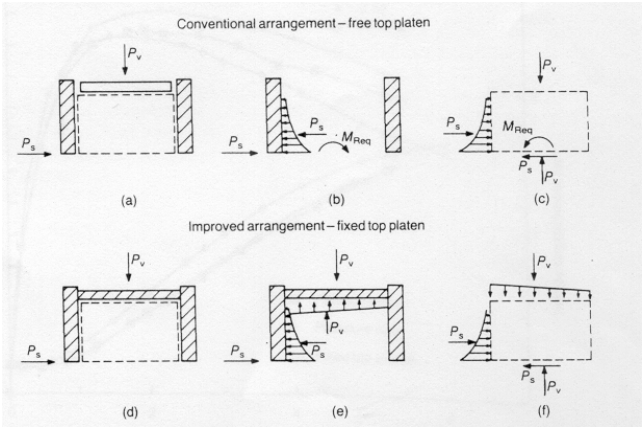

Figure 2.25. Forces in direct shear test showing couple applied by shear force. With free top platen (a) to (c) this results in non-uniform distribution of stress on central plane; symmetrical test with fixed top platen (d) to (f) provides more uniform stress distribution on central plane (Jewell, 1989).

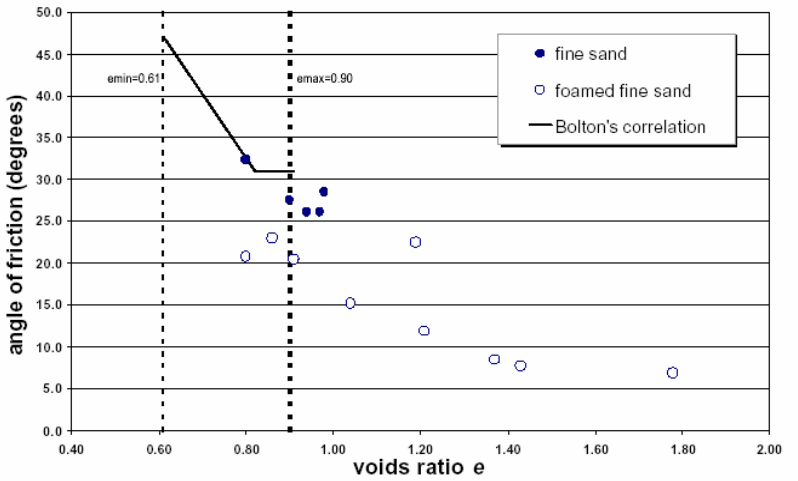

Figure 2.27. Variation of angle of friction with void ratio: fine sand (Houlsby and Psomas, 2001).

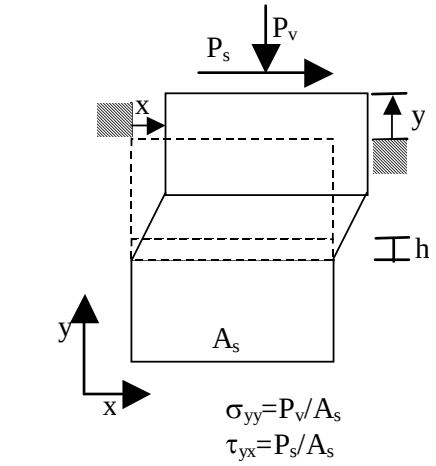

Figure 2.26. Definitions for direct shear test (Jewell, 1989).

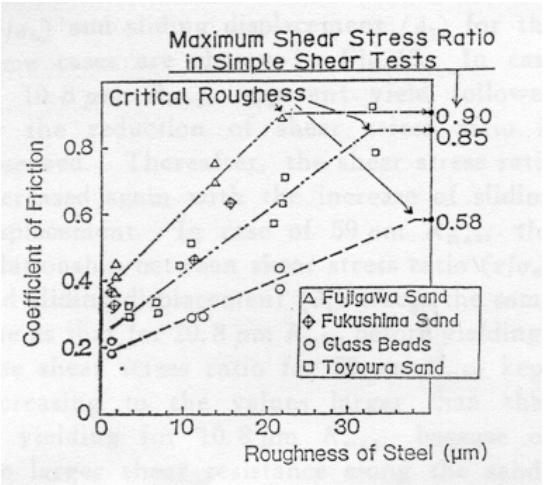

Figure 2.28. Effects of steel roughness and sand type on frictional coefficient (Uesugi and Kishida, 1986a).

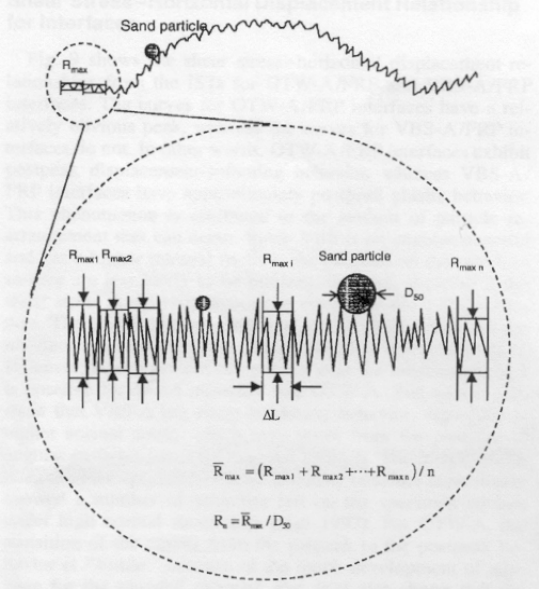

Figure 2.29. Definition of R_{max} and R_n (Uesugi and Kishida, 1986a).

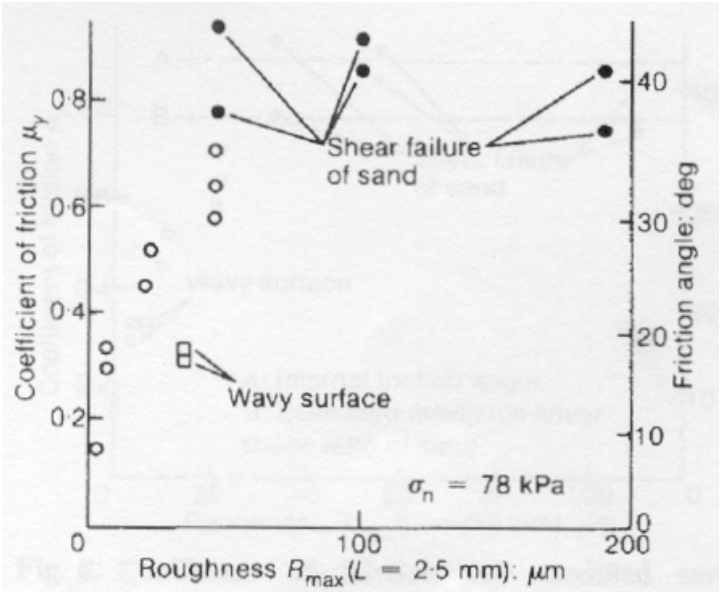

Figure 2.30. Coefficient of frictional and surface roughness (Kishida and Uesugi, 1987)

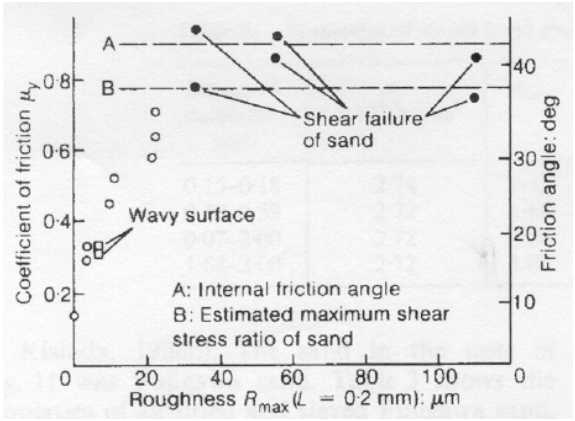

Figure 2.31. Coefficient of friction and modified surface roughness (Kishida and Uesugi, 1987)

Figure 2.32. Experimental apparatus developed by Vinai (2006): 1) displacement wire Transducer, 2) top EPC, 3) bottom EPC, 4) pressure cell 1, 5) pressure cell 2, 6) pressure cell 3, 7) torque meter, 8) weighting platform (scale).

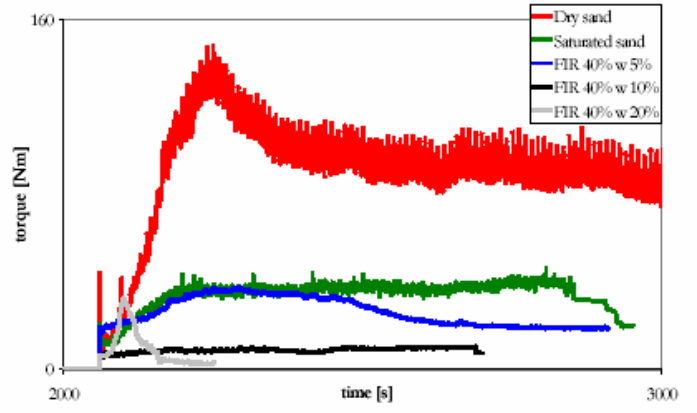

Figure 2.33. Torque required for different conditioned parameter set applied on the reference sand (Vinai, 2006).

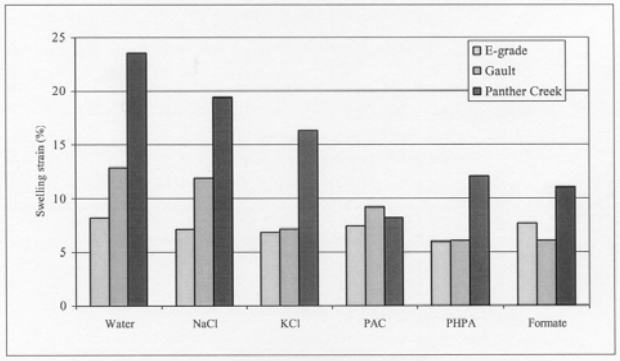

Figure 2.34. One dimensional swelling indices k* of normally consolidated E-grade kaolin, Panther Creek and Gault Clay samples conditioned with various inhibiting agents (Merritt and Mair, 2001).

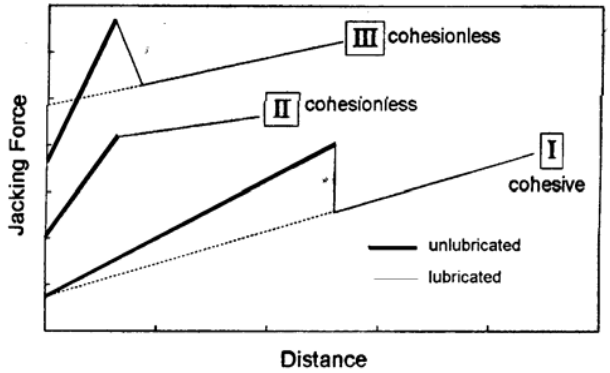

Figure 2.35. Effect of lubrication in different soils (Marshall, 1998).

Figure 2.36. Overview of model EPB machine screw conveyor system at Cambridge University (Merritt, 2004)

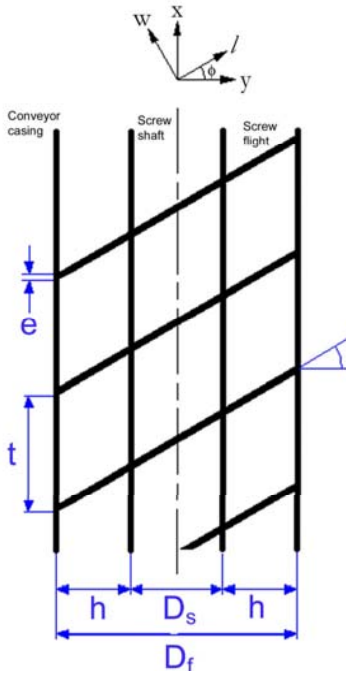

Figure 2.37 Cambridge University screw geometry plan view at top of the screw channel (Merritt, 2004).

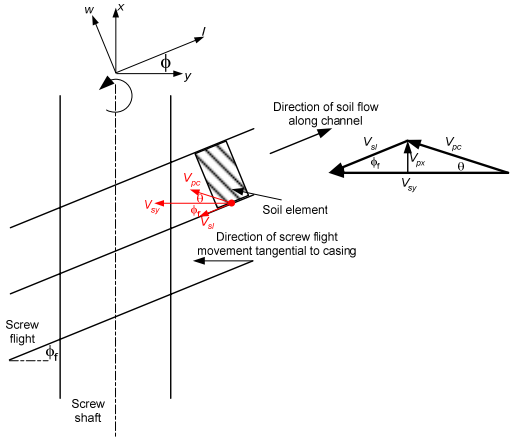

Figure 2.38. Movement of soil plug along the screw channel: plan view at top of the screw channel (Merritt, 2004)

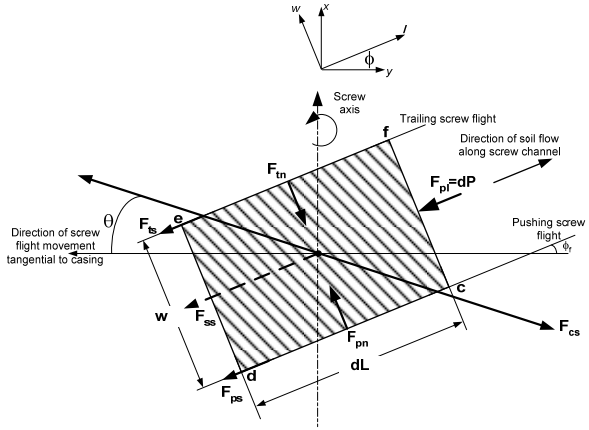

Figure 2.39. Simplified free body diagram of soil element in screw channel: viewed in plan (Merritt, 2004).

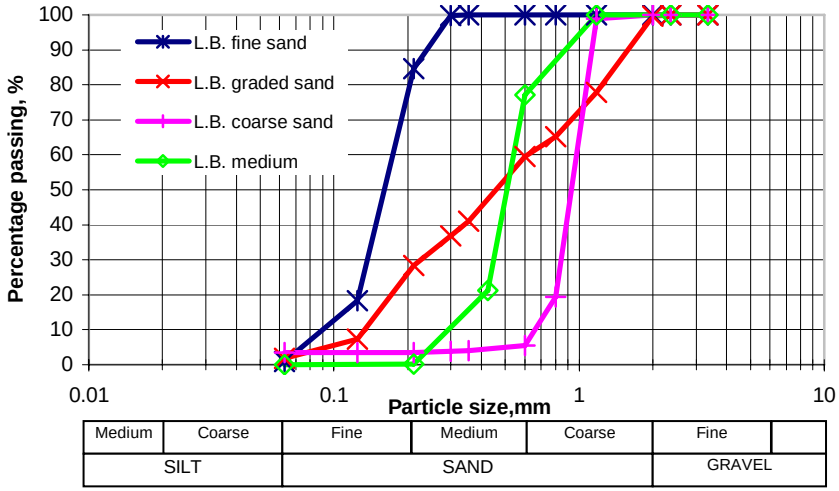

Figure 3.1. Grading curve of L.B. fine sand, L.B. coarse sand, L.B. graded sand and L.B. medium coarse sand.

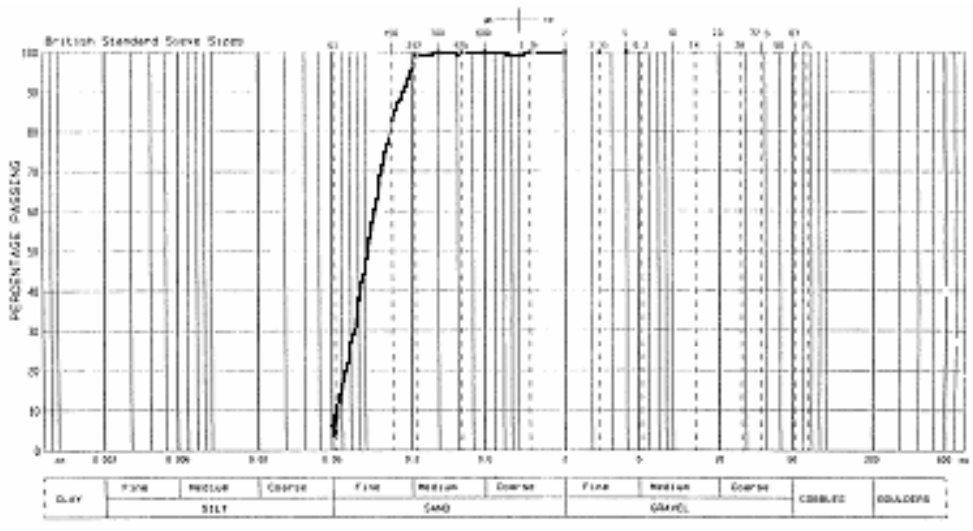

(a)

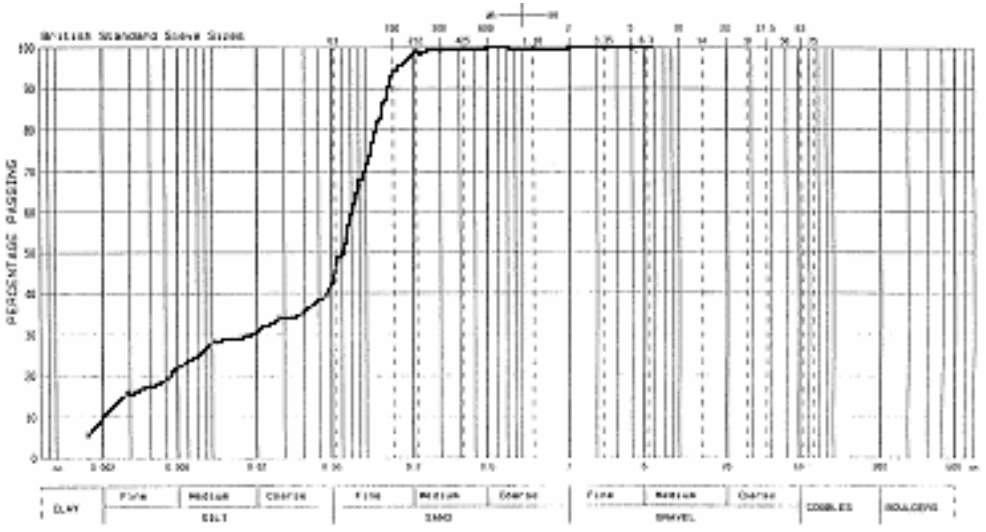

(b)

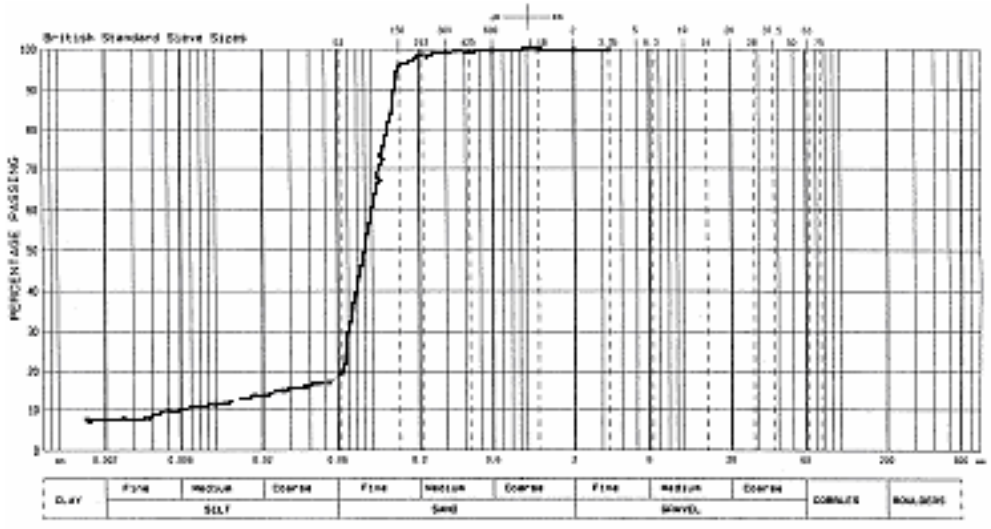

(c)

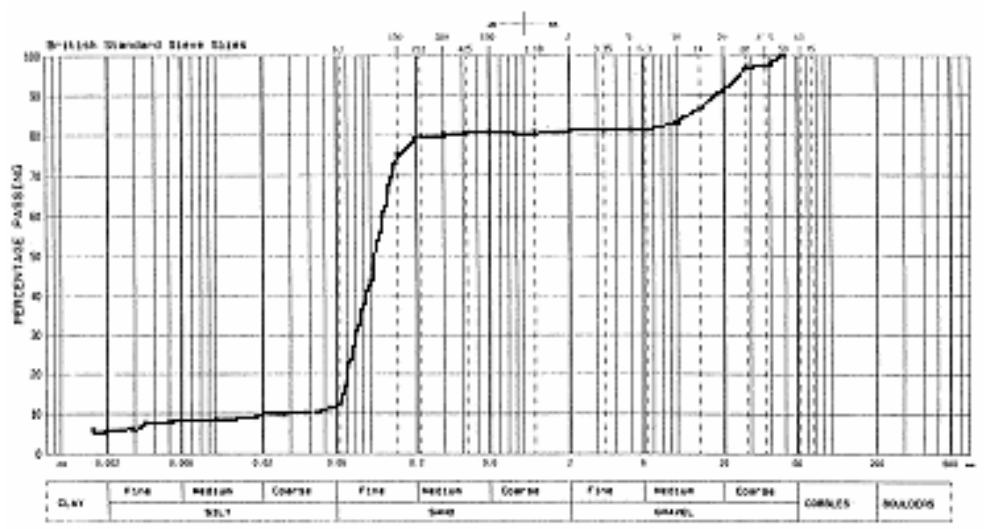

(d)

Figure 3.2. Representative grading curve of Thanet sand (a) Test 16, (b) Test 27, (c) Test 32 and (d) Test 34.

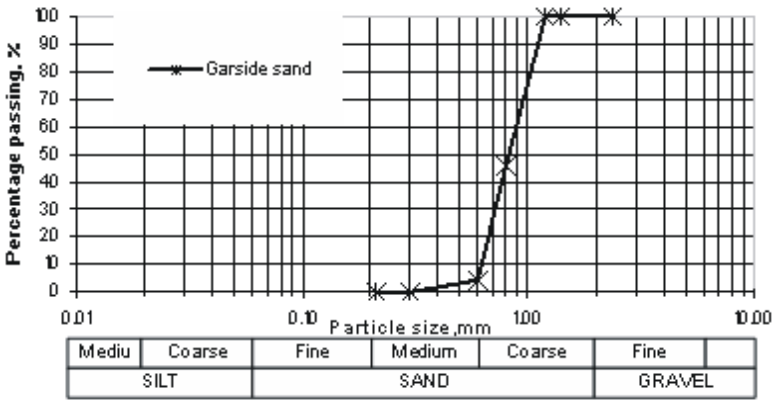

Figure 3.3. Grading curve of Garside sand.

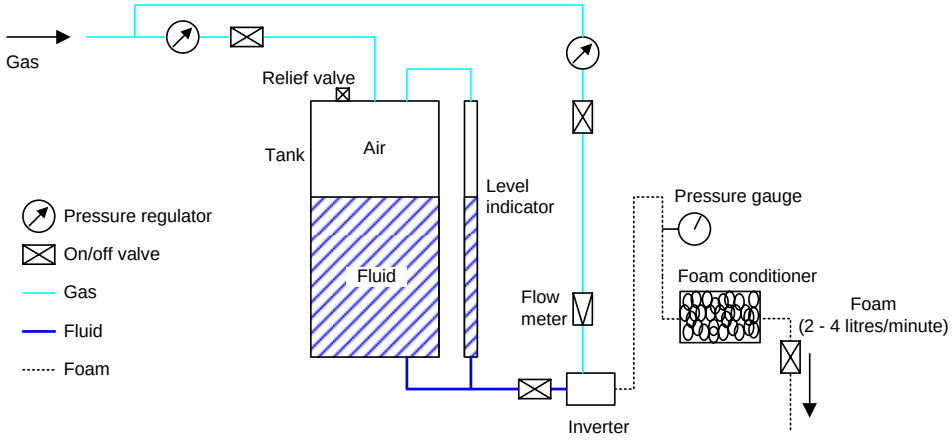

Figure 3.4. Layout of foam generator (Psomas, 2001).

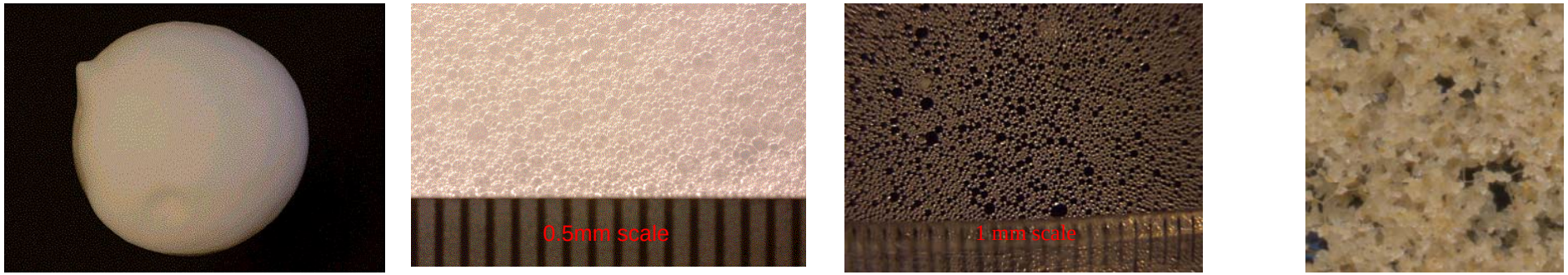

(a) **(b)** **(c)** **(d)**

Figure 3.5. Bubble images: (a) foam sample in plastic container, (b) picture from top of plastic container, (c) picture of foam between acrylic plates and (d) L.B. fine sand and foam scanned.

(a)

(b)

Figure 3.6. Brass drainage pan: (a) front view, (b) valve of drainage pan.

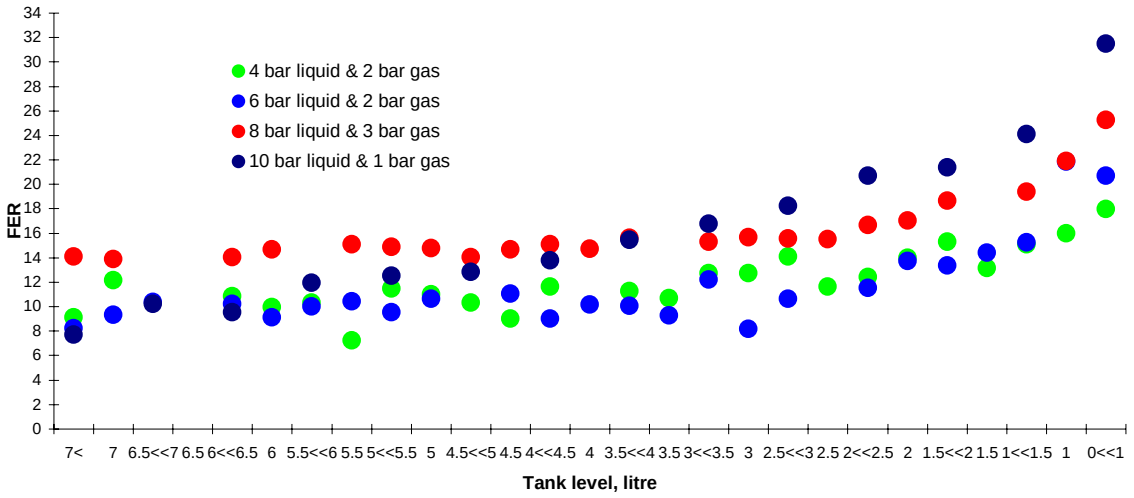

Figure 3.7. FER variation of Versa foam (2% concentration) at different pressure settings in the Oxford foam generator.

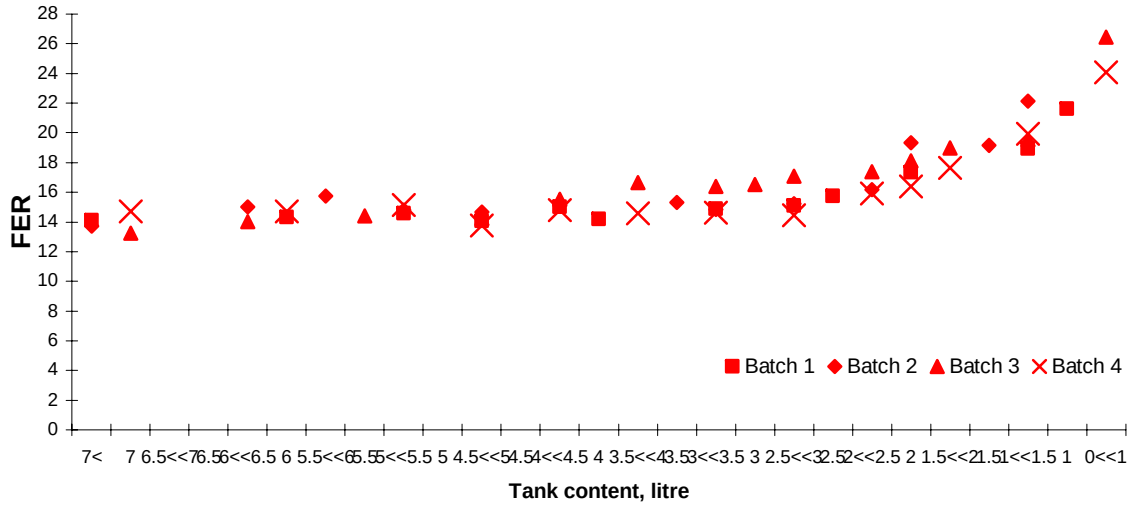

Figure 3.8. Different FER tests on Versa foam (2% concentration) at 8 bar liquid pressure and 3 bar gas pressure in foam generator.

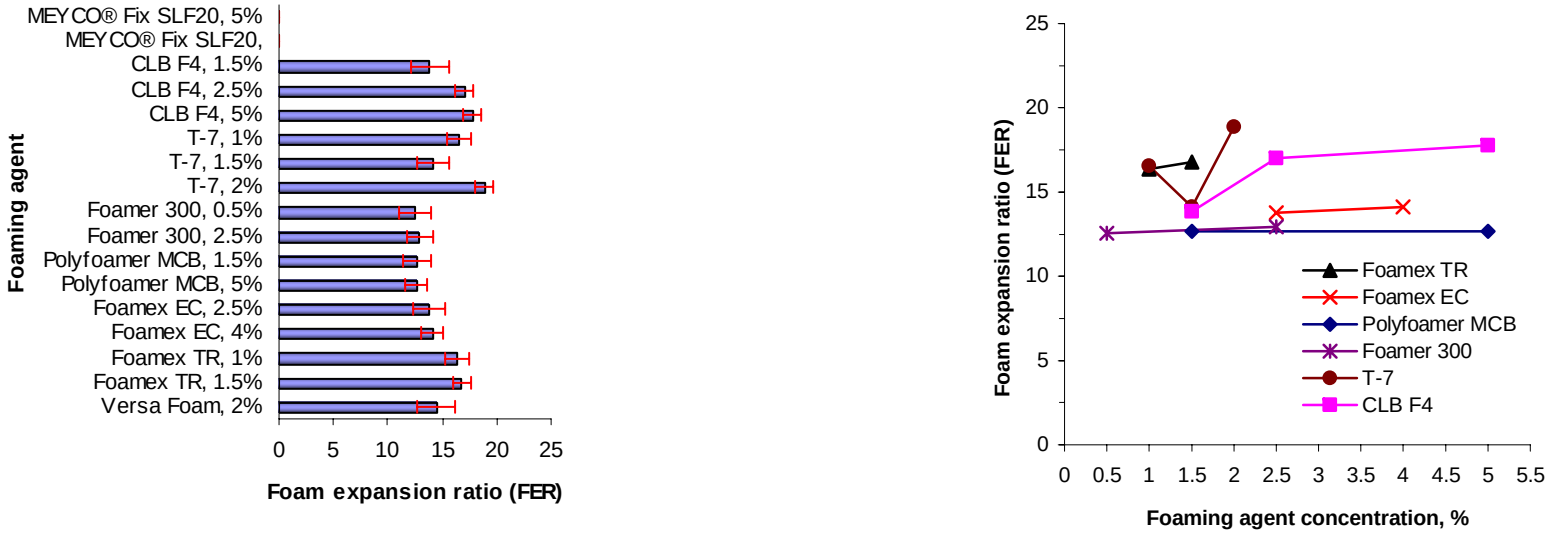

(a) **(b)**

Figure 3.9. FER of Foaming agents: (a) Foaming agents vs FER, (b) FER vs concentration of foaming agents.

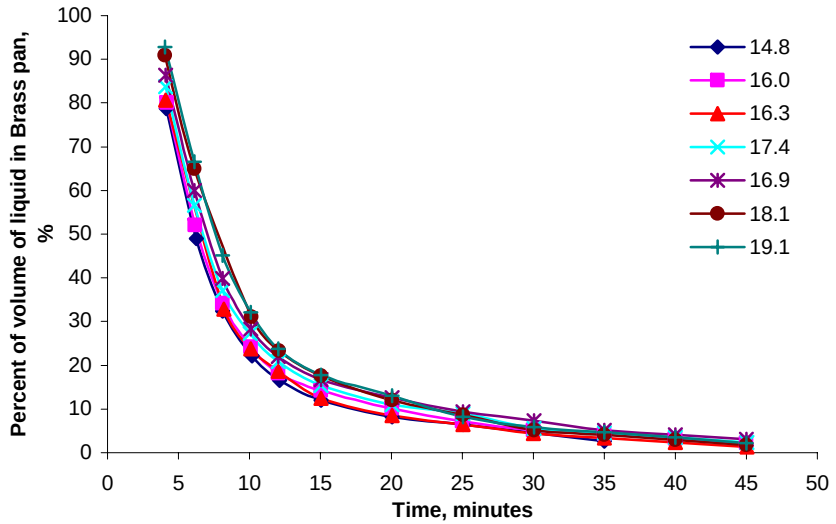

Figure 3.10. Variation of percentage of volume of liquid in the brass pan of T7, 1% concentration, at different FER.

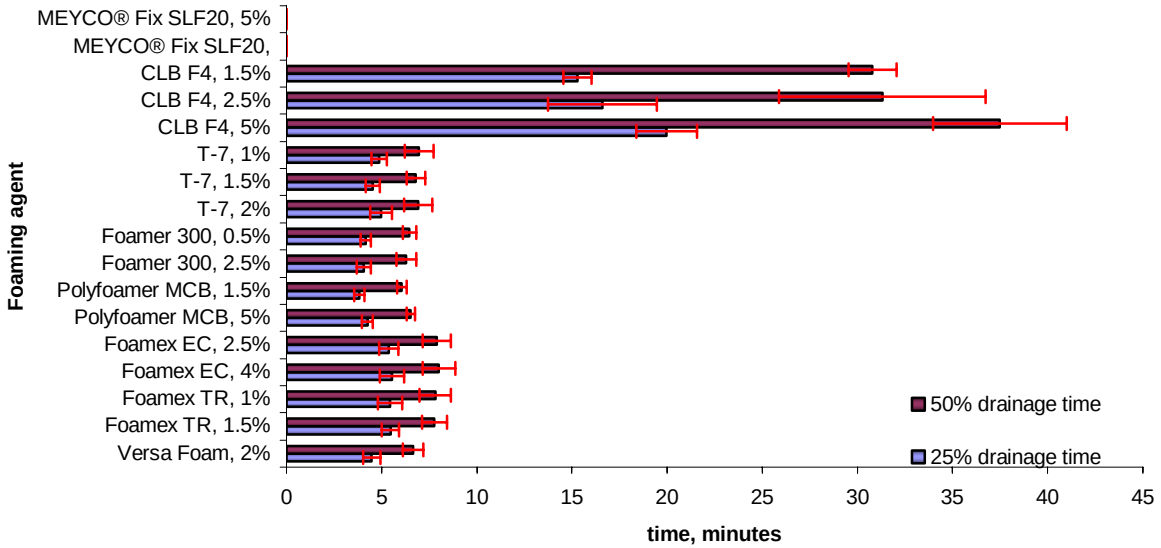

Figure 3.11. 25% and 50% drainage times of different foaming agents at different concentrations.

Figure 3.12. Multi-flow mixer.

Figure 3.13. Acrylic plungers.

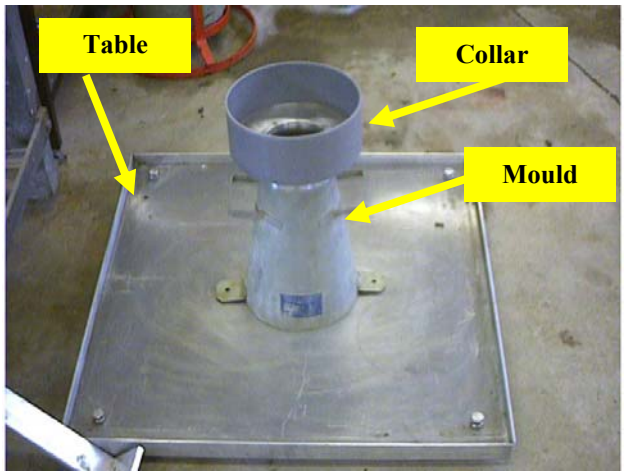

Figure 3.14. Mould and table for Slump test.

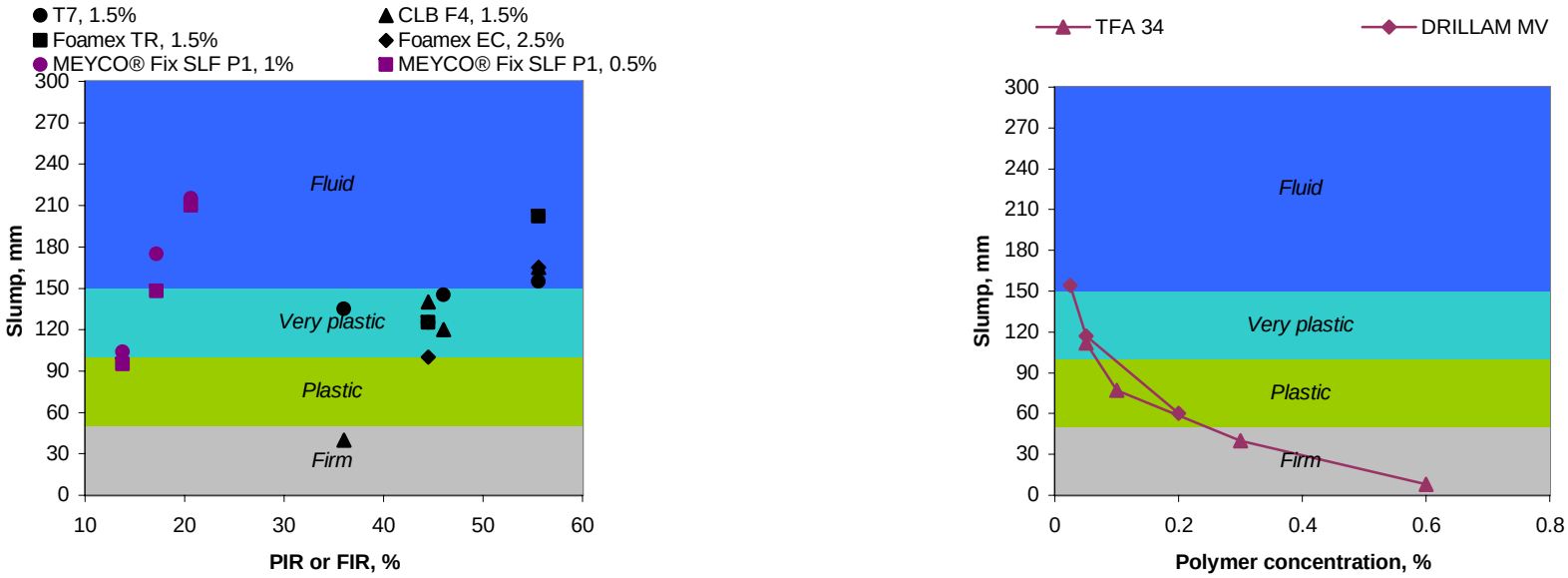

(a) **(b)**

Figure 3.15. Slump variation on conditioned Thanet sand: (a) Slump vs PIR or FIR (b) Slump vs polymer concentration.

(a) **(b)** **(c)**

Figure 3.16. L.B. sands slump images: (a) L.B. fine sand, (b) L.B. coarse sand, (c) L.B. graded sand.

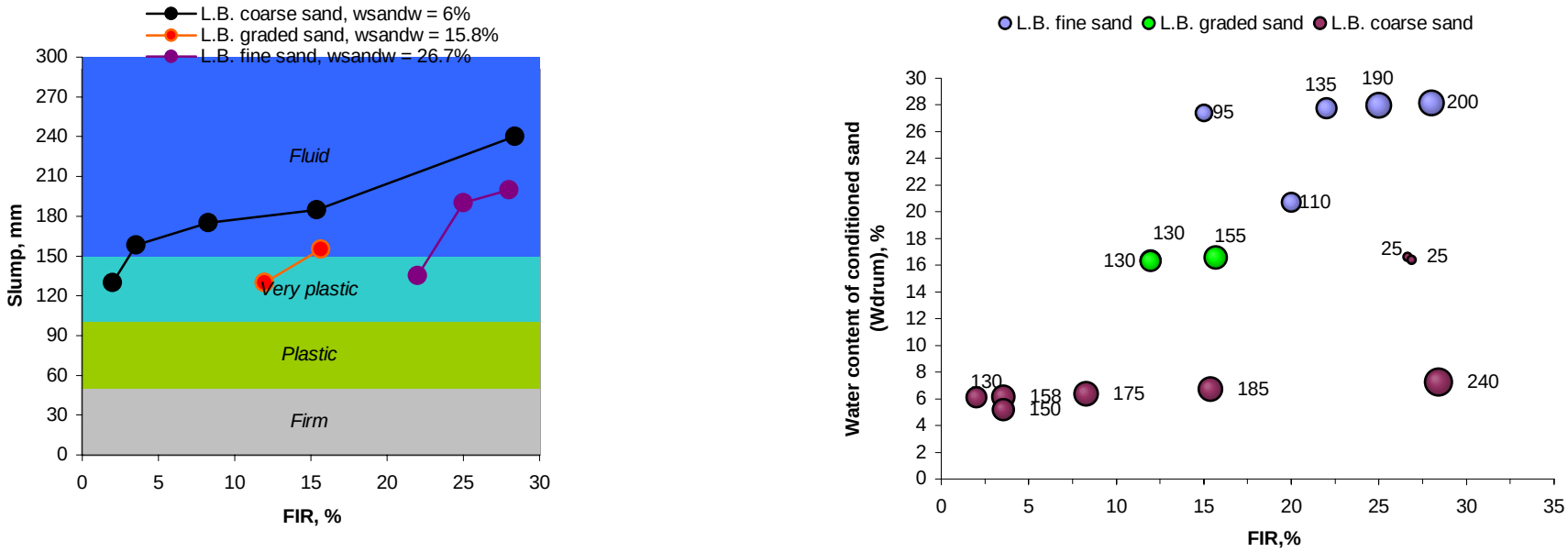

(a) (b)

Figure 3.17. Slump variation on conditioned L.B. sands: (a) Slump vs FIR (b) w_{drum} vs FIR

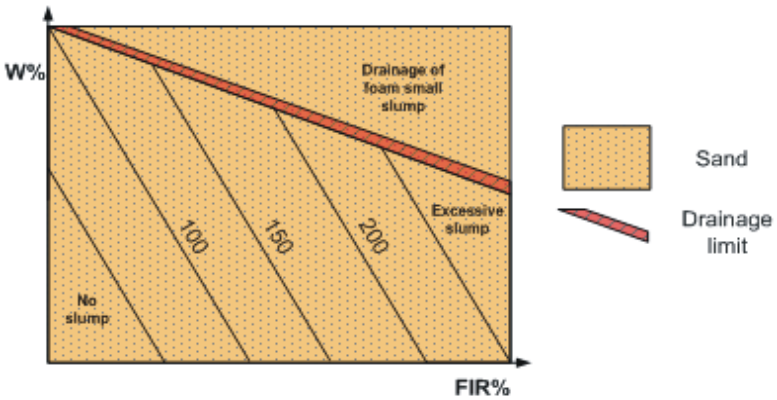

Figure 3.18. General slump behaviour of conditioned sands

(a) (b)

Figure 3.19. Flow cone: (a) front view, (b) top view.

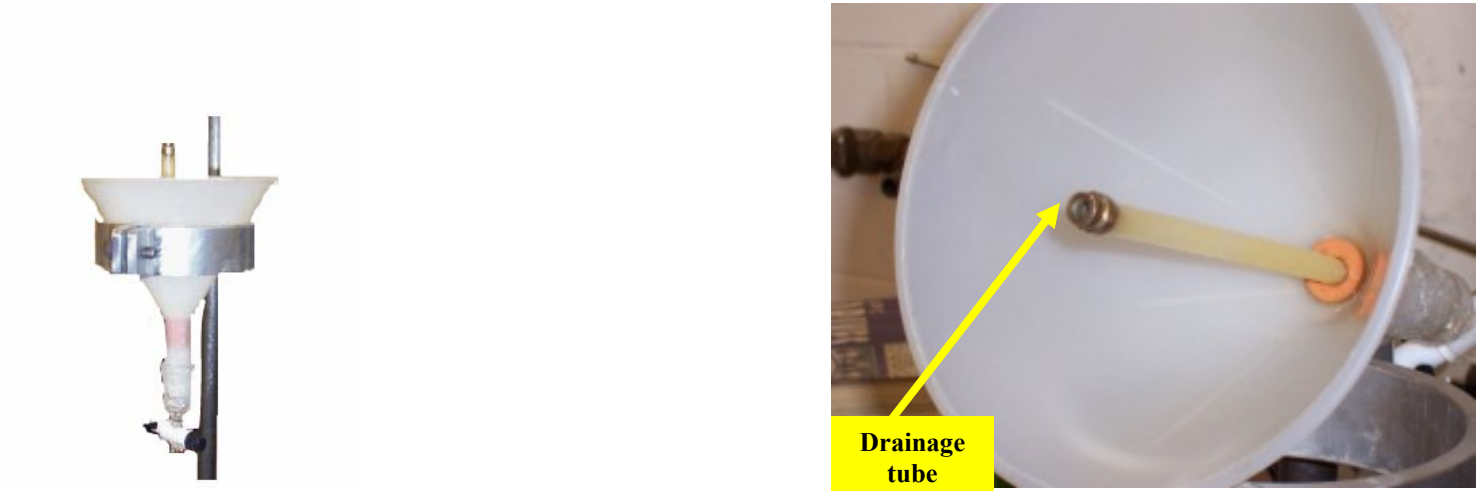

(a) (b)

Figure 3.20. Funnel for conditioned sand stability test: (a) overview (b) inside view.

(a) (b) (c)

Figure 3.21. Container for under pressure conditioned sand stability test: (a) overview, (b) conditioned sand in container and (c) dead weight applied to container.

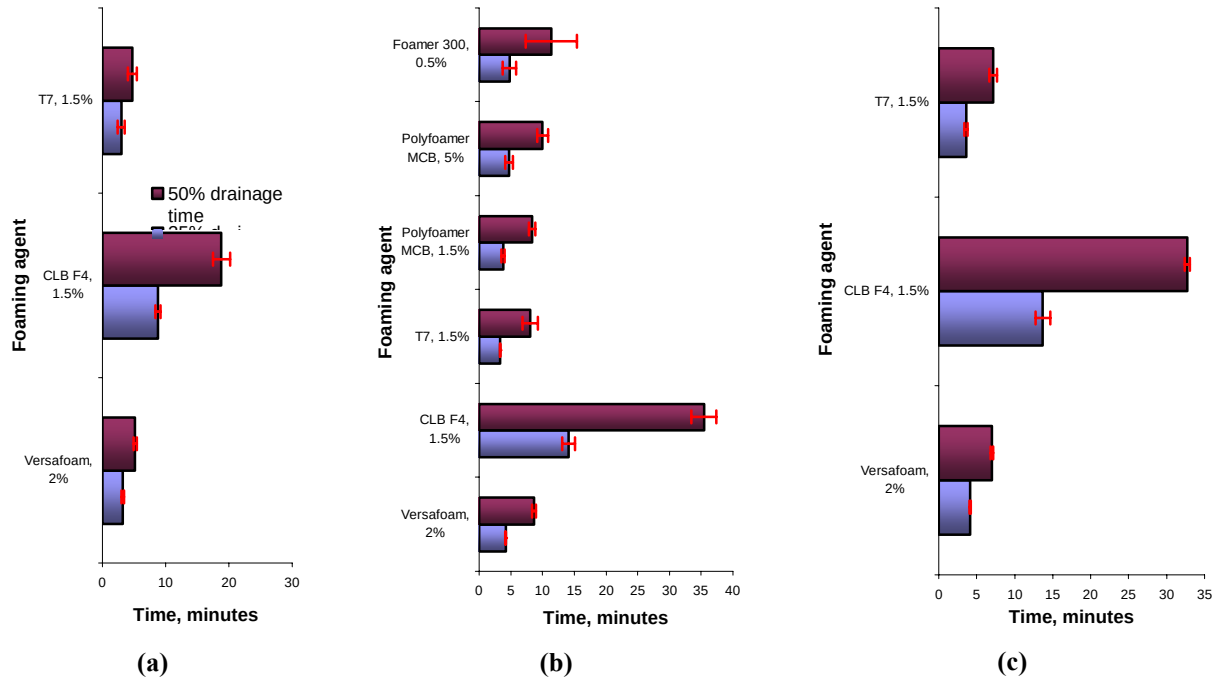

Figure 3.22. 25% and 50% drainage times in funnel device for (a) foam, (b) conditioned L.B. medium coarse sand at 500% FIR and (c) conditioned L.B. medium coarse sand at 600% FIR.

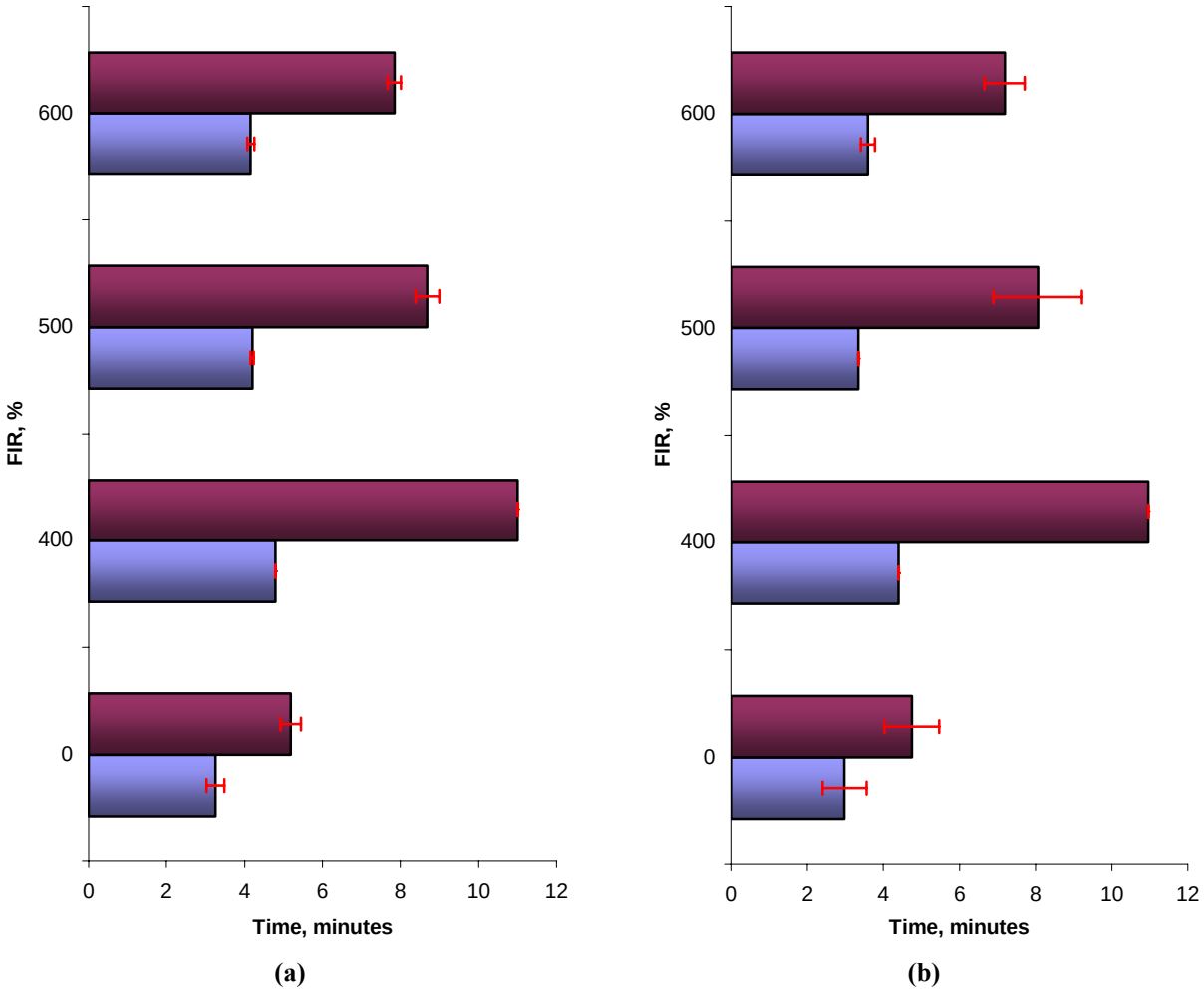

Figure 3.23. 25% and 50% drainage time in funnel device for (a) sand conditioned with Versa foam (2%) at different FIR and (b) sand conditioned with T7 (1.5%) at different FIR.

(a) **(b)**

Figure 3.24. Conditioned L.B. medium coarse sand stability test under pressure at different FER: (a) Versa foam at 1% concentration (b) CLB F4 at 1.5% concentration.

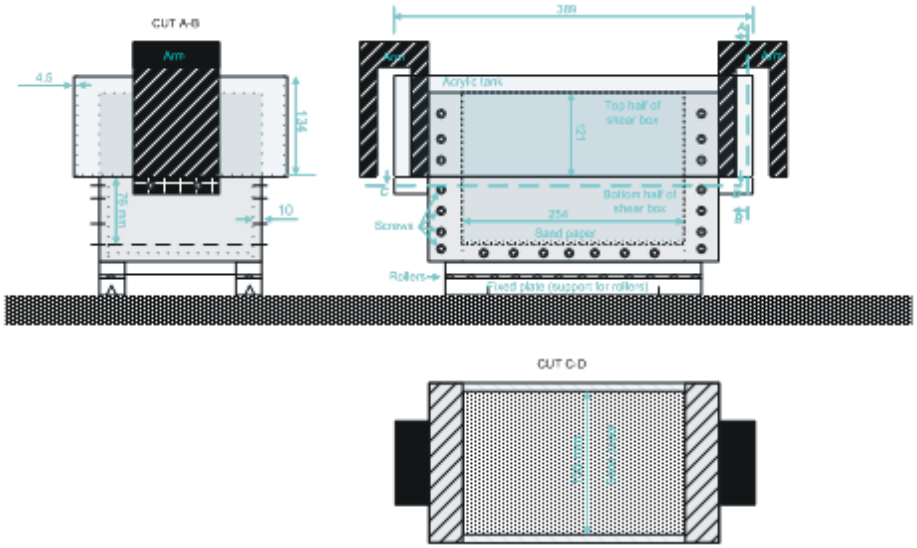

Figure 4.1. Shear box layout

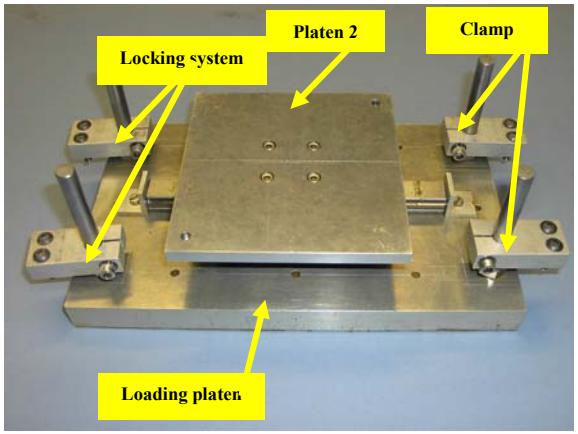

(a) Overview loading platen and clamps

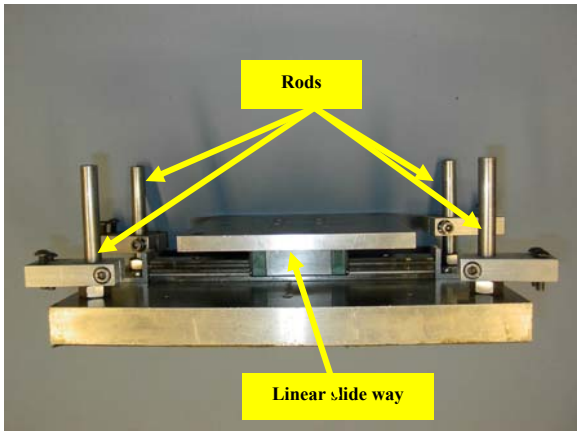

(b) Side view loading platen and clamps.

Figure 4.2. Shear box loading platen and clamps

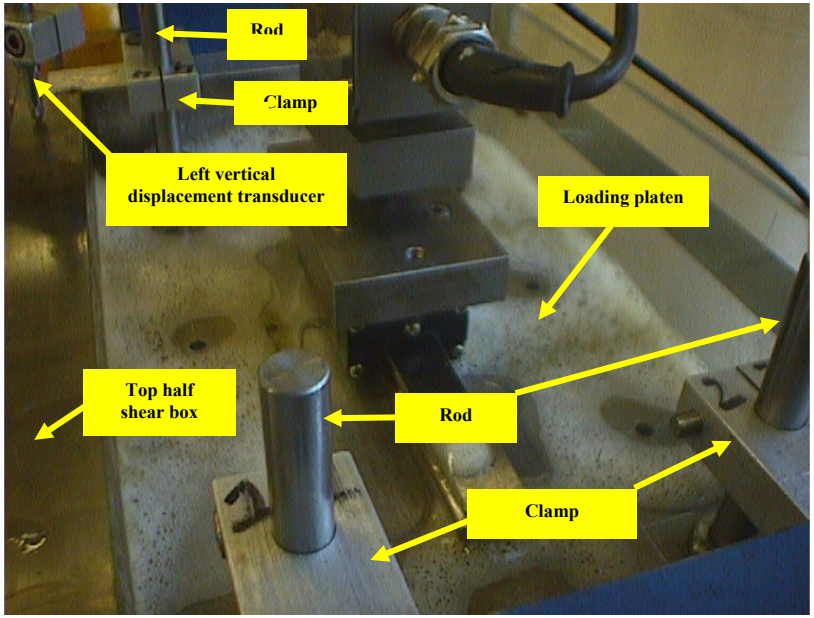

Figure 4.3. Shear box top half, loading platen and clamps all together as one body during a conditioned Thanet sand test

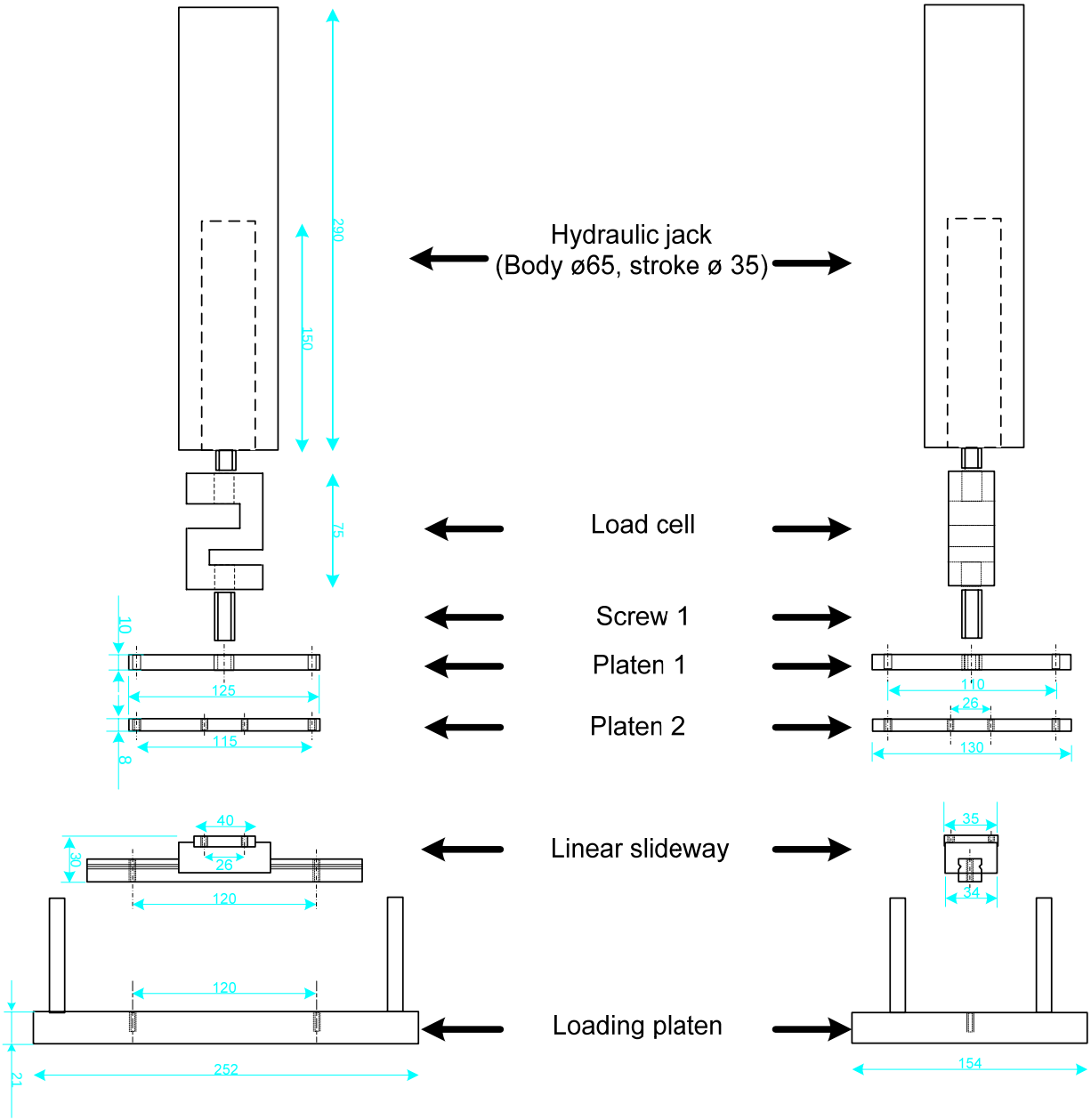

Figure 4.4. Linear slide way, load cell and ram.

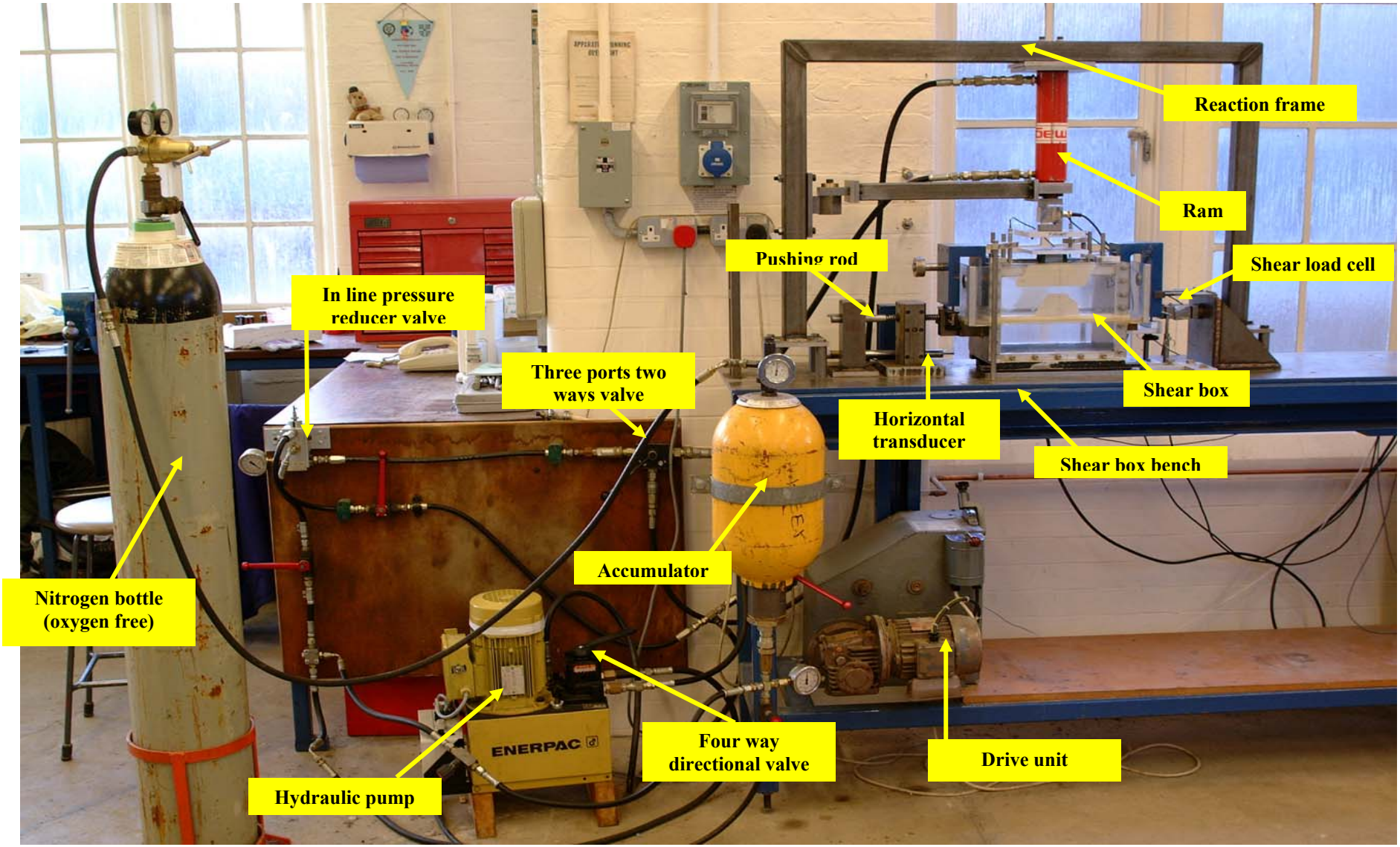

Figure 4.5 Hydraulic system and of MSSA.

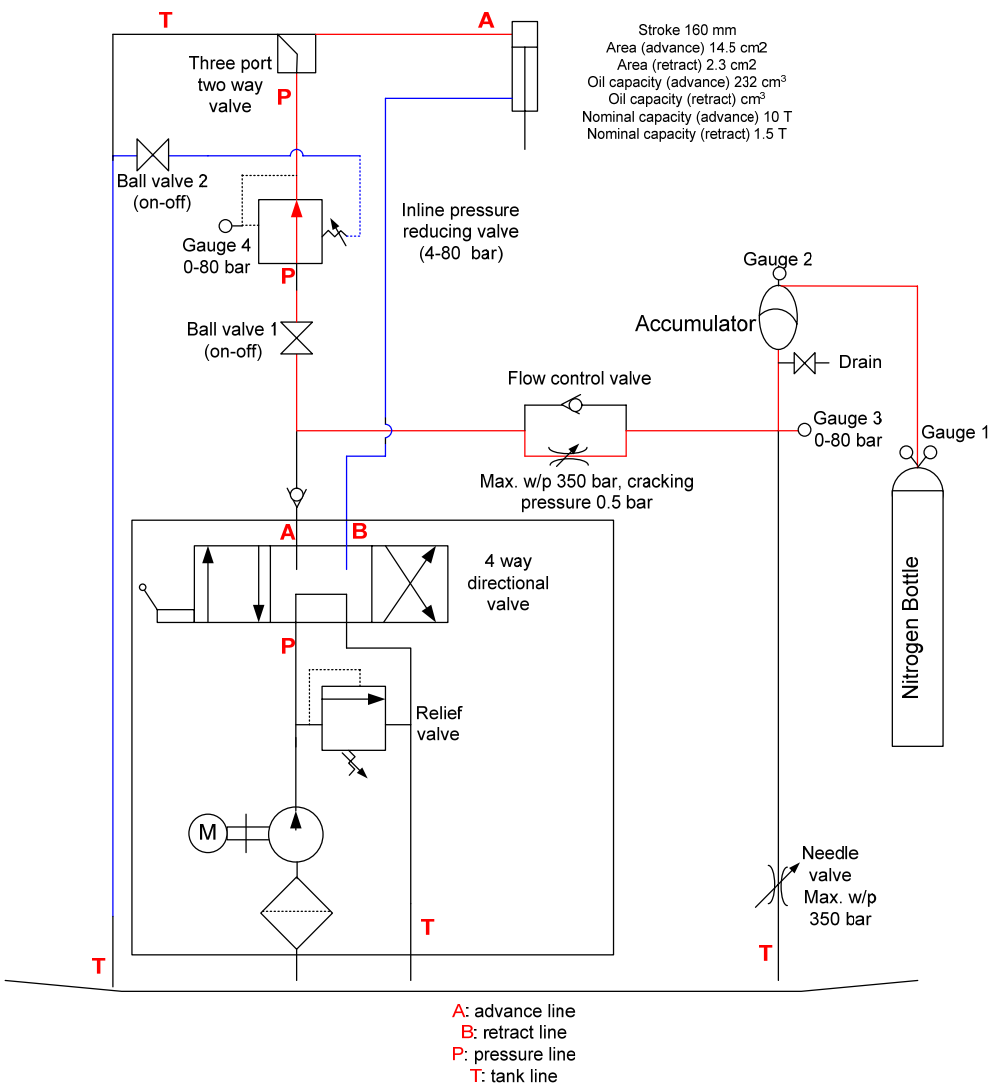

Figure 4.6. Hydraulic circuit.

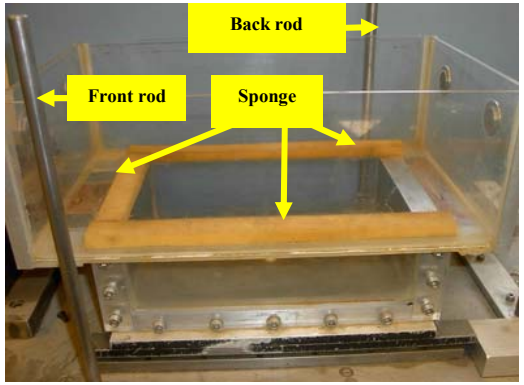

(a) Strips of sponge on the bottom half of MSSA.

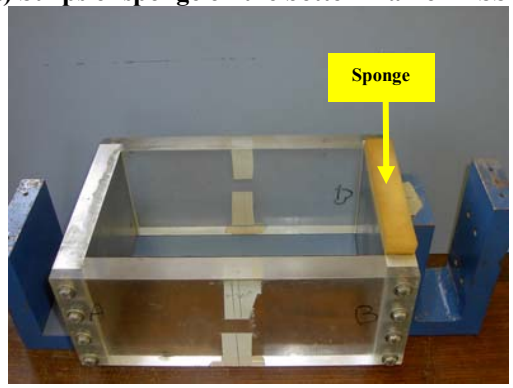

(b) Strips of sponge on the top half of MSSA.

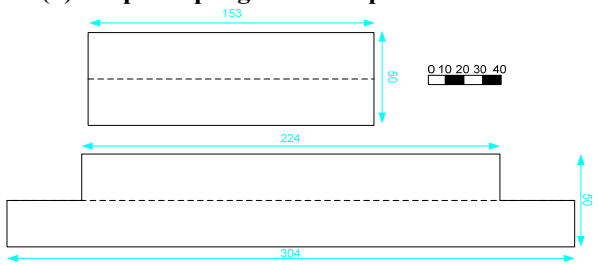

(c) Metal channels dimensions.

Figure 4.7. Strips of sponge and metal channels on MSSA.

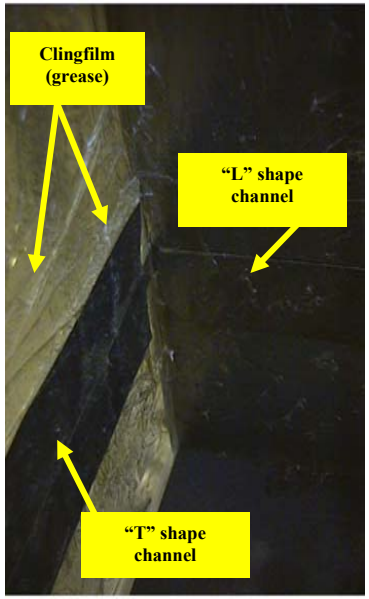

Figure 4.8. Cling film sealing system inside the middle part of MSSA.

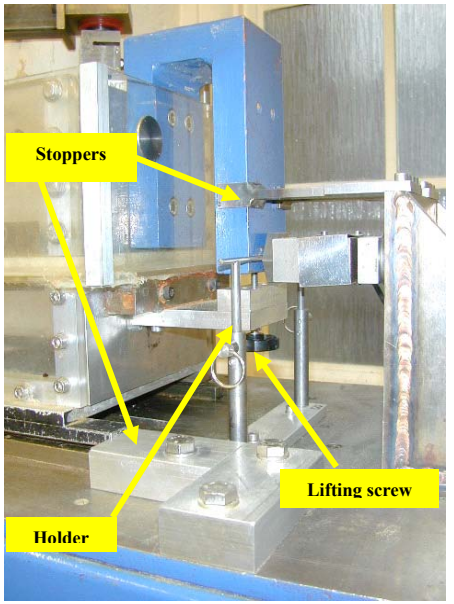

Figure 4.9. Stopper system for MSSA.

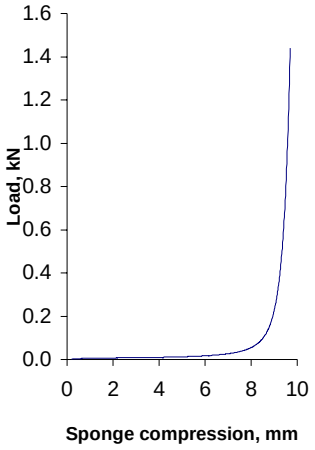

(a)

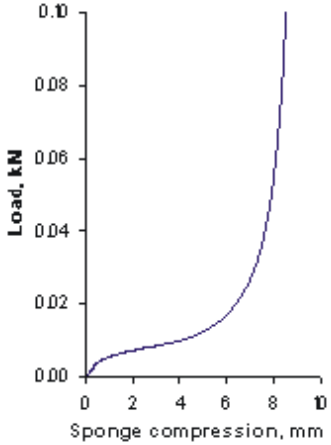

(b)

Figure 4.10. Relation load-compression of sponge: (a) full load graph, (b) load graph till 0.1 kN.

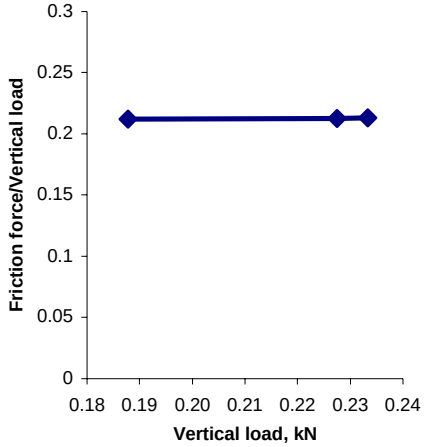

Figure 4.11. Friction force/vertical load coefficient.

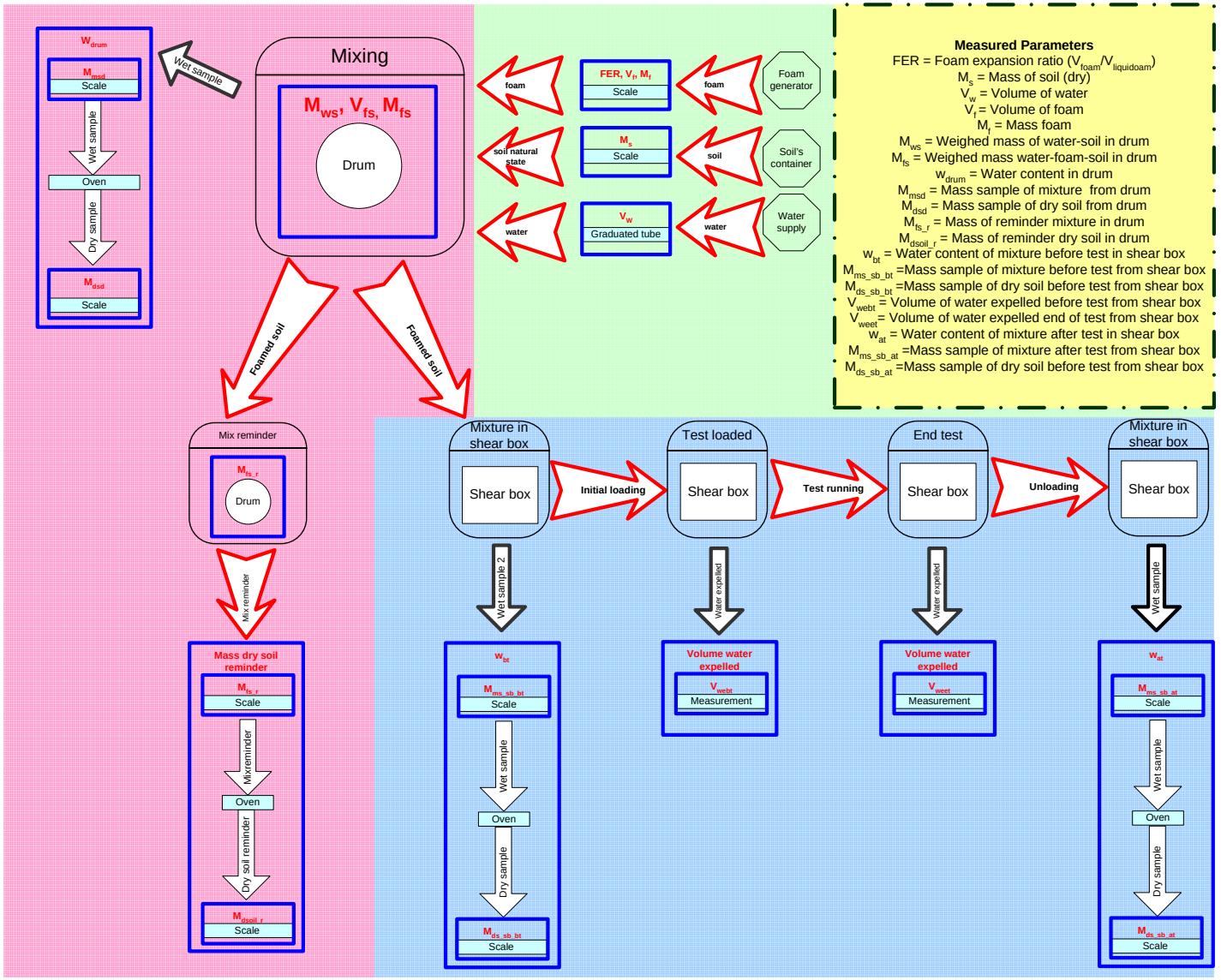

Figure 4.12. Scheme quality control Shear box test.

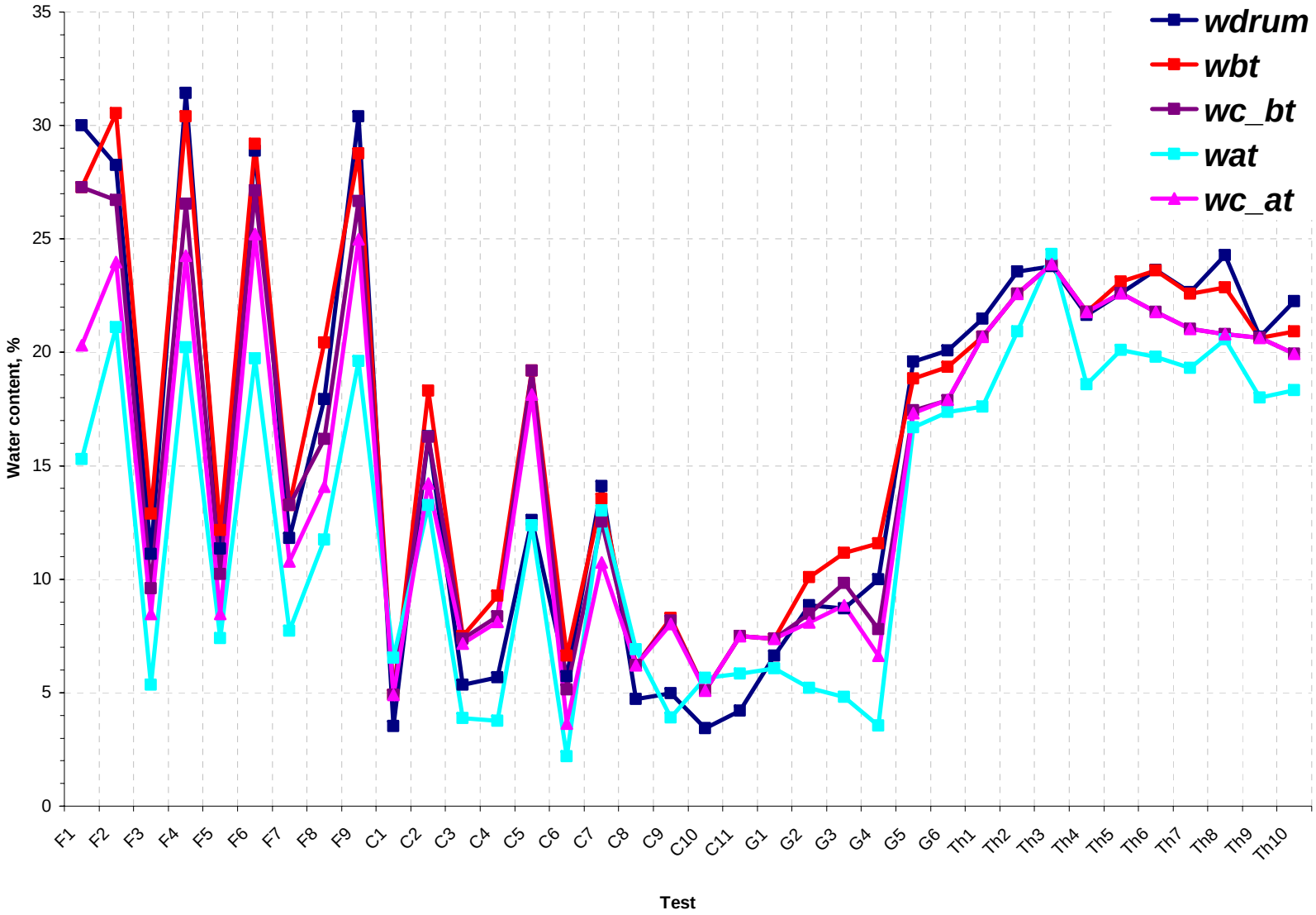

Figure 4.13. Quality control process: water content variation.

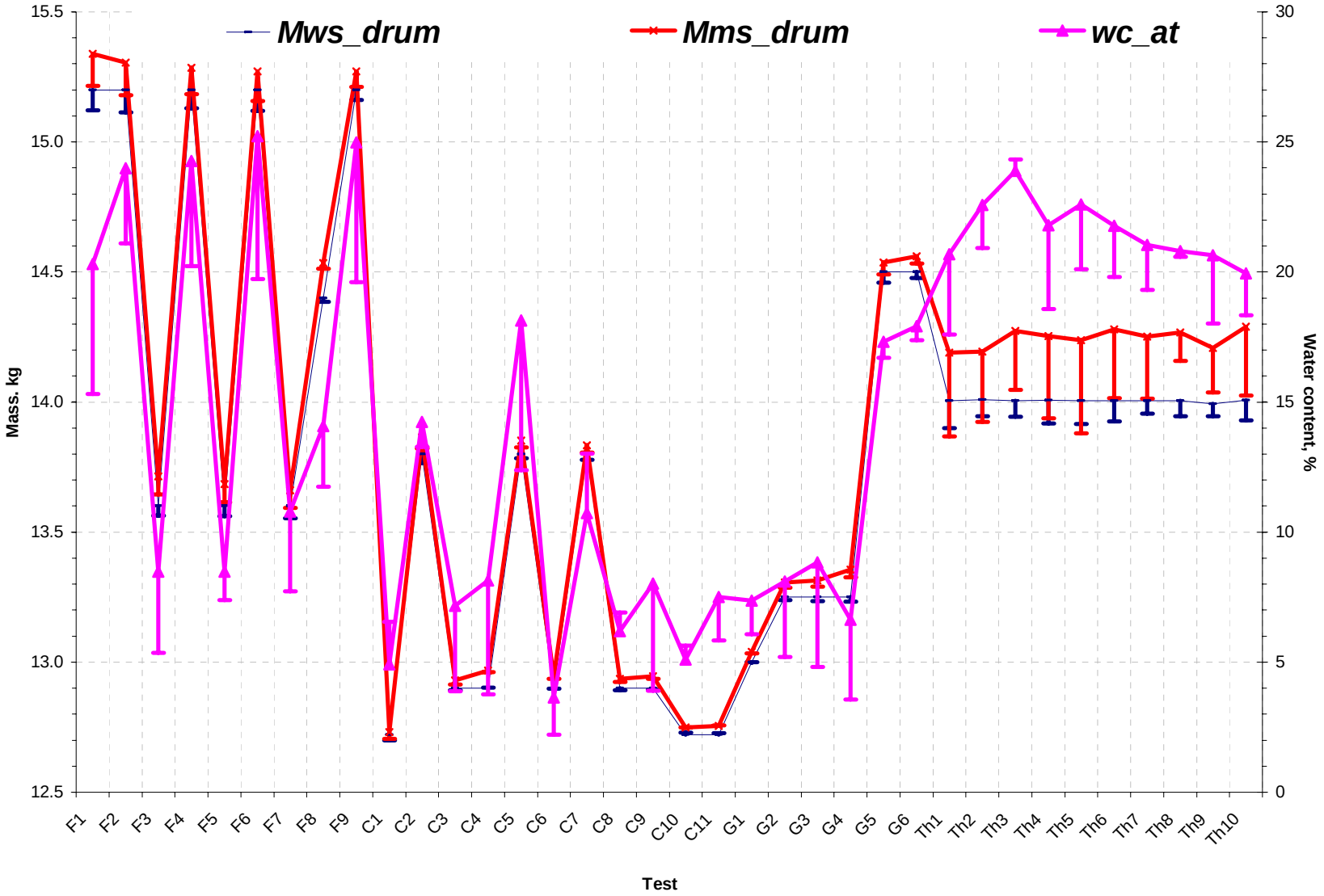

Figure 4.14. Quality control process: mass of water-soil, mass of water-foam-soil and calculated water content after test.

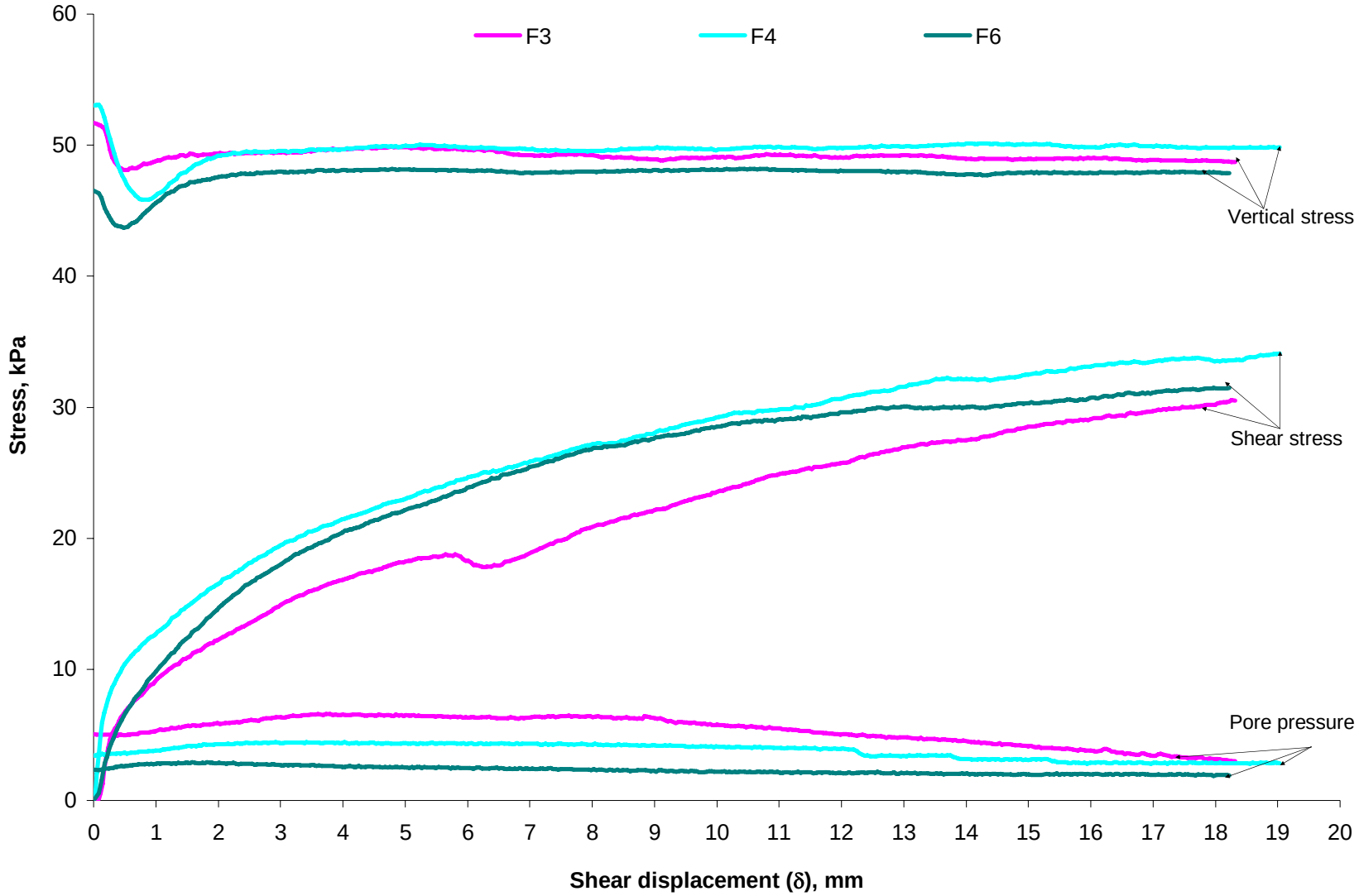

Figure 4.15. Shear stress, normal stress and pore water pressure measured for tests F3, F4 and F6.

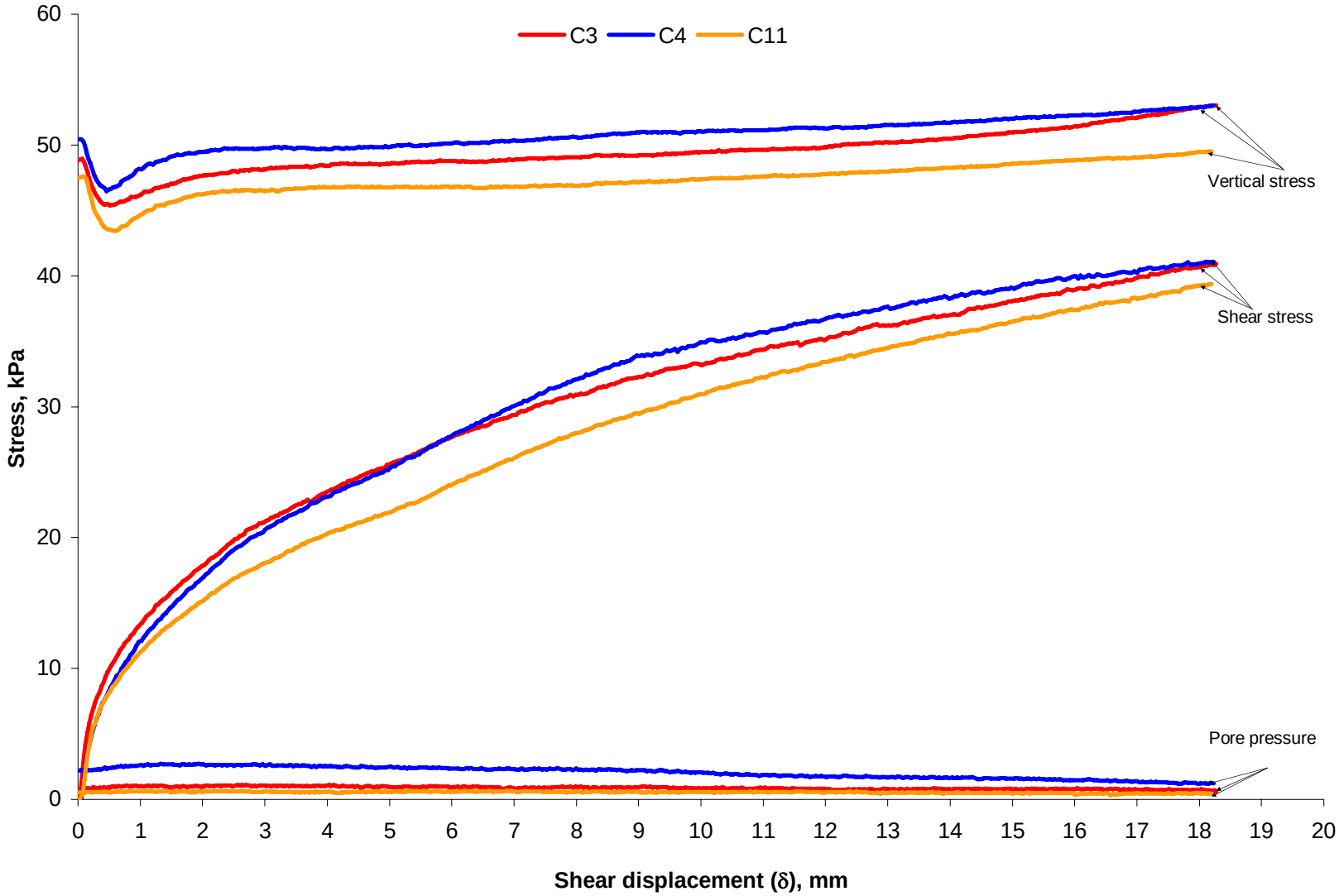

Figure 4.16. Shear stress, normal stress and pore water pressure measured for tests C3, C4 and C11.

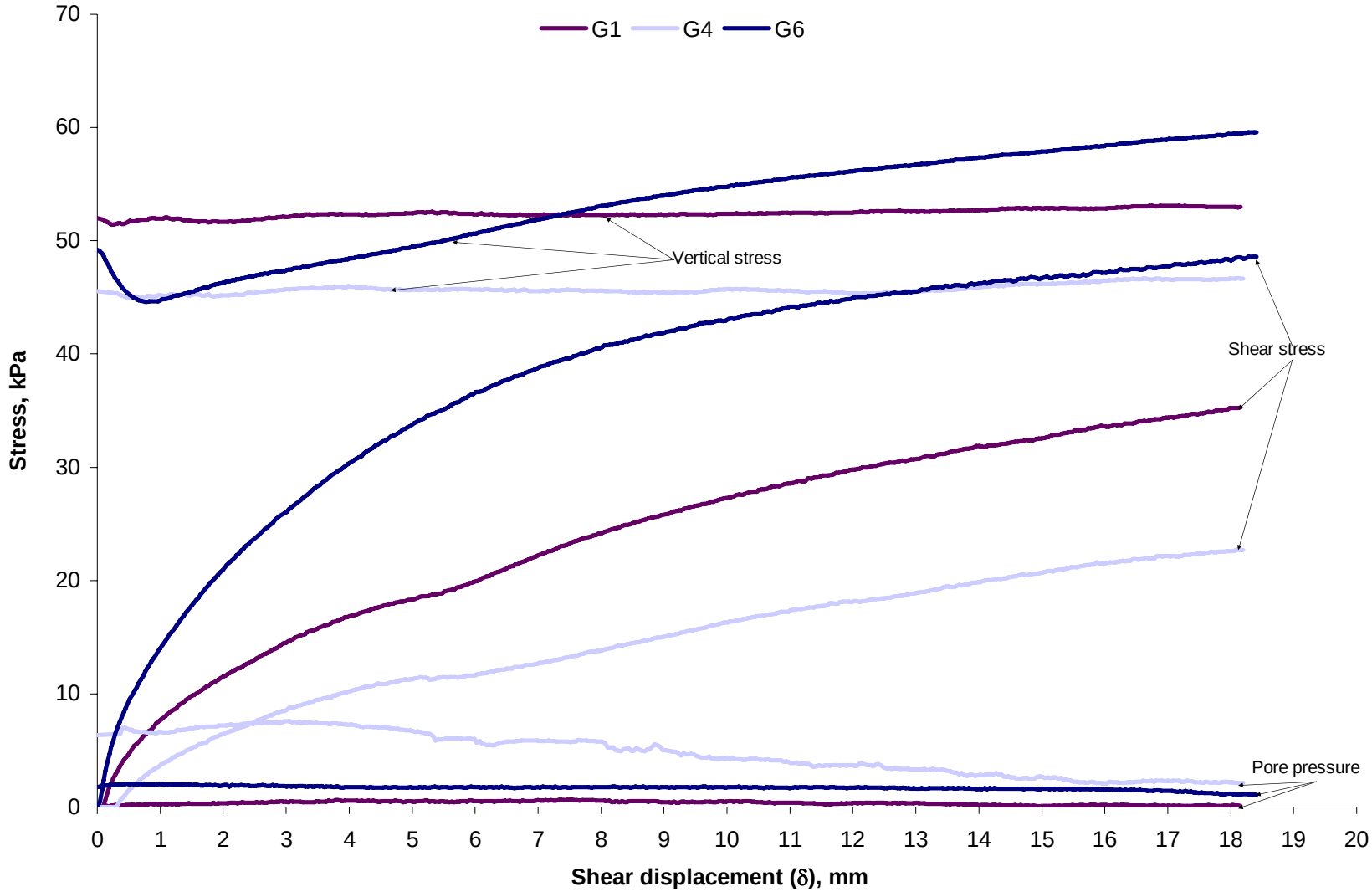

Figure 4.17. Shear stress, normal stress and pore water pressure measured for tests G1, G4 and G6.

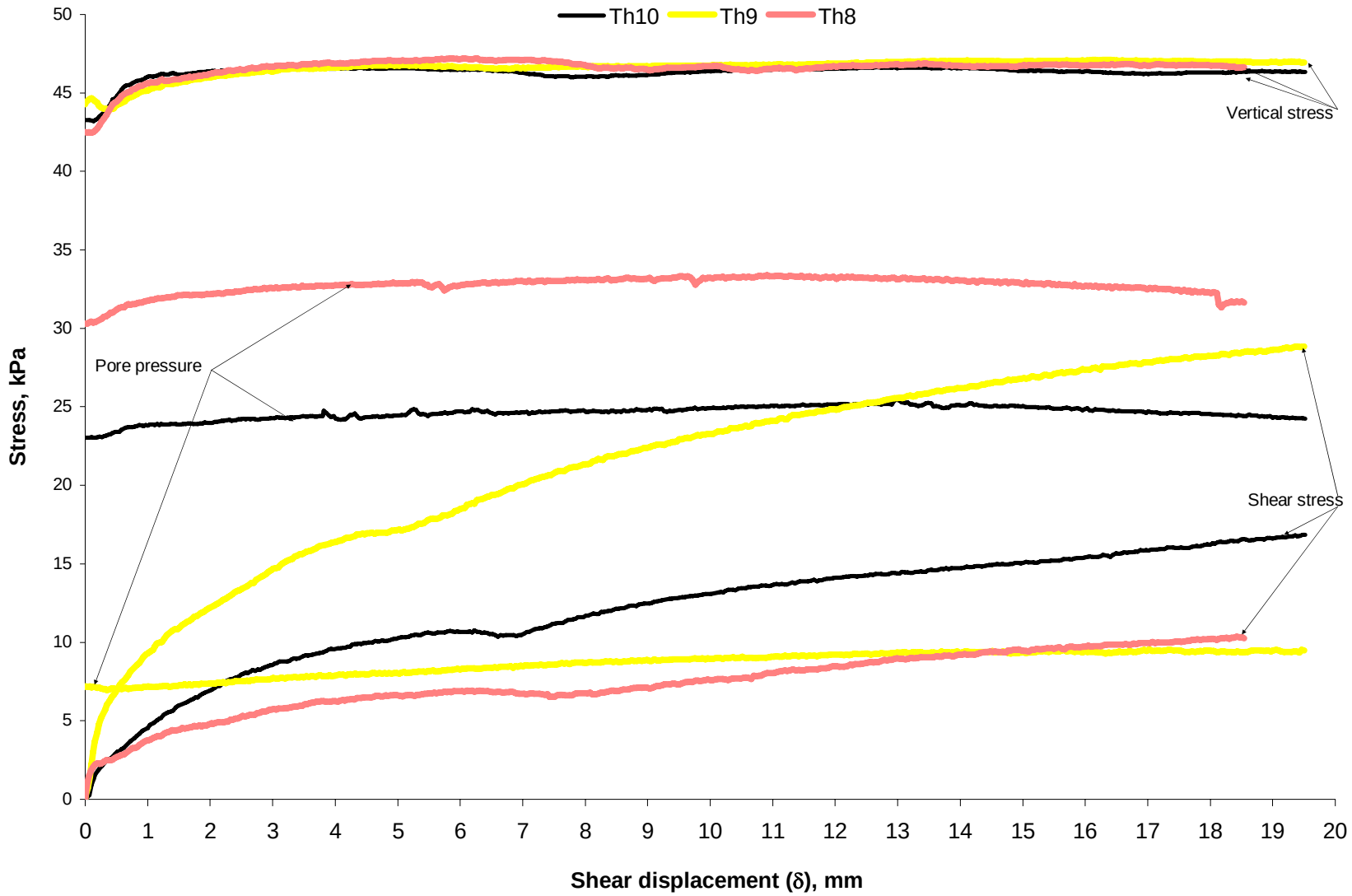

Figure 4.18. Shear stress, normal stress and pore water pressure measured for tests Th8, Th9 and Th10.

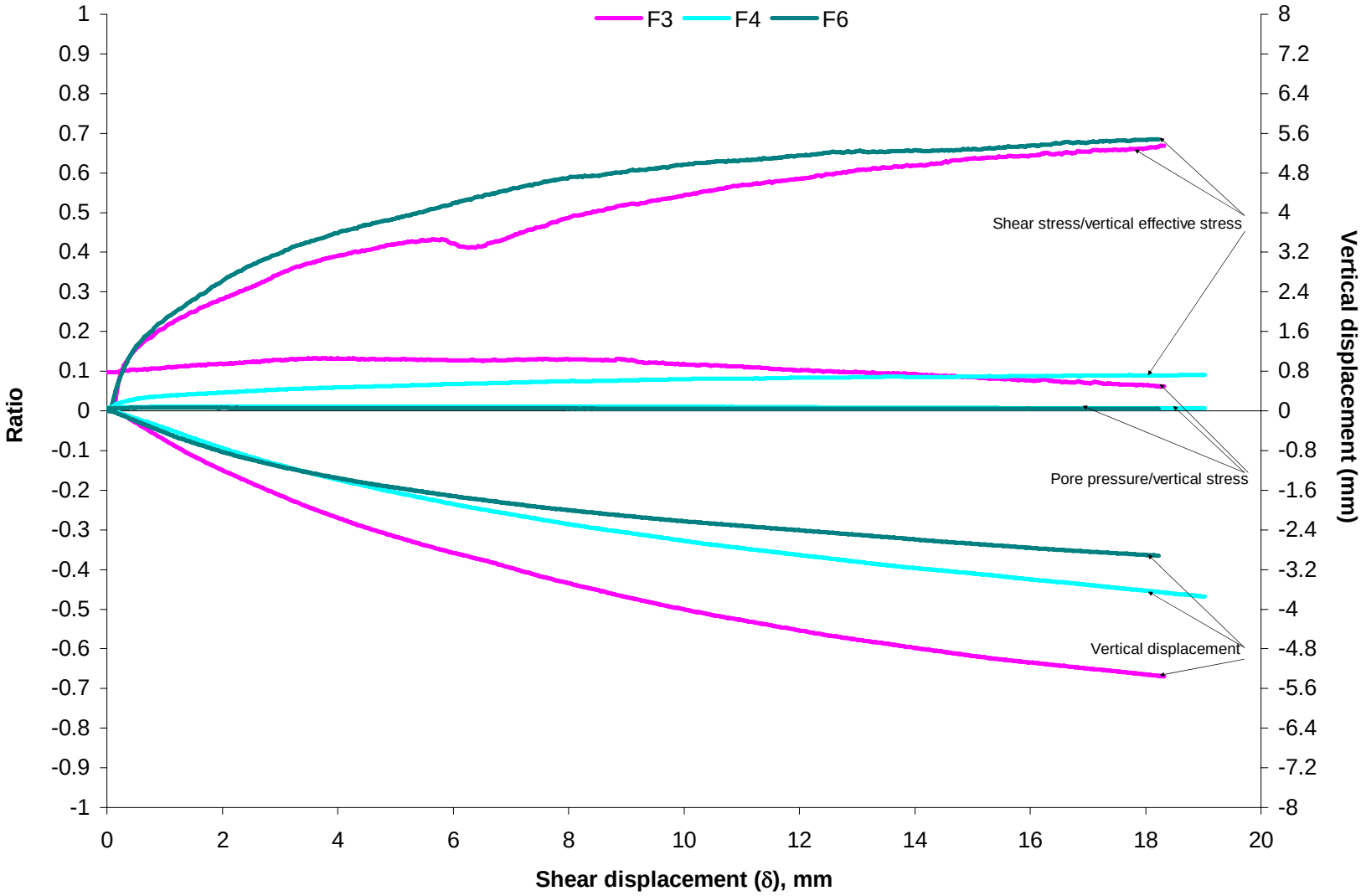

Figure 4.19. Shear stress/ vertical effective stress ratio, pore pressure/ vertical stress ratio and vertical displacement for tests F3, F4 and F6.

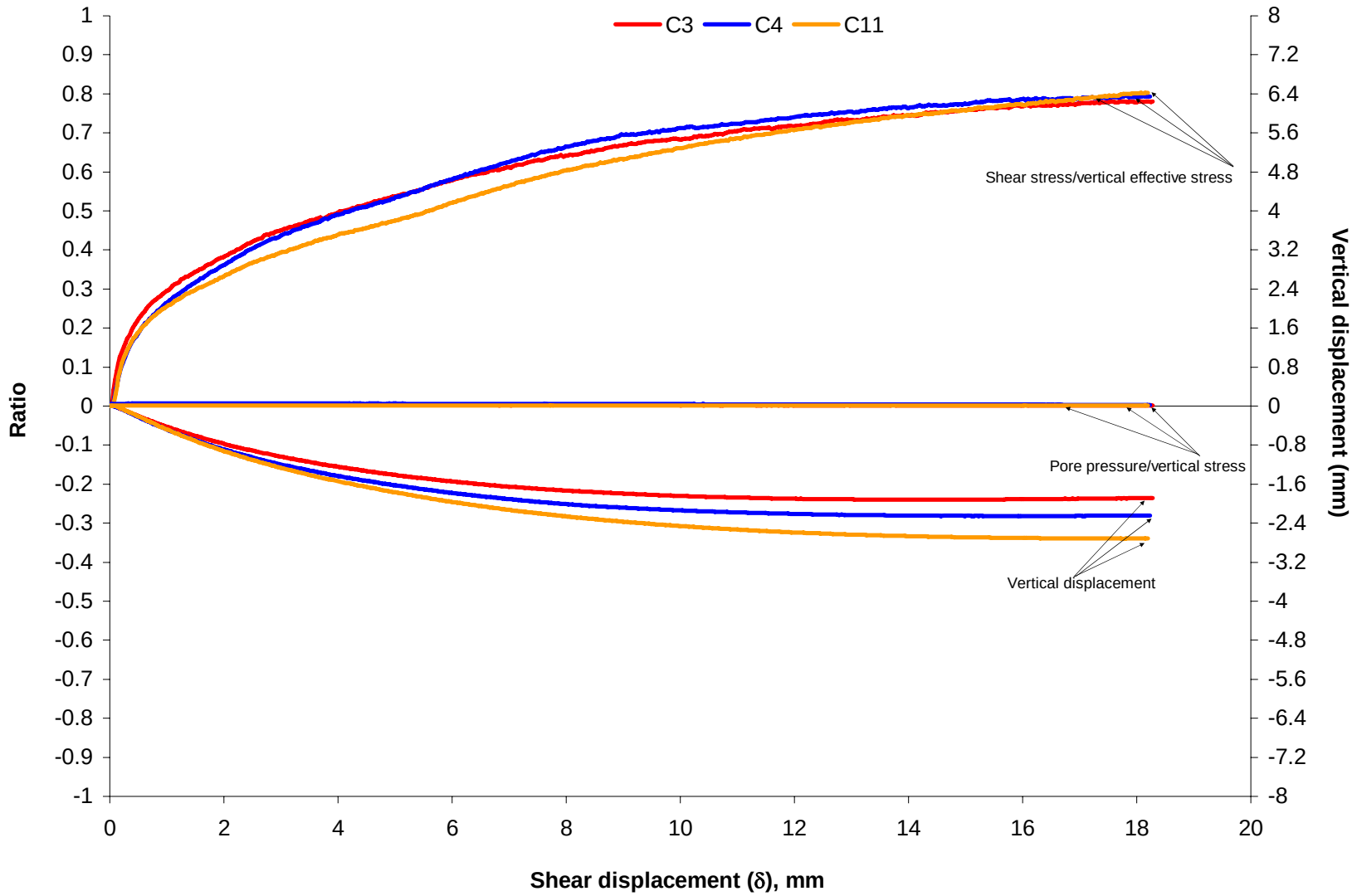

Figure 4.20. Shear stress/ vertical effective stress ratio, pore pressure/ vertical stress ratio and vertical displacement for tests C3, C4 and C11.

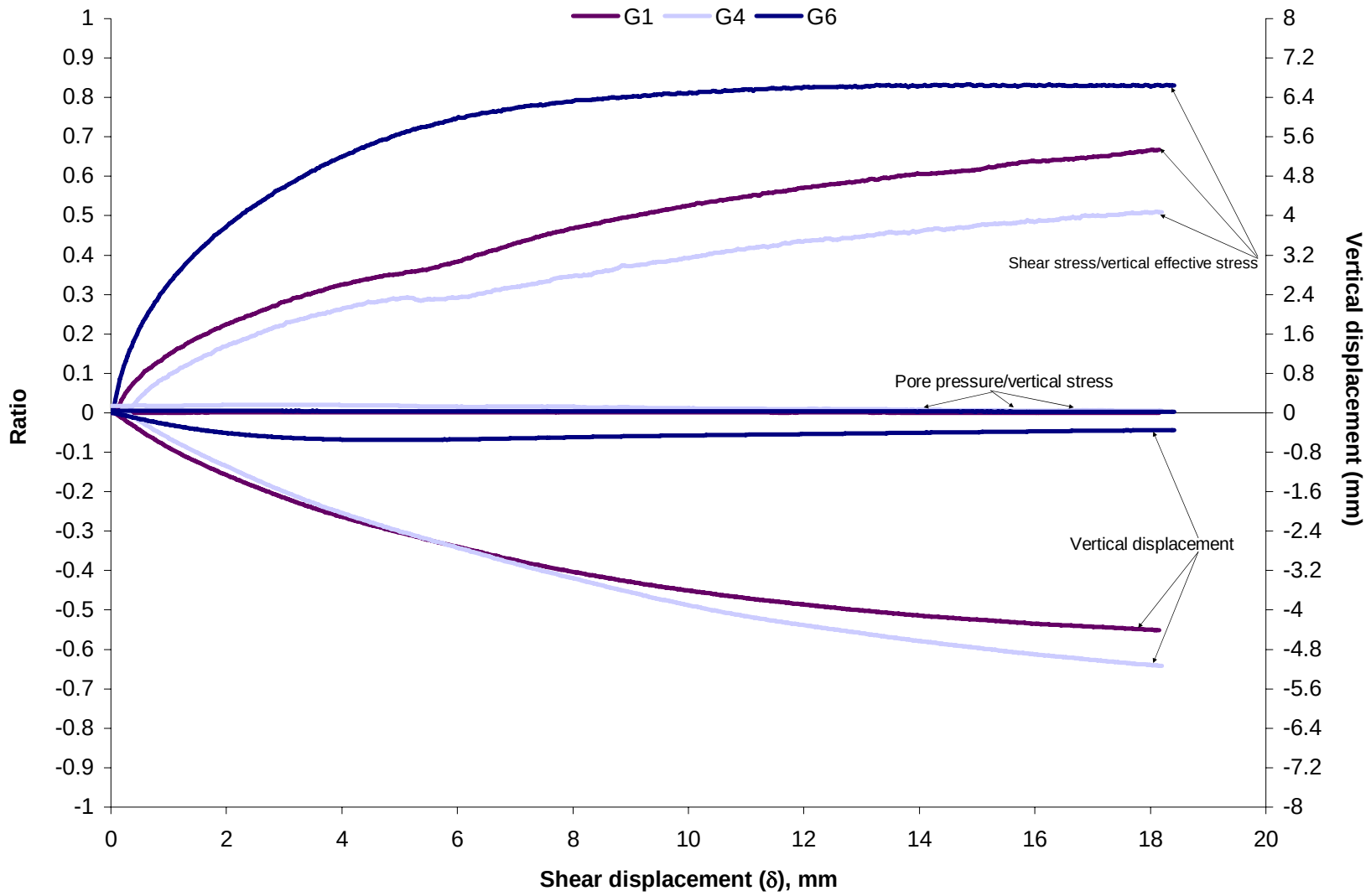

Figure 4.21. Shear stress/ vertical effective stress ratio, pore pressure/ vertical stress ratio and vertical displacement for tests G1, G4 and G6.

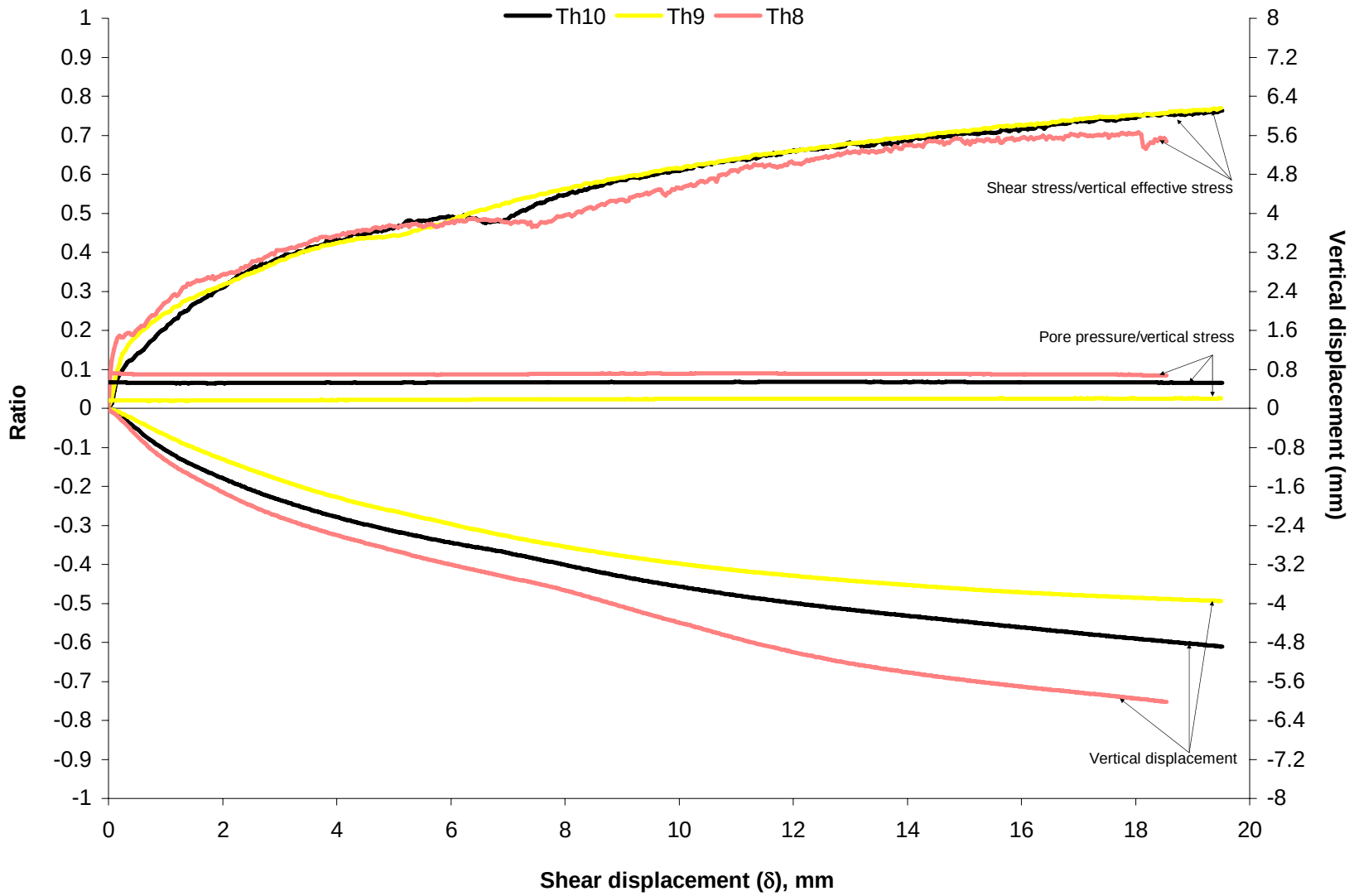

Figure 4.22. Shear stress/ vertical effective stress ratio, pore pressure/ vertical stress ratio and vertical displacement for tests Th8, Th9 and Th10.

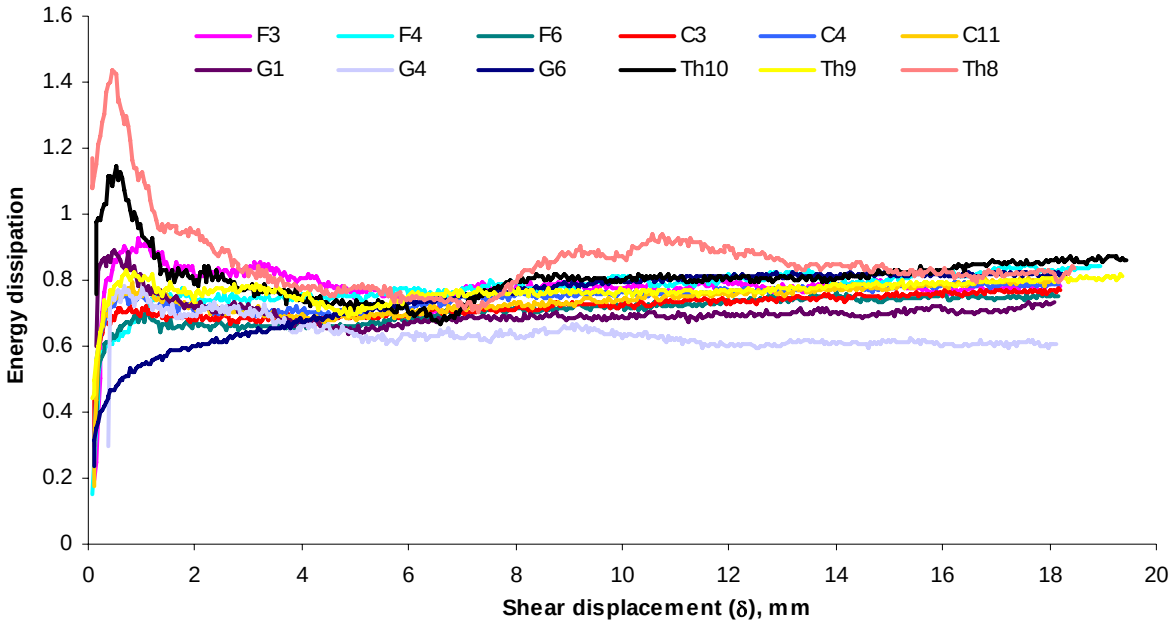

Figure 4.23. Energy dissipation for F3, F4, F6, C3, C4, C11, G1, G4, G6, Th8, Th9 and Th10.

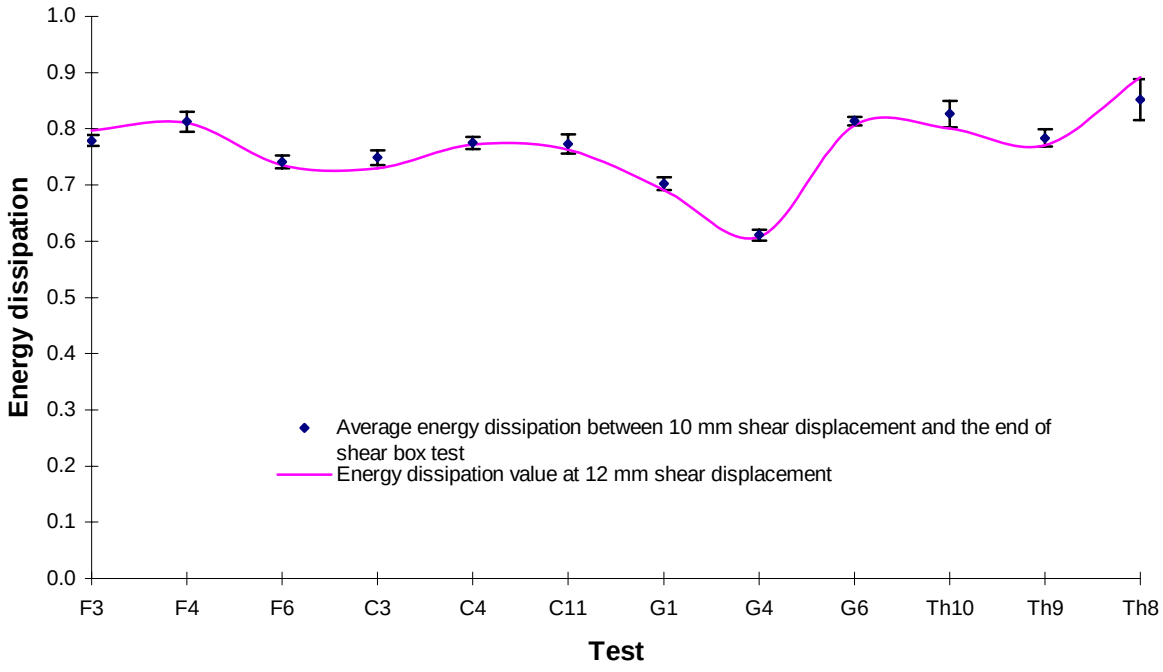

Figure 4.24. Energy dissipation for F3, F4, F6, C3, C4, C11, G1, G4, G6, Th8, Th9 and Th10 for shear displacement after 10 mm and at 12 mm of shear displacement..

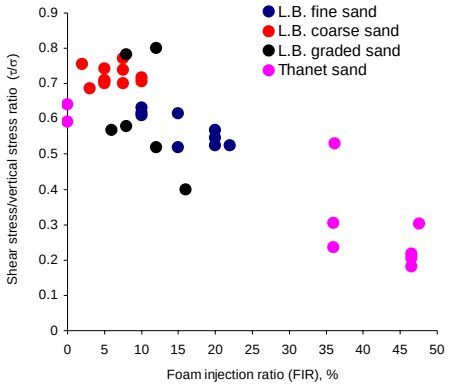

Figure 4.25. Variation of shear stress/vertical stress ratio with FIR at 12 (mm) of horizontal displacement through the shear box test (Tests with Condition "ok" plotted).

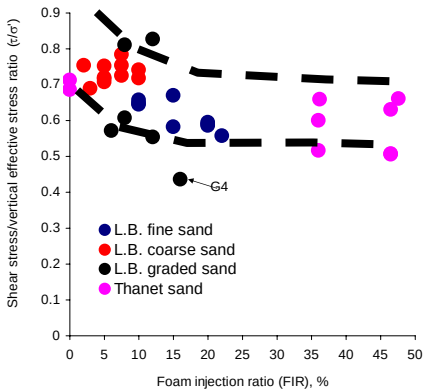

Figure 4.26. Variation of shear stress/vertical effective stress ratio with FIR at 12 (mm) of horizontal displacement through the shear box test (Tests with Condition "ok" plotted).

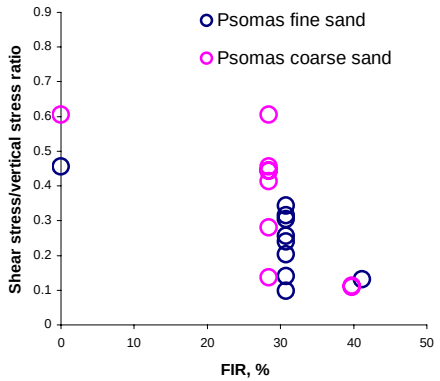

Figure 4.27. Results of shear box tests of Psomas (Psomas, 2001).

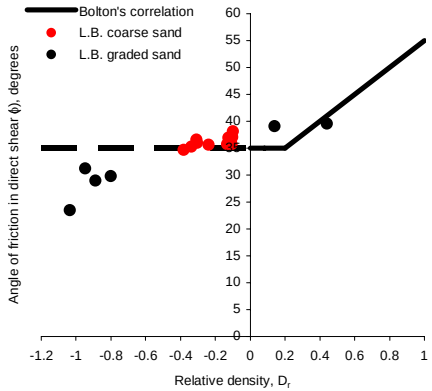

Figure 4.28. Variation of angle of friction with relative density at 12 (mm) of horizontal displacement through the shear box test for sands with coarse content ≥ 50%.(Tests with Condition "ok" plotted).

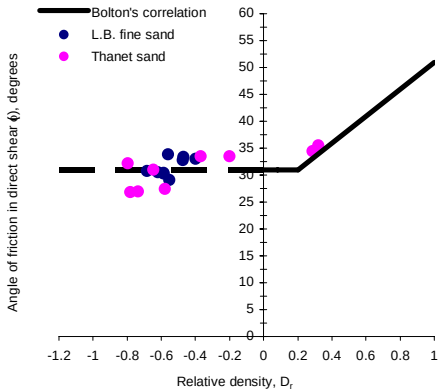

Figure 4.29. Variation of angle of friction with relative density at 12 (mm) of horizontal displacement through the shear box test for sands with fine content ≥ 50% and no coarse content. (Tests with Condition "ok" plotted).

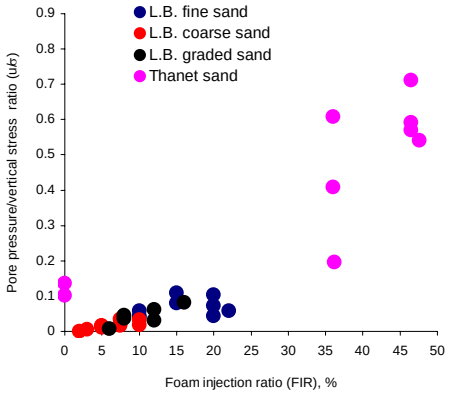

Figure 4.30. Variation of pore pressure/vertical stress ratio with FIR at 12 (mm) of horizontal displacement through the shear box test (Tests with Condition "ok" plotted).

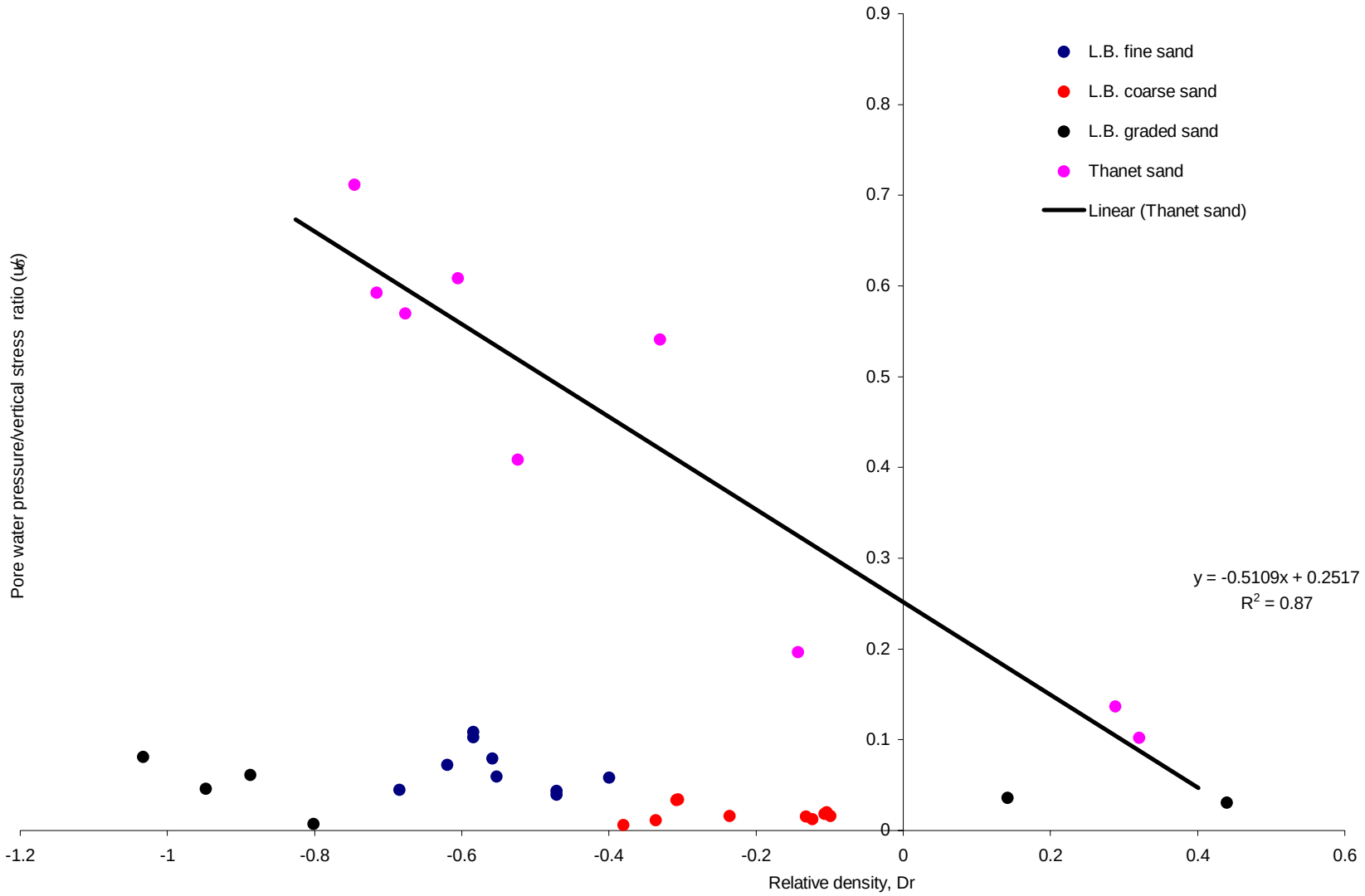

Figure 4.31. Variation of pore pressure/vertical stress ratio with Relative density at 12 (mm) of horizontal displacement through the shear box test (Tests with Condition "ok" plotted).

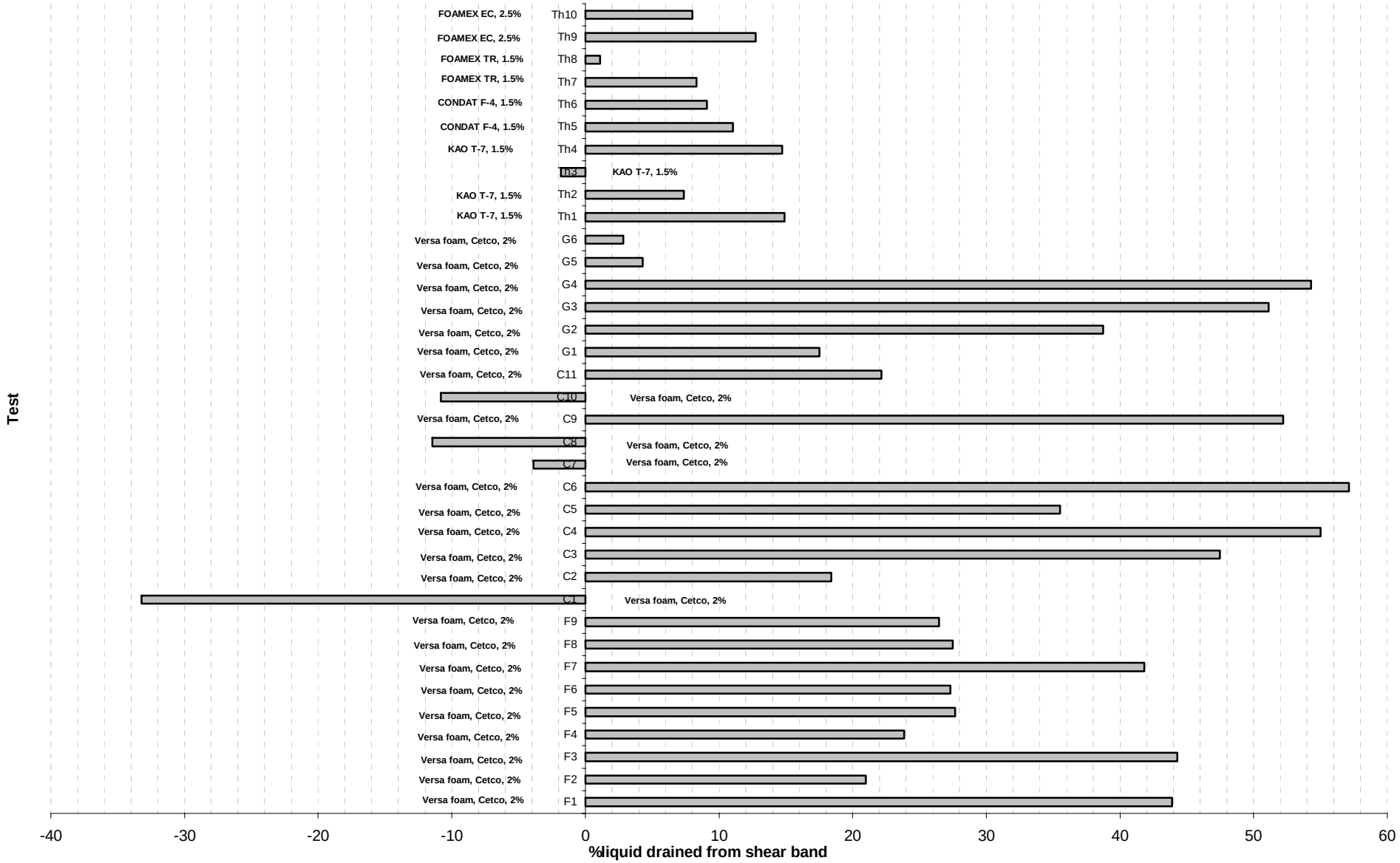

Figure 4.32. Drainage of liquid from shear band: Test vs % liquid drained fro shear band.

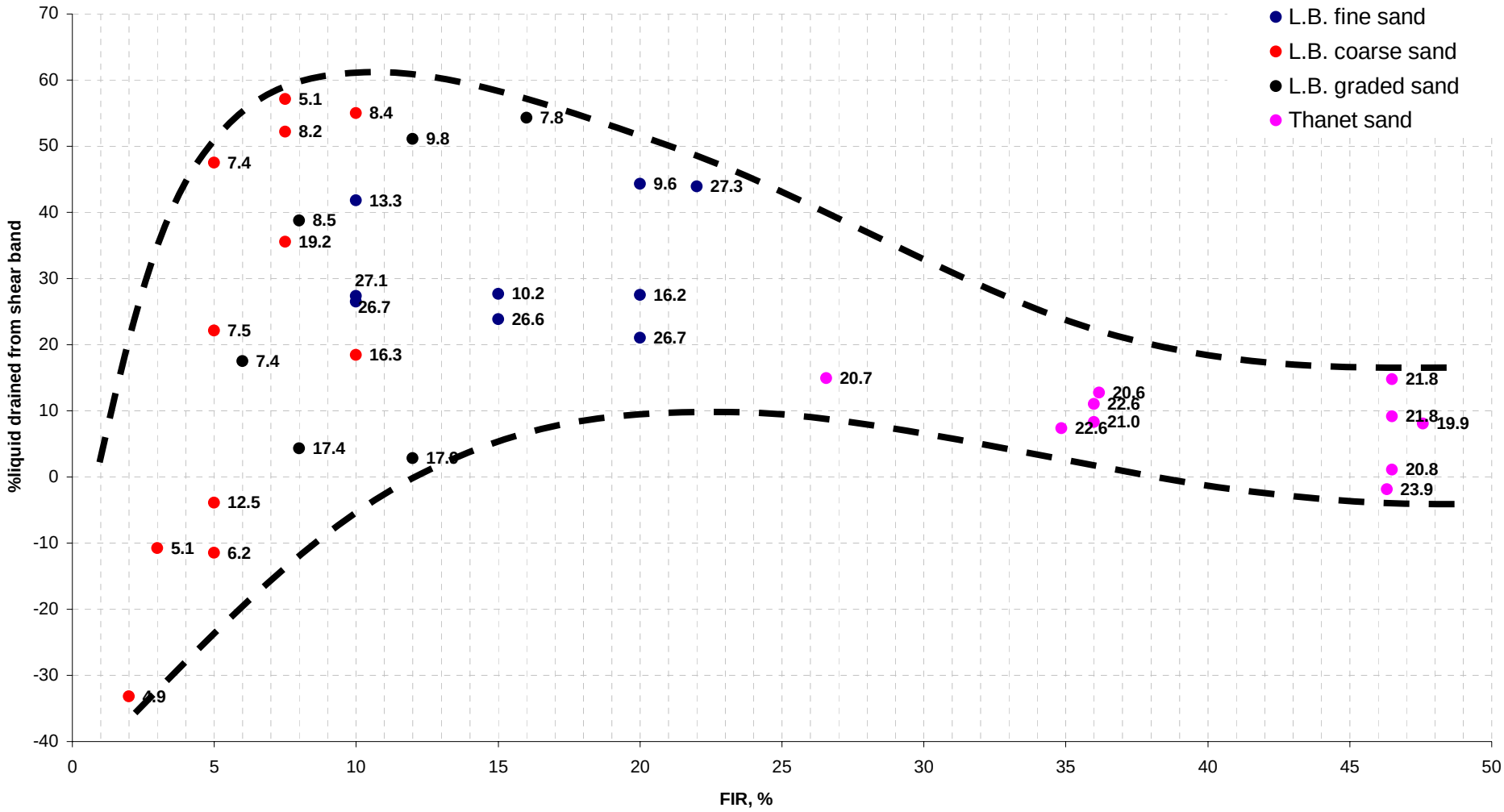

Figure 4.33. Drainage of liquid from shear band: %Liquid drained from shear band vs FIR.

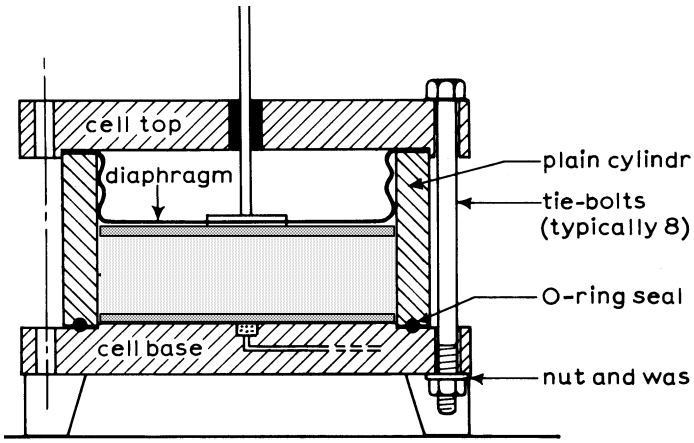

Figure 5.1. Main features of 250 mm diameter Rowe hydraulic consolidation cell (Head, 1986)

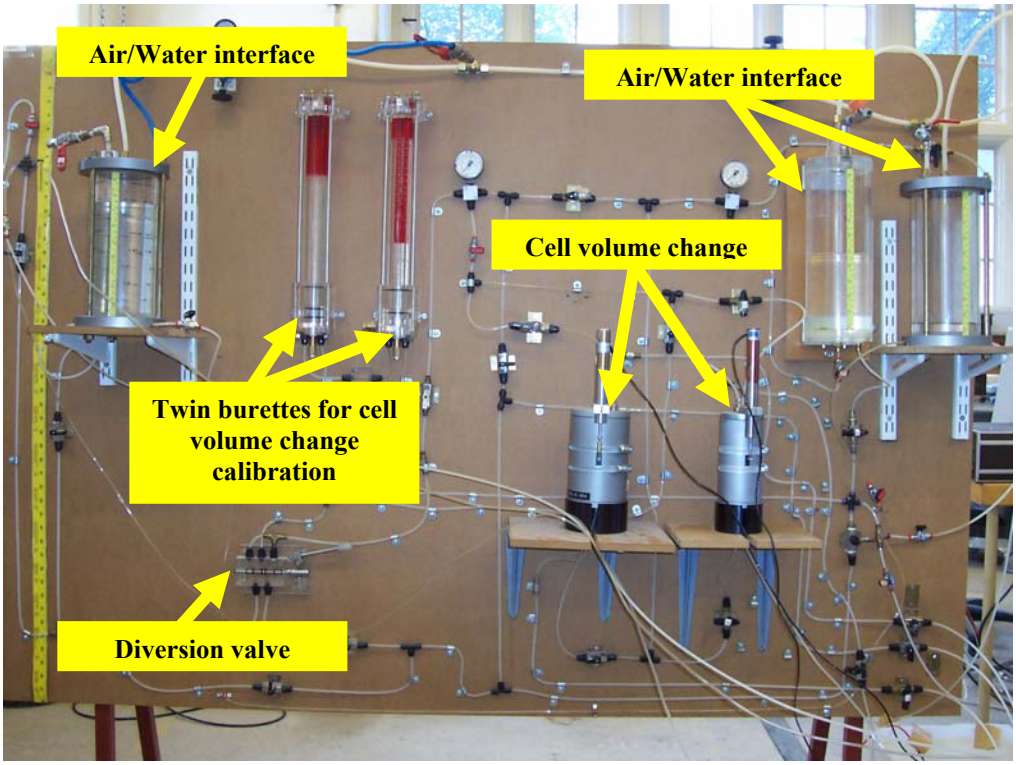

Figure 5.2. Front view piping system which connects to MAPC.

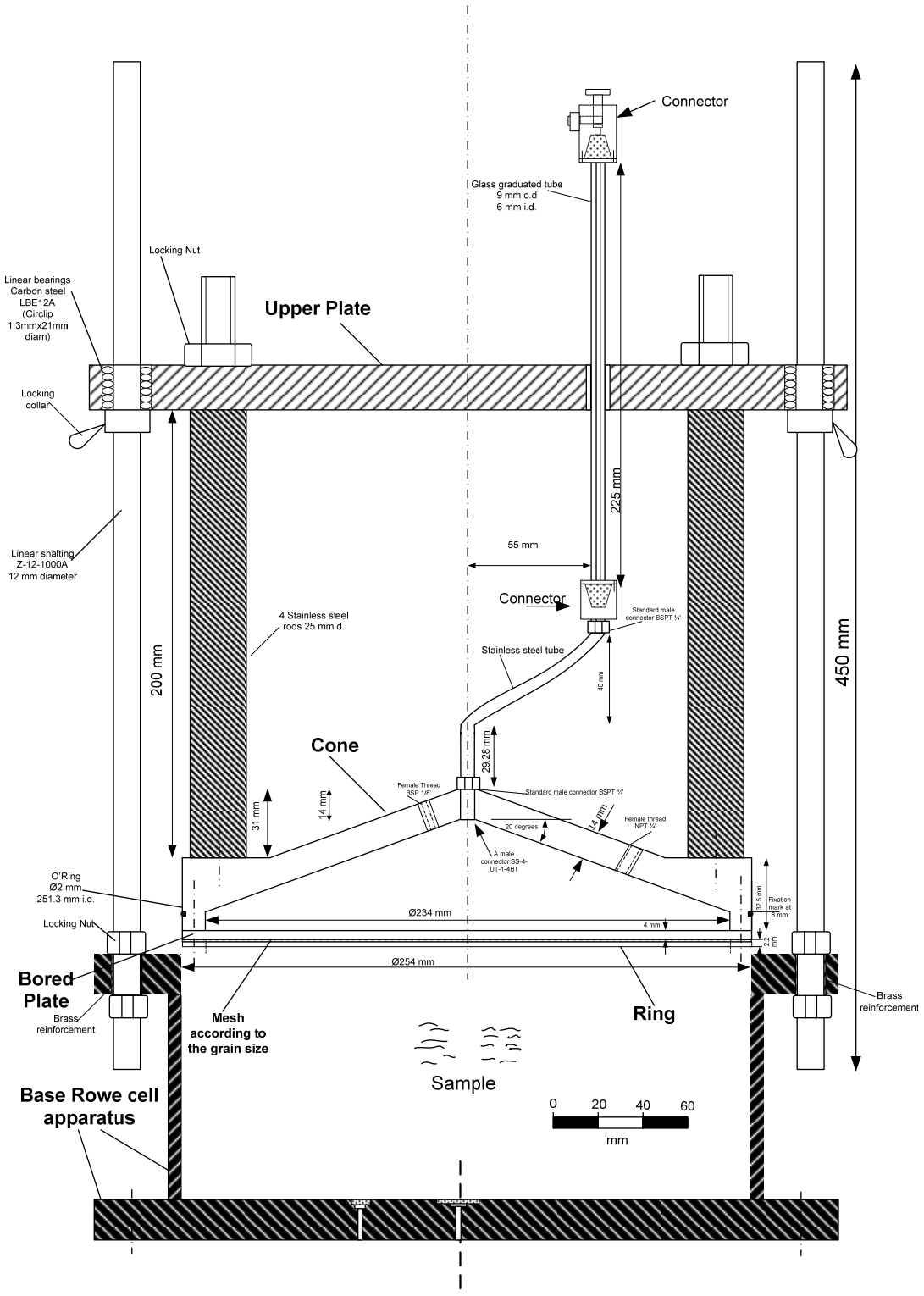

Figure 5.3. MAPC section.

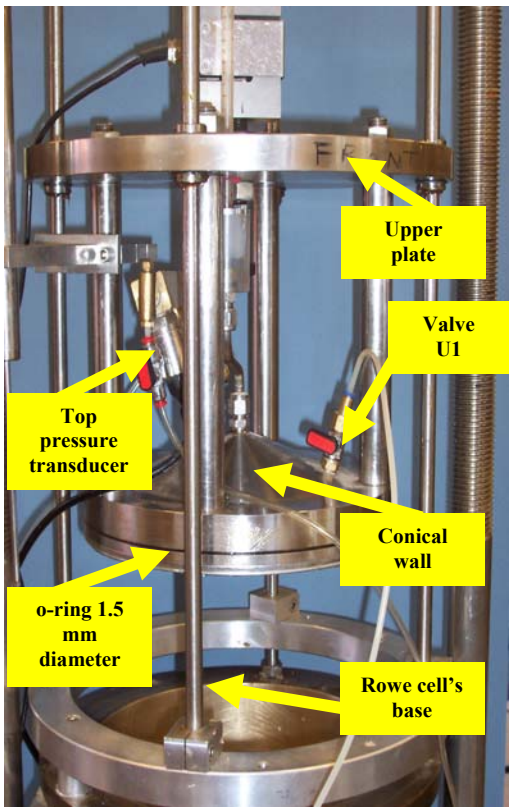

Figure 5.4. MAPC top view.

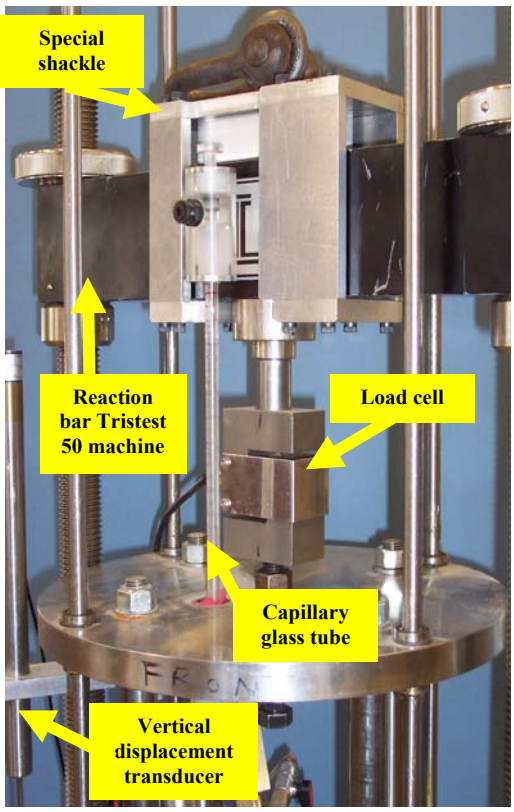

Figure 5.5. MAPC top: upper plate together with Tritest 50 reaction bar.

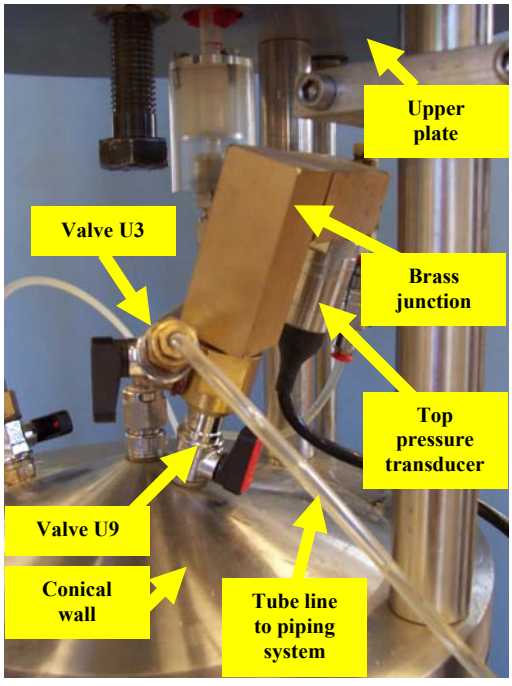

Figure 5.6. MAPC top: gap between upper plate and conical wall magnified.

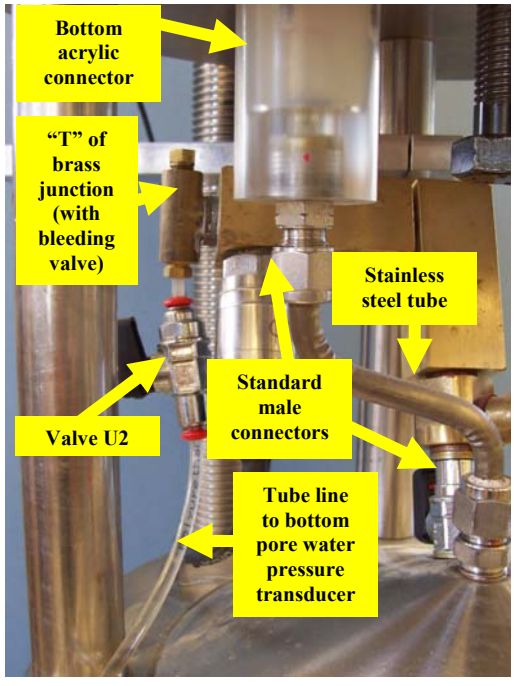

Figure 5.7. New capillary tube system: stainless steel tube and bottom acrylic connector.

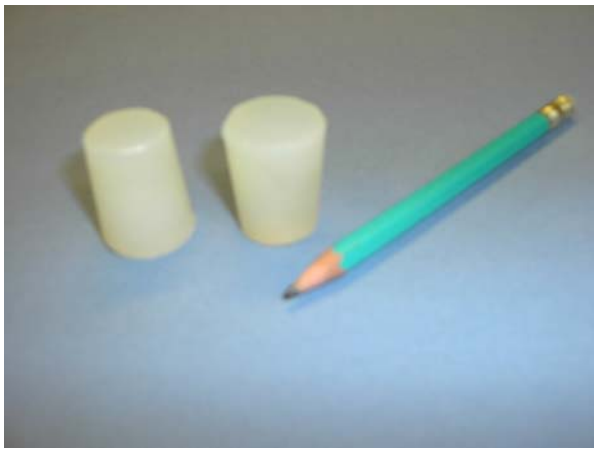

Figure 5.8. Silicone rubber stoppers.

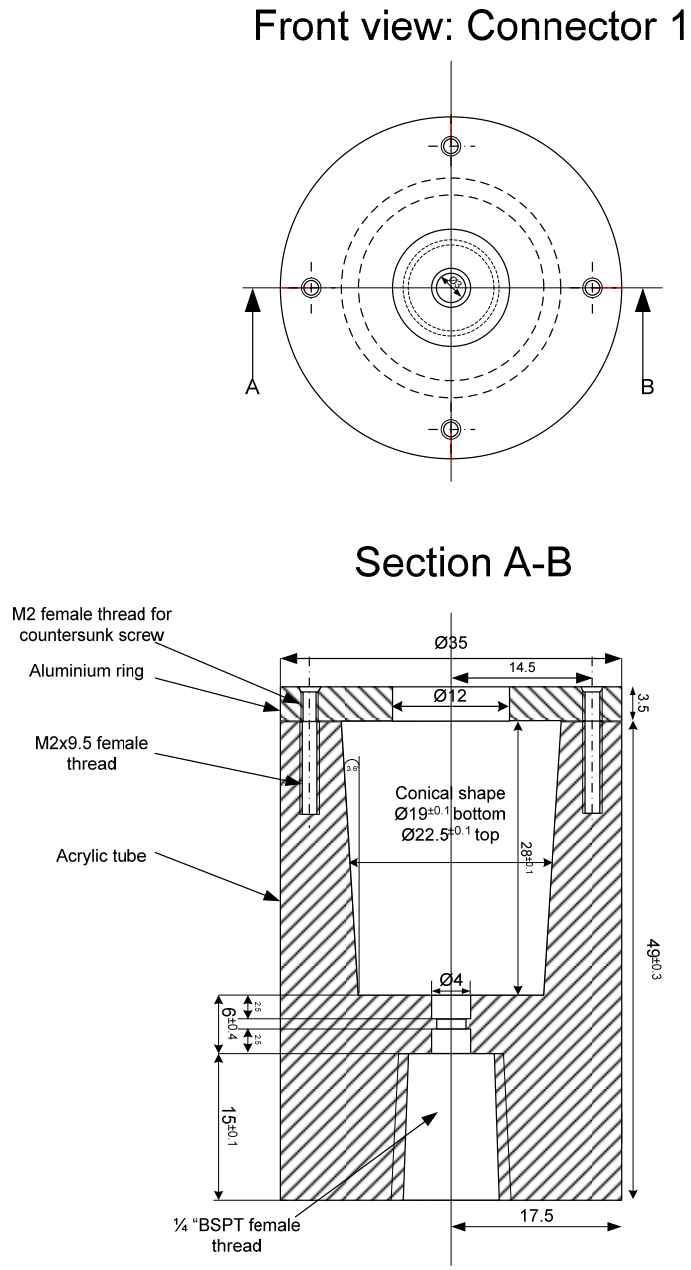

Figure 5.9. New capillary tube system: bottom connector (all units in millimetres).

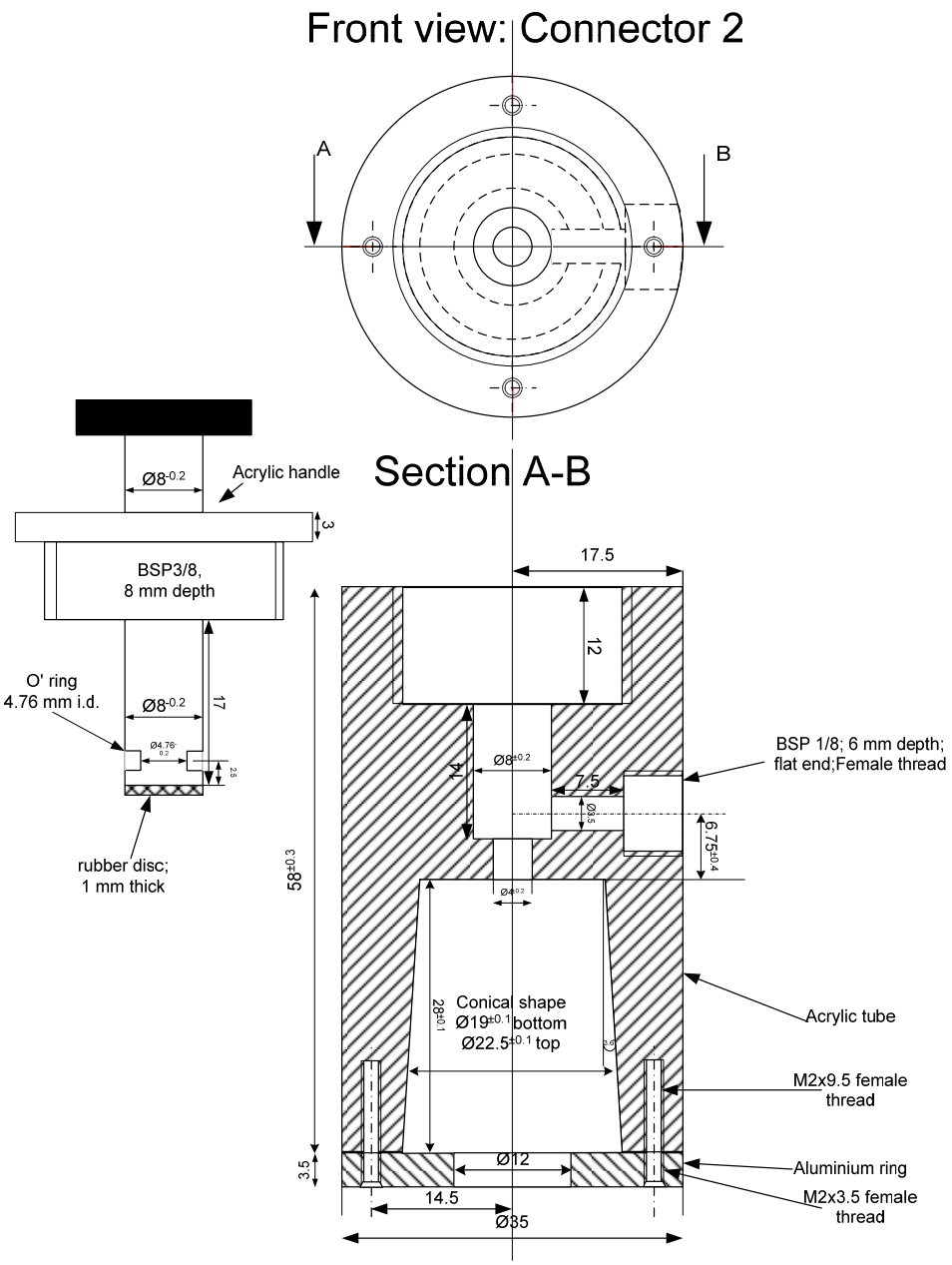

Figure 5.10. New capillary tube system: top connector (all units in millimetres).

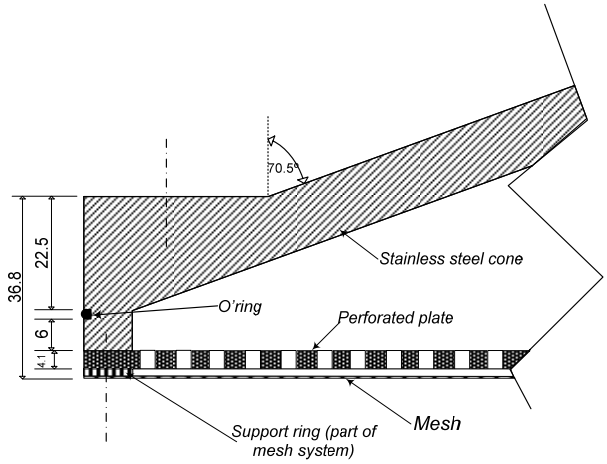

Figure 5.11. MAPC top section: symmetrical cut which shows the single o-rings arrangement (all units in millimetres).

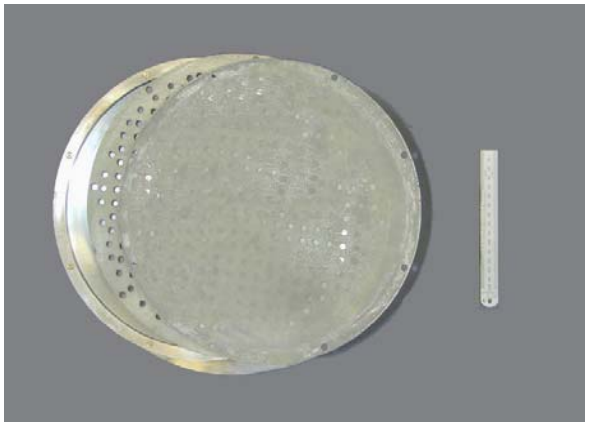

Figure 5.12. Frontal view of (left to right) inverted conical wall, perforated plate and filter mesh.

Figure 5.13. Side view of inverted conical wall and (left to right) perforated plate and filter mesh

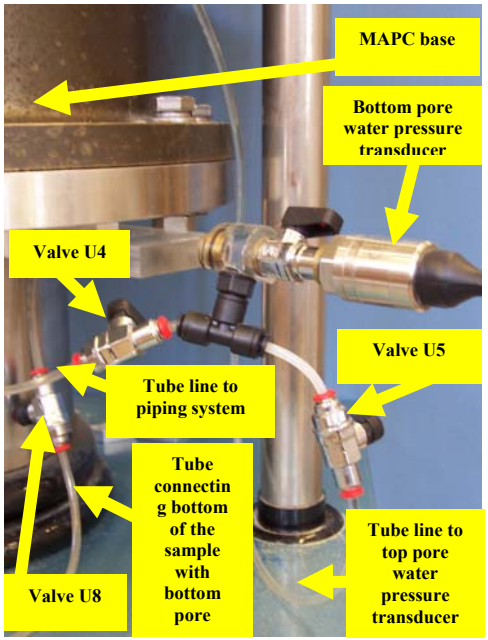

Figure 5.14. MAPC bottom pore water pressure transducer

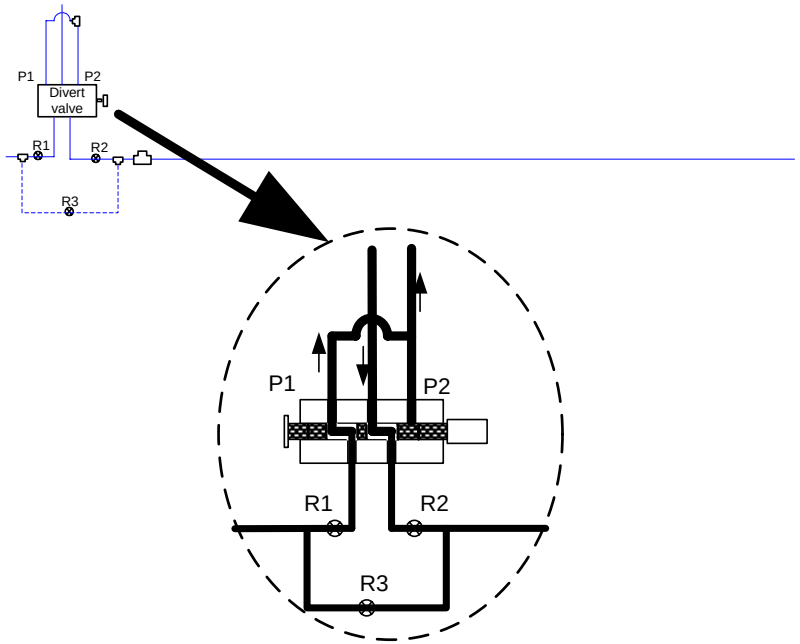

Figure 5.15. Diversion valve of MAP consolidometer system

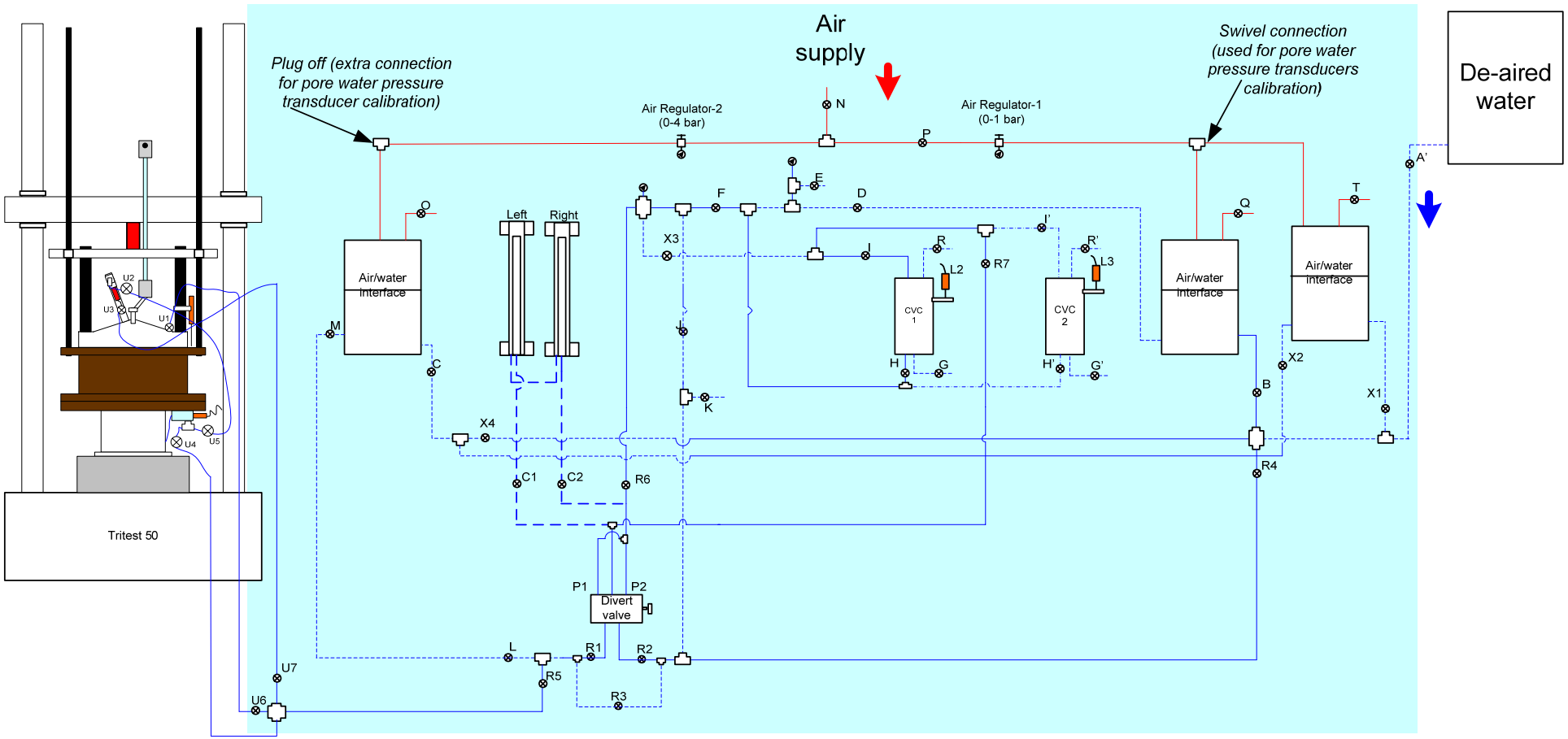

Figure 5.16. Overview of entire MAP consolidometer system

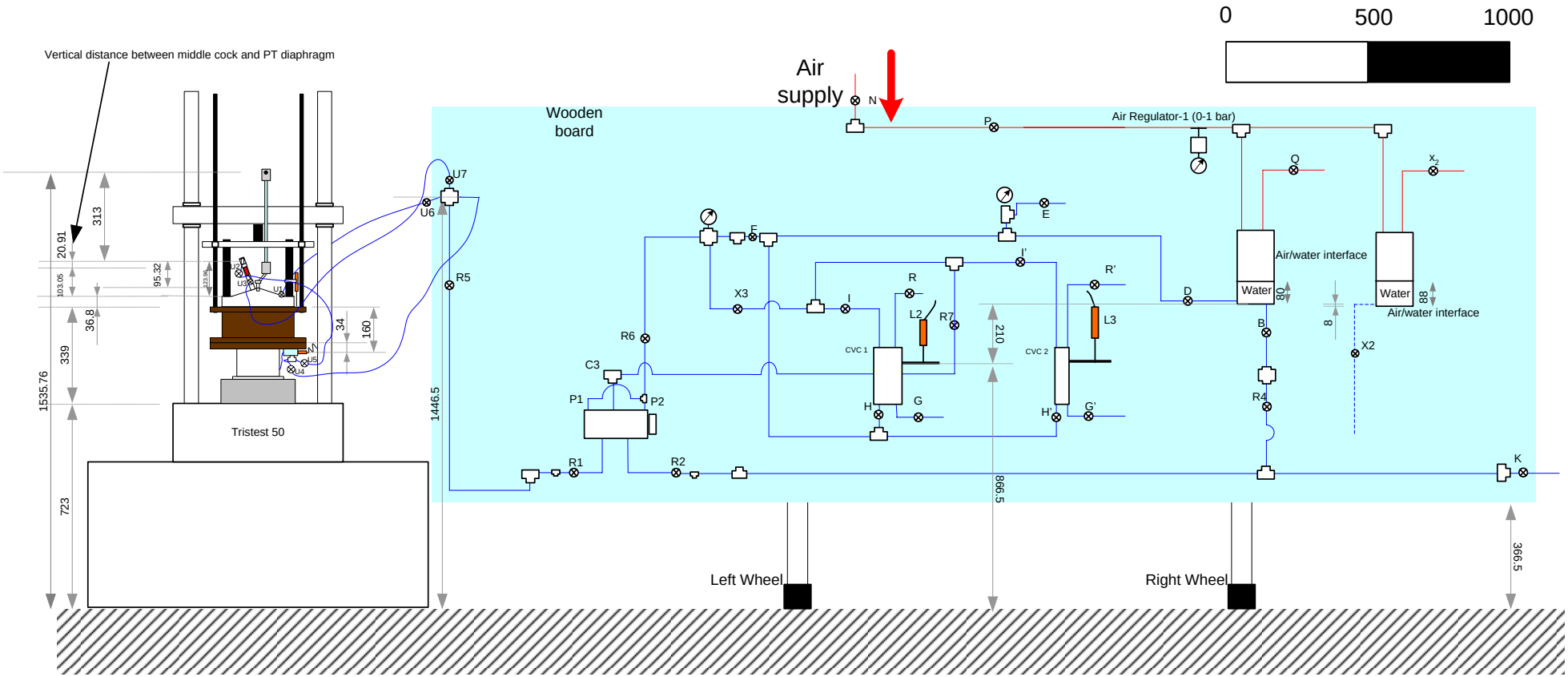

Figure 5.17. Main heights in MAP consolidometer system (all units in millimetres)

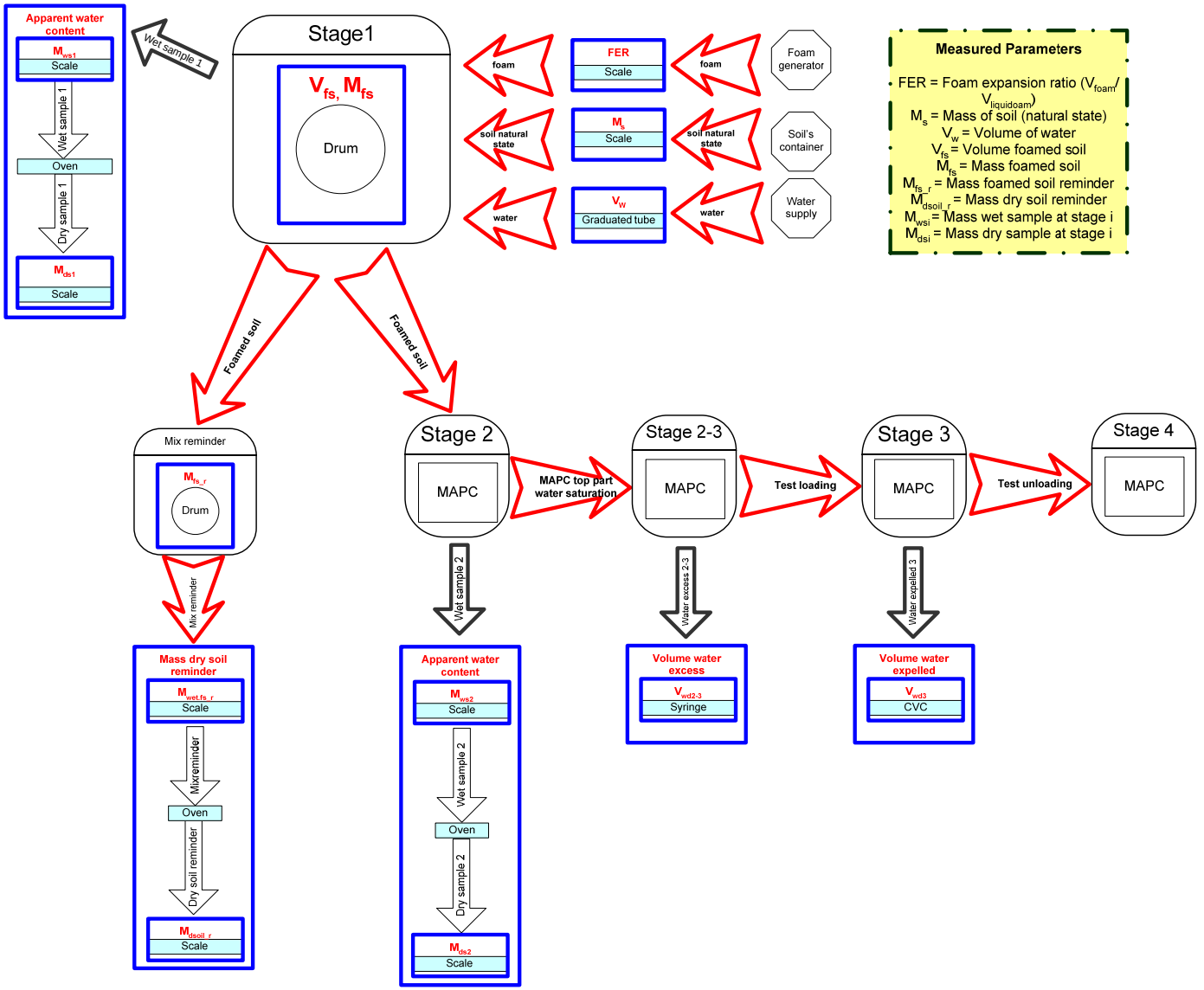

Figure 5.18. Scheme quality control compressibility test.

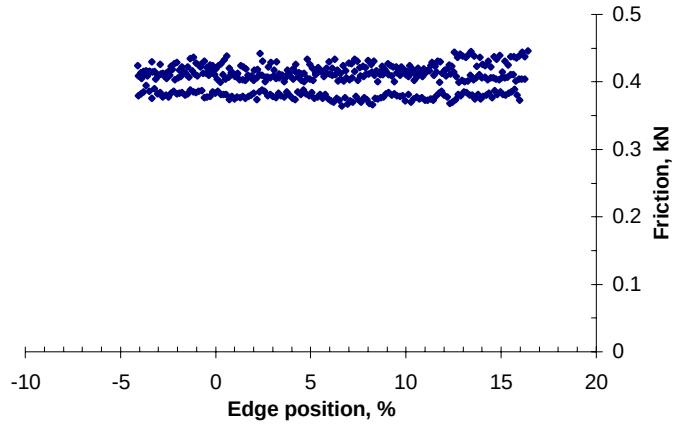

Figure 5.19. Friction- loading, displacement rate 5 mm/min-

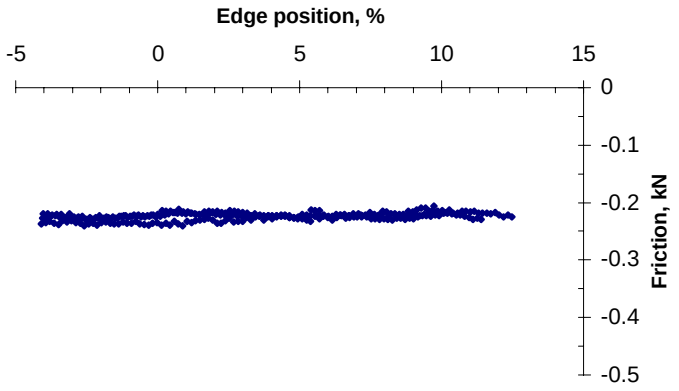

Figure 5.20. Friction- unloading, displacement rate 5 mm/min-

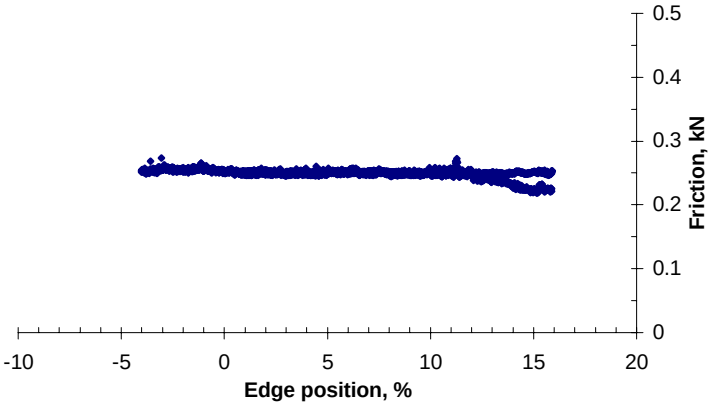

Figure 5.21. Friction- loading, displacement rate 0.3 mm/min

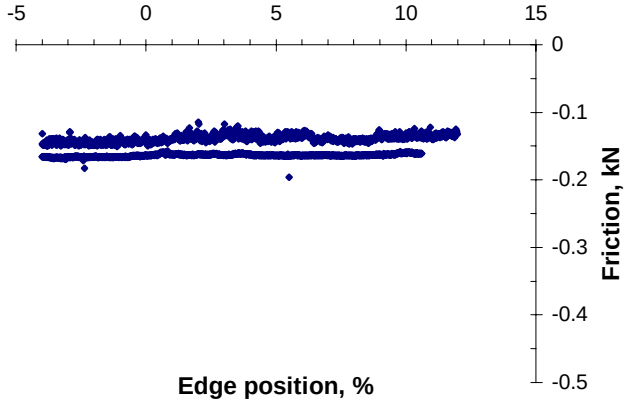

Figure 5.22. Friction- unloading, displacement rate 0.3 mm/min-

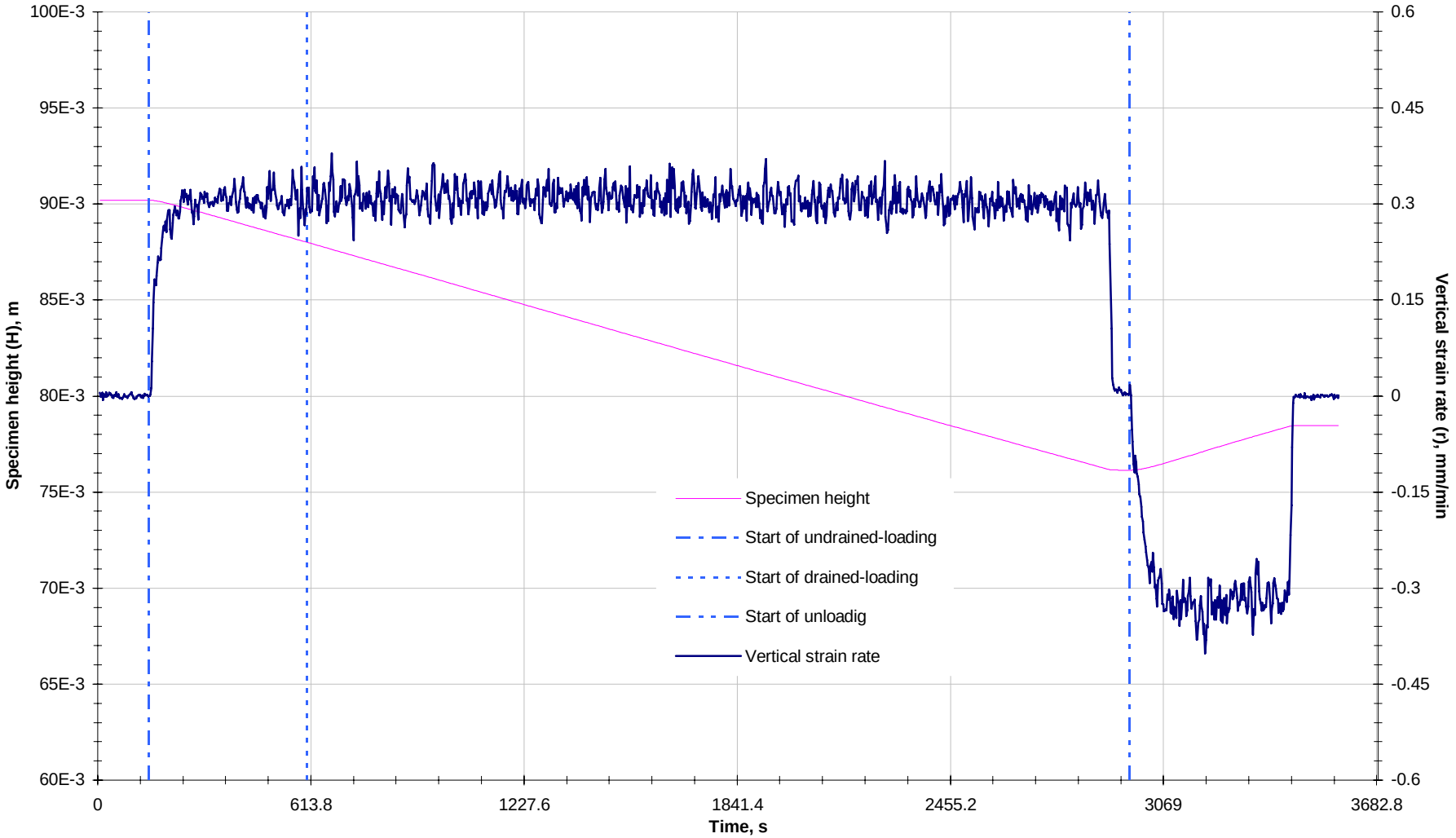

Figure 5.23. Specimen height and vertical displacement rate. Finesand13foamR.

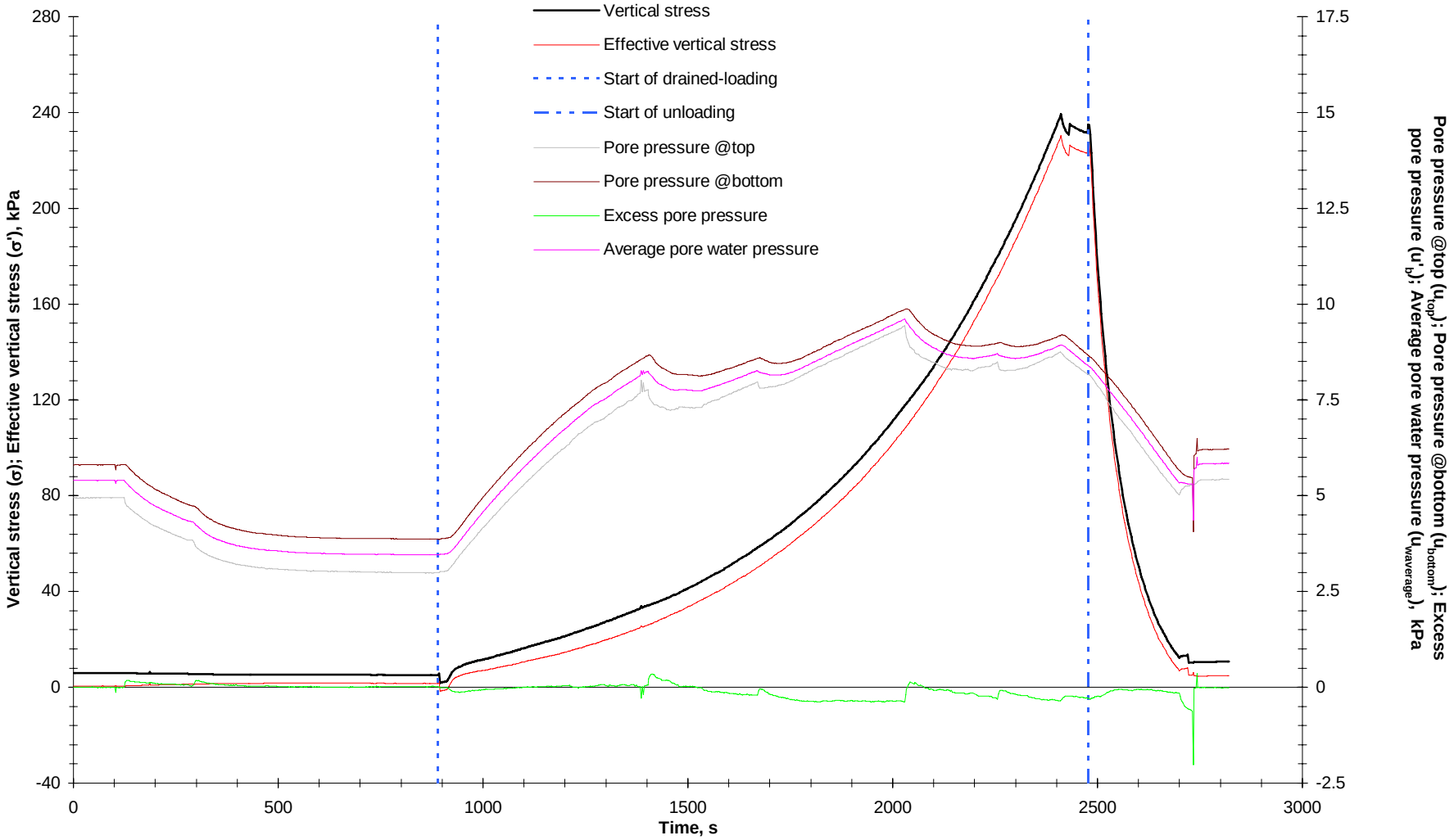

Figure 5.24. Stresses and pore water pressures. Finesand25foamR.

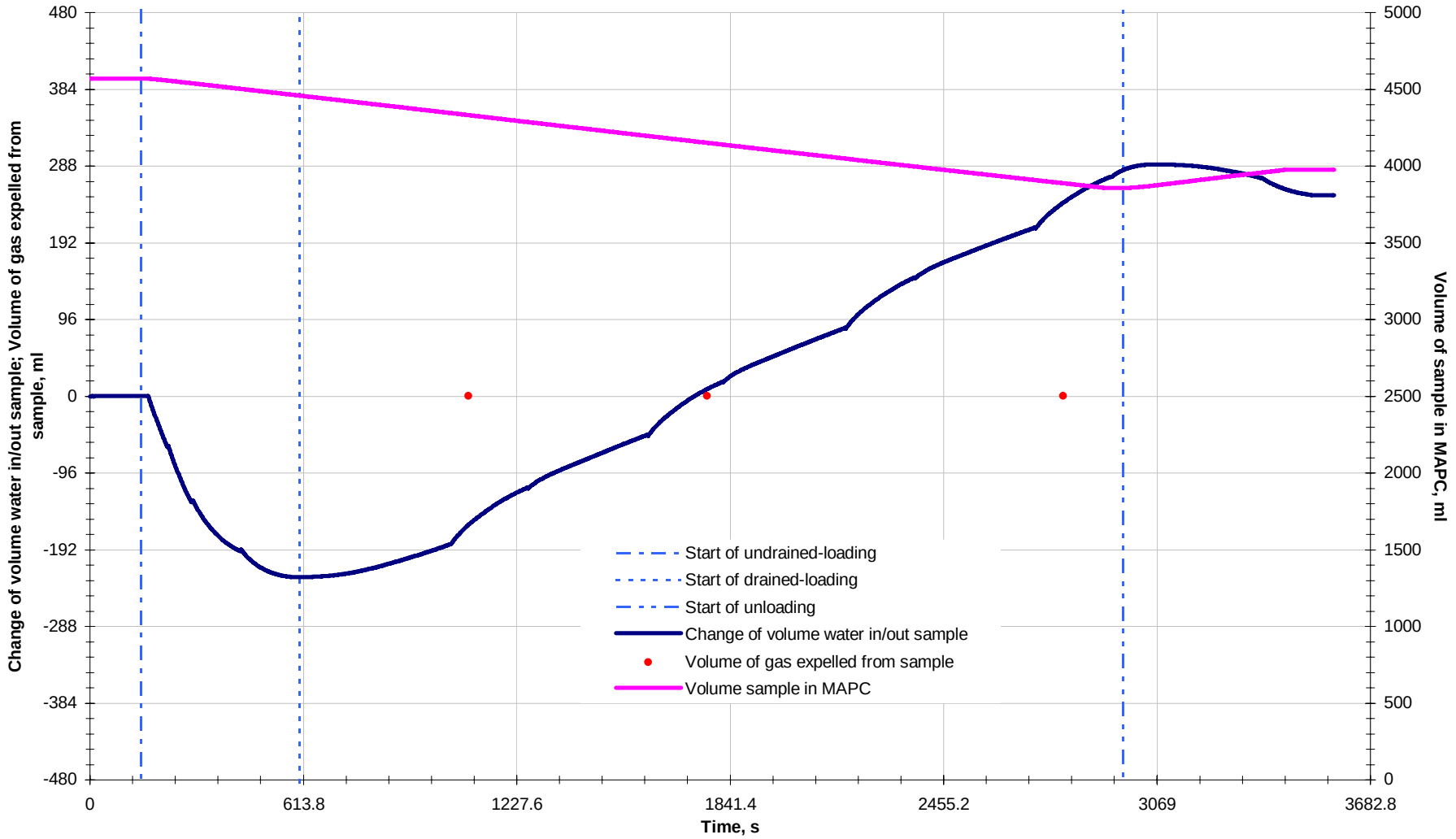

Figure 5.25. Change of volume water in/out sample, volume of gas expelled from sample and volume of sample in MAPC. Finesand13foamR

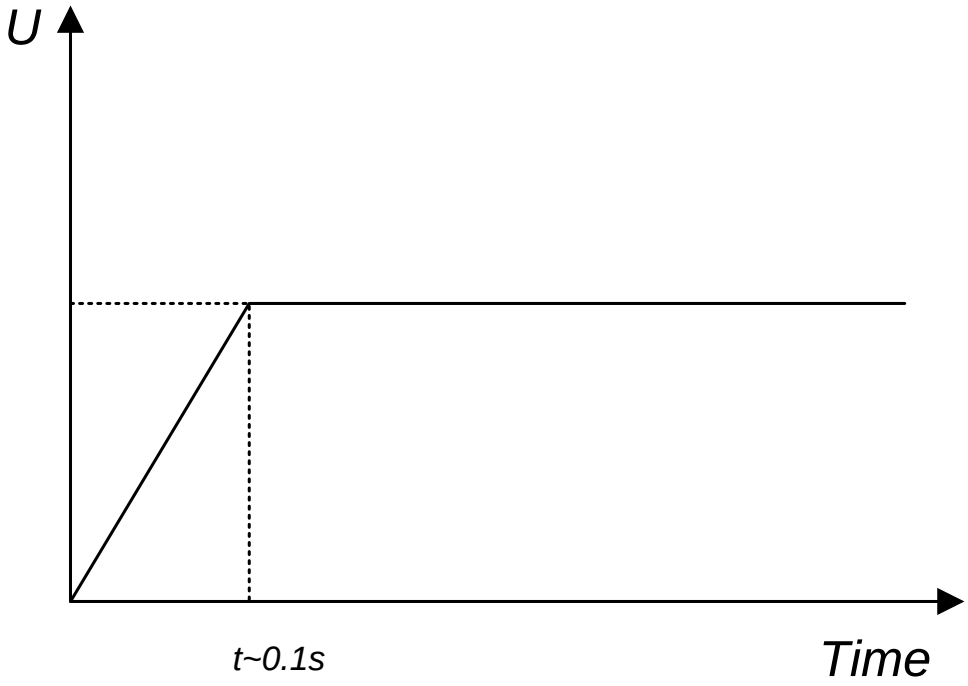

Figure 5.26. Terminal velocity of bubble.

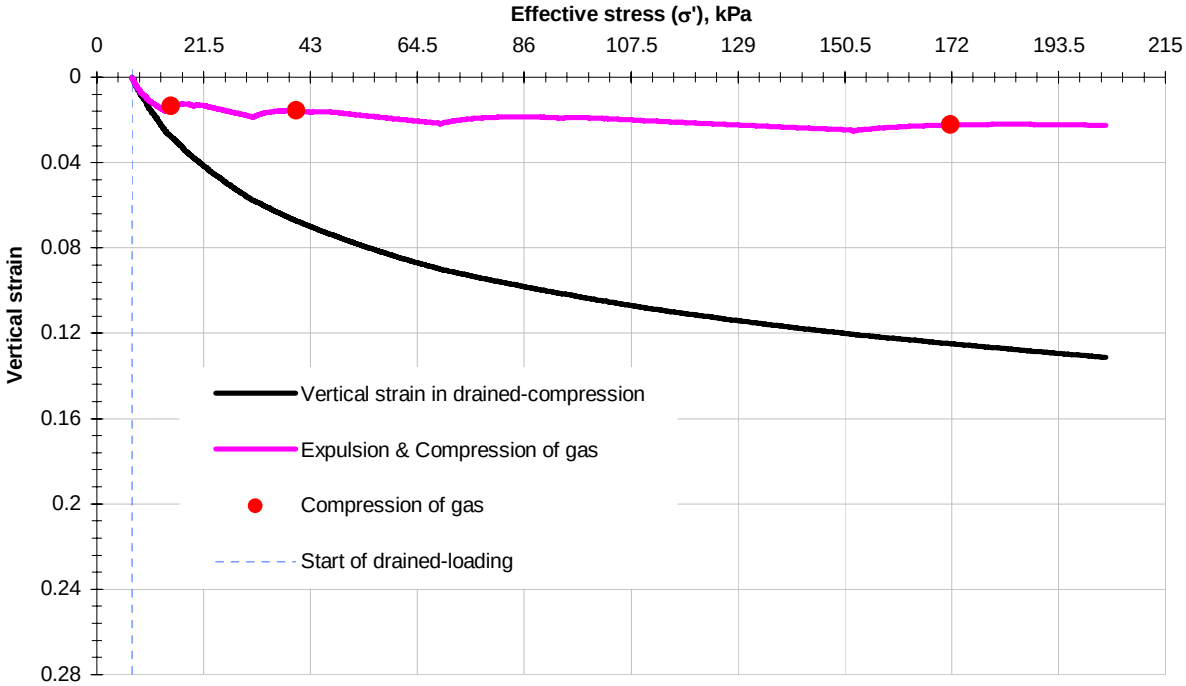

Figure 5.27. Ratio of compression. Finesand13foamR.

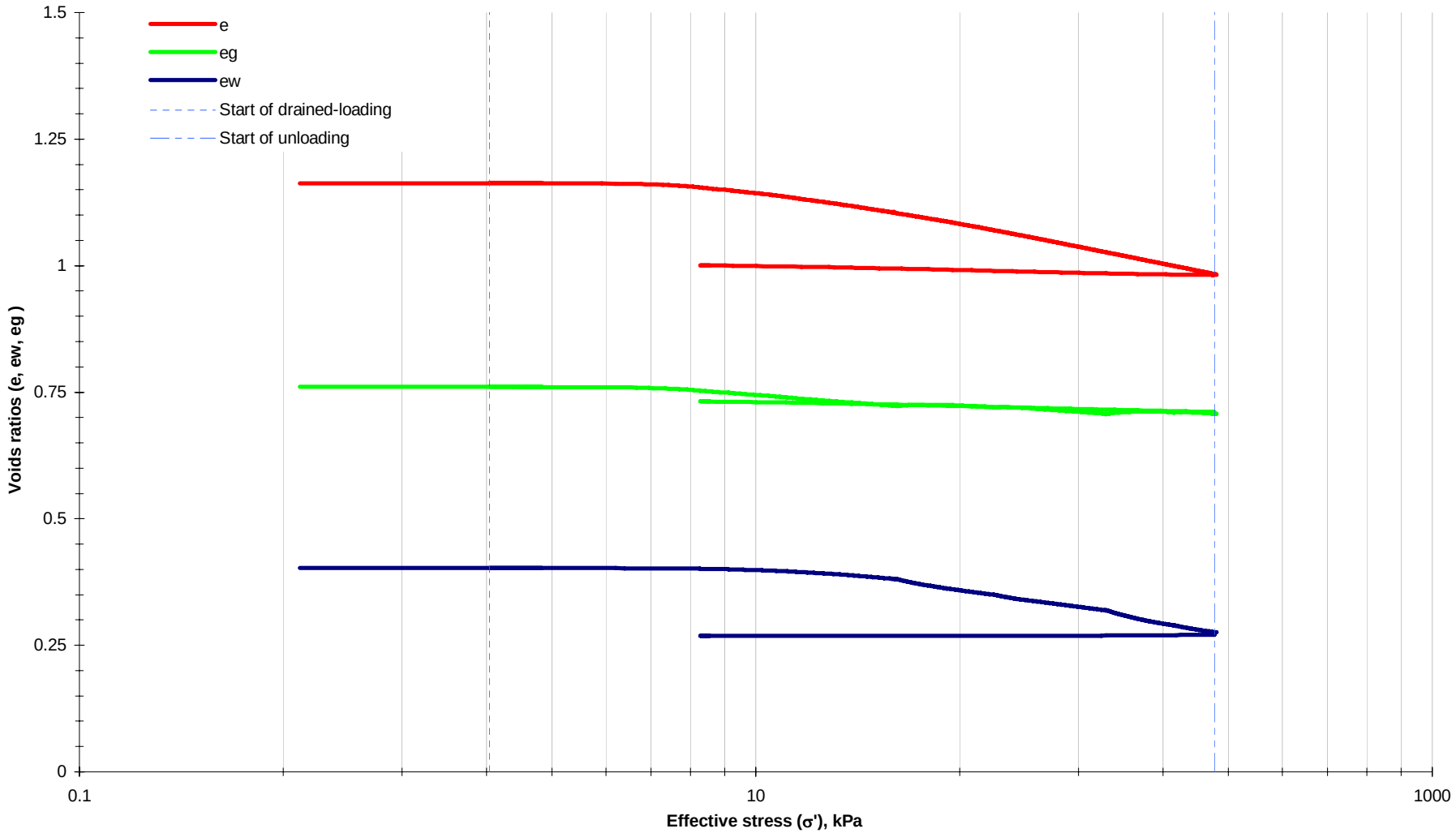

Figure 5.28. Voids ratios. Finesand25foamR.

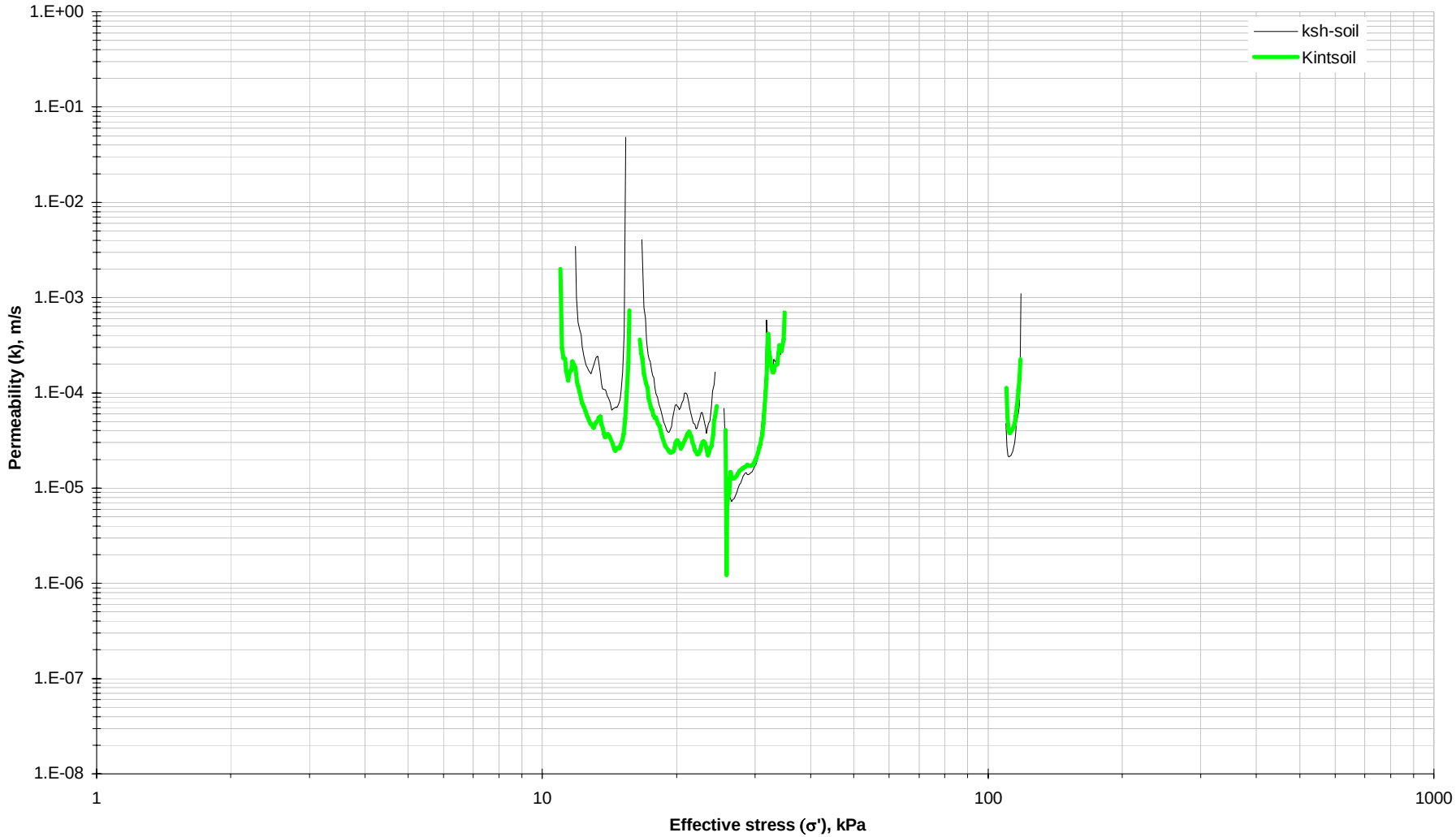

Figure 5.29. Coefficients of permeability. Finesand25foamR.

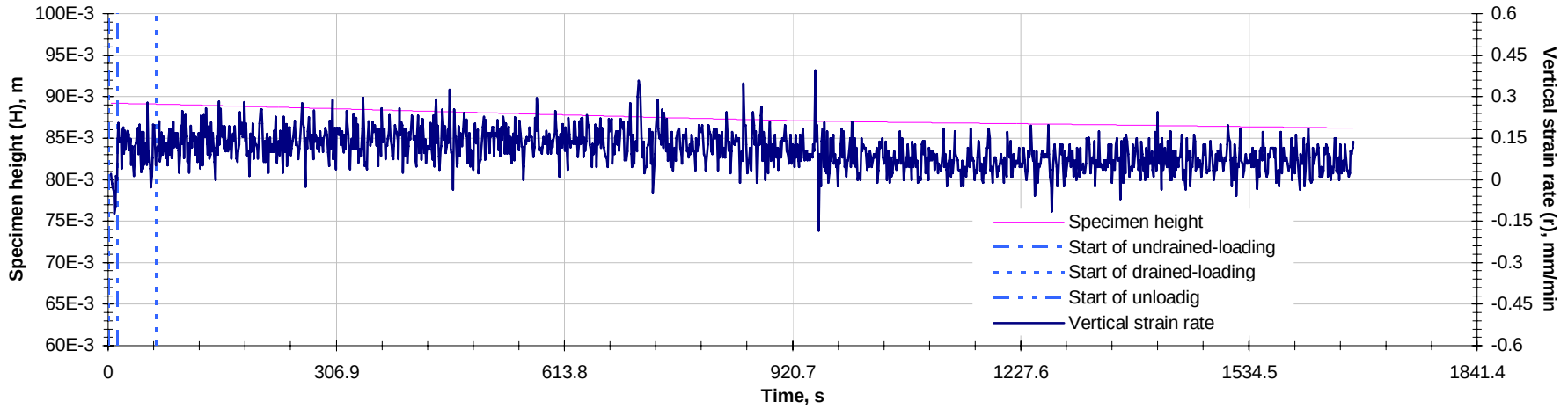

(a)

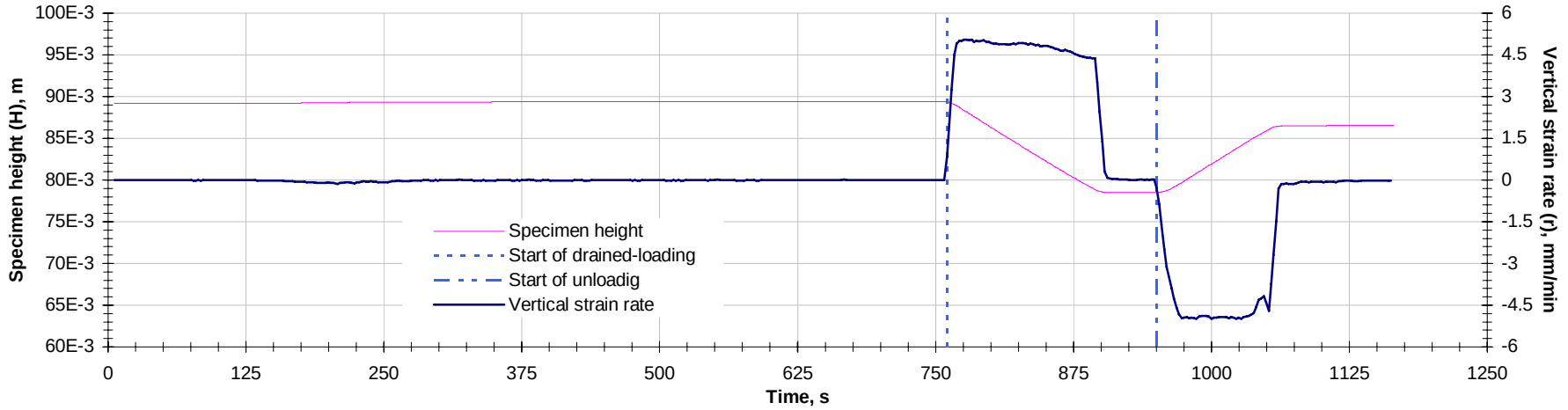

(b)

Figure 5.30. Specimen height and vertical displacement rate: (a) Finesand10 and (b) Finesand26foamR.

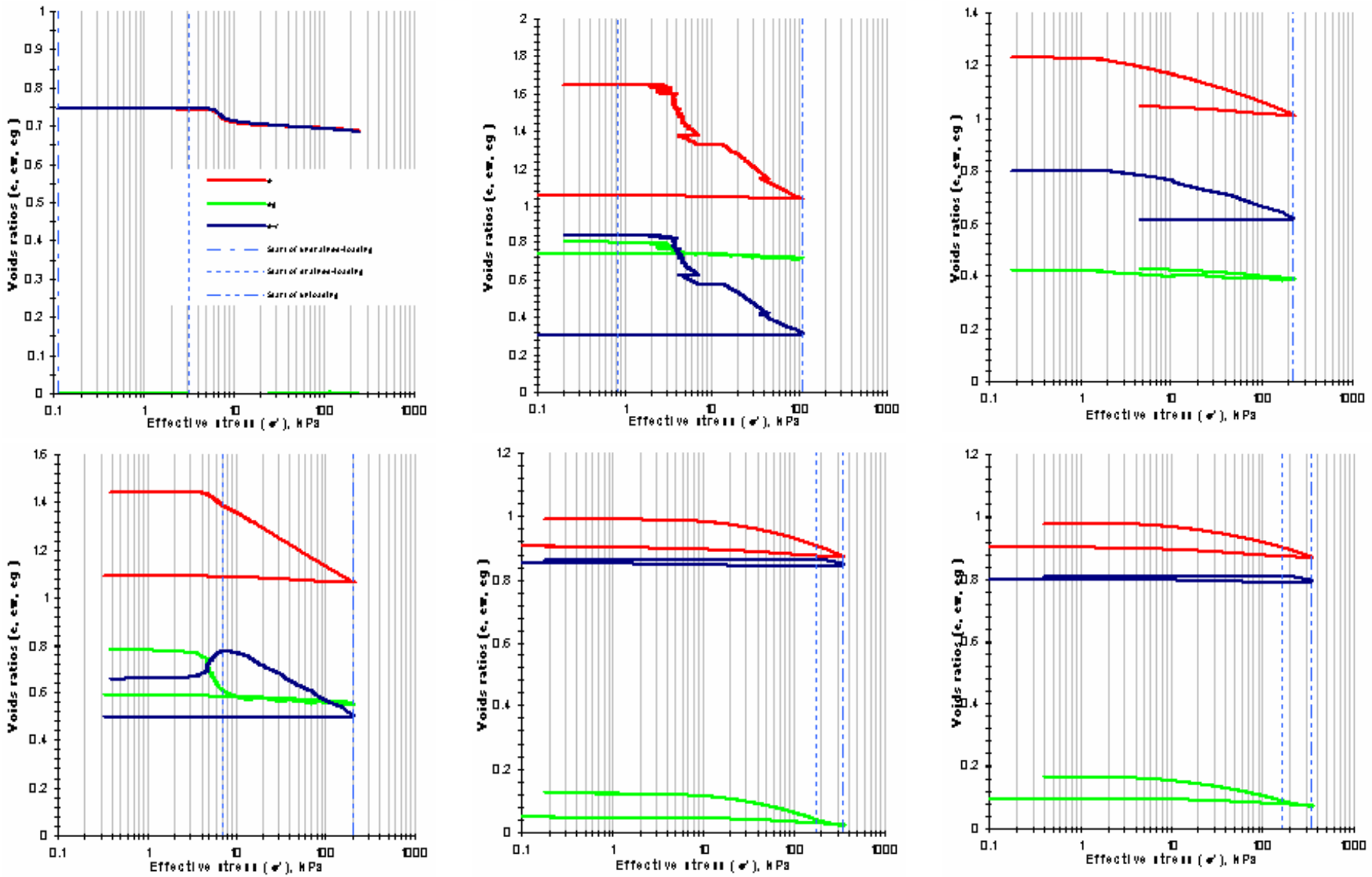

Figure 5.31. Voids ratio (From left to right and from top to bottom) : Finesand10, Finesand11foamR, Finesand12foamR, Finesand13foamR, Finesand14foamR and Finesand15foamR.

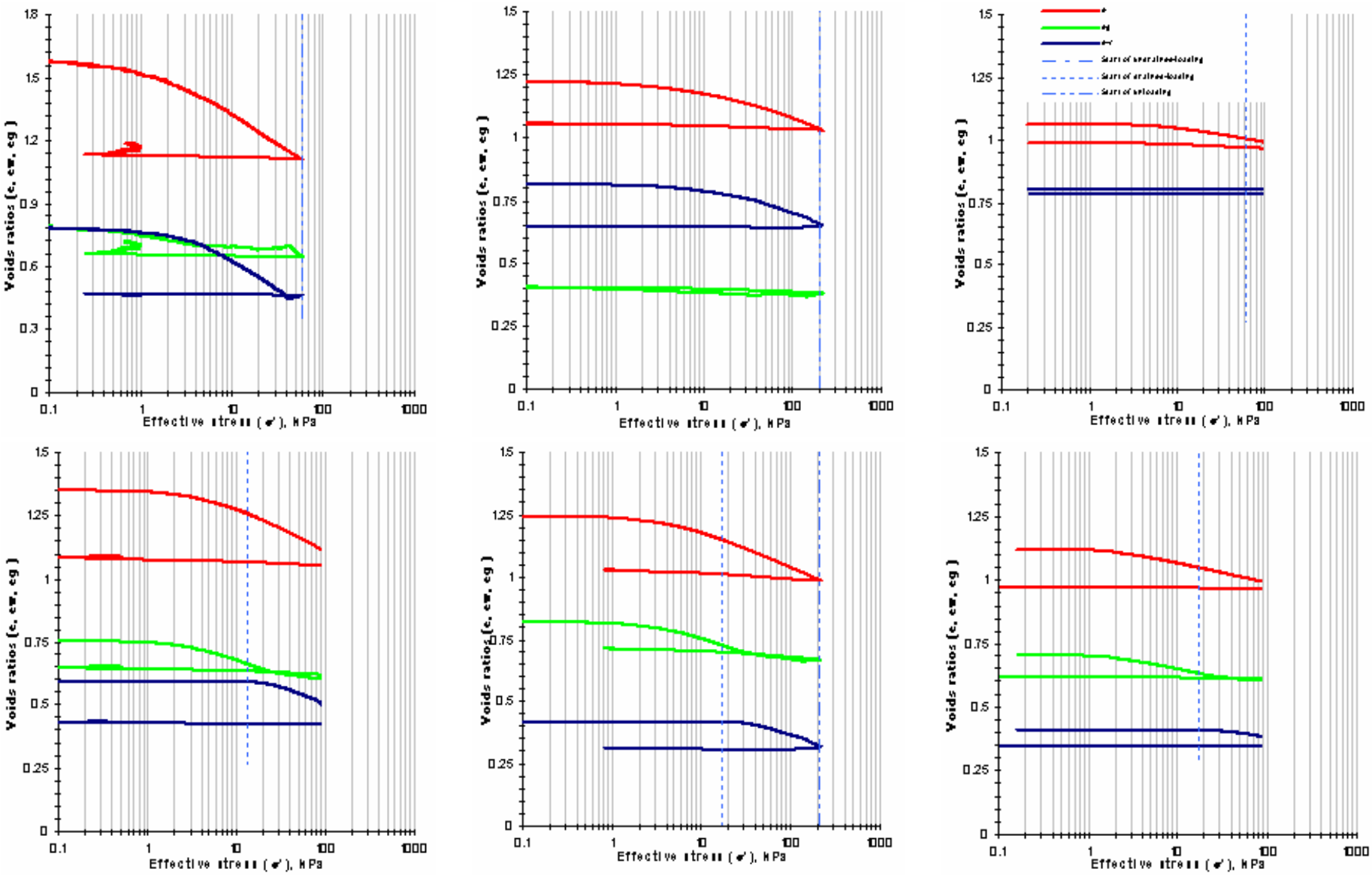

Figure 5.32. Voids ratio (From left to right and from top to bottom): Finesand16foamR, Finesand17foamR, Finesand18foamR, Finesand19foamR, Finesand20foamR and Finesand21foamR.

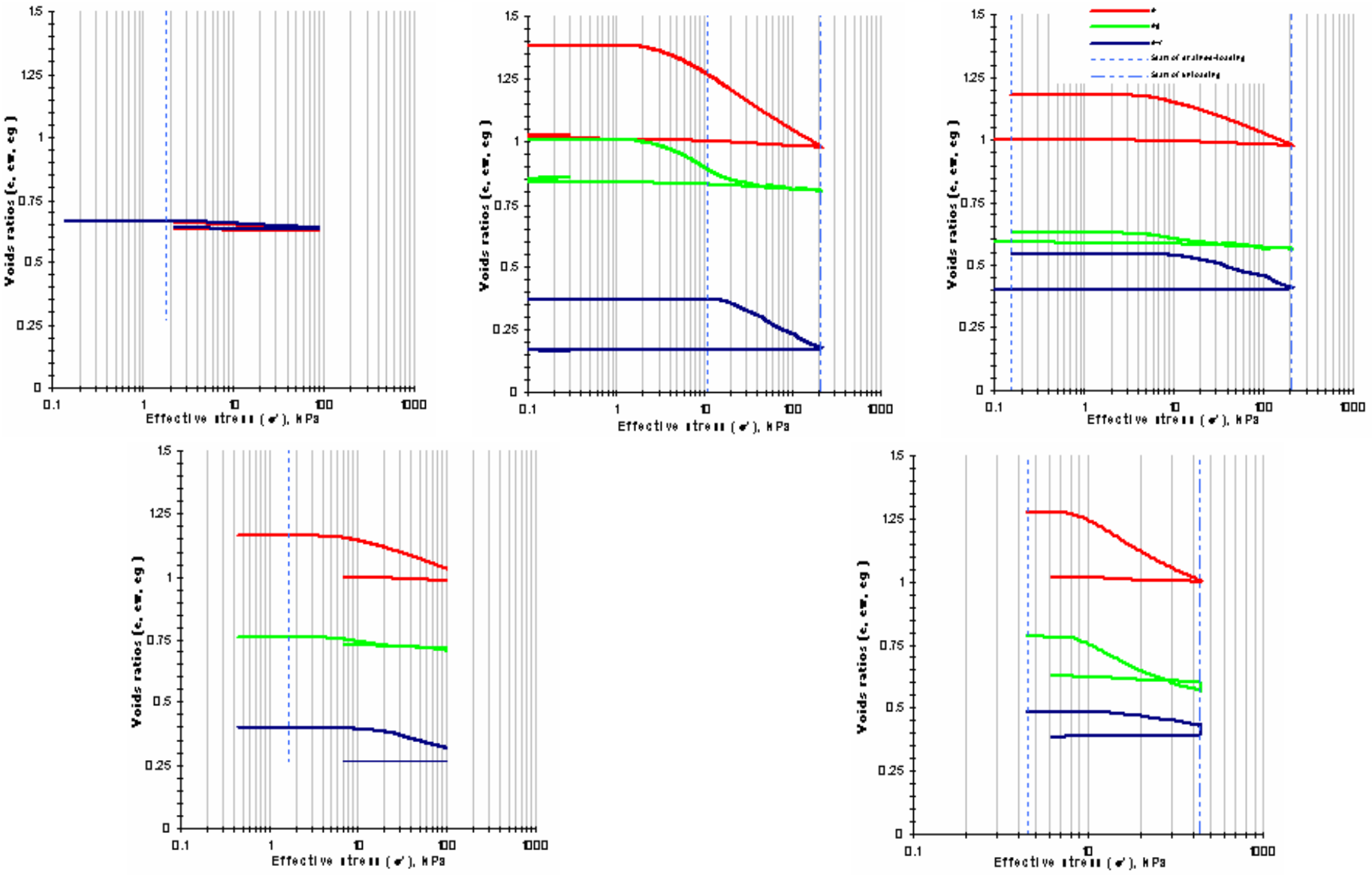

Figure 5.33. Voids ratio (From left to right and from top to bottom): Finesand22R, Finesand23foamR, Finesand24foamR, Finesand25foamR and Finesand26foamR.

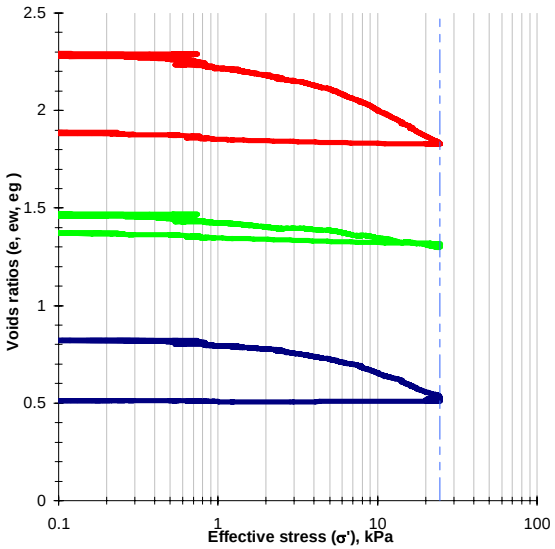

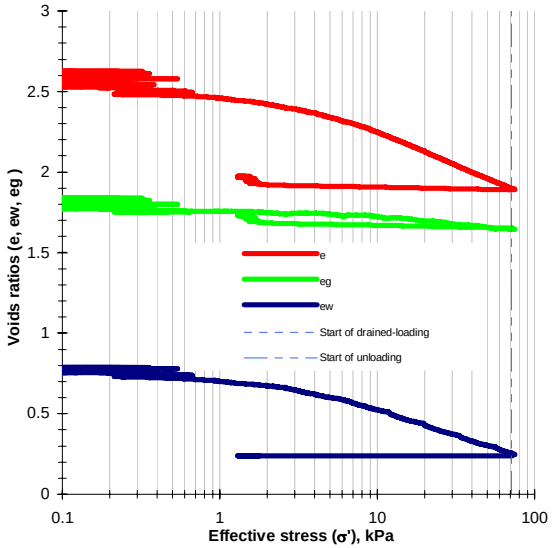

Figure 5.34. Voids ratio (From left to right):: Thanetsand1foamR and Thanetsand2foamR.

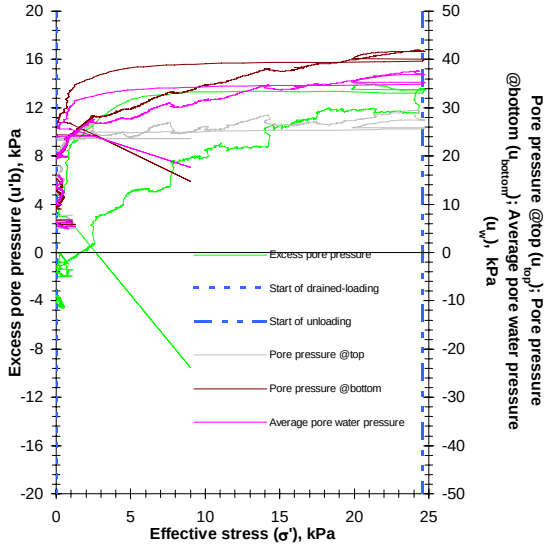

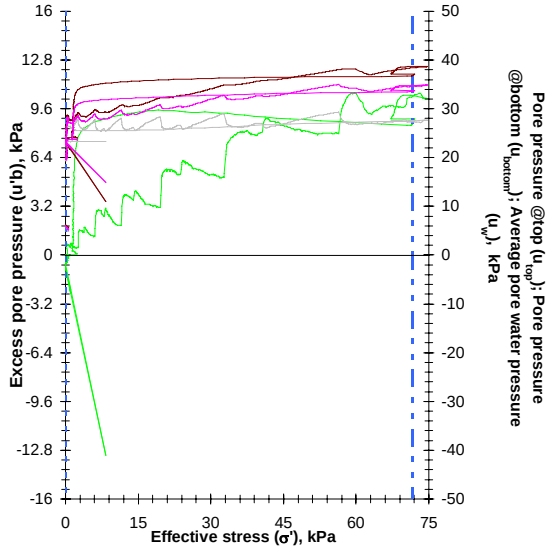

Figure 5.35. Pore water pressure and excess pore water pressure: Thanetsand1foamR and Thanetsand2foamR

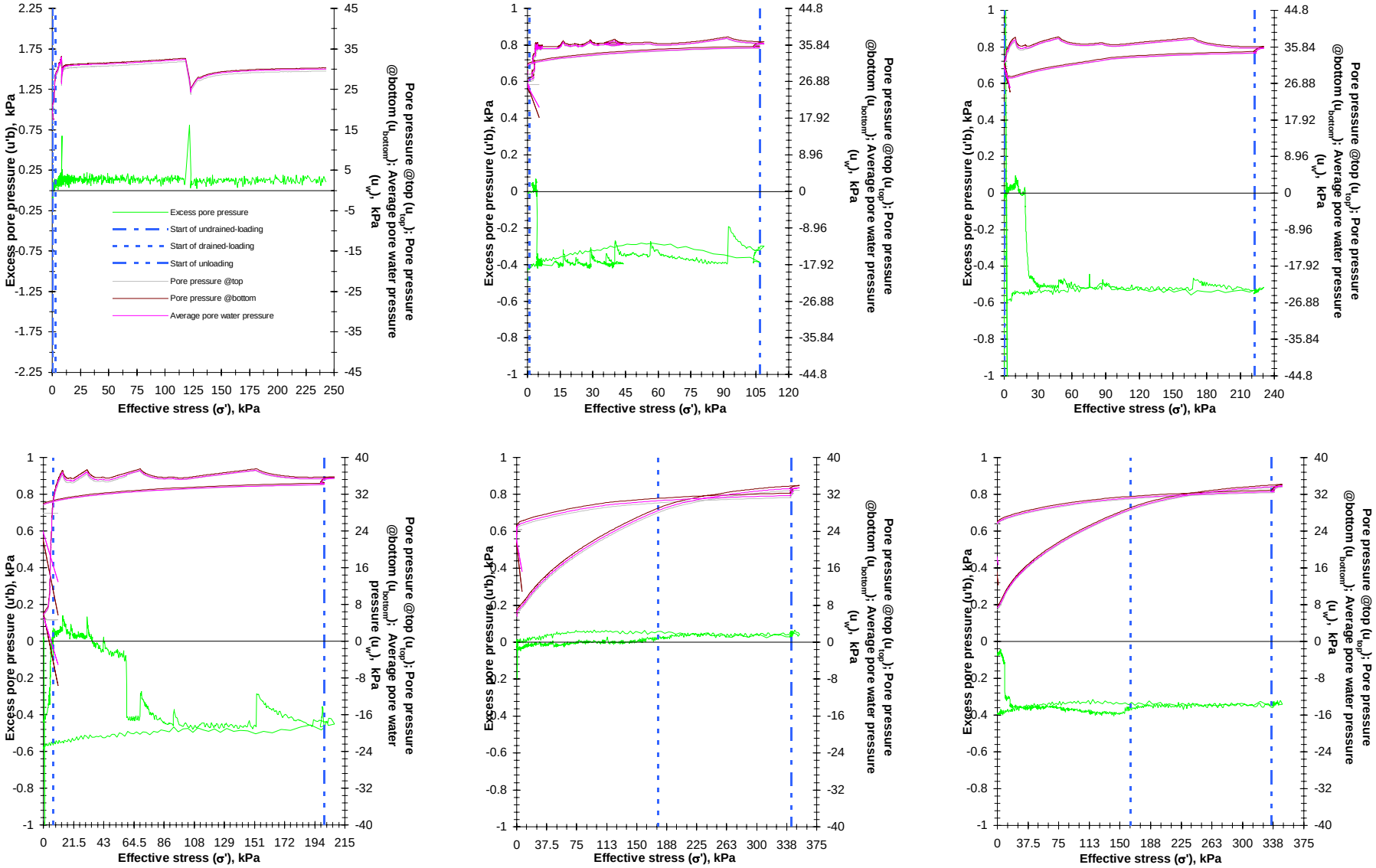

Figure 5.36. Pore water pressures and excess pore pressures (From left to right and from top to bottom): Finesand10, Finesand11foamR, Finesand12foamR, Finesand13foamR, Finesand14foamR and Finesand15foamR.

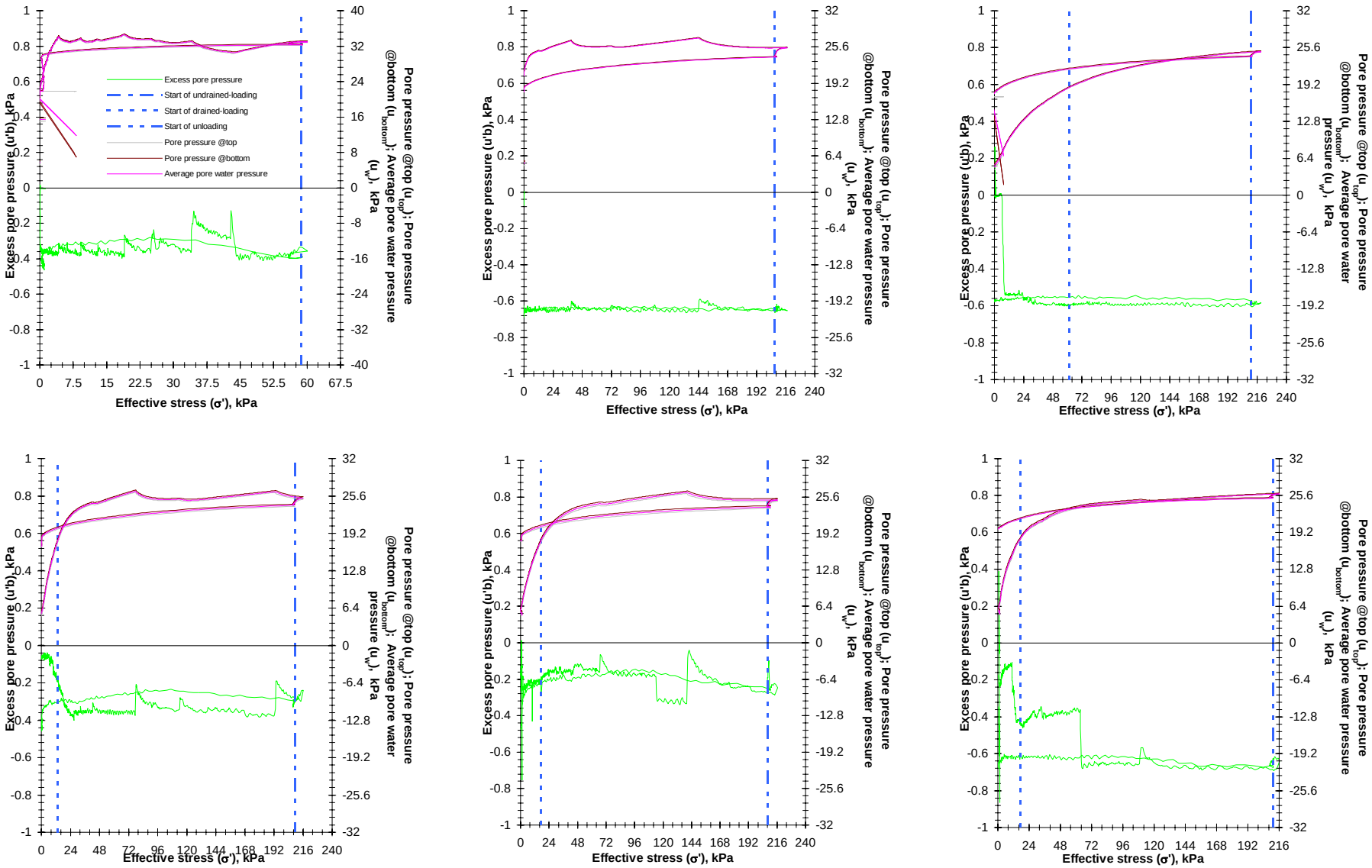

Figure 5.37. Pore water pressures and excess pore pressures (From left to right and from top to bottom): Finesand16foamR, Finesand17foamR, Finesand18foamR, Finesand19foamR, Finesand20foamR and Finesand21foamR..

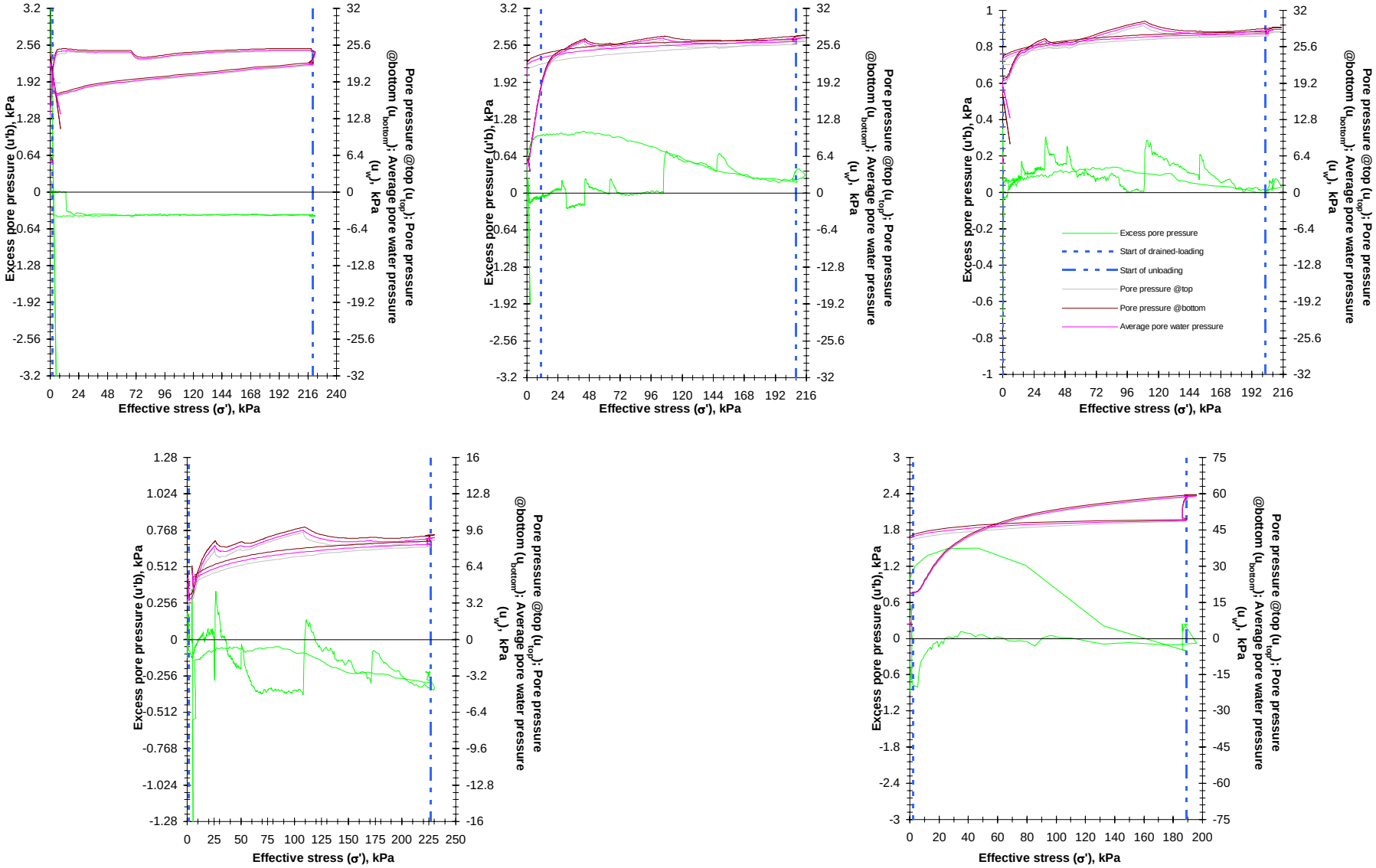

Figure 5.38. Pore water pressures and excess pore pressures (From left to right and from top to bottom): Finesand22R, Finesand23foamR, Finesand24foamR, Finesand25foamR and Finesand26foamR.

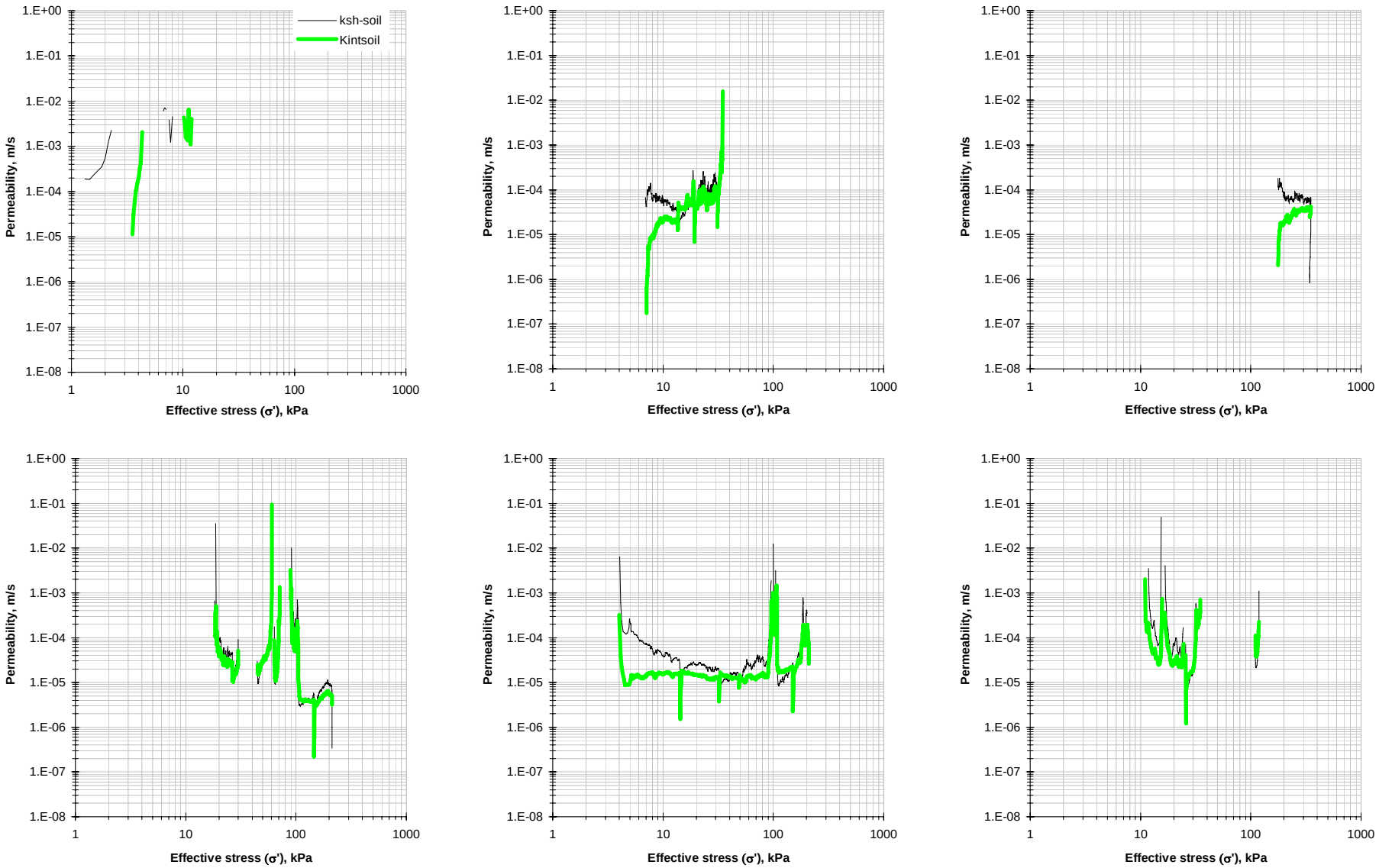

Figure 5.39. Coefficient of permeability (From left to right and from top to bottom): Finesand22, Finesand13foamR, Finesand14foamR, Finesand23foamR, Finesand24foamR and Finesand25foamR.

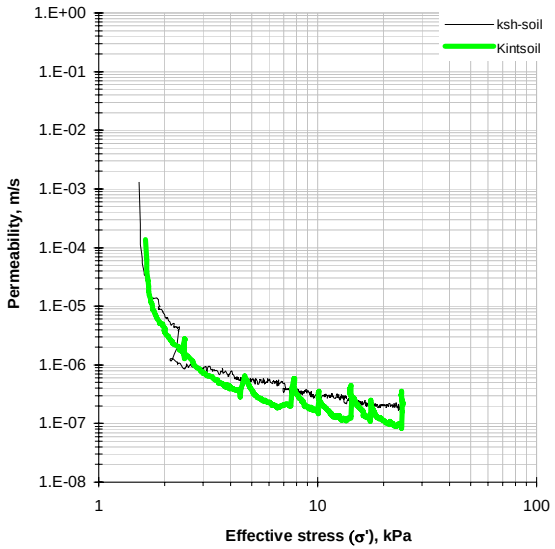

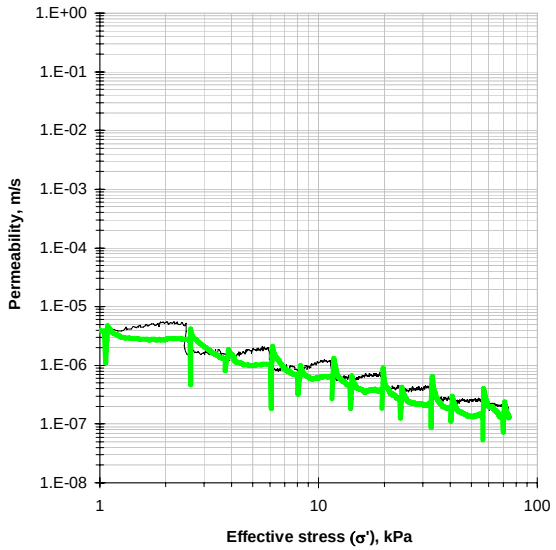

Figure 5.40. Coefficient of permeability (From left to right): Thanetsand1foamR and Thanetsand2foamR.

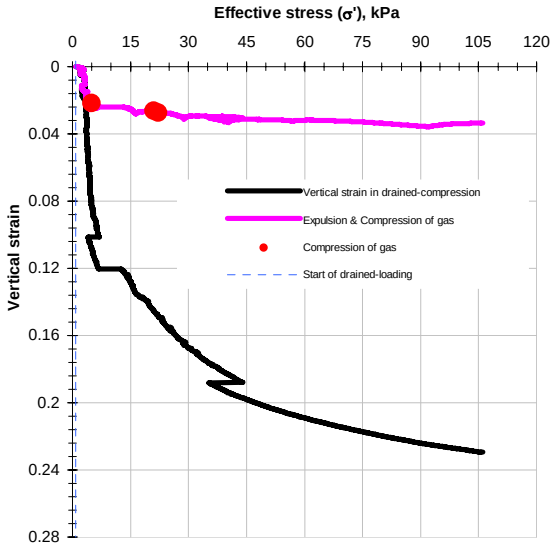

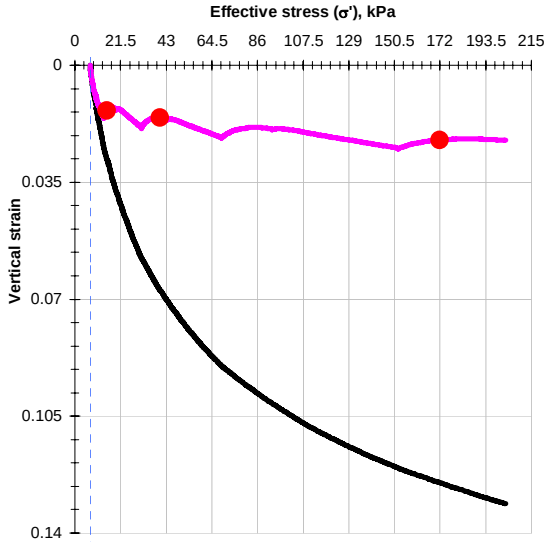

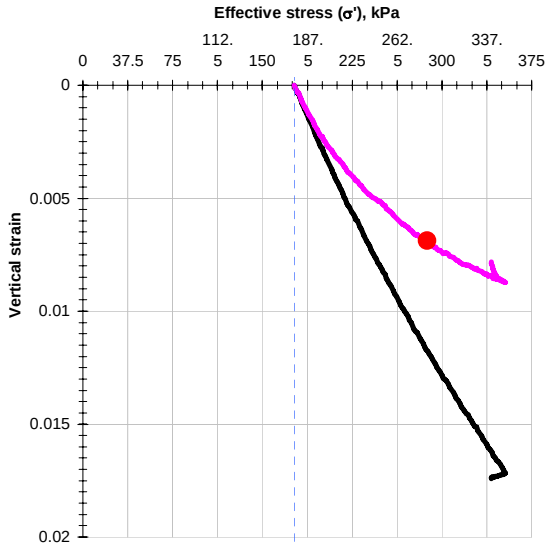

Figure 5.41. Ratio of compression (From left to right): Finesand11foamR, Finesand13foamR and Finesand14foamR.

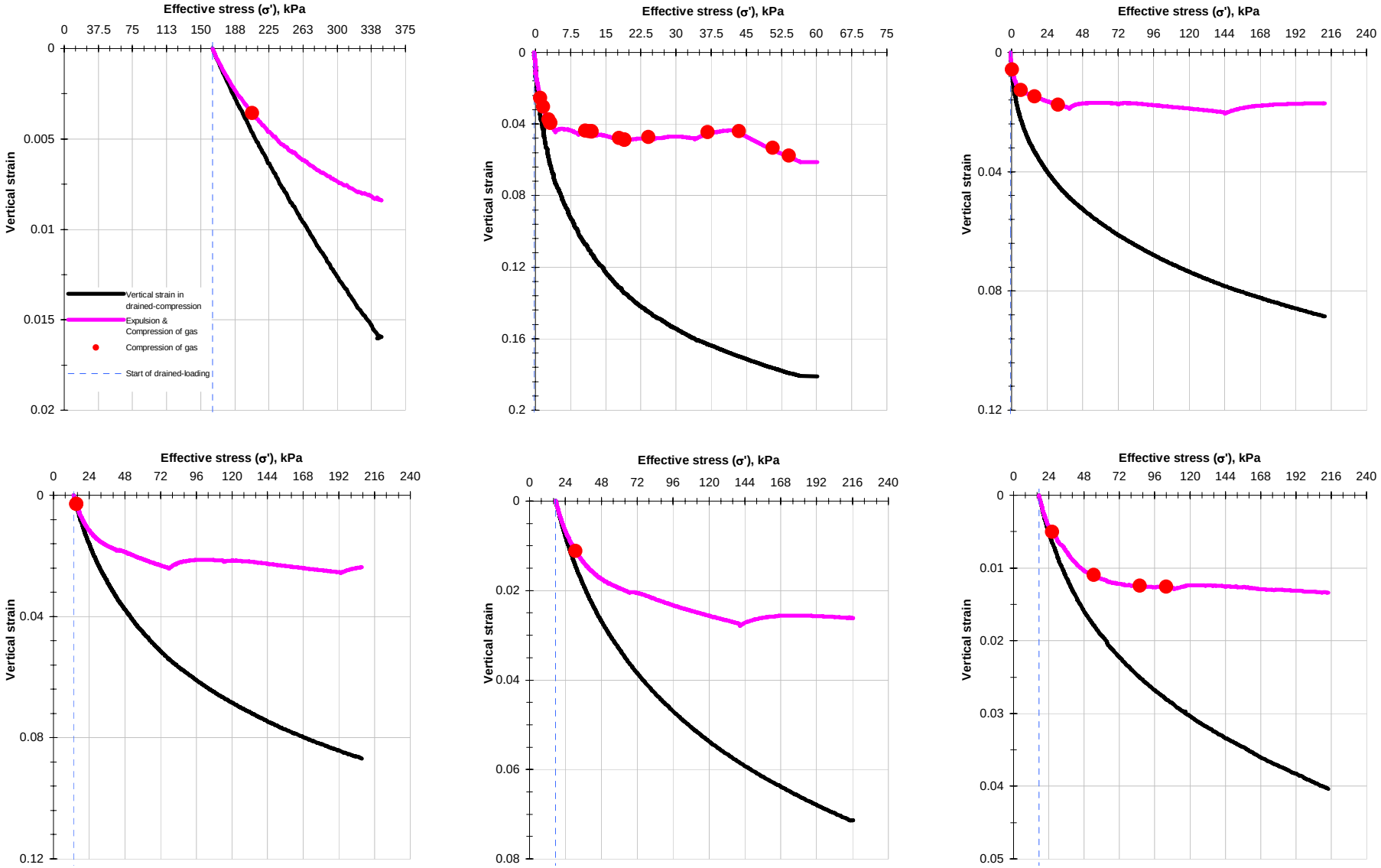

Figure 5.42. Ratio of compression (From left to right and from top to bottom): Finesand15foamR, Finesand16foamR, Finesand17foamR, Finesand19foamR, Finesand20famR and Finesand21foamR,

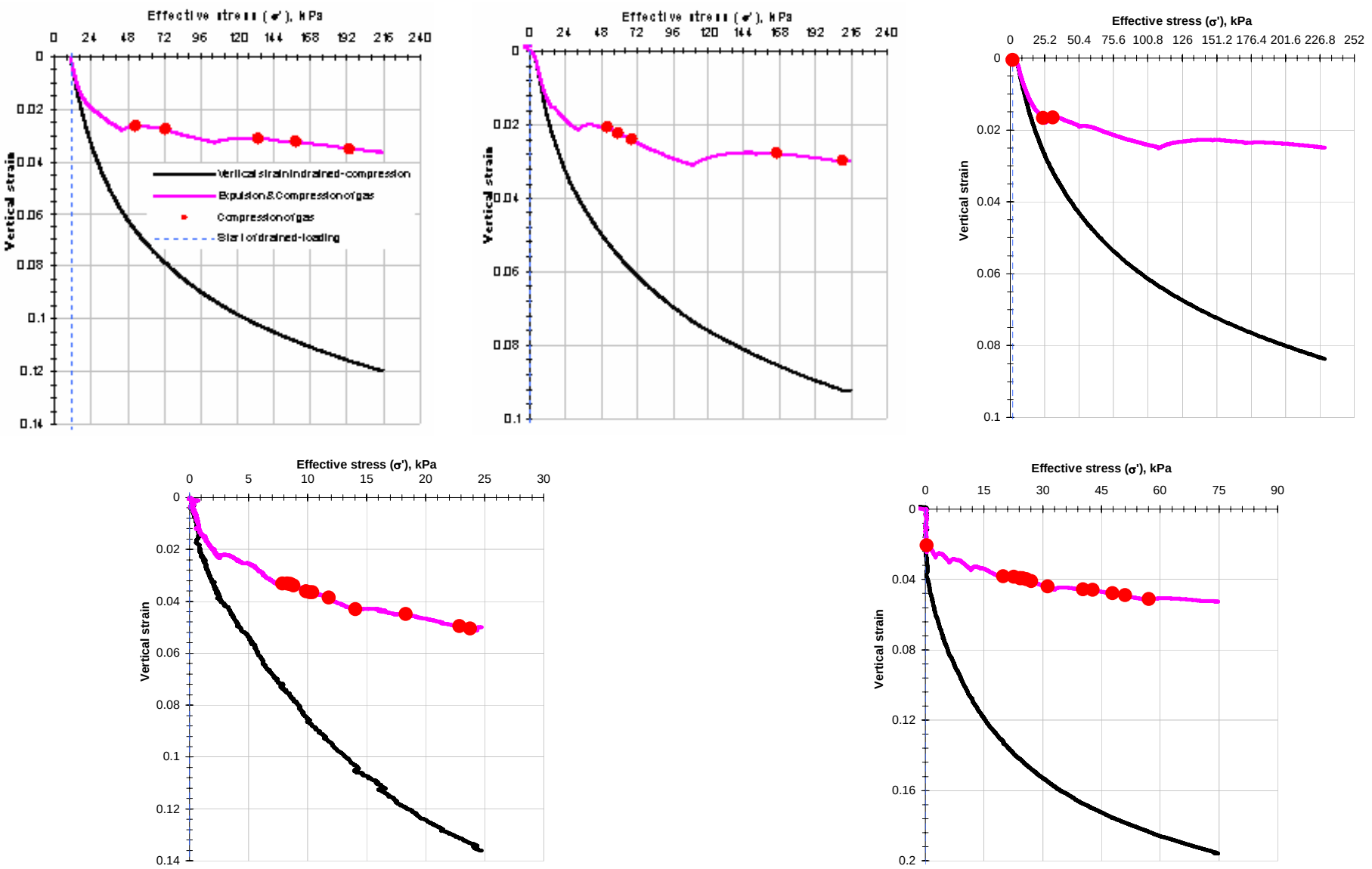

Figure 5.43. Ratio of compression (From left to right and from top to bottom): Finesand23foamR, Finesand24foamR, Finesand25foamR, Thanetsand1foamR and Thanetsand2foamR.

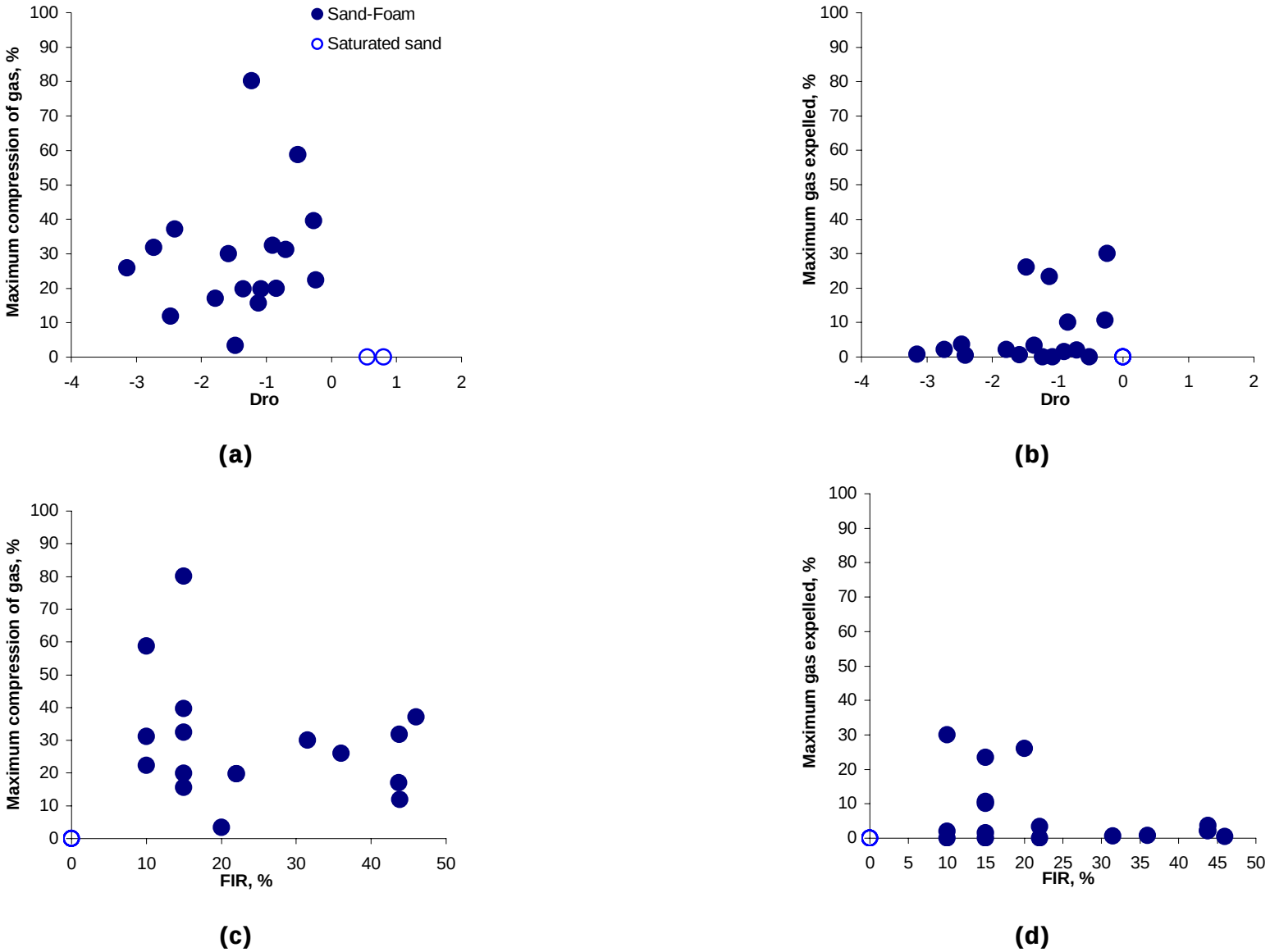

Figure 5.44. Ratios of Maximum compression of gas and Maximum gas expelled versus relative density ((a) and (b) respectively) and versus FIR ((c) and (d) respectively)

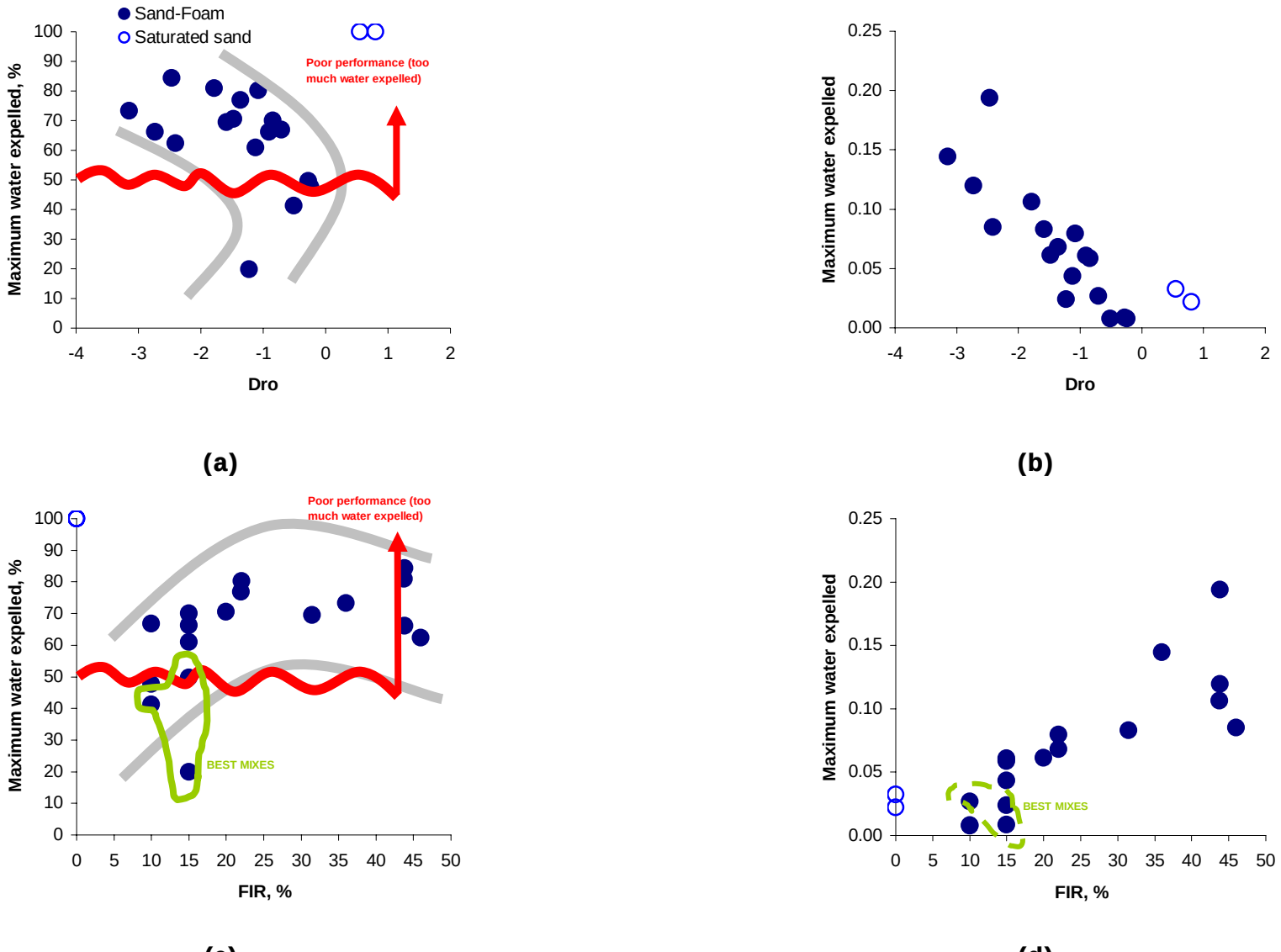

Figure 5.45. Ratios of Maximum water expelled in percentage and absolute terms versus relative density ((a) and (b) respectively) and versus FIR ((c) and (d) respectively)

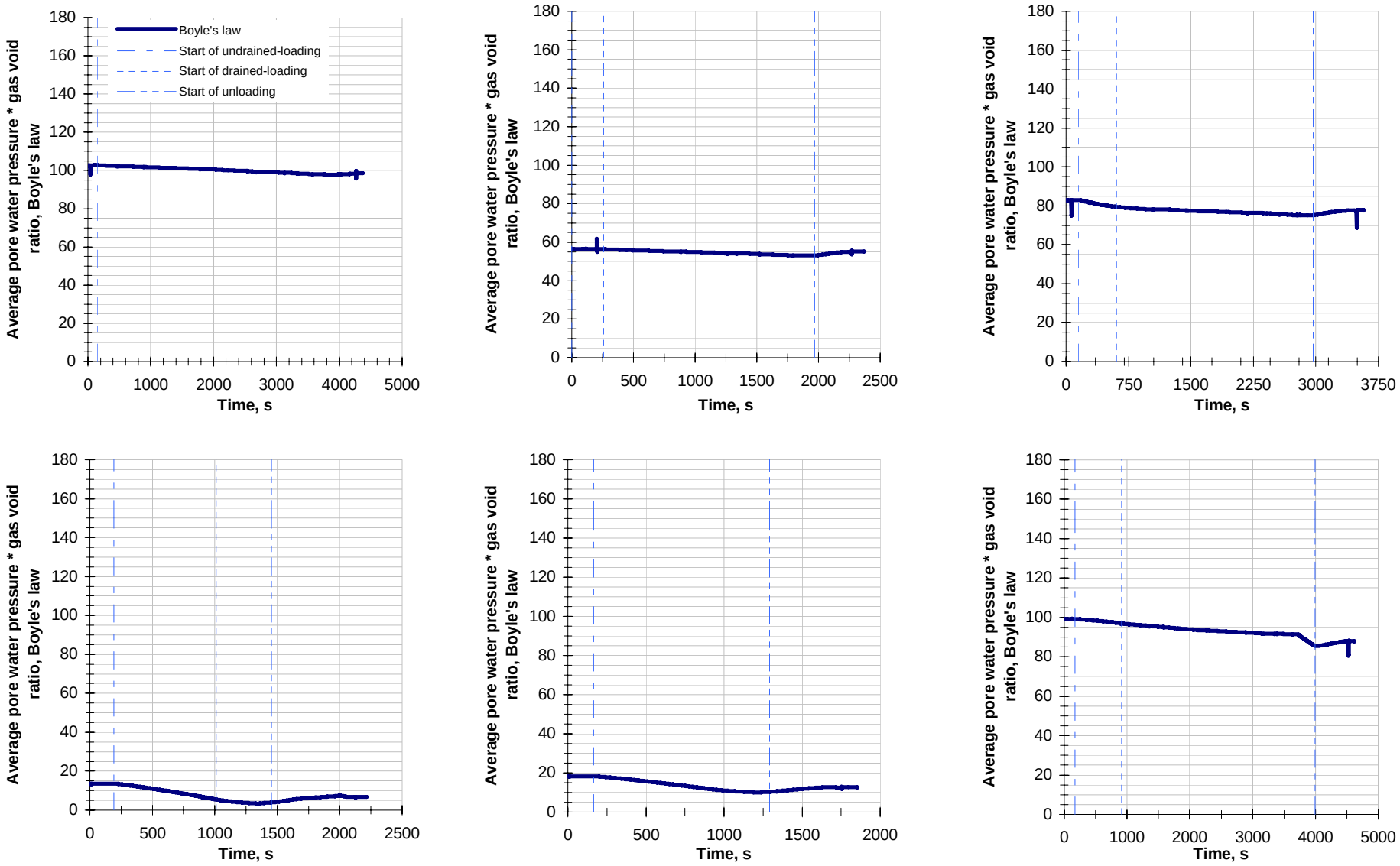

Figure 5.46. Boyle's law (From left to right and from top to bottom): Finesand11foamR, Finesand12foamR, Finesand13foamR, Finesand14foamR, Finesand15foamR and Finesand16foamR.

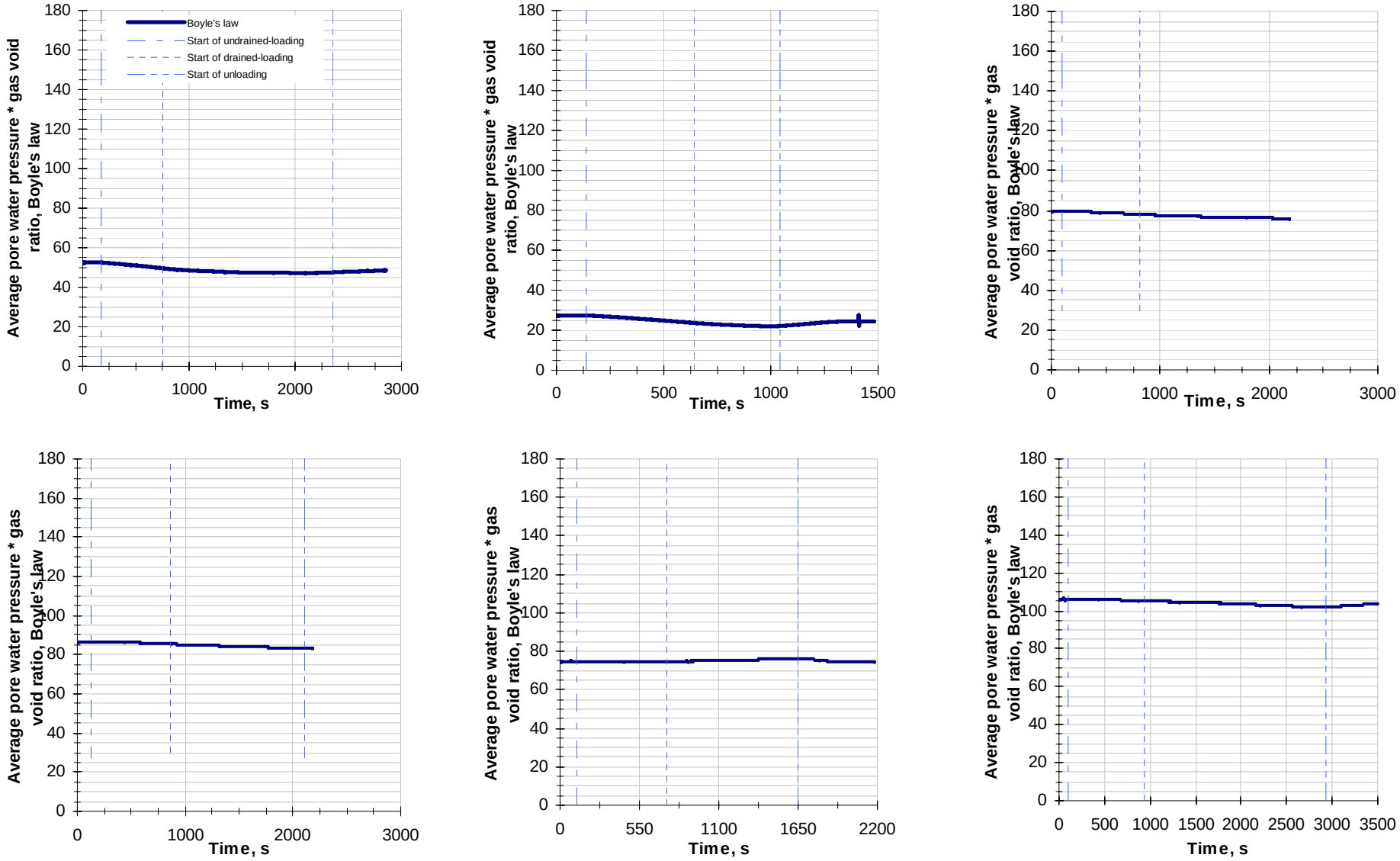

Figure 5.47. Boyle's law (From left to right and from top to bottom): Finesand17foamR, Finesand18foamR, Finesand19foamR, Finesand20famR, Finesand21foamR and Finesand23foamR.

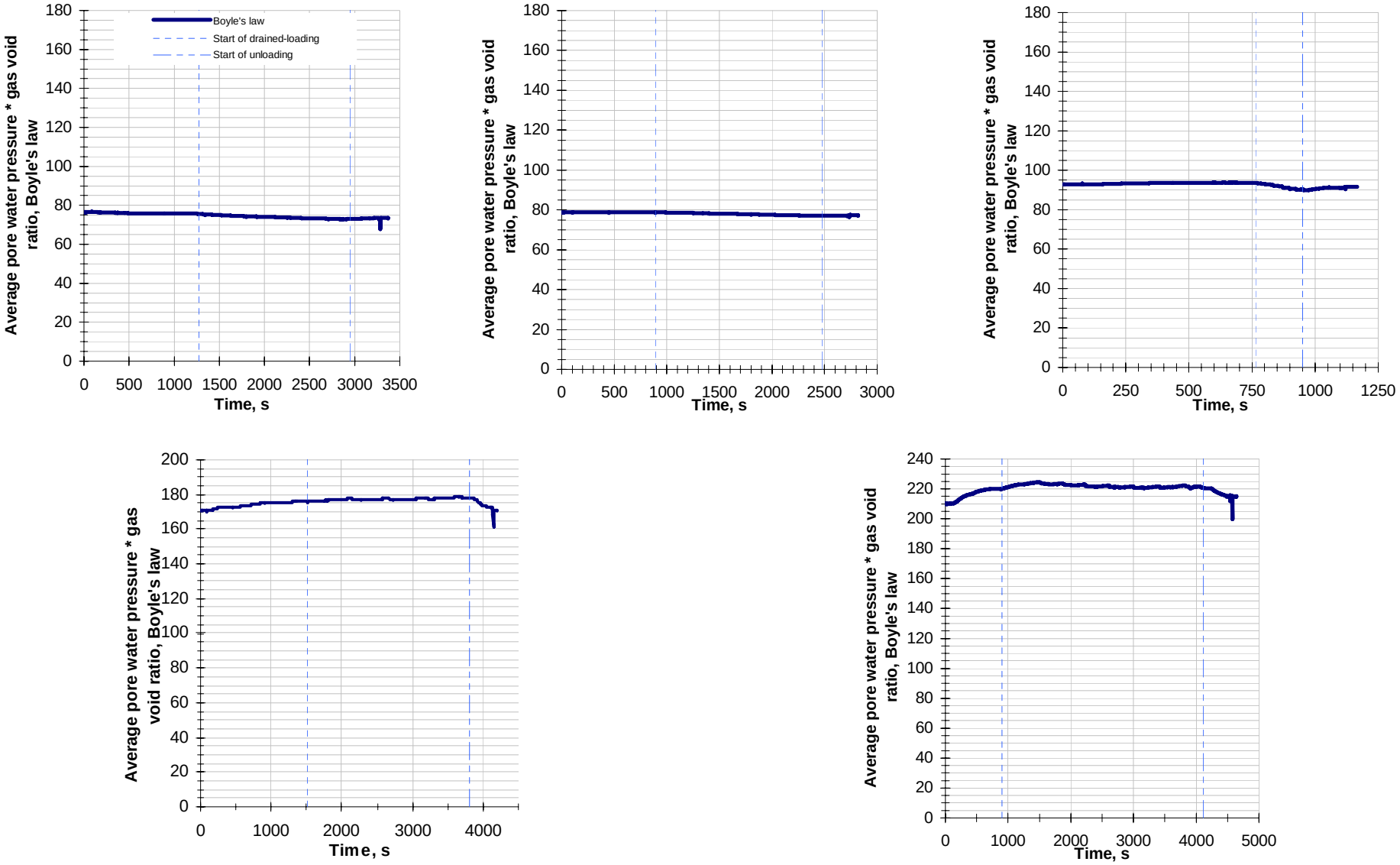

Figure 5.48. Boyle's law (From left to right and from top to bottom): Finesand24foamR, Finesand25foamR, Finesand26foamR, Thanetsand1foamR and Thanetsand2foamR..

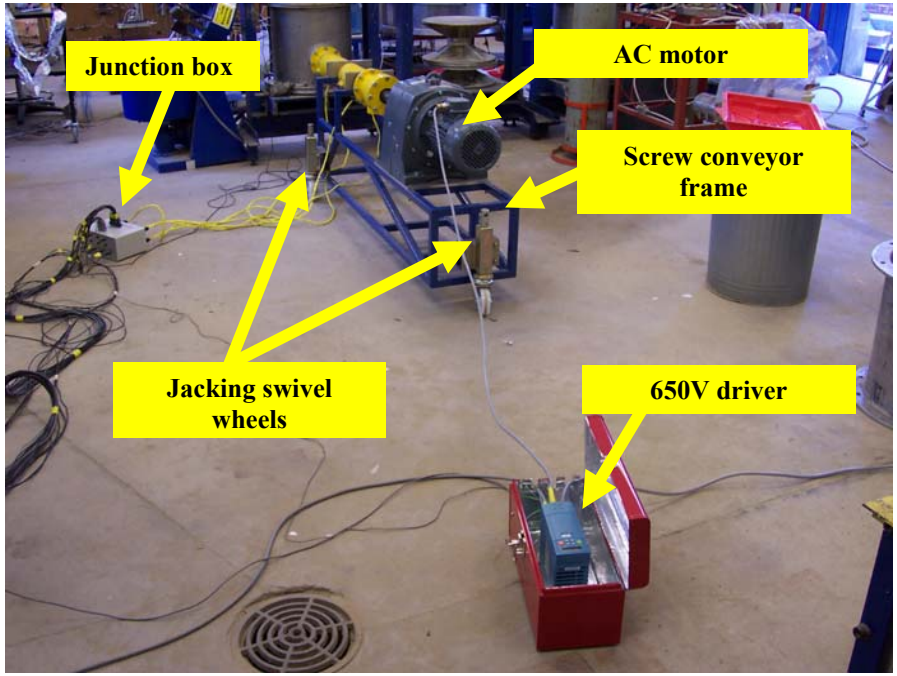

Figure 6.1. Frontal overview Oxford screw conveyor.

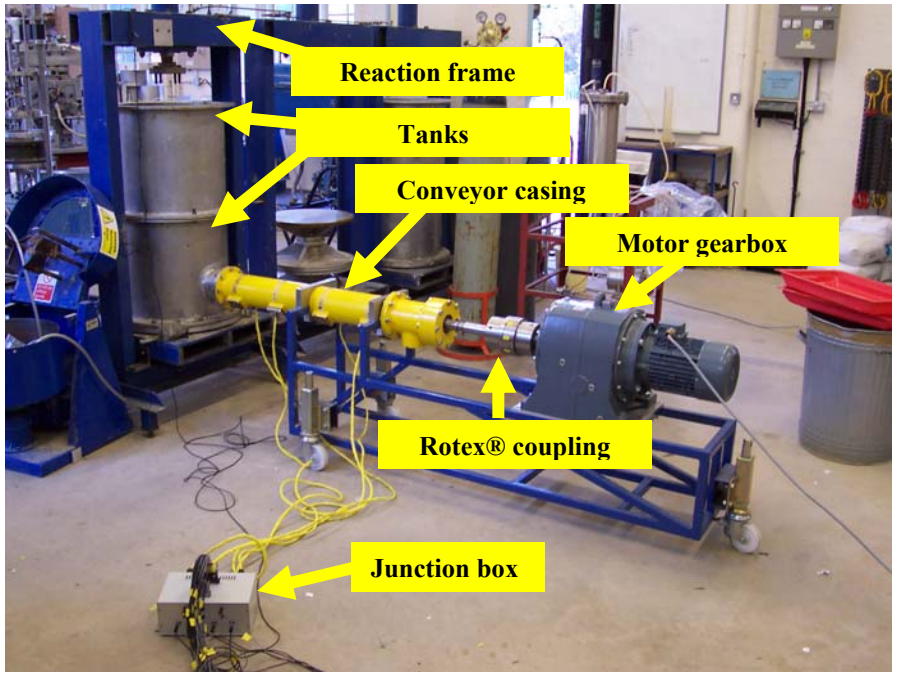

Figure 6.2. Side overview Oxford screw conveyor.

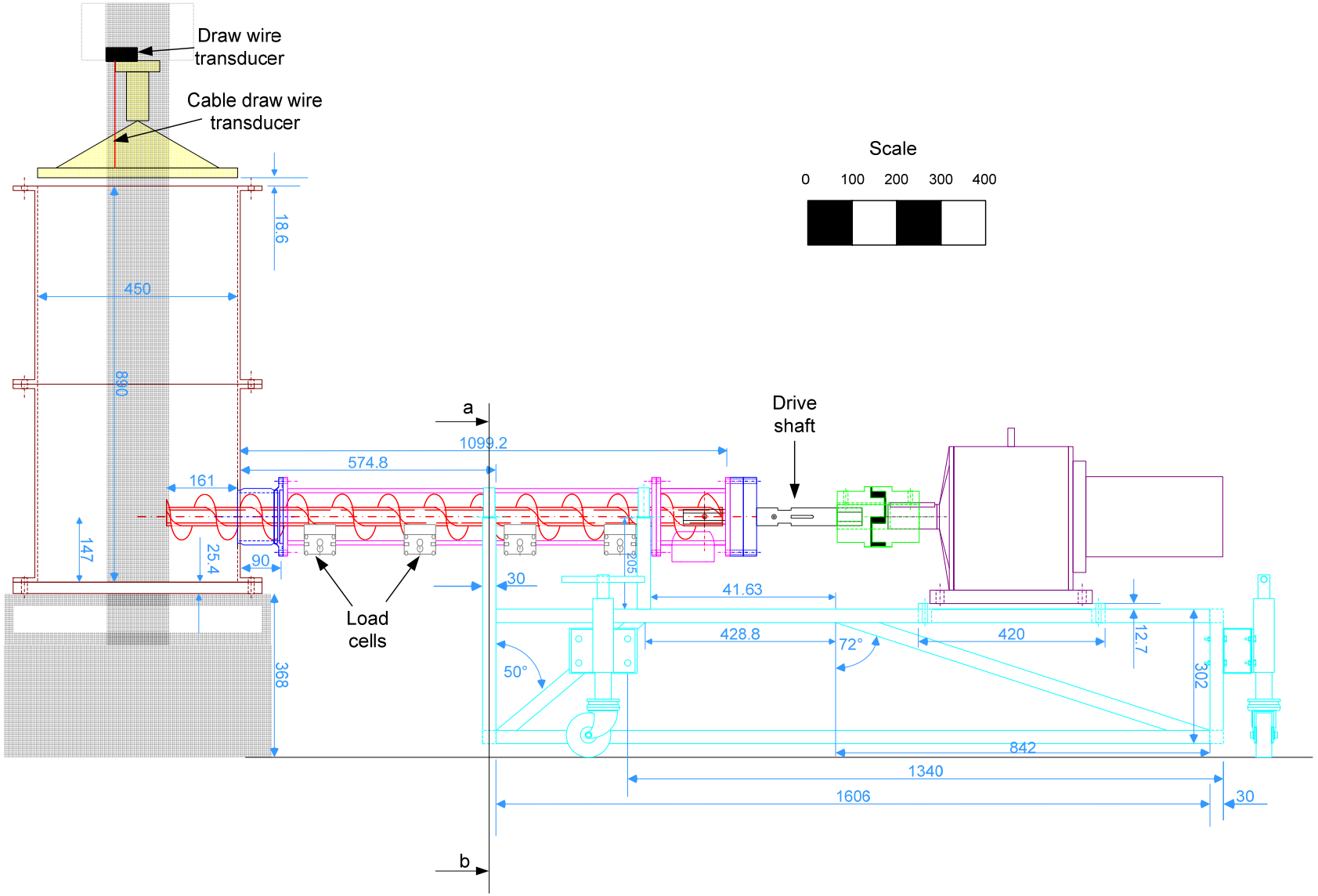

Figure 6.3. Side view general arrangement of Oxford screw conveyor.

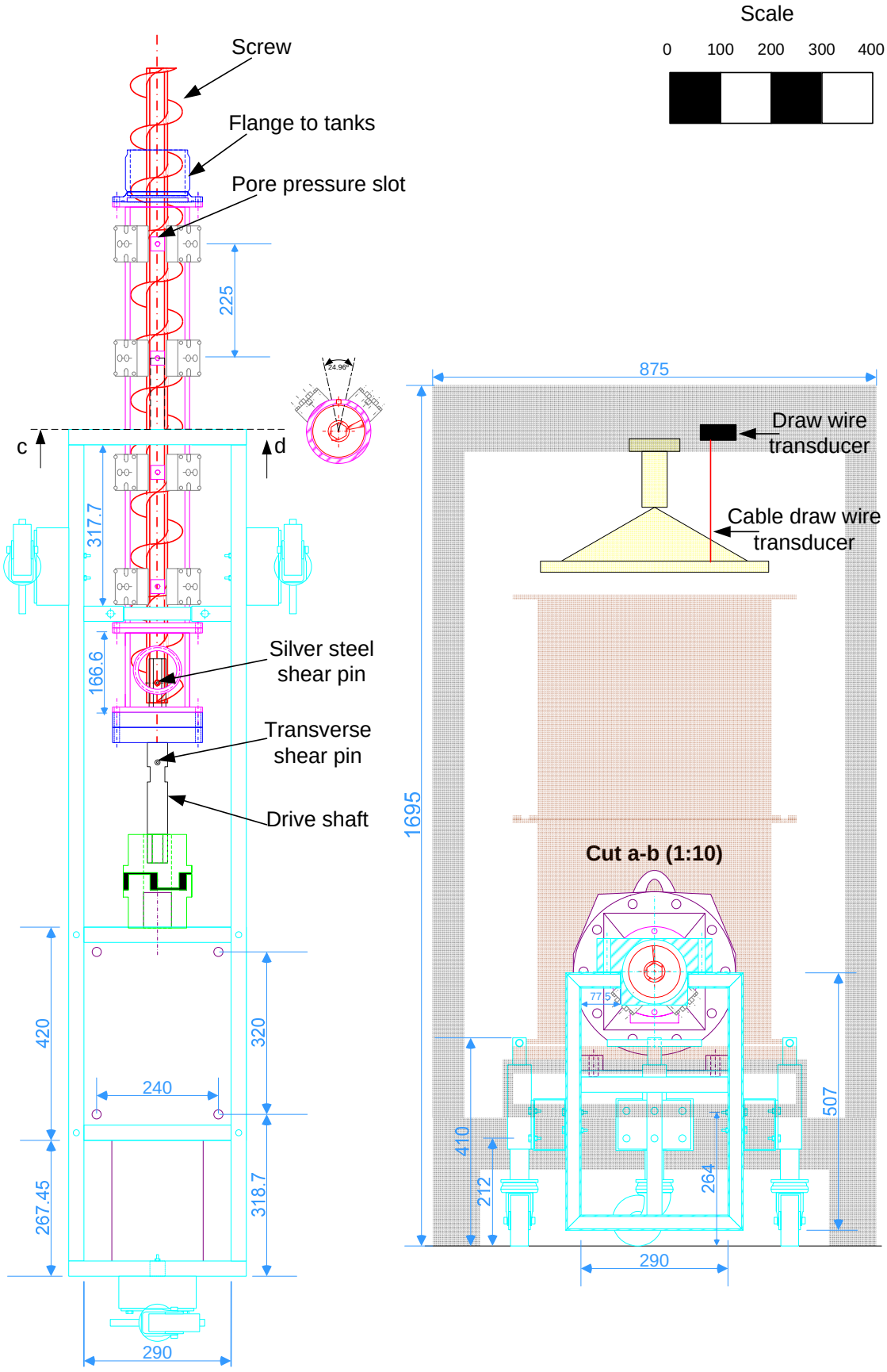

Figure 6.4. Bottom view general arrangement and cut a-b of Oxford screw conveyor

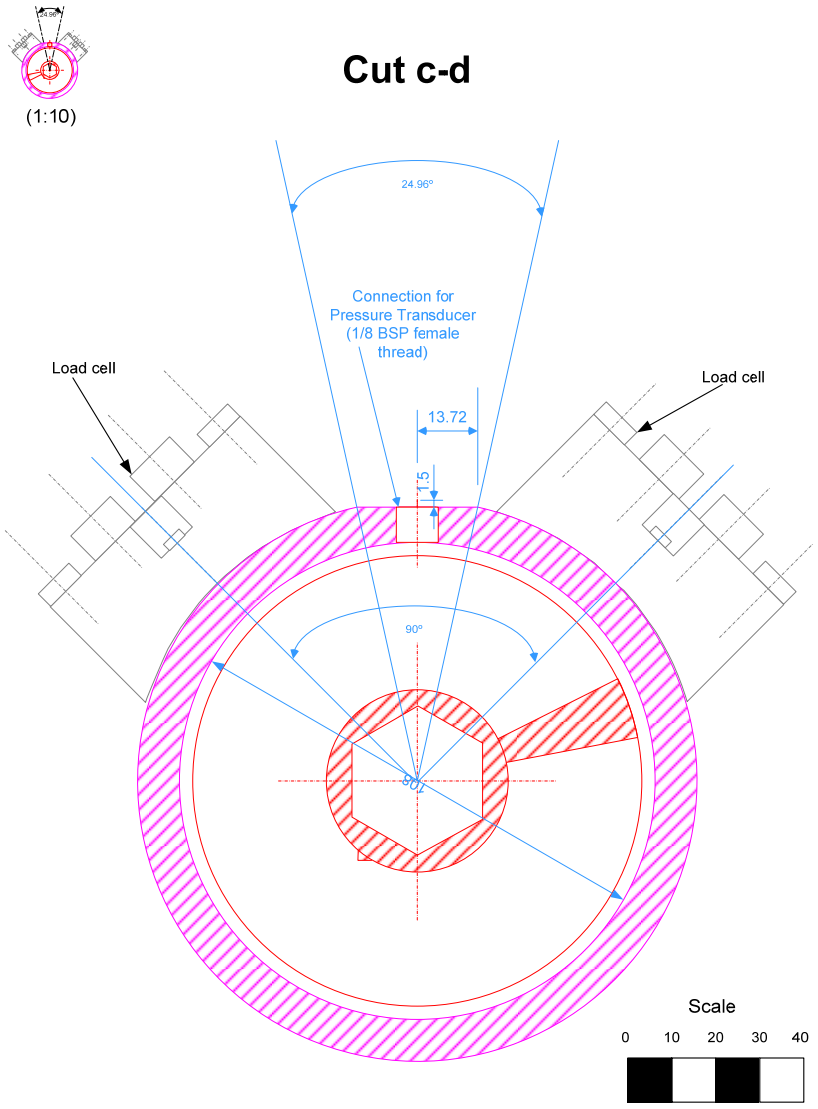

Figure 6.5. Cut c-d of Oxford screw conveyor

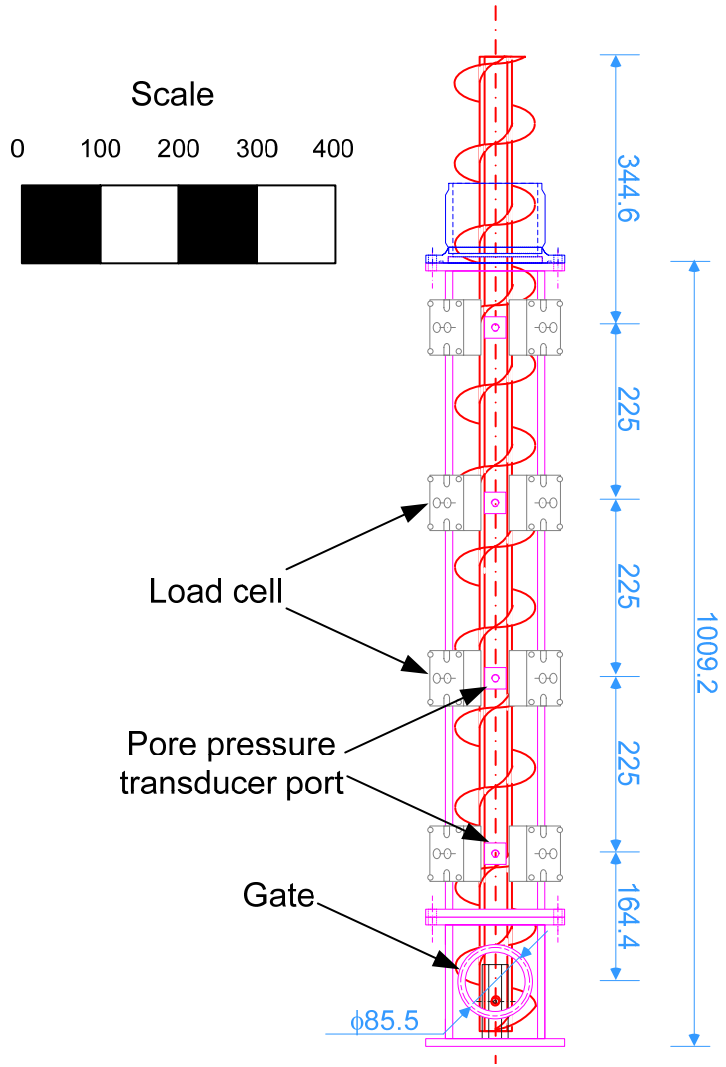

Figure 6.6. Casing overview.

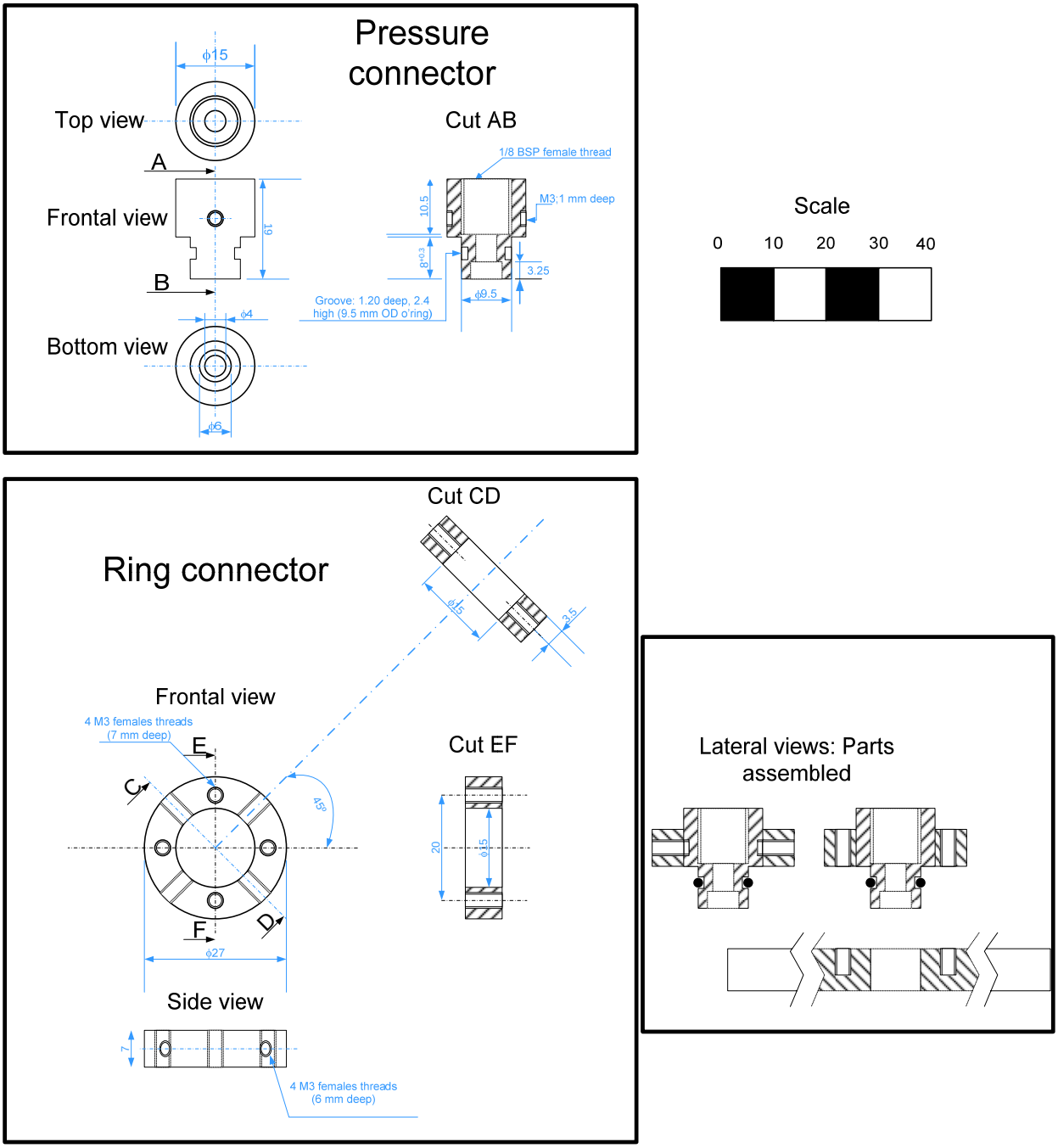

Figure 6.7. Pressure transducer connectors

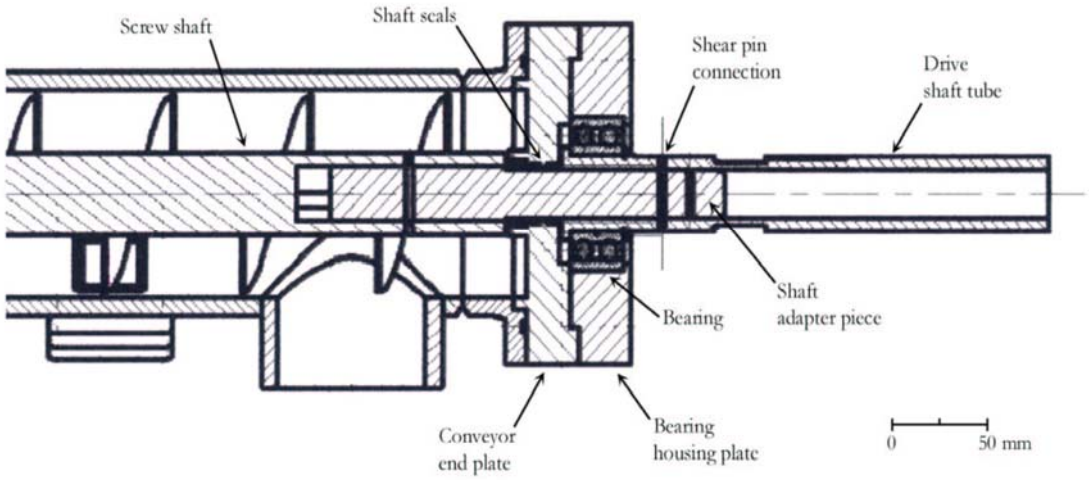

Figure 6.8. Merritt's drive shaft layout (Merritt, 2004).

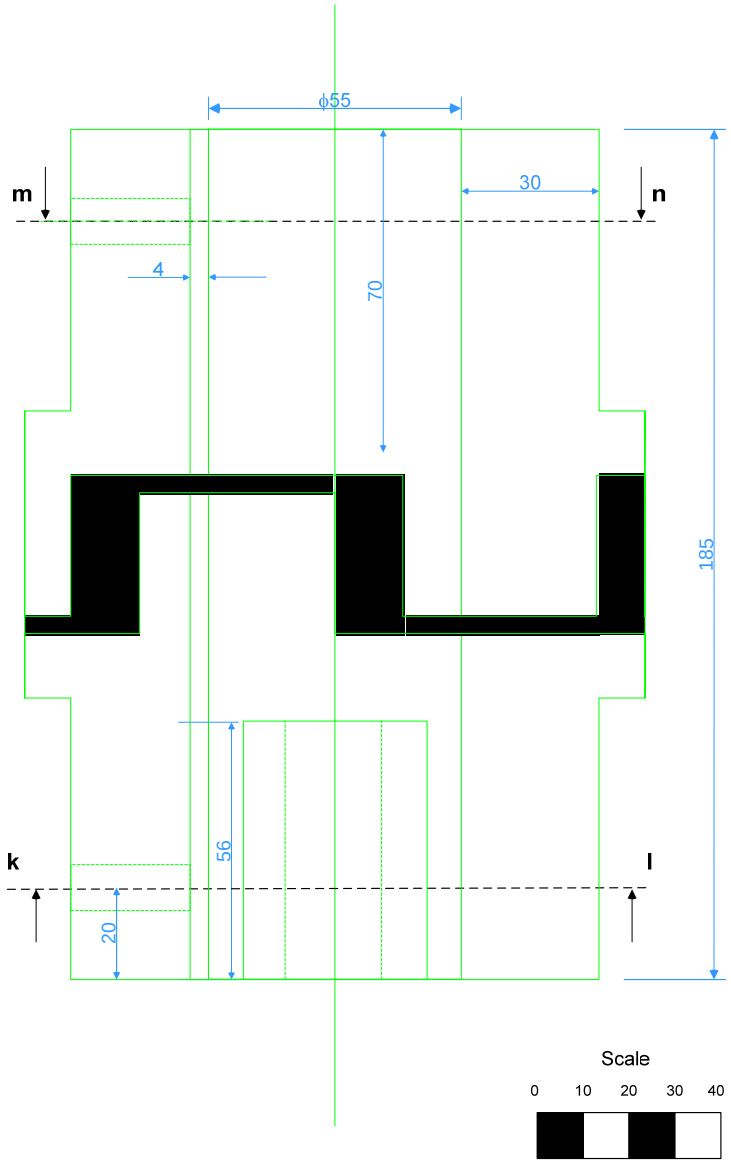

Figure 6.9. Torque coupling.

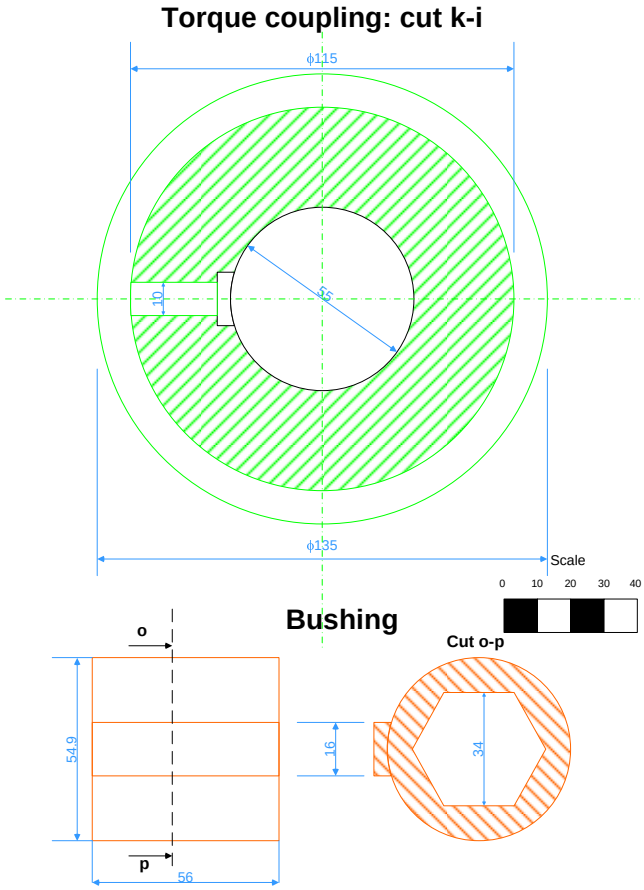

Figure 6.10. Torque coupling: cut k-i and bushing.

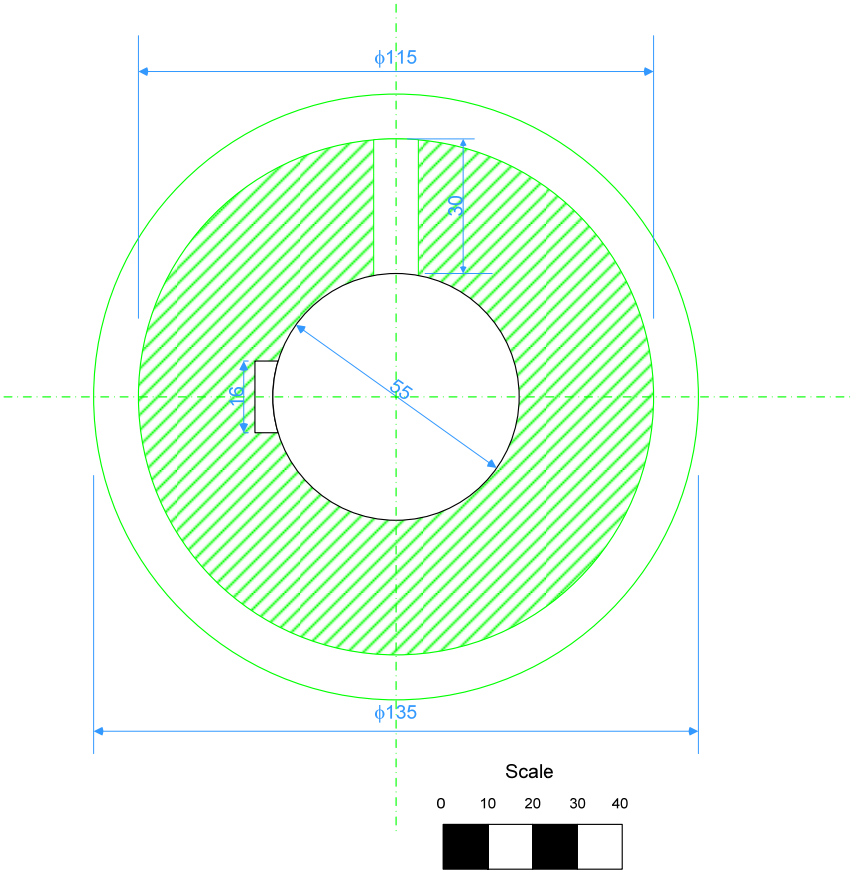

Figure 6.11. Torque coupling: cut m-n..

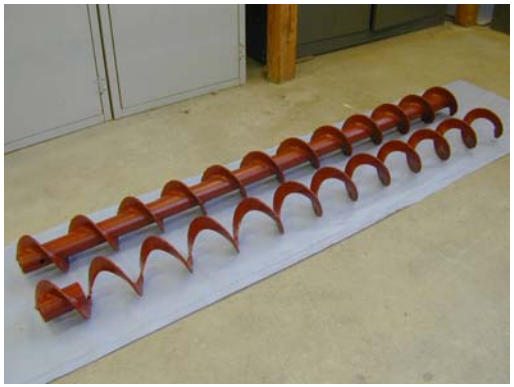

Figure 6.12. Screws.

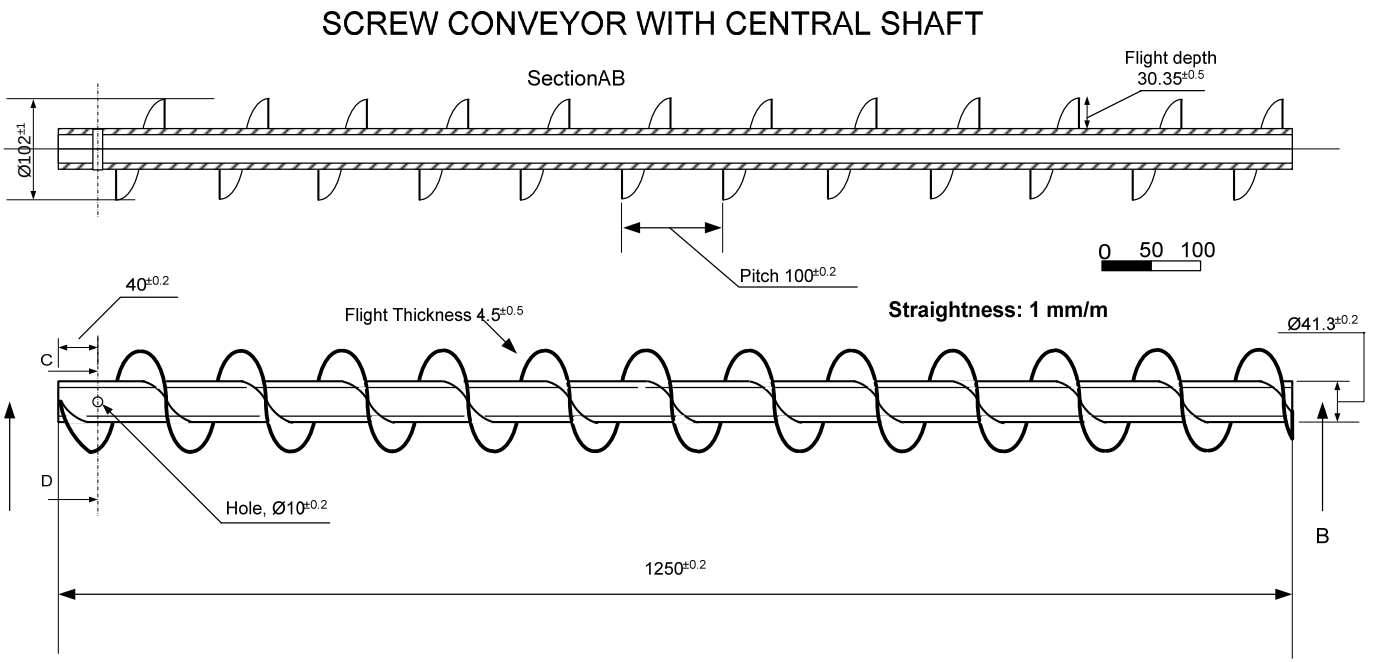

Figure 6.13. Screw with central shaft.

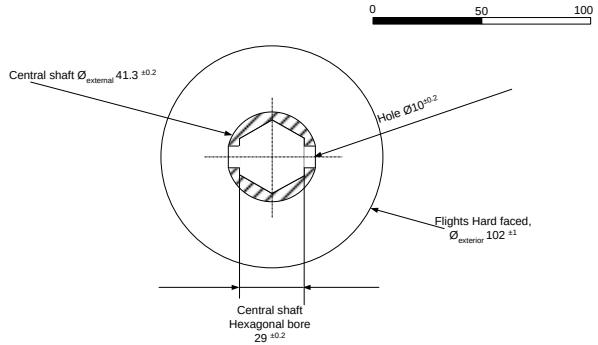

Figure 6.14. Screw cut c-d..

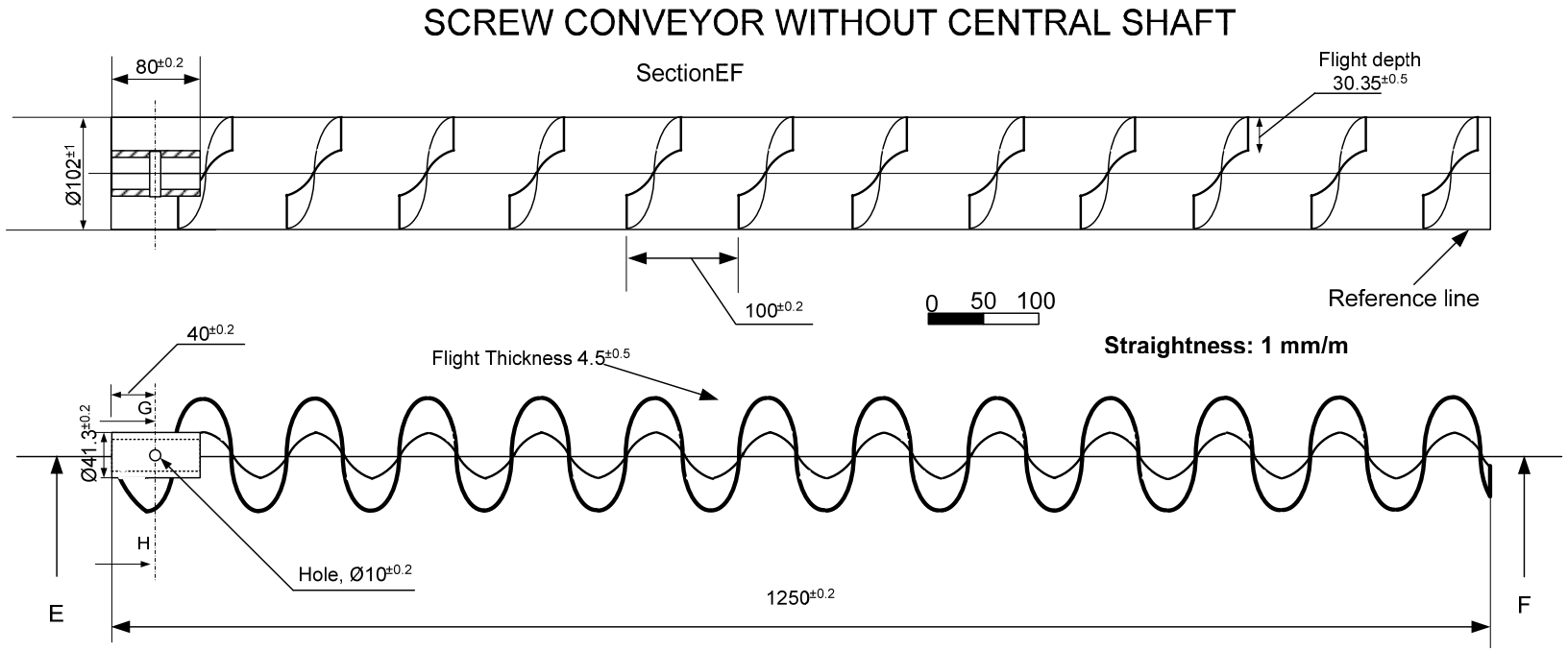

Figure 6.15. Screw without central shaft.

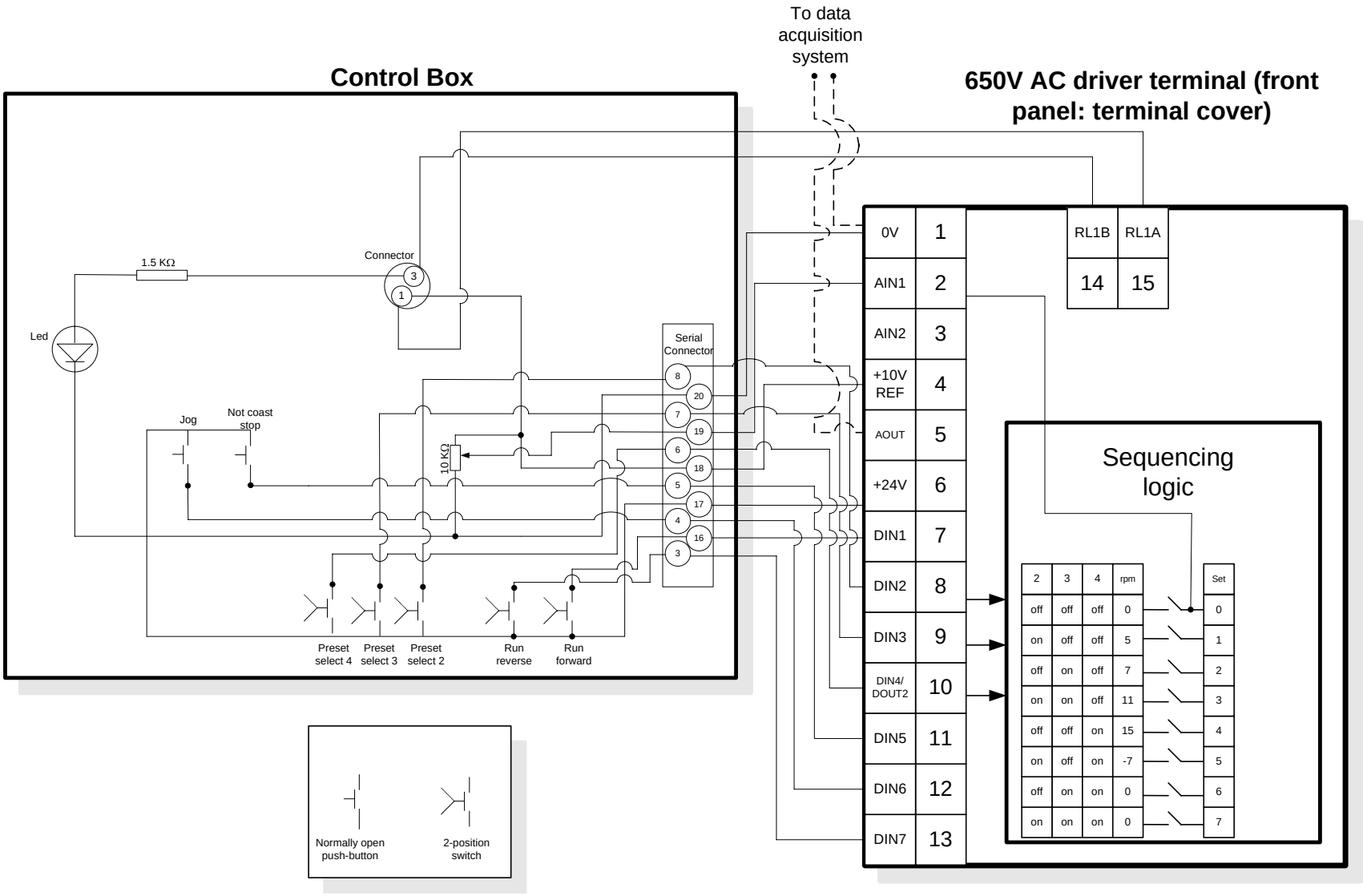

Figure 6.16. Internal circuit control box and internal panel 650V driver.

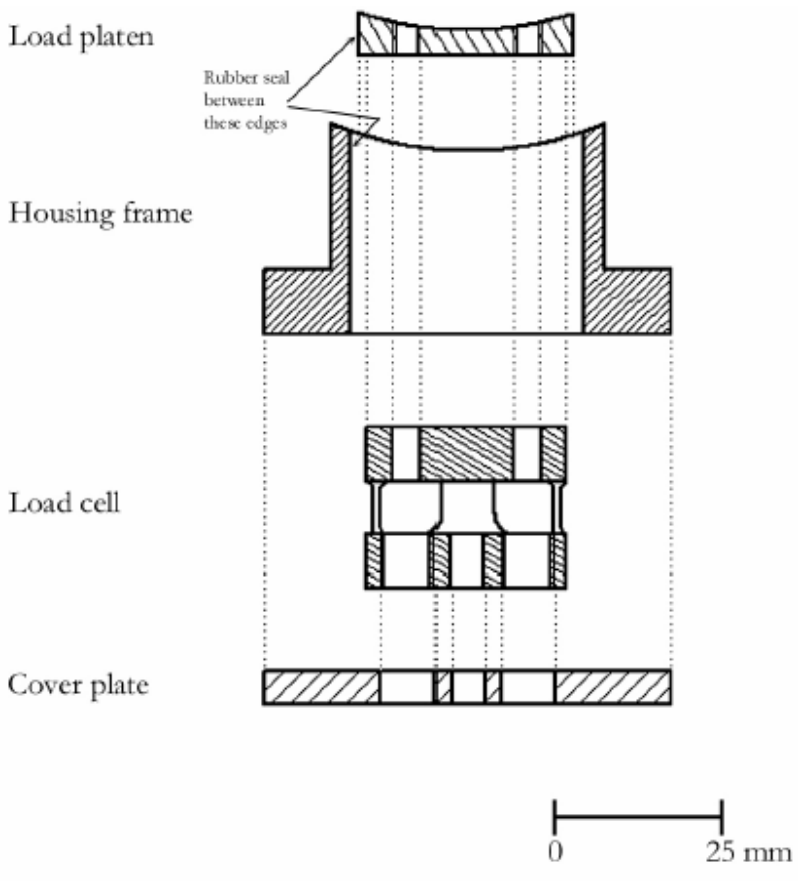

Figure 6.17. Load cell and housing components (Merritt, 2004)

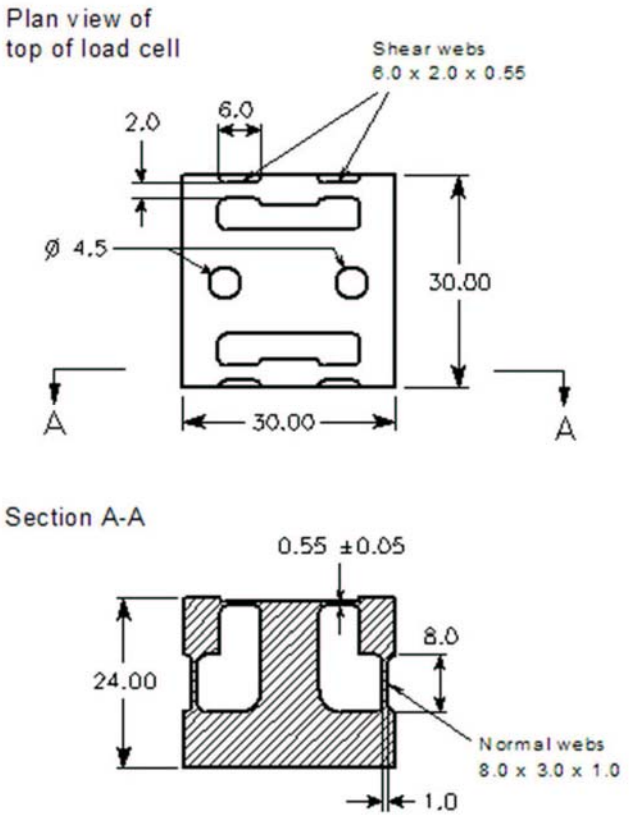

Figure 6.18. Load cell design drawing (Merritt, 2004)

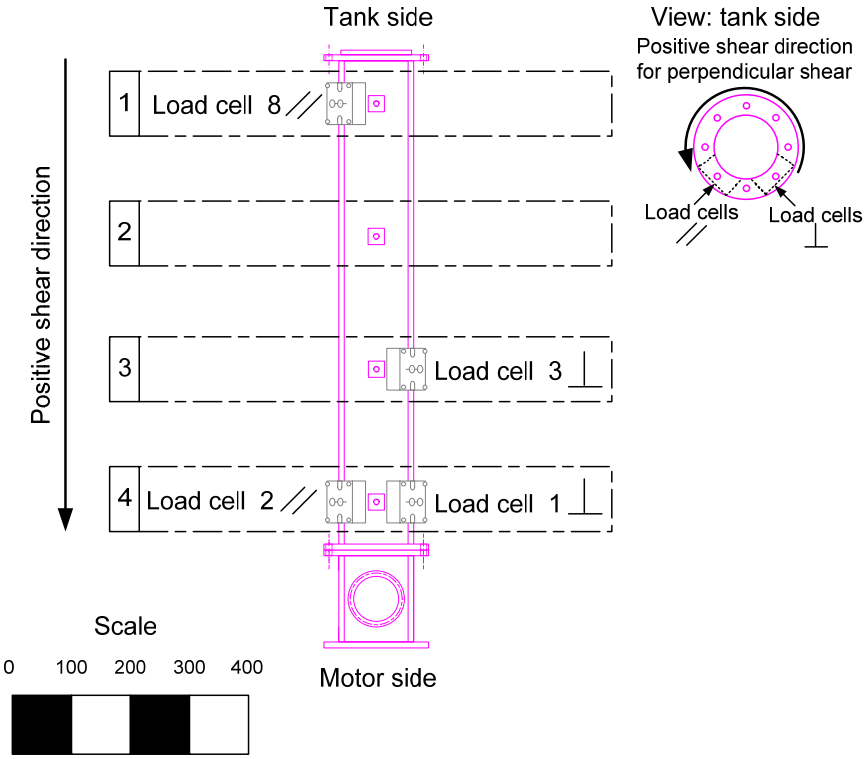

Figure 6.19. OSC Cambridge type load cells layout for SCOD 1 test.

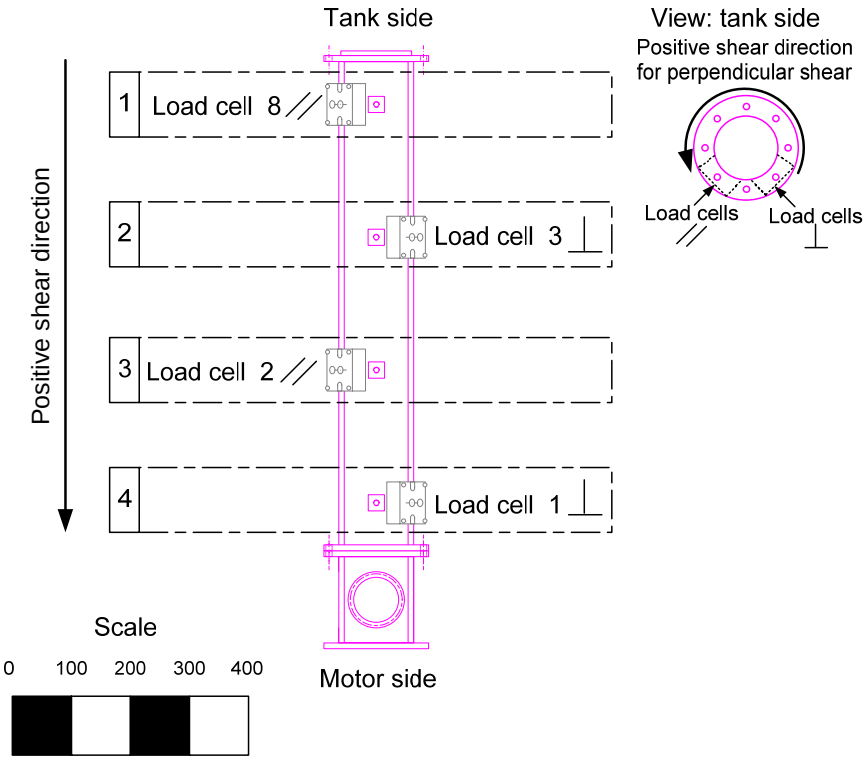

Figure 6.20. OSC Cambridge type load cells layout for SCOD 2 to SCOD 16.

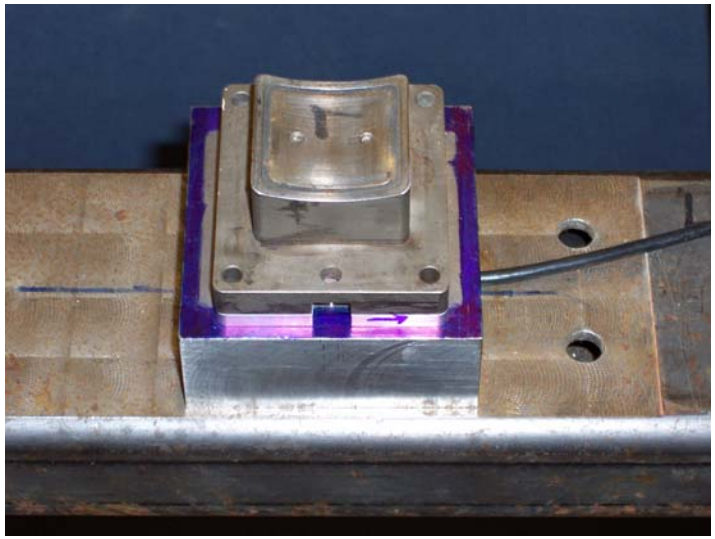

Figure 6.21. Cambridge type load cell.

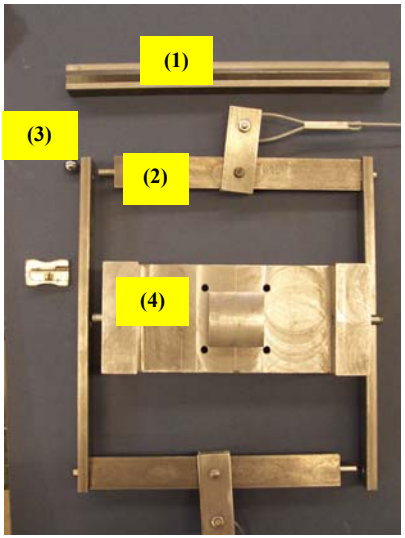

Figure 6.22. Loading system, (1) angular bar, (2) pull frame, (3) ball bearing and (4) block.

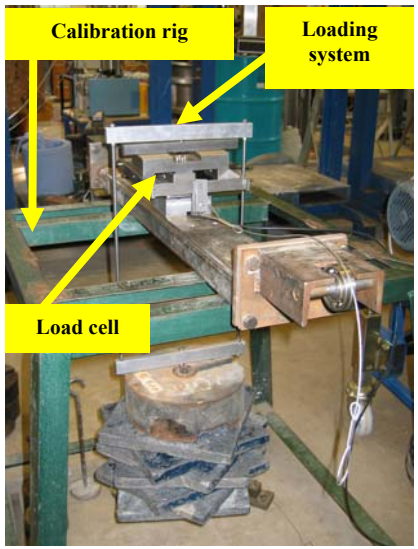

Figure 6.23. Loading rig and loading system.

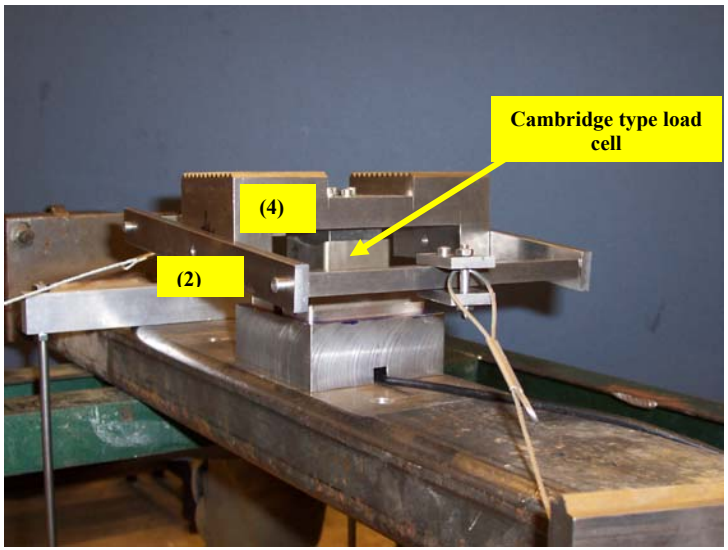

Figure 6.24. Calibration type load cell and loading system parts (4) and (2).

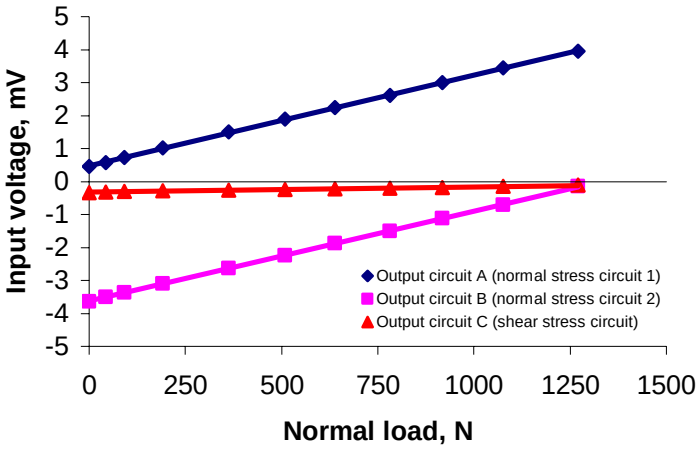

(a). Normal load calibration

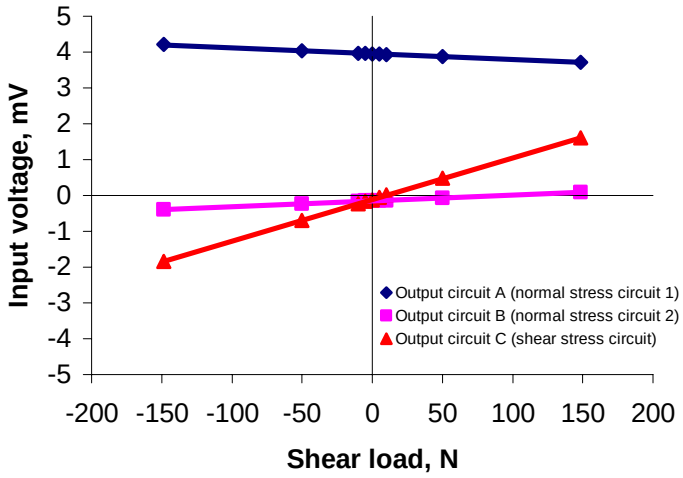

(b). Shear load calibration.

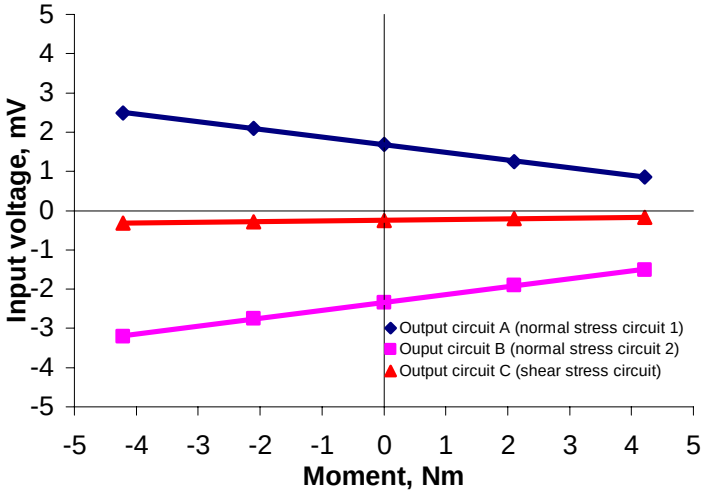

(c). Moment calibration

Figure 6.25. Example load cell calibration results.

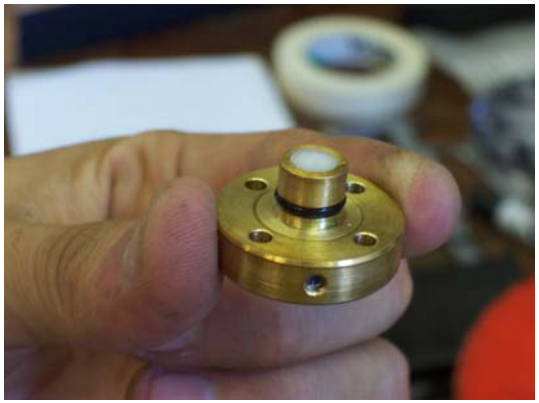

(a). Overview of pressure transducer connector.

(b). Bottom view of pressure transducer connector.

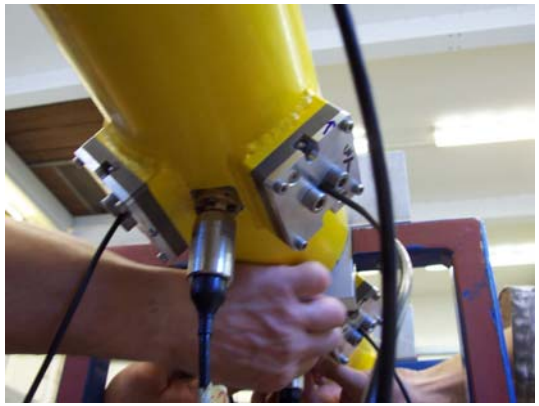

(c). Pressure transducer placed in OSC casing.

Figure 6.26. Pressure transducer connector assembled

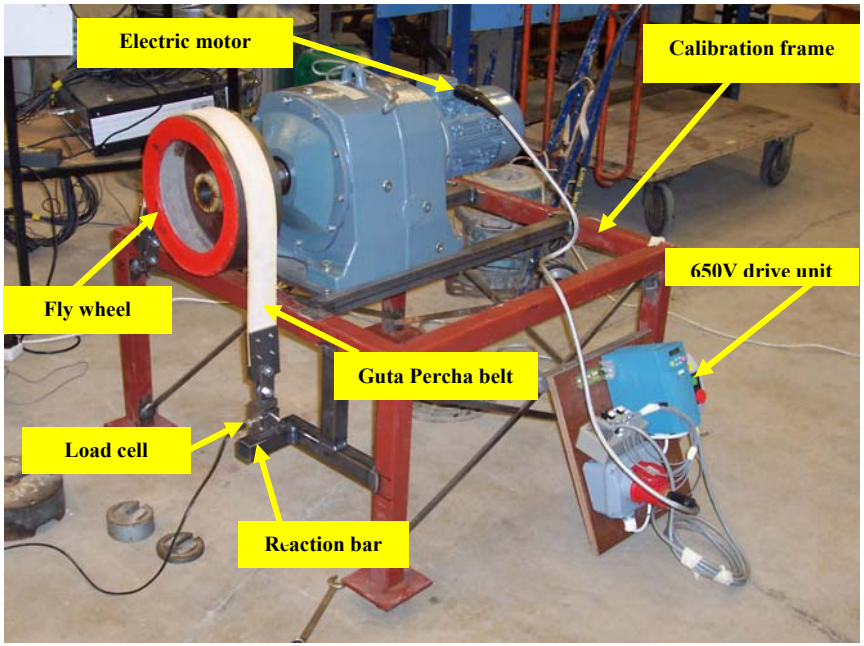

(a) Overview.

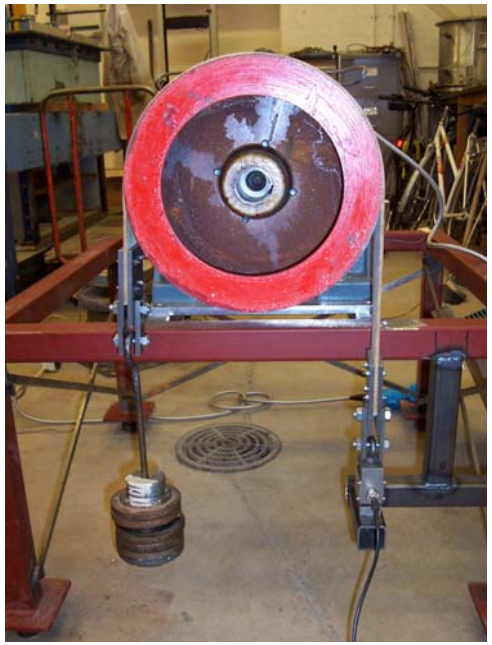

(b) Flywheel loaded.

Figure 6.27. Torque calibration system.

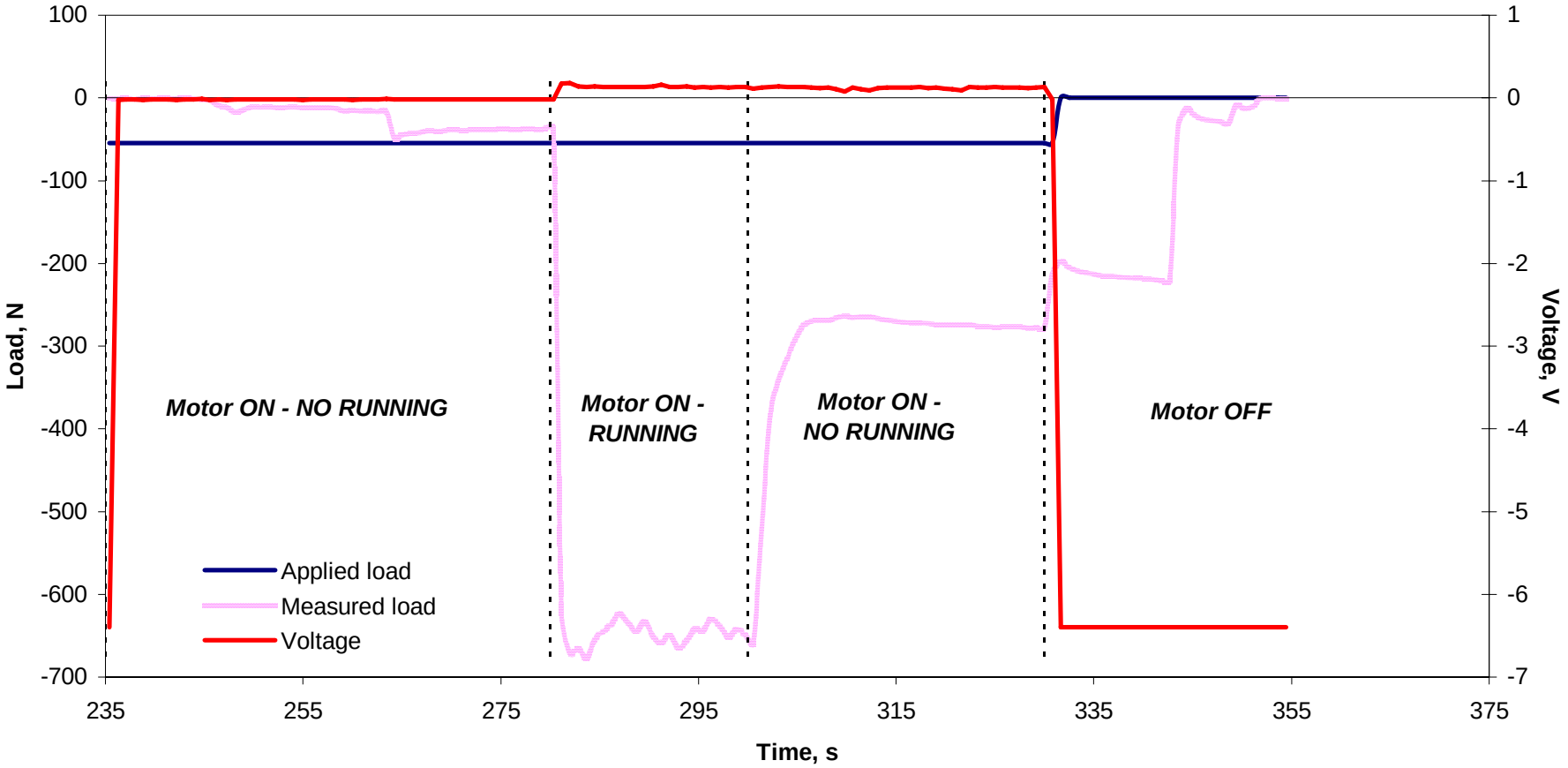

Figure 6.28. Example calibration series at 7 rpm and 54.21 N of constant load.

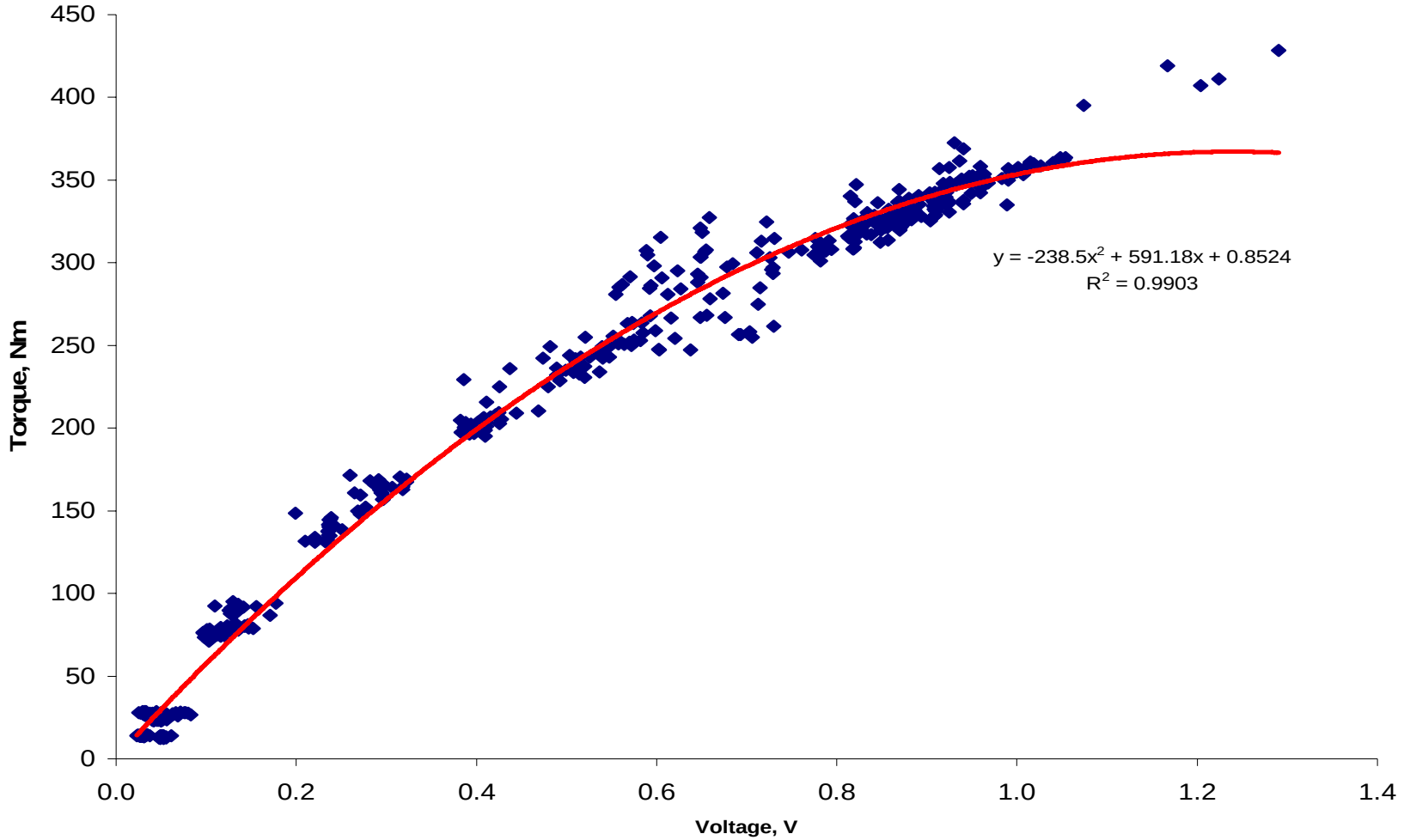

Figure 6.29. Torque calibration curve.

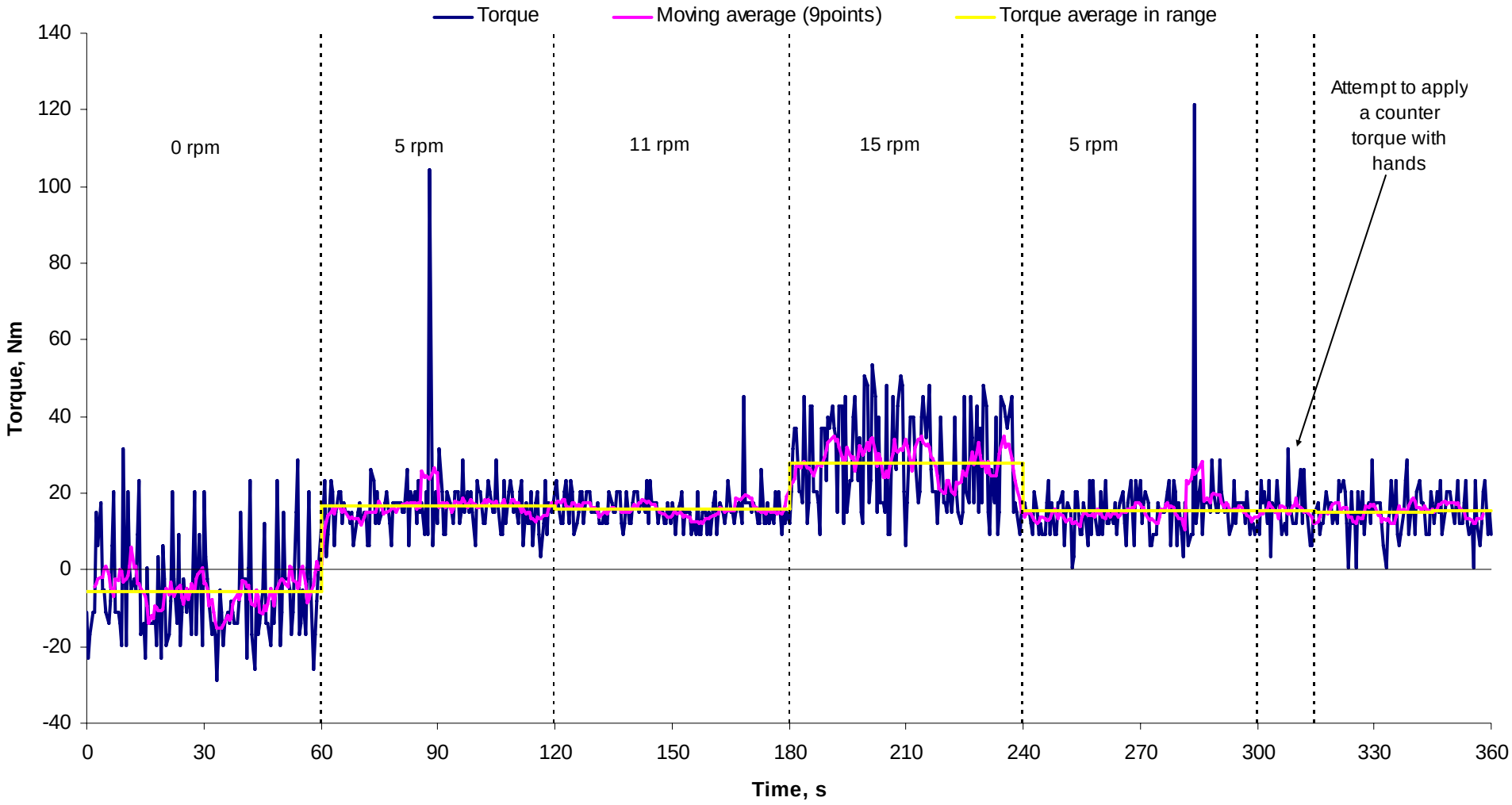

Figure 6.30. Torque supplied by motor to rotate screw conveyor without any soil material in casing.

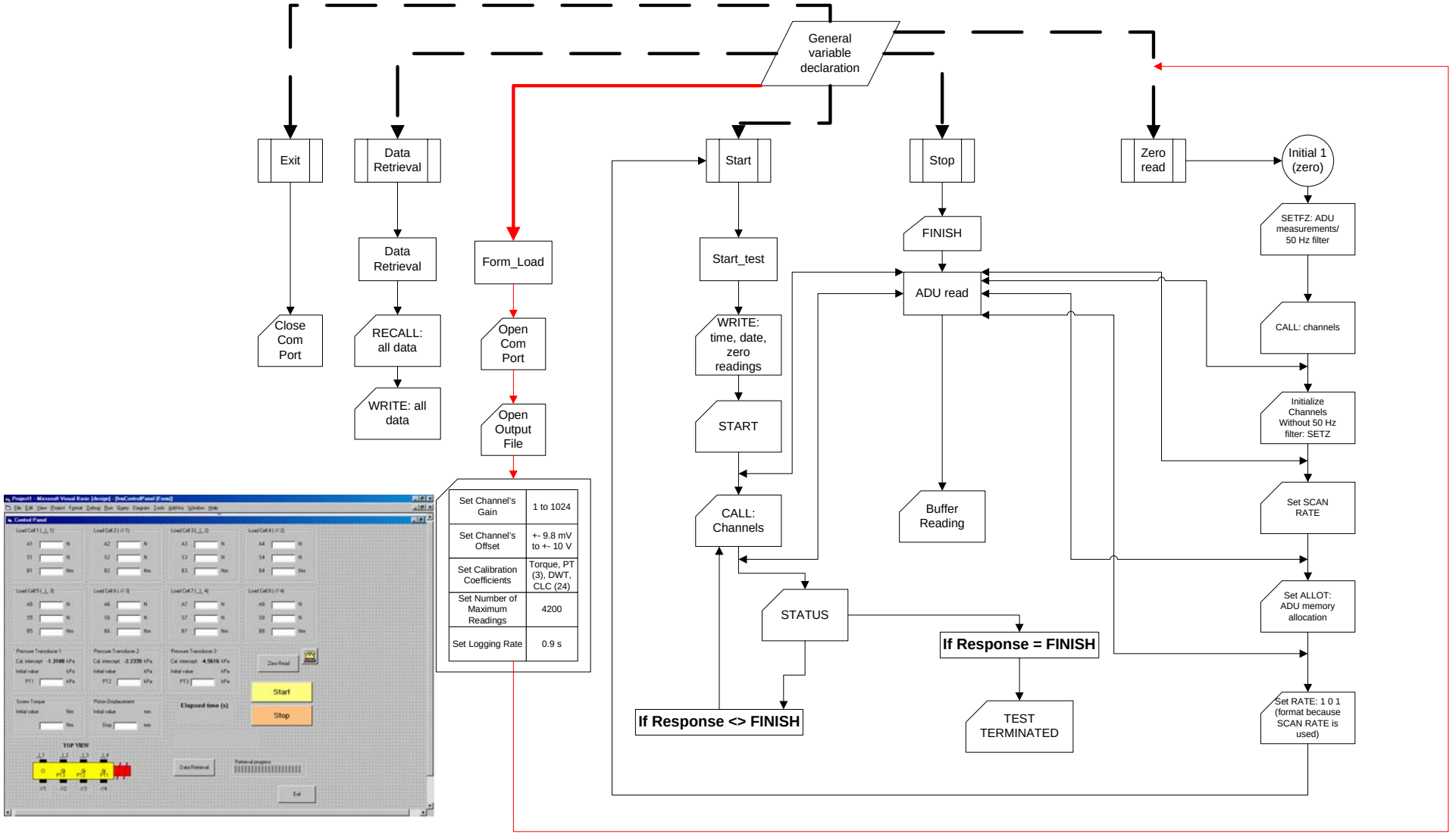

Figure 6.31. Control Panel programme: screen interface and flow diagram.

Figure 6.32. Gate discharge connectors and plugs; Diameters B = 71.5 mm, C = 45 mm, D = 51.5 mm.

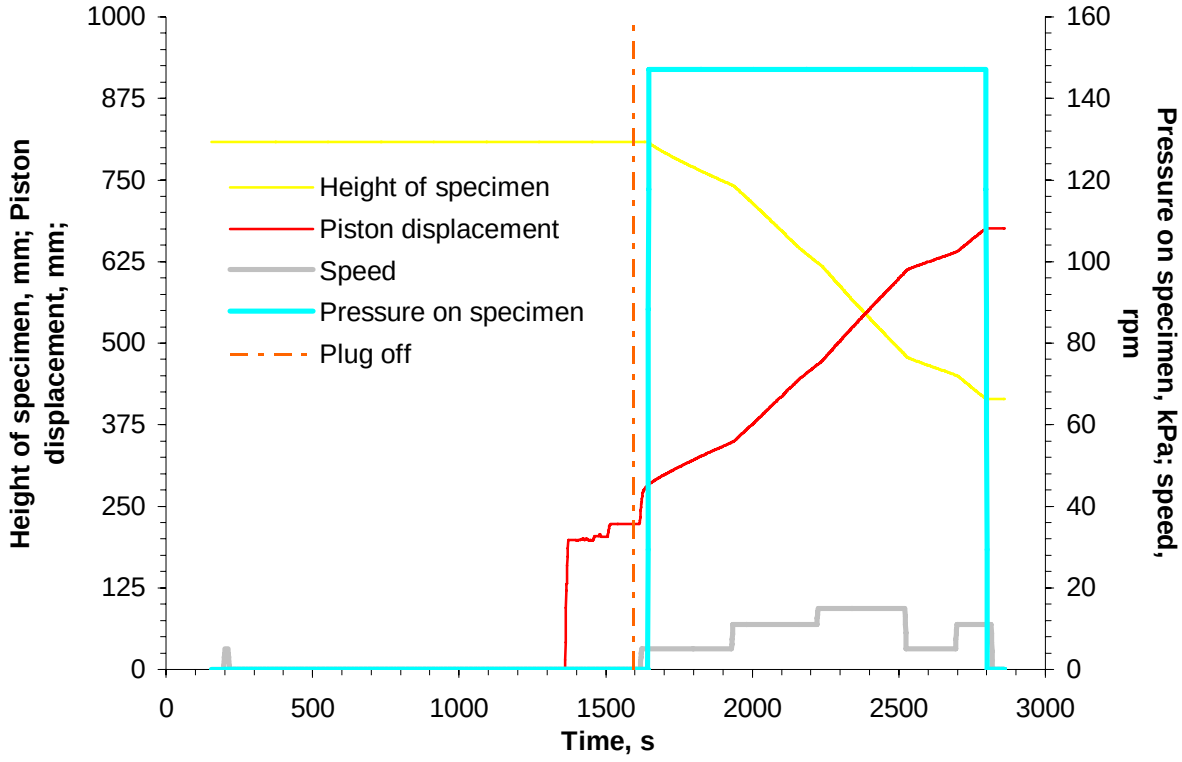

Figure 6.33. Height of specimen, piston displacement, pressure specimen and speed variation during SCOD 9 test.

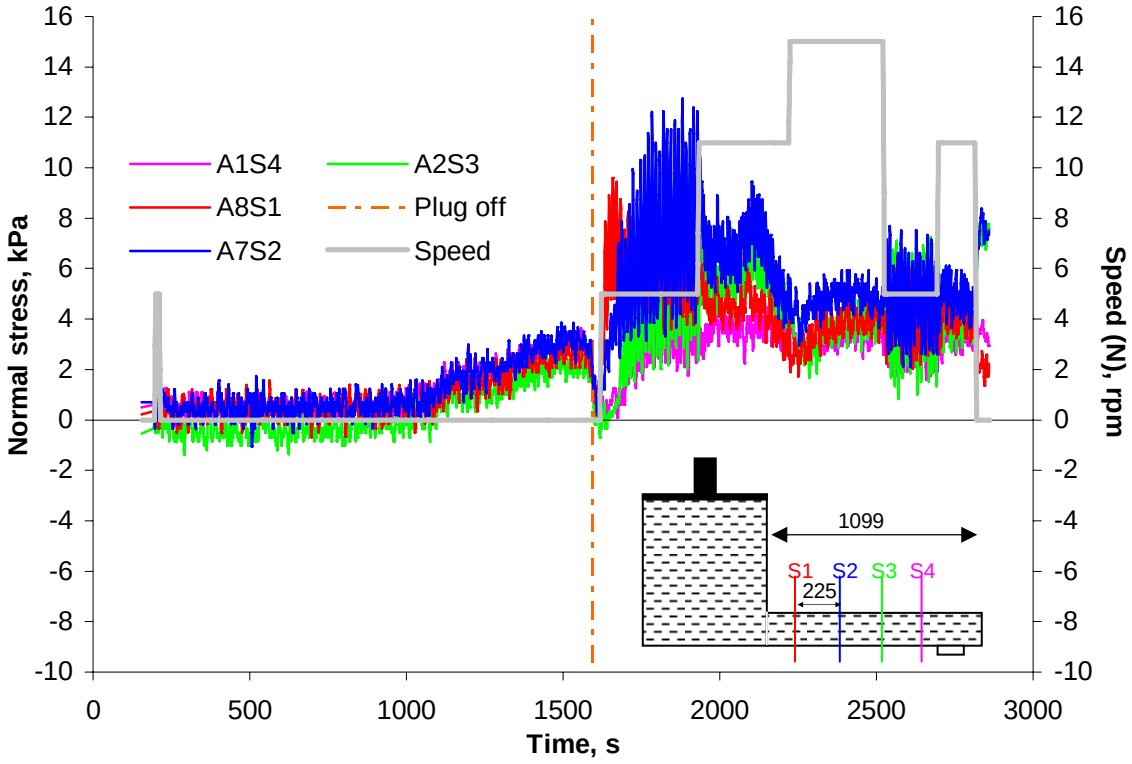

Figure 6.34. Normal stresses measured for SCOD9 test.

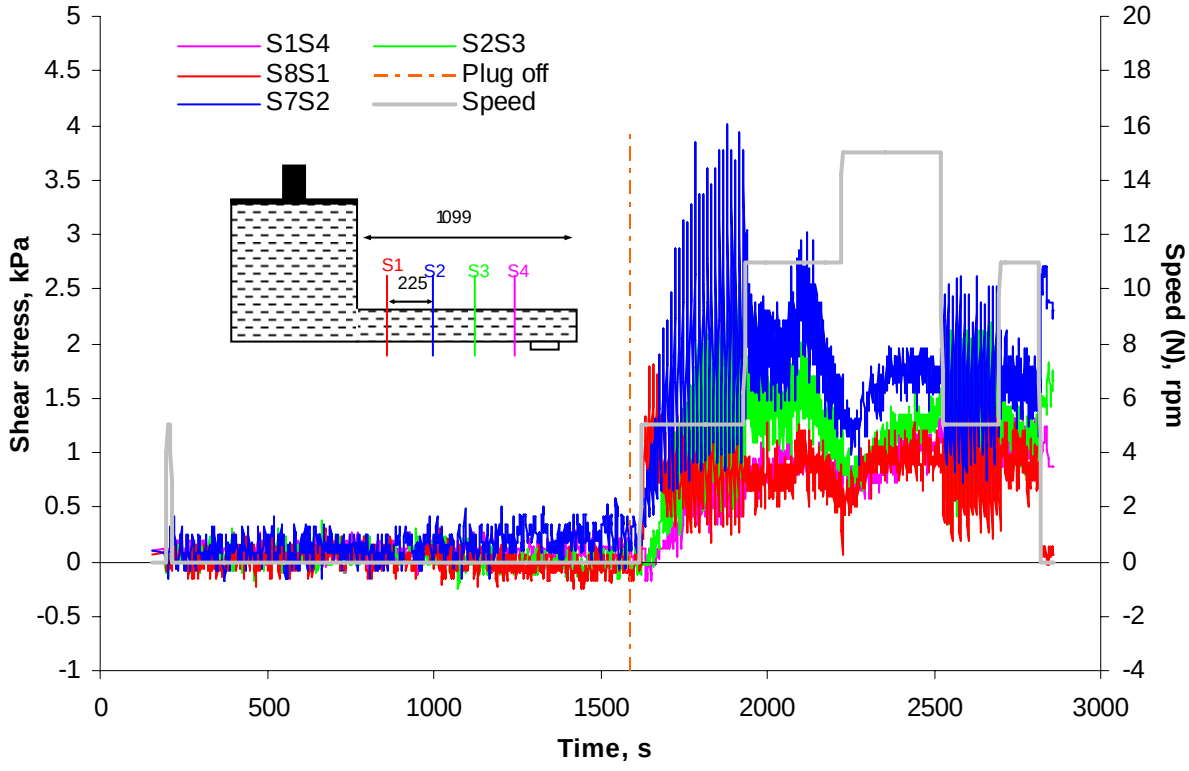

Figure 6.35. Shear stresses measured for SCOD 9 test.

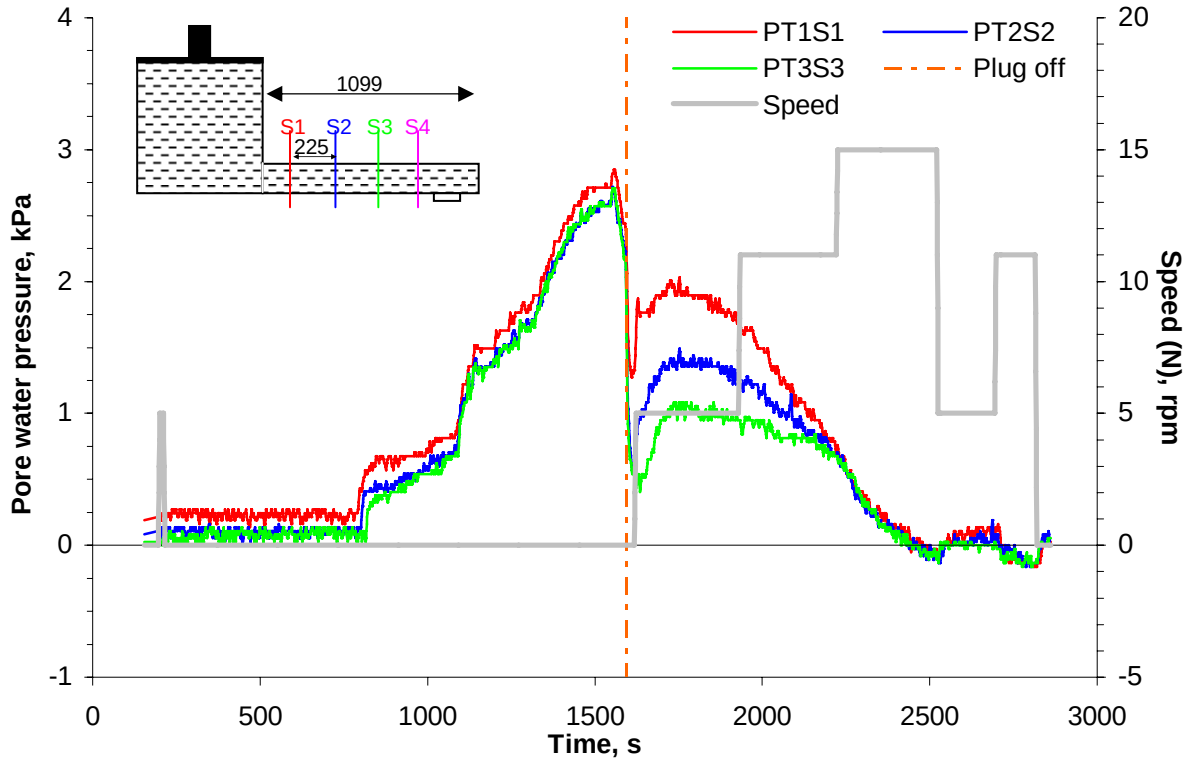

Figure 6.36. Pore water pressures measured for SCOD9 test.

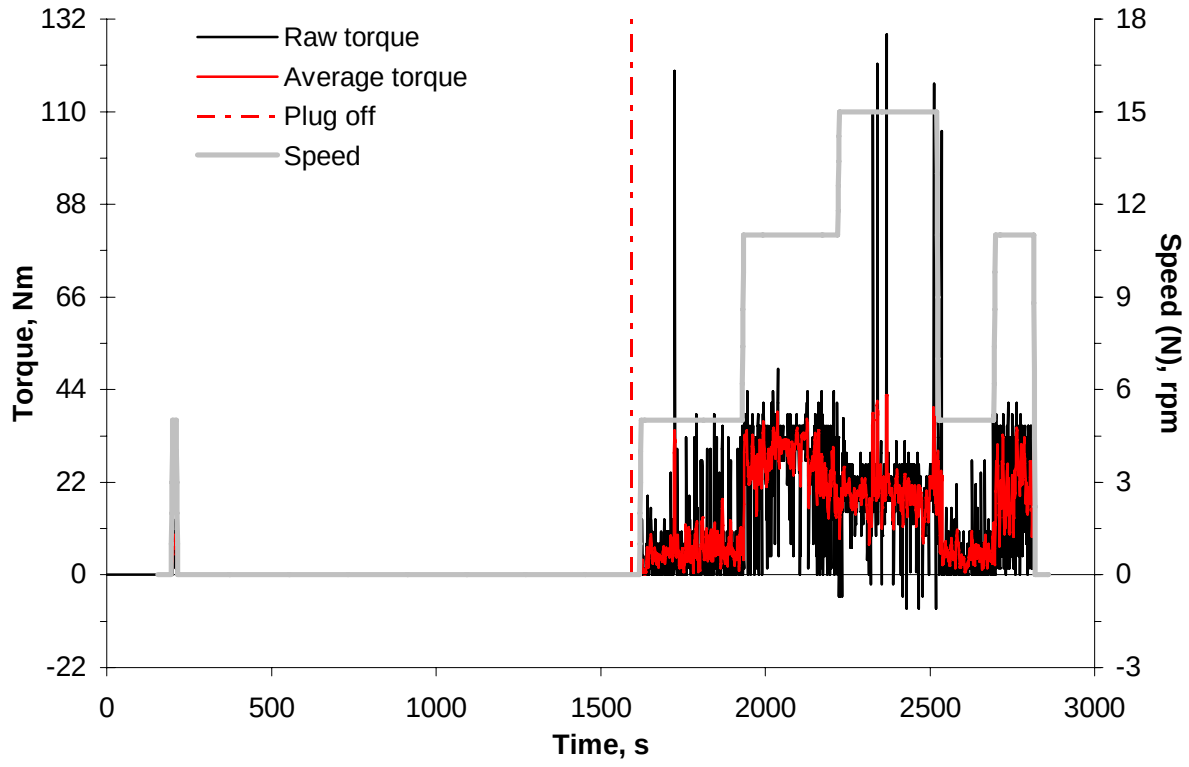

Figure 6.37. Torque calculated for SCOD 9 test.

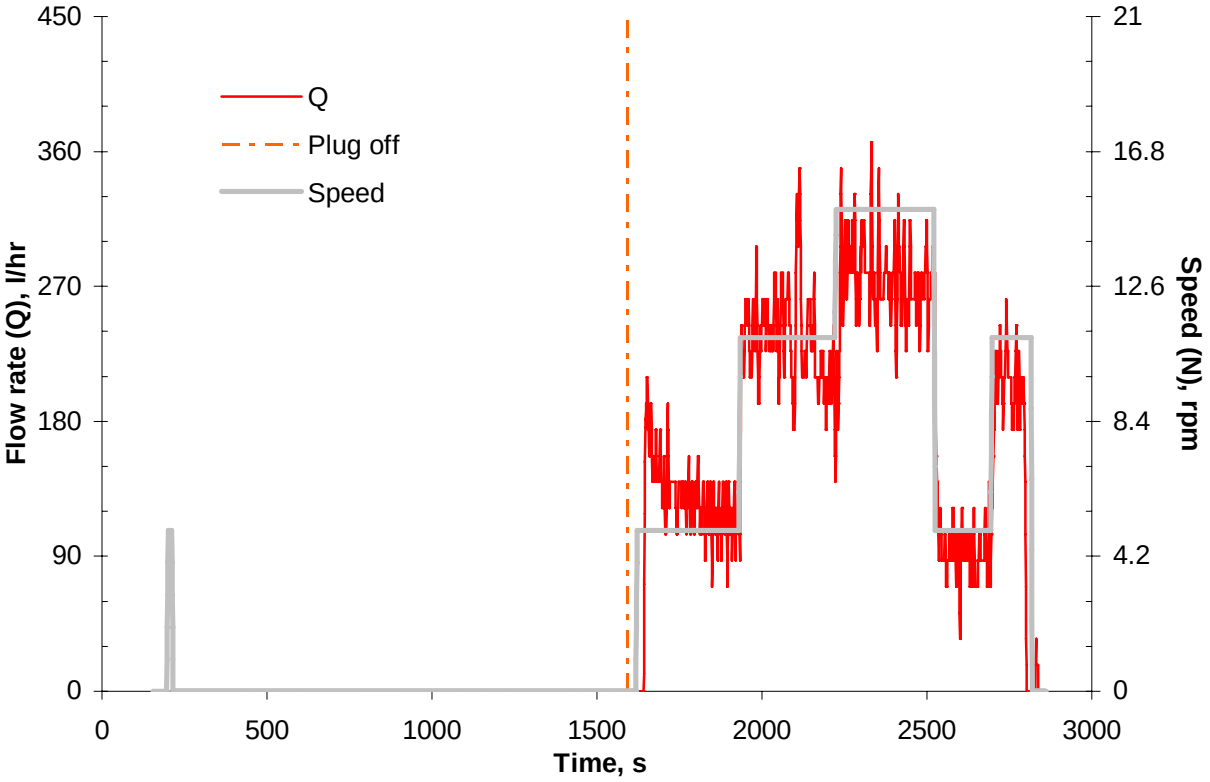

Figure 6.38. Flow rate for SCOD9 test.

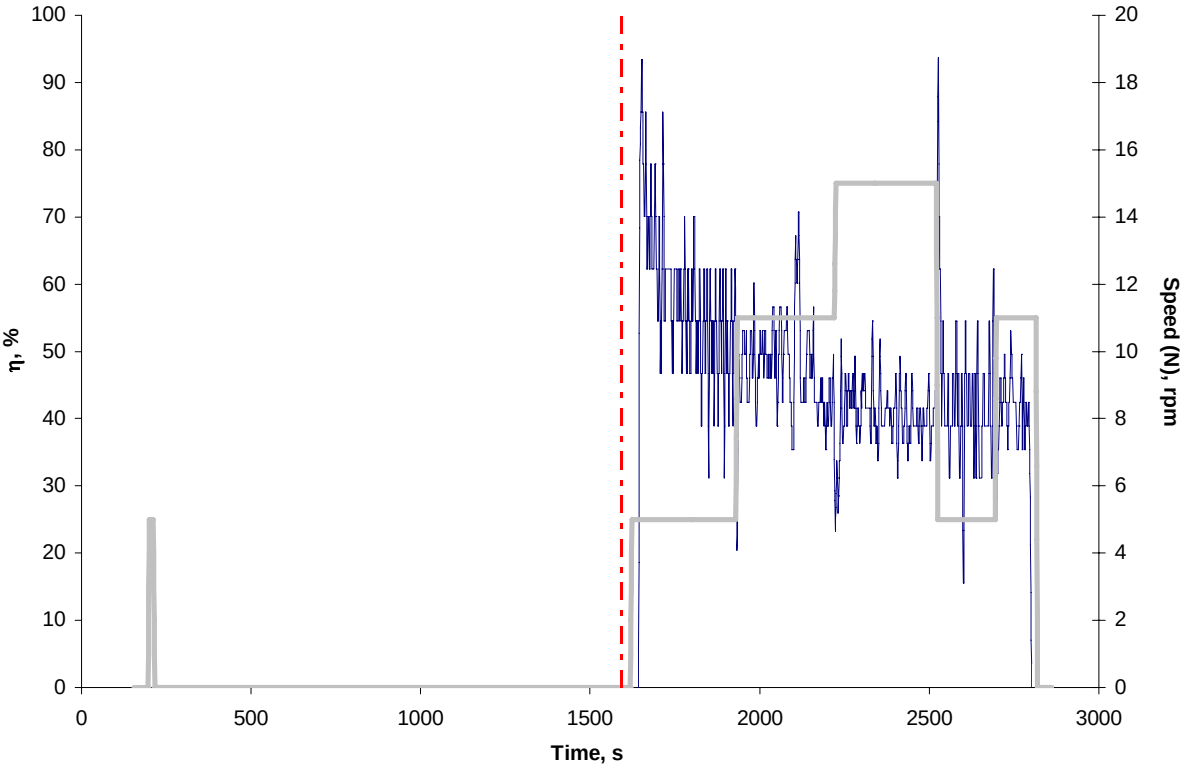

Figure 6.39. Efficiency for SCOD 9 test.

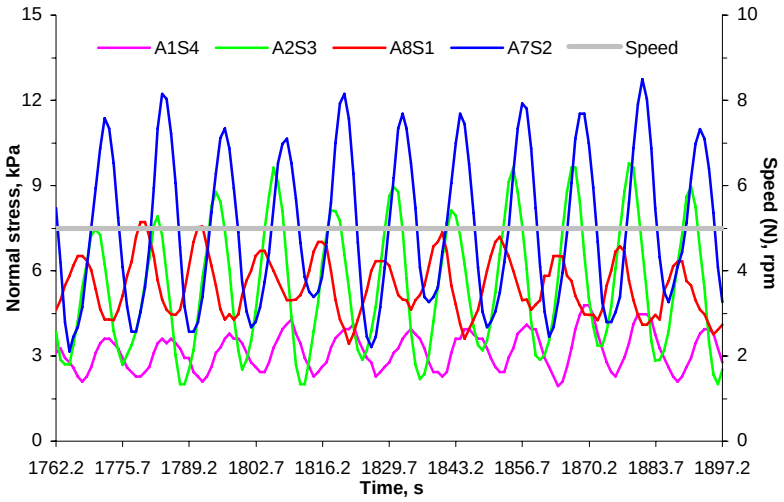

(a) Normal stress.

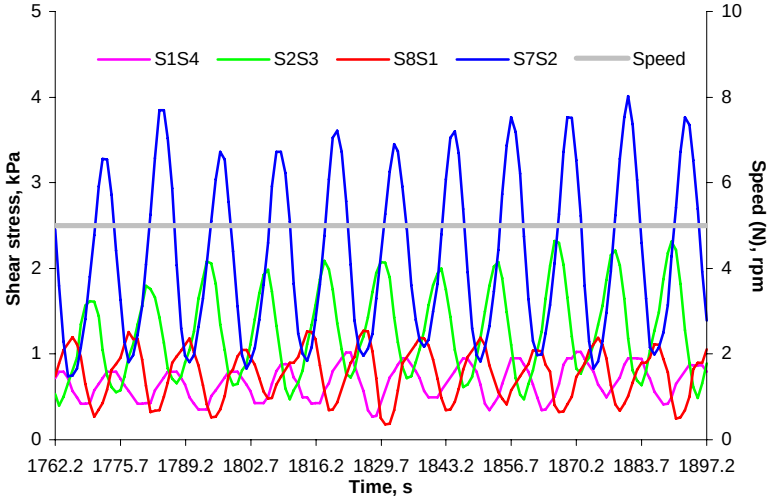

(b) Shear stress.

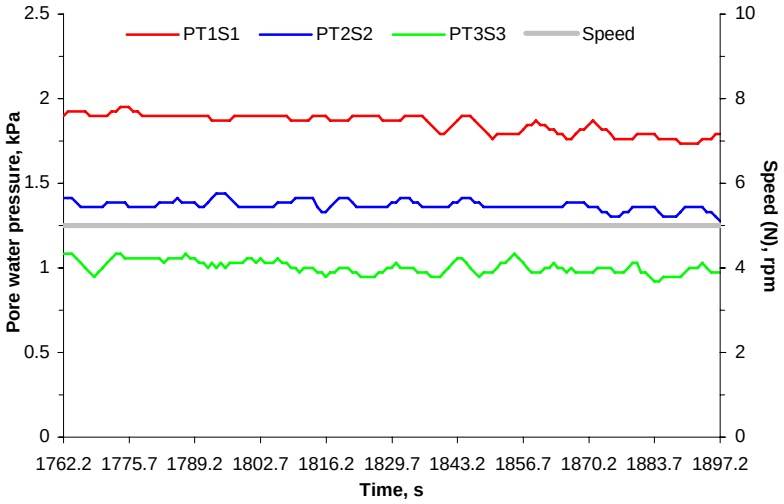

(c) Pore water pressure

Figure 6.40. SCOD9: Normal stress, shear stress and pore water pressure in a steady state event in stage 2 (SCOD9-5.2).

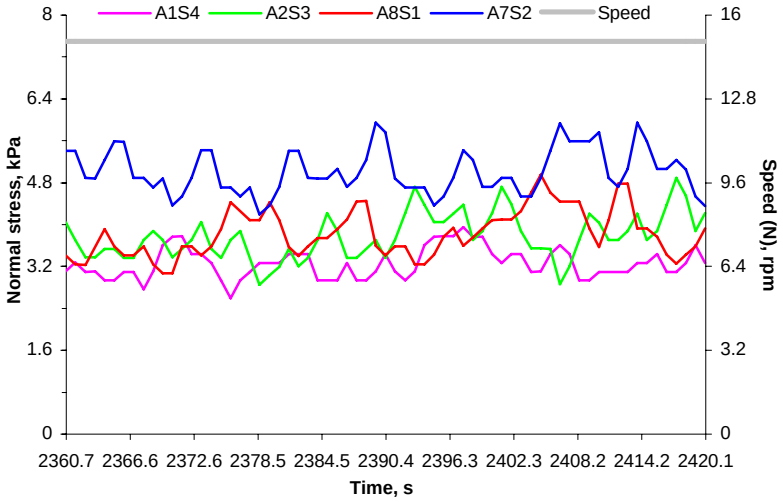

(a) Normal stress.

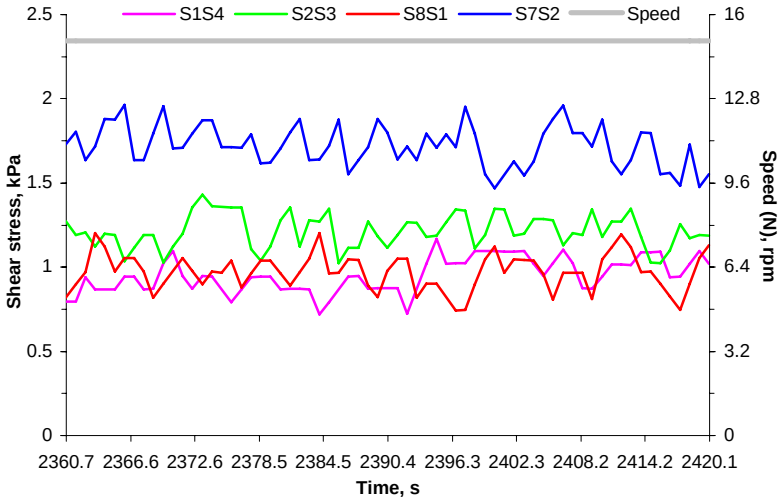

(b) Shear stress.

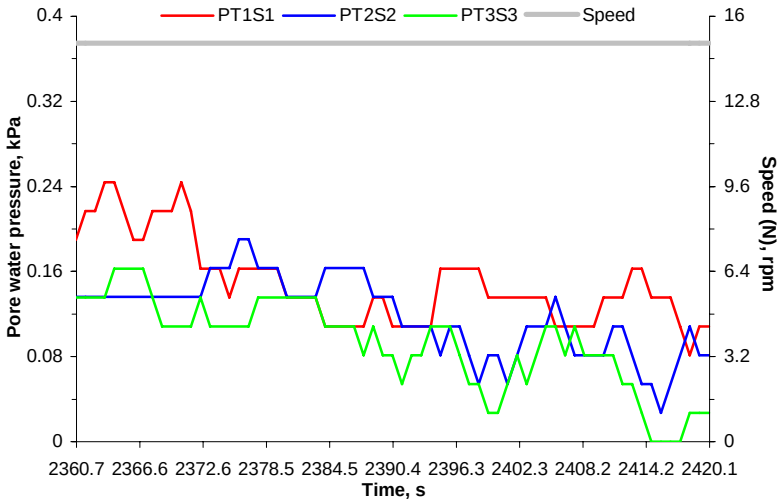

(c) Pore water pressure

Figure 6.41. SCOD9: Normal stress, shear stress and pore water pressure in a steady state event in stage 4 (SCOD9-15.4).

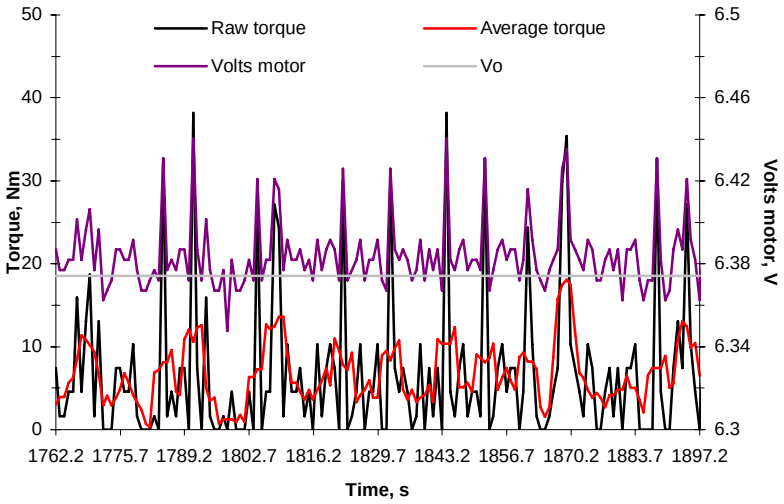

(a) Stage 2 at 5rpm.

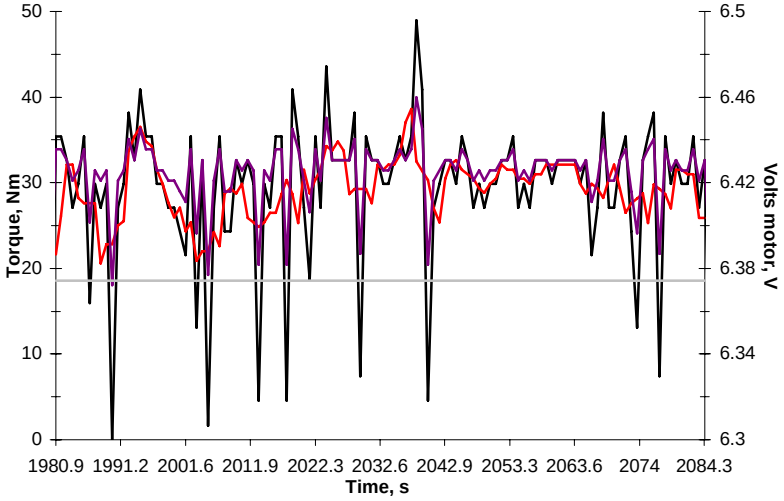

(b) Stage 3 at 11 rpm.

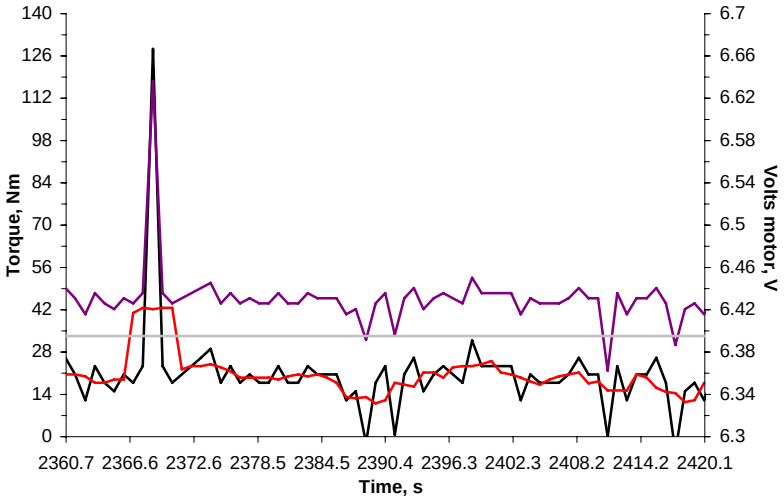

(c) Stage 4 at 15 rpm.

Figure 6.42. SCOD9: Torque values in a steady state event in stage 2 (SCOD9-5.2), stage 3 (SCOD9-11.3) and stage 4 (SCOD9-15.4).

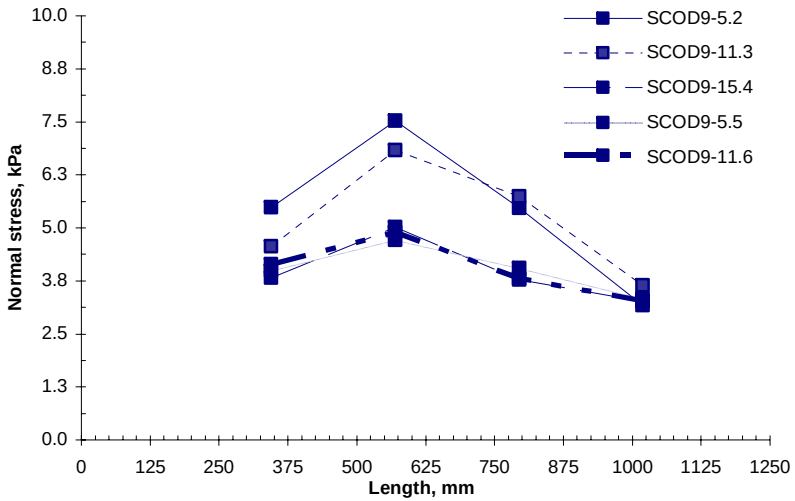

(a) Normal stress.

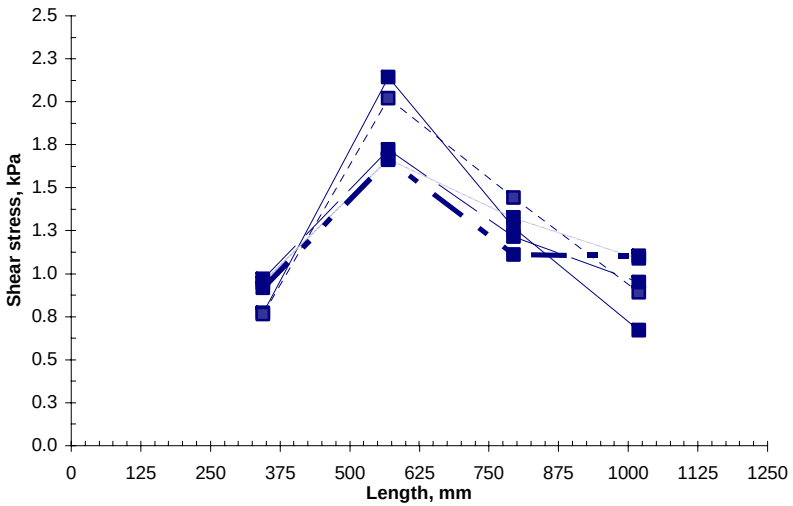

(b) Shear stress.

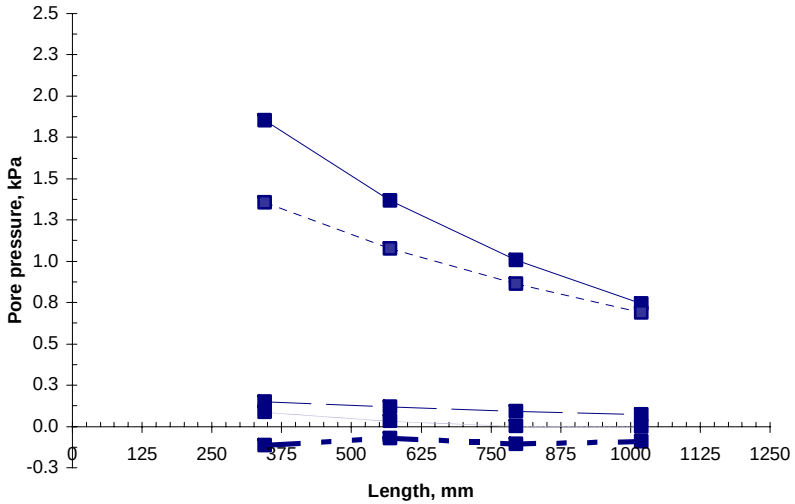

(c) Pore water pressure.

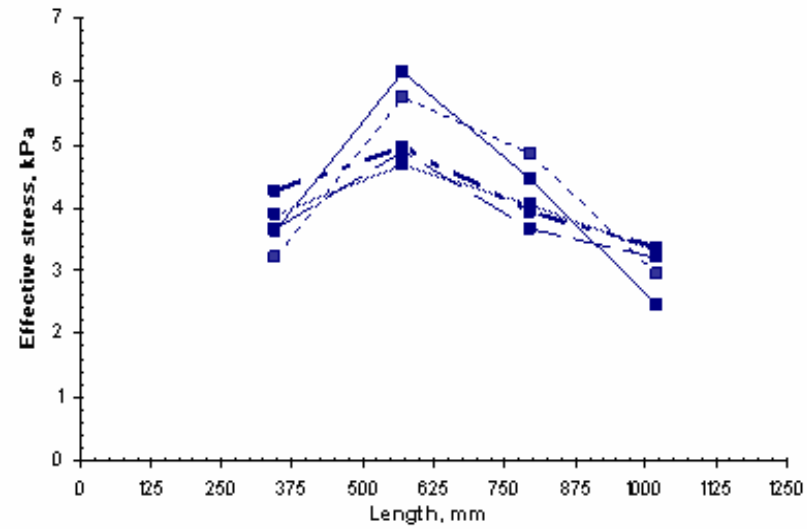

(d) Effective stress.

Figure 6.43. SCOD9: Average steady state values of normal stress, shear stress, pore water pressure and effective stress along the screw length.

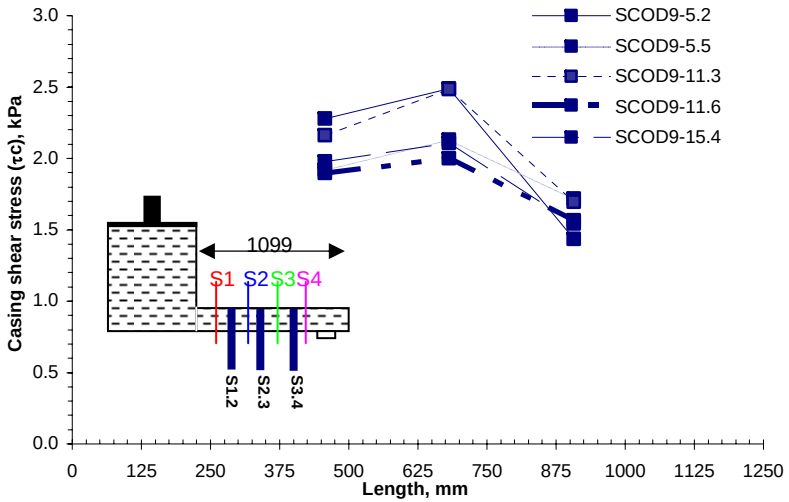

(a) Total shear stress.

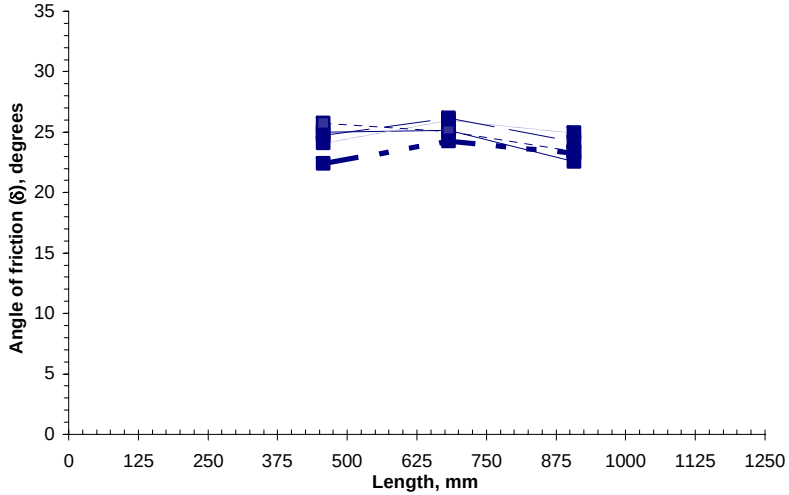

(b) Angle of friction.

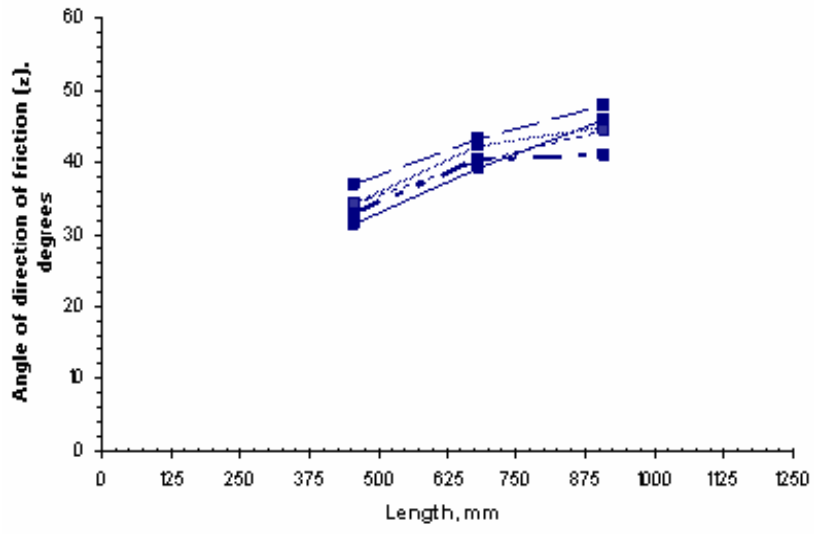

(c) Direction of friction.

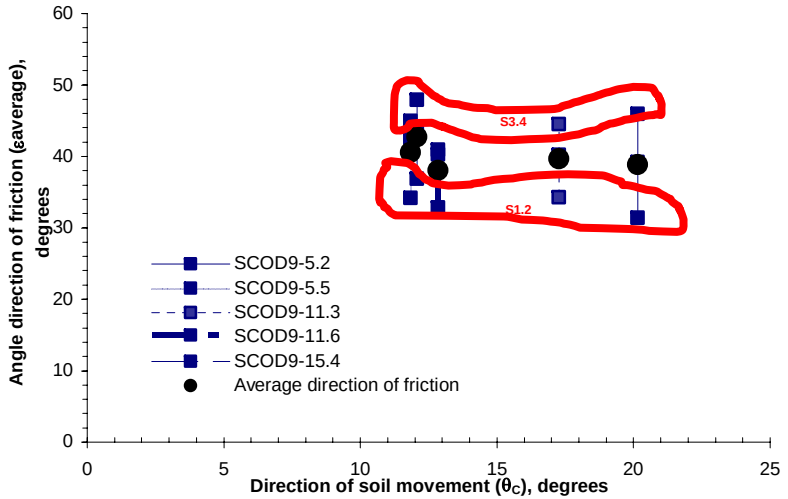

(d) Direction of friction v/s Direction of soil movement..

Figure 6.44. SCOD9: Average steady state values of total shear stress, angle of friction and direction of friction in section S1.2, S2.3 and S3.4.

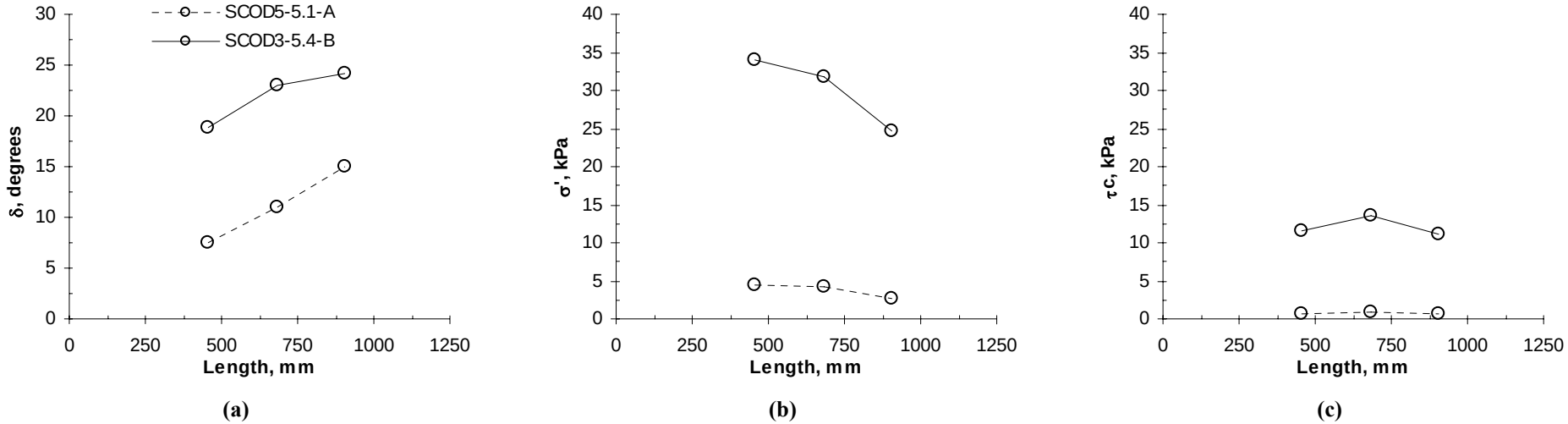

Figure 6.45. Discharge gate effect in conditioned L.B. fine sand at 5 rpm and 73.9 kPa: (a) angle of friction (b) effective stress and (c) casing shear stress.

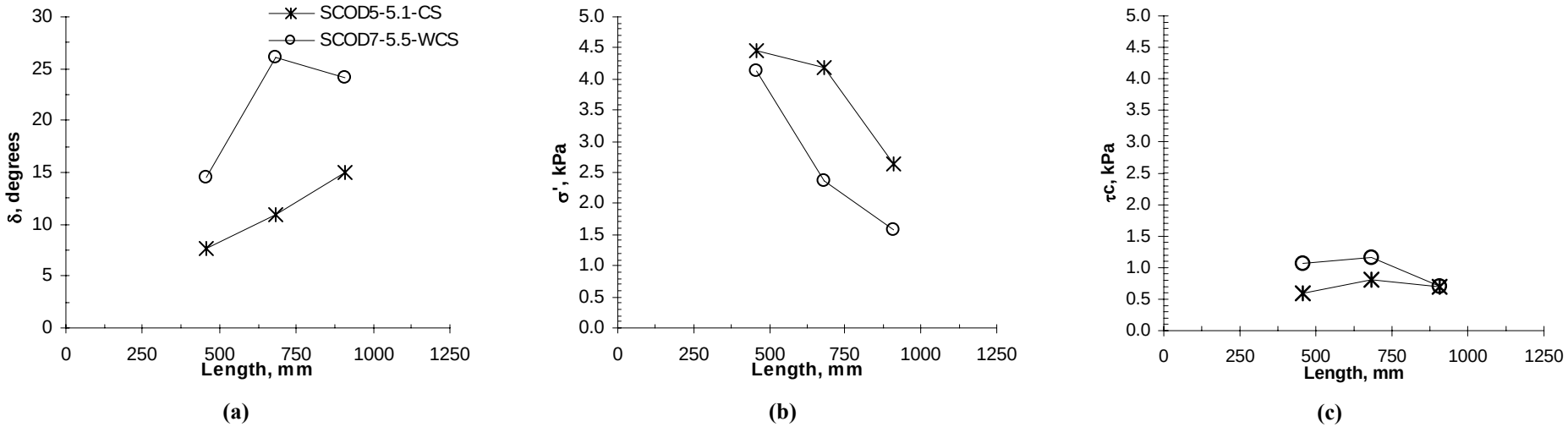

Figure 6.46. Screw type effect in conditioned L.B fine sand at 5 rpm and 73.9 kPa: (a) angle of friction (b) effective stress and (c) casing shear stress.

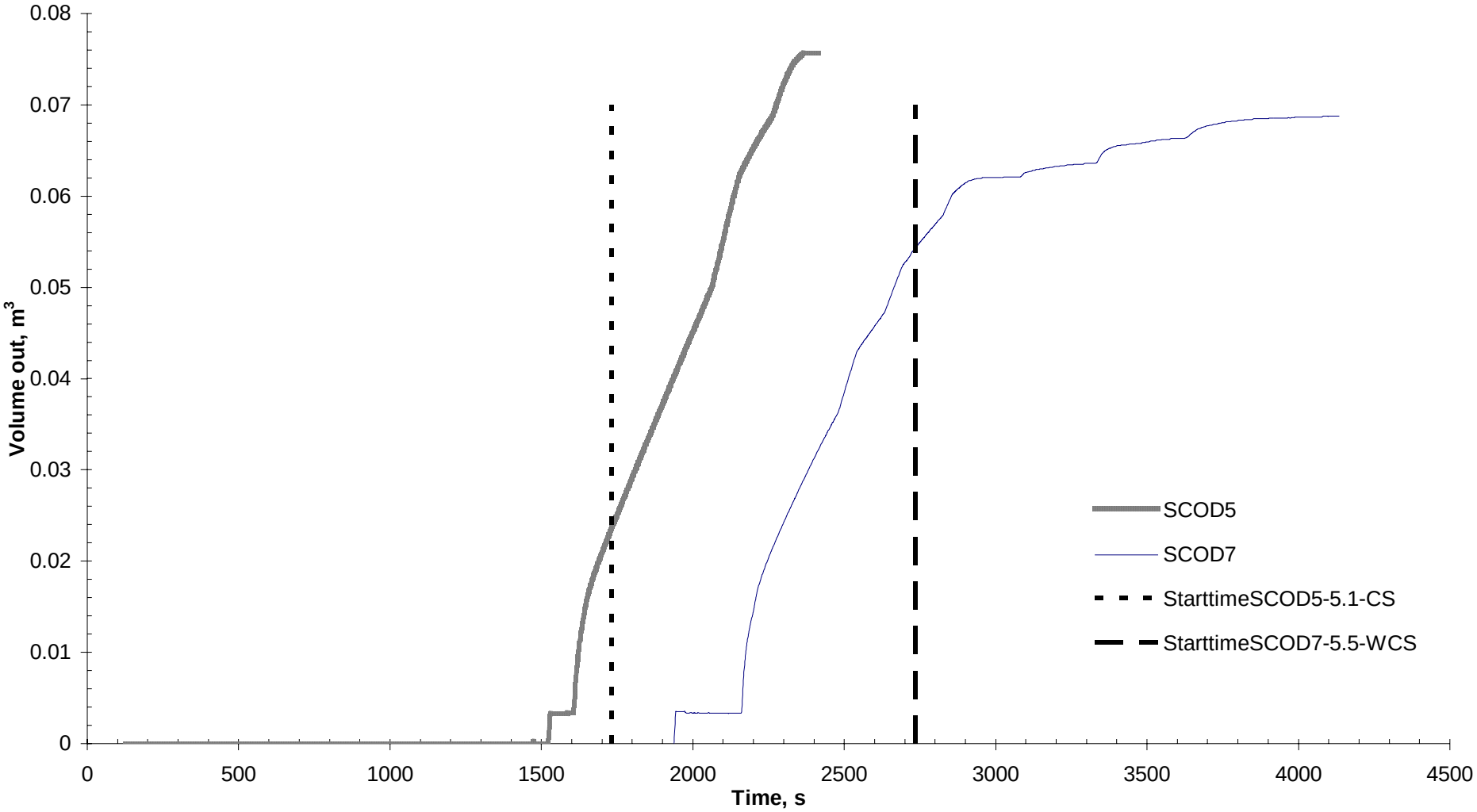

Figure 6.47. Volume of conditioned L.B soil out of tank:.

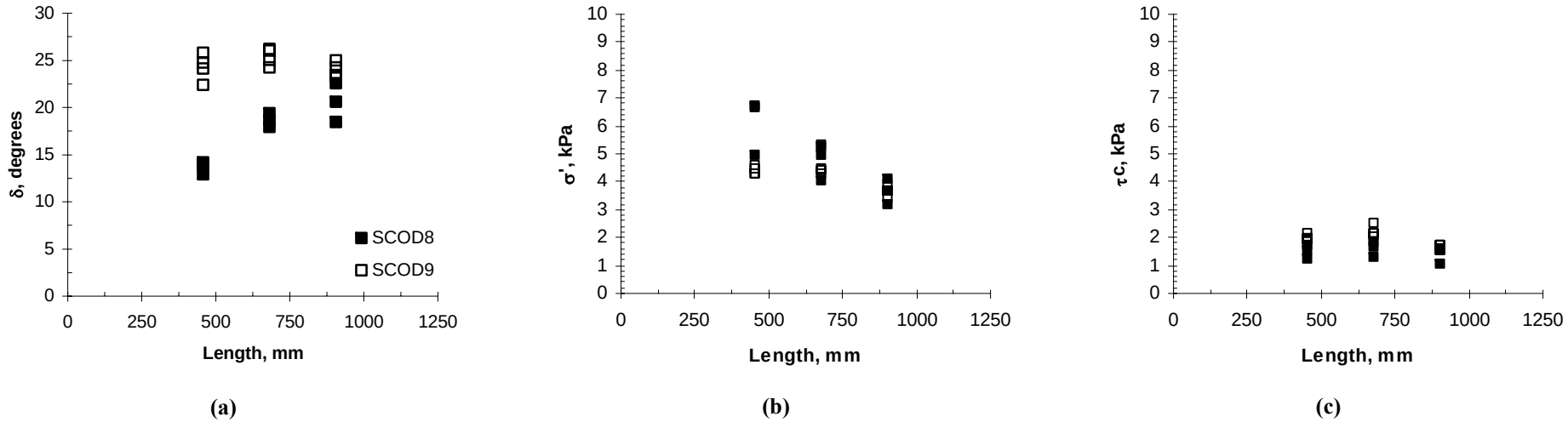

(a) (b) (c)

Figure 6.48. Pressure on top of the specimen effect in saturated Garside sand at 98.3 kPa and 147.1 kPa: (a) angle of friction (b) effective stress and (c) casing shear stress.

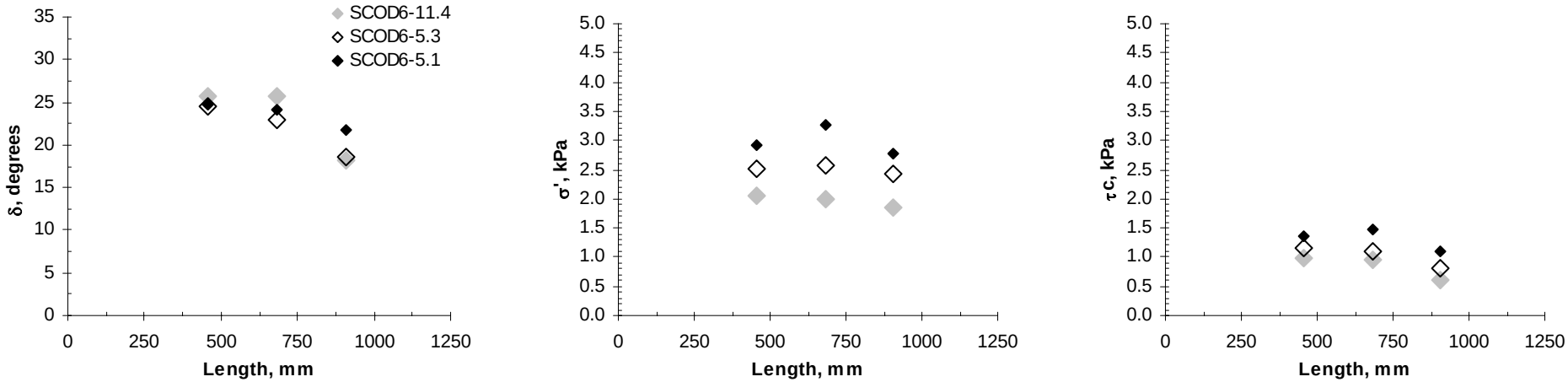

(a) (b) (c)

Figure 6.49. Effect of speed of motor. 5 rpm and 11 rpm for saturated L.B. fine sand at 73.9 kPa: (a) angle of friction (b) effective stress and (c) casing shear stress.

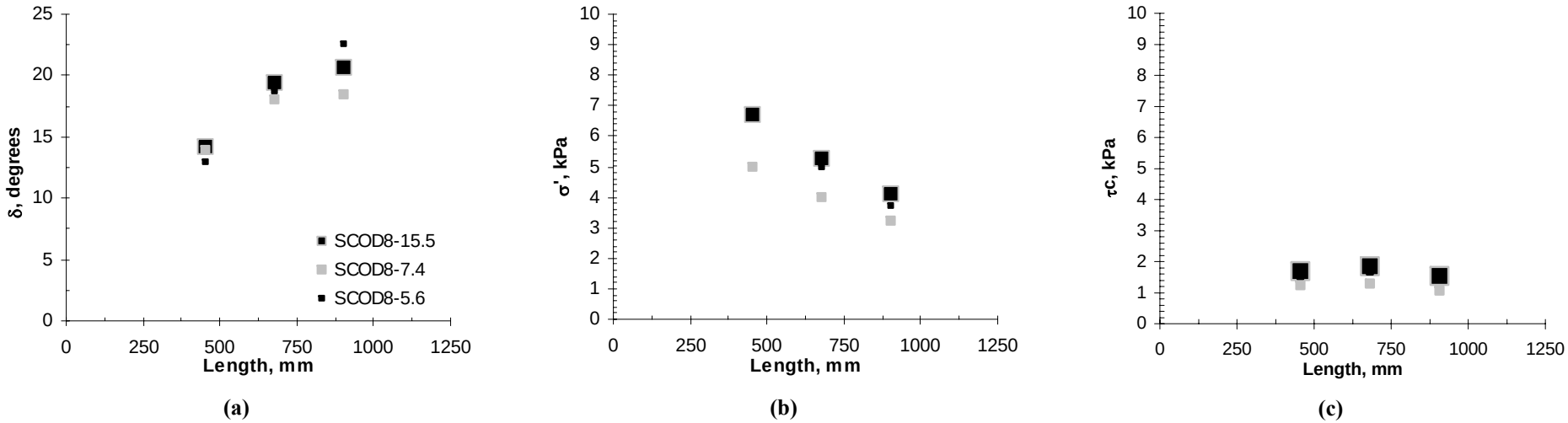

(a) (b) (c)

Figure 6.50. Effect of speed of motor. 5 rpm, 7 rpm and 15 rpm for saturated Garside sand at 98.3 kPa: (a) angle of friction (b) effective stress and (c) casing shear stress.

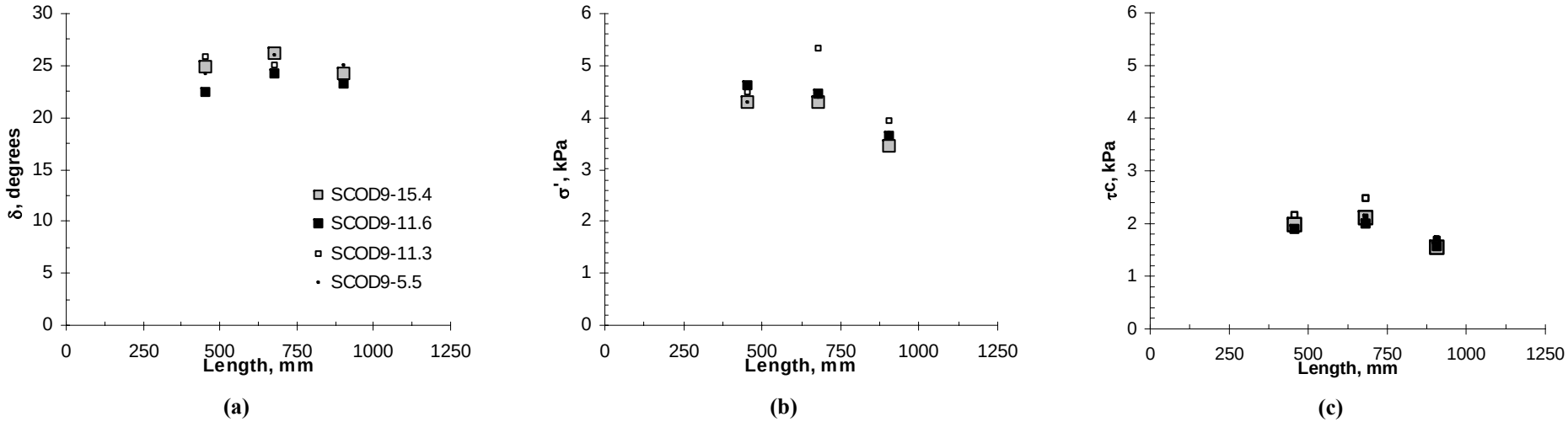

(a) (b) (c)

Figure 6.51. Effect of speed of motor. 5 rpm, 11 rpm and 15 rpm for saturated Garside sand at 147.1 kPa: (a) angle of friction (b) effective stress and (c) casing shear stress.

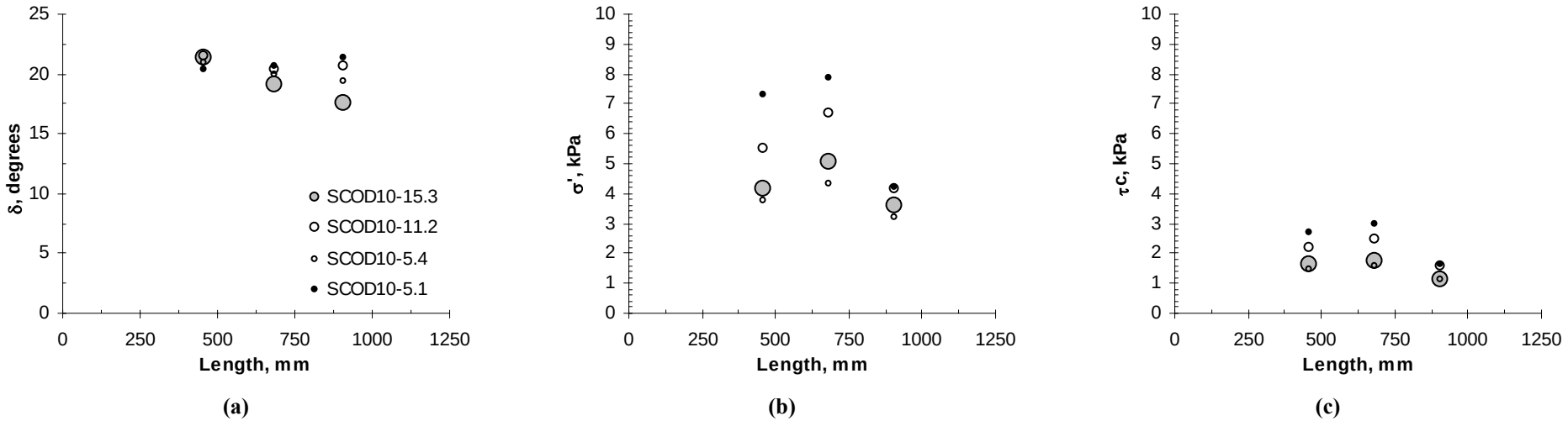

Figure 6.52. Effect of speed of motor. 5 rpm, 11 rpm and 15 rpm for conditioned Garside sand at 73.9 kPa: (a) angle of friction (b) effective stress and (c) casing shear stress.

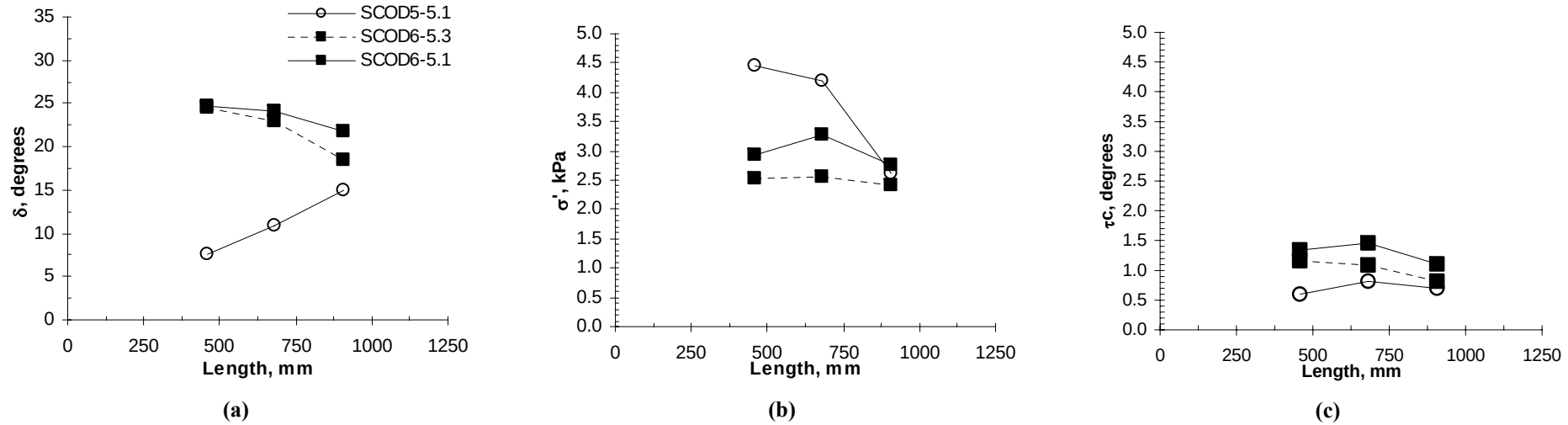

Figure 6.53. Effect of foam injection ratio (FIR). 5 rpm and gate A for L.B. fine sand at 73.9 kPa: (a) angle of friction (b) effective stress and (c) casing shear stress.

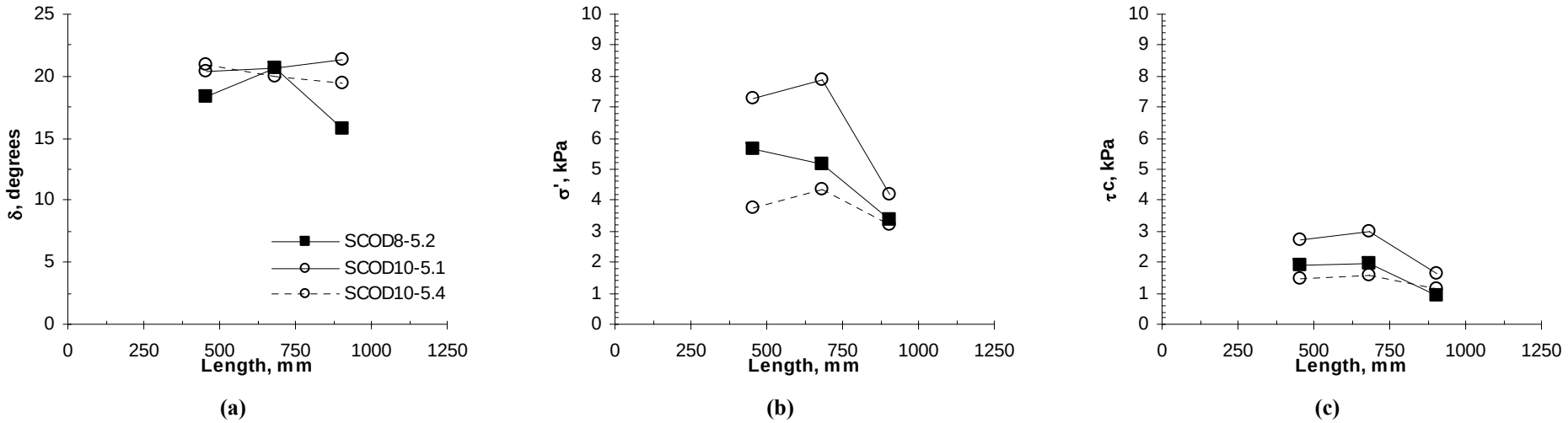

Figure 6.54. Effect of foam injection ratio (FIR). 5 rpm and gate A for Garside sand at 73.9 kPa: (a) angle of friction (b) effective stress and (c) casing shear stress.

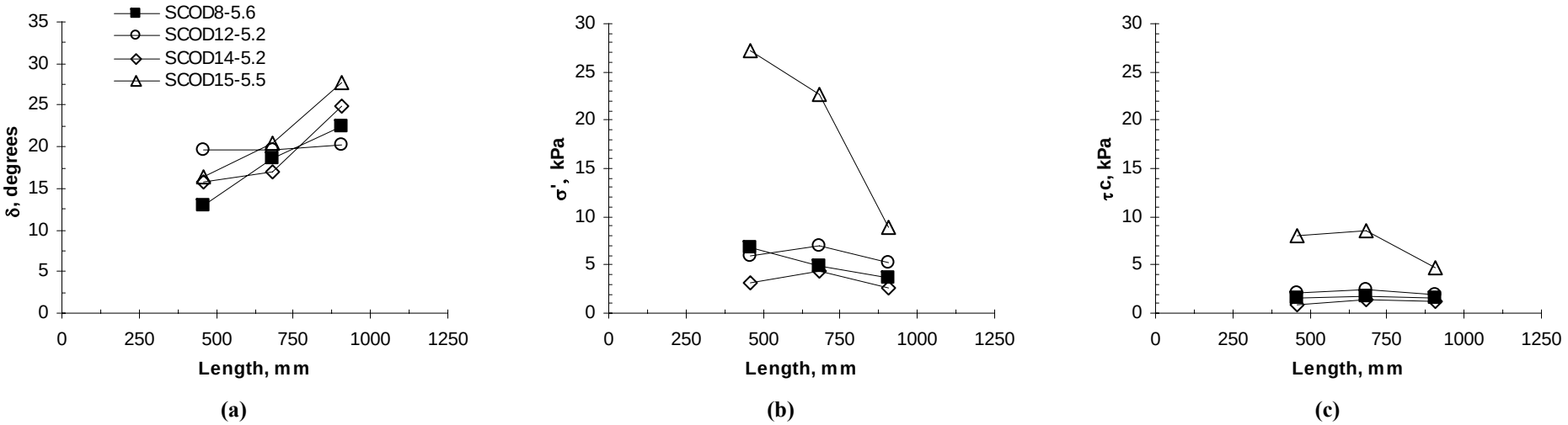

Figure 6.55. Effect of foam injection ratio (FIR). 5 rpm and gate A for Garside sand at 98.3 kPa: (a) angle of friction (b) effective stress and (c) casing shear stress.

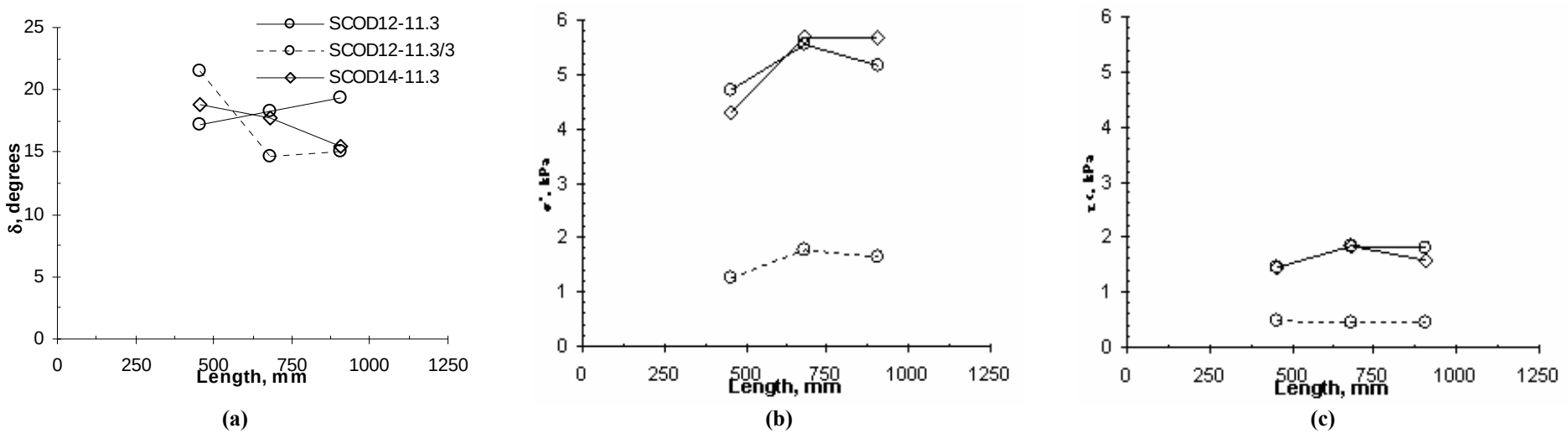

Figure 6.56. Effect of foam injection ratio (FIR). 11 rpm and gate A for Garside sand at 98.3 kPa: (a) angle of friction (b) effective stress and (c) casing shear stress.

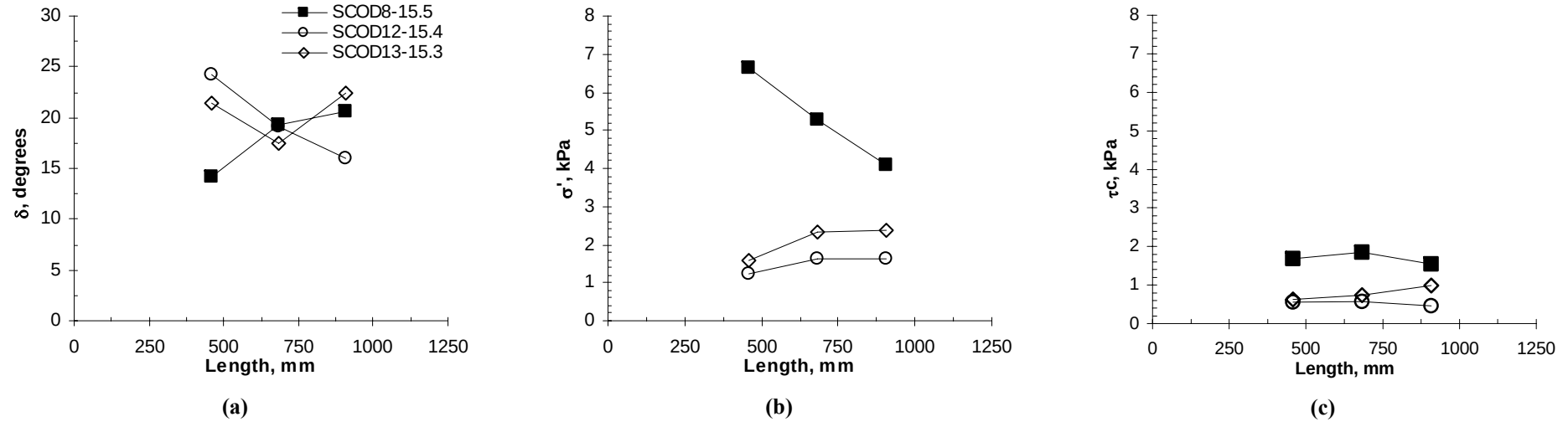

Figure 6.57. Effect of foam injection ratio (FIR). 15 rpm and gate A for Garside sand at 98.3 kPa: (a) angle of friction (b) effective stress and (c) casing shear stress.

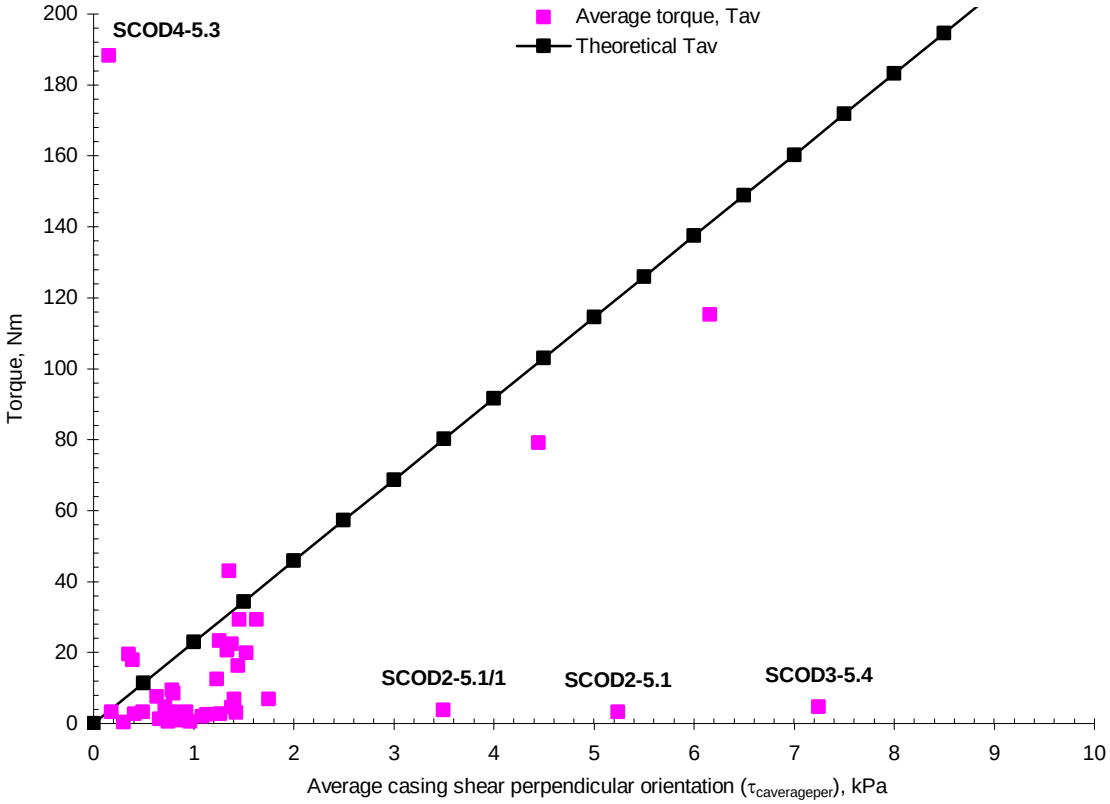

(a)

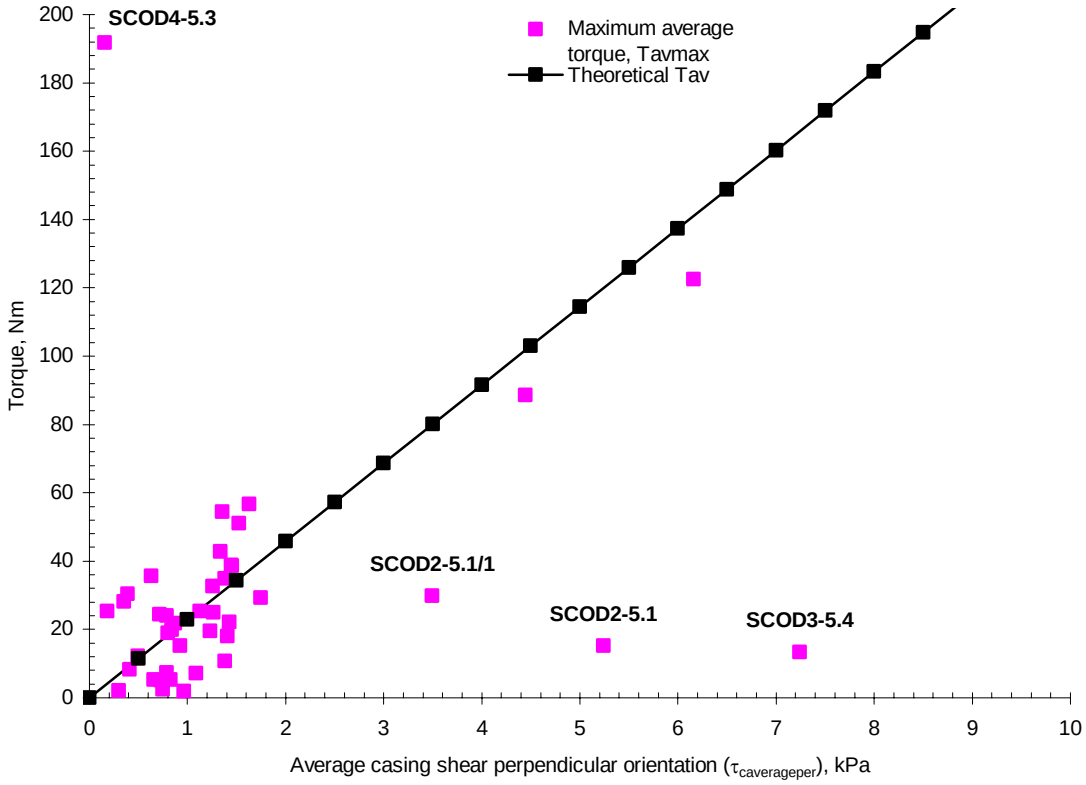

(b)

Figure 6.58. Torque recorded vs versus average casing shear perpendicular orientation, $\tau_{caverageper}$, for OSC tests: (a) average torque, Tav, (b) maximum average torque, T_{avmax}.

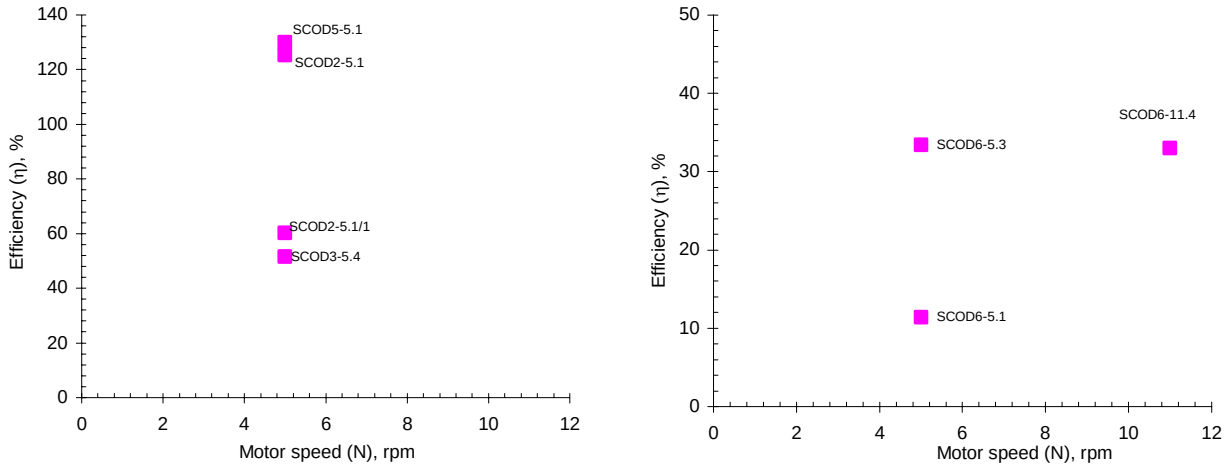

(a) Conditioned L.B. fine sand **(b) Saturated L.B. fine sand.**

Figure 6.59. Discharge efficiency vs motor speed for L.B. fine sand tests.

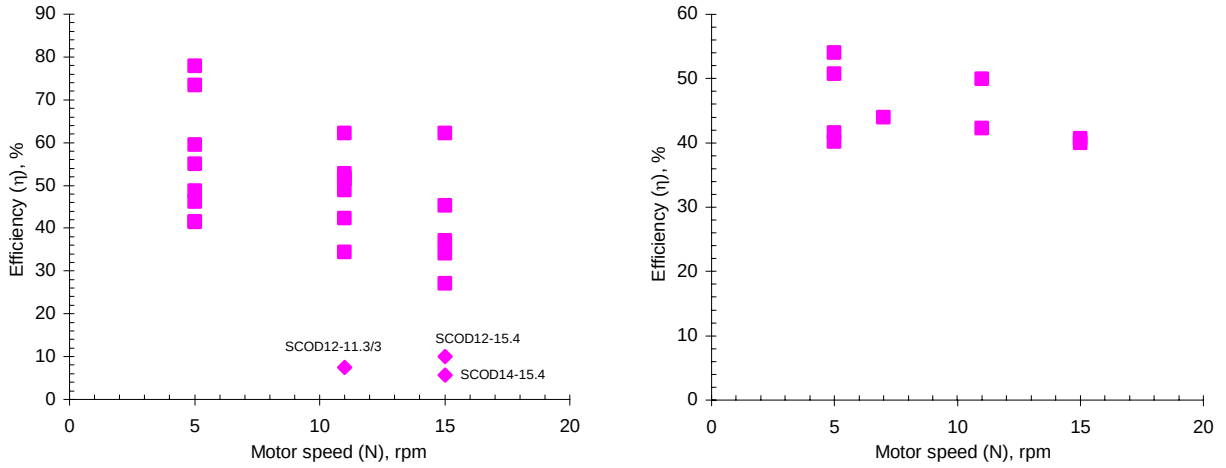

(a) Conditioned Garside sand **(b) Saturated Garside sand.**

Figure 6.60. Discharge efficiency vs motor speed for Garside sand tests.

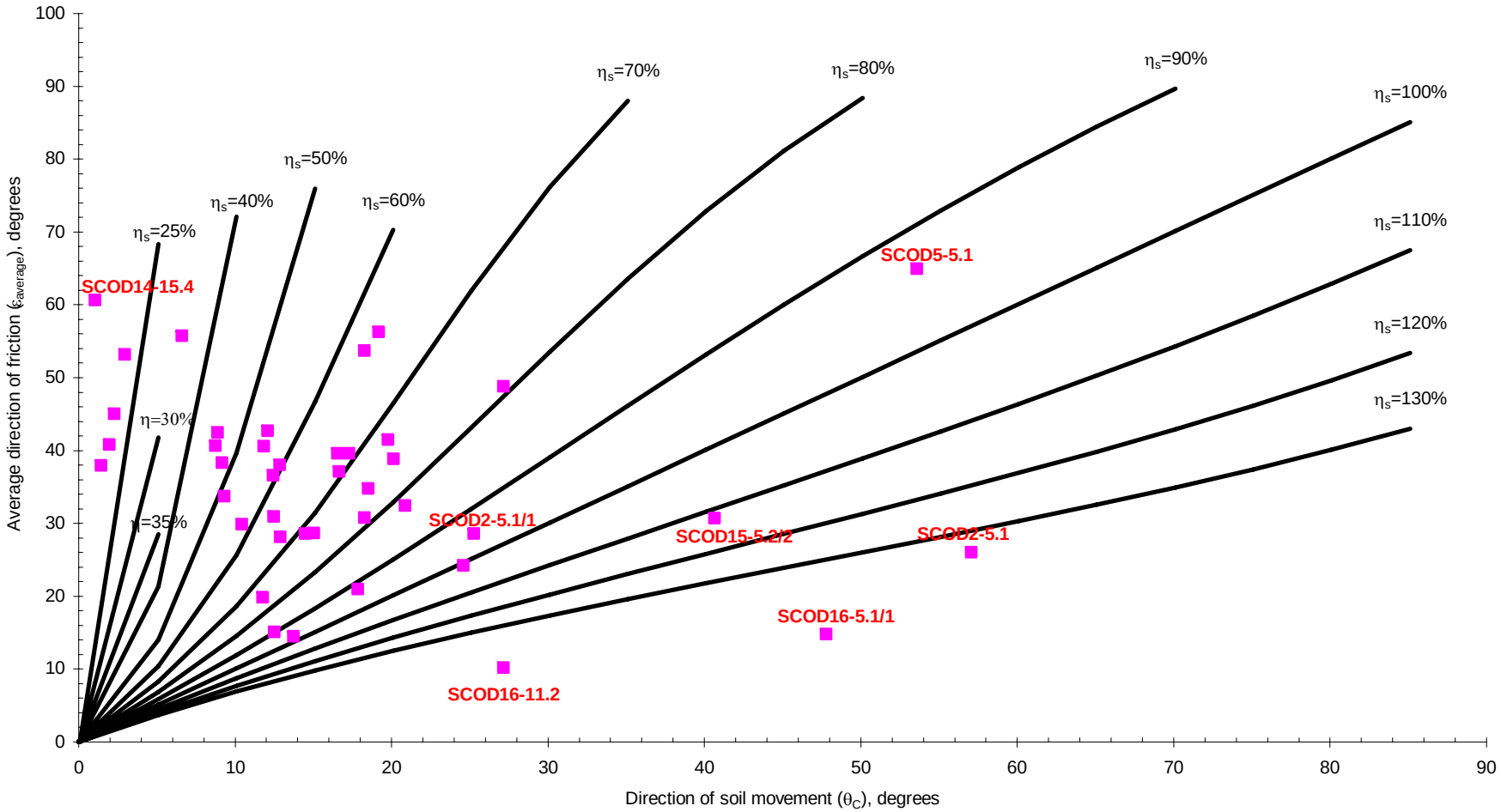

Figure 6.61. Average direction of friction vs direction of soil movement calculated for OSC tests.

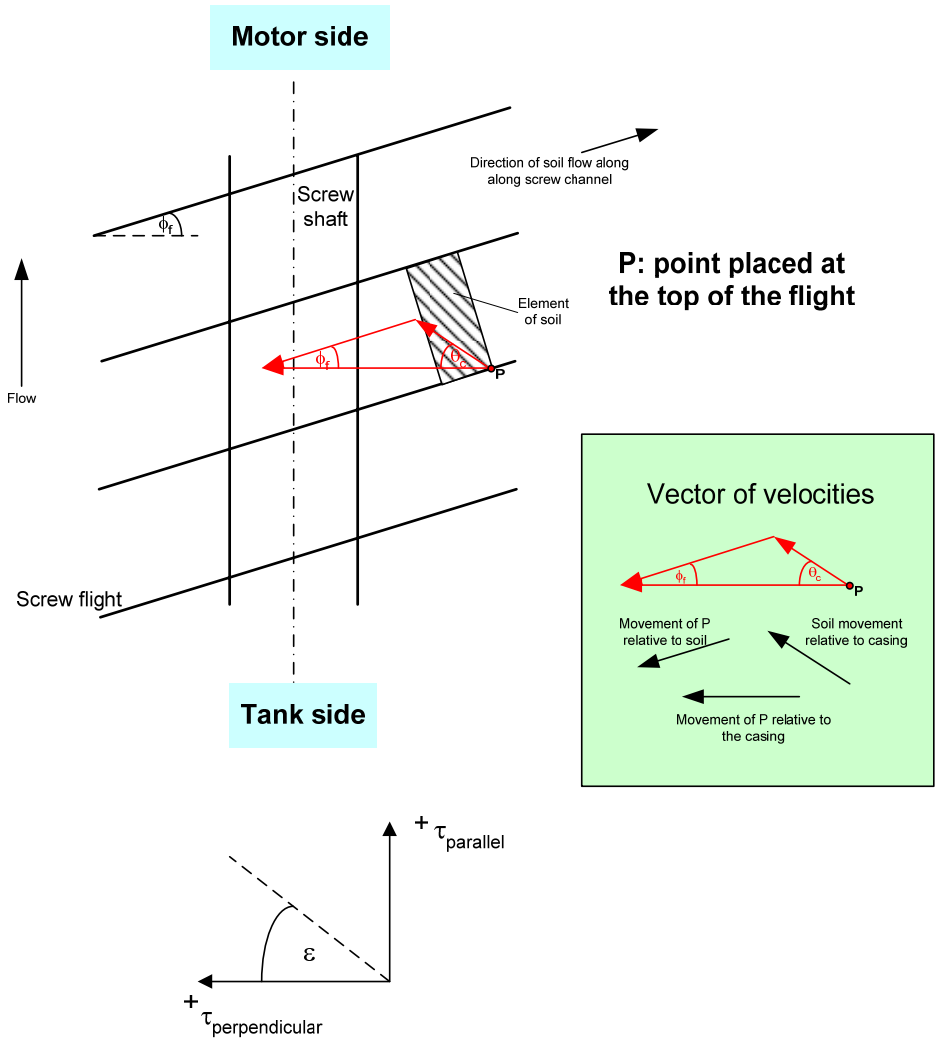

Figure 6.62. Movement of soil element along screw channel.

APPENDIX A

Correction of permeability of a porous layer backed by a perforated plate.

Dufrêche et al (2002) studied the flow of a fluid through a perforated plate. The apparent permeability of the porous layer was studied as a function of the thickness of the layer and as a function of the size and spacing of the performations in the plate. The apparent permeability is shown to be significantly lower than the intrinsic permeability of the porous layer when the layer is sufficiently thin.

Figure A.1 shows schematic illustration of the situation studied by Dufrêche et al (2002). They assumed that the average flow is perpendicular to the plate. As the stream lines in the porous medium must bend towards the discrete perforations in the wall, at least in the near wall region, the apparent permeability of the porous layer is lower than the intrinsic permeability.

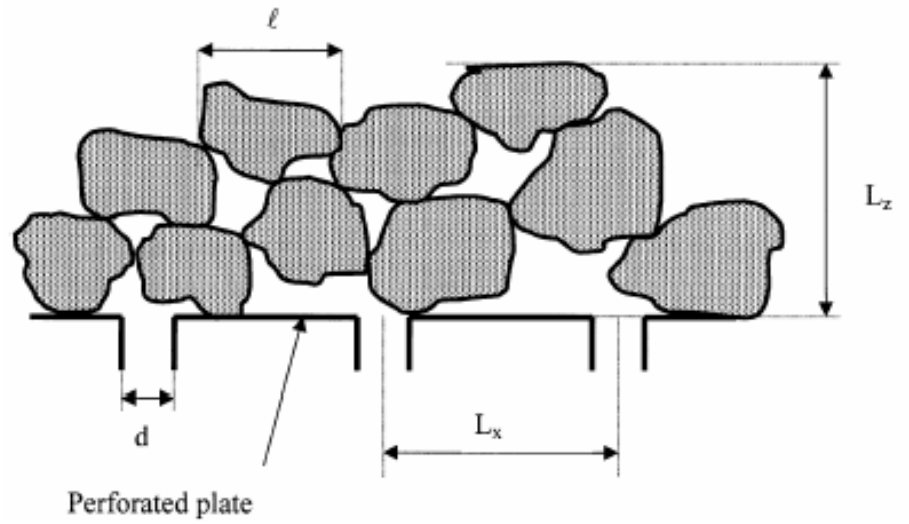

Figure A.1. Schematic illustration of the situation studied (Dufrêche et al, 2002)

In Figure A.1, L_z is the thickness of the porous layer, l is the size of the particles forming the layer, L_x is the average distance between two perforations in the plate and d is the size of the perforations. It was assumed that the porous layer is homogenous and isotropic thus it was ignored any variation of porosity near the plate.

Dufrêche et al (2002) define the following dimensionless numbers,

$$L_z' = \frac{L_z}{L_x} \qquad [A.1]$$

$$d' = \frac{d}{L_x} \qquad [A.2]$$

Where,
L_z': Dimensionless number of the length.

d': Dimensionless number of the diameter.

For thick layers ($L_z' \geq 0.5$) Dufrêche et al (2002) arrived at the following expression,

$$\frac{k_s}{k_i} = \frac{\pi * L_z'}{\pi * L_z' - \ln\left(\sin\left(d' * \frac{\pi}{2}\right)\right)} \qquad [A.2]$$

Where,

K_i: Intrinsic permeability of the porous medium.

K_s= Apparent permeability.

Table A.1 shows the different values that the ratio Ks/Ki can have for different values of L'_z and d'.

L'z	d'	sin(π*d'/2)	K_s/K_i
0.5	0.437	0.633	0.775
0.6	0.437	0.633	0.805
0.7	0.437	0.633	0.828
0.8	0.437	0.633	0.846
0.9	0.437	0.633	0.861
1	0.437	0.633	0.873
1.5	0.437	0.633	0.912
2	0.437	0.633	0.932
2.5	0.437	0.633	0.945
3	0.437	0.633	0.954
3.5	0.437	0.633	0.960
4	0.437	0.633	0.965
4.5	0.437	0.633	0.969
5	0.437	0.633	0.972
5.5	0.437	0.633	0.974
6	0.437	0.633	0.976
6.5	0.437	0.633	0.978
7	0.437	0.633	0.980
7.5	0.437	0.633	0.981
8	0.437	0.633	0.982
8.5	0.437	0.633	0.983
9	0.437	0.633	0.984
9.5	0.437	0.633	0.985
10	0.437	0.633	0.986

Table A.1. Dufrêche et al (2002) permeability ratio.